Experimental Analysis of an Actuator Disk under cyclic unsteady loading

M.Sc Thesis

Karanbir Kaur

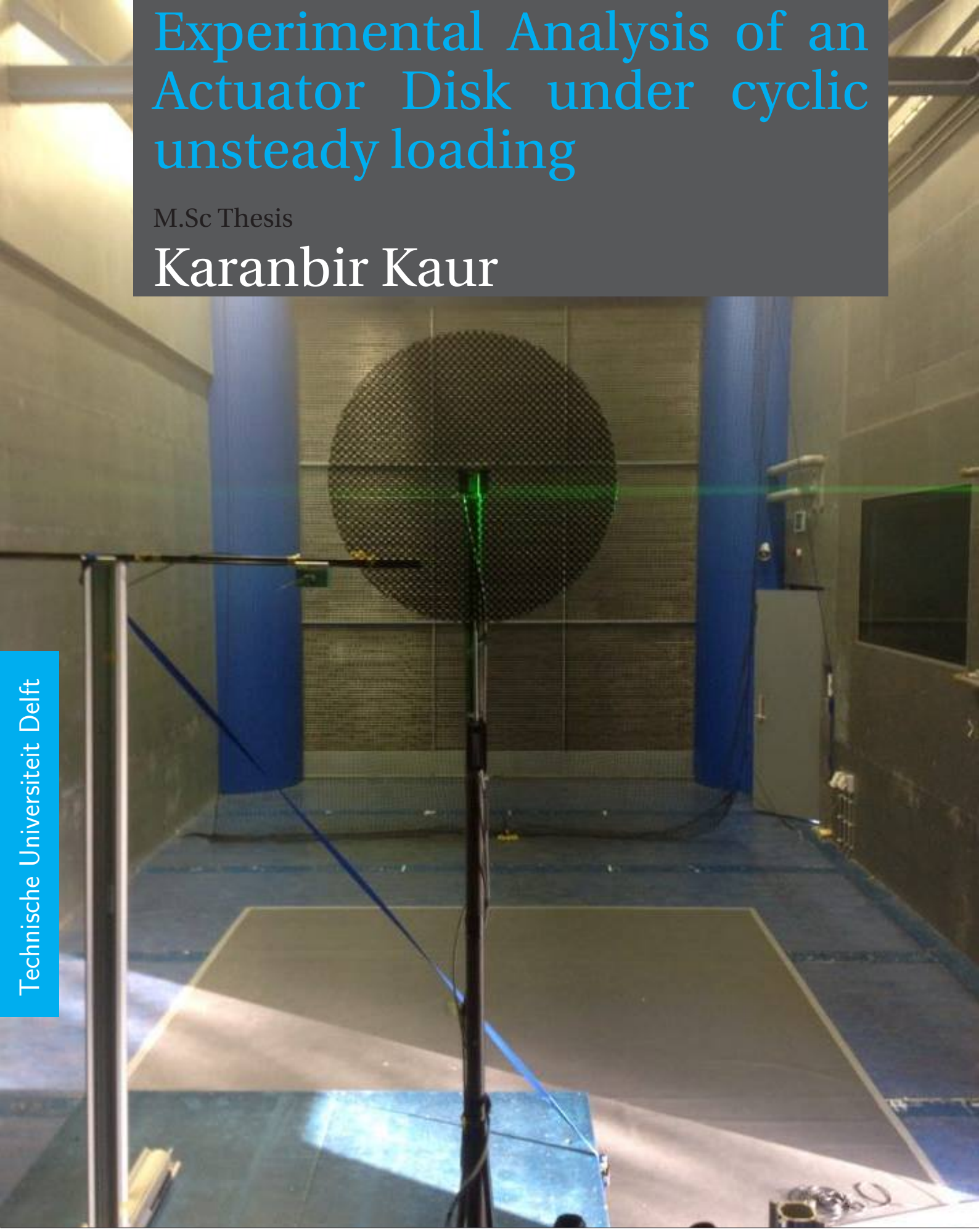

Technische Universiteit Delft

TU Delft Delft University of Technology

Challenge the future

Experimental Analysis of an Actuator Disk under Cyclic Unsteady Loading

M.Sc Thesis

by

Karanbir Kaur

to obtain the degree of

Master of Science
in Aerospace Engineering

at the Delft University of Technology,
to be defended publicly on Thursday, 6th July 2017 at 3:00 PM.

Student number:	4175018	
Project duration:	April 15th 2016 - July 6th 2017	
Supervisor:	Dr. ir. C. Simao Ferreira	
Thesis committee:	Dr. ir. C. Simao Ferreira,	TU Delft
	Dr,. D. Ragni,	TU Delft
	Dr. A. Sciacchitano,	TU Delft

TU Delft Delft University of Technology

ACKNOWLEDGEMENT

I would like to express my gratitude to everyone, without whom completion of this project was not possible. First of all, I would like to express my sincere gratitude to my supervisor, Dr.ir. Carlos J. S. Ferreira, who constantly supported and motivated me throughout the project. Without his guidance, it would not have been possible to realize this project.

I would also like to thank Dr. Daniele Ragni, who helped me a lot in processing of the data and was always ready to answer my questions. I am also grateful to Dr. Francesco Avallone, who guided me during the experiment and post-processing of data. I want to thank Wei Yu, Bruce LeBlanc and all the technicians at the TU Delft wind tunnel who helped me with the experiment. I would also like to thank my friend, Vasu, and my sister, Amtu, who helped me with editing of the report.

I would like to thank my friends and family. A special thank you to my parents, my siblings and my cousins. I am really grateful to my parents for having given me all the chances, especially my father. He taught me that hard work always pays off. A special appreciation goes to my mother and my sister for their unconditional support and encouragement throughout this project. I would like to take this opportunity to say thank you to my younger brother and a really good friend, Gurchetan, for just being there to uplift my mood and to motivate me.

Lastly, I would like to express my gratitude to all my previous teachers. They taught me the value of education and knowledge and always guided me towards the right path.

EXECUTIVE SUMMARY

Wind Energy is one of the cleanest forms of energy. It does not contribute to greenhouse gas emissions and is also one of the least expensive forms of renewable energy. Due to this, number of wind turbines are increasing annually. Therefore, it is crucial to understand the physics behind a wind turbine (WT) wake and how to optimize its power production. One of the most common tools used in designing a wind turbine is Blade Element Momentum theory (BEM), which is based on the classic momentum theory (or Actuator disc (AD) theory). In momentum theory, flow is assumed to be steady, stationary, incompressible and inviscid. But in reality, wind turbines operate in highly unsteady conditions such as gust, pitching, yawing, turbulence, etc. So, it is very important to study an actuator disc wake under unsteady loading.

Hong [1] studied a step-change in loading by taking an experimental approach. In this project, a similar method is used to study an actuator disc under cyclic unsteady load. A porous disc is used to simulate an actuator disc in the experiment. This disc's porosity ranges between 14%-65%. The disc porosity is modified sinusoidally to simulate the effect of cyclic loading. Data is acquired using both Particle Image Velocimetry and hot-wire in the open jet wind tunnel facility(OJF). Wake for steady loading is captured up to 1 rotor diameter downstream and 0.8 rotor diameters in radial direction. For unsteady load cases, data is collected up to 2 rotor diameters. For unsteady loading, three different reduced frequencies (k) are tested. The load on the disc is estimated using momentum integration of the flow field. Finally, the results from the experiment are compared to the velocity fields estimated using Vortex Ring (VR) model.

The results from the experiment for the steady loading are coherent with the results from previous work [1–6]. As porosity is increased, the loading on the disc decreases. Due to this, with lower porosity, wake expansion is smaller than that for the higher porosity cases. For higher loading on the disc, the velocity induction across the disc is also higher. The results from VR model are in good agreement with the experimental results, barring the regions just behind the disc and disc hub, where a difference of more than 100% of free-stream velocity is seen. This is because of the fact that the vorticity due to the disc porosity and the hub is not taken in to account in the VR model. The mesh of the disk causes vorticity discontinuity, which is seen in the experimental results but not in the results from VR model.

For unsteady loading on the disc, it is found that loading on the disc also forms a loop with sinusoidal change in porosity. Although the porosity cycle is same, the range of loading for the three cases is not exactly the same. However, it could be due to the uncertainty in the PIV measurements. It is noticed that for higher reduced frequencies, difference between the loading for the same porosity with different phase of the cycle is higher. The axial and radial velocity also forms a cycle with a small difference between the first and the last point, which could result from the small difference in the loading between the two measurements. For the same loading with different phase (increasing side of sinusoidal or decreasing), the velocity induction is different. It is also observed that wake expands and contracts for the cyclic loading on the disc. However, this behaviour of the wake varies for the different reduced frequency. For a higher reduced frequency, the wake expands and contracts more frequently. This is because of the different amount of wake expansion at the disc tip owing to the changing loading. For higher reduced frequency, the vorticity starts rolling up closer to

the disc. This could be interpreted as the 'new' and 'old' vortices packed closer due to fast changing porosity. Hence, due to difference in their velocities, they catch up to each other and roll-up. Similar to the steady loading, the results from VR model are similar to the experiment except in the regions behind the disc and hub.

CONTENTS

List of Figures

List of Tables

List of Symbols

Symbol	Explanation	Units
1D	One directional	[−]
a	Velocity Induction (AD Model)	[−]
A_1	Area of the wake (AD Model)	$[m^2]$
A_{cv}	Area of the contour field (AD Model)	$[m^2]$
A_{disc}	Are of the disc (AD Model)	$[m^2]$
A_k	Area of the ring (FWVR Model)	$[m^2]$
C_d	Drag coefficient	[−]
C_p	Pressure Coefficient	[−]
C_T	Thrust Coefficient	[−]
D	Disc Diameter	$[m]$
d_i	Height of the image (PIV)	$[m]$
d_o	Height of the object (PIV)	$[m]$
$E(m)$	Complete elliptical integrals of second kind (FWVR Model)	[−]
$\vec{f}$	Force per unit area	$[N/m^2]$
$\vec{F}$	Force	$[N]$
$\vec{F}_{visc}$	Force due to viscous effects	$[N]$
$f\#$	Camera-lens set-up	
Γ	Circulation	$[m^2/s]$
γ_{flux}	Flux term in Noca's method	
	Reduced frequency	[−]
k	Constant in (Stig Øye Model)	[−]
	Number of rings that actuator disc is divided into (Pitt Peters Model)	[−]
I	Identity Matrix	[−]
$K(m)$	Complete elliptical integrals of first kind (FWVR Model)	[−]
M	Magnification factor	[−]
$\dot{m}_{side}$	Rate of mass flowing out of contour (AD Model)	$[kg]$
$\vec{n}$	Normal vector	[−]

Symbol	Explanation	Units
N	Number of samples (PIV)	[−]
	Number of directions (Noca's method)	[−]
μ	Dynamic (shear) viscosity	$[Ns/m^2]$
ν	Kinematic viscosity	$[m^2/s]$
$\vec{\omega}$	Vorticity	$[1/s]$
ω	Circular Frequency	$[rad/s]$
P_0 or P_∞	Free-stream static pressure	$[Pa]$
r	Radial distance	$[m]$
ρ	Density	$[kg/m^3]$
ρ_p,ρ_f	Density of the seeding particle and the fluid (PIV)	$[kg/m^3]$
r_i	Radial position of the vortex ring (FWVR Model)	$[m]$
r_p	Radial position of the point where velocity needs to be calculated (FWVR Model)	$[m]$
t	Time	$[s]$
T	Temperature	$[^\circ C]$
	Stress Tensor (Noca's method)	$[Pa]$
τ	Viscous stress tensor	$[Pa]$
	Time scale associated with the dynamic inflow phenomenon	$[s]$
τ_1,τ_2	Constants (Stig Øye Model)	[−]
T_k	Thrust of the kth ring (Pitt Peters Model)	$[N]$
δt	Duration of the load unsteadiness	$[s]$
u_1	Axial velocity at the wake (AD Model)	$[m/s]$
u_i	Induced Velocity	$[m/s]$
V_0 or V_∞	Free-stream velocity	$[m/s]$
$V_{i,k}$	Induced velocity (Pitt Peters Model)	$[m/s]$
V_{int}	Intermediate value of induced velocity (Stig Øye Model)	$[m/s]$
V_{qs}	Quasi steady (Stig Øye Model)	$[m/s]$
$\varepsilon_{\Delta t}$	Uncertainty in time	$[s]$
$\varepsilon_{\Delta t}$	Uncertainty in velocity	$[m/s]$
$\varepsilon_{\Delta x}$	Uncertainty in axial distance	$[m]$
x	Axial distance	$[m]$
x_i	Axial position of the vortex ring (FWVR Model)	$[m]$
x_p	Axial position of the point where velocity needs to be calculated (FWVR Model) (AD Model)	$[m]$

Symbol	Explanation
AD	Actuator disc
BEM	Blade Element Momentum Theory
CFD	Computational Fluid Dynamics
CTA	Constant Temperature Anemometry
FWVR	Free Wake Vortex Ring
HAWT	Horizontal Axis Wind Turbine
HWA	Hot-wire Anemometry
LES	Large Eddy Simulation
MT	Momentum Theory
OJF	Open Jet Wind Tunnel
PIV	Particle Image Velocimetry
RANS	Reynolds-Averaged Navier Stokes
SPIV	Stereoscopic Particle Image Velocimetry
VR	Vortex Ring
WT	Wind turbine

1

INTRODUCTION

As population is increasing, demand for energy supply is growing exponentially. Due to this, there is an increased pressure on traditional sources of energy such as coal, natural gas, oil. etc. Since these sources are scarce and also not eco-friendly, there is a need for development of sustainable sources of energy. One of which is wind energy. Wind energy is one of the cleanest sources of energy and also one of the least expensive of the renewable sources of energy. Consequently, the number of wind turbines has also been increasing annually. It is estimated to increase by 22.6% in 2030 [23].

Wind turbines convert kinetic energy of the incoming flow into electricity. This results in momentum deficit in the flow causing velocity behind the wake to be lower than the free-stream conditions and increase in the turbulent intensity of the wake.[24] Wind turbines operate in groups known as wind farms. Depending on the spatial distance between the wind turbines, power extraction process of the downstream wind turbines is influenced by the wake losses caused by the upstream wind turbine. Along with the wake-induced turbulence, there is already existing ambient turbulence which also affects wind turbine performance. Depending on these factors, velocity field has been observed to take up to 40 rotor diameters behind the wind turbine to fully recover. [1] However, a general rule of thumb is to have at-least 10 rotor diameters of distance between wind turbines. Hence, wind turbines operate in the wake affected by the upstream wind turbine. Due to these dynamic inflow, wind turbines experience unsteady aerodynamic loadings. This results in an increased fatigue of wind turbines, affecting its lifetime and maintenance expenses. Thus, it is important to understand the physics of the wake of a wind turbine under such unsteady loads. In the following sections, overview of the project is discussed, which explains the basis of this research and aim of the project.

1.1. PROJECT OVERVIEW

Actuator disk models are commonly used to simulate a wind turbine and simplify numerical implementation of flow field behind a horizontal axis wind turbine (HAWT). Momentum theory (MT) on which the AD model is based on was first proposed by Froude in 1989. [25] It assumes an infinitely thin disc with uniform loading in an incompressible, steady, inviscid flow. However in reality, wind turbines operate in highly unsteady flows caused by many reasons such as rotor controls, turbulence, gust, wind shear, etc. There are mainly two types of models used to simulate these conditions: dynamic inflow engineering models and Computational fluid dynamics (CFD) models. The actuator disk model is based on the steady flow field assumption, so it does not represent the unsteady condition accurately. Currently, in order to overcome this limitation, dynamic inflow engineering models are used. These models use Blade Element momentum theory (BEM) in combination with

time-derivation parameters. These engineering models have been discussed in [26]. Other methods used to model unsteady load conditions are Free Wake Vortex Ring (FWVR) model and vortex tube model.

Yu *et al.* [27] used FWVR method to estimate the velocity field behind an actuator disk under unsteady loading namely, step-change and harmonic change in loading. The method is also compared to the basic momentum theory and two of the most commonly used dynamic inflow engineering models. The study was further continued by V. Hong in [1]. Here, actuator disk is modelled by a porous disk in an experiment and step change in the porosity is studied. Then the results from the experiment are used to validate Reynolds-averaged Navier–Stokes (RANS) model and engineering models by Pit-Peters [28] and Stig Øye [29]. In this project, the same porous disk model is used in a similar set-up to study the wake of an actuator disk under cyclic unsteady loading.

1.1.1. PROJECT OBJECTIVE AND APPROACH

Main Objective: In this M.Sc thesis project, steps are taken to further extend the research on using AD model to unsteady flows. The main research objective is to study the behaviour of near wake behind an actuator disk under cyclic unsteady loading. As learnt during the literature review, only a small number of studies have been dedicated to this research topic. In order to fulfil the objective, an experimental approach is taken. Particle Image Velocimetry (PIV) is used to acquire data in order to study the flow field behind the disk. As mentioned earlier, actuator disk is modelled using a porous disk. The porosity of the disk is used to change unsteadiness of the flow field. By doing so, unsteady effects can be simulated. Cyclic frequency of the load change is simulated by varying porosity in a sinusoidal way. This harmonic frequency was based on the reduced frequency $\left(k = \frac{\omega D}{2V_0}\right)$. For this experiment, k between 0.2 and 2 are used.

The approach taken to realize this objective is shown in Figure 1.1

1 First step is to review previous work related to this research topic. Works related to Actuator Disk theory, horizontal axis wind turbines(HAWT), dynamic inflow, engineering models, FWVR method, flow measurement techniques, load determination methods, etc. are reviewed.

2 Second step is to design an experiment to study cyclic unsteady loading over an actuator disk. For this purpose, porous disk model from [1] is used and porosity is varied sinusoidally to periodically change loading on the disk.

3 Third step is post-processing of the acquired data using `DaVis` to estimate flow field characteristics. Although load during the experiment is directly measured during the experiment using a load cell, load is required to be calculated using momentum integration of flow-field.

4 Fourth step is to validate Vortex Ring (VR) model. In order to do so, wake strength is quantified using experimental results and then axial and radial velocities are estimated using VR model.

5 Final step is to report all the results and conclusions drawn. Results from both steady and unsteady loadings are discussed.

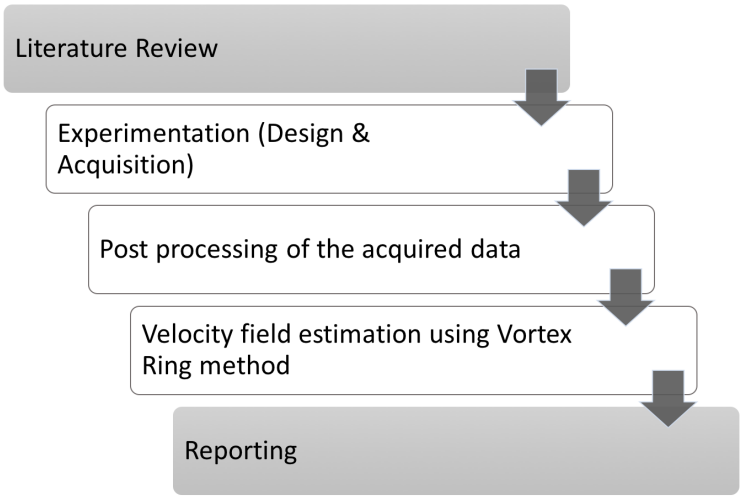

Figure 1.1: The approach taken to realize the objective

1.2. REPORT OUTLINE

The report can be structured into four main parts:

- **Introduction**: chapter 2 and chapter 3 explain the theory behind AD model and aerodynamics of wind turbine wake respectively.

- **Methodology**: In chapter 4, engineering models and vortex ring model are explained. Then the experimental set-up is explained in chapter 5.

- **Results and Discussion**: Results for steady loading on an actuator disk are presented and analysed in chapter 6. chapter 7 presents and discusses results for the unsteady loading on the disk. After this uncertainty in results is estimated in chapter 8.

- **Conclusion and Recommendations**: Finally, the report ends with conclusion from all the results and recommendations for further research in chapter 9.

- **Appendices**: The flow measurement techniques used in the experiment are explained in Appendix A and Appendix B. Followed by method on estimating load from flow field in Appendix C. Pressure fields for unsteady loading on the disk are presented in Appendix D. Then some extra velocity plots related to the unsteady load cases are presented in Appendix E.

2

ACTUATOR DISC MODEL

Actuator disc (AD) model is a well-accepted model to simulate wind turbines in many numerical codes. It simplifies the simulations and avoid scaling issues such as unrealistic swirls caused by scaling down of a wind turbine with same rotational speed as that of an actual wind turbine. In previous works such as [31],[32],[29],[33],[4],[5],[6],[34], it has been extensively studied for steady loading and wake of WT and AD are compared. The AD model is based on the 1D momentum theory. In this chapter, theory behind this model is reviewed. At first, the 1D momentum theory is discussed and then relevance and limitations of the AD model are studied.

2.1. THEORY

The Actuator disc model is based on the 1D momentum theory, which is base of the Blade Element Momentum (BEM) theory. The model assumes a hypothetical thin disc. This disc acts as a drag device by creating a pressure drop across it. The disc here is not a physical disc, but a hypothetical one which is represented by a momentum sink.[1] As shown in Figure 2.1, it slows down the free-stream velocity to u. Then velocity is assumed to to decrease to u_1 before recovering back to V_0. These wake development phenomena are shown in Figure 2.1. [7]

The figure shows that free-stream pressure, p_0, increases to value p just before the disc, and drops by Δp after the disc and then starts recovering back to free-stream conditions. The momentum exchange of the disc and the wind turbine being modelled should be same, thereby the thrust coefficient of the wind turbine and the disc should also be same. [7] Power generated can be found using application of mass, momentum and energy conservation to the control volume shown in Figure 2.2 (All the equations in this chapter are derived based on [7])

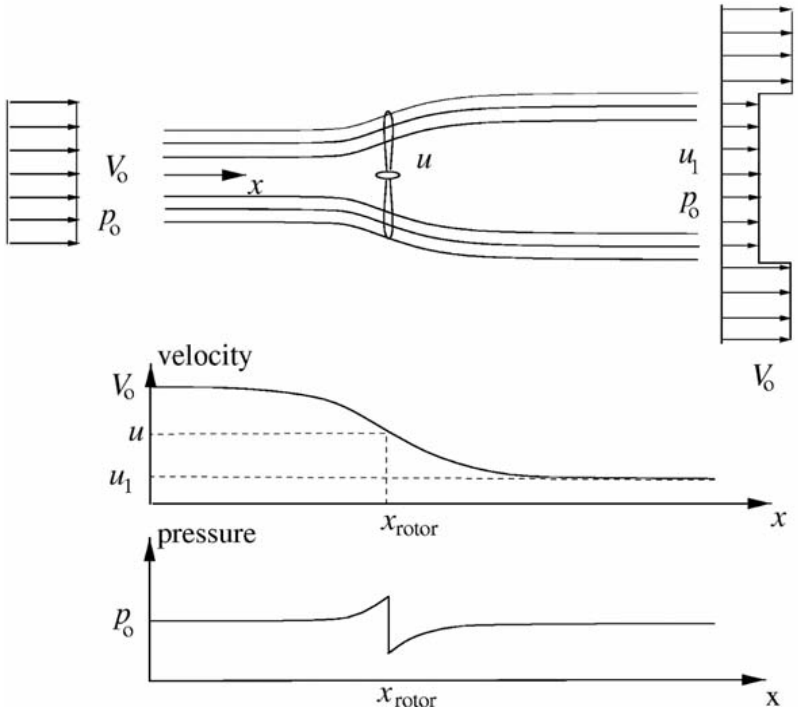

Figure 2.1: Schematic of streamlines past a rotor along with axial velocity and pressure profiles across it [7]

2.1.1. MODEL WITHOUT ROTATION

Assumptions: 1D momentum theory is derived by application of conservation laws, which are simplified by making following assumptions:

- Ideal Disc: Actuator disc is assumed to be an ideal disc which is friction-less and there is no rotational velocity component.[7]
- Incompressible, friction-less flow and no external forces act on the flow: The operating tip speed of a wind turbine is usually 80m/s, which results in Mach number of 0.3, therefore flow can be assumed to be incompressible. [7]
- Inviscid: Flow is assumed to be inviscid, however in reality this is not true. [7]
- One Dimensional: This also does not have to be true, as wind turbines operate in yawed conditions due to different wind directions and wake meandering from upstream wind turbines.[7]
- Uniforms loading : As the disc is assumed to be a turbine with infinite number of blades, it is assumed that loads act uniformly on the disc.[7]
- Stationary Conditions: It is assumed that the flow in the wake adapts to any changes in the incoming flow or in the loads instantaneously. [14]

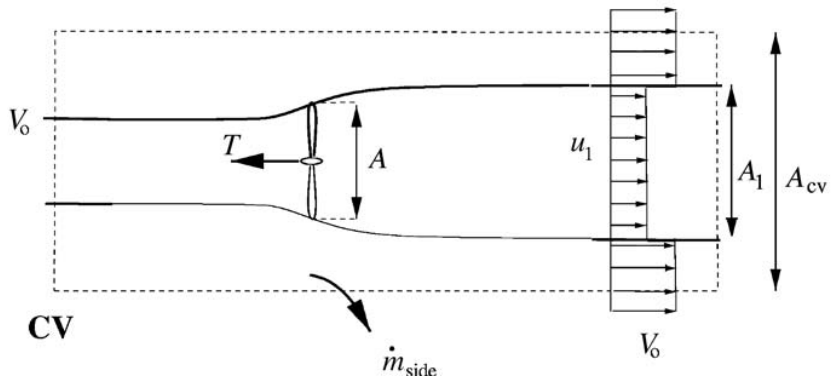

Figure 2.2: Control volume around a wind turbine schematic [7]

Figure 2.2 shows an actuator disc control volume. (In this chapter, V_0 represents the free-stream velocity, u is the velocity at the disc and u_1 is the velocity infinitely far downstream of the rotor.) By application of conservation of mass to the closed volume, Equation 2.1-Equation 2.3 can be derived.

$$\rho \cdot V_0 \cdot A_{cv} = \rho \cdot u_1 \cdot A_1 + \rho \cdot V_0 \cdot (A_{cv} - A_1) + \dot{m}_{side} \tag{2.1}$$

where ρ represents density, V_0 is the free-stream velocity, A_{cv} is the area of the control volume, A_1 is the area of the expanded wake as shown in Figure 2.2, u_1 is the wake velocity and $\dot{m}_{side}$ is the mass flow.

$$\dot{m}_{side} = \rho \cdot A_1 \cdot (V_0 - u_1) \tag{2.2}$$

$$\dot{m} = \rho \cdot A_1 \cdot u_1 \tag{2.3}$$

Equation 2.4-Equation 2.8 is derived by applying of conservation of momentum to the closed volume:

As the total momentum is conserved in a flow. Therefore:

$$\rho \cdot {V_0}^2 \cdot A_{cv} = \rho \cdot {u_1}^2 \cdot A_1 + \rho \cdot {V_0}^2 \cdot (A_{cv} - A_1) + \dot{m}_{side} \cdot V_0 + T \tag{2.4}$$

$$\rho \cdot {V_0}^2 \cdot A_{cv} = \rho \cdot {u_1}^2 \cdot A_1 + \rho \cdot {V_0}^2 \cdot (A_{cv} - A_1) + \rho \cdot A_1 \cdot (V_0 - u_1) \cdot V_0 + T \tag{2.5}$$

Using Equation 2.2 and Equation 2.5, thrust equation can be derived in terms of free-stream velocity and wake velocity. This equation shows that the momentum loss at the disc depends on the thrust. [7]

$$T = \dot{m}\,(V_0 - u_1) \tag{2.6}$$

It is assumed that the flow is friction-less and no change in internal energy takes place, and by applying integral form of energy equation to the control volume, power is found to be as shown in Equation 2.7 [7]:

$$P = \dot{m}\left(\frac{1}{2}V_0^2 + \frac{p_0}{\rho} - \frac{1}{2}u_1^2 - \frac{p_0}{\rho}\right) \tag{2.7}$$

Using conservation of mass $m = \rho \cdot A \cdot u$, Equation 2.7 can be written as:

$$P = \frac{1}{2}\rho u A_{cv}\left({V_0}^2 - {u_1}^2\right) \tag{2.8}$$

Although there is no change in internal energy, but there is discontinuity at the disc as kinetic energy is converted into mechanical energy, therefore Bernoulli's equation is applied in two sections.

The first section is from far upstream (where pressure is p_0) till just before the rotor (where pressure is p) as shown in Figure 2.1.

$$p_0 + \frac{1}{2}\cdot\rho\cdot{V_0}^2 = p + \frac{1}{2}\cdot\rho\cdot u^2 \tag{2.9}$$

Then Bernoulli's equation is applied from just after the disc (where pressure is $p + \Delta p$) till downstream of the rotor [1],[9],[7]:

$$(p - \Delta p) + \frac{1}{2}\cdot\rho\cdot u^2 = p_0 + \frac{1}{2}\cdot\rho\cdot {u_1}^2 \tag{2.10}$$

Using Equation 2.9 and Equation 2.10, jump in pressure can be defined as:

$$\Rightarrow \Delta p = \frac{1}{2}\cdot\rho\cdot({V_0}^2 - {u_1}^2) \tag{2.11}$$

Thrust can be defined in terms of pressure and also by equation Equation 2.6:

$$\Rightarrow T = \Delta p \cdot A = \dot{m}_{side}\cdot(V_0 - u_1) \tag{2.12}$$

Therefore thrust is given by:

$$\rho\frac{1}{2}\left({V_0}^2 - u_1^2\right)A_{disc} = \dot{m}_{side}\cdot(V_0 - u_1) \tag{2.13}$$

Hence:

$$\rho\frac{1}{2}\left({V_0}^2 - u_1^2\right)A_{disc} = \rho u_1 A_1 (V_0 - u_1) \tag{2.14}$$

Using equation Equation 2.3:

$$\rho\frac{1}{2}\left({V_0}^2 - u_1^2\right)A_{disc} = \rho u A_{disc} (V_0 - u_1) \tag{2.15}$$

By rearranging Equation 2.15, equation of velocity (u) at the rotor can be derived as:

$$u = \frac{1}{2}(V_0 + u_1) \tag{2.16}$$

As shown by the equation, velocity at the disc is mean of velocities far upstream and downstream of rotor.

Upon deriving thrust, power and velocity at the rotor in terms of free-stream velocity and u_1„ i.e., velocity induction at the disc can be defined [1],[9],[7]:

$$u = (1-a)\cdot V_0 \tag{2.17}$$

where a is the induction factor and it can also be defined as:

$$u_1 = (1-2a)\cdot V_0 \tag{2.18}$$

Now thrust and power coefficients can be written in terms of induction factor:

$$T = 2\cdot\rho\cdot {V_0}^2\cdot a\cdot(1-a)\cdot A \tag{2.19}$$

$$C_T = T\left(\frac{1}{2}\cdot\rho\cdot A\cdot {V_0}^2\right) = 4\cdot a\cdot(1-a) \tag{2.20}$$

Hence, with increase in C_T, wake expansion and velocity jump over the disc will also increase. The ratio of wake expansion can be derived using continuity equation: $\frac{A_0}{A_1} = 1-2a$. [7]

$$P = 2\cdot\rho\cdot {V_0}^3\cdot a\cdot(1-a)^2\cdot A \tag{2.21}$$

$$C_P = P\left(\frac{1}{2}\cdot\rho\cdot A\cdot {V_0}^3\right) = 4\cdot a\cdot(1-a)^2 \tag{2.22}$$

Figure Figure 2.3 shows thrust and pressure coefficient as function of induction factor. From the curve for pressure coefficient it can be seen that there is a limit on the maximum power coefficient. This limit is called 'Betz limit', and is equal to 16/27 which occurs at a = 1/3. The actuator disc model assumes ideal disc, therefore no wind turbine can surpass this limit of maximum pressure coefficient.

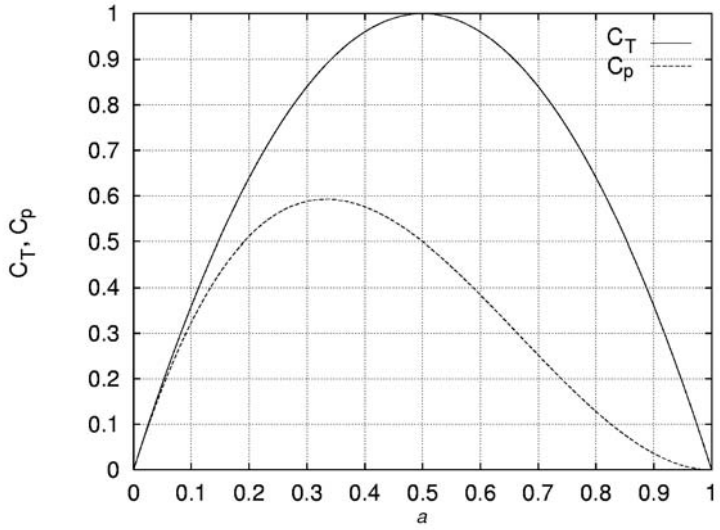

Figure 2.3: C_P and C_T as a function of the axial induction factor a for an ideal HAWT [7]

2.2. LIMITATIONS AND RELEVANCE

- Incompressible and inviscid flow : As mentioned before, AD model assumes that the flow is incompressible and inviscid. In order to correct for incompressibility, either corrections such as Prandtl-Glauert correction or airfoil characteristics for actual Mach number can be applied. But usually these are neglected, as the tip speed is generally less than 80m/s (Mach number of around 0.25). [14]

  Although the viscous effects are taken into account in the Blade-element momentum (BEM) theory in terms of drag, they are neglected in the momentum theory. This is one of the reasons why power generated by a wind turbine will always be less than 'Bletz Limit'.[14]

  The momentum theory assumes a simplified stream-tube concept, therefore the viscous effects are neglected. In the momentum theory, there is a discontinuity in the velocity and pressure at the edge of the disc. However generally, momentum theory is applied to annular rings over the disc, and therefore allowing for some radial variation in the flow over the disc plane.[14] From experiment in the Mexico project (Schepers (ECN) [14]), it is found that in the near wake, stream-tube concept is followed well.

- Actuator Disc model: A hypothetical 'actuator disc' concept is used in the momentum theory to model a wind turbine. In momentum theory, the disc is assumed to be uniform loaded. However in reality, the loading is non-uniform. For this purpose, in BEM, Prandtl tip loss correction is applied.[14]

- Turbulent wake state: Experiments have shown that due to the assumption of ideal flow conditions, model is only valid for induction factor less than 0.5. If induction factor is higher than 0.5, velocity in the wake becomes negative, as shown by Equation 2.18. This is physically not possible as this will result in stationary mass of fluid.[7]

  Based on the momentum theory, the flow becomes stationary or moves backwards if induction factor is higher than 0.5. However, in reality 'turbulent wake state' is formed in the flow. This flow condition is shown in Figure 2.4. For high loadings, i.e., for high thrust coefficient, axial induction factor is high even at low wind speeds. If induction factor is higher than 0.5, this results in an unstable shear layer at the wake edge because of large difference in free-stream velocity and wake velocity. Due to this turbulent eddies form in the wake, which aid in momentum mixing from outside the wake into inside. [7],[14]

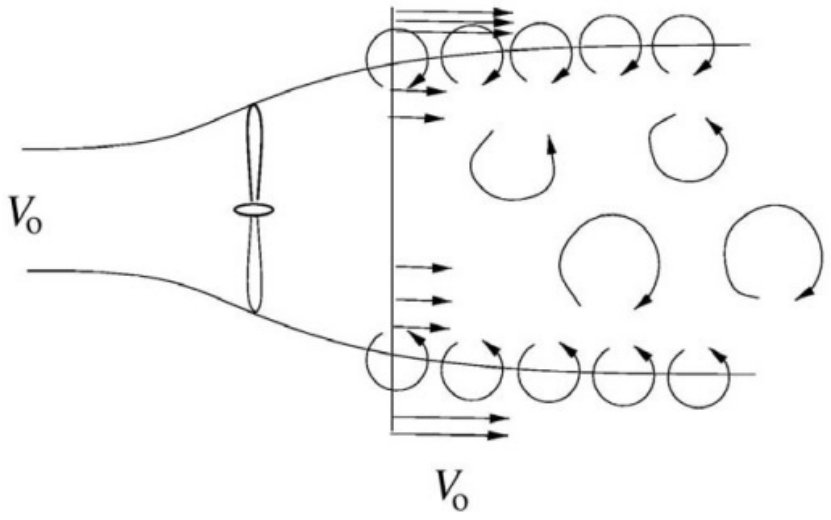

Figure 2.4: Turbulent wake state created due to unstable shear layer near the edge of wake [7]

- Another drawback of simple momentum theory is that it assumes no rotation in wake, which is not true. Even a single rotor turbine possesses some rotation hence an azimuthal induction is required. [7]
- Stationary conditions: One of the reasons for wind turbines operating under unsteady conditions is unsteady aerodynamics due to flow around airfoil which is not taken into account in the AD model. Unsteady aerodynamics occurs at time scale of $\frac{c}{V_0}$. For wind turbines, dynamic stall plays an important role which results in unsteady loads on the rotor.[14]

  Another condition with causes unsteady conditions is dynamic inflow. Dynamics inflow is mainly defined as the lag caused in velocity due to sudden change in loads on the turbine. This concept is discussed in detail in chapter 4

- Annular independence and axisymmetric: The fact that the momentum theory assumes streamtube, which is divided into independent annular rings, makes the flow axisymmetric. However according to Sørensen and van Kuik [35], there is a large radial gradient in pressure which violates this assumption. This assumption is also violated due to finite number of blades, wind shear and yaw effects.[14]

2.3. CHANGE OF VORTICITY WITH LOAD

Vorticity is a vector that describes the local rotation of fluid at a point in the flow. This means that the fluid particle needs to be rotating about its centre of mass to have non-zero vorticity. Mathematical definition of vorticity is given by curl of velocity.

VORTICITY TRANSPORT EQUATION

Unsteady momentum equation for an actuator disc is given by Equation 2.23:

$$\rho \frac{D\vec{V}}{Dt} = -\nabla p + \vec{f} + \mu \nabla^2 \vec{V} \tag{2.23}$$

where ρ is the density, $\vec{V}$ is the velocity vector, p is the pressure, f is the body force and μ is kinematic viscosity.

The Equation 2.23 can also be written as Equation 2.24:

$$\rho\frac{\partial\vec{V}}{\partial t}+\rho\left(\vec{V}\cdot\nabla\vec{V}\right)=-\nabla p+\vec{f}+\upsilon\nabla^2\vec{V} \tag{2.24}$$

Taking the curl of equation Equation 2.24:

$$\nabla\times\left(\rho\frac{\partial\vec{V}}{\partial t}+\rho\left(\vec{V}\cdot\nabla\vec{V}\right)\right)=\nabla\times-\nabla p+\nabla\times\vec{f}+\nabla\times\left(\mu\nabla^2\vec{V}\right) \tag{2.25}$$

Representing the curl of rate of velocity change in terms of vorticity as shown by equation Equation 2.26:

$$\nabla\times\left(\rho\frac{\partial\vec{V}}{\partial t}\right)=\rho\frac{\partial\vec{\omega}}{\partial t} \tag{2.26}$$

Substituting Equation 2.26 into Equation 2.25 gives equation Equation 2.27:

$$\left(\rho\frac{\partial\vec{\omega}}{\partial t}+\nabla\times\rho\left(\vec{V}\cdot\nabla\vec{V}\right)\right)=\nabla\times-\nabla p+\nabla\times\vec{f}+\nabla\times\left(\mu\nabla^2\vec{V}\right) \tag{2.27}$$

Now, Equation 2.27 can be rewritten using calculus vector identities and conservation laws:

(a)
Using vector identities and mathematical definition for vorticity ($\vec{\omega}=\nabla\times\vec{V}$), $\nabla^2\vec{V}$ is given by Equation 2.28:

$$\begin{aligned}&\nabla^2\vec{V}=\nabla\left(\nabla\cdot\vec{V}\right)-\nabla\times\left(\nabla\times\vec{V}\right)\\&\nabla^2\vec{V}=\nabla\left(\nabla\cdot\vec{V}\right)-\nabla\times\vec{\omega}\\&\nabla\cdot\vec{V}=0\leftarrow Conservation\,of\,mass\\&\therefore\nabla^2\vec{V}=-\nabla\times\vec{\omega}\end{aligned} \tag{2.28}$$

and

$$-\nabla\times\left(\nabla\times\vec{\omega}\right)=\nabla^2\vec{\omega}-\nabla\cdot\left(\nabla\times\vec{\omega}\right)=\nabla^2\vec{\omega} \tag{2.29}$$

Substituting Equation 2.28-Equation 2.29 into Equation 2.27 gives Equation 2.30:

$$\rho\left(\frac{\partial\vec{\omega}}{\partial t}+\nabla\times\left(\vec{V}\cdot\nabla\vec{V}\right)\right)=\nabla\times-\nabla p+\nabla\times\vec{f}+\mu\nabla^2\vec{\omega} \tag{2.30}$$

(b)
Using calculus identities, second term of the L.H.S of Equation 2.30 can be expressed as Equation 2.31:

$$\begin{aligned}\nabla\times\left(\vec{V}\cdot\nabla\vec{V}\right)&=\nabla\times\left(\tfrac{1}{2}\nabla\left(\vec{V}\cdot\vec{V}\right)-\vec{V}\times\nabla\times\vec{V}\right)\\ \nabla\times\left(\vec{V}\cdot\nabla\vec{V}\right)&=\nabla\times\left(\tfrac{1}{2}\nabla\left(\vec{V}\cdot\vec{V}\right)-\vec{V}\times\vec{\omega}\right)\\ \nabla\times\left(\vec{V}\cdot\nabla\vec{V}\right)&=\left(\nabla\times\tfrac{1}{2}\nabla\left(\vec{V}\cdot\vec{V}\right)-\nabla\times\vec{V}\times\vec{\omega}\right)\end{aligned}\tag{2.31}$$

As $\nabla\times\frac{1}{2}\nabla\left(\vec{V}\cdot\vec{V}\right)=0\leftarrow\nabla\times\nabla(scaler\ quantity)=0$:

$$\therefore\nabla\times\left(\vec{V}\cdot\nabla\vec{V}\right)=-\nabla\times\vec{V}\times\vec{\omega}\tag{2.32}$$

Rearranging the terms of the equation Equation 2.32:

$$\therefore\nabla\times\left(\vec{V}\cdot\nabla\vec{V}\right)=\nabla\times\left(\vec{\omega}\times\vec{V}\right)\tag{2.33}$$

In turn, $\nabla\times\left(\vec{\omega}\times\vec{V}\right)$ can be expressed as:

$$\begin{aligned}\nabla\times\left(\vec{\omega}\times\vec{V}\right)&=\vec{V}\cdot\nabla\vec{\omega}-\vec{\omega}\cdot\nabla\vec{V}+\vec{\omega}\left(\nabla\cdot\vec{V}\right)-\vec{V}\left(\nabla\cdot\vec{\omega}\right)\\ \nabla\times\left(\vec{\omega}\times\vec{V}\right)&=\left(\vec{V}\cdot\nabla\vec{\omega}+\vec{\omega}\left(\nabla\cdot\vec{V}\right)\right)-\left(\vec{\omega}\cdot\nabla\vec{V}+\vec{V}\left(\nabla\cdot\vec{\omega}\right)\right)\\ \nabla\times\left(\vec{\omega}\times\vec{V}\right)&=\left(\vec{V}\cdot\nabla\right)\vec{\omega}-\left(\vec{\omega}\cdot\nabla\right)\vec{V}\end{aligned}\tag{2.34}$$

Substituting Equation 2.34 into Equation 2.30 gives:

$$\rho\left(\frac{\partial\vec{\omega}}{\partial t}+\left(\vec{V}\cdot\nabla\right)\vec{\omega}-\left(\vec{\omega}\cdot\nabla\right)\vec{V}\right)=\nabla\times-\nabla p+\nabla\times\vec{f}+\mu\nabla^2\vec{\omega}\tag{2.35}$$

(c)
As $\nabla\times-\nabla p=0$, equation Equation 2.35 becomes:

$$\rho\left(\frac{\partial\vec{\omega}}{\partial t}+\left(\vec{V}\cdot\nabla\right)\vec{\omega}-\left(\vec{\omega}\cdot\nabla\right)\vec{V}\right)=\nabla\times\vec{f}+\mu\nabla^2\vec{\omega}\tag{2.36}$$

Rearranging the terms of Equation 2.36:

$$\rho\left(\frac{\partial\vec{\omega}}{\partial t}+\left(\vec{V}\cdot\nabla\right)\vec{\omega}\right)=\nabla\times\vec{f}+\mu\nabla^2\vec{\omega}+\rho\left(\vec{\omega}\cdot\nabla\right)\vec{V}\tag{2.37}$$

The term $\left(\vec{\omega}\cdot\nabla\right)\vec{V}$ represents the vortex stretching and for 2D axisymmetric flows:

$$\left(\vec{\omega}\cdot\nabla\right)\vec{V}=0\tag{2.38}$$

The momentum theory assumes inviscid flow, therefore:

$$\mu\nabla^2\vec{\omega}=0\tag{2.39}$$

As shown by Equation 2.40, generation of vorticity is determined by $\nabla\times f$ [36]

$$\frac{D\vec{\omega}}{Dt} = \nabla \times \vec{f} \tag{2.40}$$

It implies that if there is no generation and transport of vorticity, curl of force field is zero and vice versa. Hence, vorticity is only created if there is a non-uniform force acting the body and vice-versa.[1]

2.4. RELEVANT PAST EXPERIMENTAL RESEARCH

In this section, past experiments which are relevant for this project (especially the experiment) are reviewed. The project is about actuator disc and dynamic inflow modelling, projects related these two topics are discussed. Although the project focuses on unsteady actuator discs, review of experiments related to AD under steady loading is also made as there are not many experiments done on unsteady actuator discs.

The recent project on actuator disc under unsteady loading was done by V.Hong (presented in [1]). The aim of this experiment was to analyse an actuator disc under unsteady loading. Actuator disc was modelled using a porous disc. This porous disc was created using a metal-wire mesh like in [37],[38]. The set-up of the experiment is shown in Figure 2.5. The set-up and results of this experiment are very relevant for this case study, as current M.Sc. thesis project aims to extend the research in same field.

The unsteady profile for both the experiment and numerical simulation is shown in Figure 2.6. As shown in the figure, unsteadiness factor in this experiment was a step change in the load. Three different time-steps were used for this step change: $\delta t^* = 0.2$,0.4 and 0.8. $\left(\delta t^* = \frac{\delta t V_0}{D}\right)$ Thrust Coefficient range was 0.61-0.82. To keep the load cases same for experiment and numerical models, these C_T were given as input to the engineering models, FWVR model (see section 4.2) and 3D RANS model.

Figure 2.5: Experimental set-up for unsteady actuator discs experiment used in [1]

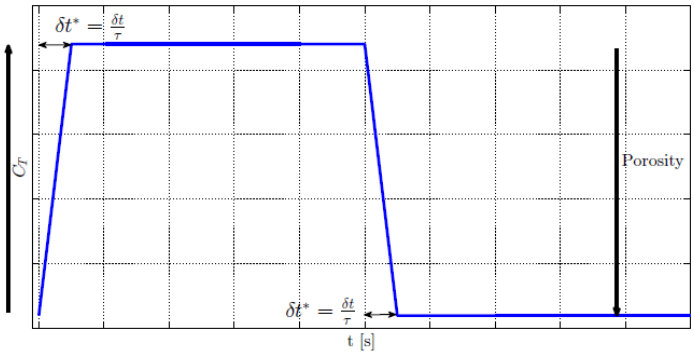

Figure 2.6: Profile of the unsteady load cycle used in [1]

At first, the experiment was done for steady cases. Figure 2.7 show the results. In this figure, effect of the tower can be seen as mean velocity deficit is maximum at the centre of the disc. A clear jump in velocity at r/D = 0.5 can be seen due to the shed vortices from edge of the disc. Presence of shear layer can be seen before x = 2.5D. Before this point, mean velocity gradient is more gradual than beyond this point. This also indicates shear layer breakdown and expansion. It can also be seen by increase of turbulence intensity. [1]

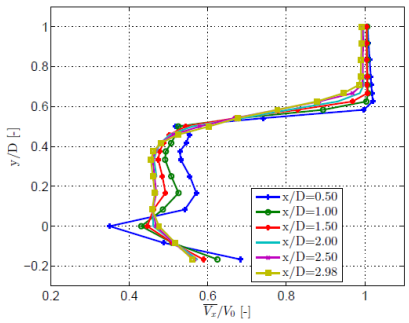

(a) High Porosity configuration: $C_T = 0.61$.

(a) Time-averaged velocity profile for low porosity [1]

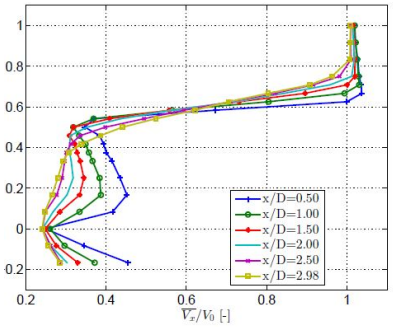

(b) Low Porosity configuration: $C_T = 0.82$.

(b) Time-averaged velocity profile for high porosity state [1]

Figure 2.7: Time-averaged velocity profile for disc under steady loading

The figure shows that for higher porosity configuration, shear layer is more stable. This is because for lower porosity (i.e. higher C_T) velocity deficit is higher, which means difference between velocity in the wake and free-stream is more. Due to this, there are more turbulent eddies to entrain momentum from free-stream, which resulted in faster velocity recovery. In Figure 2.8, it can be noticed that as the wake progresses, deviations in the turbulent intensity also starts decreasing. [1]

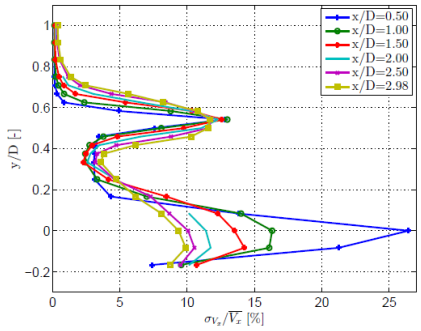

(a) High Porosity configuration: $C_T = 0.61$.

(a) Turbulent intensity profile for low porosity state [1]

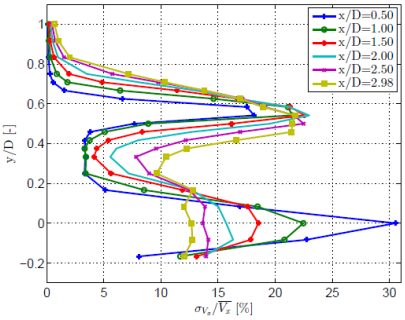

(b) Low Porosity configuration: $C_T = 0.82$.

(b) Turbulent intensity profile for high porosity state[1]

Figure 2.8: Turbulent intensity profile for disc under steady loading

The project compares the experimental results with 3D-RANS and then 3D-RANS with engineering models. The results for steady load cases are shown in Figure 2.10,Figure 2.11 and Figure 2.9. The results show that the 3D-RANS model gives a slight overestimation of velocity deficit. It is pointed in [1] that this might have resulted due to error in thrust coefficient calculated in the experiment which was used as input to all other models. The results also show effect of the tower. Figure 2.9 shows that the 3D-RANS model underestimates the turbulence intensity.

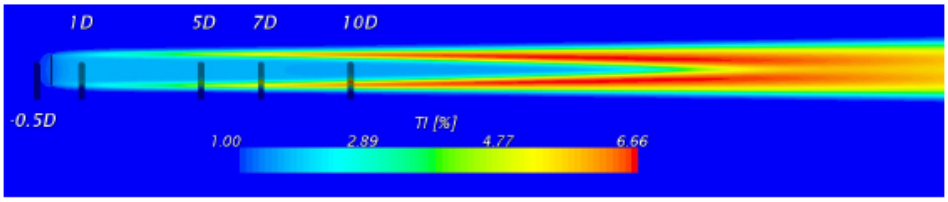

(a) $C_T = 0.61$.

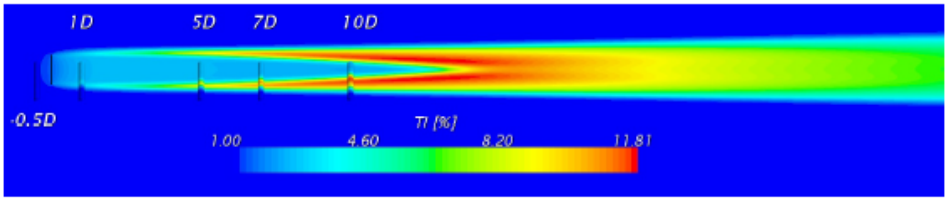

(b) $C_T = 0.82$.

Figure 2.9: Turbulent Intensity contour maps by 3D RANS model [1]

The experimental results for the unsteady loading cases were also compared to the 3D-RANS modelling. Step was made from low porosity to high porosity. It shows that the flow in the shear layer around y = 0.5D is most turbulent and shed vortices are prominent there. The results show that for flow with higher C_T (low porosity) is more turbulent. It is also seen that after 2 rotor diameters downstream, the shear layer starts to expand. This effect is longer for lower C_T. [1]

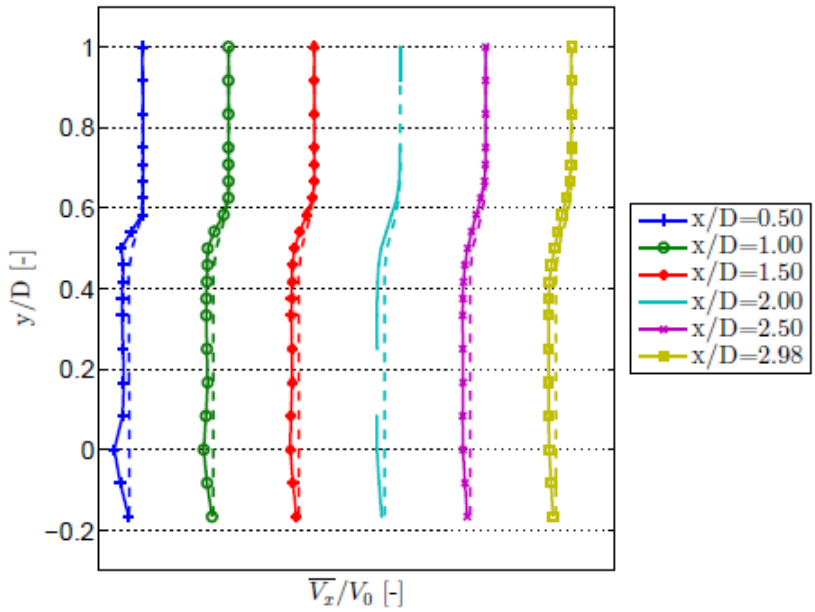

(a) $C_T = 0.61$.

Figure 2.10: Wake velocity profile for experiment(-) and 3D-RANS(–) for thrust coefficient = 0.61 [1]

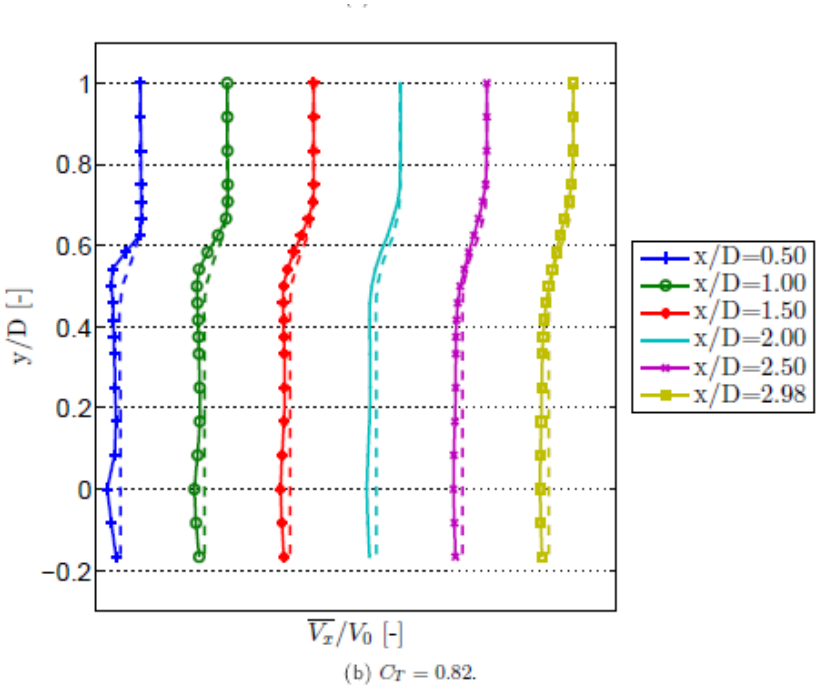

(b) $C_T = 0.82$.

Figure 2.11: Wake velocity profile for experiment(-) and 3D-RANS(–) for thrust coefficient = 0.82 [1]

Both the experimental and the 3D-RANS model show an overshoot in the wake velocity when the step change was made. After this, it decays to a steady value. The 3D-RANS vorticity contour maps show the reason behind it. It is due to formation 'new' and 'old' vortices and their passage over hot-wire probe. When there is a sudden increase in load, it results in stronger shed vortices due to lager wake expansion and lower mean velocity. These 'new' vortices lag behind the 'old' vortices as the wake expands, these vortices roll-up and eventually interact. This passage of vortices over the hot-wire leads to this overshoot. A similar but opposite effect is seen when load is suddenly decreased. [1]. The results from the experiment and the 3D-RANS model are different with respect to time required to decay to steady value. Decay time is shorter for the experimental results. According to Hong [1], this can result from different set-up as the numerical model does not have tower shadow effects and no small-scale turbulence. The results from 3D-RANS are compared to dynamic inflow models and FWVR model. It shows that the dynamic inflow models predict smaller time decay needed to reach the steady value. The results are shown in Figure 2.12. It shows that results from FWVR model are closer to 3D-RANS results.

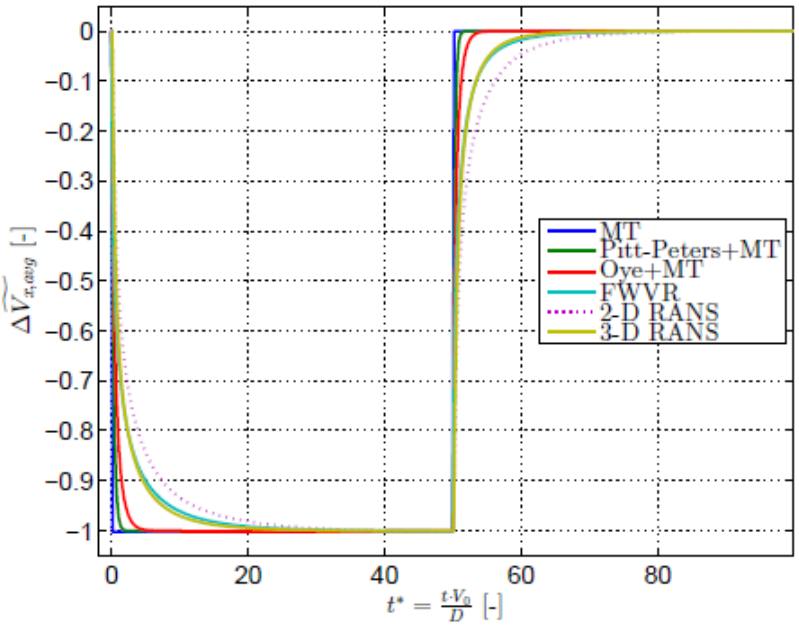

Figure 2.12: Inflow velocity response calculated by Momentum theory, Dynamic Inflow Engineering Models, FWVR model and 3D RANS simulations. [1]

Unlike actuator discs under unsteady loading, there are many experiments related to actuator discs under steady loading which use porous discs. Medici and Alfredsson [3] used a circular disc with perforated holes to model an actuator disc. In this experiment, two bladed rotor was compared to discs with different porosity values. It shows that the major difference exits in the near wake. The near wake of a bladed rotor is characterized by the helical structure of tip vortices which do not exist in the case of a porous disc. A similar phenomena of large scale vortex shedding is seen for both turbine and disc, but it is more clear for the turbine. The results show that there is a 'critical rotor speed' after which the plane of the rotor starts to behave like a disc. It also shows that for high tip speed ratios, Strouhal number of the rotor is similar to that of a disc. This means that when the tip speed is very high, the rotor behaves like a rotor with infinite number of blades.

A similar experiment was done by Lignarolo *et al.* [4], where wake of a two bladed rotor was compared to that of porous disc. The results were similar. The study focused on the near and the intermediate wake. According to this study, there is a difference in the oscillations in the wake of the disc and turbine. This might have been caused due to the difference in the method of wake generation and holes in the disc. It was also noticed that for the turbine, the velocity gradients at the edge are higher due to tip vorticity and also turbulence in the wake of turbine is anisotropic.[4]

Like in [1] and [5], experimental results were compared to the FWVR model and four large eddy simulation (LES). However, the loading is steady and experimental results are gathered using Stereoscopic Particle Velocimetry (SPIV). It was found that the FWVR model (see subsection 4.3.1) is better at estimating the centre-line velocity and the wake expansion than the LES models. As for LES code, it was seen that they can predict the velocity deficit fairly good with a coarser grid, but for the turbulence intensities, a finer grid is needed. [5]

As AD model is used to simulate a wind turbine, it is important to understand aerodynamics of a wind turbine wake. This is vital for validation purposes. Next chapter studies wake of horizontal axis wind turbine.

3

AERODYNAMICS OF HORIZONTAL AXIS WIND TURBINES

In order to understand and compare wake behind an actuator disc to that of a wind turbine (WT), it is crucial to understand aerodynamics of wake behind the wind turbine first. Wake behind a wind turbine is highly complex. It is influenced by many factors such as blade airfoil, number of blades, operating conditions, presence of turbulence, height, etc. As a wind turbine extracts energy from the incoming flow, the wake behind it has a lower velocity and momentum. After a point in the wake, the flow starts recovering back to the free-stream conditions due to the momentum mixing process. This process is aided by the presence of shear layer, and other turbulent eddies in the wake. Turbulence in the wake is due to many elements such as presence of shear layer, tip vorticity, atmospheric turbulence, wake meandering, etc. Along with this, the wake of a wind turbine comprises of many other important characteristics such as helical structure of tip vortices, shear layer formation, momentum mixing, leap-frogging, etc. In order to understand, how the wake behind a wind turbine develops, it is important to understand basics involved.

The wake of a wind turbine can be broadly divided into two main components: Near wake and Far wake. The wake of a HAWT is characterized by a momentum sink in the near wake and recovery of momentum in the far wake. [1], [9]

Figure 3.1 shows wake development behind an HAWT and Figure 3.2 shows a schematic drawing of velocity profile behind it.

3.1. NEAR WAKE REGION

In this section, region just behind wind turbine known as 'Near Wake' and its properties are investigated. This is the region behind a wind turbine where direct effects of a wind turbine geometrical design can be seen on the flow properties. Different models use different lengths for the extent of the near wake, but it is generally described till the shear layer expansion meets the turbine axis. Therefore, the length can be different for different wind turbines depending on the wind turbine design and thrust coefficient. The distance between two subsequent wind turbines depends on the length of this region. The length of this region is generally considered between 1 and 2 rotor diam-

eters [39], but according to van Kuik [36] it extends till around 1 rotor diameters while [2] takes it to be 10 rotor diameters. This region is generally modelled using the actuator disc theory (discussed in chapter 2)

Figure 3.1: Helical structure formed of tip vortices shed from wind turbine [8]

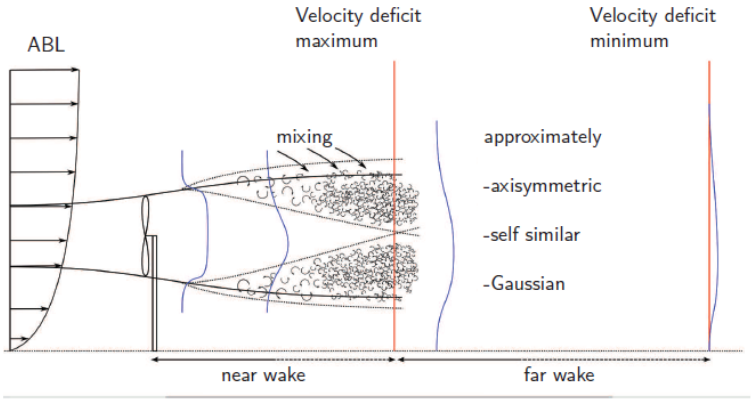

Figure 3.2: Velocity profile inside a wind turbine wake [9]

The wake of a wind turbine is combination of a 3D-wing aerodynamics and effects of rotation. Like in 3D wing aerodynamics, it consists of tip and bound vorticity formation due to difference in pressure on both sides and difference in loading along the span of the blade. However, it is more

complex, as it is characterized by helical structured tip vortices formation due to blade rotation, as shown in Figure 3.1. This rotation of tip vortices is in opposite direction to that of blades. As shown in Figure 3.1 and Figure 3.3, the near wake region is characterized by two main phenomena: shear layer expansion and tip vortices creation, which will be further discussed in detail. After diffusion of shear layer, velocity deficit has reached its maximum and velocity starts recovering. [1],[9]

3.1.1. SHEAR LAYER CHARACTERISTICS

As the velocity behind a wind turbine is lower than the free-stream velocity, it results in high velocity gradients in the wake especially near the wake boundaries. Figure 3.3 clearly shows formation and expansion of the shear layer. This shear layer is formed due to difference in velocities in the wind turbine wake and outside the wake. In this region, turbulent eddies are formed due to shearing of fluid. This decreases the flow velocity further more. According to Ainslie [39], maximum deficit occurs at 1-2 rotor diameters. As explained later in the chapter (see Figure 3.1.2), length of shear layer also depends on the ambient turbulence. For lower ambient turbulence, the length might be longer due to lower momentum mixing (studied later in the chapter). [9] According to Schepers [40], based on past experimental studies, an average length of shear layer is 2.25 rotor diameters.

3.1.2. WAKE MIXING PHENOMENA

Mixing of momentum in the wake of a wind turbine is mainly due to factors (as shown in Figure 3.3):

- **Wake Induces mixing**: This is mainly due to helical structure of tip vorticity, its instability and its breakdown. [10]
- **Atmospheric turbulence**: Atmospheric turbulence also plays an important role in wake mixing especially at on-shore farms.

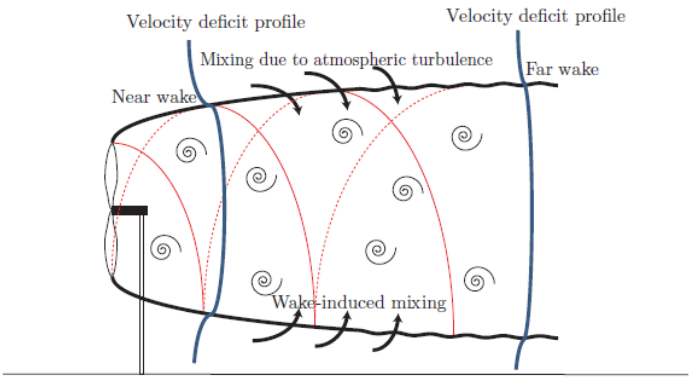

Figure 3.3: Velocity profile inside a wind turbine wake along with factors influencing momentum mixing [10]

WAKE INDUCED MIXING

One of the main sources of turbulence in the wake is turbulence created by tip vortices generated by blades. Like 3D wing, tip vortices are formed as there is higher pressure on the pressure side and lower pressure on the suction side of the blade. This results in reduced lift at the tip of the blade. Along with this, as there is a span-wise variation of load on the blade, bound vorticity is

formed.[41],[9],[1]

Lignarolo *et al.* [12] investigates origins of tip vortices behind a wind turbine in detail. It uses Stereoscopic Particle Image Velocimetry (SPIV) to investigate the initiation of tip vortices. It is found that the tip vortices behind a wind turbine are created due to varying distribution of vorticity along blades of the wind turbine.[12] There are other works such as [42], [43], [44], [45], [46], etc. These previous works discuss structure of the tip vortices in detail. At first, tip vortices decrease in size as there is vortex shedding. As wake expands, tip vortices are pushed outwards in radial direction. After this, their size increase because of viscous effects and ultimately they breaking down.[41]

As these tip vortices are shed at different azimuthal angle, they form a helical structure as shown in Figure 3.4. [47] Therefore as the rotational speed of wind turbine increases, these tip vortices are formed closer to each other, forming a 'tubular vortex sheet'. This also happens when number of blades increase.[47] [9],[1]

Figure 3.4: Smoke flow visualization showing helical structure of tip vortices for the NREL turbine in the NASA-Ames wind tunnel [11]

AMBIENT TURBULENCE

Along with the turbulence in the shear layer, wind turbines have to operate in ambient turbulence and wind shear due to the ground effects. According to Hong [1], for lower ambient turbulence, shear layer is stable for a longer distance. Due to this, there will be a larger velocity deficit as there is less turbulence to promote momentum mixing. [1],[9]

MOMENTUM MIXING

As there is a difference in the velocity and momentum in the wake and outside the wake, the difference causes momentum exchange between the two regions. There have been many past research projects which explain this concept. In [12], vorticity of a wind turbine wake is investigated using Stereoscopic Particle Image Velocimetry (SPIV) (see Appendix A). The experiment was performed in the Open Jet Facility at TU Delft. The results show vortex pairing (also known as 'leap-frogging phenomena'). Figure 3.5 shows this phenomenon, where one vortex of each tip vortex pair catches

up with the other. The results from the experiment show that this instability plays an important role in diffusion of shear layer as this helps in momentum mixing in the wake. According to Hong [1] and Winant and Browand [48], the leap frogging phenomena takes place due to flow perturbations, which can be caused by different blade pitch angles and presence of the ambient turbulence. Due to these perturbations, each vortex pair has its own path and velocity, resulting in the vortex pairing. Also seen in Figure 3.5, for a higher tip speed ratio, this tip vortex instability occurs earlier. The reason for this can be, as stated before, with higher rotational speed, tip vortices are placed closer to each other, resulting in earlier tendency of catching up with each other. [1],[9]

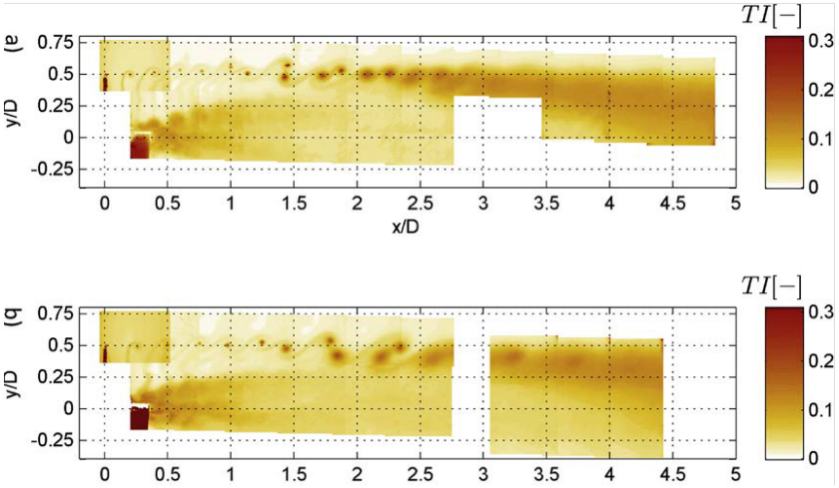

Figure 3.5: Average turbulence intensity field for tip-vortices of (a) $\gamma = 6$ and (b) $\gamma = 4$ [12]

As the thrust coefficient of a wind turbine increases, maximum wake velocity deficit increases. [9] This results in higher difference between outside and inner wake velocities, which in turn causes increase in shearing effect, and hence there will be stronger vorticity and higher turbulence intensities. These turbulence eddies act as a momentum mixing agent. Momentum from outside the wake is mixed with inside, resulting in wake expansion and decrease in velocity deficit. [9],[49]. Therefore, length of shear layer and turbulent wake depends on:

- Operating Thrust Coefficient: velocity deficit, strength of vorticity, etc.
- Ambient Turbulence, wind shear, topographical effects, other flow perturbations etc. [49]

Other sources of turbulence in the wake are turbulent boundary layer leaving the blade and turbulence due to presence of nacelle and tower (which is known as mechanical turbulence), ambient turbulence and wake meandering. [9].

3.2. FAR WAKE REGION

This is the region after the near wake. In this region, wake starts to recover back to the free-stream conditions. Velocity profile is generally assumed to be self-similar and axisymmetric in this region. This region is known as 'far wake' region. The wake is generally assumed to be fully developed in this region, so there is no more velocity deficit. Usually velocity profile is modelled using Gaussian profile.
There are many engineering models used to simulate wake in this region. Most commonly used models for this region are Ainslie model, Jensen model, Frandsen model, Larsen model, etc.[9]

3.2.1. WAKE RECOVERY IN THE FAR WAKE

After the shear layer has diffused as a result of momentum mixing and leap frogging, velocity field starts recovering. As explained earlier, this happens mainly due to mixing of the wake by atmospheric turbulence and wake induced mixing. The pressure gradients are of less importance in this region and focus is more on the velocity profiles. Characteristics of velocity profile in a wind turbine wake are shown in Figure 3.2. This region is characterized by small velocity gradients, high turbulence and wake meandering. [9] The models, which are dedicated solely to this region, generally assumes that wake is axisymmetric, i.e. $\frac{dp}{dx} = 0$, $\frac{d^2u}{dx^2} = 0$. [9] Assumption of self similar solutions for velocity profile and turbulence intensities is also made, which is not completely true as there is presence of the ambient shear and the ground effects.

Like the recovery of velocity, turbulence intensity also starts to recover to ambient value. It is found that due to tower effects, maximum velocity deficit is found below turbine axis while maximum turbulence intensity (TI) above it. [9],[47] The process of TI recovery is guided by Energy Cascade Process (transfer of energy from larger eddies to smaller ones).

3.2.2. WAKE MEANDERING

Sanderse [9] defines wake meandering as a large scale movement of the wind turbine wake. It is considered to be caused due to the movement of large-scale eddies larger than the wake. Due to this, wake reaching the downstream wind turbine can be yawed, which might result in the periodic variations in the angle of attack. This can lead to increased load fluctuations and fatigue of the downstream wind turbine. [50],[41]
Wake meandering was first modelled by Ainslie. This model has been documented in [39]. According to Ainslie [39] and Larsen *et al.* [51], wake meandering has a huge effect on decreasing the velocity deficit. This can be a result of large scale movement of wake, encouraging entrainment of the turbulent eddies, and hence increased mixing process.

There have been experimental studies done in [2] and [50] related to the wake meandering process. The wake meandering is caused by wake instability. [2] These studies also show that wake meandering depends on the tip speed ratio, thrust coefficient, number of blades and pitch angle of blades. As per Medici and Alfredsson [3], for low tip speed ratios, there is almost no wake meandering. In [52], an experiment to study the wake meandering behind a wind turbine model is discussed. In this study, it was found that the main cause of the wake meandering is the presence of turbulence eddies in the surrounding atmosphere, which are larger than the size of wake. These result in moving the wake as whole.

3.2.3. EFFECT OF YAW

As discussed in the section before, yawed flow can lead to increased load fluctuations and fatigue loading. Yawed flow can be caused due to wind in varying directions, wake meandering, etc. This also leads to a lower WT efficiency. As yawed flow causes deflection of the wake, it can be used to deflect the wake in desired direction as well. [9]

3.3. WIND TURBINE FARM

The previous section discusses aerodynamics of a single HAWT, but in reality, turbines operate in cluster. So the wake of one wind turbine has an effect on the performance of the other turbines downstream. It should also be noted that as the wake of a wind turbine is unsteady, the downstream

wind turbines have to operate in unsteady inflow conditions. This is where this project plays an important role. It aims to study the properties of wake behind an actuator disc under unsteady loading.

In this section, how these effects vary with different variables is discussed. In order to optimize power generation and to decrease loads due to fatigue, it is important to study how performance and loads vary for a wind turbine operating in the wake of a wind turbine. There have been many studies done in order to analyse these effects. Barthelmie *et al.* [13], Adaramola and Krogstad [53], Lissaman [54], Aagaard Madsen *et al.* [55], Elliott [56] and Milborrow and Ross [57] analyse the effect of a farm geometry, operational settings of the wind farm and ambient turbulence. Lissaman [54] states that there are two main factors effecting the power output: wind farm geometry and ambient turbulence. The effect of wind farm geometry is very obvious. For example, shorter the distance between two turbines, larger the effect of the upstream turbine can be seen on the power output of downstream turbine. [53].

With respect to ambient turbulence, as is discussed in section Figure 3.1.2, higher the ambient turbulence, higher the turbulence mixing, resulting in faster recovery of the velocity and turbulence intensities in the wake. This means downstream wind turbine will experience less effects of the wake. According to Lissaman [54], offshore wind farms have lower ambient turbulence due to lower roughness lengths, this results in more "persistent wakes". [53]

In [56], effects of thrust coefficient on power performance are studied. According to this report, as the operating thrust coefficient decreases, the wake effects decrease as well. This could be because as the thrust coefficient decreases, the velocity deficit decreases, hence smaller wake effects. According to Aagaard Madsen *et al.* [55], mechanical turbulence (turbulence due to nacelle and tower) might affect wind turbine performance. In general, higher the turbulence, higher the fatigue load on the downstream turbine.[55] According to Adaramola and Krogstad [53], power losses of a downstream wind turbine ranges between 20% and 25%. According to McTavish *et al.* [58], by decreasing the lateral space between the turbine to 0.25 rotor diameters or 0.5 rotor diameters, accumulative power output can be increased.

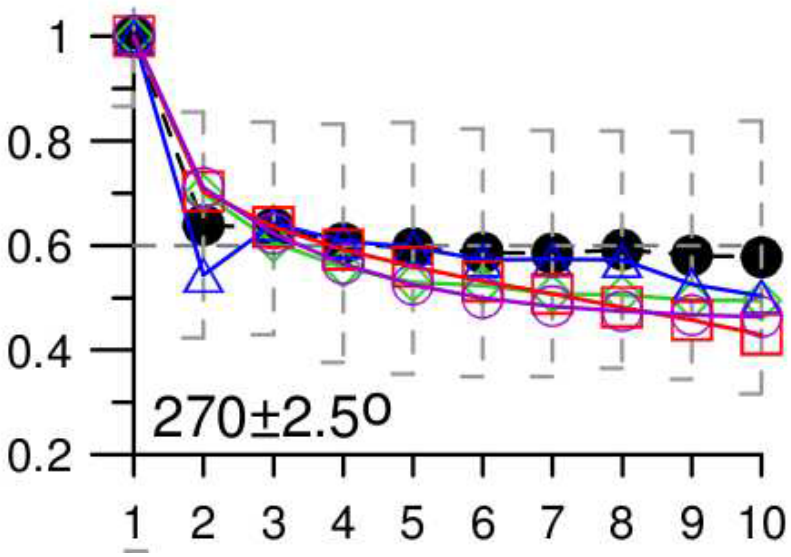

Figure 3.6: Normalized Power of wind turbines Vs. downstream rows of wind turbines [13]

Figure 3.6 shows normalized power of wind turbines. It shows that after a certain point the power

loss reaches an asymptote, i.e., after certain number of wind turbines, the power loss of downstream wind turbines do not increase any more. Hong [1] suggests that reason for this behaviour might be that after a point turbulence reaches its saturation level.

This chapter analysed the aerodynamics of wake behind a wind turbine. As wind turbine operate in unsteady conditions, there are different models used to simulate these conditions. In next chapter, few of these models and concept of dynamic inflow are studied.

4

DYNAMIC INFLOW

Dynamic inflow is caused due to changes in the loading on the rotor, such as during wind gusts and/or sudden and fast change in blade pitch angles. It is dynamic response of inflow velocity to the changes in the rotor plane. The inflow is not always in equilibrium. Flow takes time to respond, and to reach a new equilibrium after a sudden change as there is no instantaneous change in the flow conditions. Due to a sudden change in the blade pitch angle, there is an 'overshoot' in the local angle of attack. This overshoot in the angle of attack results in an overshoot in the loads.[16] A similar phenomena is observed for conditions with wind gust as it changes the induced velocity. Hence this phenomenon describes that the steady state is achieved only after some time delay. As this flow change is related to the complete wake flow, the time scale of this flow is D/V (where D is the diameter of the rotor), while unsteadiness caused due to airfoil aerodynamics has a smaller time scale of c/V. [16]

The phenomenon of dynamic inflow can also be explained using change in the vorticity. [26] The trailed vorticity formed at the blades is convected downstream at a certain local velocity. Wake with this trailed vorticity will have a certain induced velocity. As load on the blades change, the bound vorticity also changes. With this shed vorticity will also change, as explained by the Kelvin's theorem. The new trailed vorticity travels with a new changed local velocity, hence the wake becomes mixture of 'old' and 'new' vorticity. Therefore, this wake will have a different induced velocity. So until these new vortices replace the old vortices (or have travelled far enough that their effect is negligible), induced velocity experiences a gradual change to a steady state. This is why it is also known as 'dynamic induction'. [16, 26] Process is also shown in Figure 4.1

As mentioned earlier, momentum theory assumes stationary conditions, i.e., the wake is always in an equilibrium and responds instantaneously to any changes in the load. However as stated above, when load changes, the velocity lags behind and gradually approaches a new equilibrium as an appreciable amount of air needs to be accelerated. [26]. Due to the lag in the induced velocity, there is a temporary increase in the loads especially during sudden pitch changes.[59]

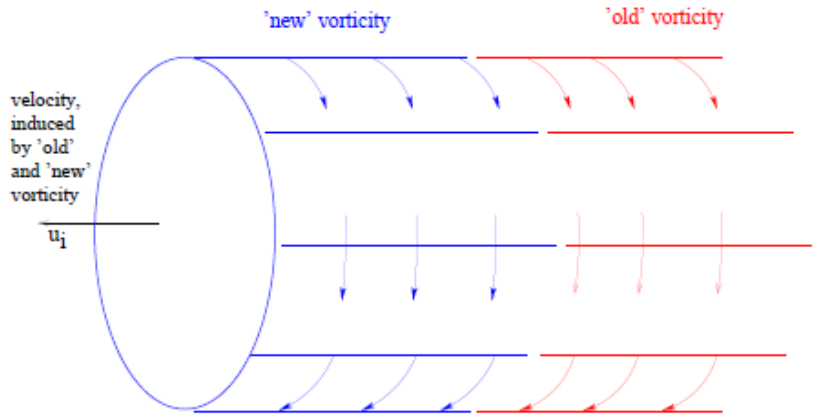

Figure 4.1: Wake with mixed vorticity as result of pitch angle change [14]

There have been many experiments done in the past to evaluate the phenomena of dynamic inflow. In NREL's Phase VI(NASA-Ames) experiments, effects of dynamic inflow were studied. [26],[15] Figure 4.2 shows fast variation of pitch angle from -5.9 degrees to 10 degrees. Figure 4.3 presents results for this fast change in the pitch angle.

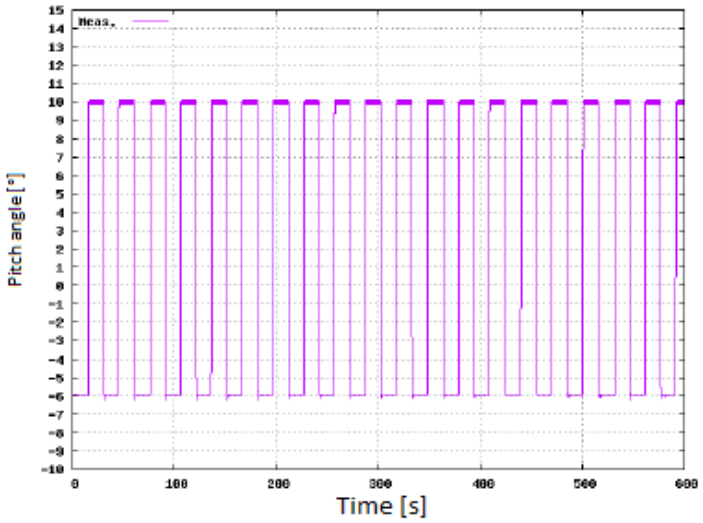

Figure 4.2: Pitch angle vs. time used in [15]

Along with this, in-depth experiments related to dynamic inflow effects have been documented in [16]. Several models have been developed in [16] to simulate dynamic inflow. To validate these models, experiments with Tjæreborg turbine were conducted. During these experiments, effect of a sudden and fast change in the blade pitch angle on the blade root flapping movement and root shaft torque were analysed.

Figure 4.4 shows some of the results from the experiment. There were two main results found during these experiments:

1. First effect that can be seen was that due to the rapid change in the blade pitch angle, due to which the angle of attack changes rapidly. Due to this, there is a sudden and fast change in

the torque. This first effect is due to unsteady airfoil aerodynamics.

2. The second effect is that change in the torque due to the induced velocity reaching a new equilibrium. It was seen that as the induced velocity is larger than the axial velocity, torque decreases, and decreasing the first effect.

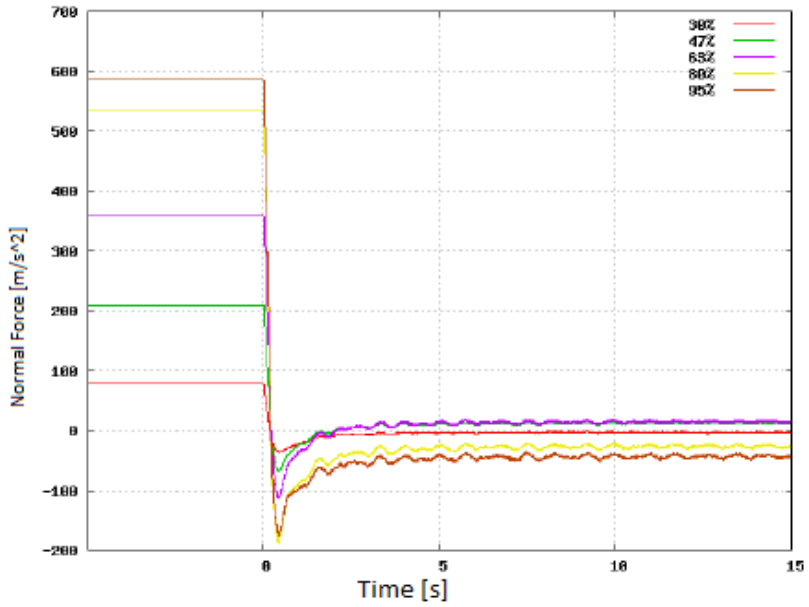

Figure 4.3: Measured normal force at 5 radial positions for rapidly changing pitch angle [15]

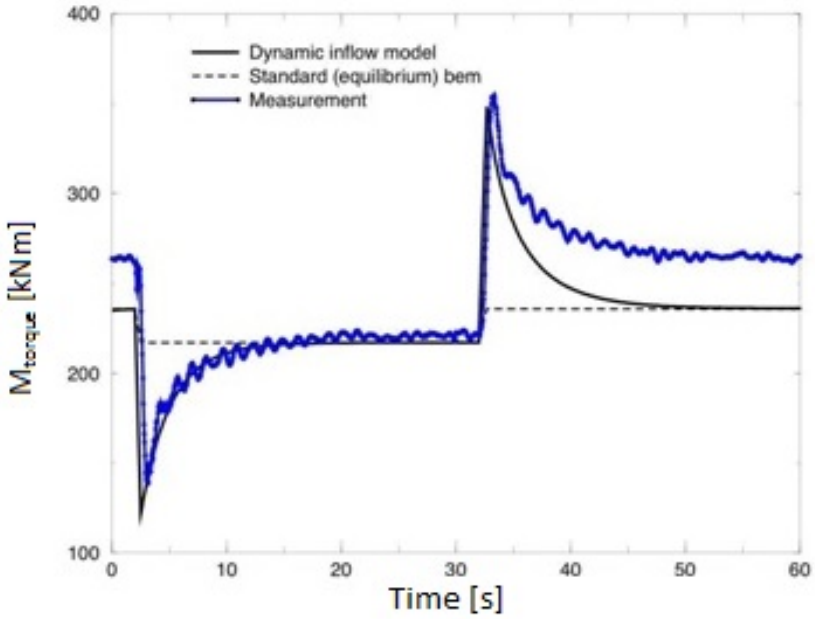

Figure 4.4: Rotor shaft torque with step change in pitch angle [16]

From these results it can be seen although characteristic time scales of two types of unsteadiness (airfoil and dynamic inflow) are different, effect of both unsteady airfoil aerodynamics and dynamics induction can be seen. The experiments also show that effects of coherent wind gust is relatively small.

4.1. MODELLING OF DYNAMIC INFLOW

As stated in chapter 2, drag/thrust coefficient (C_d) and velocity in the wake (u_1) is given by:

$$\begin{aligned} C_d &= 4a(1-a) \\ u_1 &= V_0(1-2a) \end{aligned} \tag{4.1}$$

Dynamic inflow is generally modelled by adding a time derivative of the induced axial velocity as in Equation 4.2: [14]

$$C_d = \frac{1}{V_0}\left(4u_i(1-u_i) + \tau\frac{du_i}{dt}\right) \tag{4.2}$$

where τ is a time constant and u_i is the induced velocity. As this time constant decreases, the time to a new equilibrium decreases as well.

4.2. ACTUATOR DISC THEORY BASED MODELS

In this section, models that are used for dynamics inflow behind an unsteady actuator disc are reviewed. These models are based on either the fluid physics or empirical data or both. Although BEM gives sufficiently good results at uniform load conditions [60], it assumes the equilibrium assumption of the 'momentum theory', so it cannot be used for unsteady flows. An example of a model for unsteady flows is model by Sorensen and Myken, which is a non-linear and time-dependent actuator disc model. However Chattot [61] states that it contains errors as diffusion of vorticity is unrealistic.

There are other models which are based on Reynold's Average Navier-Stokes Equations (RANS). Although these models give very good results, they are time consuming. Engineering models are preferred as they offer reliable results with less computational time. In this section: two of the commonly models are presented.

4.2.1. STIG ØYE

This model was presented by S. Øye, in [29]. It calculates induced velocity by using a quasi-steady induced velocity in two first-order-linear-ordinary differential equations.[27] This quasi-steady induced velocity is given as an input to the model and is calculated using BEM. Induced velocity is given by Equation 4.3:

$$\begin{aligned} V_{\text{int}} + \tau_1\frac{dV_{\text{int}}}{dt} &= V_{qs} + k\tau_1\frac{dV_{qs}}{dt} \\ V + \tau_2\frac{dV_{\text{int}}}{dt} &= V_{\text{int}} \end{aligned} \tag{4.3}$$

where V_{int} is defined as an intermediate value of induced velocity, V_{qs} is quasi steady velocity and V is the induced velocity. $k = 0.6$ is used for vortex ring models. τ_1 and τ_2 are given by Equation 4.4.

These two coefficients are found using Vortex Ring models in [62],[29]

$$\begin{aligned}\tau_1 &= \frac{1.1}{1-1.3a}\frac{R}{V_0}\\ \tau_2 &= \left[.39-0.26\left(\frac{r}{R}\right)^2\right]\tau_1\end{aligned} \tag{4.4}$$

where r is the radial distance and R is the rotor radius.

As these equations are first-order-ordinary differential equations, they can be solved using backward or forward or central differentiation method. However as for the forward and the central differentiation methods, information of next time step is required, backward difference method will be less time consuming.
Using backward difference method:

In this method, time derivatives of all terms are found using backward difference method:

$$\begin{aligned}\frac{dV_{qs}}{dt} &= \frac{{V_{qs}}^{i}-{V_{qs}}^{i-1}}{\Delta t}\\ \frac{dV_{\text{int}}}{dt} &= \frac{{V_{\text{int}}}^{i}-{V_{\text{int}}}^{i-1}}{\Delta t}\\ \frac{dV}{dt} &= \frac{V^{i}-V^{i-1}}{\Delta t}\end{aligned} \tag{4.5}$$

Substituting Equation 4.5 into Equation 4.3 gives:

$${V_{\text{int}}}^{i}+\tau_1\frac{{V_{\text{int}}}^{i}-{V_{\text{int}}}^{i-1}}{\Delta t} = {V_{qs}}^{i}+k\tau_1\left(\frac{{V_{qs}}^{i}-{V_{qs}}^{i-1}}{\Delta t}\right)$$
$$\Rightarrow {V_{\text{int}}}^{i} = \frac{\left[{V_{qs}}^{i}+k\tau_1\left(\frac{{V_{qs}}^{i}-{V_{qs}}^{i-1}}{\Delta t}\right)+\frac{{V_{\text{int}}}^{i-1}}{\Delta t}\right]}{1+\frac{\tau_1}{\Delta t}} \tag{4.6}$$

$$V^{i}+\tau_2\frac{V^{i}-V^{i-1}}{\Delta t} = V_{\text{int}}$$
$$\Rightarrow V^{i} = \frac{\left[V_{\text{int}}+\frac{V^{i-1}}{\Delta t}\right]}{1+\frac{\tau_2}{\Delta t}} \tag{4.7}$$

4.2.2. PITT PETERS

This model is presented in [28]. It is used to estimate thrust and induced velocity at the rotor plane. It is based on the momentum theory and is used in commercial codes such as Bladed and AeroDyn. The equation for dynamic inflow at each annular ring is found as: [27]

$$T_k = \frac{8}{3\pi}\rho A_k r\frac{dV_{i,k}}{dt}+2\rho A_k V_{i,k}\left(V_0+V_{i,k}\right) \tag{4.8}$$

where k is the number of rings that actuator disc is divided into, A_k is the area of the ring, r is the radial distance from the centre of the disc and $V_{i,k}$ is the induced velocity. [26]

Thrust can be estimated using backward difference method: [1]

$$
\begin{aligned}
T^j &= \frac{8}{3\pi}\rho \cdot {A_k}^j \cdot r^j \cdot \left[\frac{{V_{i,k}}^j - {V_{i,k}}^{j-1}}{\Delta t}\right] + 2\rho \cdot {A_k}^j \cdot {V_{i,k}}^j \cdot \left(V_0 + V_{i,k}^j\right) \\
{V_{i,k}}^j &= \frac{1}{2}\left[V_0 + \frac{4r}{3\pi\Delta t} - \sqrt{\left(V_0 + \frac{4r}{3\pi\Delta t}\right)^2 + \frac{16r}{3\pi\Delta t}{V_{i,k}}^{j-1} - C_{T,qs}V_0^2}\right]
\end{aligned}
\tag{4.9}
$$

where $C_{T,qs}$ is the input loading and j represents time.

4.3. VORTEX METHODS

There is another set of models which use vorticity transport to estimate flow field. Advantage of these methods are that they are reliable and straightforward. There are many models based on this method, some of them are summarized in [62],[27] and [63]. In [64], this method is derived using *Bio-Savart* Law. These methods use transport of vorticity in space and time. Using this law, influence of vortex particles on different locations in the wake can be found. This is repeated for all particles for next time steps. [1] In this section, system of equation for velocity field in the near wake is presented.

4.3.1. FREE WAKE VORTEX RING METHOD FOR NEAR WAKE REGION

This method is presented in [6]. In this model, wind turbine is modelled using an actuator disc which is uniformly loaded and sheds discrete vortex rings downstream. [6] Figure 4.5 shows the wake model. As shown in the figure, the first vortex ring coincides with the disc. The model is divided into two parts: Near wake (from disc till 15 rotor diameters and) and Far wake (from 15 rotor diameters onward). In this section, only near wake calculations are reviewed.

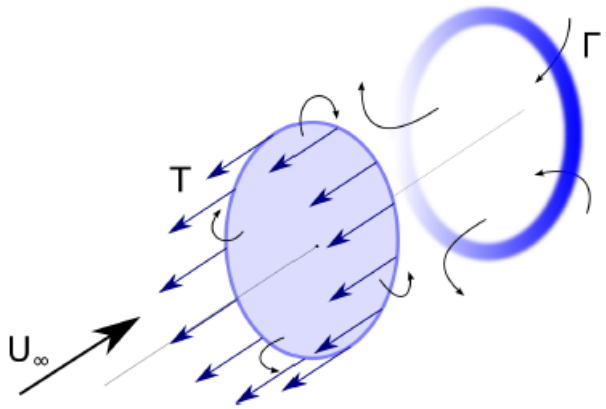

Figure 4.5: Wind turbine modelled as a uniformly loaded actuator disc [17]

The flow in this model is considered incompressible and inviscid. Therefore steady Euler equation is used:

$$
\rho\frac{D\vec{v}}{Dt} = -\nabla p + \vec{f} \tag{4.10}
$$

where ρ is density, v is velocity, ∇p is the pressure change and f is the force density vector which body acts on the flow.

As the flow is considered incompressible, the continuity equation becomes:

$$\nabla \cdot \vec{v} = 0 \tag{4.11}$$

The vortex sheet is discretized into vortex rings with strength Γ. These vortex rings are shedding from the parts of the disc where pressure jump is non-zero. [27] In an axial and axisymmetric flow, force density is given by:

$$\vec{f} = \vec{e}_x f$$

Integration of Equation 4.10 in the axial direction from upstream to the downstream of the disc gives:

$$\Delta p = \int f dx \tag{4.12}$$

van Kuik [36] gives relationship between strength of vortex rings and pressure gradient by:

$$\frac{D\Gamma_{edge}}{Dt} = \frac{\Delta p}{\rho} \tag{4.13}$$

This shows that the strength of unsteady vortex increase with time. The gain in vortex strength from new vortex rings developed is:

$$\frac{\Gamma}{\Delta t} = \frac{\Delta p}{\rho} \tag{4.14}$$

As the pressure jump across the disc can be defined as thrust acting over the frontal area of the disc. Hence, thrust coefficient is defined by Equation 4.15, the relationship between vortex strength and thrust coefficient is given by Equation 4.16.

$$C_T = \frac{T}{1/2 \rho A V_\infty^2} = \frac{A \Delta p}{1/2 \rho A V_\infty^2} \tag{4.15}$$

$$\Gamma = \frac{C_T \left(1/2 V_\infty^2\right)}{\Delta t} \tag{4.16}$$

Axial velocity (V_x) and radial velocity (V_r) induced at any arbitrary point ($P(r_p, \theta, x_p)$) by a vortex ring at $[r_i, 0, x_i]$ (as shown in Figure 4.6) is represented by Equation 4.17 and Equation 4.18 respectively: [65]

$$V_x = \frac{\Gamma}{2\pi\rho_2}\left(K(m) + \frac{{r^2}_i - {r_p}^2 - \left(x_p - x_i\right)^2}{\rho_1^2} E(m)\right) \tag{4.17}$$

$$V_r = \frac{\Gamma}{2\pi r_p \rho_2}\left(K(m) - \frac{{r^2}_i + {r_p}^2 + \left(x_p - x_i\right)^2}{\rho_1^2} E(m)\right) \tag{4.18}$$

where $K(m)$ and $E(m)$ are the complete elliptical integrals of first and second kind and $\rho_1 = \sqrt{(r_i - r_p)^2 + (x_p - x_i)^2}$ $\sqrt{(r_i + r_p)^2 + (x_p - x_i)^2}$ and $m = \frac{4 r_p r_i}{\rho_1^2}$ [6]

Equation 4.17 and Equation 4.18 are valid for all points in the near wake, except at the position of the ring, i.e. $x_p = x_i$ and $x_p = x_i$.

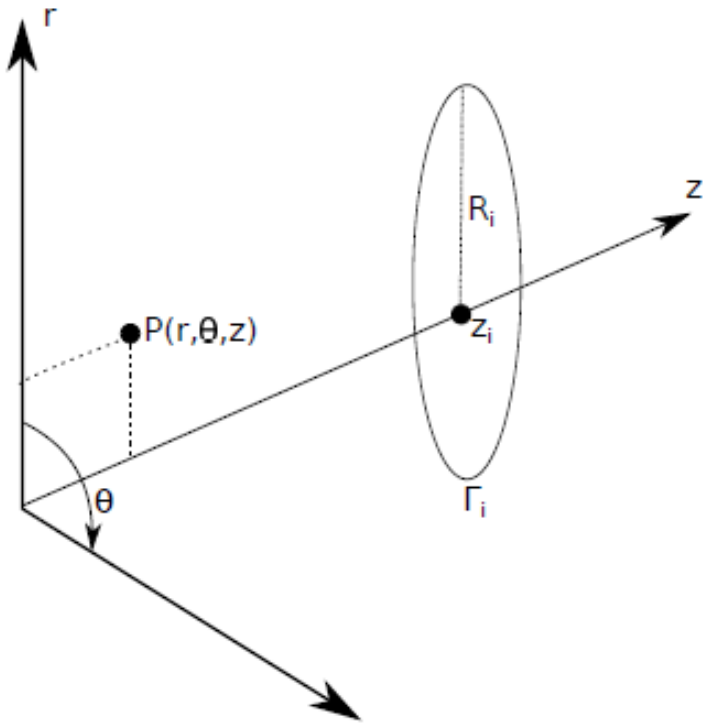

Figure 4.6: Coordinate system used for velocity calculations [17]

5

ACTUATOR DISC MODEL AND EXPERIMENTAL SET-UP

This chapter details the actuator disc model used in the experiment and set-up used to capture velocity field behind wake of the disc under steady and unsteady load. At first, the properties of the actuator disc model are listed. Then explanation on the wind tunnel and flow measurement techniques used to collect data is given

5.1. ACTUATOR DISC MODEL

Actuator disc is modelled using a porous disc shown in Figure 5.1. It is the same porous disc as used by Hong [1]. Requirements for the disc are that it should be as thin as possible such that it should not be flexible and not yield under load. The disc consists of two separate discs consisting of $2 \times 2mm^2$ square holes, which are aligned on top of each other. The front disc is moved to change porosity of the disc. The proximity of the discs is required to be as small as possible without any friction between them. This is because the discs are supposed to behave as close to a single disc as possible. It is found that with maximum porosity (see Figure 5.1a), a thrust coefficient of 0.55 can be achieved and with minimum porosity, a thrust coefficient of 0.81 can be achieved.(see chapter 6)

During the experiment same model for actuator disc is used as in [1] since experimental conditions are similar. In [1], step change in load was analysed while in this experiment periodic loading on the disc will be analysed. In [1], several designs of porous disc were investigated however, it was found that this model is the best as a comparable range of thrust coefficients with respect to a wind turbine can be achieved without any no reverse flow. Along with this it was possible to change porosity to a maximum of 64% with speed required for the load cases in that experiment without any reverse flow. Difference between complete models in that experiment and this experiment is height of the tower used. The tower used in [1],[27] was longer, which might result in different resonance frequencies of the towers. Also the tower was welded at the middle with a rod to reduce the vibrations.

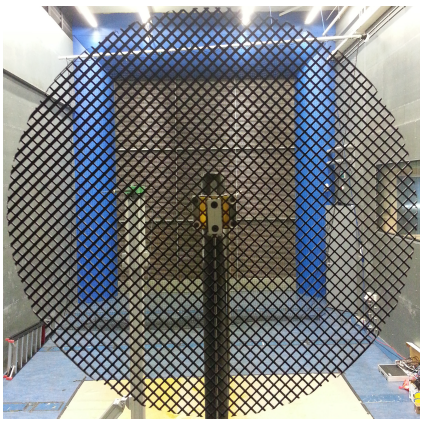

(a) Maximum porosity configuration [1]

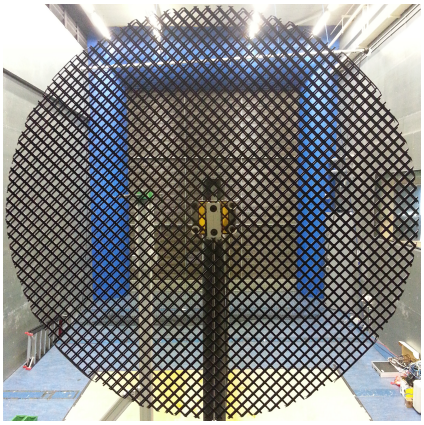

(b) Minimum porosity configuration [1]

Figure 5.1: Porous disc model used in the experiment

In order to change porosity of the disc, an actuating motor (see Figure 5.2) is used. This motor is a linear actuator. It is used as it fulfils stroke-length and speed requirements needed for the experiment.

Figure 5.2: Actuating Motor used in the experiment

5.2. WIND TUNNEL

The wind tunnel used for the experiment is the Open Jet Facility (OJF) at TU Delft High Speed Laboratory (HSL). It is a closed-loop jet tunnel with an octagonal nozzle (see Figure 5.4). It has a contraction ratio of 4:1. It is driven by a large turbo-fan with a rated power of 500kW, achieving a maximum speed of 120km/h (33.3m/s). Figure 5.3 shows its different parts. At first air is rotated 180◦ through a large diffuser and 2 sets of vanes. After this, it enters a 'settling chamber' through a small diffuser, and then velocity fluctuations and turbulence are decreased using five fine-mesh screens. It enters the 'test sections' through a contraction. After this, air is cooled down using a heat exchanger and rotated again 180◦ using turning vanes, returning back to the fan.

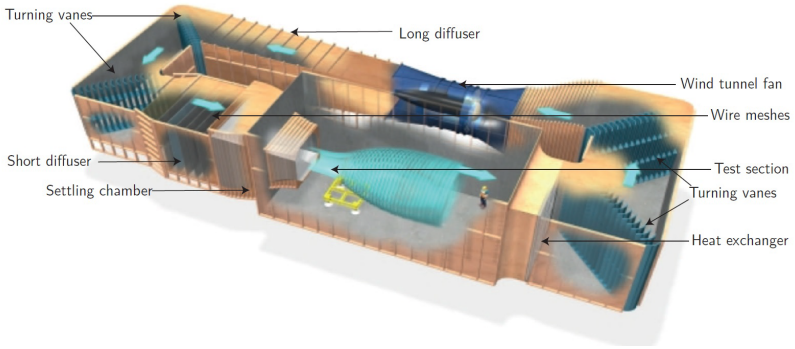

Figure 5.3: Schematic of Open Jet Facility (OJF) at TU Delft [10]

Figure 5.4: Octagonal Nozzle of OJF [1]

The dimensions of the test section dimensions are 6×6.5 m^2 and 11m in length in the inflow direction. Flow entering the test section is uniform flow with maximum turbulence intensity of 5% and remains steady till 3m after the nozzle. Turbulence intensity of the flow is less than 0.5% till 1m after the nozzle and less than 2% till 6m after the nozzle. The large test section of OJF allows for a bigger

testing model and smaller blockage effects. (OJF has less than 3% blockage effect at the nozzle)

5.3. SET-UP

Data for analysis are collected using both Particle Image Velocimetry (PIV) and hot-wire anemometry (HWA). In this section, set-ups for both of these are explained.

In order to fix the actuator disc model in the test section, a metal tower of 5cm diameter is used. The height and location of this OJF platform is adjusted such that the disc is at vertical centre of the wind-tunnel test section. The disc is not placed at horizontal centre of the test section as the camera set-up is not able to reach it.

5.3.1. PIV-SETUP

Figure 5.5 shows the set-up of PIV system for velocity measurement. As the figure shows, two sets of camera (*LaVision Imager pro LX 16M*) are used to capture flow field. These cameras have pixel pitch of $7.4\mu m/px$. Each camera has a field of view of 310 × 496 mm^2. Digital resolution for the measurements is 13.6px/mm. The cameras and the laser system are installed on a traverse system. This is done to ensure that cameras and the laser system will move equally in same direction when traverse system is moved. By doing so, PIV-system does not need to be calibrated every time it is moved to measure. Traverse system can move in two directions, 130cm in x-direction and 35cm in y-direction. For the experiment, PIV-system and traverse system are positioned such that it is only required to move in x-direction to measure phase-locked velocity measurements.

Laser system that is used to illuminate the tracer particles is low speed Quantal Evergreen Nd:YAG laser system. It has a pulse energy of 200mJ/pulse with maximum frequency of 15Hz and wavelength of 527nm. Using a combination of two spherical and one cylindrical lens, a thin sheet of 2.5mm thickness is obtained at the field of view.

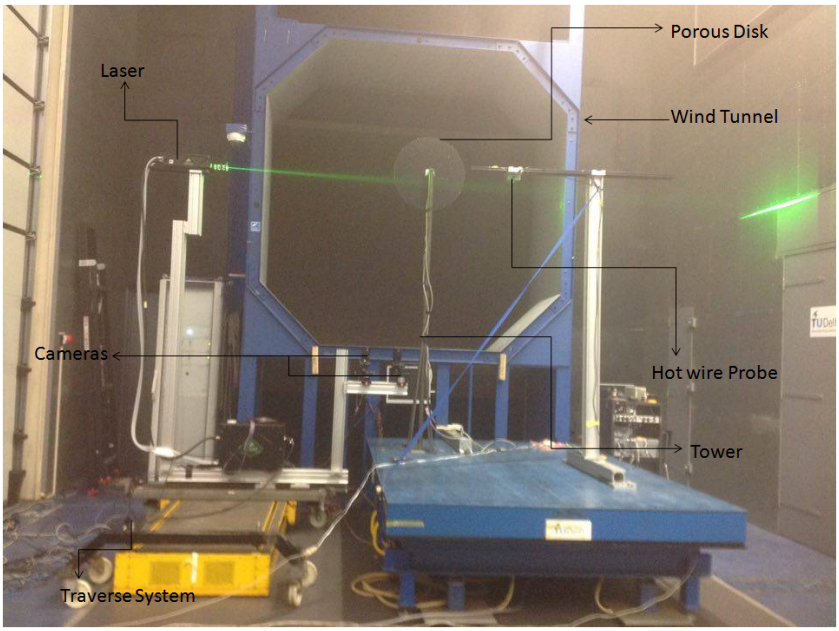

Figure 5.5: Set-up of the experiment showing PIV and hot-wire set-up

Figure 5.6 shows a schematic of complete set-up of the experiment:

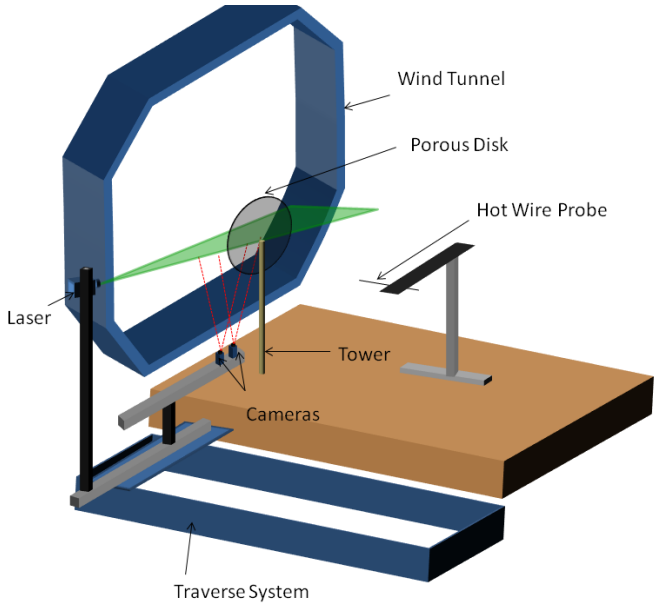

Figure 5.6: Schematic of experimental set-up

A SAFEX smoke generator is used to generate tracer particles. It uses SAFEX mix, which is dropped over an electrically heated plate and evaporates to create smoke. The particle density is controlled using a remote control in the control room.

Laser control and image acquisition are synchronized using a programmable transfer unit (PTU), trigger box and `DaVis`. A pulse, generated by a code to control porosity, is sent to the trigger box, which in turn sends signal to `DaVis` and then using the PTU, laser and images are synchronized. The time after which image is to be required is controlled using `DaVis`.

Load Measurement Device: In order to measure load on the disc with changing porosity, a load cell is attached directly to the disc as shown in Figure 5.7. Before using this load cell to measure loading on the disc, it is calibrated using known weights and voltage change in the strain gauge. Using this relationship between voltage and weight, force on the disc can be found.

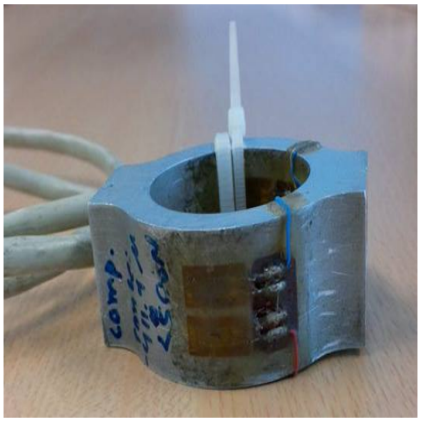

(a) Load cell used in the experiment

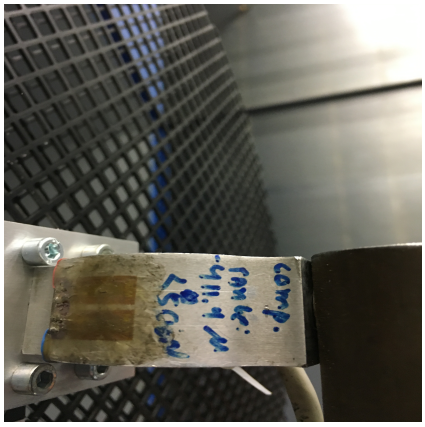

(b) Load cell and disc attachment

Figure 5.7: Load Cell attached to the porous disc

5.3.2. HOT-WIRE ANEMOMETRY SET-UP

The HWA set-up used in the experiment is explained in this section.

Calibration: Hot-wire probe needs to be calibrated before measurements. `TSI Model 1127 Manual Velocity Calibration` [1] (see Figure 5.8) is used to calibrate the probe. This calibrator consists of an exit nozzle which is connected to a settling chamber and then to a pressure vessel via a secondary nozzle. The calibrator comes with three different secondary nozzle sets. For the experiment, `Nozzle set 1` is used as it is optimum for velocity range of $1 m/s$ to $8 m/s$. (See section B.2 for theory behind HWA calibration.)

Figure 5.8: TSI Model 1127 Manual Velocity Calibrator

In order to calibrate the probe, flow speed at the nozzle is varied by manually changing the pres-

[1] http://www.tsi.com/products/_product-accessories/manual-velocity-calibrator-without-pressure-transducer-11 aspx

sure inside the pressure vessel. Pressure inside the pressure vessel is measured using a manometer. By measuring temperature using a thermocouple, flow speed at the nozzle is calculated using isentropic relations. This process is repeated 10 times to obtain a relationship between velocity and voltage variation across the probe as explained in section B.2

5.4. DESCRIPTION OF LOAD CASES

Experiment can be divided in terms of load cases studied as:

1. **Steady Load cases**: Here porosity is kept constant. Table 5.1 presents the table with test matrix for steady load measurements. As the table shows, for each steady load case, 70 images are collected per FOV and the measurement distance ranged from 0.5 rotor diameters upstream till 1 rotor diameter downstream.

Table 5.1: Test Matrix for Steady Cases

Load Case	Porosity [%]	number of images per FOV	Free-stream Velocity $[m/s]$	Upstream Distance [−]	Downstream Distance [−]
steady	64	70	6	0.5D	1D
	43.4	70	6	0.5D	1D
	29.7	70	6	0.5D	1D
	14.1	70	6	0.5D	1D

Figure 5.9 shows field of views captured with PIV for steady load cases. Windows in the figure represent field of views for the two different cameras used. The darker regions represent overlaps between the two cameras and also between two adjacent fields of views for a camera. The positions of these fields of view are controlled using traverse system controller.

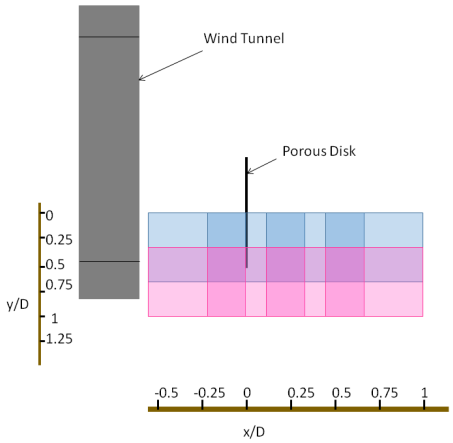

Figure 5.9: Measurement matrix for steady load cases

2. **Unsteady Load cases**: Here porosity is varied harmonically with three different frequencies and phase-locked velocity measurements are made. Table 5.2 presents the table with test matrix for unsteady loading measurements. The table shows that for each steady load case, 100

images are collected per FOV and the measurement distance ranged from 0.5 rotor diameters upstream till 2 rotor diameters downstream.

Table 5.2: Test Matrix for Unsteady Cases

Load Case	**Frequency** [Hz]	**Reduced Frequency** [−]	**Number Number of images per FOV**	**Free-stream Velocity** [m/s]	**Upstream Distance** [−]	**Downstream Distance** [−]
unsteady	5	1.57	100	6	0.5D	2D
cyclic	3	0.94	100	6	0.5D	2D
loading	1.5	0.47	100	6	0.5D	2D

Figure 5.10 shows field of views captured with PIV for unsteady load cases. The frequency of the load variation depends on the reduced frequency $\left(k = \frac{\omega \cdot D}{2V_0}\right)$. For an airfoil, k is larger than 0.05 for unsteady flow. However, no such data is available for discs, so different frequencies are tested during the experiment to see unsteadiness of the flow. Table 5.2 summarizes the load cases.

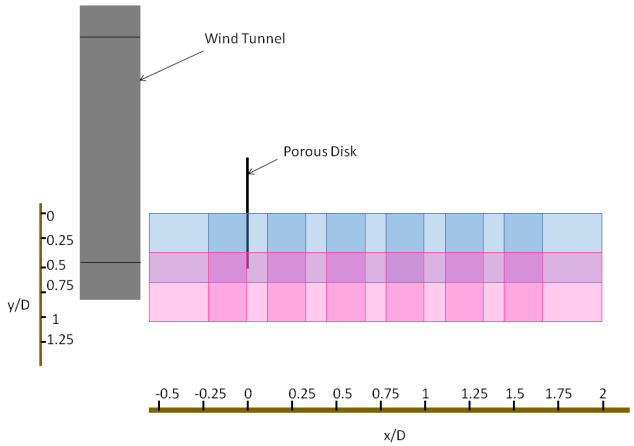

Figure 5.10: Measurement matrix for unsteady load cases

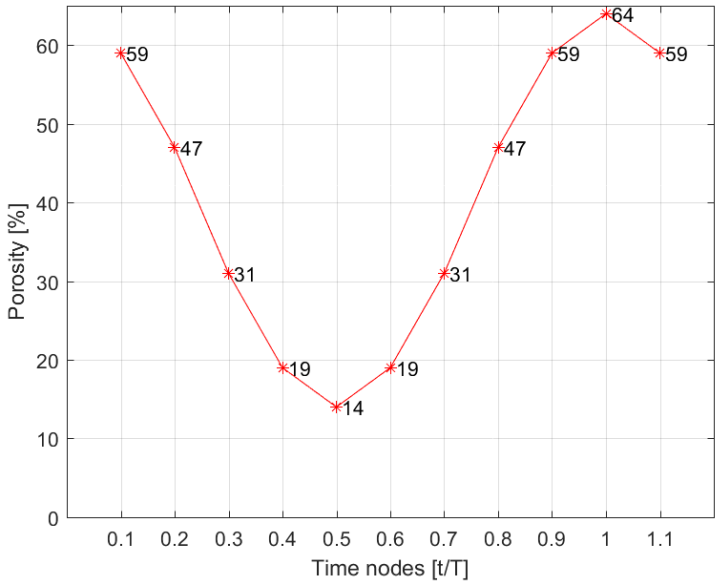

Figure 5.11: Disc porosity cycle for unsteady load cases

5.5. IMAGE PROCESSING

Images collected from the experiment are processed using `DaVis 8.0`. Table 5.3 shows the parameters used for PIV. Image post processing involves the following steps:

- First step is to select the images to process and create geometrical mask over the disc and reflections from the laser.
- Subtracting average minimum: There are different settings in `DaVis 8.0` to remove background noise from raw images. For the experiment, average minimum of raw images set is subtracted from the raw images.
- Cross-Correlation: Next step is cross-correlating the images. This process is explained in section A.4. For this project, sequential cross correlation is used. The interrogation window size used for it is 24×24 $pixels$ with overlap ratio of 50%. After this median filter is applied to delete artificial velocity vectors.
- The final step is to stitch images from all the FOV to get the full wake.

Table 5.3: PIV parameters and image processing settings

Parameters	Value
Field of View per camera	310×496 mm^2
Ensemble size (images)	70 (steady), 100 (unsteady)
Digital Resolution	13.6 px/mm
Type of image processing	Sequential cross-correlation
Overlap	50%
Interrogation window size (pixels)	24×24 px^2

5.5.1. ERROR IN CAMERA POSITIONING

As stated before, velocity field upstream and downstream of the AD is scanned by moving the camera set-up with the traverse system. As this system has a low uncertainty of 2mm, the fields are first stitched together using the distance moved and the averaged over the overlapping regions.

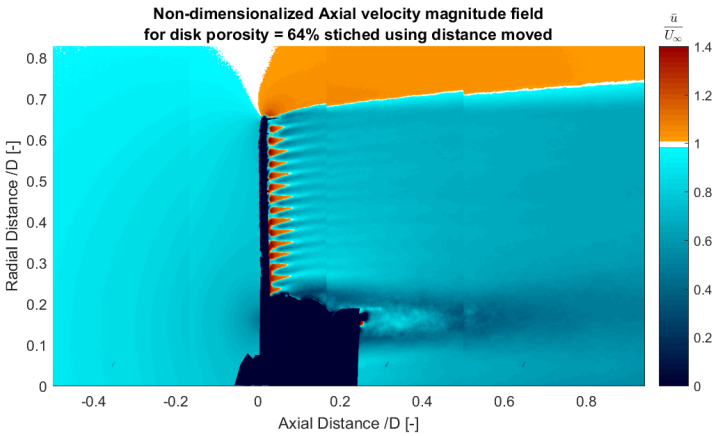

Figure 5.12: Normalized axial velocity field stitched together using distance moved with the traverse system

Figure 5.12 shows the velocity fields stitched together using distance moved with the transverse system. The figure show that there are discontinuities at the joints, so the fields are stitched again using correlation at the overlap region (see Figure 5.13). The figure shows that the discontinuity at the joint area is reduced, however some discontinuity is still present.

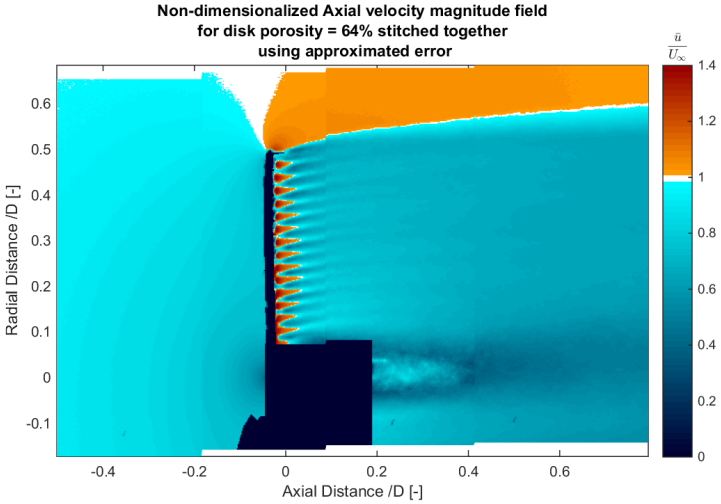

Figure 5.13: Normalized axial velocity field stitched together using correlation of the fields in the overlap region

6

Actuator Disc under Steady Loading

In this chapter, actuator disc is analysed for four different steady load cases. At first, loading on the disc is determined. This is followed by evaluating phase-locked velocity and vorticity fields for these load cases. The chapter ends with the analysis of results from the Vortex Ring (VR) model, discussed in section 4.3.

After the experiment, it was found that data from the camera 2 was lost, so data from only camera 1 is used for all the analysis. Figure 6.1 shows the FOV used.

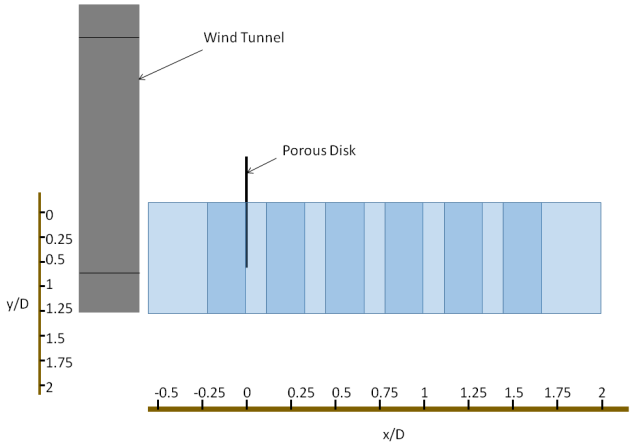

Figure 6.1: Overview of final field of view for PIV

6.1. Load Determination from Flow Field

In this section, for different disc porosities, load is estimated from the obtained flow field. It is calculated using two different methods and then solutions are compared.

6.1.1. 1D Actuator Disc Momentum-model Approximation

At first, load on the disc is estimated using 1D Actuator disc momentum-model, used by Lignarolo *et al.* [4]. The model is given by Equation 6.1-Equation 6.3:

$$A = \pi \left(R_{tip}^2 - R_{root}^2 \right) \tag{6.1}$$

$$a = \frac{\pi}{A} \int_{R_{root}}^{R_{tip}} \left[1 - \frac{u(x)}{U_\infty} \right] \cdot r\, dr \tag{6.2}$$

$$C_t = 4a(1-a) \tag{6.3}$$

As the data at x/D = 0 is not available due to the reflections, equation Equation 6.2 for velocity profile in the wake at x/D = 1 is used.

Table 6.1 shows the estimated thrust coefficient for different porosity values. The table shows that when the disc has maximum porosity, thrust coefficient is minimum and vice-verse. This is also found in the past experiments reviewed in section 2.4.

Table 6.1: Thrust Coefficients calculated using 1D Actuator disc momentum-model approximation

Porosity [%]	Thrust Coefficient [-]
64%	0.5581
43.40%	0.6290
29.70%	0.7195
14%	0.7545

According to this model, thrust coefficient for this porous disc ranges from 0.558 to 0.755. The range is different from the experiment done with the same porous disc model used in [1]. This can arise from many differences, few of which are listed below:

- **Different load estimation techniques**: Hong [1] used a load cell to determine load on the disc. Although load cell was used in this experiment as well, it was found that the data from the load cell cannot be used as set-up needed to be dismounted due to change of motors, but load cell was not calibrated again.

- **Differences in Experimental set-up**: Few parts of the set-up were different such as the tower, the actuating motor and tower fixation in the middle to reduce tower vibrations.

  The 1D actuator disc model assumes steady, incompressible, one directional, inviscid flow and uniform loading on the disc. However, in reality, these assumptions are not true. So the results from this method cannot be accurate enough to draw strong conclusions, hence another method described in Appendix C is used to estimate load from the velocity profile.

6.1.2. FLOW MOMENTUM INTEGRATION

In this section, load on the disc is estimated using momentum integration of the flow field as described in section C.1. Steps to calculate thrust coefficient are as follows:

1. **Pressure Estimation**: First step is to calculate static pressure field from the flow field. Pressure field is calculated using Poisson Integration explained in Appendix C [22]. In order to estimate pressure distribution, axial velocity field, radial velocity field, boundary conditions, mask over the disc reflection region and rate of change velocity over time (du/dt and dv/dt) are required.

   As the flow is steady in this case, $\frac{du}{dt}$ and $\frac{dv}{dt}$ are zero. The boundary conditions are calculated from the Bernoulli equation. The pressure is estimated using Poisson integration. (see subsection C.2.1)

   Figures 6.2 shows the normalized pressure distribution for the steady load cases. The figures show that at upstream position of the disc, pressure coefficient is positive. This means that the pressure is higher than the free-stream pressure. As the flow approaches the disc, pressure increases. After the disc, the pressure coefficient is calculated to be negative. This indicates that the pressure after the disc is lower than the free-stream pressure. Past the disc, pressure is minimal near the disc, where the velocity jump takes place. Along the radial direction, the pressure is increasing towards the inner-wake edge. This results from the velocity distribution (discussed in the next section). The figures show that the pressure is increasing after the pressure jump across the disc but does not fully recover for any of the cases. It is increasing as the wake is expanding (see next section).

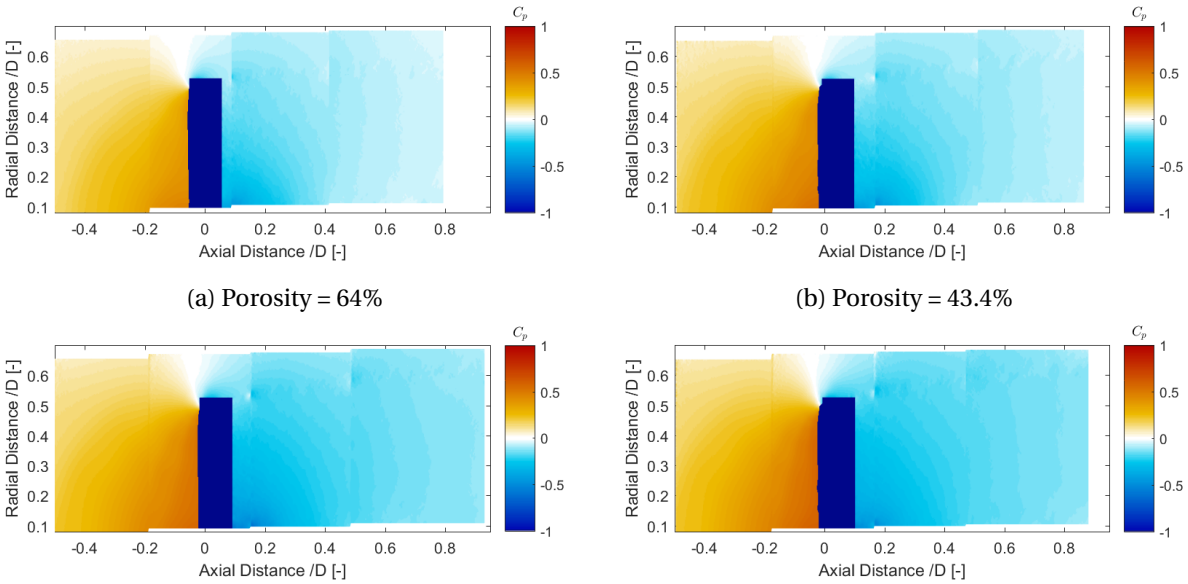

(a) Porosity = 64%

(b) Porosity = 43.4%

(c) Porosity = 29.7%

(d) Porosity = 14%

Figure 6.2: Pressure distribution at the disc for steady load cases

Figures 6.3 show pressure jump across the disc for all the steady load cases. The figures display the pressure distribution from r/D = 0.1 to r/D = 0.5. Near the disc due to reflection, velocity data is unknown, so pressure cannot be found. As the figures show, pressure upstream and downstream the disc both reach free-stream while approaching r/D = 0.5. It was mentioned earlier that it is assumed that the disc is uniformly loaded. However, it is not completely true as the figure shows, there is a gradient in pressure distribution in the radial direction. This is mainly due to gradient of velocity.

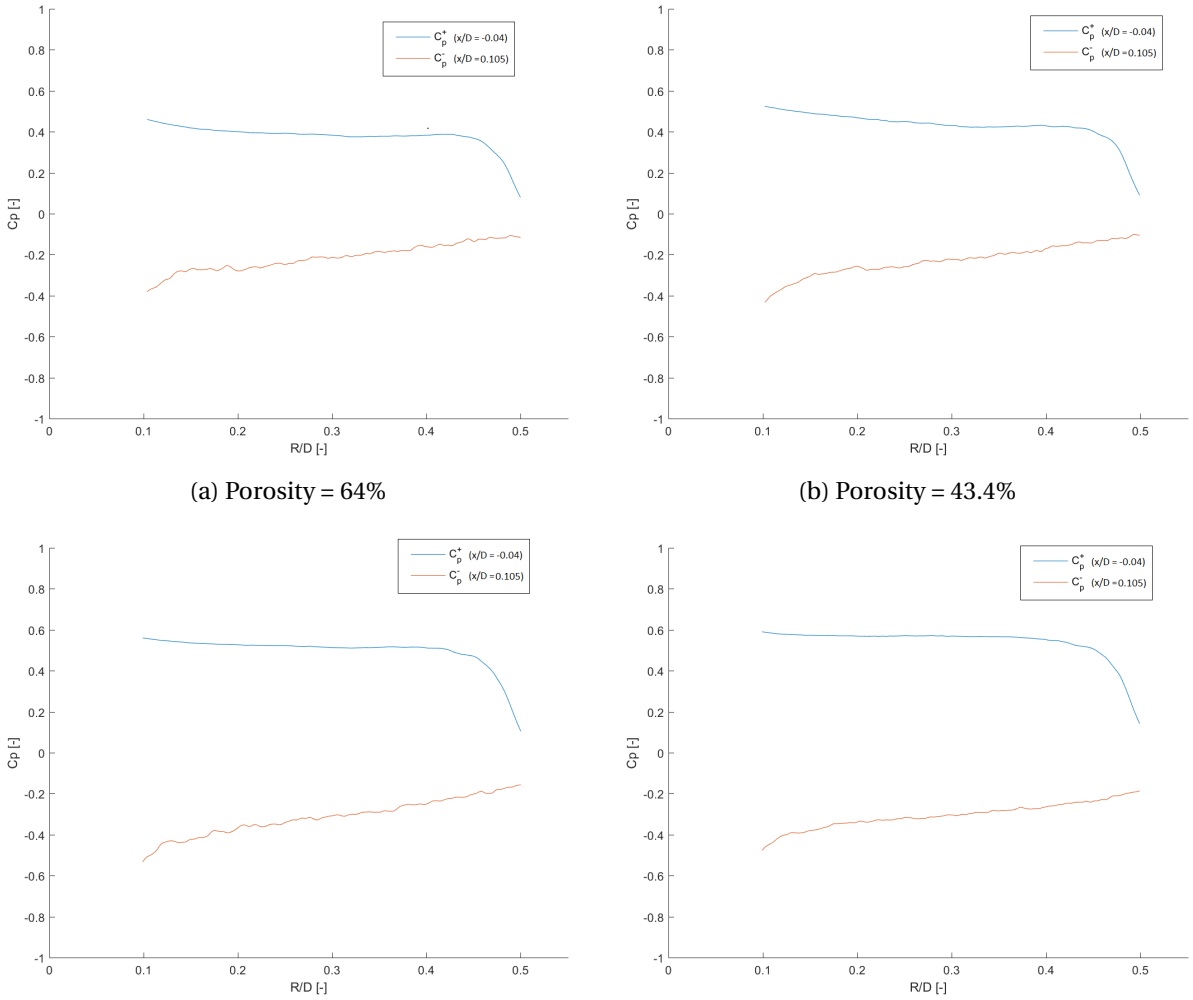

(a) Porosity = 64%

(b) Porosity = 43.4%

(c) Porosity = 29.7%

(d) Porosity = 14%

Figure 6.3: Pressure distribution along the upwind and the downwind surface of disc for steady load cases

Figures 6.4 show the stream-wise development of pressure across the disc. Similar to figures 6.3, it can be seen that the pressure jump is maximum near the hub and decreases with increasing radial distance. Figures also show that for the same axial position, the pressure distribution is not uniform. Hence, the disc is not uniformly loaded which is assumed to be so in the AD model.

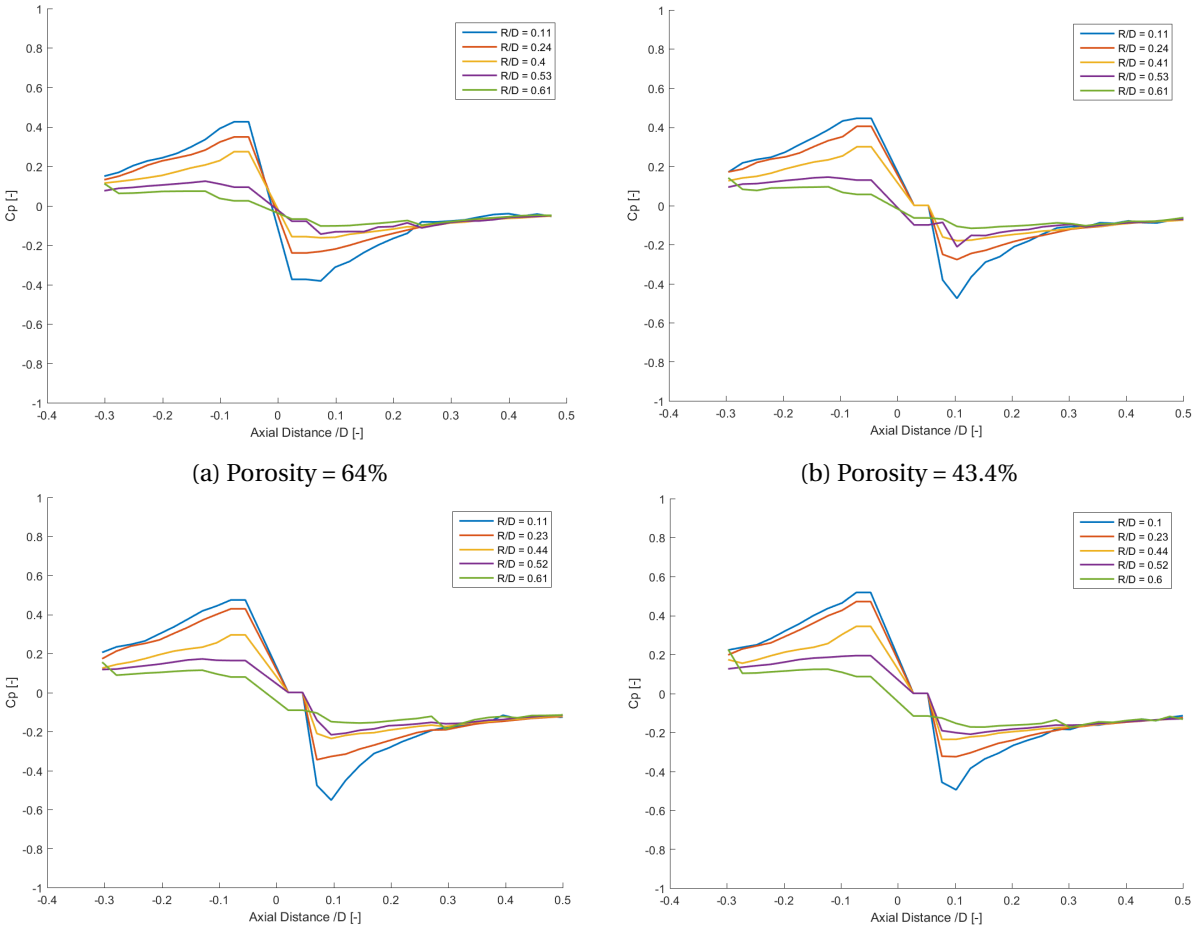

(a) Porosity = 64%

(b) Porosity = 43.4%

(c) Porosity = 29.7%

(d) Porosity = 14%

Figure 6.4: Stream-wise development of pressure across the disc for steady load cases

2. **Momentum Integration**: Second step in calculating load on the disc is momentum integration of the flow field. It is done using Equation 6.4.

$$\begin{bmatrix} F_x \\ F_y \end{bmatrix} = -\int\int \rho \begin{bmatrix} uu & uv \\ uv & vv \end{bmatrix} \cdot \vec{n} ds - \int \begin{bmatrix} p & 0 \\ 0 & p \end{bmatrix} \cdot \vec{n} ds \tag{6.4}$$

As stated in Appendix C, if boundary contour is taken to be big enough and far from the disc, viscous terms in Equation C.8 can be neglected.

3. Steps 1-2 are repeated for all 4 porosity values. The figures show that the general trends for pressure are similar. It can be noted that with decreasing porosity, pressure jump increases. This coincides with the fact that the velocity jump across the disc also increases with decreasing porosity as discussed in the next section.

Table 6.2 shows the results for thrust coefficients calculated for different porosity using momentum integration of the flow field. For porosity of 64%-14%, C_T ranges from 0.55 to 0.81. Similar to the

results from 1D actuator disc model and past experiments, load over the disc increases with decreasing porosity.

Table 6.2: Thrust Coefficients calculated using flow momentum integration

Porosity [%]	Thrust Coefficient [-]
64%	0.5545
43.40%	0.6117
29.70%	0.7599
14%	0.8073

6.1.3. COMPARISON

Figure 6.5 and Figure 6.6 show the results for load calculated using 1D Actuator disc momentum-model approximation and momentum integration of the flow field. As the figures show, the load calculated using the 1D actuator disc model is higher than that calculated using momentum integration for the first two porosities. For the two lowest porosity cases, 1D AD model predicts lower thrust coefficient values than that from the momentum integration method. The main reasons for the difference between calculations from the AD model and momentum integration are that for 1D actuator disc model velocity at the disc location is required which is not available and also the flow assumptions made in the AD model such as uniformly loaded disc, in-viscid flow, etc. are not true.

The figure shows that as porosity increases, difference between the two methods decreases and the trend is not linear. It is likely due to the fact that with increasing C_T, velocity jump across the disc increases and hence downstream distance for flow to reach minimum before it starts to recover increases (see section 6.2). As discussed in section 2.1, velocity used (u_1) in Equation 2.18 has to be at location infinitely far downstream of the rotor, but this was not the case for these velocity fields.

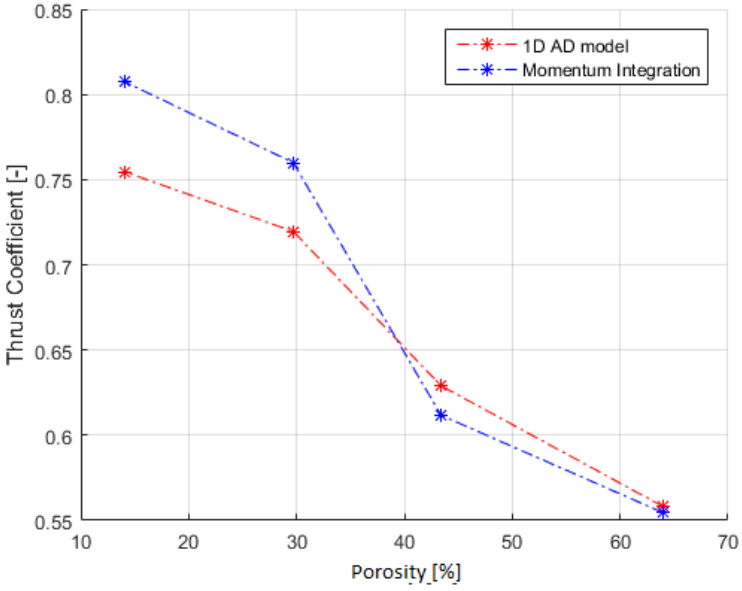

Figure 6.5: Thrust coefficient Vs. porosity for 1D Actuator disc momentum-model approximation and momentum integration of the flow field

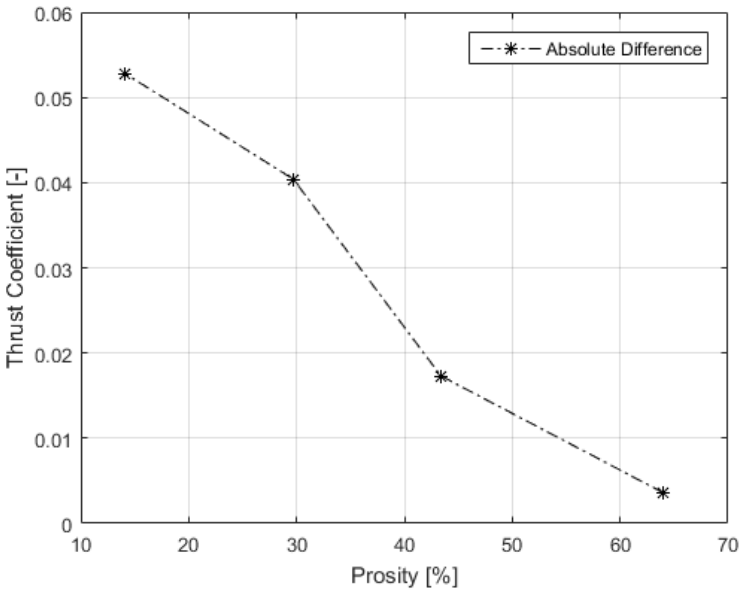

Figure 6.6: Difference between thrust coefficients calculated using 1D Actuator disc momentum-model approximation and momentum integration of the flow field

6.2. VELOCITY AND VORTICITY FIELDS FOR DIFFERENT DISC LOADING

In this section, velocity and vorticity fields obtained from the experiment are discussed for four different steady load cases.

6.2.1. DISC POROSITY = 64% AND THRUST COEFFICIENT = 0.555

Figure 6.7,Figure 6.8 and Figure 6.9 show the velocity fields and vorticity field for the maximum disc porosity, i.e., 64% and minimum load, C_T = 0.56. The figures show that axial velocity decreases as the flow approaches the disc. This is similar to the actuator disc theory as discussed in chapter 6. Downstream the disc, the velocity profile is non-uniform. The velocity at $y/D = 0$ downstream the disc is lower than the velocity at the other radial positions for the same axial position. This higher reduction in the velocity field directly behind the disc hub is due to the tower-shadow effect.

The figure also shows that the increase in velocity towards $y/D = 0.5$. This is due to tip vorticity and expansion of the wake. The effect of the disc mesh on the velocity just behind the disc is also shown. The velocity just behind the disc is discontinuous. This discontinuous velocity field disappears around x/D = 0.1. The axial velocity behind the disc decreases with the downstream distance. So no velocity recovery can be seen till the downstream distance of $x/D = 1$. However, from Figure 6.19a, it can be seen that the rate of decrease of velocity is decreasing, which means that the velocity field can be expected to reach a global minimum at some point in the downstream distance and then starts recovering as discussed in chapter 6.

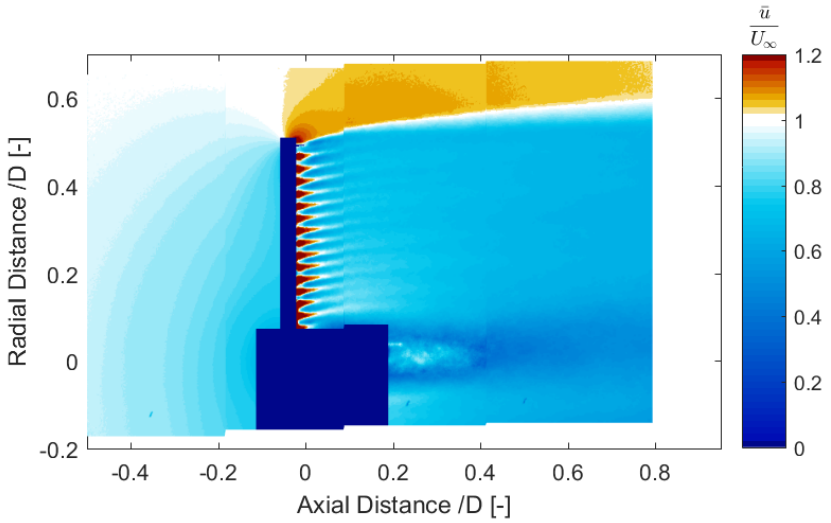

Figure 6.7: Normalized Axial Velocity field for AD under steady loading for maximum porosity of 64% and Thrust coefficient = 0.555

Figure 6.8 shows the normalized radial velocity field around the disc with C_T of 0.56. Positive direction in the velocity indicates outward movement of the flow towards the free-stream, while the negative direction implies movement toward the nacelle. The velocity in the radial direction is much smaller than the axial velocity. The radial velocity is positive everywhere in the field except the region directly affected by the tower and the hub of the disc. The direct effect of the disc mesh can also be seen on the radial velocity in the wake just behind the disc. It can also be seen that the radial velocity increases near the disc edge, indicating outward movement of the flow near the disc edge.

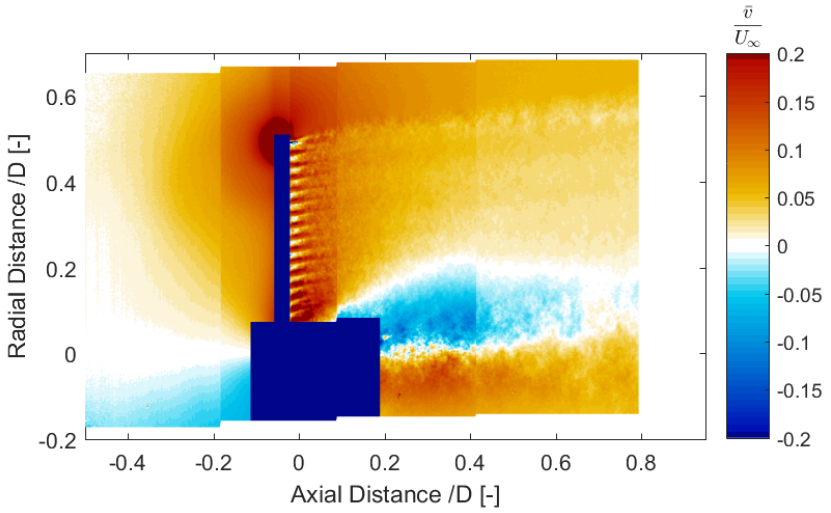

Figure 6.8: Normalized Radial Velocity field for AD under steady loading for maximum porosity of 64% and Thrust coefficient = 0.555

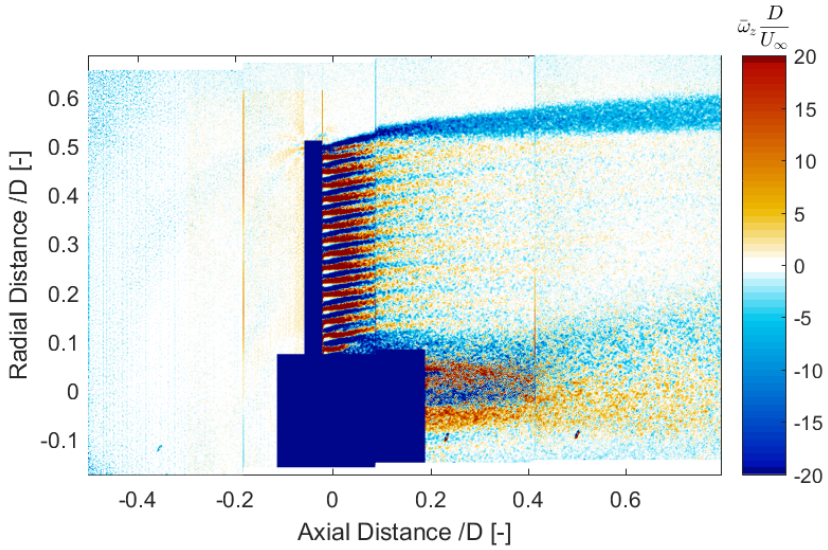

Figure 6.9: Normalized Vorticity fields fir AD under steady loading for maximum porosity of 64% and Thrust coefficient = 0.555

Figure 6.9 shows the normalized vorticity field for the maximum disc porosity and $C_T = 0.56$. The figures show a strong positive and negative vorticity originating from porosity of the disc. The positive vorticity dissipates around $x/D = 0.3$, leaving the field with only negative vorticity. It can also been seen that other two regions of the strong vorticity are the regions behind the disc hub and region around $y/D = 0.5$. The vorticity behind the disc hub is mainly negative. The figures show that there is concentrated sheet of negative vorticity around the disc edge, which expands and decreases in strength. Around $x/D = 0.2$, the sheet diffuses into a broader region and by $x/D = 0.8$, the absolute strength of the sheet has decreased from $\omega \frac{D}{U_\infty} \geqslant 50$ to $\omega \frac{D}{U_\infty} \leqslant 10$.

6.2.2. DISC POROSITY = 43.4% AND THRUST COEFFICIENT = 0.612

Figure 6.10-Figure 6.12 show the normalized velocity fields and vorticity field for the AD with porosity of 43.4% and $C_T = 0.61$. Velocity field outside the inner wake has velocity higher than the free-stream velocity and inside the inner wake, it is lower than the free-stream velocity. Although trends are similar to the results for the AD with $C_T = 0.56$, the velocity jump across the disc, wake expansion, etc. are different.

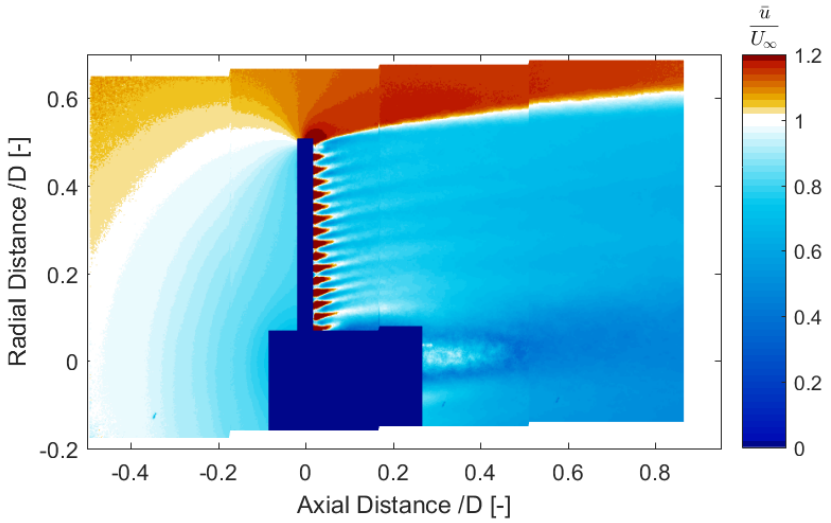

Figure 6.10: Normalized Axial Velocity field for AD under steady loading for porosity of 43.4% and Thrust coefficient = 0.612

Figure 6.11 shows the radial velocity field for the disc porosity of 43.4% with thrust coefficient = 0.612. The figure shows that like the previous load case, the radial velocity increases near the disc edge. Also, effects of the disc hub and tower can also be seen.

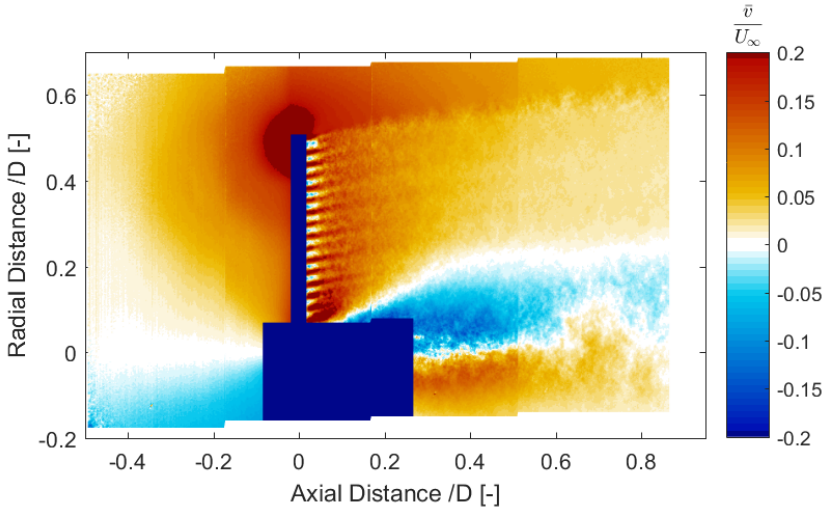

Figure 6.11: Normalized Radial Velocity field for AD under steady loading for porosity of 43.4% and Thrust coefficient = 0.612

Figure 6.12 shows the normalized vorticity field for disc porosity of 43.4% and C_T = 0.61. By comparing the two cases, it can be noted that for the higher load, dissipation takes longer downstream distance.

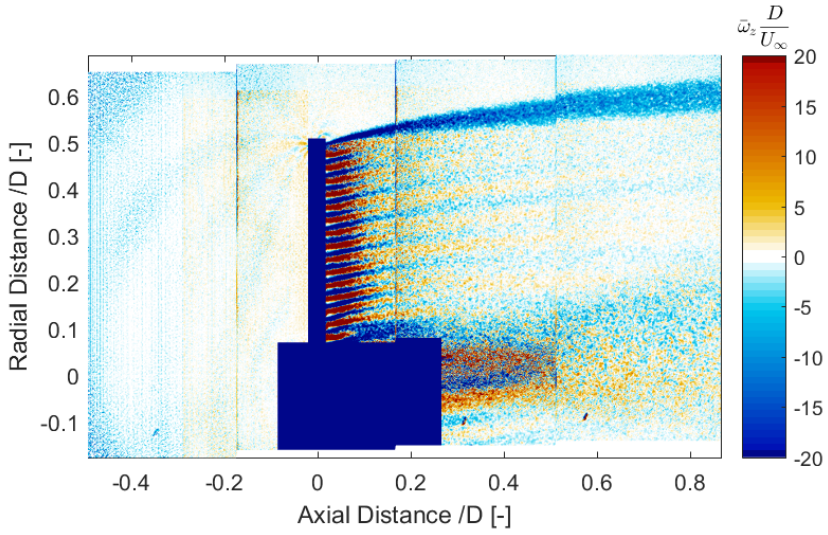

Figure 6.12: Normalized Vorticity fields fir AD under steady loading for porosity of 43.4% and thrust coefficient = 0.612.

6.2.3. DISC POROSITY = 29.7% AND THRUST COEFFICIENT = 0.76

Figure 6.13 shows the normalized axial velocity field for C_T = 0.76. The figure shows that the axial velocity is decreasing with downstream distance. It also shows the discontinuity in the axial velocity behind the disc due to the mesh of the disc. The effect of the disc hub can also be seen as the velocity induction in the region behind the hub is maximum. However, these two effects quickly dissipate. The figure also shows that the wake is expanding with downstream distance.

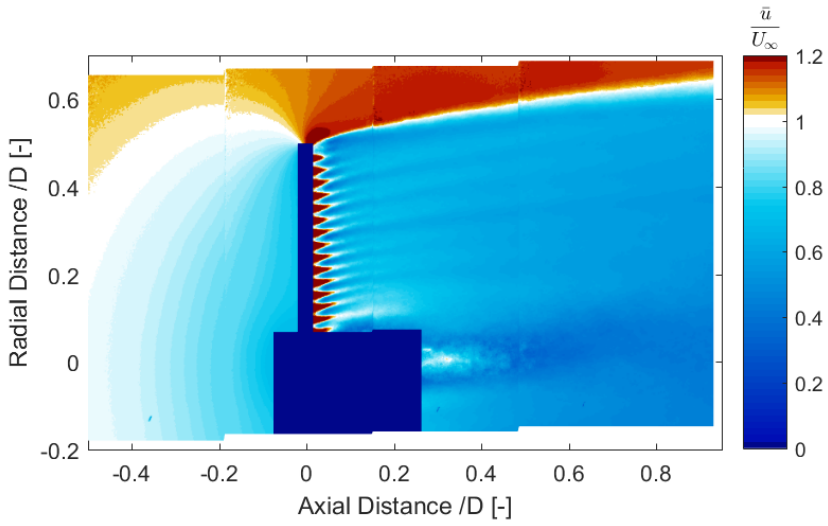

Figure 6.13: Normalized Axial Velocity field for AD under steady loading for porosity of 29.7% and thrust coefficient = 0.76

Figure 6.14 shows the normalized radial velocity field for thrust coefficient = 0.76. Due to the expanding wake, radial velocity is mainly positive in the wake exception being the region behind the disc hub.

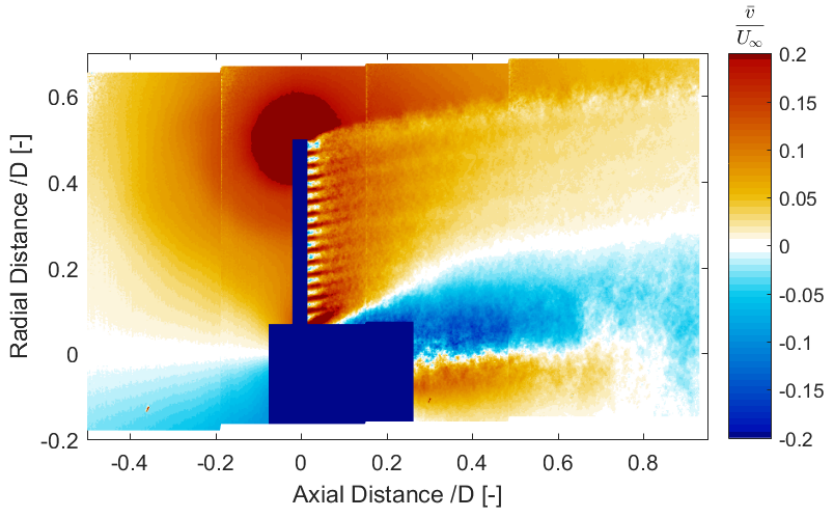

Figure 6.14: Normalized Radial Velocity field for AD under steady loading for porosity of 29.7% and thrust coefficient of 0.76 and thrust coefficient = 0.76

Figure 6.15 displays the normalized vorticity field for thrust coefficient = 0.76. The figure shows the region in blue shades where vorticity is negative. It is shown that as the wake expands, the strength of vorticity decreases. This is due to dissipation of vorticity.

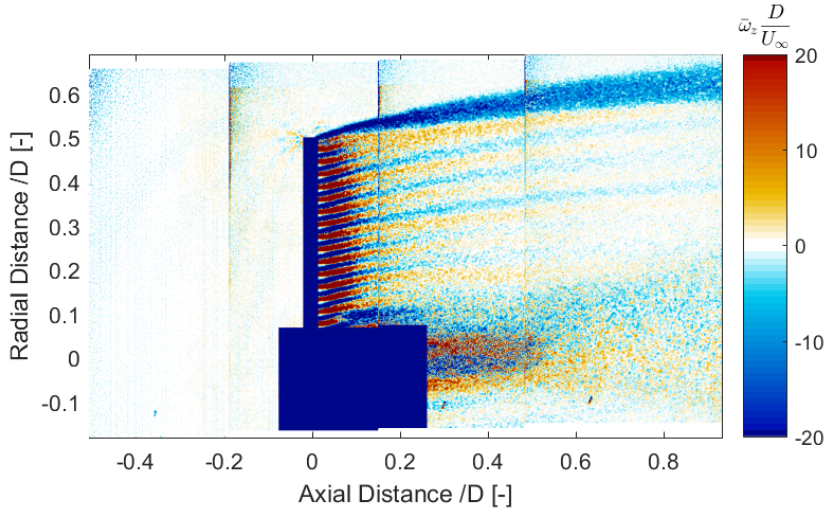

Figure 6.15: Normalized Vorticity fields fir AD under steady loading for porosity of 29.7% and thrust coefficient of 0.76 and thrust coefficient = 0.76

6.2.4. DISC POROSITY = 14% AND THRUST COEFFICIENT = 0.807

The normalized axial velocity field for thrust coefficient = 0.807 is shown in Figure 6.16. The velocity decreases as the flow advances towards the disc. Across the disc, there is a velocity induction. This is because of kinetic energy dissipation across the disc. Effect of the mesh of the disc and disc hub is noticed for this case as well.

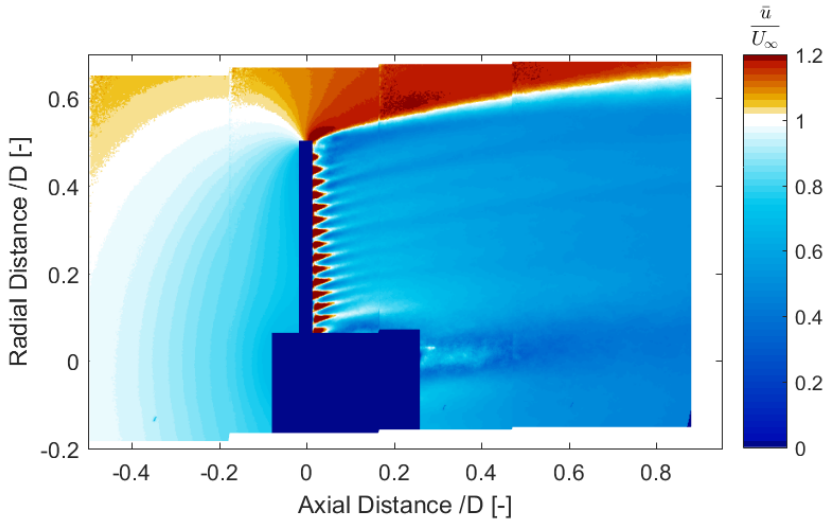

Figure 6.16: Normalized Axial Velocity field for AD under steady loading for minimum porosity of 14% and thrust coefficient = 0.807

The normalized radial velocity field for thrust coefficient = 0.807 is shown in Figure 6.17. The radial velocity increases towards the disc as the flow moves outwards towards the free-stream due to presence of the disc. Region behind the hub has a negative radial velocity.

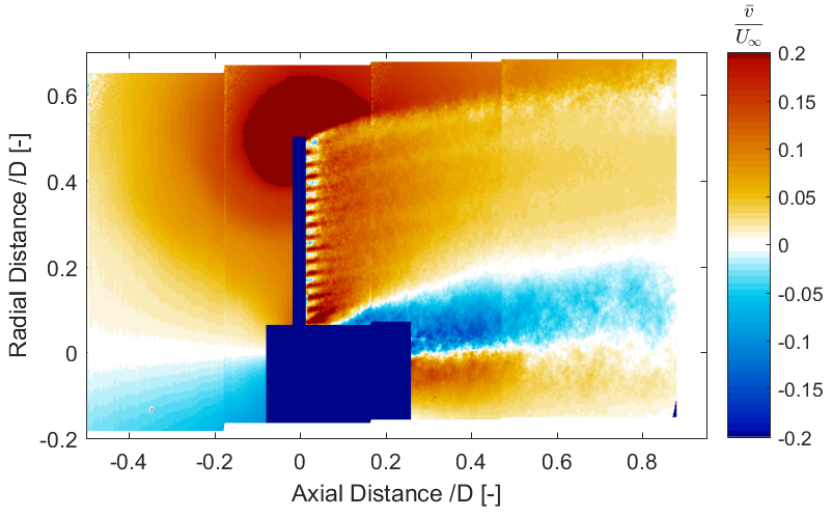

Figure 6.17: Normalized Radial Velocity field for AD under steady loading for minimum porosity of 141% and thrust coefficient = 0.807

The normalized vorticity field for thrust coefficient = 0.807 is shown in Figure 6.18. The regions of strong vorticity are wake edge, behind the disc and behind the disc hub. It can be explained by strong velocity gradient in these regions.

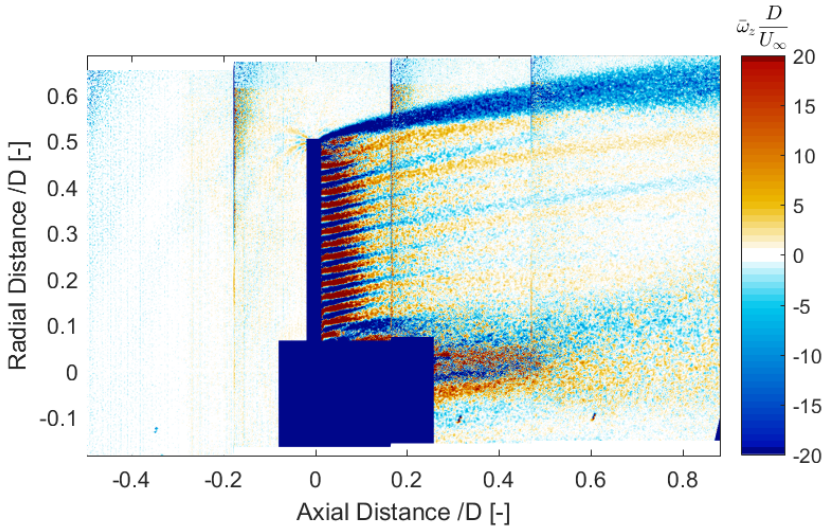

Figure 6.18: Normalized Vorticity fields fir AD under steady loading for minimum porosity of 14% and thrust coefficient = 0.807

6.2.5. COMPARISON OF VELOCITY FIELDS FOR DIFFERENT LOAD CASES

By comparing all the fields, following salient points can be made:

1. **Axial Velocity**: Figures 6.19 show the radial variation of the normalized axial velocity for different axial positions. As the figure shows, for all load cases, the normalized axial velocity behind the disc is lower than the free-stream velocity. It approaches V_∞ while reaching towards the radial position of 0.5 rotor diameters (i.e. the disc tip).

   The figures show that as the axial position increases, the normalized axial velocity decreases. This means that the velocity has not started recovering yet. However, it can also be noticed that the rate of decrease of velocity over increasing the downstream axial position also decreases. From this figure, it can be inferred that at a certain point at the downstream axial position, velocity can be expected to reach its global minimum and starts recovering.

   According to the normalized axial velocity plots, as the load increases, the velocity induction also increases. This means that with increasing load, more kinetic energy is dissipated by the disc. However, for C_T = 0.56 and C_T = 0.61, there not much difference between the velocity induction. On contrary, near the disc (until x/D = 0.5), there are regions where C_T = 0.61 has higher velocity than C_T = 0.56. This is caused by the mesh of the disc and hub. However, average induction over the disk for C_T = 0.56 is lower than that for C_T = 0.61. According to [1], as loading on the disc increases, the rate of velocity change over the axial distance increases due to higher momentum exchange. However, from Figure 6.19, no such conclusions can be made. Although rate of velocity change decreases for all the load cases, but the rate of change in velocity profiles are not very different from each other for all the load cases. This is possibly because the flow is yet to reach the recovery point, so that the its recovery locations can be compared.

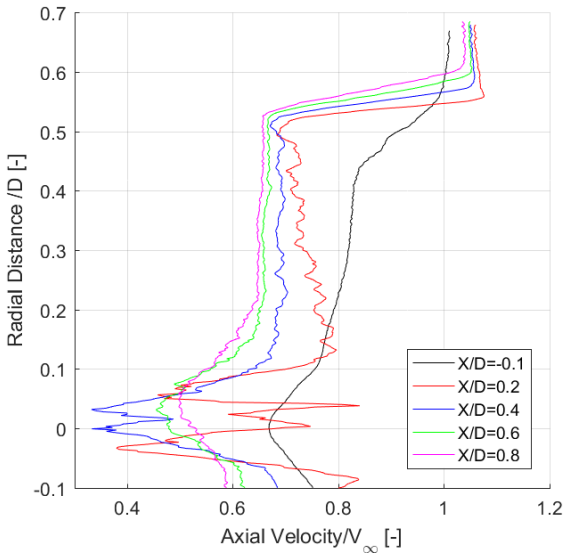

(a) Porosity = 64% and thrust coefficient = 0.555.

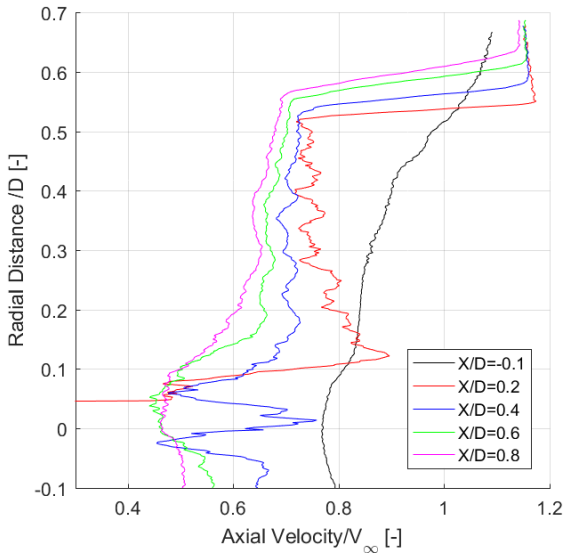

(b) Porosity = 43.4% and thrust coefficient = 0.612.

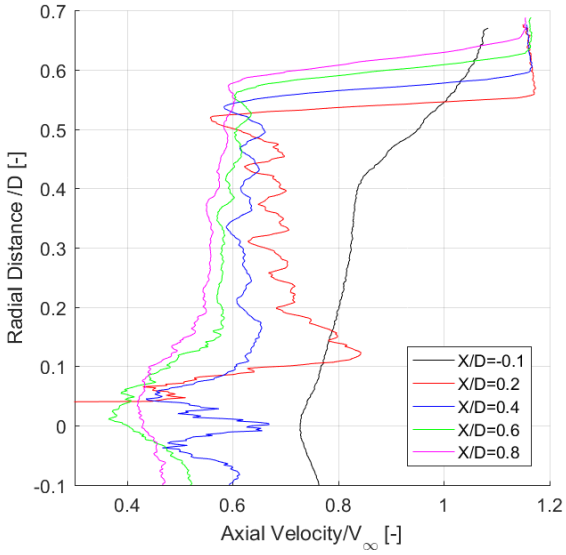

(c) Porosity = 29.7% and thrust coefficient = 0.76.

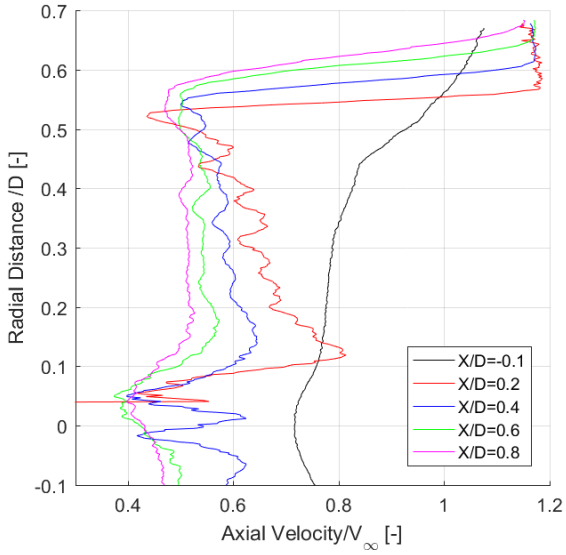

(d) Porosity = 14% and thrust coefficient = 0.807.

Figure 6.19: Radial variations of normalized axial velocity for different axial positions

2. **Radial Velocity**: Figures 6.20 show the radial variation of the normalized radial velocity for different downstream axial positions. As the figure shows, jump in the radial velocity is quite small for all load cases. However, it can be observed, that unlike axial velocity, jump of the radial velocities is higher for the lower loading. This is likely cause due to a higher wake expansion for higher load. Thus, with increased expansion, flow field is directed towards the positive radial positions, hence increase in the radial velocity. However, it should be noted that the difference is small.

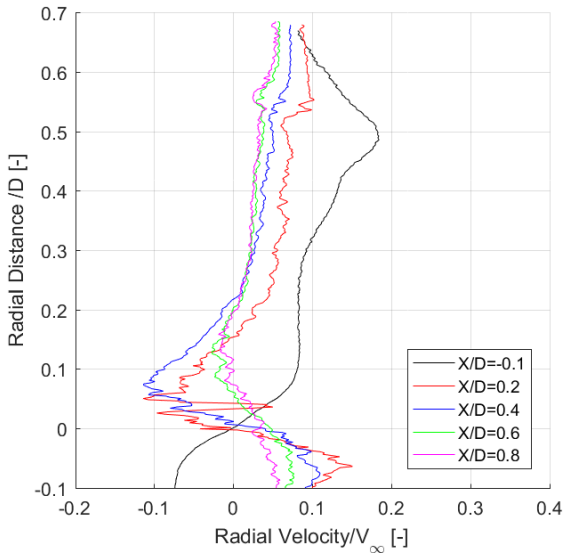

(a) Porosity = 64% and thrust coefficient = 0.555.

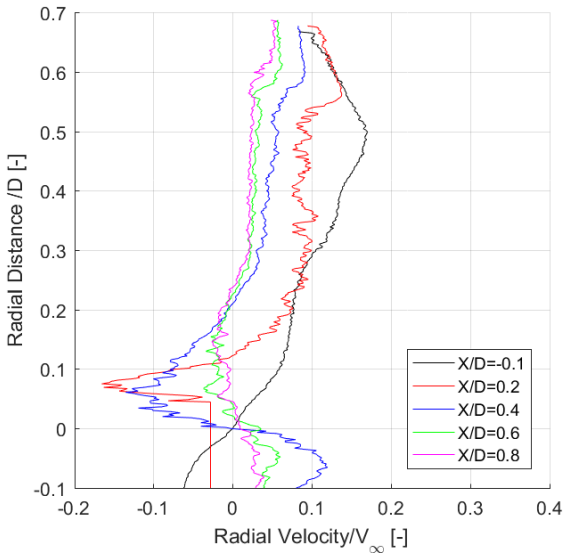

(b) Porosity = 43.4% and thrust coefficient = 0.612.

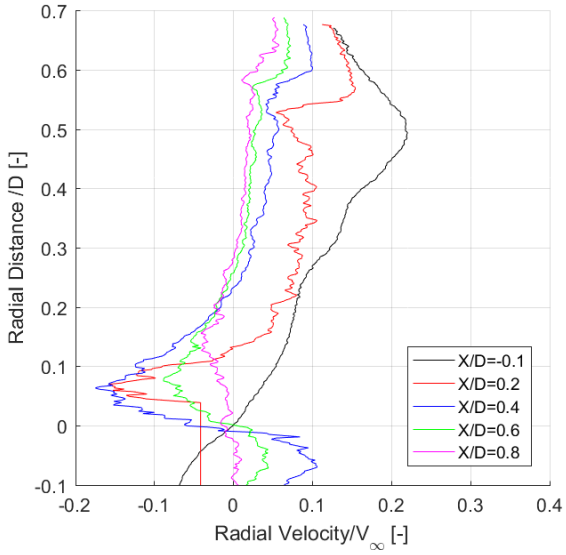

(c) Porosity = 29.7% and thrust coefficient = 0.76.

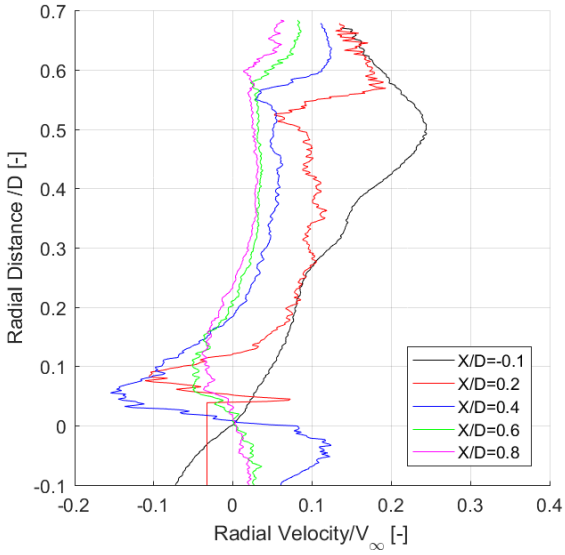

(d) Porosity = 14% and thrust coefficient = 0.807.

Figure 6.20: Radial variations of normalized radial velocity for different axial positions

3. **Wake Expansion**: Figures 6.21 show the field expansion for the four different load cases. As shown in the figures, for lower load on the disc, expansion of the field decreases. This result is also consistent with the past experiments (section 2.4) as with increasing porosity, thrust coefficient is decreased and less kinetic energy is dissipated by the AD, resulting in a smaller wake expansion.

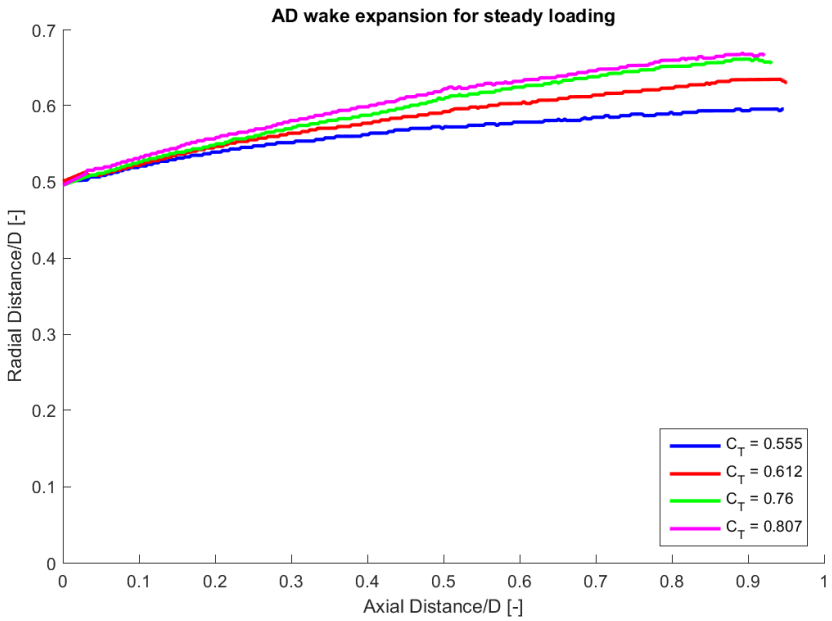

Figure 6.21: AD wake expansion for steady load cases. The curves represent the points where the velocity is equal to the free-stream velocity

6.3. VORTEX RING SOLUTION OF THE FLOW FIELD USING EXPERIMENTAL DATA

In this section, velocity solutions from the Vortex Ring model described in section 4.3 are analysed and compared to the experimental results. In order to do so, strength of the wake is required. There are two ways to estimate it:

1. **Free Wake Vortex Ring model**: This is the method used by Hong [1], Yu *et al.* [27]. Strength of the wake is calculated based on thrust coefficient using Equation 4.16. Position of the Vortex Ring is estimated for each time step and velocity field is estimated using strength and position of these vortex rings using Equation 4.17 and Equation 4.18.

2. **Prescribed Wake Vortex Ring model**: Load data was not available at first, so the FWVR model could not be used for this project, instead Prescribed Wake Vortex Ring (VR) Method is used. In this method, instead of estimating wake strength from thrust coefficient, it is estimated using vorticity near the inner-wake edge. Vorticity near the inner-wake edge is estimated from the experimental results. Hence, the wake expansion is already prescribed. Therefore, only velocity field calculations can be validated for this method. For far wake region, a mean value of vorticity around x/D = 0.8 - 1 (for unsteady load cases, x/D = 1.8 - 2) is used as shown in Figure 6.22. This is done as the vorticity near the wake edge is the most important as it takes longest to dissipate but data is not collected after x/D = 1 for steady load cases (x/D = 2 for unsteady load cases). As shown in the previous section, vorticity in the other regions dissipate quickly, so its influence is assumed to be not as strong as the vorticity near the wake boundary.

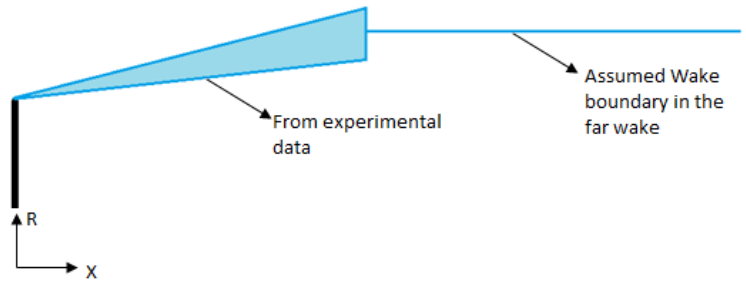

Figure 6.22: Wake expansion for Prescribed Wake Vortex Ring model

The figure shows that the wake boundary up to x/D = 1 is estimated using inner-wake edge from the experimental data. After that point as velocity data is not available, wake is assumed to stop expanding and mean value of vorticity between point x/D = 0.8 and 1 is used to estimate wake strength after x/D = 1. This is done to take the effect of vorticity after that point and also assuming that after a certain point, wake recovers and does not expand any-more. The flow fields in the previous section show that for neither of the load cases, wake has fully recovered, so the wake will still be expanding after x/D = 1. Hence, the method of assuming that wake stops expanding after x/D = 1 (x/D = 2 for unsteady load cases) will introduce an error in the velocity estimation using the VR model.

(a) At first, vorticity is calculated using Equation 6.5 from the velocity data.

$$\omega = \nabla \times \vec{u} \tag{6.5}$$

(b) From vorticity, strength of the wake is calculated using Equation 6.6

$$\Gamma = \int\int_{S} \omega \cdot dS \tag{6.6}$$

(c) Next step is to extend the wake strength to far wake. For all load cases, the wake is extended till downstream distance of 4 rotor diameters. Figure 6.23 shows the wake strength in the shear layer for different load cases.

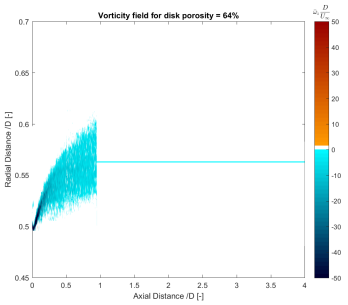

(a) Wake strength in the shear layer for porosity 64% and thrust coefficient = 0.555

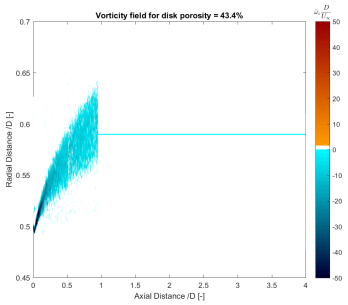

(b) Wake strength in the shear layer for porosity 43.4% and thrust coefficient = 0.612

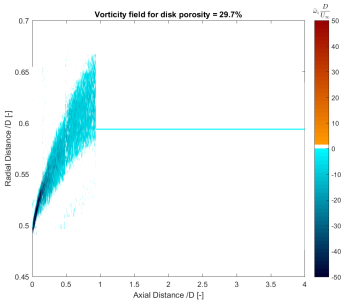

(c) Wake strength in the shear layer for porosity 29.7% and thrust coefficient = 0.76

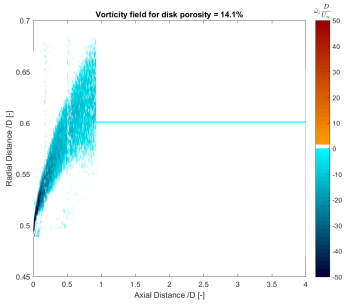

(d) Wake strength in the shear layer for porosity 14% and thrust coefficient = 0.807

Figure 6.23: Vorticity Field used for Vortex Ring model

(d) After this, axial and radial velocity fields are calculated using Equation 4.17 and Equation 4.18 for same field as for experimental data.

6.3.1. AXIAL VELOCITY

Figure 6.24 shows the normalized axial velocity field for all steady load cases estimated using Vortex Ring model. Equation 4.17 is used to calculate axial velocity. It shows that as the flow approaches the disc, the axial velocity decreases. Across the disc, there is a velocity induction for all cases and velocity decreases with downstream distance. It can also be noticed that the wake expansion increases with increase in loading on the disc.

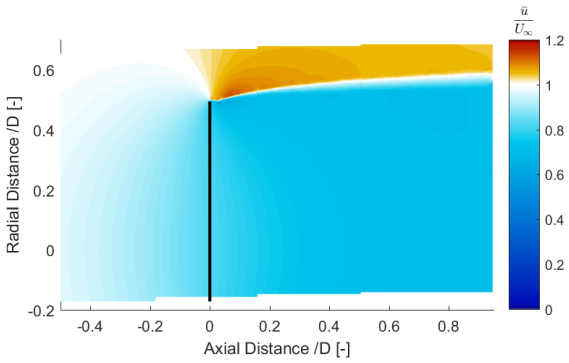

(a) Porosity = 64% and thrust coefficient = 0.555

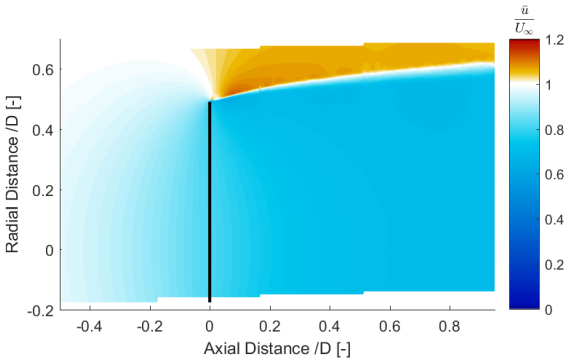

(b) Porosity = 43.4% and thrust coefficient = 0.612

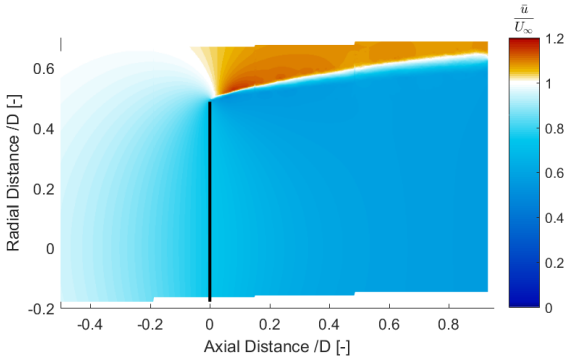

(c) Porosity = 29.7% and thrust coefficient = 0.76

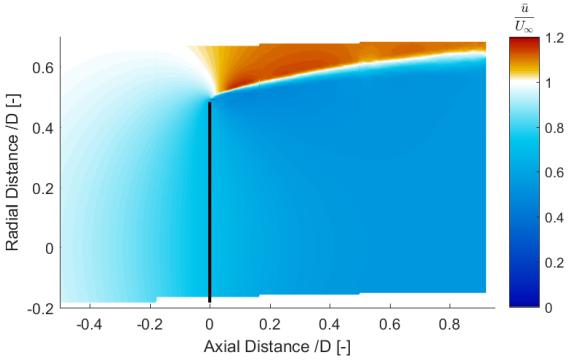

(d) Porosity = 14% and thrust coefficient = 0.807

Figure 6.24: Normalized Axial Velocity field for AD under steady loading estimated using the Vortex Ring model

6.3.2. RADIAL VELOCITY

Figure 6.25 shows the normalized radial velocity field for all steady load cases estimated using Vortex Ring model. Equation 4.18 is used to calculate the radial velocity. The figures show that radial velocity is maximum near the tip of the disc for all load cases. It is close to zero along the centre line of axis and increases further from the hub. The radial velocity is mainly positive, except at few locations in the shear layer. This is possibly because of the effect of estimation of the wake strength in the region where experimental data was unavailable. Due to this assumption, the model assumes that wake has stopped expanding resulting in negative radial velocity near x/D = 1.

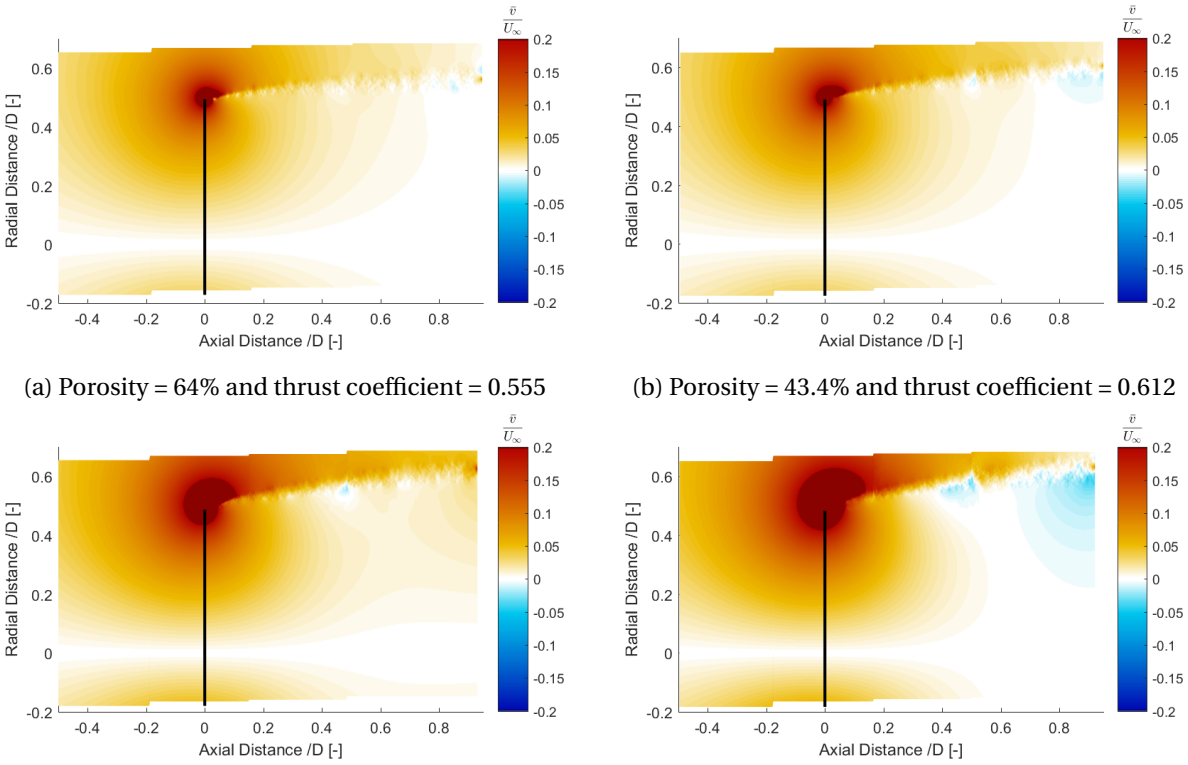

(a) Porosity = 64% and thrust coefficient = 0.555

(b) Porosity = 43.4% and thrust coefficient = 0.612

(c) Porosity = 29.7% and thrust coefficient = 0.76

(d) Porosity = 14% and thrust coefficient = 0.807

Figure 6.25: Normalized Radial Velocity field for AD under steady loading estimated using the Vortex Ring model

6.3.3. COMPARISON OF VELOCITY FIELDS FOR DIFFERENT LOAD CASES

In this section, velocity fields for the different loads on the disc are compared and discrepancies between them are analysed.

1. **Axial Velocity**: Figure 6.26 shows the radial variation of the normalized axial velocities for different axial positions. The figure illustrates that the general trends for all the load cases are similar. The velocity profiles are not uniform behind the disc. However, with downstream distance they become more uniform. The figures also show that velocity increases to free-stream conditions for the radial positions near 0.5 rotor diameters. As stated earlier, this is because of the presence of tip vortices in the shear layer.

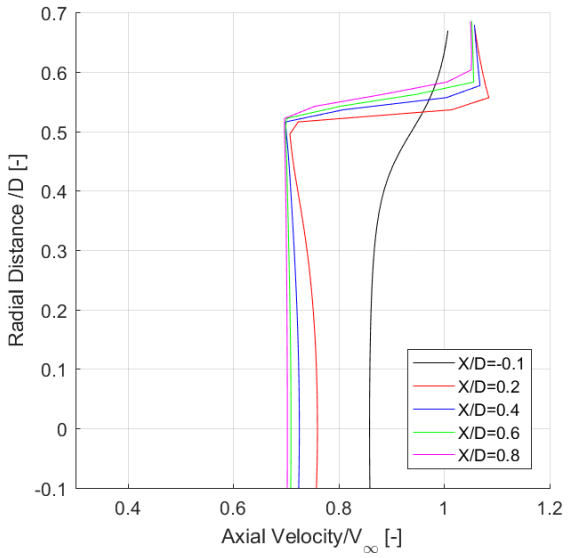

(a) Porosity = 64% and thrust coefficient = 0.555

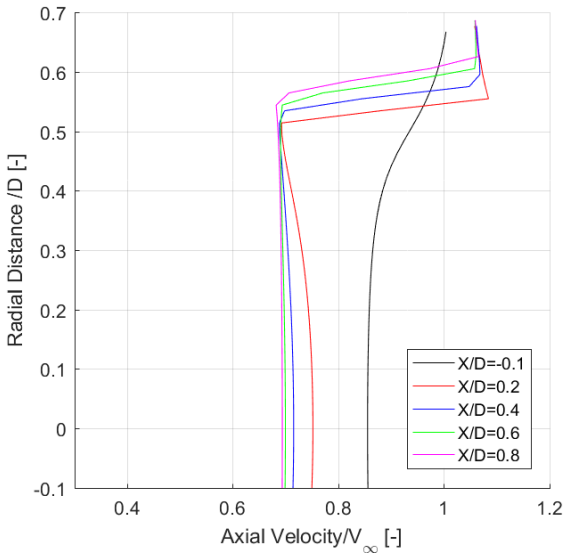

(b) Porosity = 43.4% and thrust coefficient = 0.612

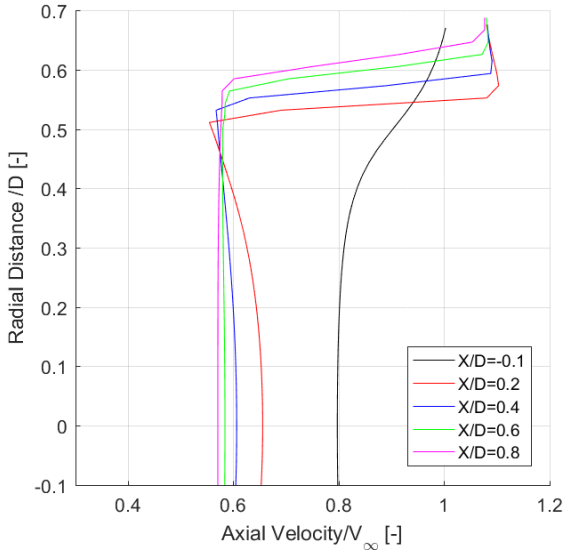

(c) Porosity = 29.7% and thrust coefficient = 0.76

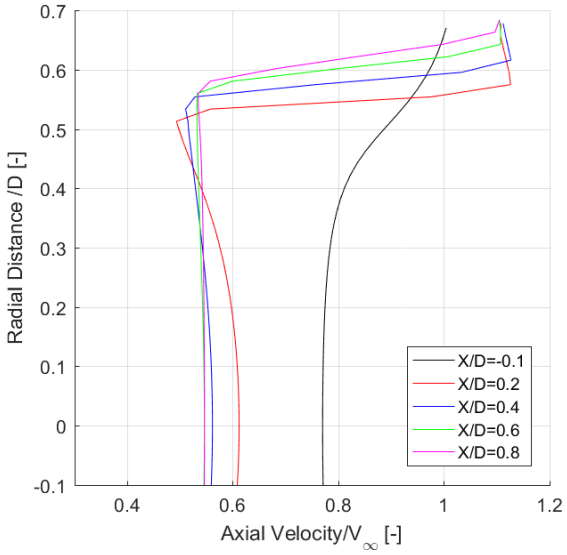

(d) Porosity = 14% and thrust coefficient = 0.807

Figure 6.26: Radial variations of normalized axial velocity calculated using Vortex Ring model for different axial positions

There is velocity induction across the disc. The axial velocity is still decreasing till x/D = 1. The rate of decrease of velocity with downstream axial distance is decreasing. Figure 6.26 shows that the difference between porosity of 64% and 43.4% (C_T = 0.555 and 0.612 respectively) is very small for all the axial positions. For porosity of 43.4% (C_T = 0.612), the average velocity induction is slightly larger. The figures show that the velocity induction across the disc increases with load.

2. **Radial Velocity**: Figure 6.27 show the radial variation of the normalized radial velocity field for the four steady load cases. Similar to radial variation of the normalized axial velocity, the normalized radial velocity also decreases with increasing downstream position. At r/D = 0.5, it decreases to 0 as in the far outer wake the flow is mainly in the axial direction.

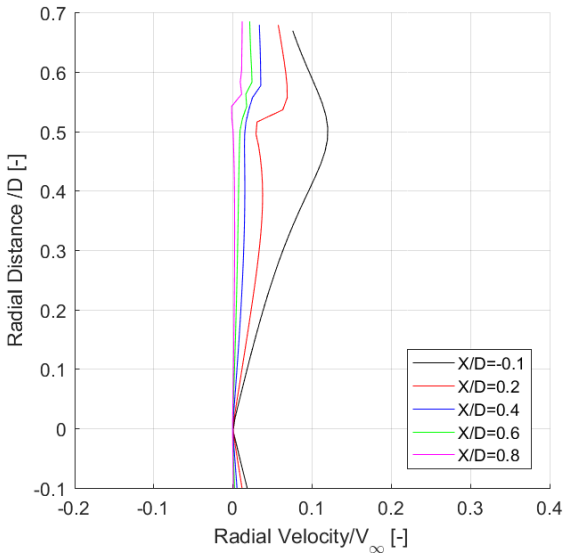

(a) Porosity = 64% and thrust coefficient = 0.555

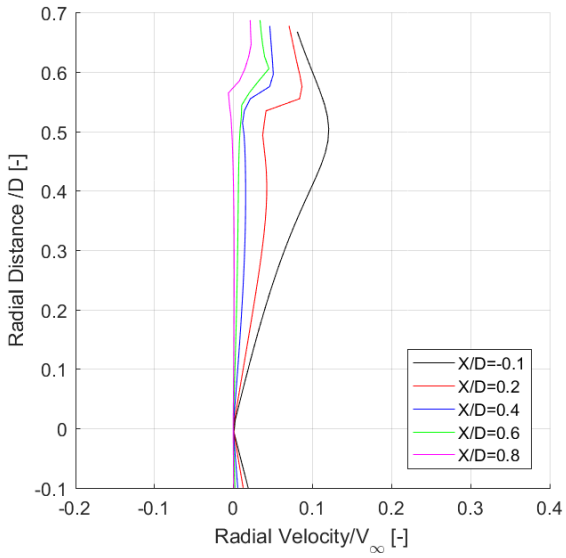

(b) Porosity = 43.4% and thrust coefficient = 0.612

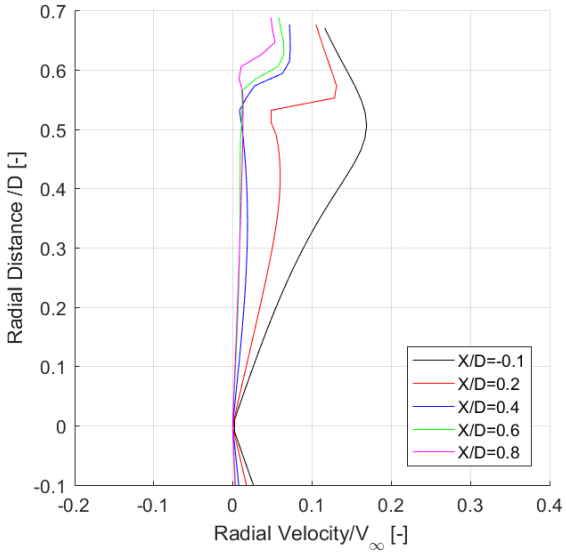

(c) Porosity = 29.7% and thrust coefficient = 0.76

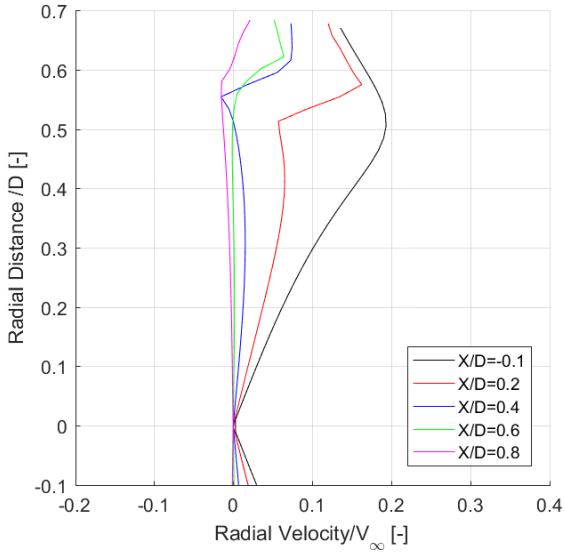

(d) Porosity = 14% and thrust coefficient = 0.807

Figure 6.27: Radial variations of normalized radial velocity calculated using Vortex Ring model for different axial positions

3. **Wake Expansion**: Figure 6.28 shows the field expansion for the four different steady load cases. As indicated, with a lower load on the disc, expansion of the field decreases. These results are also consistent with the past experiments (section 2.4). With increasing porosity, thrust coefficient is decreased and less kinetic energy is dissipated by the AD, resulting in the smaller wake expansion.

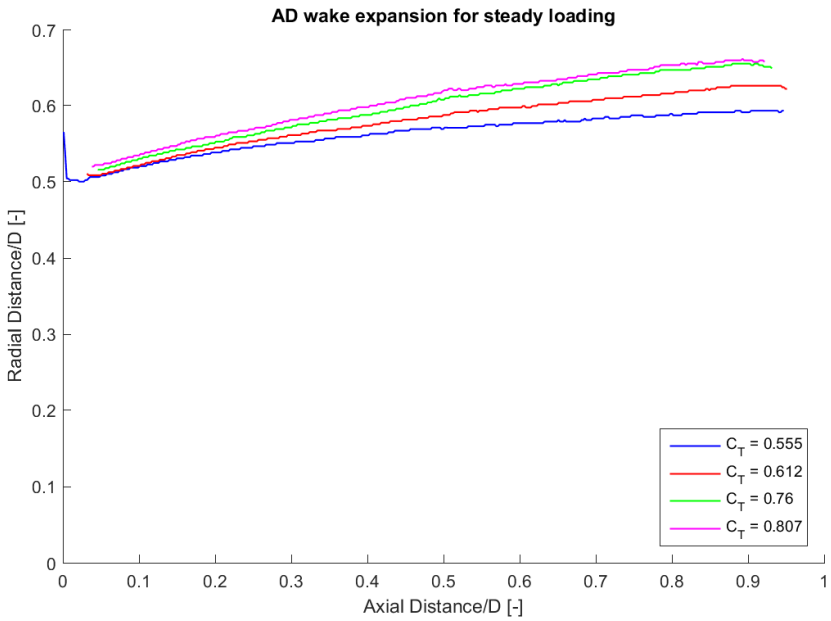

Figure 6.28: AD wake expansion for different porosity. The curves represent the points where the velocity is equal to the free-stream velocity

6.3.4. VALIDATION OF THE MODEL

In this section, results from the Vortex Ring model are validated using the experimental results. This is done by calculating the difference between the two results.

AXIAL VELOCITY

Figures 6.29 show the radial variation of the normalized axial velocity measured experimentally and computed via Vortex Ring model. From the figures, it is evident that the velocity profiles from the experiment and Vortex Ring model are more similar near the r/D = 0.5 region. This is because wake strength is estimated using flow field near the wake boundary. Behind the disc, velocity profile for all the load cases is more uniform for the Vortex Ring model than that from the experiment. In the experimental results, effect of the disc mesh is seen, which is not taken into account for the Vortex Ring model. Another big difference is near the hub region as the Vortex Ring model does not take the effect of hub into account.

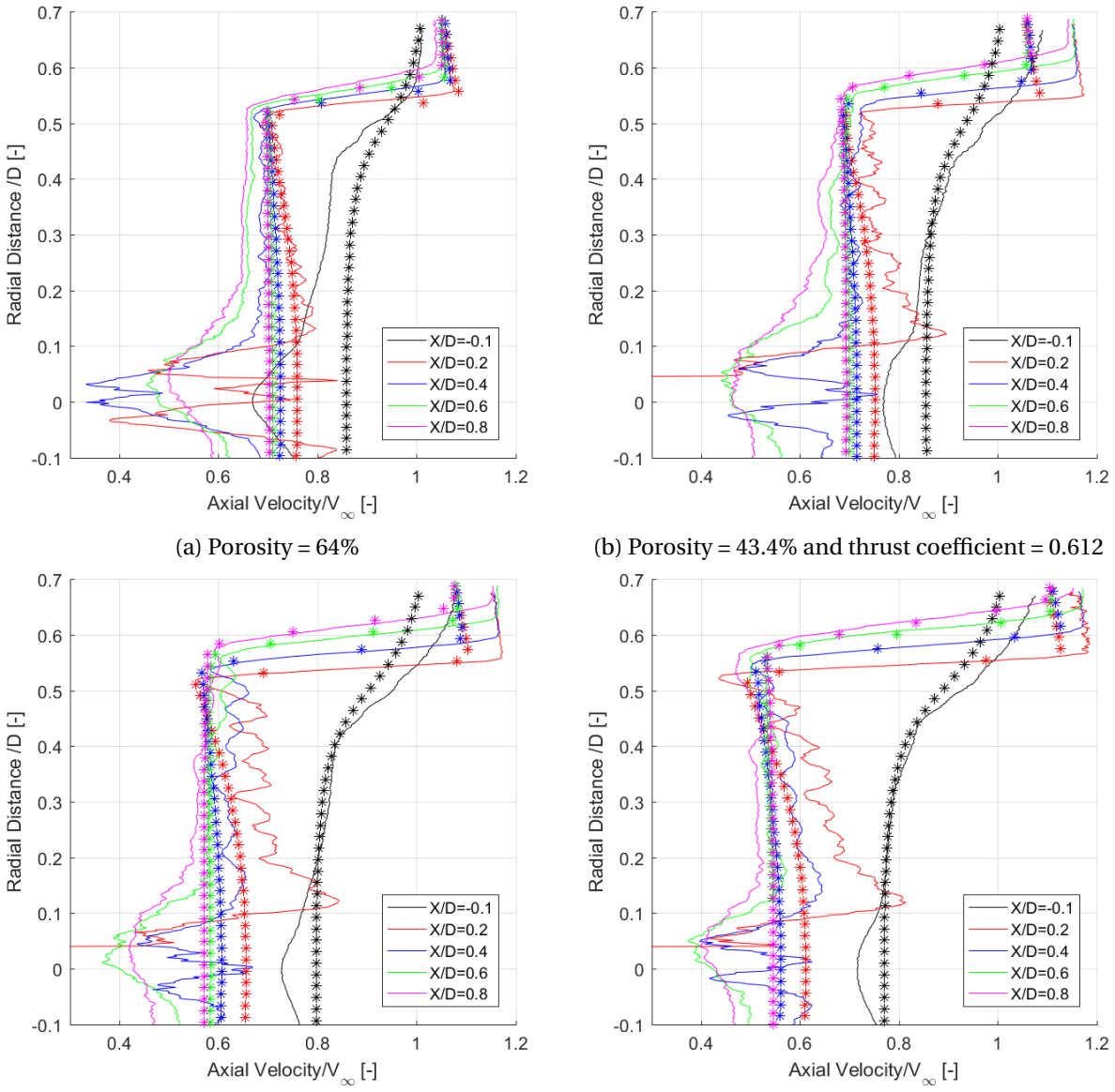

(a) Porosity = 64%

(b) Porosity = 43.4% and thrust coefficient = 0.612

(c) Porosity = 29.7% and thrust coefficient = 0.76

(d) Porosity = 14% and thrust coefficient = 0.807

Figure 6.29: Radial variation of normalized axial velocity from the Experiment (–) and Vortex Ring model (**) different axial positions

Figure 6.30 shows the difference between normalized axial velocity fields from the experiment and the Vortex Ring model. This difference is found as:

$$\bar{\varepsilon}_x = \frac{V_{x,\text{exp}} - V_{x,VRM}}{V_\infty} \tag{6.7}$$

The figures show that the difference is higher just behind the disc due to the disc mesh and nacelle. Further downstream from the disc, the difference decreases. The figures illustrate that the difference between the velocity fields outside the wake is minimum. For all the load cases, Vortex Ring model underestimates the axial velocity profile in the region just behind the disc by over 50% of the free-stream velocity. This is due to not taking effect of the disc mesh into account. In other regions , the difference ranges between -10% and 10% of the free-stream velocity..

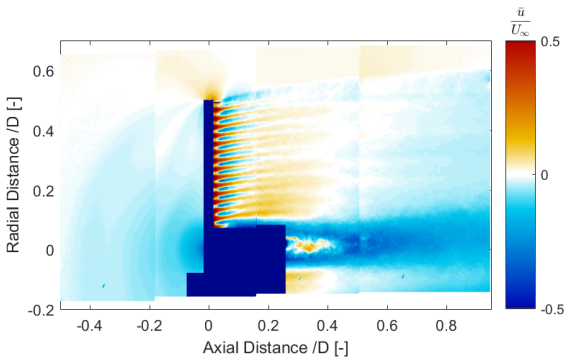

(a) Porosity = 64% and thrust coefficient = 0.555

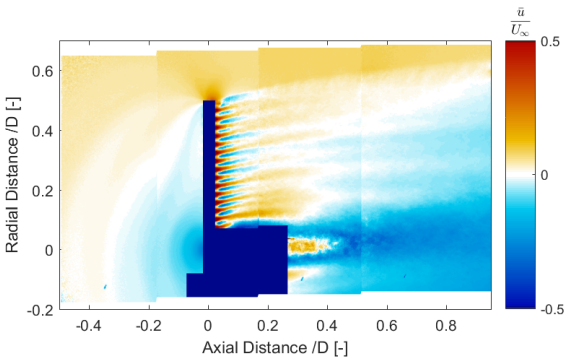

(b) Porosity = 43.4% and thrust coefficient = 0.612

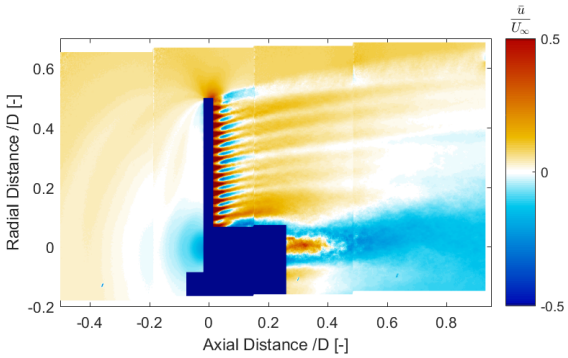

(c) Porosity = 29.7% and thrust coefficient = 0.76

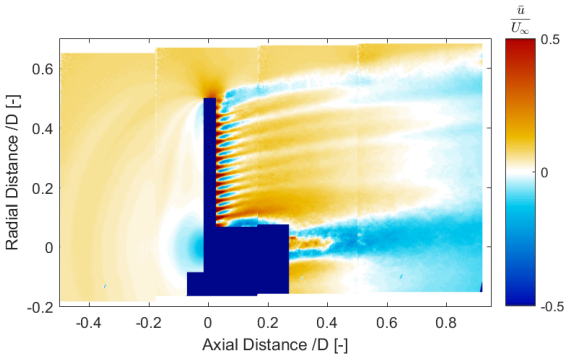

(d) Porosity = 14% and thrust coefficient = 0.807

Figure 6.30: Difference between normalized axial velocity fields from the experiment and the Vortex Ring model

RADIAL VELOCITY

Figure 6.31 shows the difference between normalized radial velocity fields from the experiment and the Vortex Ring model. This difference is found as:

$$\bar{\varepsilon}_r = \frac{V_{r,\text{exp}} - V_{r,VRM}}{V_\infty} \tag{6.8}$$

The figures show that error in the radial velocity is smaller compared to the axial velocity. This is due to the fact that radial velocity is smaller than the axial velocity. For all the cases, the error is maximum behind the disc and the hub. This is because the wake strength is assumed only using vorticity near the boundary of the inner wake. The difference ranged between -2% and 2% of the free-stream velocity.

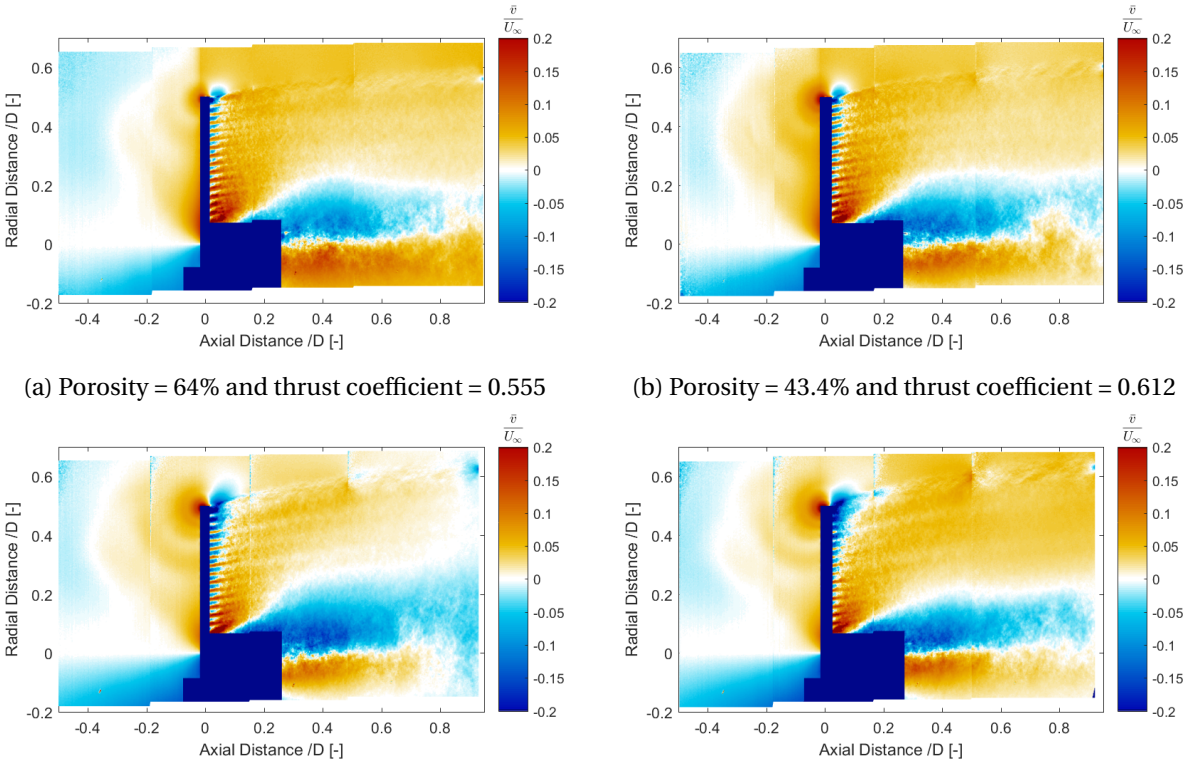

(a) Porosity = 64% and thrust coefficient = 0.555

(b) Porosity = 43.4% and thrust coefficient = 0.612

(c) Porosity = 29.7% and thrust coefficient = 0.76

(d) Porosity = 14% and thrust coefficient = 0.807

Figure 6.31: Difference between normalized radial velocity fields from the experiment and the Vortex Ring model

COMPARISON WITH HOT-WIRE DATA

Table 6.3 presents the normalized axial velocity results for the location of hot-wire from HWA and VR model. The table shows that there is a difference between both estimations. This difference is associated with errors in the two methods, namely: vibrations of the hot-wire probe, inconsistency in the calibration of the HWA probe, wake strength used for VR model, etc. The difference between the two ranges from 3.7% to 9% of the free-stream velocity.

Table 6.3: Axial Velocity comparison between hot-wire results and VRM for steady load cases

Porosity [%]	HWA $\frac{\bar{u}}{U_\infty}$	VR model $\frac{\bar{u}}{U_\infty}$
64	0.96	1.047
43.4	1.02	1.057
29.7	1.09	1.083
14	1.19	1.10

It can be concluded from the results from both the experiment and VR model that velocity induction and wake expansion increases with load on the disc. The results also show that load on the disc decrease with increase in the disc porosity. In order to study the effects of cyclic loading on the disc, porosity of the disc is varied sinusoidally. The results for load and flow field are presented in the next chapter.

7

Actuator Disc under Unsteady Loading

In this chapter, actuator disc is analysed under cyclic unsteady loading. As stated before, porosity of the disc is changed in a sinusoidal way with frequency of 5Hz, 3Hz and 1.5Hz, with reduced frequency of 1.57, 0.94 and 0.47 respectively. At first, estimation of loading on the AD is carried at with two different methods. This is followed by analysis of phase-locked normalized flow fields for these cases. Then velocity fields estimated using Vortex Ring model are then analysed and validated.

7.1. Load Determination from Flow Field

Load calculations are discussed in this section. At first, load is calculated using 1D-AD momentum model approximation, for which load trends are compared for each frequency. After this, same is repeated for calculating load using momentum integration of the flow field. Then, solutions from these two methods are compared to each other.

7.1.1. 1D Actuator Disc Momentum-model Approximation

Load on the disc is calculated using equations 6.1-6.3. Table 7.1 shows the load calculations for sinusoidal change in the disc porosity with 5Hz frequency and k = 1.57. The table shows that the thrust coefficient varies between 0.675 and 0.574. These values are different from those for the steady load cases. Unlike the steady load cases, where maximum porosity corresponds to the minimum load and vice-verse, 1D AD approximation does not result in a similar trend for cyclic unsteady loading. The maximum load is for 19% porosity just before the minimum porosity case. The minimum porosity is for 59% porosity, which is just before the maximum porosity. This is possibly because of unsteady loading on this disc which is contrary to the assumption made in the 1D AD model.

Table 7.2 shows the thrust coefficient for unsteady load case with frequency of 3Hz and k = 0.94. The thrust coefficient ranges from 0.547 till 0.684. The maximum and the minimum values are lower than those for the steady load cases. The maximum is for the same time-node and porosity of 19% as the previous unsteady load case. The minimum thrust coefficient is also for the same time-node and porosity of 59% like the previous unsteady load case. The reason is possibly that the flow is unsteady and also the wake has not reached the recovery point.

Table 7.1: Thrust Coefficients calculated using 1D Actuator disc momentum-model approximation for sinusoidal change in the disc porosity with frequency of 5Hz and k = 1.57.

Time [ms]	Porosity [%]	Thrust Coefficient [-]
20	59	0.583
40	47	0.592
60	31	0.640
80	19	0.675
100	14	0.666
120	19	0.634
140	31	0.601
160	47	0.587
180	59	0.574
200	64.0	0.579
220	59	0.583

Table 7.2: Thrust Coefficients calculated using 1D Actuator disc momentum-model approximation for sinusoidal change in the disc porosity with frequency of 3Hz and k = 0.94.

Time [ms]	Porosity [%]	Thrust Coefficient [-]
33	59	0.592
66	47	0.643
99	31	0.680
132	19	0.684
165	14	0.671
198	19	0.642
231	31	0.603
264	47	0.553
297	59	0.547
330	64.0	0.559
363	59	0.592

Load calculations with 1D-AD model for the unsteady load case with 1.5Hz frequency and k = 0.47 are shown in Table 7.3. The maximum thrust coefficient is 0.728 for porosity of 19%, which is the time-node before the minimum porosity. The minimum C_T is 0.535 for the porosity of 59%, just before the maximum porosity. This trend is same as the previous two unsteady load cases.

Table 7.3: Thrust Coefficients calculated using 1D Actuator disc momentum-model approximation for sinusoidal change in the disc porosity with frequency of 1.5Hz and k = 0.47.

Time [ms]	Porosity [%]	Thrust Coefficient [-]
67	59	0.637
134	47	0.698
201	31	0.719
268	19	0.728
335	14	0.658
402	19	0.566
469	31	0.541
536	47	0.541
603	59	0.535
670	64.0	0.567
737	59	0.640

Comparison of load with changing frequency: Figure 7.1 shows a comparison of load cycle for the three unsteady load cases. It was found in section 6.1 that for the steady load cases, thrust coefficient (using AD-model) ranges from 0.558 to 0.754 for the porosity range of 14-64%. AD model estimates that all the unsteady load cases have higher minimum load over the disc than that for the steady load cases. The unsteady load cases have lower maximum value than that for the steady load cases as estimated by the 1D AD model. The difference is likely caused as the AD model assumes steady, inviscid flow conditions.

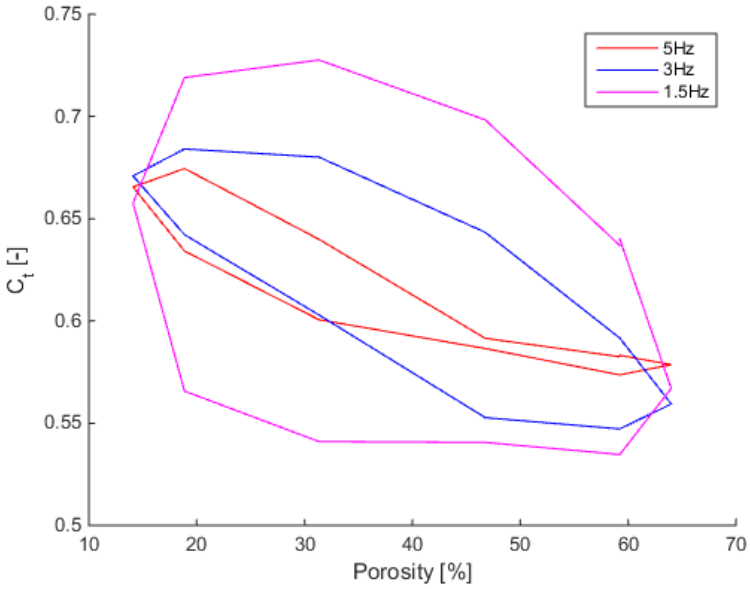

(a) Thrust Coefficient vs. Porosity

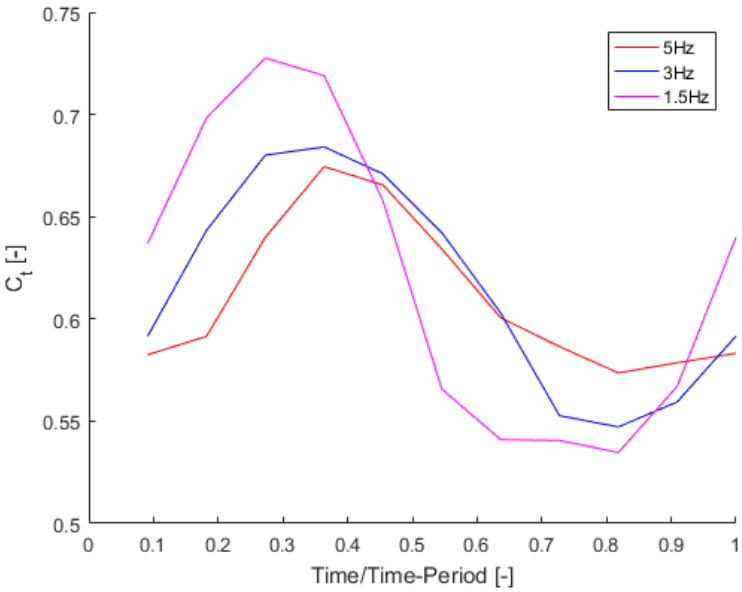

(b) Thrust Coefficient vs. Time

Figure 7.1: Thrust Coefficient calculated using AD-model for the 3 unsteady load cases

7.1.2. FLOW MOMENTUM INTEGRATION

For momentum integral of the flow field, Equation 7.1 is used. The viscous term is ignored in this equation, as the viscous effects are assumed to be negligible if the contour is taken to be sufficiently far from the disc [66]. Static pressure is calculated using Poisson integration (see section C.2). Pressure (static) fields for all the unsteady load cases are presented in Appendix D. For all cases, pressure increases as flow approaches the disc. Across the disc, there is a pressure jump, after which pressure follows the wake expansion and contraction (discussed in the next section). Due to cyclic loading on the disk, wake is expanding and contracting. This causes pressure to increase with wake expansion and decrease with wake contraction. Pressure fields show that loading on the disc is non-uniform

as the radial variation of pressure for an axial position in the field has a gradient.

In order to calculate rate change of velocity with time, central difference method is used for the middle time-nodes, forward difference method is used for the first time-node and backward difference method is used for the last time-node

$$\vec{F} = \iiint_{V(t)} \frac{\partial\left(\rho\vec{V}\right)}{\partial t} dV(t) - \oiint_{S} \rho\left(\vec{V}.\vec{n}\right)\cdot\vec{V}dS - \oiint_{S} p\vec{n}dS + \oiint_{S} \tau\vec{n}dS \tag{7.1}$$

Table 7.4 shows loading on the disc for the unsteady load case with 5Hz frequency (k = 1.57) calculated using momentum integration of the flow field. The thrust coefficient ranges from 0.55 to 0.71. The minimum load is found at the time-node of 1.0 with porosity of 64% which is the maximum porosity. The maximum load is found at the minimum porosity of 14%. The table shows that the first and the last porosity cases do not have same loading. This could be due to the uncertainties in load calculations and PIV measurements discussed in chapter 8

It can also be seen that the same porosity cases with different phases do not have same loading on the disc. This is because of the dynamic inflow discussed in chapter 4. Due to the wake being a mixture of 'new' and 'old' vorticity, when porosity changes, the change in load and vorticity strength is not the same as in the steady load cases. As explained in [1], when porosity is suddenly changed, there is a sudden increase or decrease in load before reaching a steady-state value. However, this was the case for a step change in porosity. In this experiment, porosity is continuously changing, so there is no approach to a steady-state value. Effect of the sudden increase or decrease in loading is also minimized due to sinusoidal change in porosity.

Table 7.4: Thrust Coefficients calculated using flow momentum integration for sinusoidal change in the disc porosity with frequency of 5Hz and k = 1.57.

Time [ms]	Porosity [%]	Thrust Coefficient [-]
20	59	0.5550
40	47	0.5577
60	31	0.5790
80	19	0.6200
100	14	0.7051
120	19	0.6970
140	31	0.6775
160	47	0.6574
180	59	0.5964
200	64.0	0.5501
220	59	0.5545

Table 7.5 shows results for thrust coefficient for each porosity for the unsteady load case with 3Hz frequency and k = 0.94. The minimum load is found to be 0.57 for time-node of 0.10 with porosity of 64%. The maximum load of 0.68 is found to be at the time-node 0.5 with porosity of 14%. The table shows that the first and the last porosity cases do not have same loading. This is possibly due to uncertainty in the PIV measurements and load calculations(see chapter 8). Other trends are similar

to the previous unsteady load case.

Table 7.5: Thrust Coefficients calculated using flow momentum integration for sinusoidal change in the disc porosity with frequency of 3Hz and k = 0.94.

Time [ms]	Porosity [%]	Thrust Coefficient [-]
33	59	0.5721
66	47	0.5925
99	31	0.6217
132	19	0.6490
165	14	0.6838
198	19	0.6709
231	31	0.6508
264	47	0.6115
297	59	0.5840
330	64.0	0.5690
363	59	0.5720

Results for thrust coefficient for each porosity for the unsteady load case with 1.5Hz frequency (k = 0.47) are shown in Table 7.6. The range for the thrust coefficient is 0.55-0.69. The minimum load on the disc occurs at the maximum porosity and vice-verse.

Table 7.6: Thrust Coefficients calculated using flow momentum integration for sinusoidal change in the disc porosity with frequency of 1.5Hz and k = 0.47.

Time [ms]	Porosity [%]	Thrust Coefficient [-]
67	59	0.5655
134	47	0.6050
201	31	0.6386
268	19	0.6655
335	14	0.6920
402	19	0.6750
469	31	0.6512
536	47	0.6155
603	59	0.5748
670	64.0	0.5548
737	59	0.5650

Comparison of load with changing frequency: Figure 7.2 compares load cycles for the three different unsteady load cases. The figure shows that all three load cases form cycle, but not necessarily a sinusoidal. A clearer trend can be found with more data points for each load case.

With higher frequency for porosity change, load cycle is broader. Hence, the difference between loads for same porosity value but different phase is lower for smaller frequency. This as explained before is caused by the unsteadiness of the flow field and difference in velocity induction. The range of thrust coefficient for the three load cases is comparable (difference likely due to the errors in the experiment as discussed in 6). With increased frequency, speed and acceleration of porosity cycle

is higher. Due to this, the load change between the two porosity values is also higher (similar to [1] during a step-change). As described earlier, this difference is caused by the 'dynamic inflow' effect.

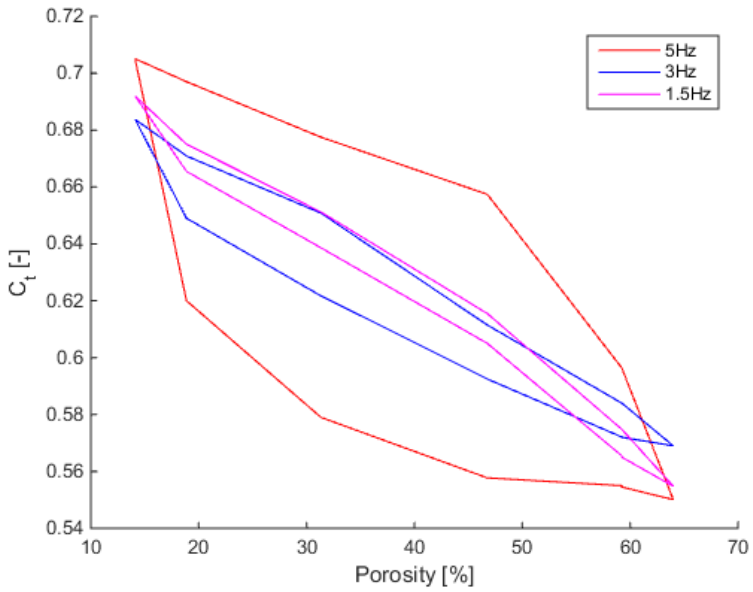

(a) Thrust Coefficient vs. Porosity

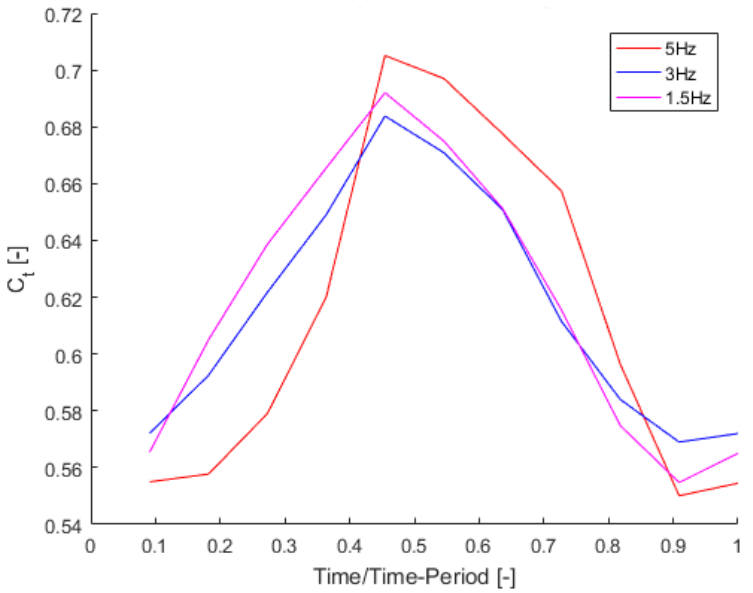

(b) Thrust Coefficient vs. Time

Figure 7.2: Thrust Coefficient calculated using momentum integration for the 3 unsteady load cases

7.1.3. COMPARISON OF THE TWO METHODS

Figure 7.3-Figure 7.5 shows the thrust coefficient calculated using 1D-AD model and momentum integration of the flow field. Results from both methods are very different from each other. According to the 1D AD model, loading with higher frequency is more similar to that for the steady load cases. This is probably because 1D-AD model assumes steady flow field which is not true for these

for these cases along with uncertainties discussed in chapter 8. Hence, calculations using 1D AD model for unsteady flow cannot be used to draw conclusions.

From load estimation, difference between step-change in porosity and sinusoidal change in porosity can be established. As seen in [1],[27], when there is a step decrease in porosity, there is an overshoot in loading and velocity, before a subsequent decay to a steady-state. This is not observed in any of the cyclic load cases. This can be explained by wake being mixture of 'new' and 'old' vortices. When step change in porosity was made, 'new' vortices of new strength were shed from the disc. Unless they replaced the 'old' vortices to the extent that effect of the 'old' vortices was negligible, effect of these 'old' vortices was observed. However, when the 'old' vortices were being transported far enough, a gradual change to a steady-state value was seen. However, in case of sinusoidal porosity change, a gradual change in load is taking place (no sudden change from maximum to minimum or opposite). Therefore, a continuous change in the strength of 'new' vortices takes place. The old vortices are also mixture of different strength (but this strength difference is not that much as seen in the vorticity fields as porosity change is gradual). Therefore, no sharp change in load is seen.

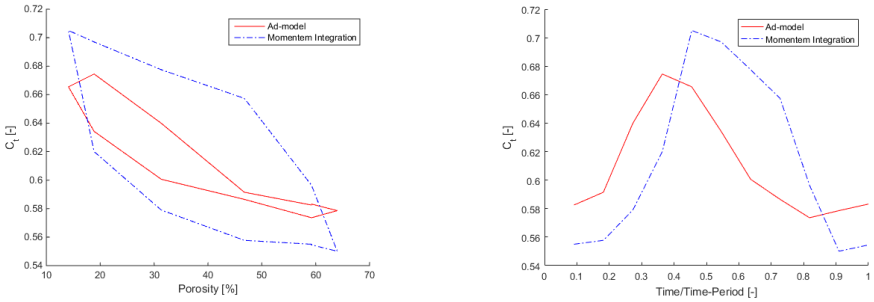

(a) Thrust Coefficient vs. Porosity (b) Thrust Coefficient vs. Time

Figure 7.3: Thrust Coefficient calculated with two different methods for sinusoidal frequency of 5Hz

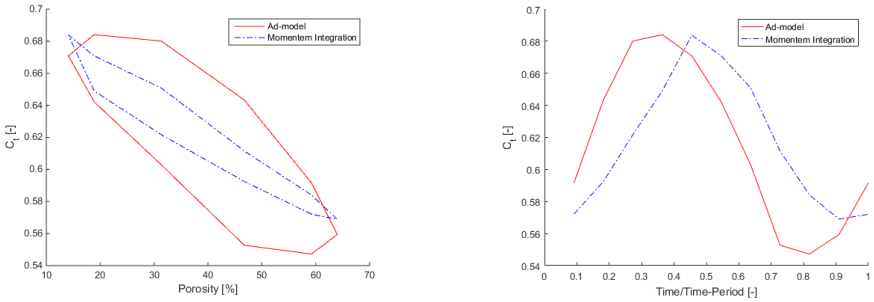

(a) Thrust Coefficient vs. Porosity (b) Thrust Coefficient vs. Time

Figure 7.4: Thrust Coefficient calculated with two different methods for sinusoidal frequency of 3Hz

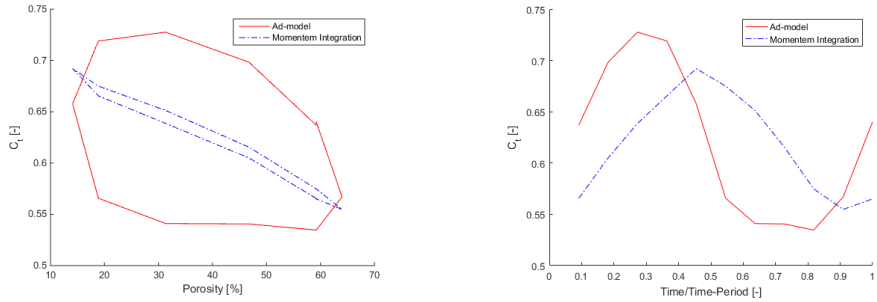

(a) Thrust Coefficient vs. Porosity (b) Thrust Coefficient vs. Time

Figure 7.5: Thrust Coefficient calculated with two different methods for sinusoidal frequency of 1.5Hz

7.2. VELOCITY AND VORTICITY FIELDS FOR DIFFERENT REDUCED FREQUENCIES

In this section, velocity and vorticity fields for all three unsteady load cases are analysed. At first, porosity changing with frequency of 5Hz is discussed, followed by frequency of 3Hz and finally 1.5Hz.

7.2.1. FREQUENCY = 5HZ AND REDUCED FREQUENCY = 1.57

In this section, velocity and vorticity fields for unsteady load case in which the disc load cycle has a frequency of 5Hz and k = 1.57 are discussed.

AXIAL VELOCITY

Figure 7.6-Figure 7.9 show the average normalized axial velocity fields for changing porosity with frequency of 5Hz and k = 1.57. The region outside the wake has u/U_∞ larger than 1 similar to the steady load cases. Inside the wake, it decreases to lower than 1. As porosity changes, progression of flow fields can clearly be seen in the figures. The figures show that as load on the disc changes, wake expansion changes. When porosity decreases at first and load on the disc increases from Figure 7.6a to Figure 7.7b, the wake immediately near the disc expands more. Because of gradual decrease in loading on the disc, the wake expansion is also gradual. Likewise, as porosity increases and disc loading decreases from Figure 7.7b to Figure 7.9a, the wake immediately near the disc expands less. Hence in contrast to steady load cases where flow field was expanding with downstream distance, in this case of cyclic loading, wake expands and also contracts with it.

The figures also illustrate that the velocity fields for this case is scanned till x/D = 2. Same fields are represented in Figure E.1-Figure E.5. In these figures, it can clearly be seen that with changing porosity, the wake is expanding and contracting with changing loading.

For all the cases, the axial velocity has not fully recovered even till the downstream distance of 2 rotor diameters. Due to the tower shadow affect, the velocity at the hub is lower than neighbouring regions.

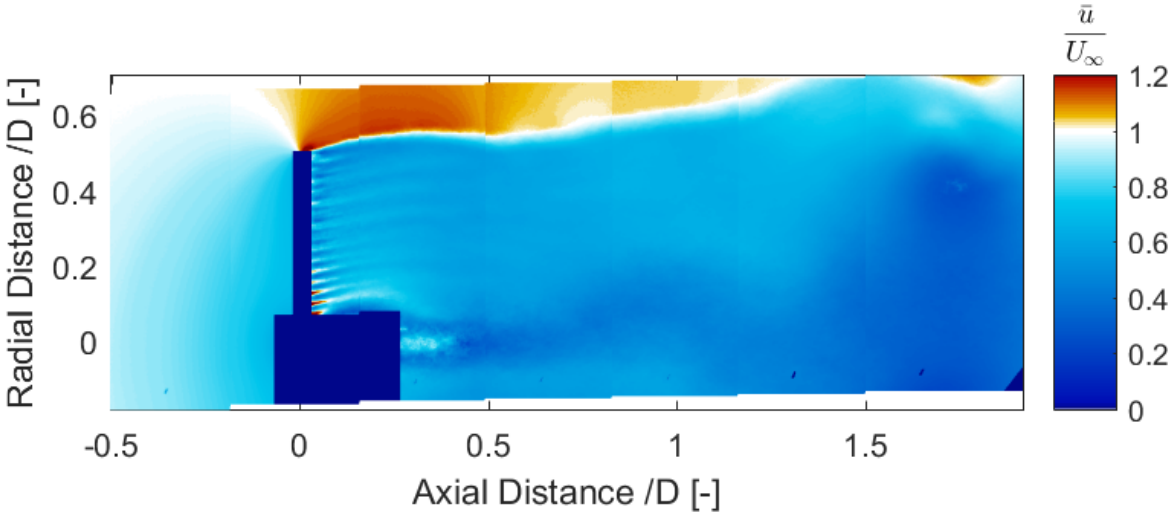

(a) Porosity = 59% (decreasing porosity) and C_T = 0.555

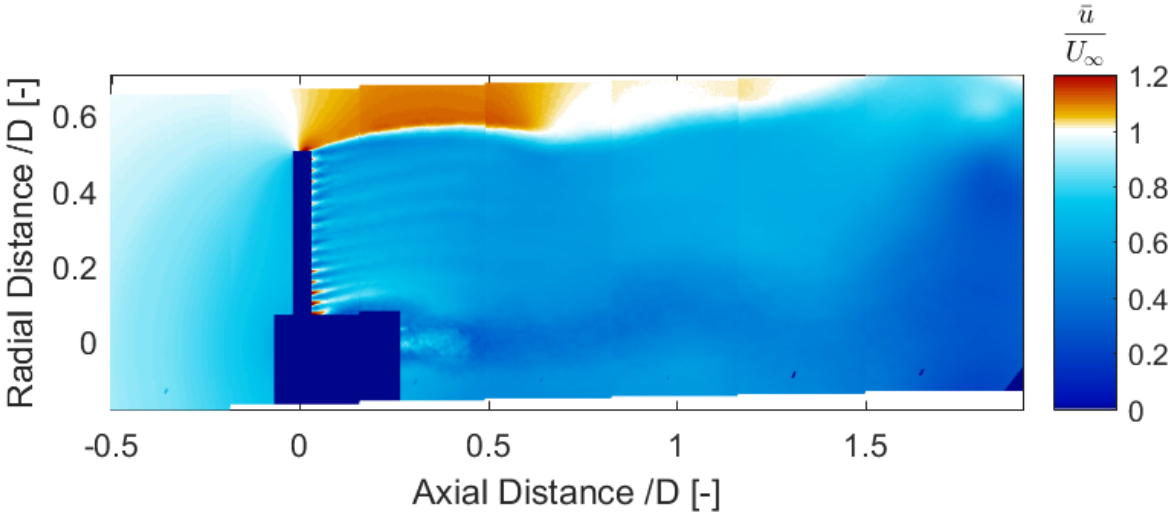

(b) Porosity = 47% (decreasing porosity) and C_T = 0.557

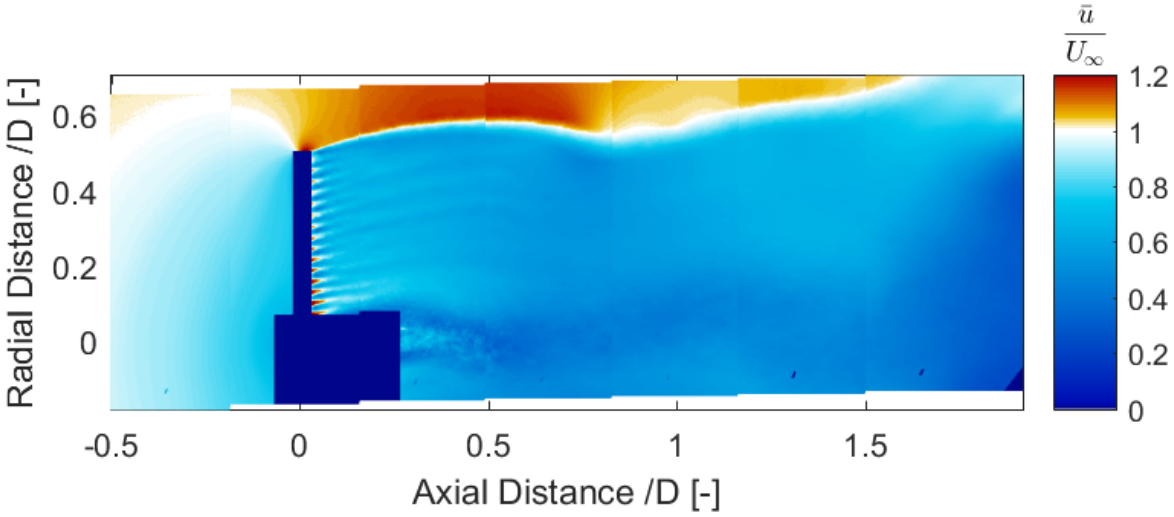

(c) Porosity = 31% (decreasing porosity) and C_T = 0.579

Figure 7.6: Normalized Axial Velocity Field used for porosity changing with frequency = 5Hz and reduced frequency = 1.57 (Experiment)

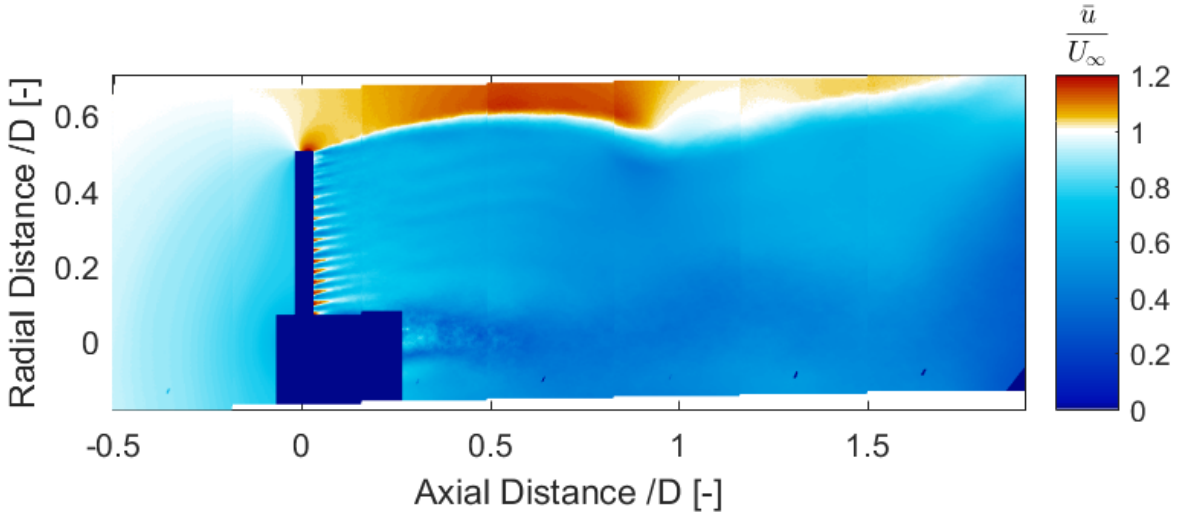

(a) Porosity = 19% (decreasing porosity) and C_T = 0.620

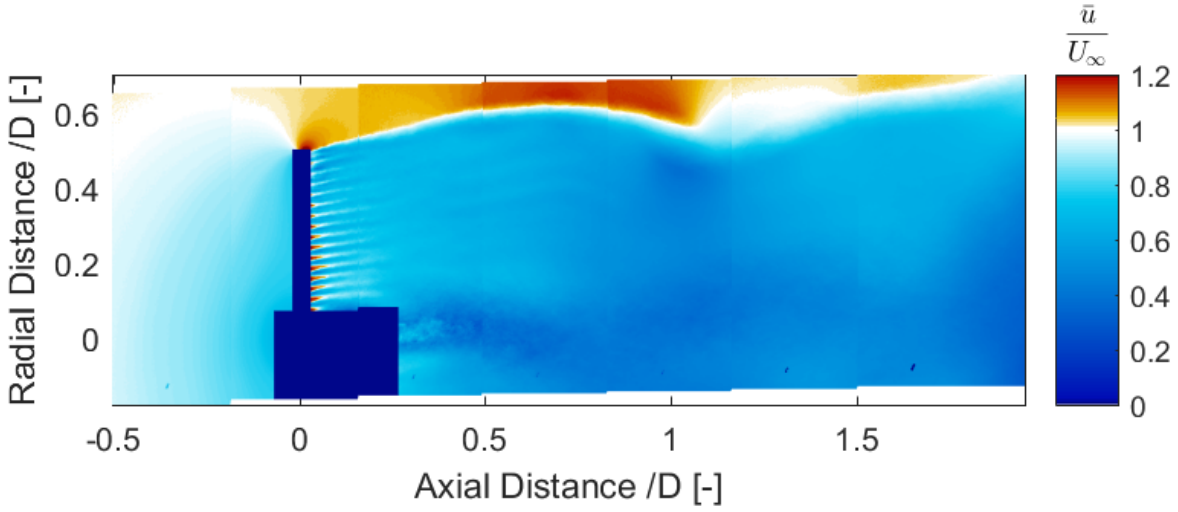

(b) Porosity = 14% (minimum porosity) and C_T = 0.705

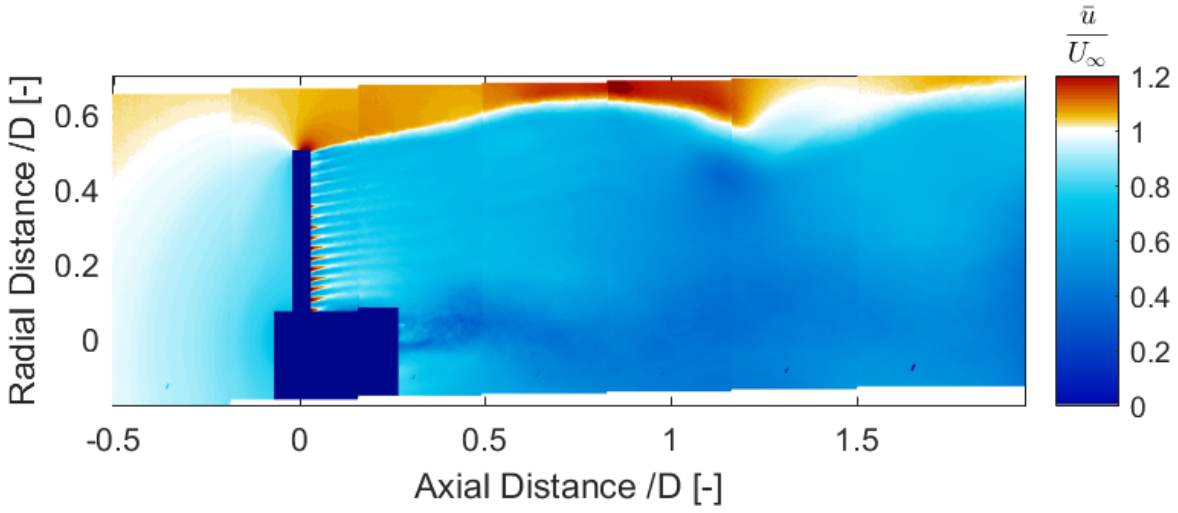

(c) Porosity = 19% (increasing porosity) and C_T = 0.697

Figure 7.7: Normalized Axial Velocity Field for porosity changing with frequency = 5Hz and reduced frequency = 1.57 (Experiment)

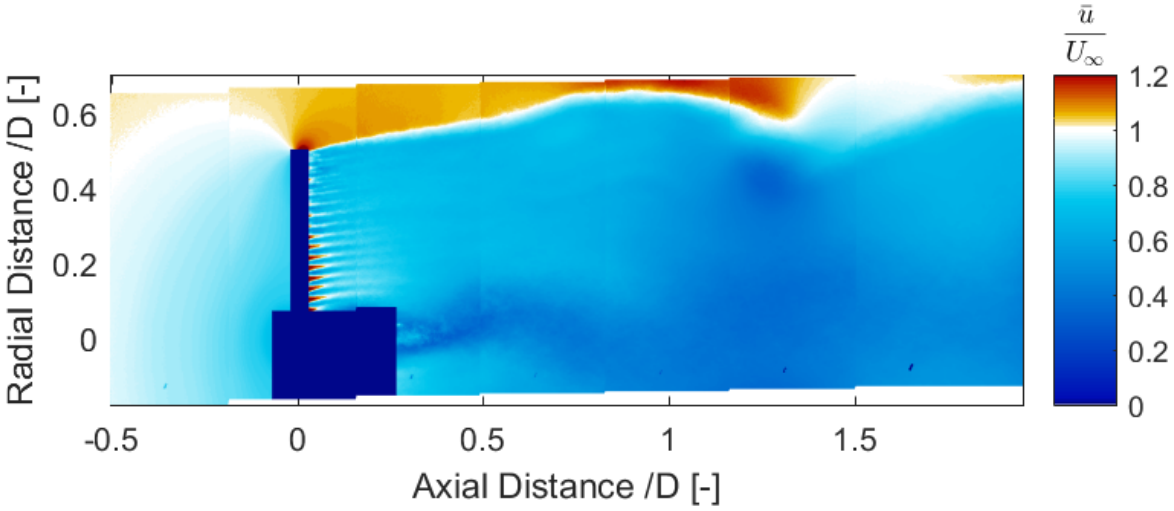

(a) Porosity = 31% (increasing porosity) C_T = 0.678

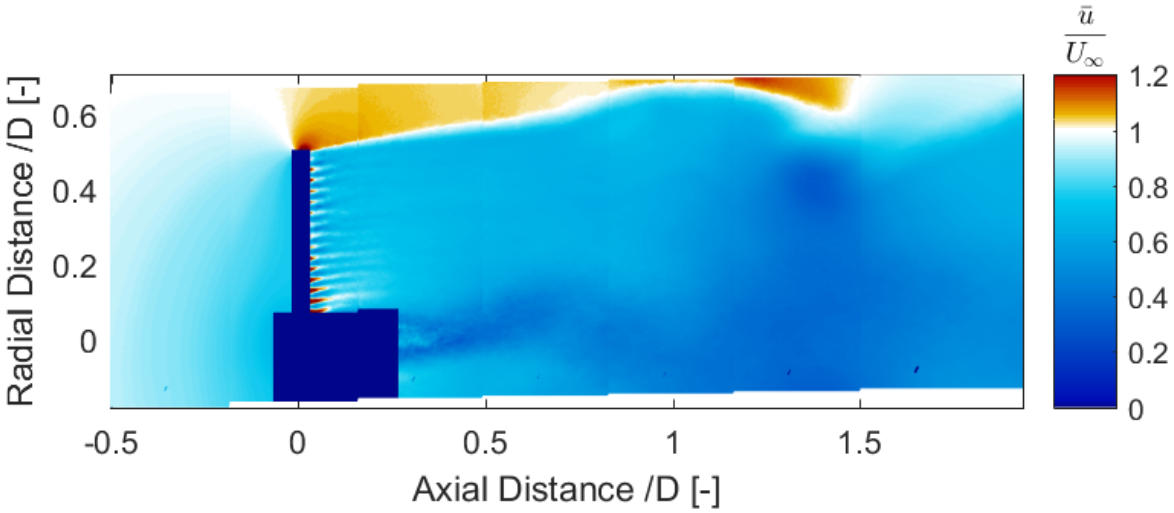

(b) Porosity = 47% (increasing porosity) and C_T = 0.657

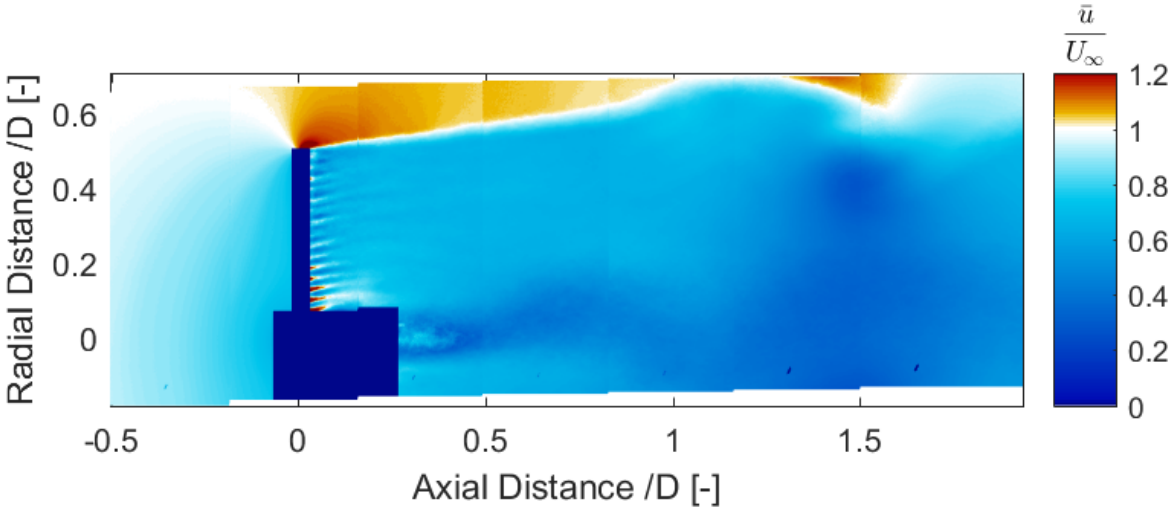

(c) Porosity = 59% (increasing porosity) and C_T = 0.596

Figure 7.8: Normalized Axial Velocity Field for porosity changing with frequency = 5Hz and reduced frequency = 1.57 (Experiment)

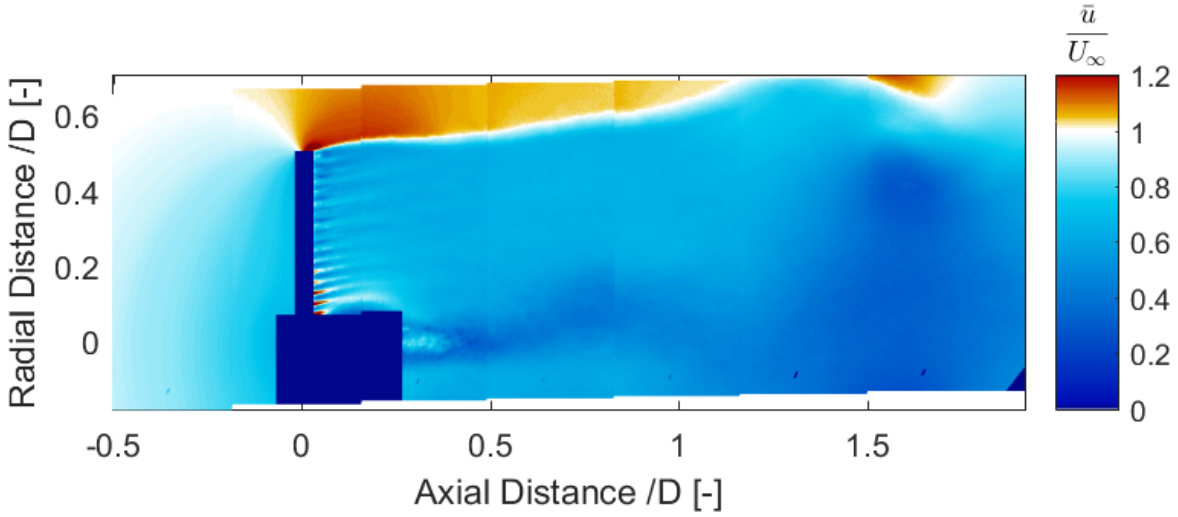

(a) Porosity = 64% (maximum porosity) and C_T = 0.550

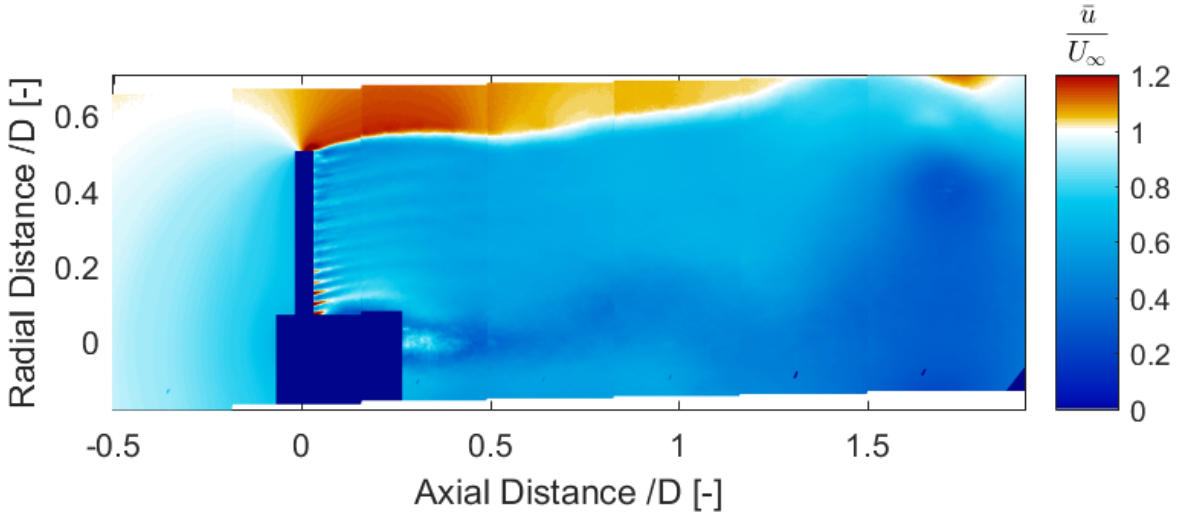

(b) Porosity = 59% (decreasing porosity) and C_T = 0.554

Figure 7.9: Normalized Axial Velocity Field for porosity changing with frequency = 5Hz and reduced frequency = 1.57 (Experiment)

RADIAL VELOCITY

Figure 7.10-Figure 7.13 show the average radial velocity fields normalized with respect to the free-stream velocity for sinusoidal change in porosity of the disc with a frequency of 5Hz and k = 1.57. Behind the hub, the radial velocity is negative. However, unlike steady load cases, where radial velocity in other regions is mainly positive up to x/D = 1, for this unsteady load case, radial velocity is both negative and positive. This is most likely due to the sinusoidal change in porosity resulting in cyclic loading on the disc. Due to this, wake is expanding and contracting as seen in the axial velocity fields. This in turn changes the magnitude and the direction of the radial velocity owing to flow moving outboards toward the free-stream and in-boards with wake expanding and contracting respectively. For the first half of the load cycle, where loading on the disc increases, radial velocity is positive next to the disc due to expanding wake. However, for the second half, region of negative radial velocity starts to appear as the wake expansion is decreasing in this half of the cycle. Compared to the axial velocity fields, magnitude of the radial velocity fields is small. The regions of a high magnitude of radial velocity indicate a strong vortex filament.

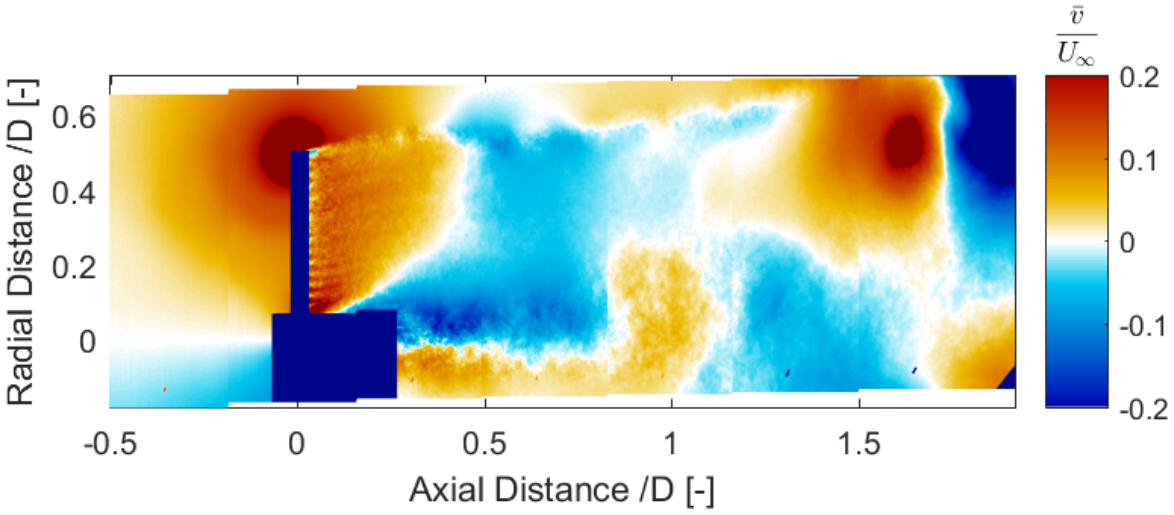

(a) Porosity = 59% (decreasing porosity) and C_T = 0.555

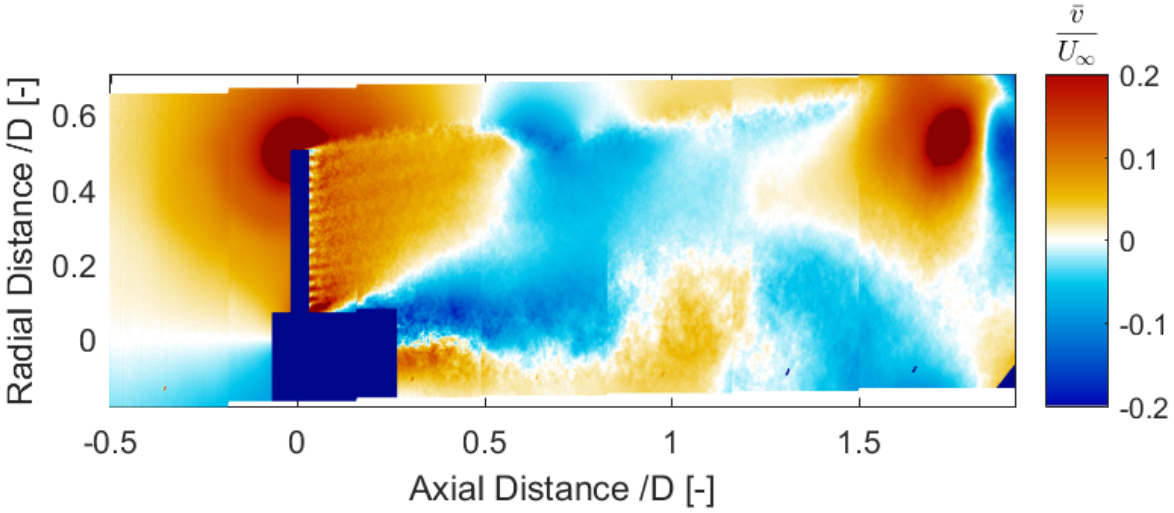

(b) Porosity = 47% (decreasing porosity) and C_T = 0.557

Figure 7.10: Normalized Radial Velocity Field for porosity changing with frequency = 5Hz and reduced frequency = 1.57 (Experiment)

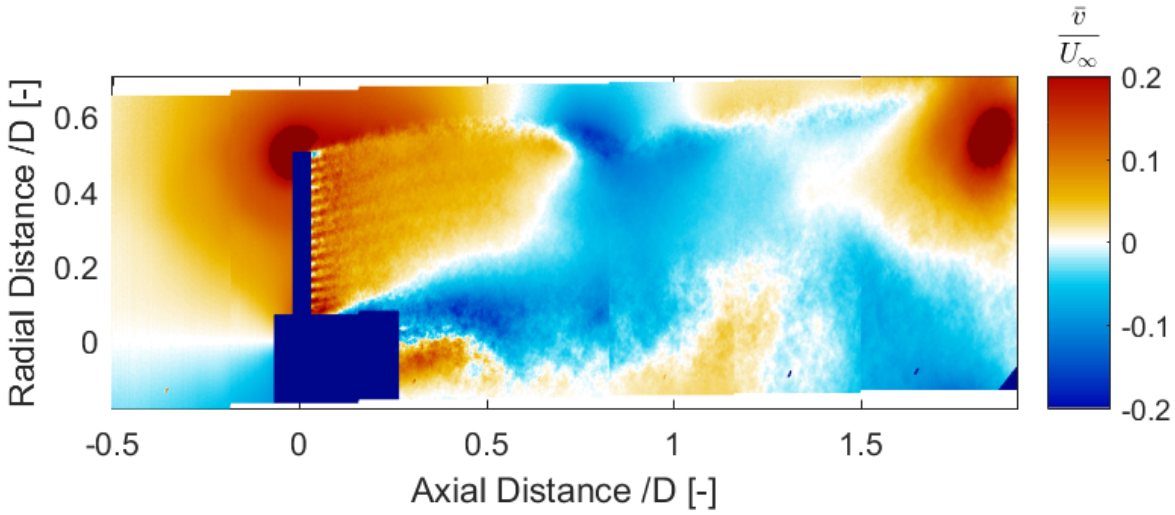

(a) Porosity = 31% (decreasing porosity) and C_T = 0.579

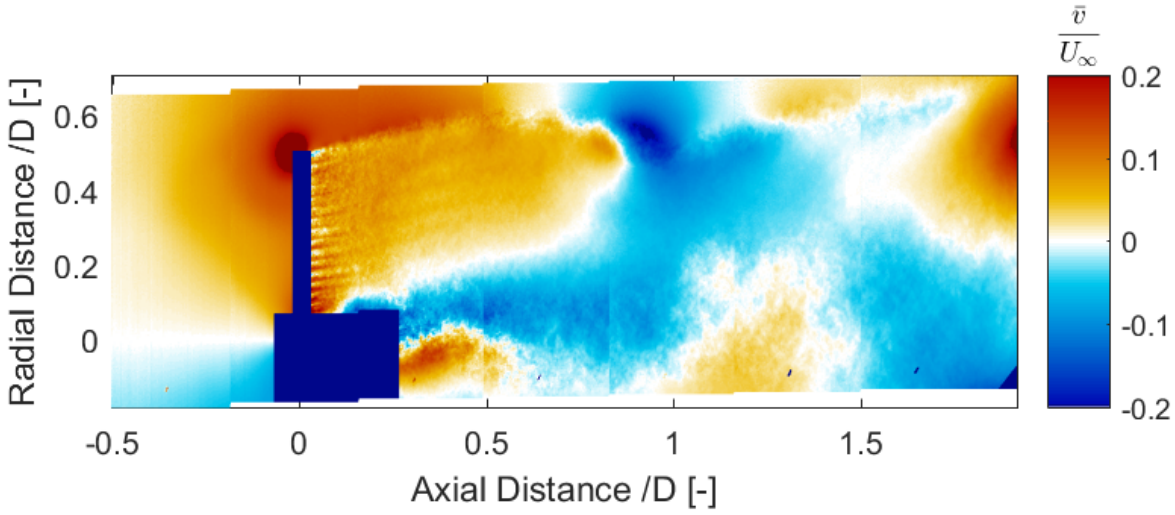

(b) Porosity = 19% (decreasing porosity) and C_T = 0.620

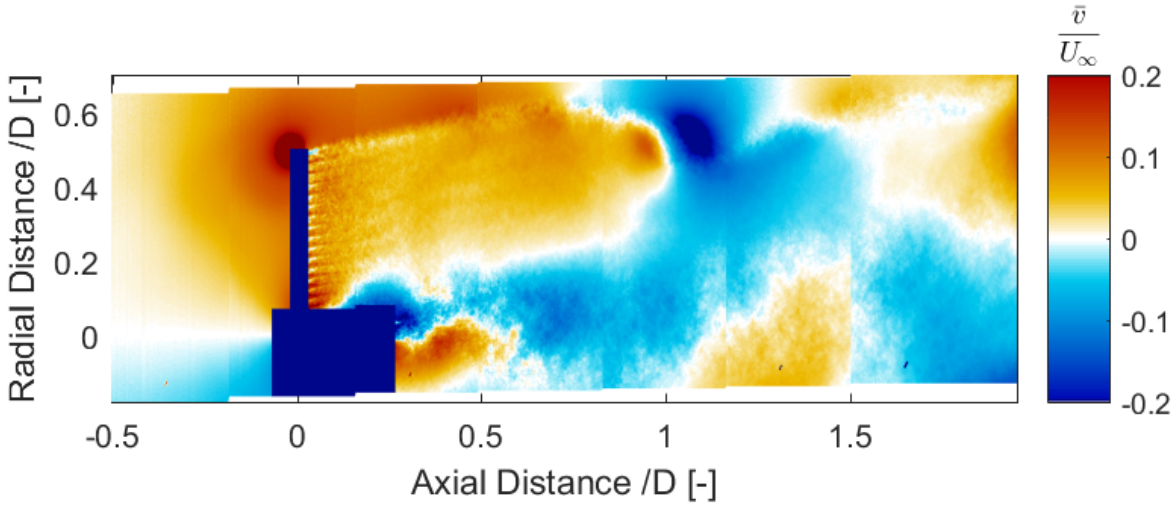

(c) Porosity = 14% (minimum porosity) and C_T = 0.705

Figure 7.11: Normalized Radial Velocity Field for porosity changing with frequency = 5Hz and reduced frequency = 1.57 (Experiment)

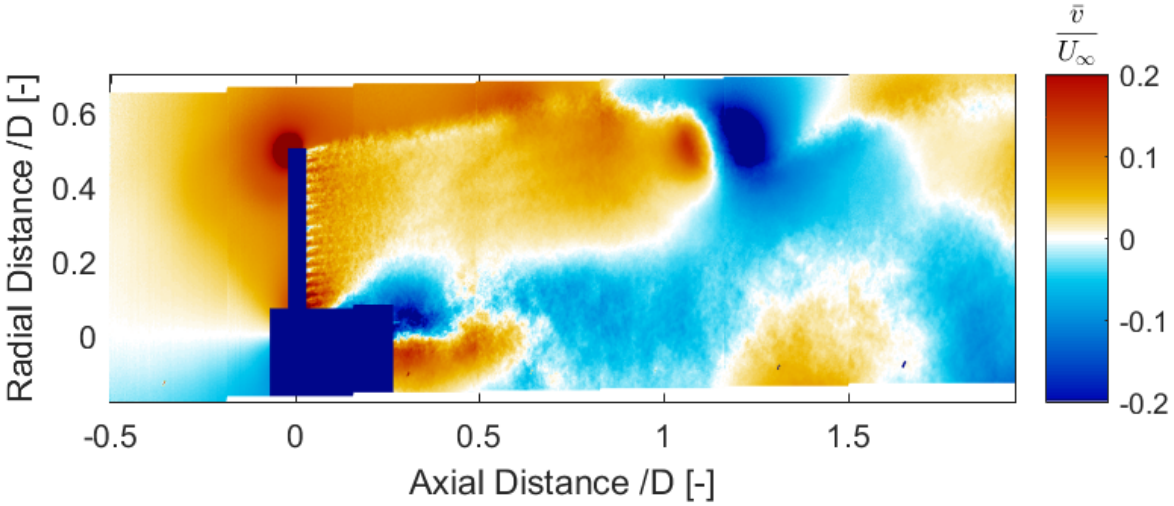

(a) Porosity = 19% (increasing porosity) and C_T = 0.697

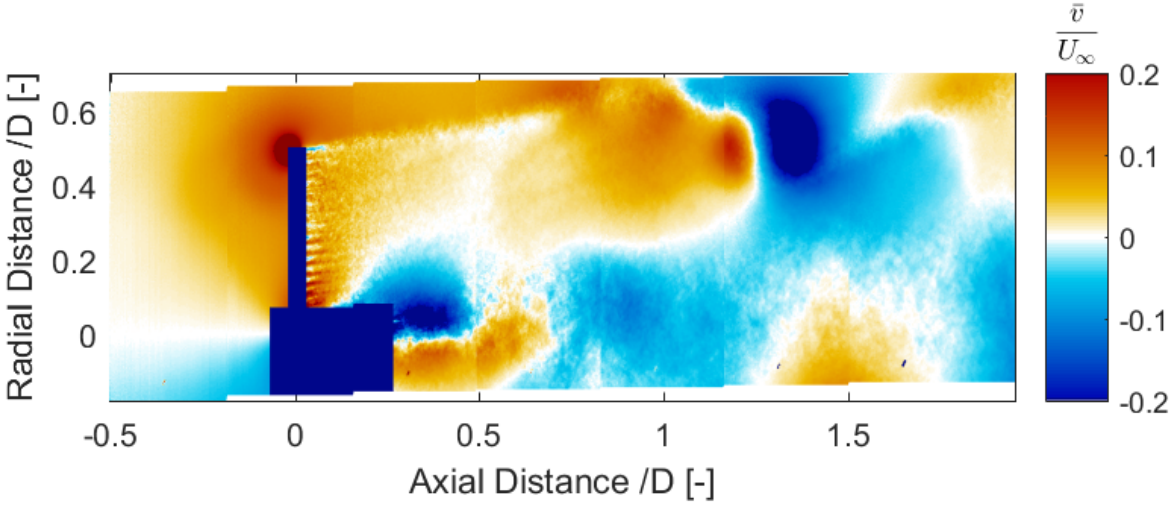

(b) Porosity = 31% (increasing porosity) C_T = 0.678

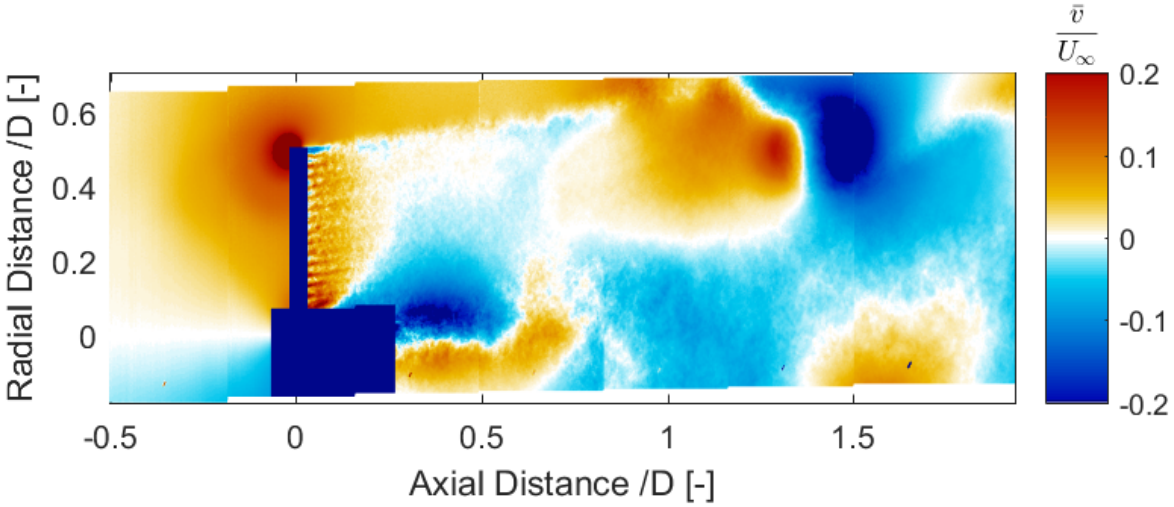

(c) Porosity = 47% (increasing porosity) and C_T = 0.657

Figure 7.12: Normalized Radial Velocity Field for porosity changing with frequency = 5Hz and reduced frequency = 1.57 (Experiment)

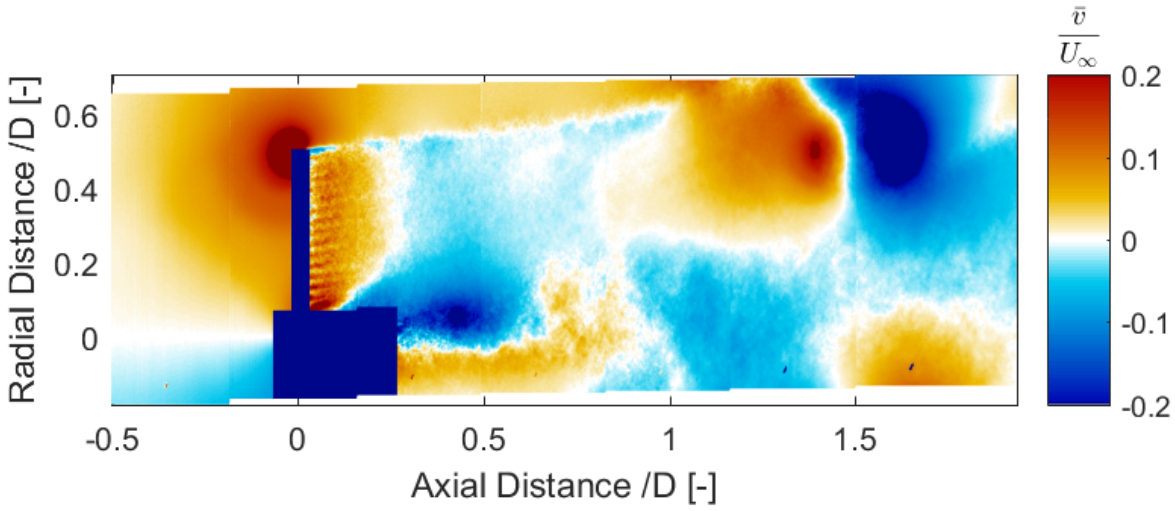

(a) Porosity = 59% (increasing porosity) and C_T = 0.596

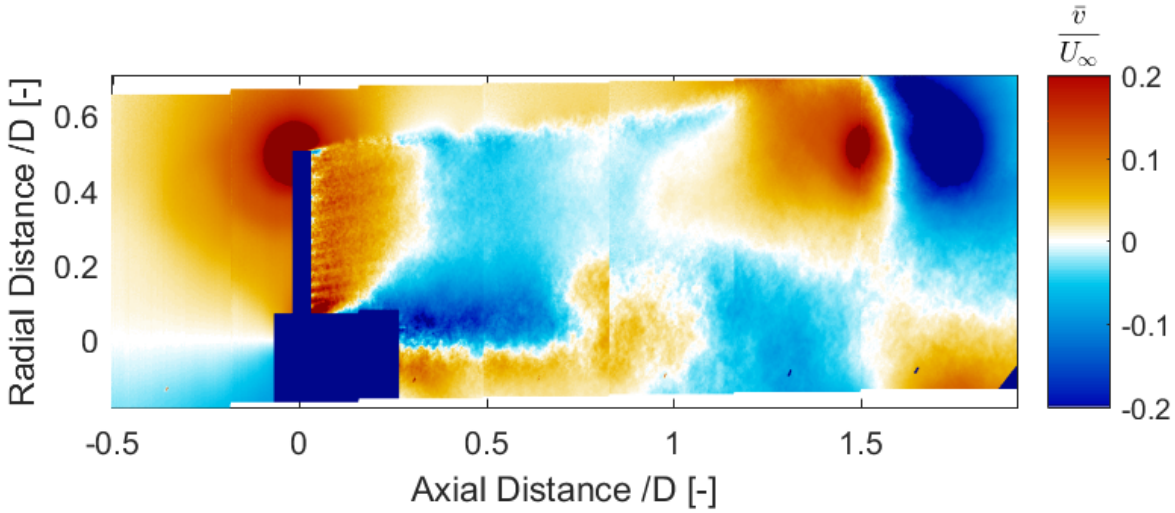

(b) Porosity = 64% (maximum porosity) and C_T = 0.550

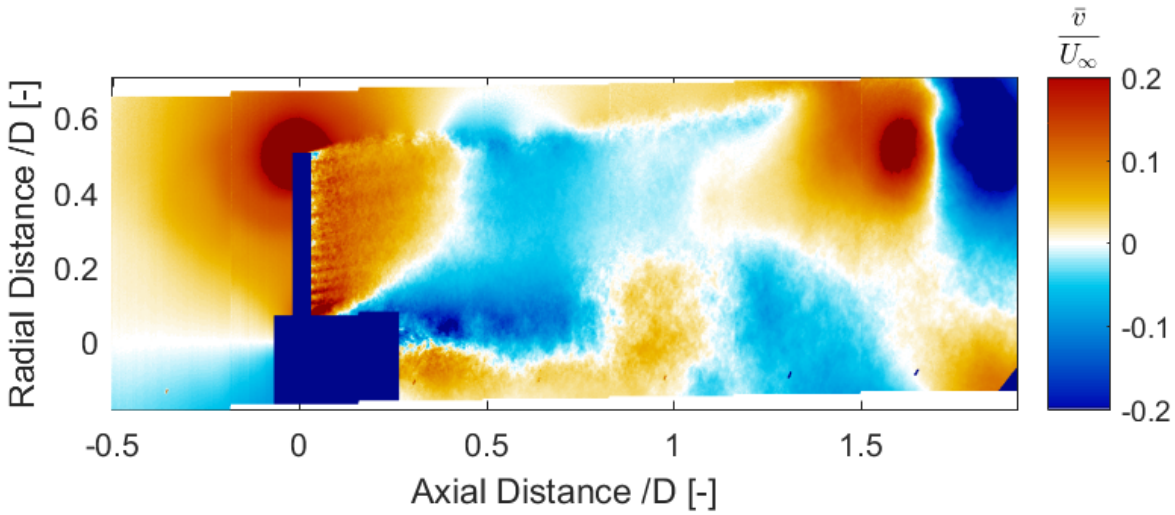

(c) Porosity = 59% (decreasing porosity) and C_T = 0.554

Figure 7.13: Normalized Radial Velocity Field for porosity changing with frequency = 5Hz and reduced frequency = 1.57 (Experiment)

VORTICITY

Figure 7.14-Figure 7.18 show the vorticity field for this case. The figures show that like the steady load cases vorticity is the strongest near the edge of the wake and just behind the disc. Behind the disc, field constitutes of both negative and positive vorticity. This is because of the mesh of the disc and the hub of the disc. Just behind the disc hub, axial velocity is really small and the radial velocity is negative, due to which, this region consists of strong vorticity. This vorticity shortly disintegrates. The magnitude of the vorticity shed from the disc edge decreases further away from the disc and also the vorticity expands.

The main change in the vorticity with changing loading in a cycle is near the edge of the wake. This is the vorticity that originates from the disc edge. As porosity changes, loading on the disc and generation and transport of vorticity changes (as discussed in section 2.3). This means with each new loading, transportation velocity and magnitude of these vortices change. This results in the so-called 'leap-frogging' phenomenon (discussed in Figure 3.1.2). As the figures show at some point in the wake, the vortices start to roll-up. The point where this happens depends on the current and the previous disc loadings and flow field. This phenomenon was not seen in the steady load cases. The first half of the load cycle has two such locations while the second half has only one such location. This is possibly due to larger velocity induction in the first half as shown in Figure 7.45a. Hence the transportation velocity is lower for the first of the cycle. So two locations of vorticity roll-up can be seen in the field up to x/D = 2.

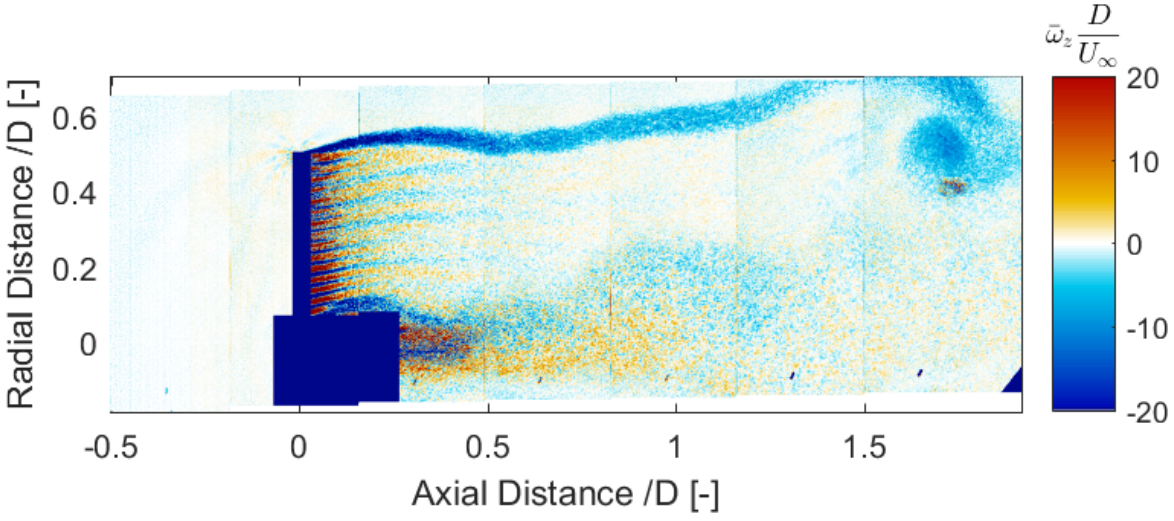

(a) Porosity = 59% (decreasing porosity) and C_T = 0.555

Figure 7.14: Normalized Vorticity Field for porosity changing with frequency = 5Hz and reduced frequency = 1.57 (Experiment)

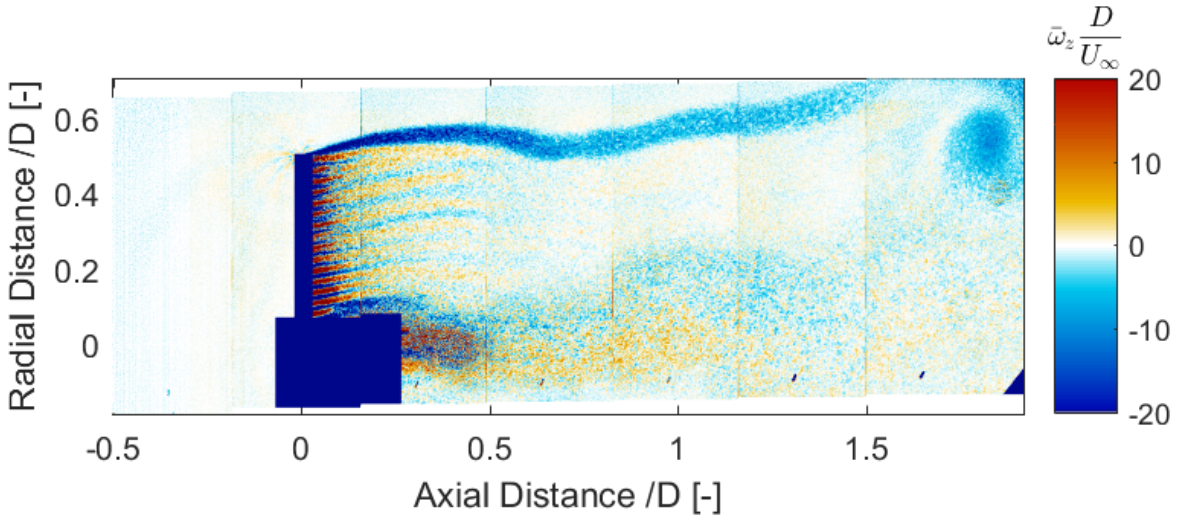

(a) Porosity = 47% (decreasing porosity) and C_T = 0.557

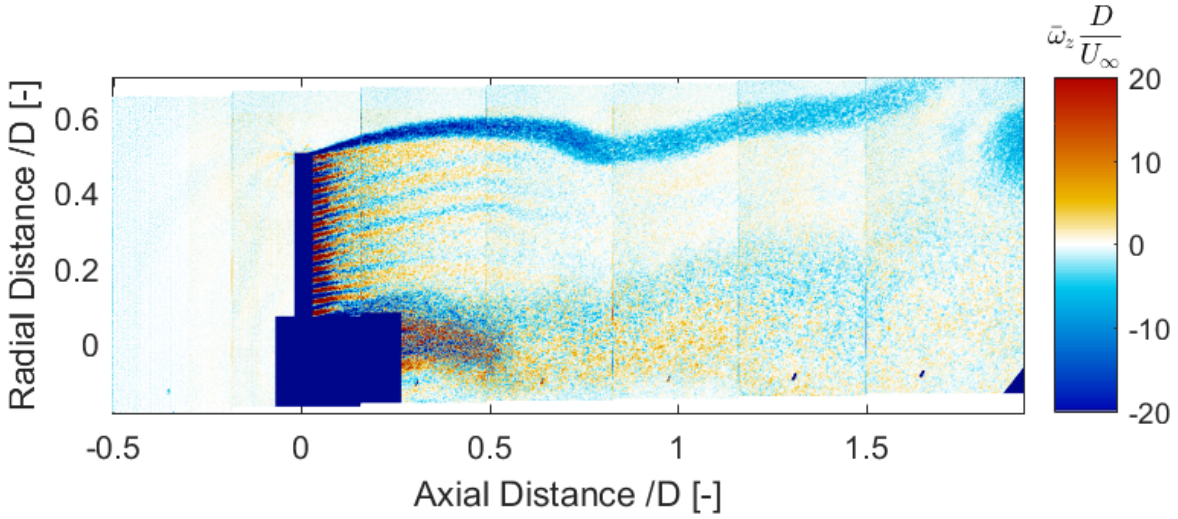

(b) Porosity = 31% (decreasing porosity) and C_T = 0.579

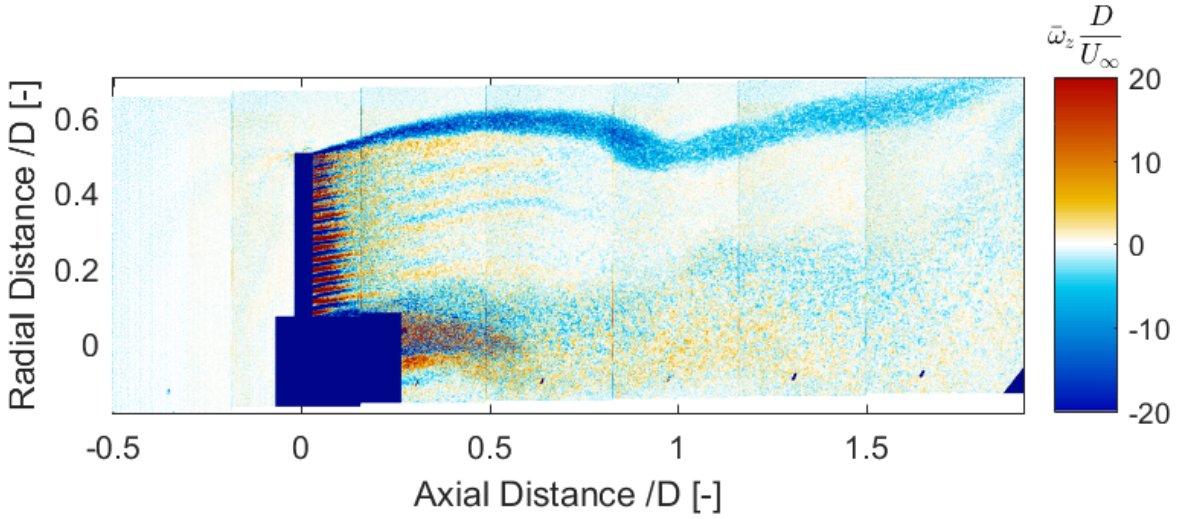

(c) Porosity = 19% (decreasing porosity) and C_T = 0.620

Figure 7.15: Normalized Vorticity Field for porosity changing with frequency = 5Hz and reduced frequency = 1.57 (Experiment)

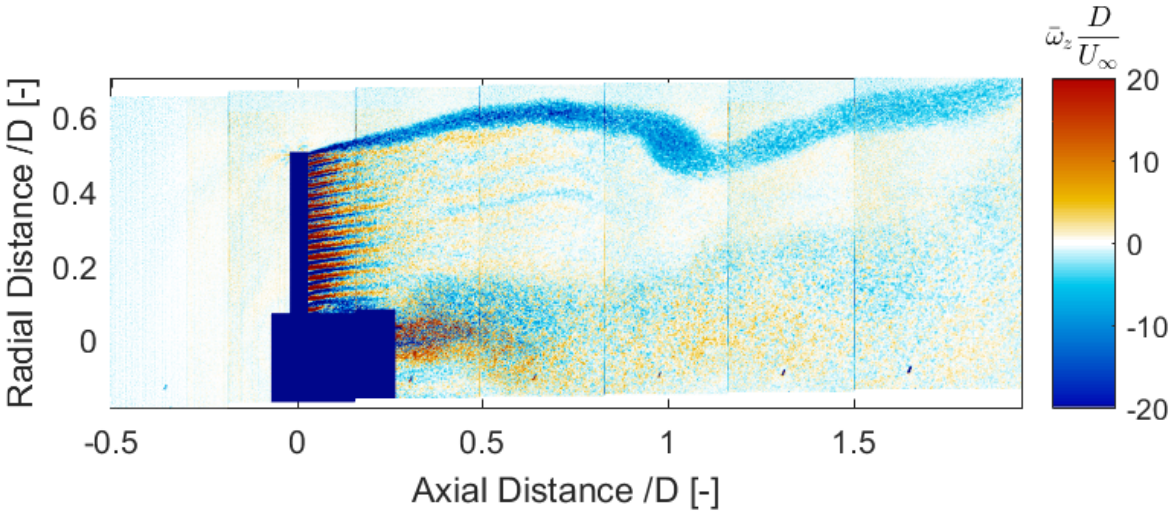

(a) Porosity = 14% (minimum porosity) and C_T = 0.705

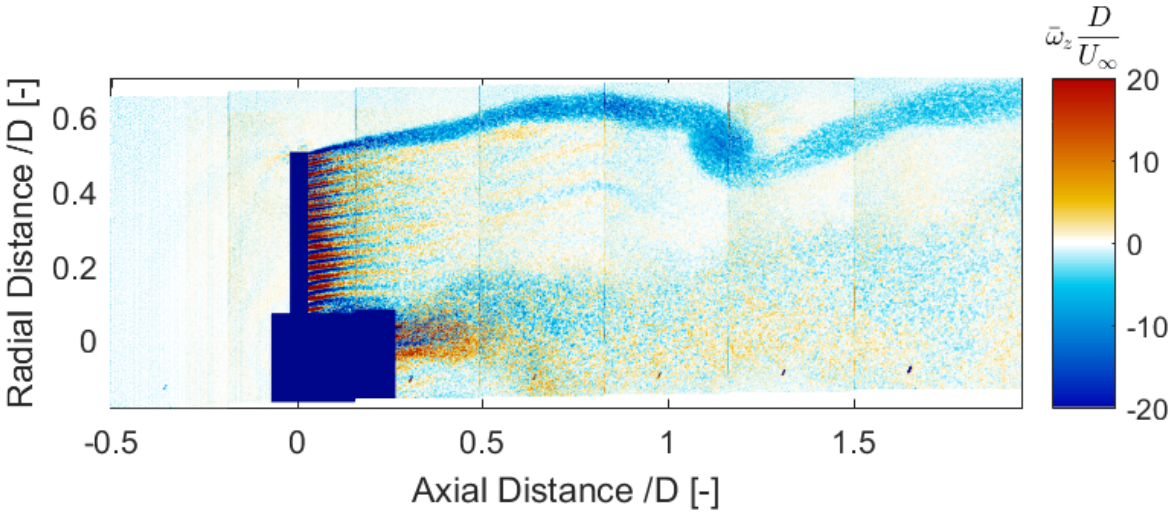

(b) Porosity = 19% (increasing porosity) and C_T = 0.697

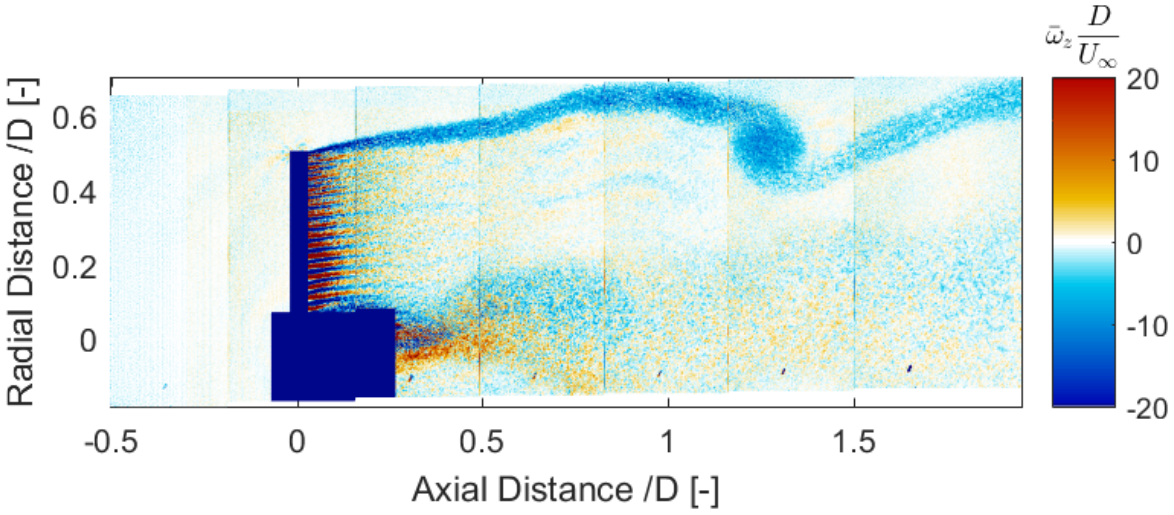

(c) Porosity = 31% (increasing porosity) C_T = 0.678

Figure 7.16: Normalized Vorticity Field for porosity changing with frequency = 5Hz and reduced frequency = 1.57 (Experiment)

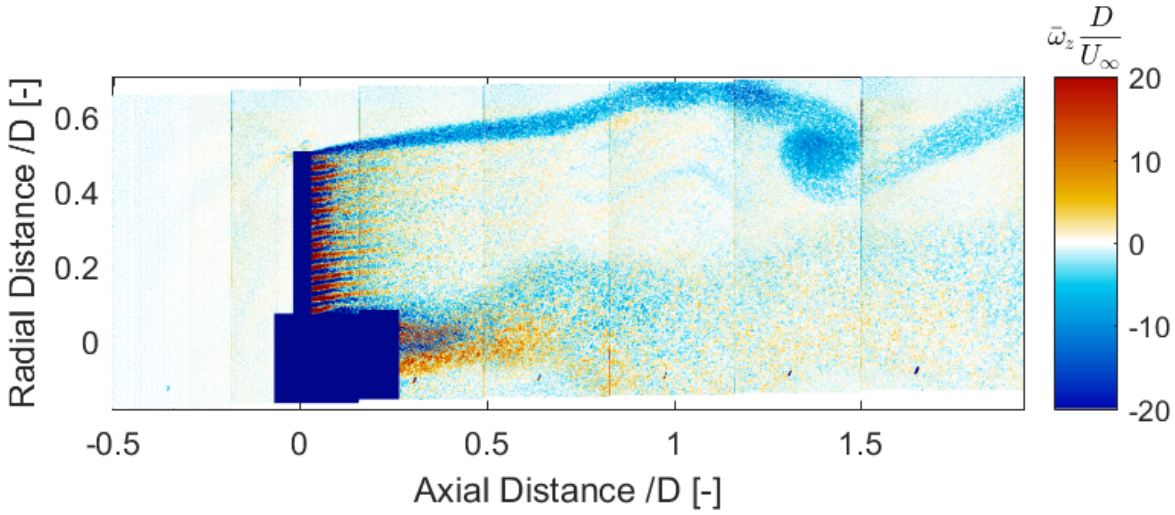

(a) Porosity = 47% (increasing porosity) and C_T = 0.657

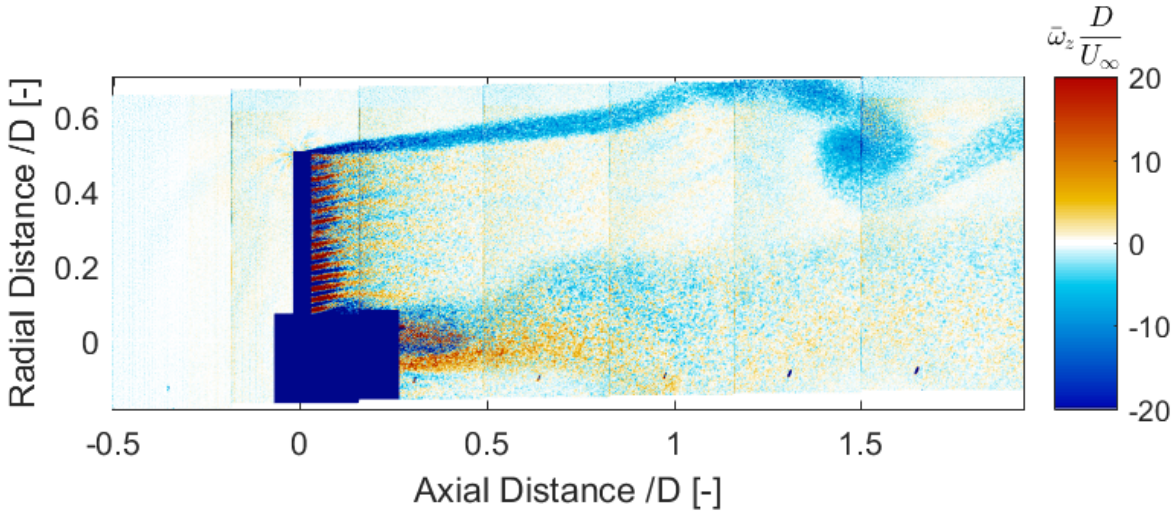

(b) Porosity = 59% (increasing porosity) and C_T = 0.596

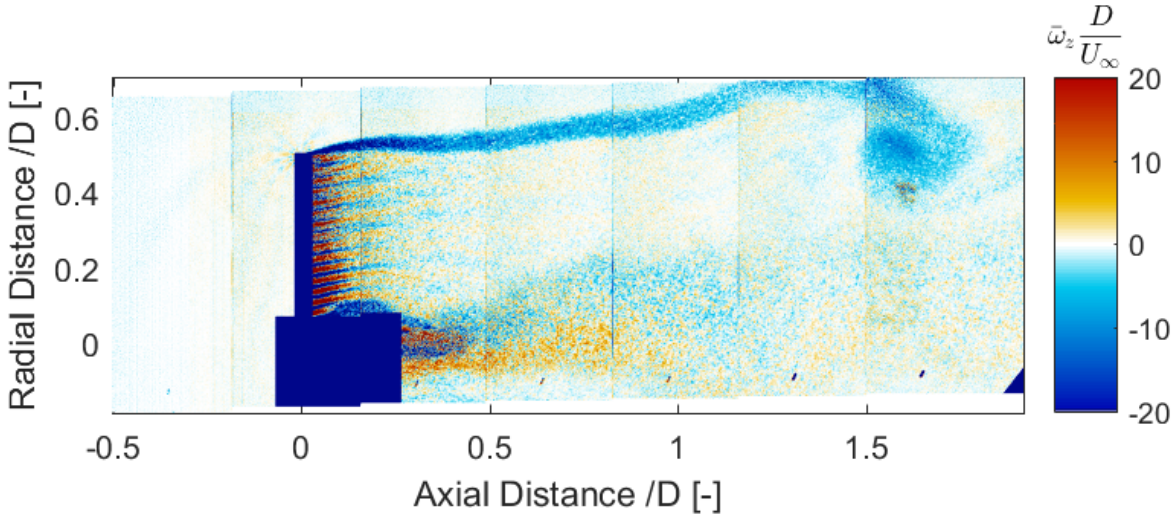

(c) Porosity = 64% (maximum porosity) and C_T = 0.550

Figure 7.17: Normalized Vorticity Field for porosity changing with frequency = 5Hz and reduced frequency = 1.57 (Experiment)

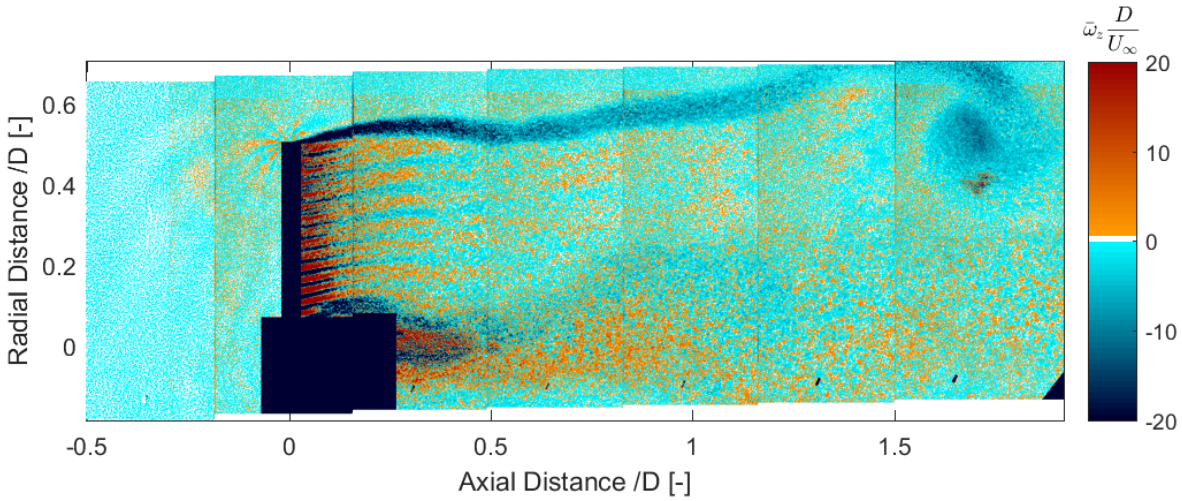

(a) Porosity = 59% (decreasing porosity) and C_T = 0.555

Figure 7.18: Normalized Vorticity Field for porosity changing with frequency = 5Hz and reduced frequency = 1.57 (Experiment)

7.2.2. FREQUENCY = 3HZ AND REDUCED FREQUENCY = 0.94

In this section, flow fields for unsteady load case in which the disc load cycle has a frequency of 3Hz and k = 0.94 are analysed.

AXIAL VELOCITY

Figure 7.19-Figure 7.22 show the normalized axial velocity field for sinusoidal porosity change with 3Hz and k = 0.94. The figures demonstrate that the general velocity trend is same as the 5Hz porosity change case. However, the major difference is the expansion and contraction of the wake. Comparing to the field of load cycle with 5Hz frequency, expansion and contraction of the wake is less frequent (or in other words stretched over the field). With decreased frequency, the change in the wake expansion is more gradual than that for the load case with the 5Hz frequency. This is most likely due to difference in loading on the disc and the speed of the load cycle. During the previous unsteady load case, load on the disc was varied faster and load cycle was broader than this case, hence wake expansion and contraction was seen more within the distance scanned.

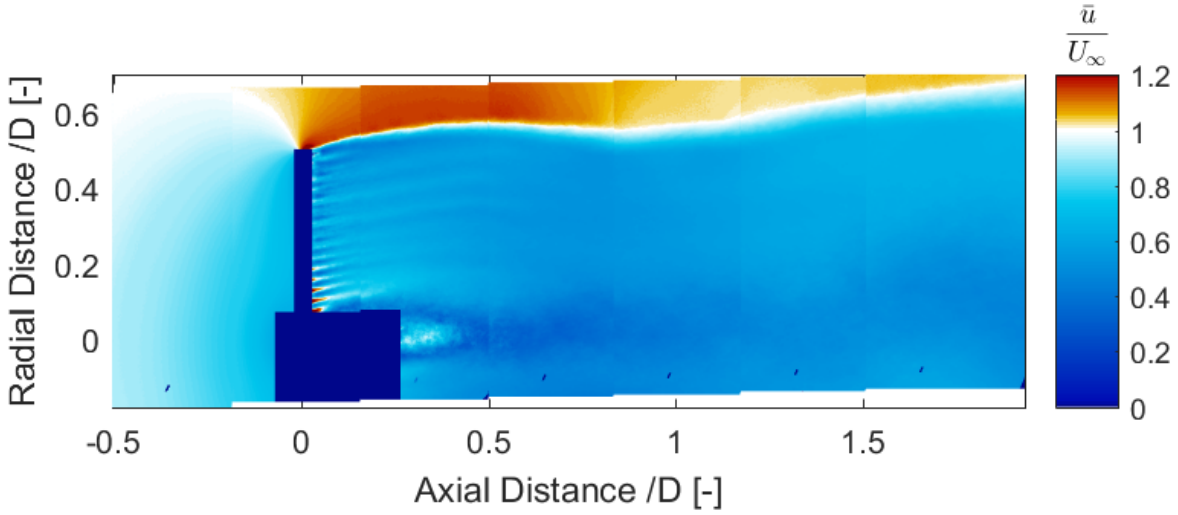

(a) Porosity = 59% (decreasing porosity) and C_T = 0.572

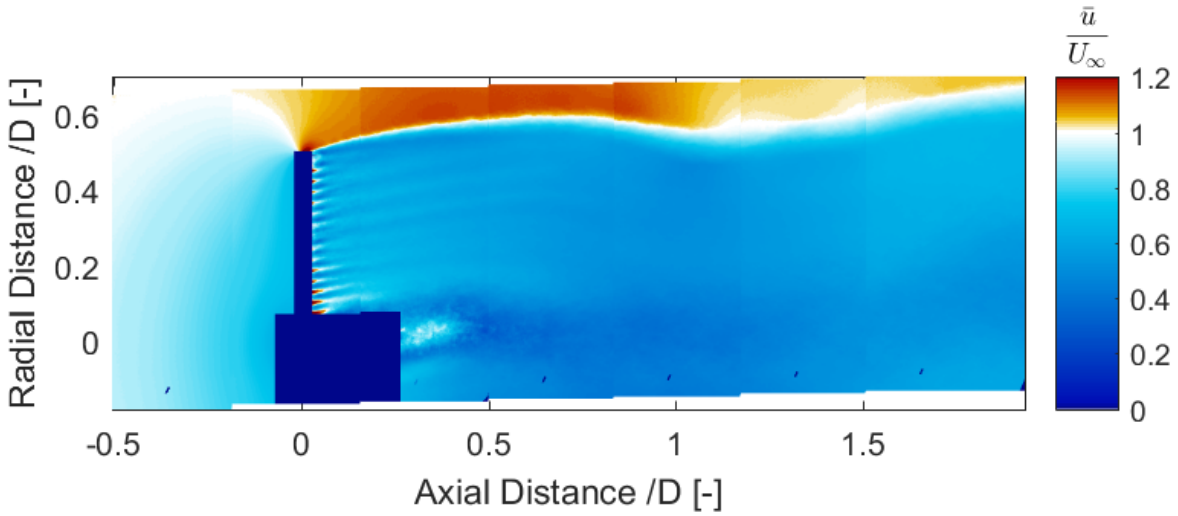

(b) Porosity = 47% (decreasing porosity) and C_T = 0.593

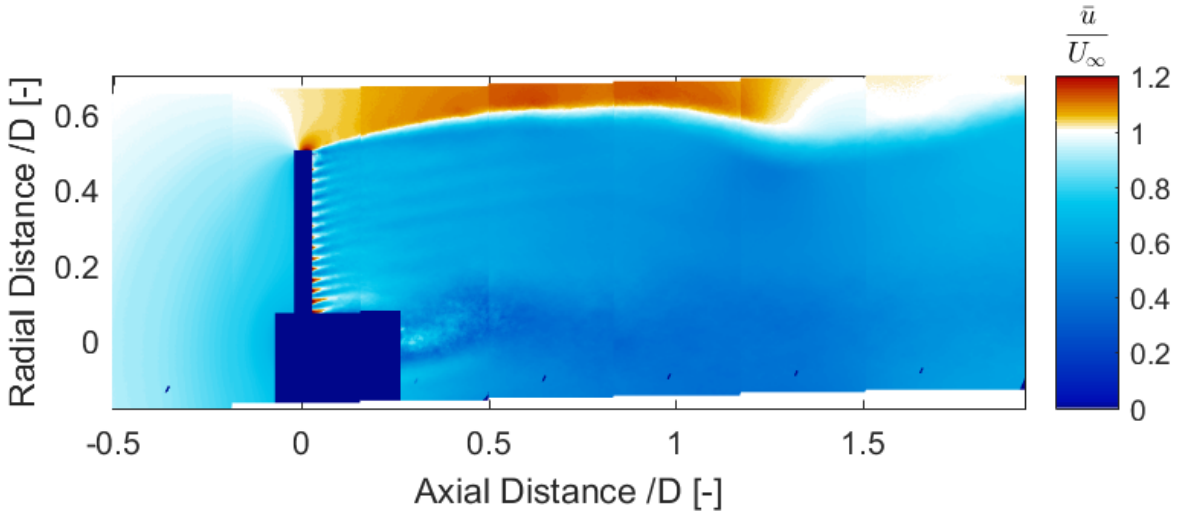

(c) Porosity = 31% (decreasing porosity) and C_T = 0.622

Figure 7.19: Normalized Axial Velocity Field for porosity changing with frequency = 3Hz and reduced frequency = 0.94 (Experiment)

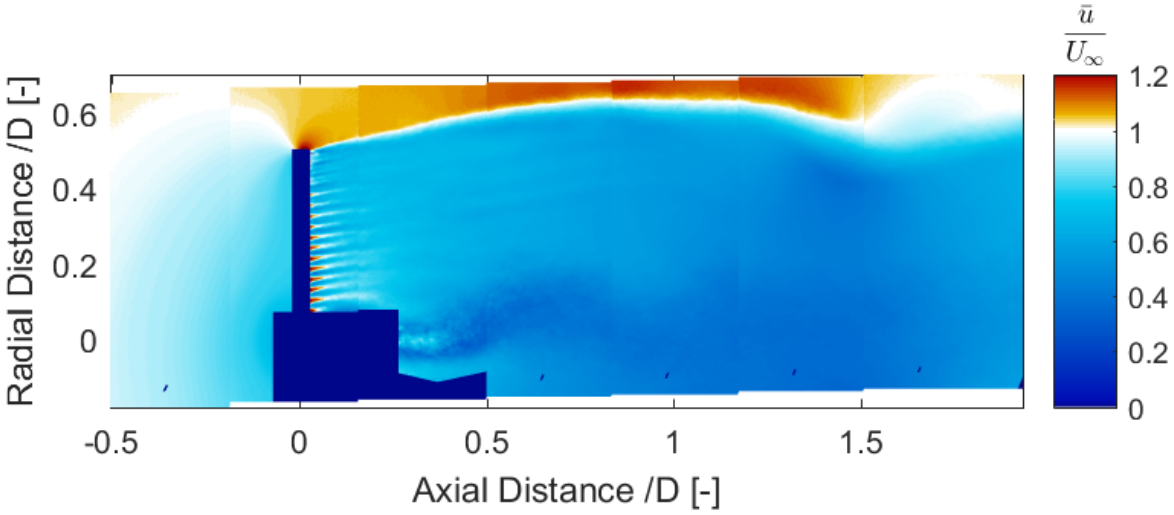

(a) Porosity = 19% (decreasing porosity) and C_T = 0.649

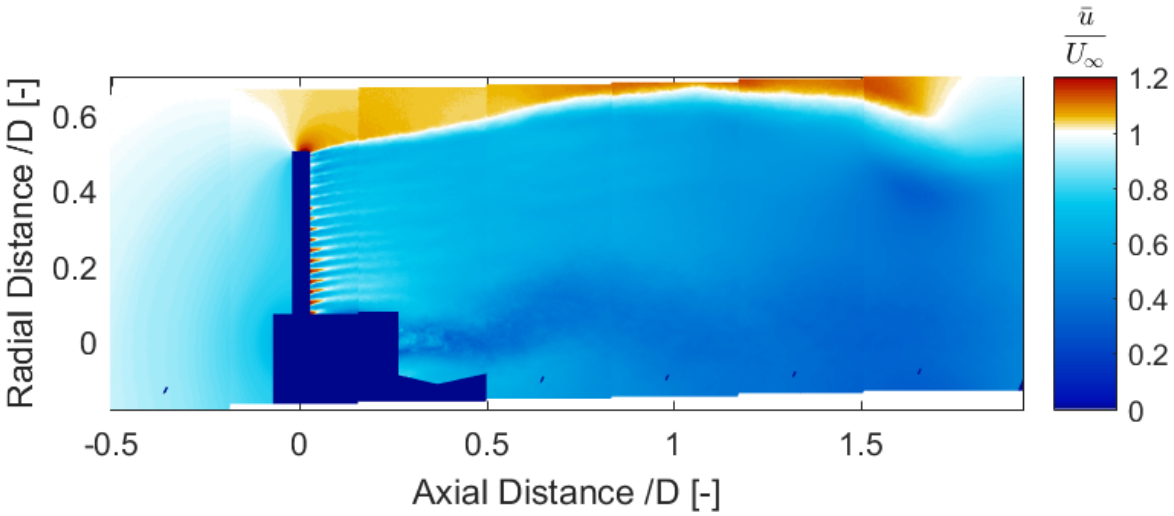

(b) Porosity = 14% (minimum porosity) and C_T = 0.684

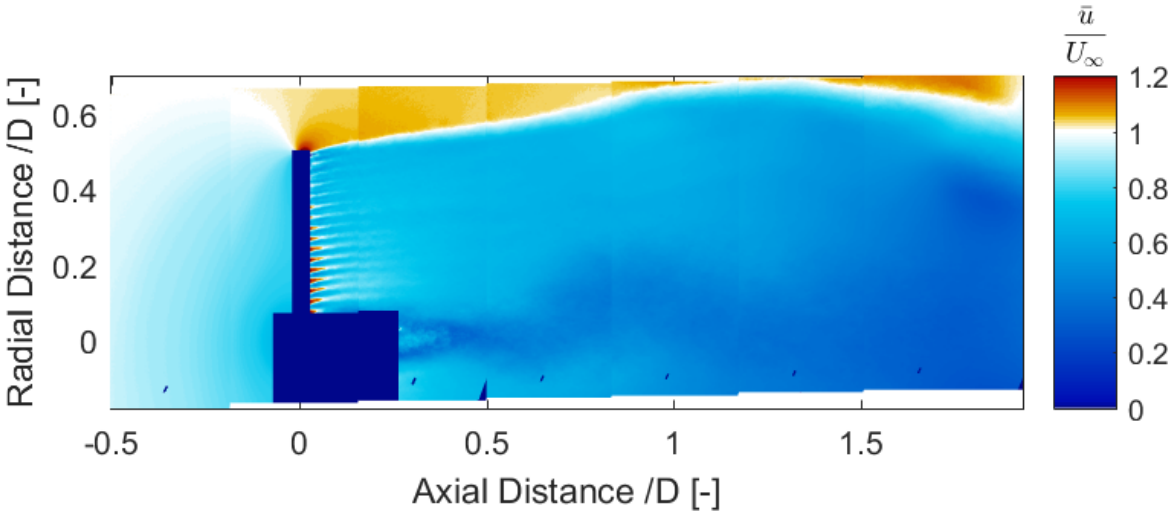

(c) Porosity = 19% (increasing porosity) and C_T = 0.671

Figure 7.20: Normalized Axial Velocity Field for porosity changing with frequency = 3Hz and reduced frequency = 0.94 (Experiment)

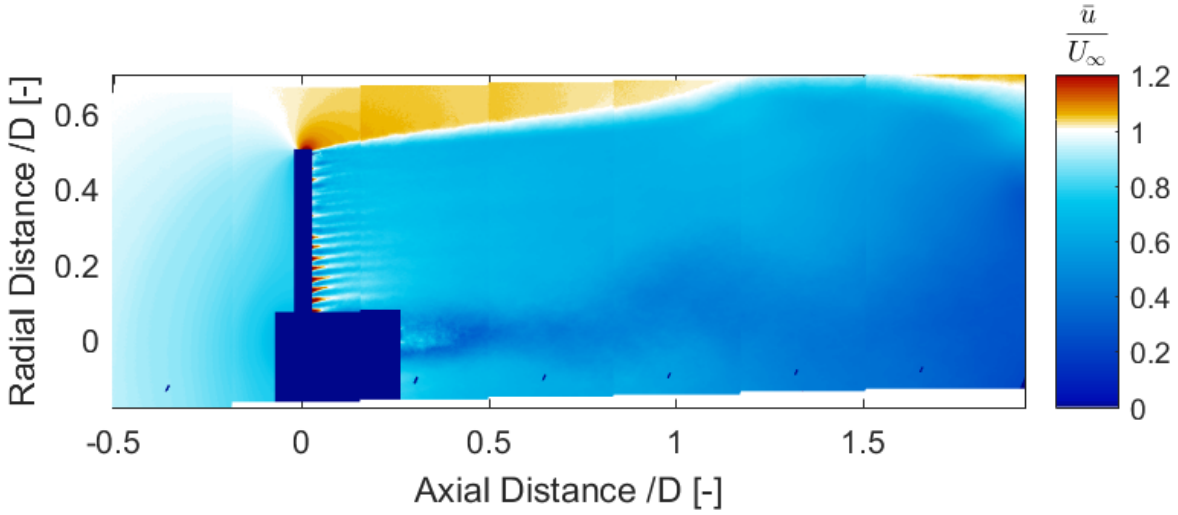

(a) Porosity = 31% (increasing porosity) and C_T = 0.651

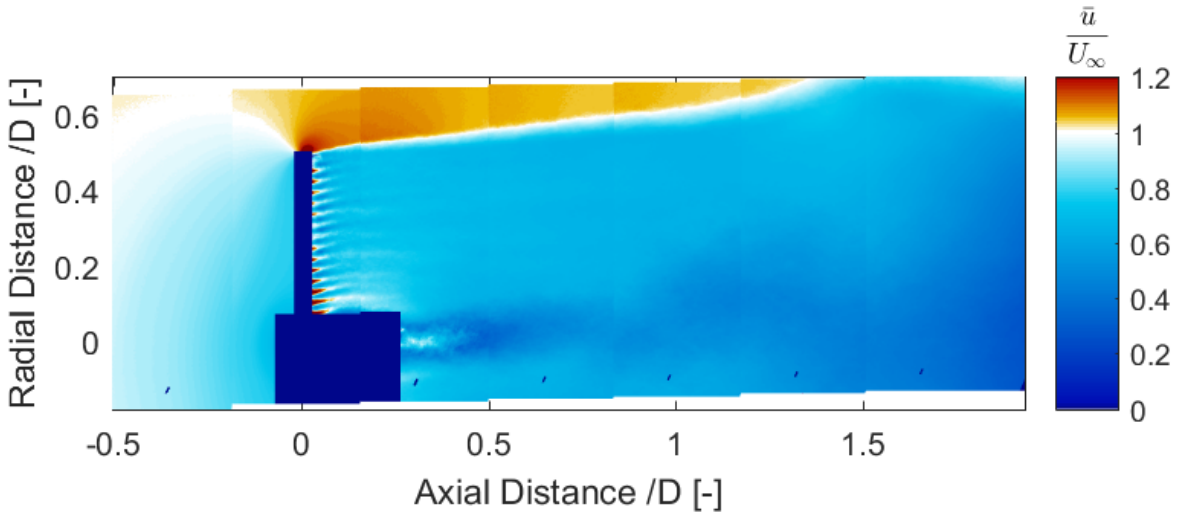

(b) Porosity = 47% (increasing porosity) and C_T = 0.612

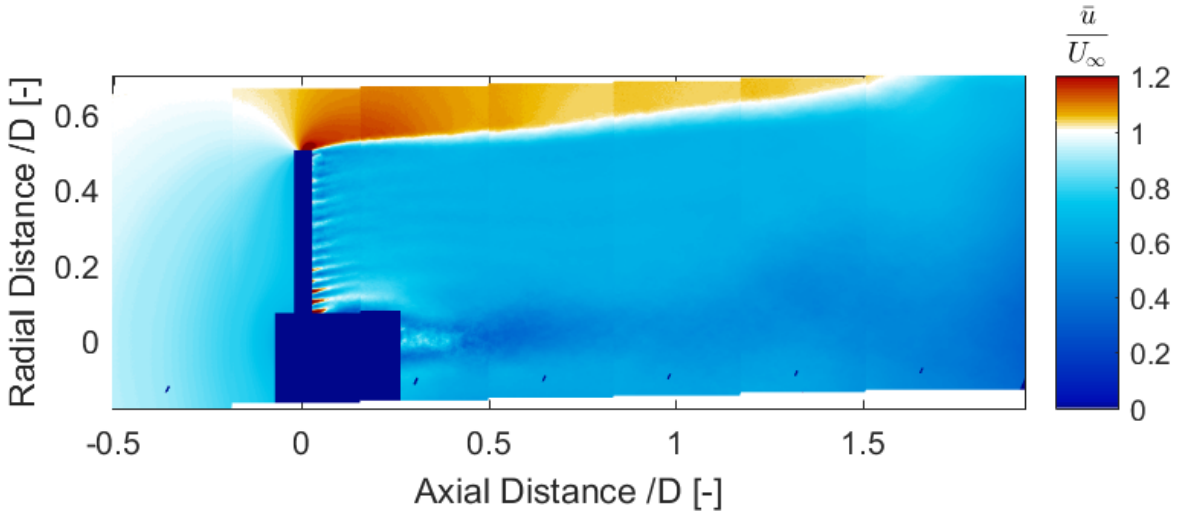

(c) Porosity = 59% (increasing porosity) and C_T = 0.584

Figure 7.21: Normalized Axial Velocity Field for porosity changing with frequency = 3Hz and reduced frequency = 0.94 (Experiment)

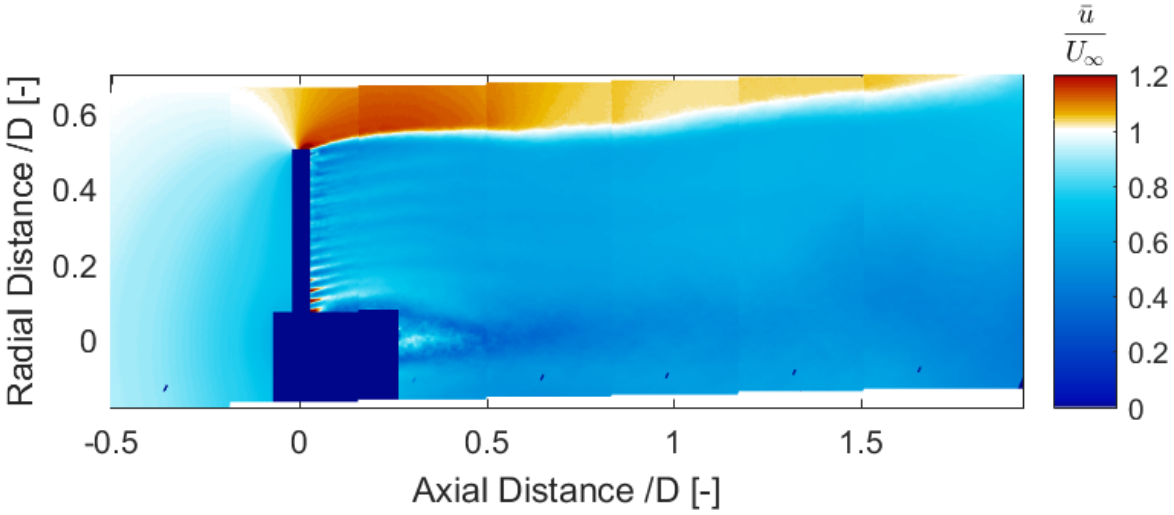

(a) Porosity = 64% (maximum porosity) and C_T = 0.569

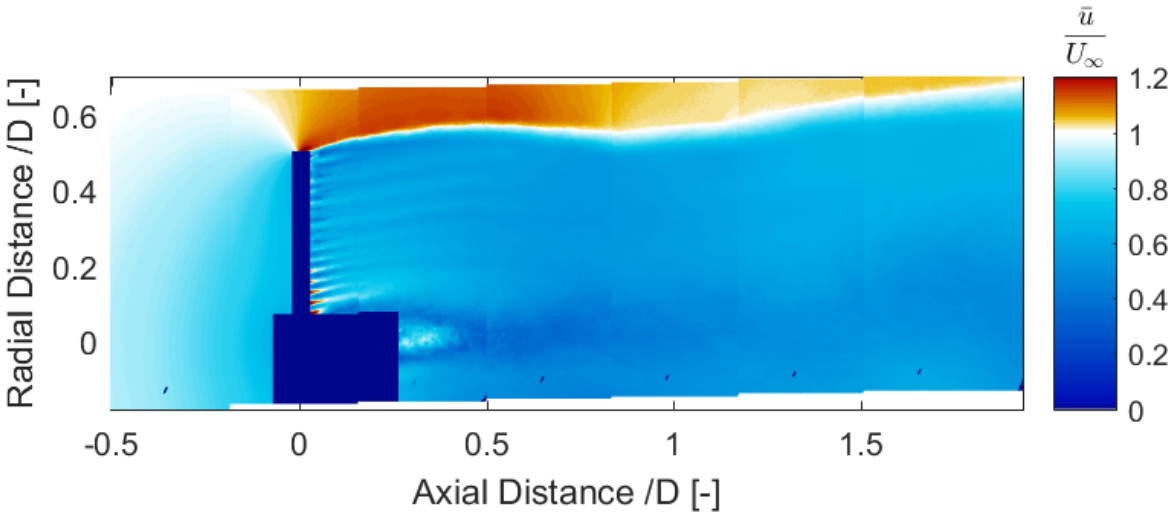

(b) Porosity = 59% (decreasing porosity) and C_T = 0.572

Figure 7.22: Normalized Axial Velocity Field for porosity changing with frequency = 3Hz and reduced frequency = 0.94 (Experiment)

RADIAL VELOCITY

Figure 7.23-Figure 7.26 show the average normalized radial velocity fields for changing load with frequency of 3Hz and k = 0.94. Like the previous cases, the general trends in the radial velocity field are similar. The fields consists both negative and positive velocity fields, with maximum around the disc edge. Compared to the previous unsteady load case (frequency = 5Hz and k = 1.57), regions with the negative and positive fields are larger for this case. This is likely because of the lower frequency of the load cycle. Similar to the previous unsteady load case, this positive and negative pattern of the radial flow field is due to the wake expansion and contraction owing to the cyclic loading. It can also be observed that some locations have higher radial velocity. These are the regions of strong vortex filament as will be seen in next section.

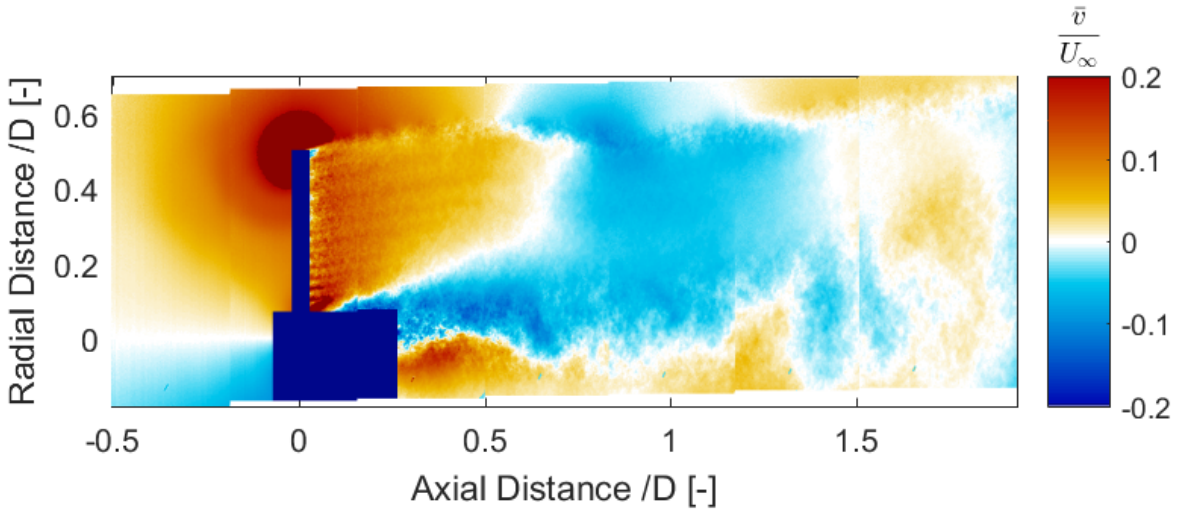

(a) Porosity = 59% (decreasing porosity) and C_T = 0.572

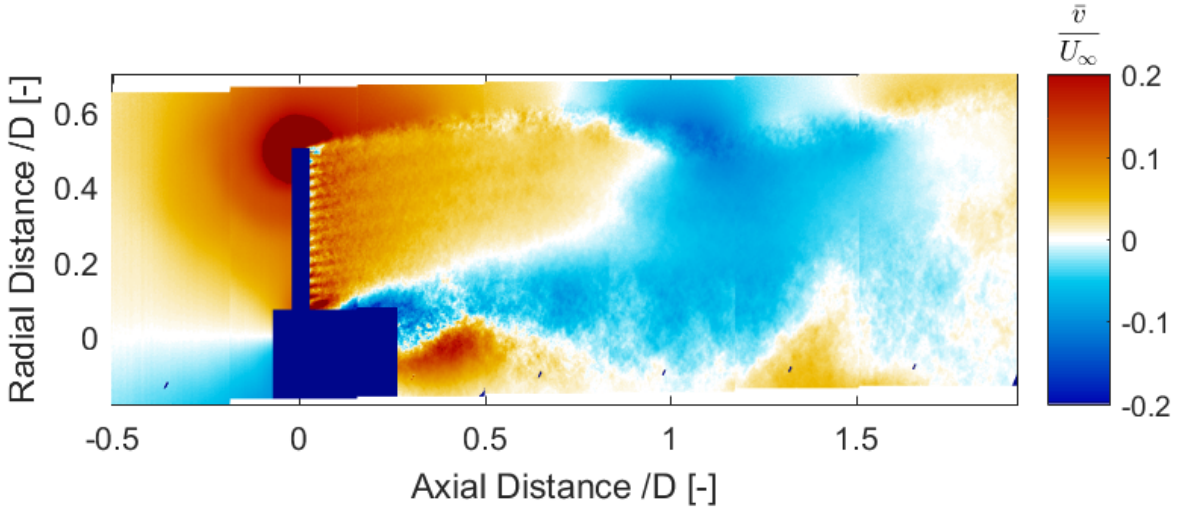

(b) Porosity = 47% (decreasing porosity) and C_T = 0.593

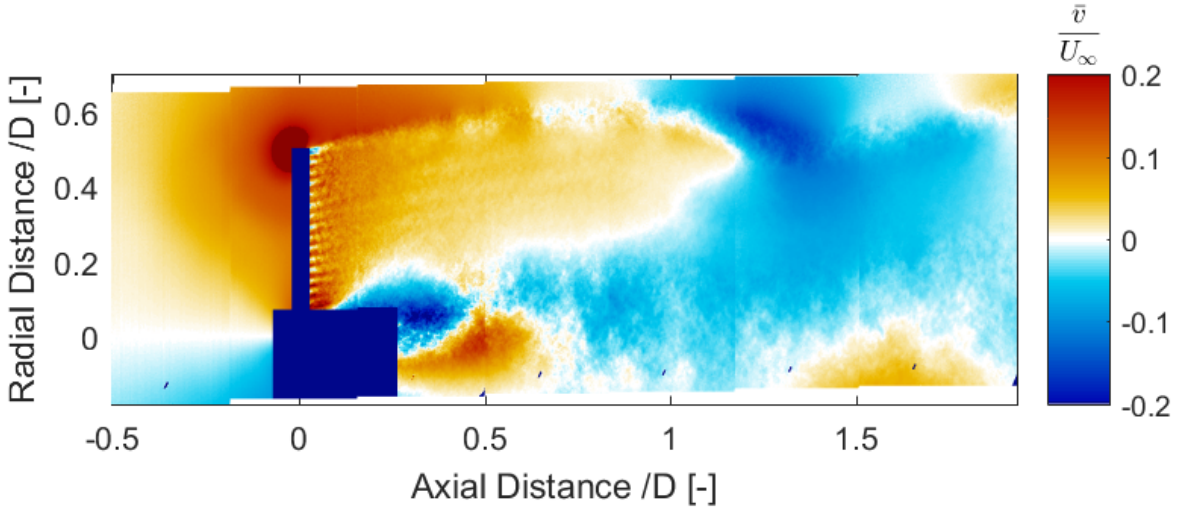

(c) Porosity = 31% (decreasing porosity) and C_T = 0.622

Figure 7.23: Normalized Radial Velocity Field for porosity changing with frequency = 3Hz and reduced frequency = 0.94 (Experiment)

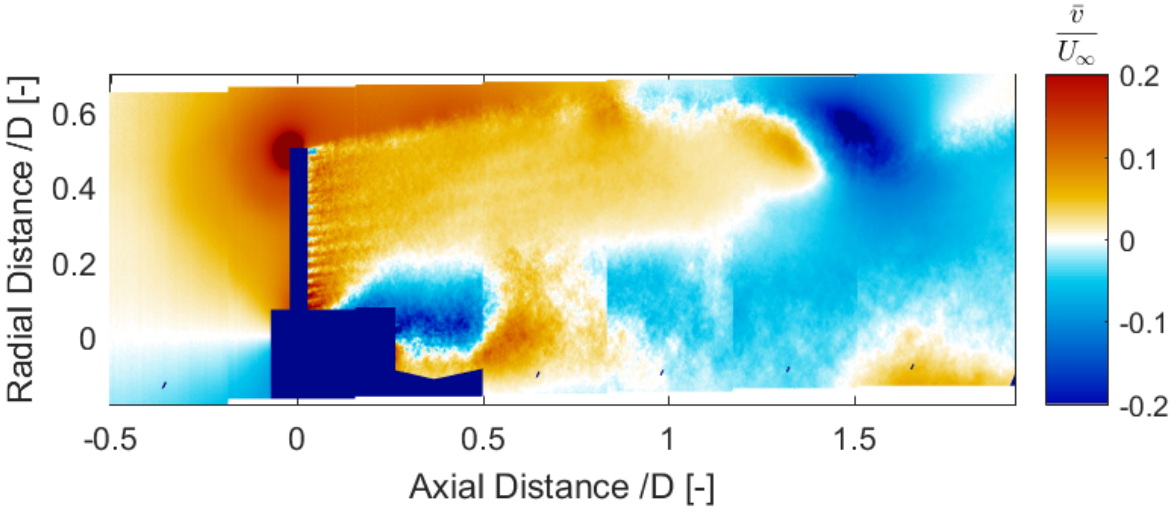

(a) Porosity = 19% (decreasing porosity) and C_T = 0.649

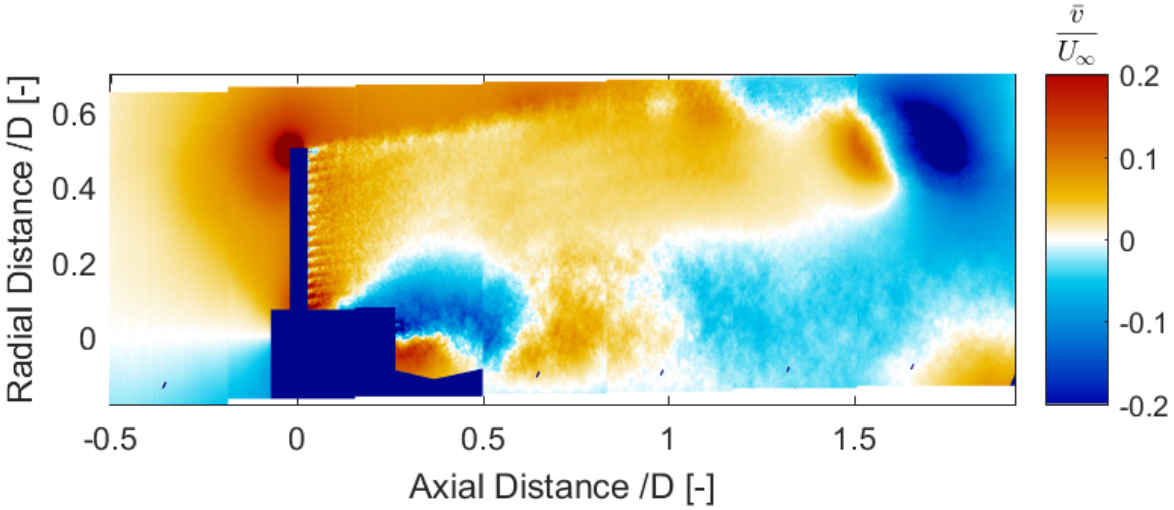

(b) Porosity = 14% (minimum porosity) and C_T = 0.684

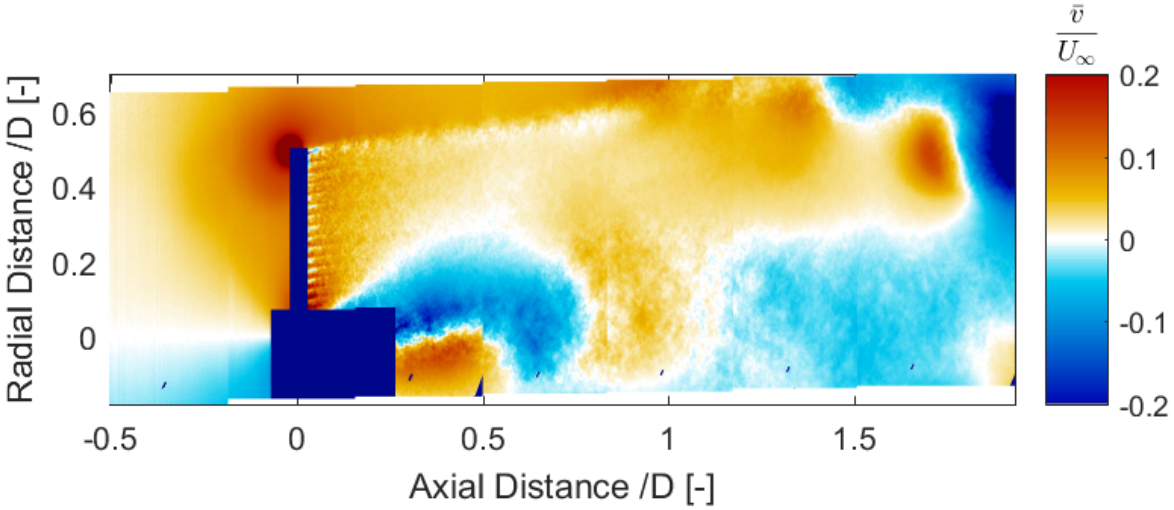

(c) Porosity = 19% (increasing porosity) and C_T = 0.671

Figure 7.24: Normalized Radial Velocity Field for porosity changing with frequency = 3Hz and reduced frequency = 0.94 (Experiment)

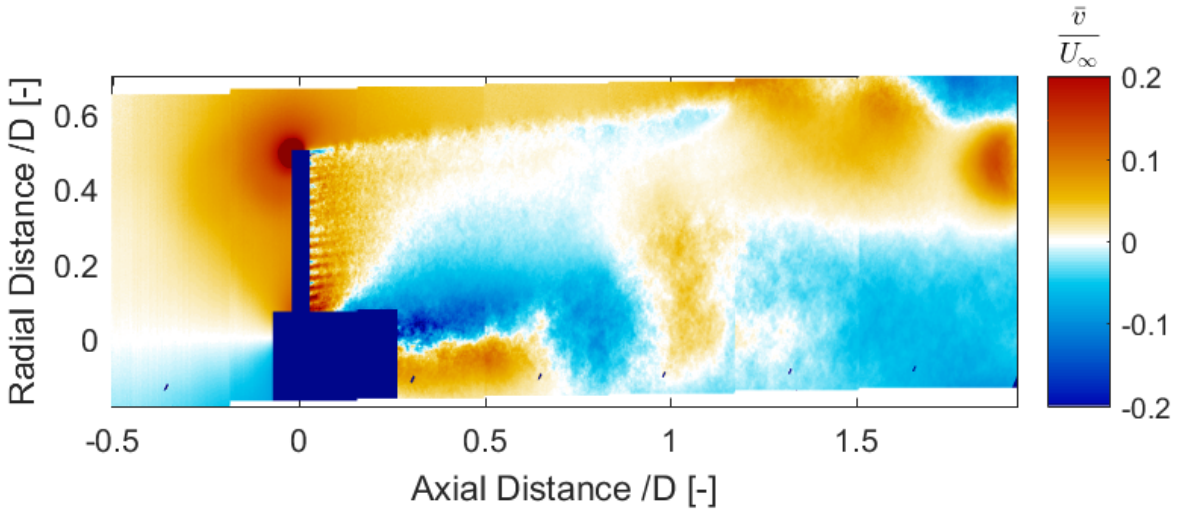

(a) Porosity = 31% (increasing porosity) and C_T = 0.651

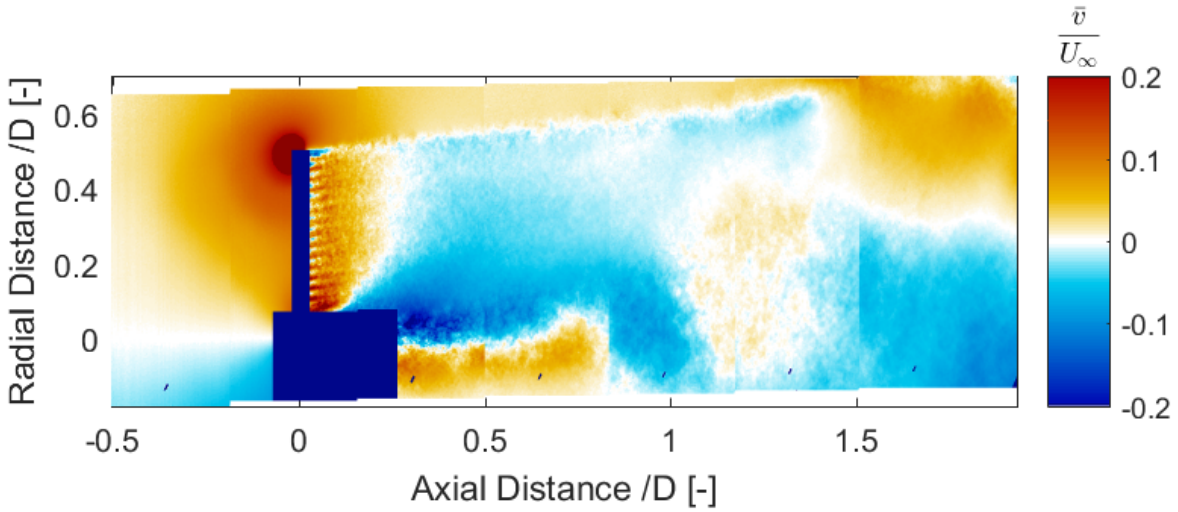

(b) Porosity = 47% (increasing porosity) and C_T = 0.612

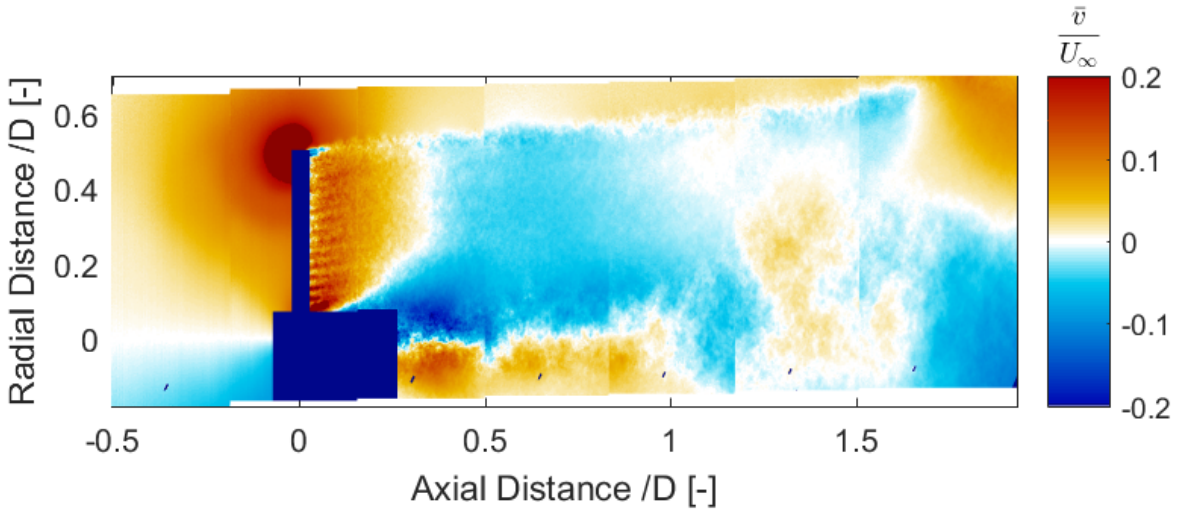

(c) Porosity = 59% (increasing porosity) and C_T = 0.584

Figure 7.25: Normalized Radial Velocity Field for porosity changing with frequency = 3Hz and reduced frequency = 0.94 (Experiment)

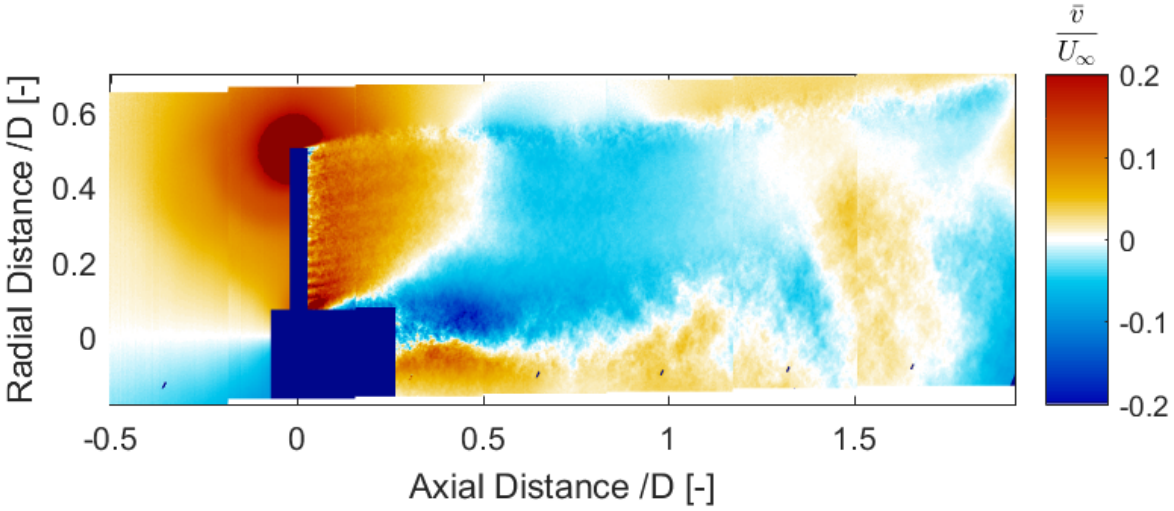

(a) Porosity = 64% (maximum porosity) and C_T = 0.569

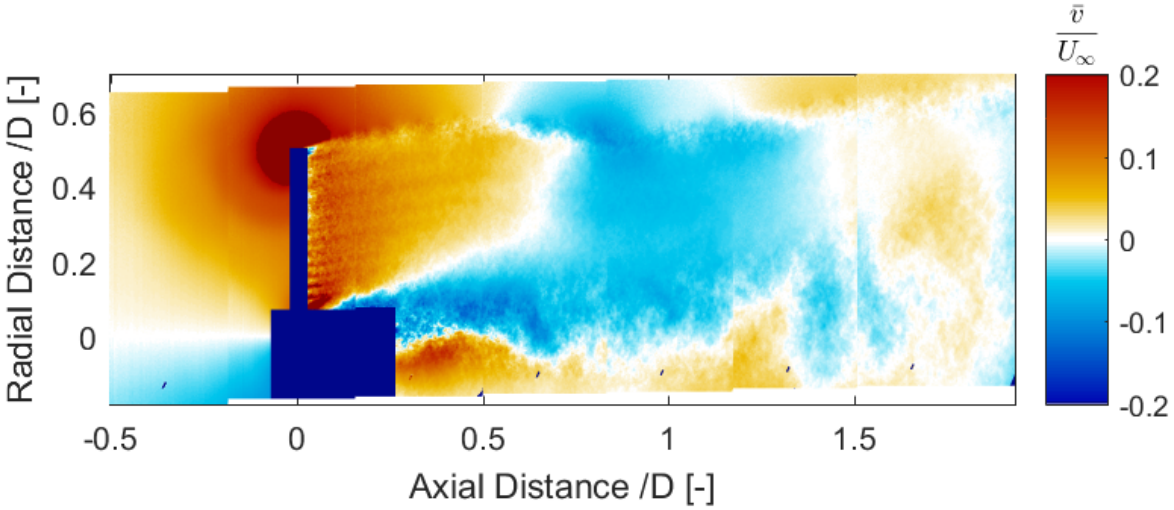

(b) Porosity = 59% (decreasing porosity) and C_T = 0.572

Figure 7.26: Normalized Radial Velocity Field for porosity changing with frequency = 3Hz and reduced frequency = 0.94 (Experiment)

VORTICITY

Figure 7.27-Figure 7.30 show the vorticity field for sinusoidal change in the disc porosity with frequency of 3Hz (k = 0.94). Similar to the previous unsteady load case which had higher reduced frequency, the vorticity is mainly negative except in the region behind the disc, which dissipates quickly. Like the previous unsteady load case, the vorticity also rolls up. A clear transportation of vorticity is visible. It can be seen that with time, the rolling up location moves downstream. When the last time-node approaches, the vorticity field also becomes more similar to the vorticity field of the first time-node. For all vorticity field, vorticity in the shear layer expands with downstream distance with different amount of expansion for different loading.

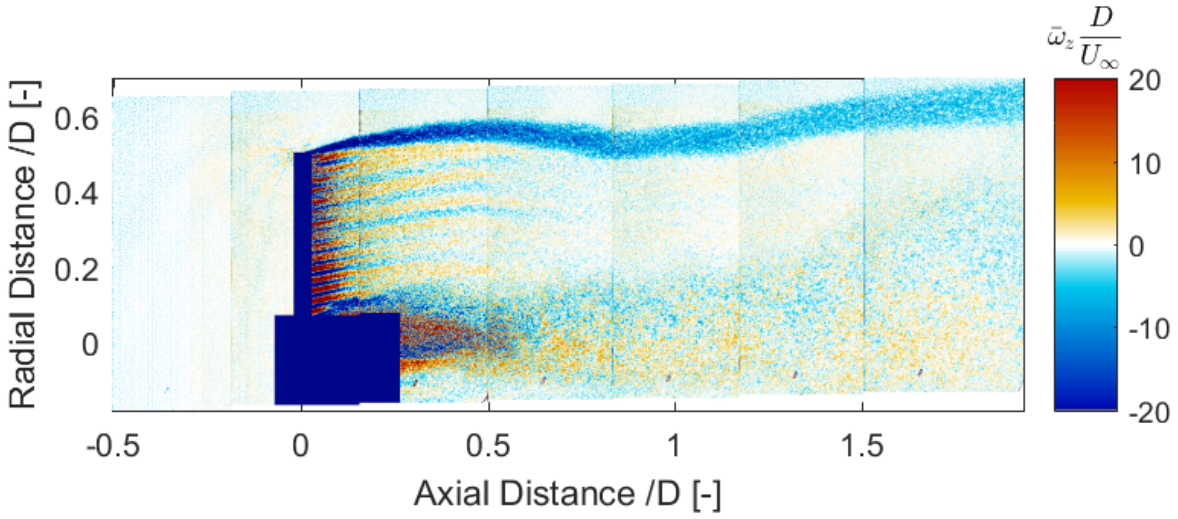

(a) Porosity = 59% (decreasing porosity) and C_T = 0.572

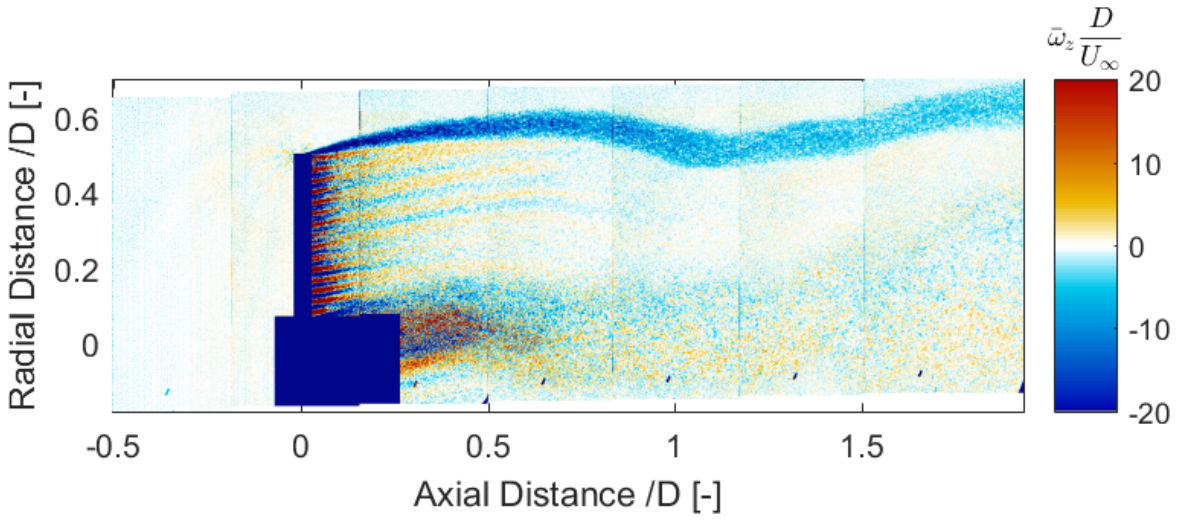

(b) Porosity = 47% (decreasing porosity) and C_T = 0.593

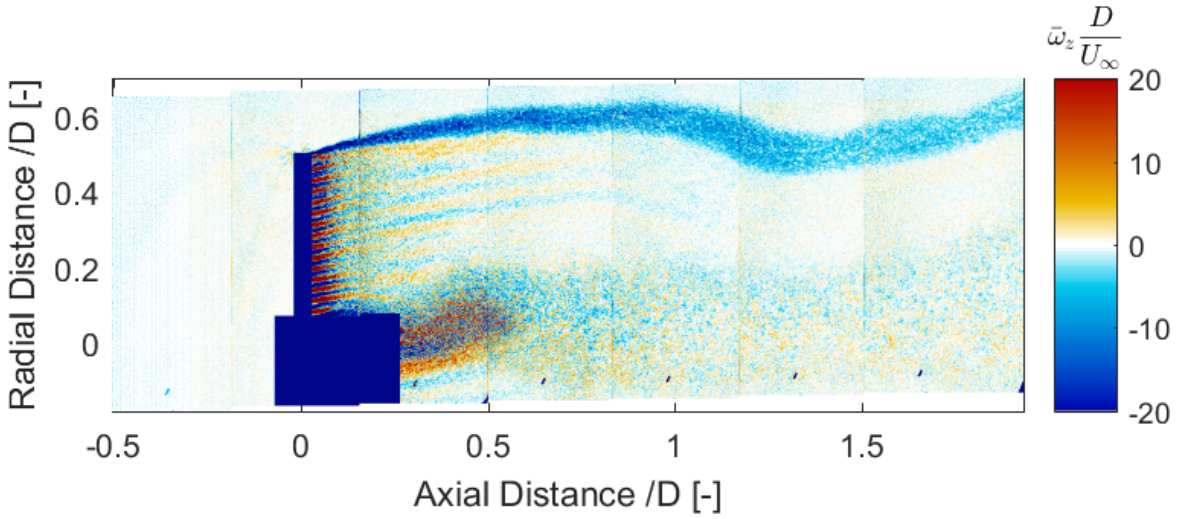

(c) Porosity = 31% (decreasing porosity) and C_T = 0.622

Figure 7.27: Normalized Vorticity Field for porosity changing with frequency = 3Hz and reduced frequency = 0.94 (Experiment)

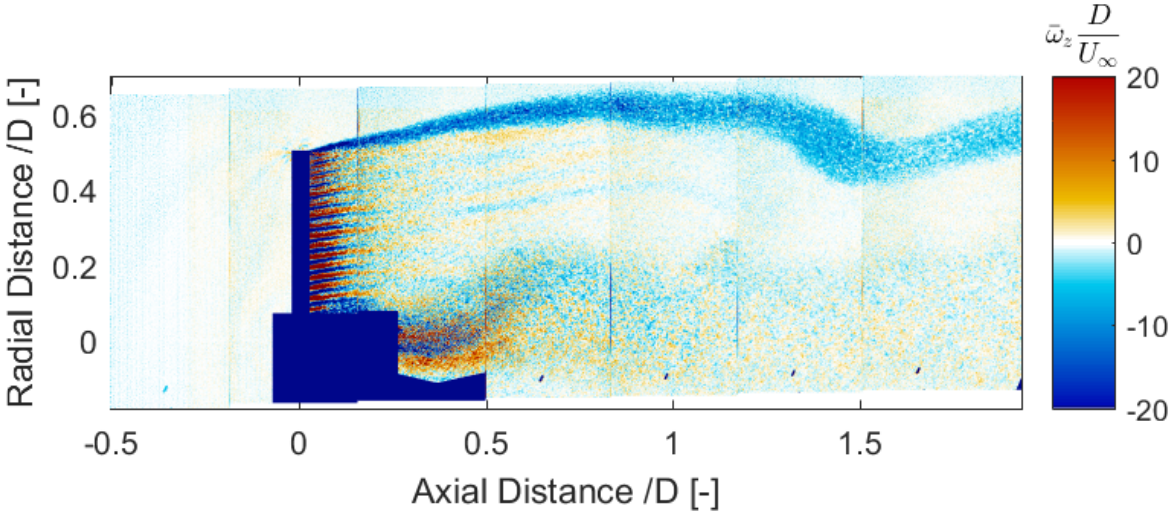

(a) Porosity = 19% (decreasing porosity) and C_T = 0.649

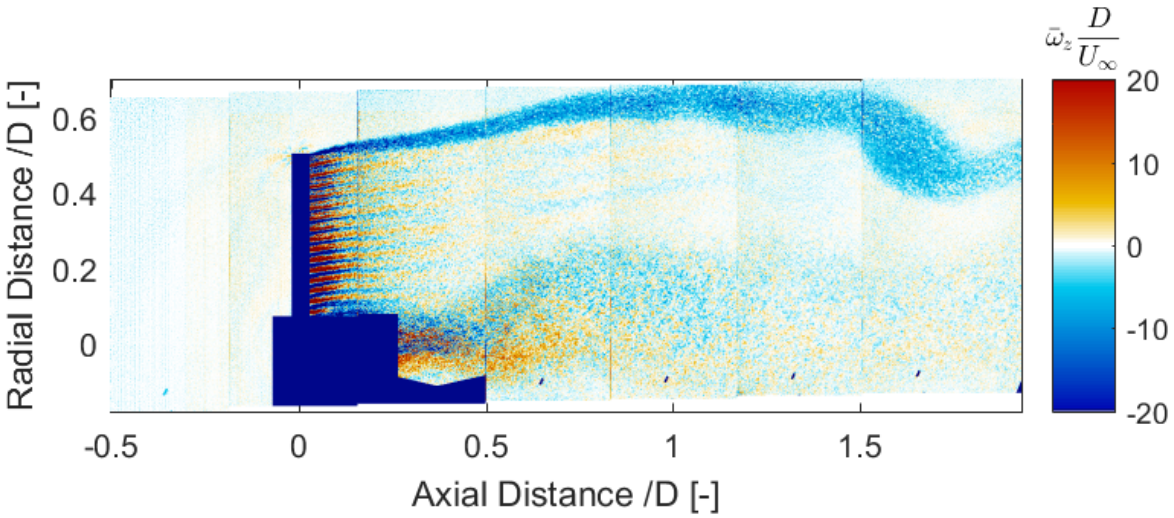

(b) Porosity = 14% (minimum porosity) and C_T = 0.684

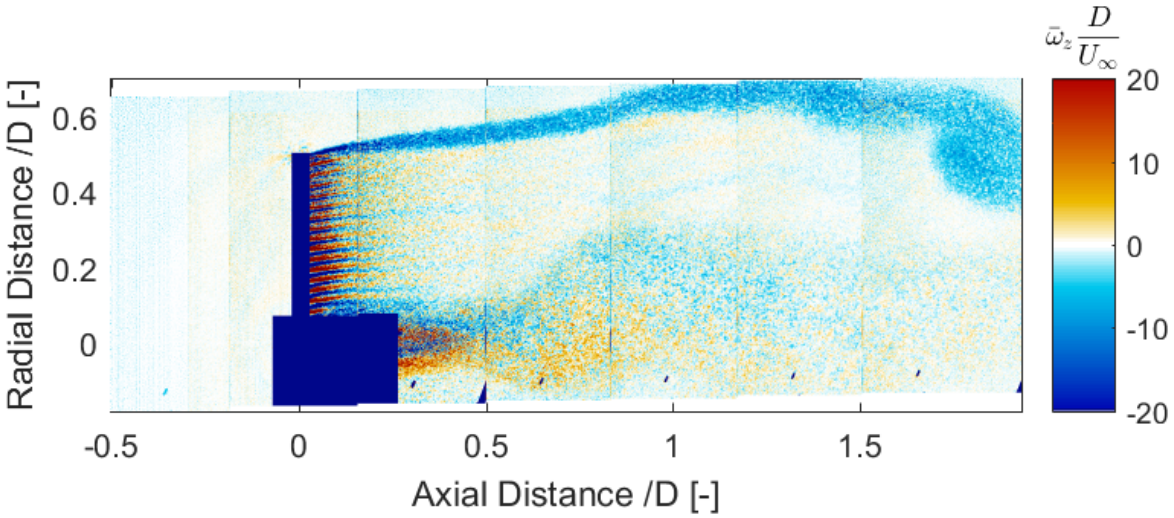

(c) Porosity = 19% (increasing porosity) and C_T = 0.671

Figure 7.28: Normalized Vorticity Field for porosity changing with frequency = 3Hz and reduced frequency = 0.94 (Experiment)

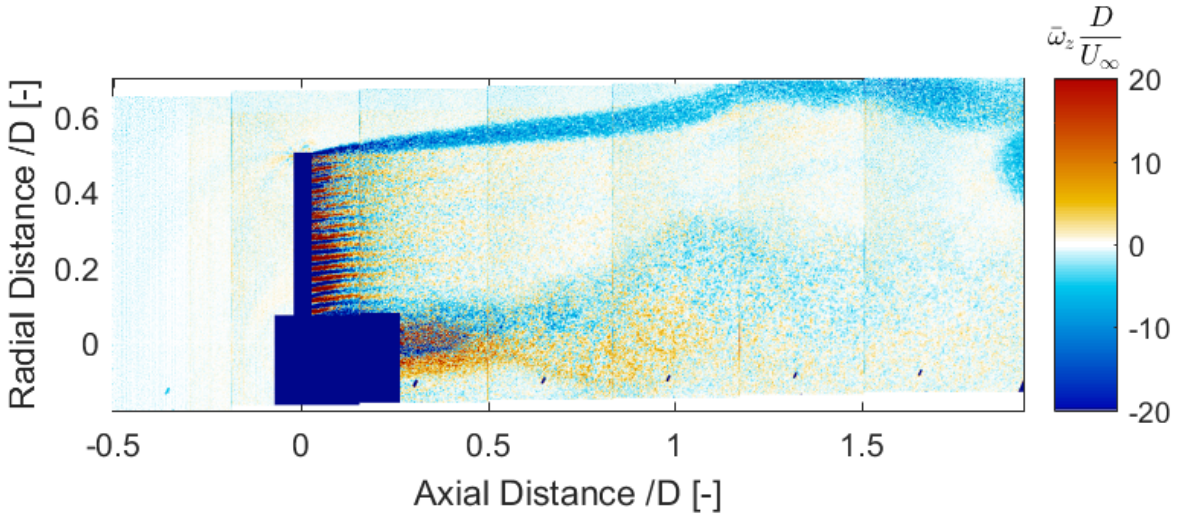

(a) Porosity = 31% (increasing porosity) and C_T = 0.651

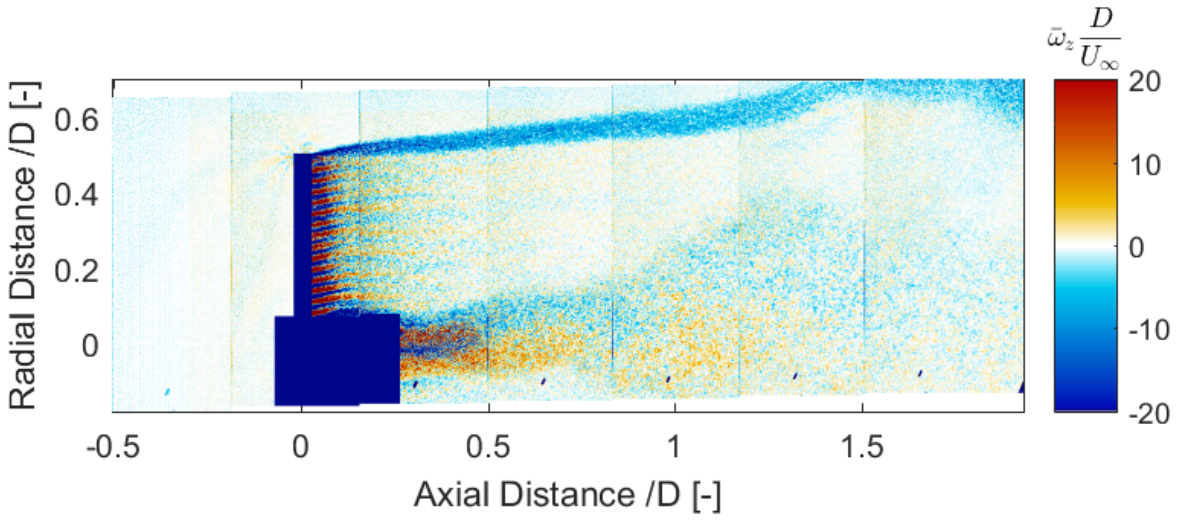

(b) Porosity = 47% (increasing porosity) and C_T = 0.612

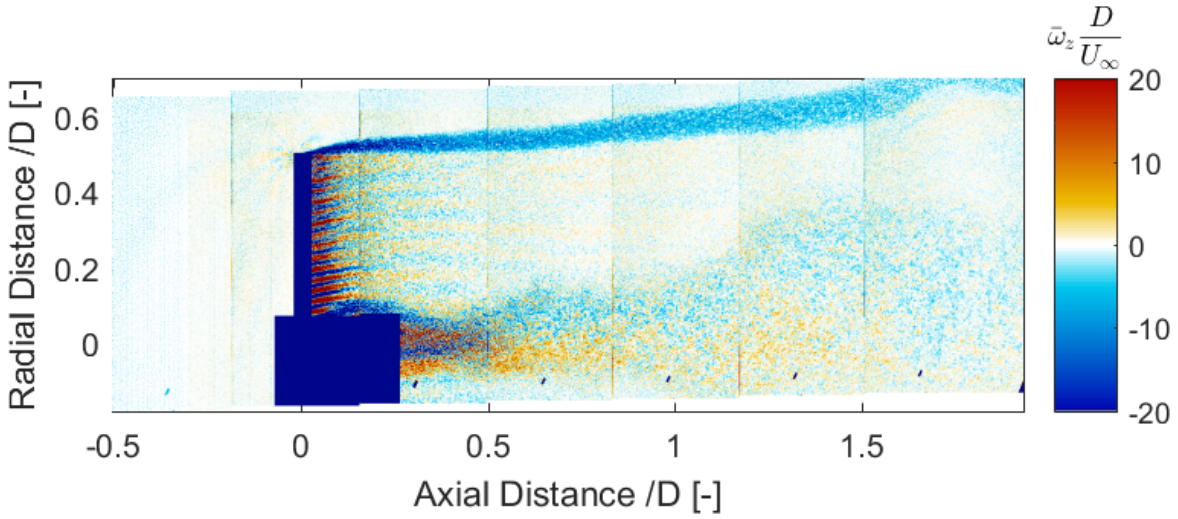

(c) Porosity = 59% (increasing porosity) and C_T = 0.584

Figure 7.29: Normalized Vorticity Field for porosity changing with frequency = 3Hz and reduced frequency = 0.94 (Experiment)

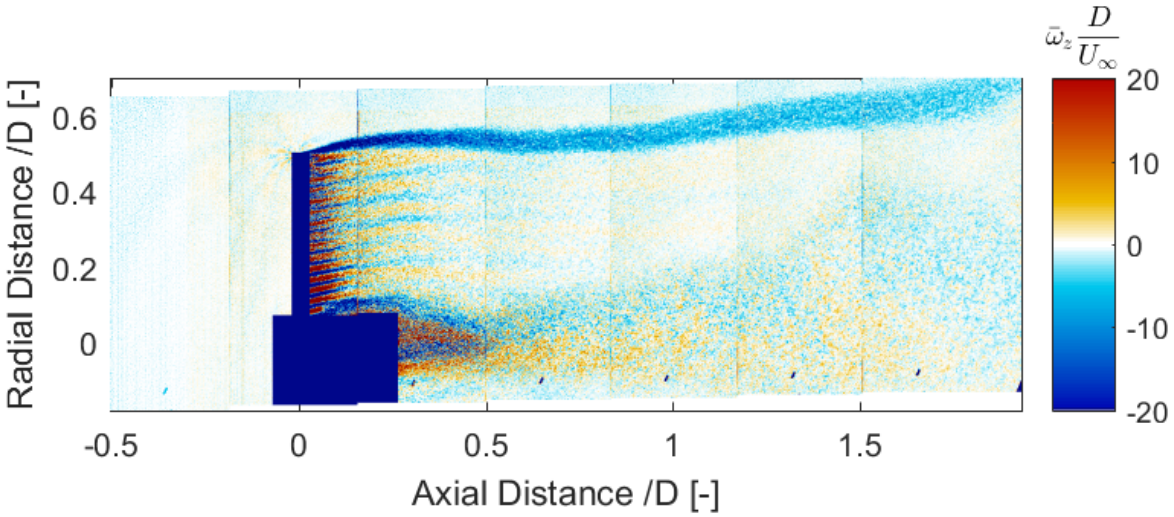

(a) Porosity = 64% (maximum porosity) and C_T = 0.569

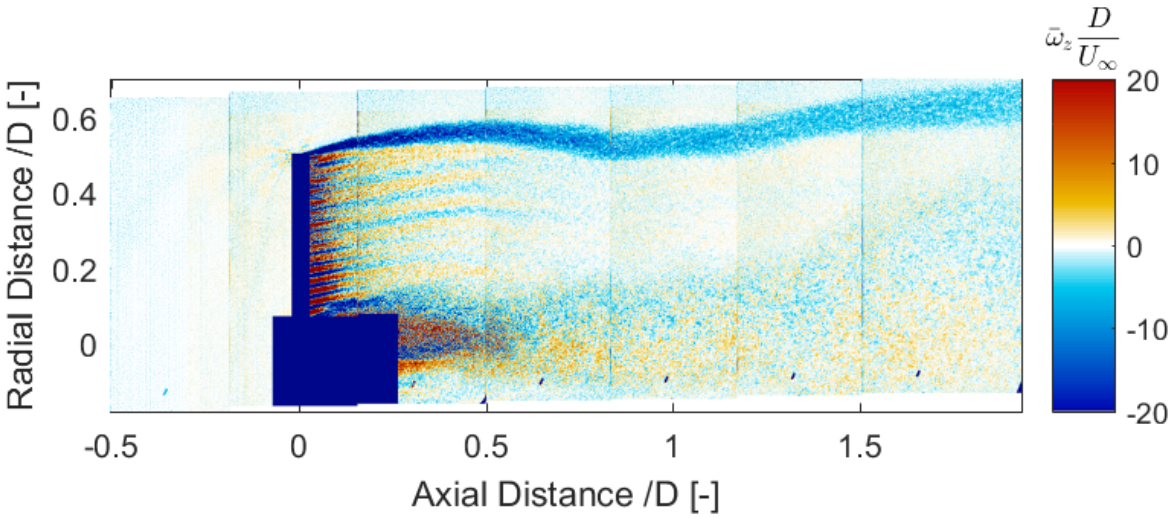

(b) Porosity = 59% (decreasing porosity) and C_T = 0.572

Figure 7.30: Normalized Vorticity Field for porosity changing with frequency = 3Hz and reduced frequency = 0.94 (Experiment)

7.2.3. FREQUENCY = 1.5HZ AND REDUCED FREQUENCY = 0.47

In this section, for unsteady load case in which the disc load cycle has a frequency of 1.5Hz and k = 0.94, velocity and vorticity fields are discussed.

AXIAL VELOCITY

Figure 7.31-Figure 7.34 display the average normalized axial velocity field for sinusoidal porosity change with the frequency of 1.5Hz (k = 0.47). This is the case with minimum frequency, so it shows the least unsteadiness in its flow fields among all the unsteady load cases. This can be seen in the axial velocity fields. Compared to the last two load cases, the wake expansion and contraction does not take place as fast over the same scanned distance. However, the effect is still present contrary to the steady cases for which the wake expansion only increases with the downstream distance. In other words, this case is the closest to the steady load cases. With decreasing porosity and increasing load, the field very near to the disc expands more. This is an effect of loading on the disc.

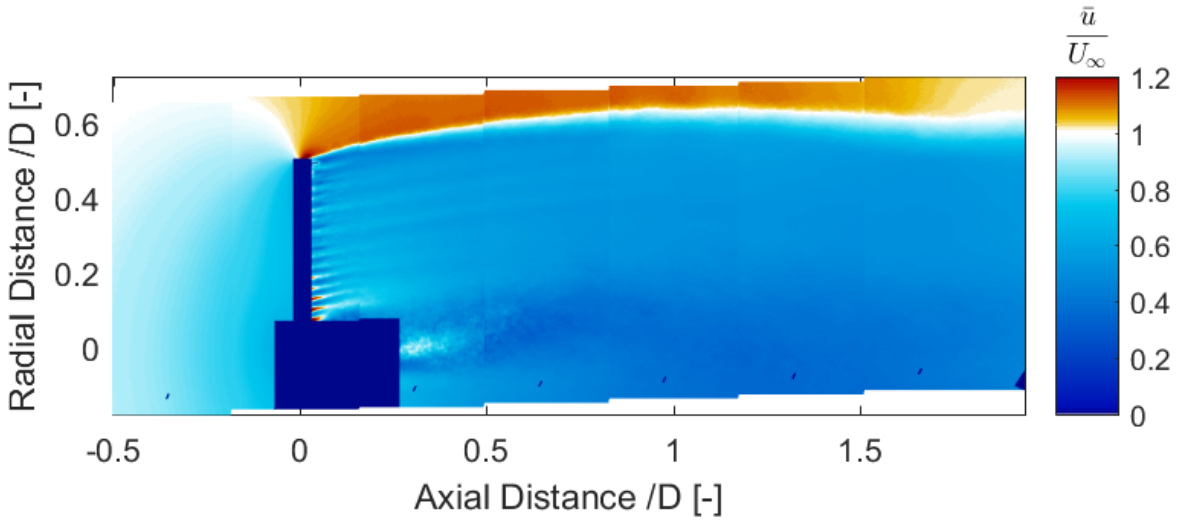

(a) Porosity = 59% (decreasing porosity) and C_T = 0.566

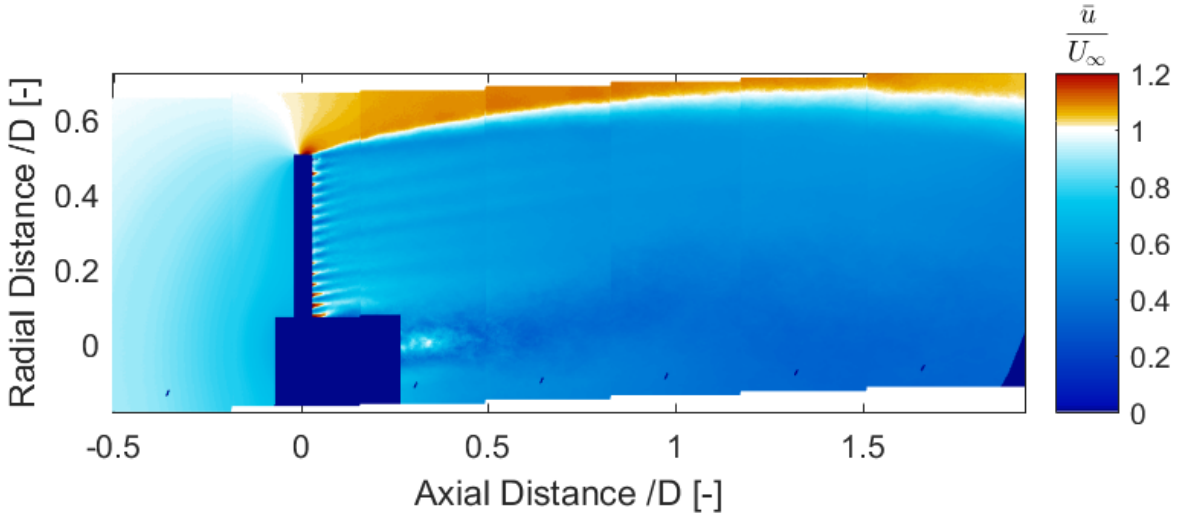

(b) Porosity = 47% (decreasing porosity) and C_T = 0.605

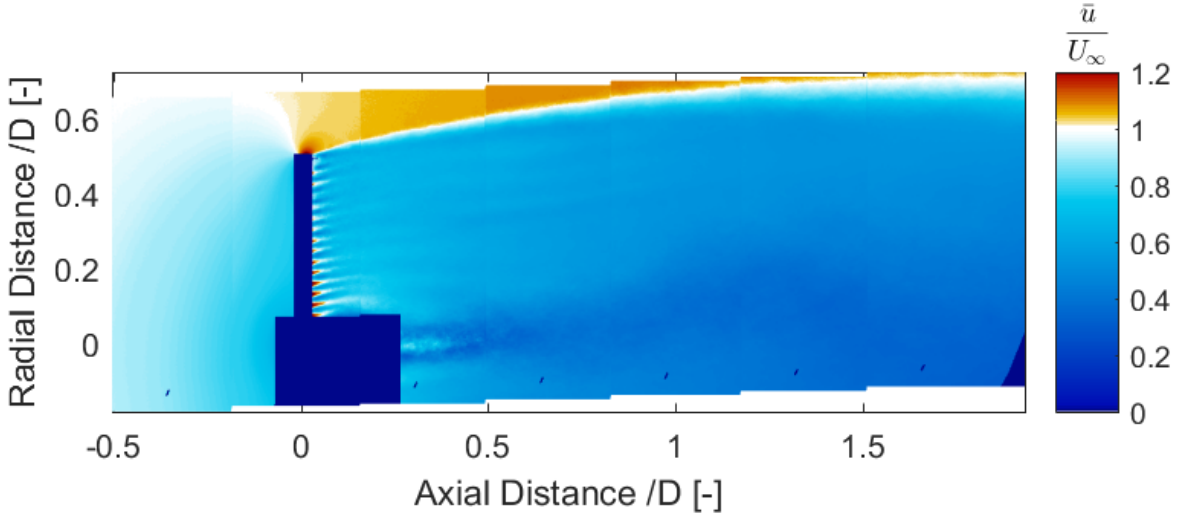

(c) Porosity = 31% (decreasing porosity) and C_T = 0.639

Figure 7.31: Normalized Axial Velocity Field for porosity changing with frequency = 1.5Hz and reduced frequency = 0.47 (Experiment)

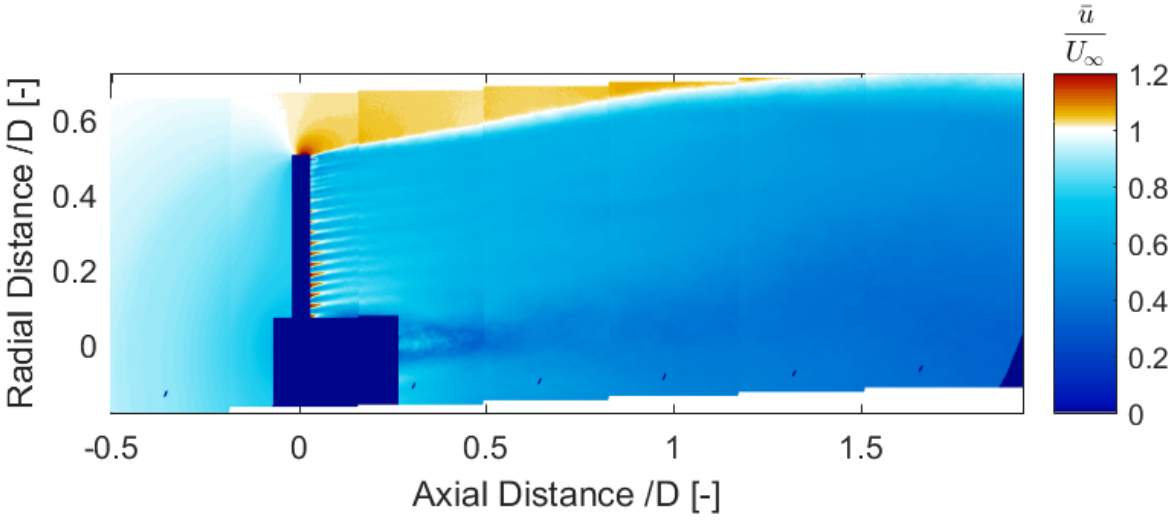

(a) Porosity = 19% (decreasing porosity) and C_T = 0.666

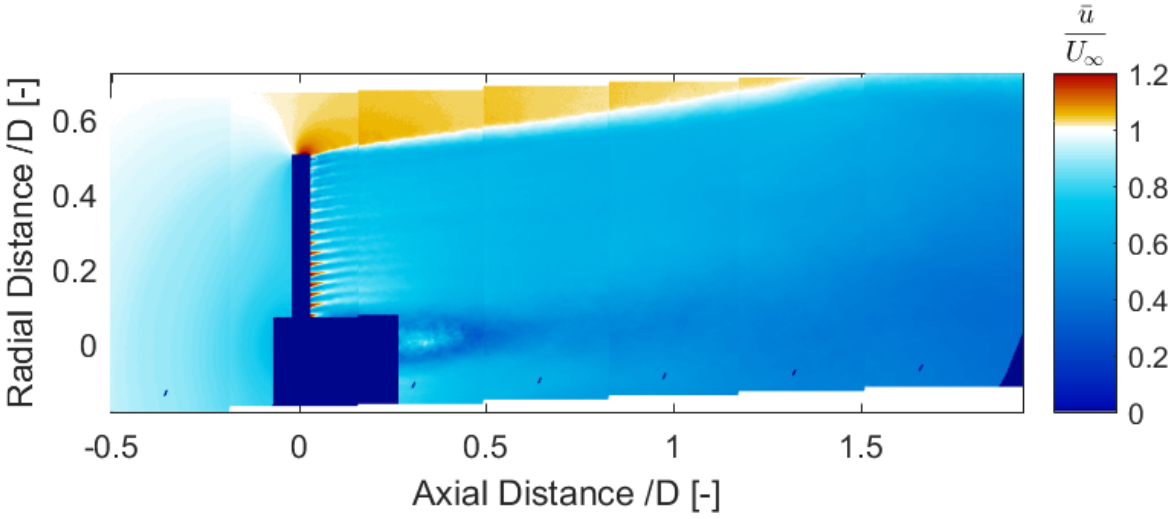

(b) Porosity = 14% (minimum porosity) and C_T = 0.692

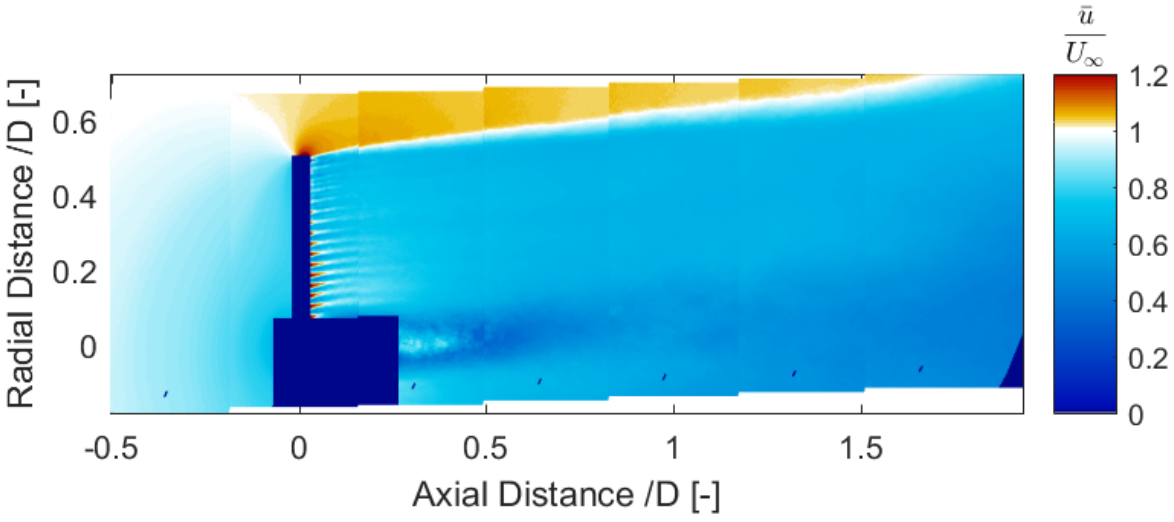

(c) Porosity = 19% (increasing porosity) and C_T = 0.675

Figure 7.32: Normalized Axial Velocity Field for porosity changing with frequency = 1.5Hz and reduced frequency = 0.47 (Experiment)

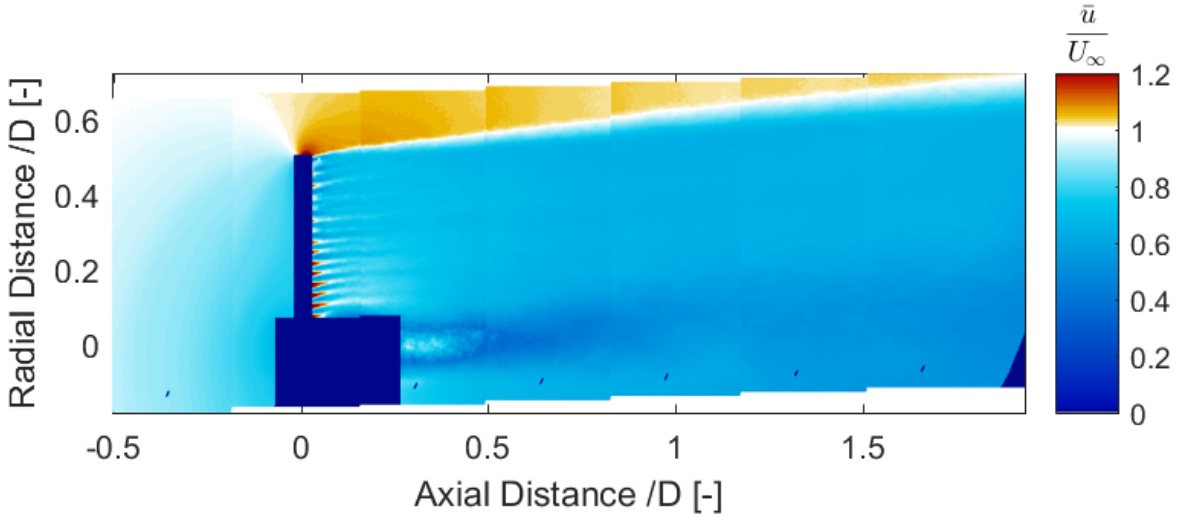

(a) Porosity = 31% (increasing porosity) and C_T = 0.651

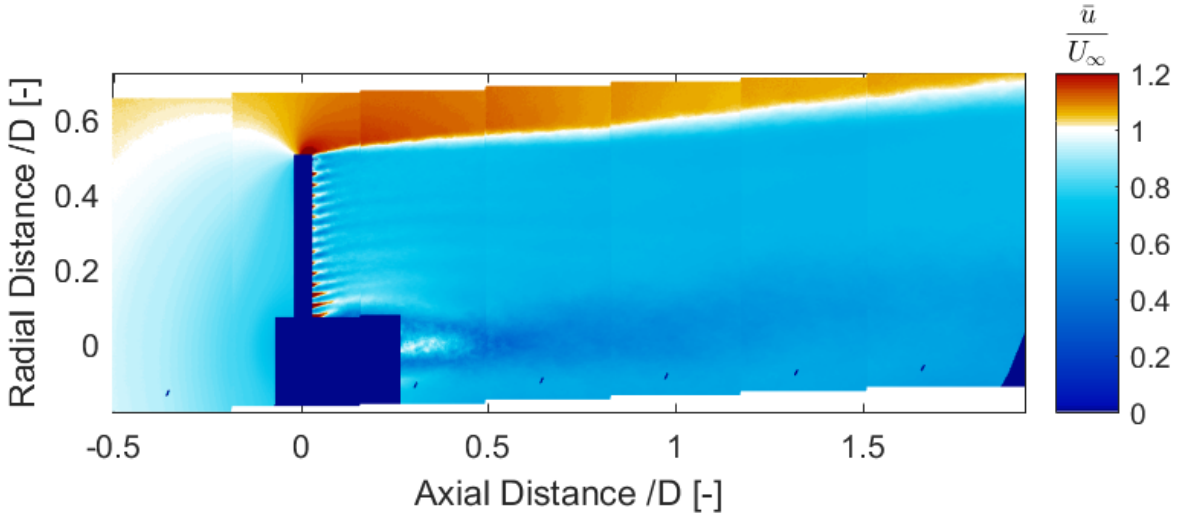

(b) Porosity = 47% (increasing porosity) and C_T = 0.616

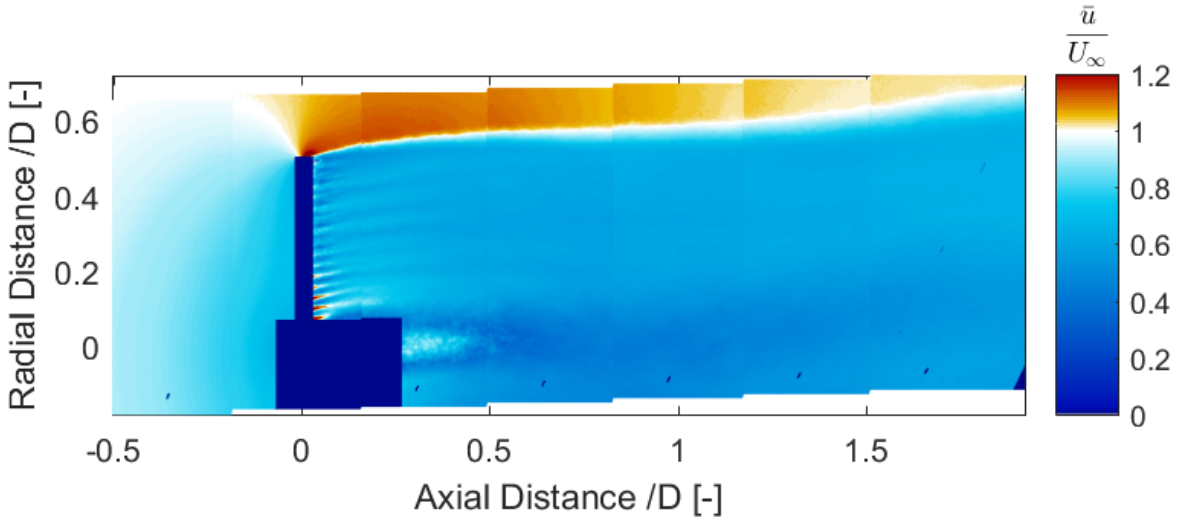

(c) Porosity = 59% (increasing porosity) and C_T = 0.575

Figure 7.33: Normalized Axial Velocity Field for porosity changing with frequency = 1.5Hz and reduced frequency = 0.47 (Experiment)

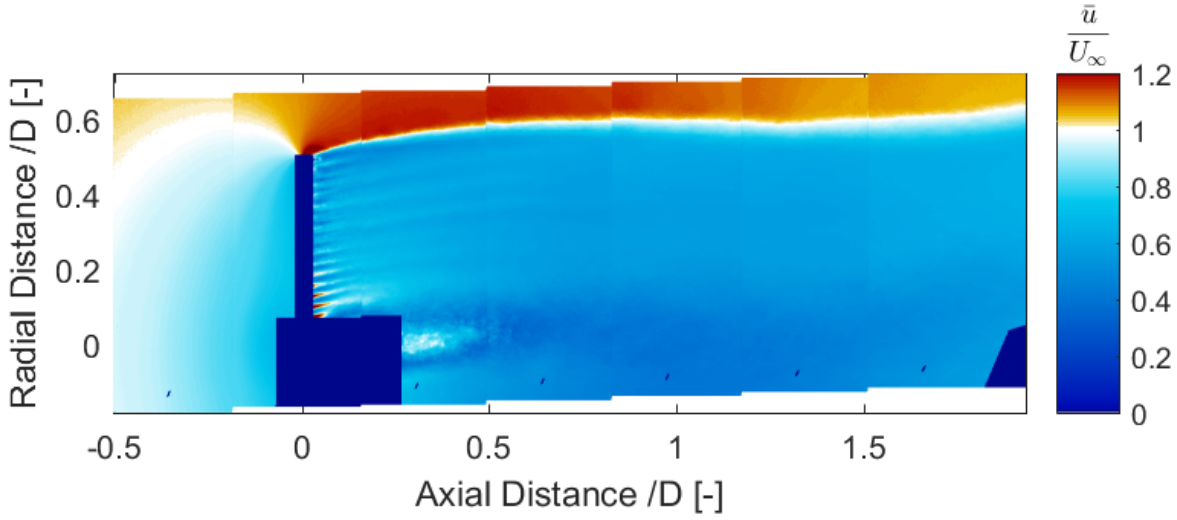

(a) Porosity = 64% (maximum porosity) and C_T = 0.555

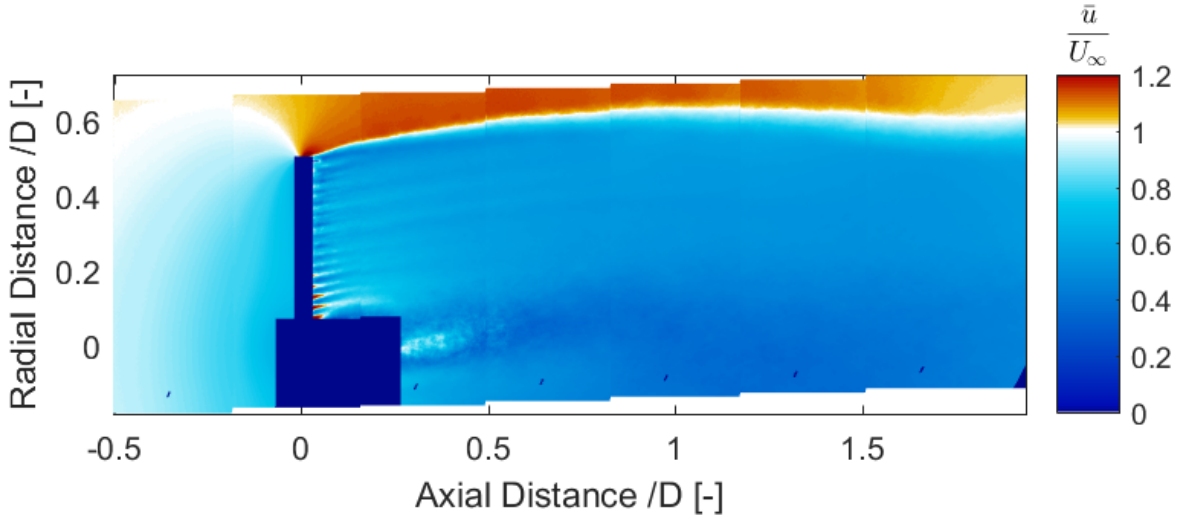

(b) Porosity = 59% (decreasing porosity) and C_T = 0.565

Figure 7.34: Normalized Axial Velocity Field for porosity changing with frequency = 1.5Hz and reduced frequency = 0.47 (Experiment)

RADIAL VELOCITY

Figure 7.35-Figure 7.38 show the average radial velocity fields for changing porosity with frequency of 1.5Hz (k = 0.47). Like the other two cases, in this case also the radial velocity is negative in the region behind the disc hub. It is maximum near the disc edge. A similar trend of positive radial velocity where wake expands and negative radial velocity where wake contracts is seen.

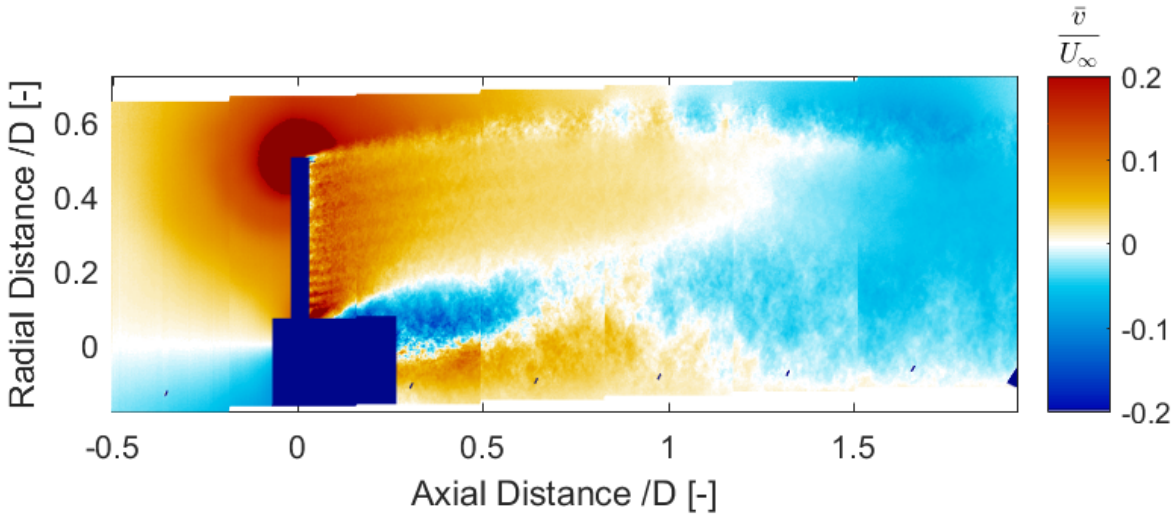

(a) Porosity = 59% (decreasing porosity) and C_T = 0.565

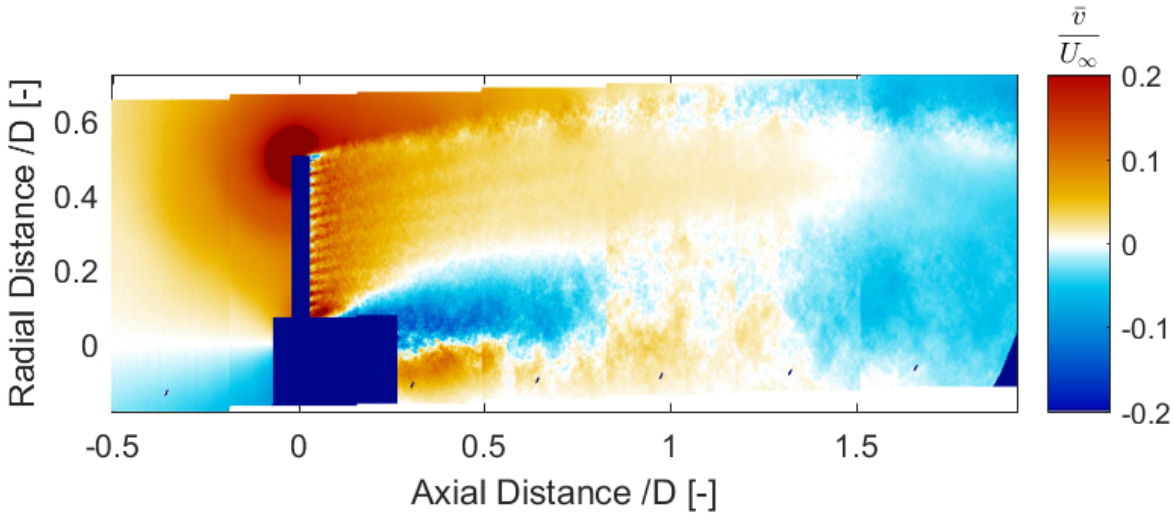

(b) Porosity = 47% (decreasing porosity) and C_T = 0.605

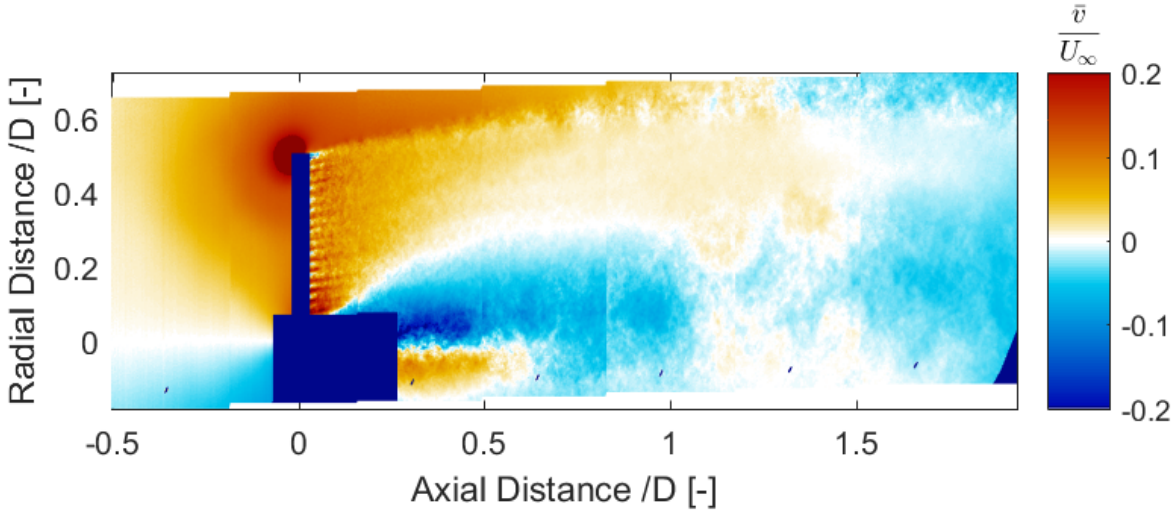

(c) Porosity = 31% (decreasing porosity) and C_T = 0.639

Figure 7.35: Normalized Radial Velocity Field for porosity changing with frequency = 1.5Hz and reduced frequency = 0.47 (Experiment)

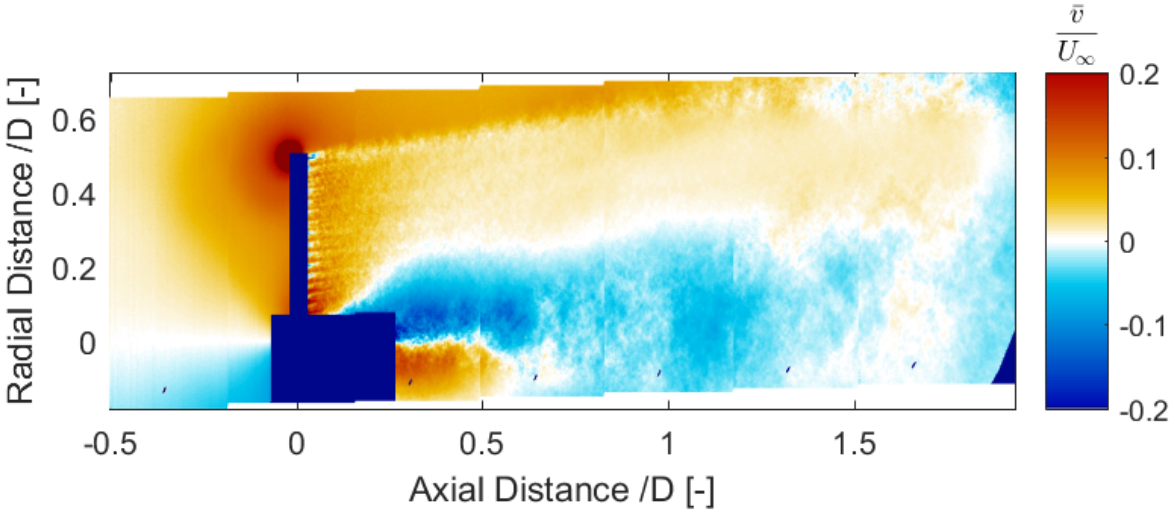

(a) Porosity = 19% (decreasing porosity) and C_T = 0.666

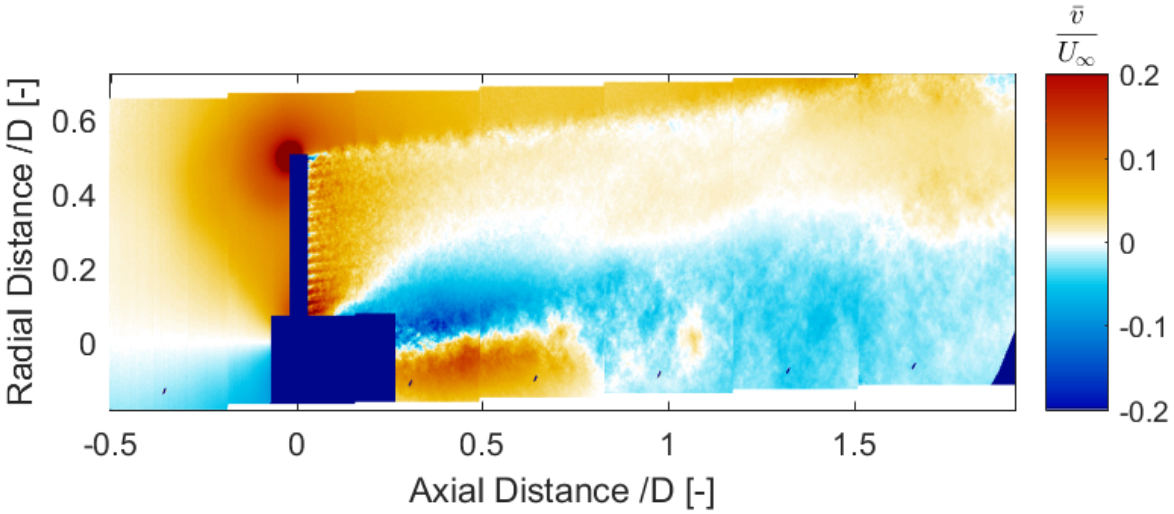

(b) Porosity = 14% (minimum porosity) and C_T = 0.692

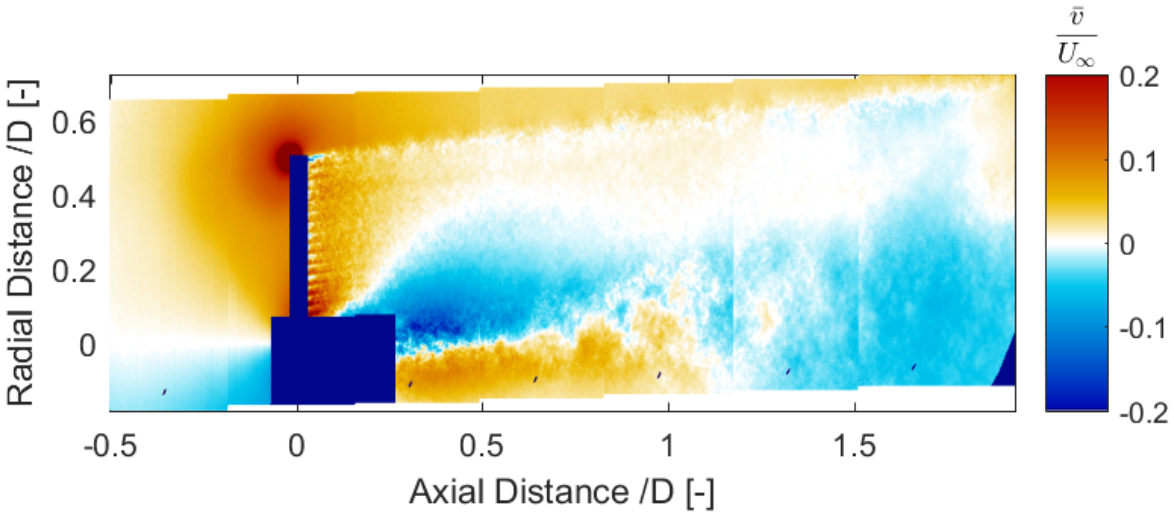

(c) Porosity = 19% (increasing porosity) and C_T = 0.675

Figure 7.36: Normalized Radial Velocity Field for porosity changing with frequency = 1.5Hz and reduced frequency = 0.47 (Experiment)

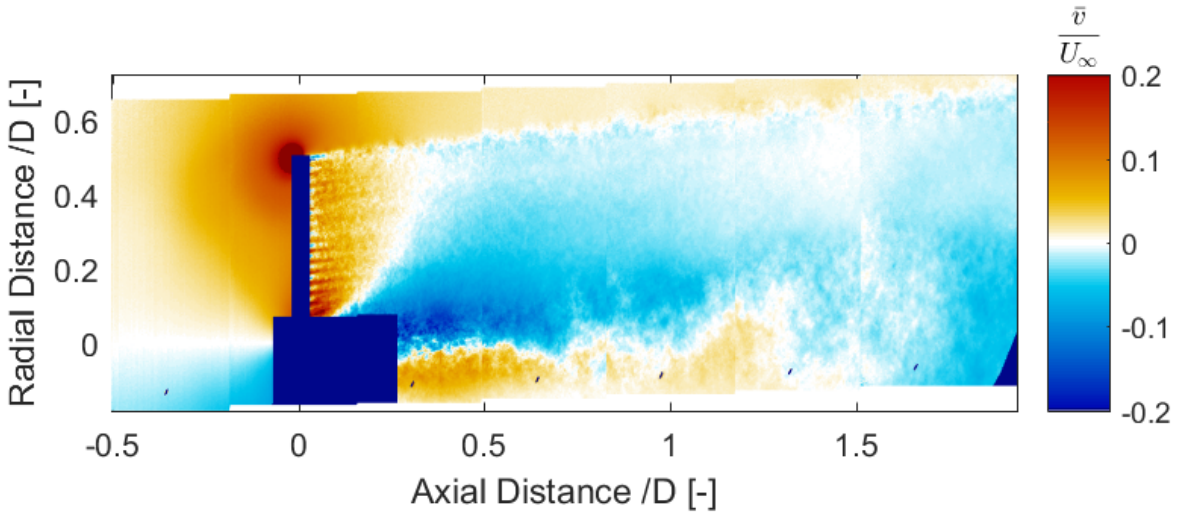

(a) Porosity = 31% (increasing porosity) and C_T = 0.651

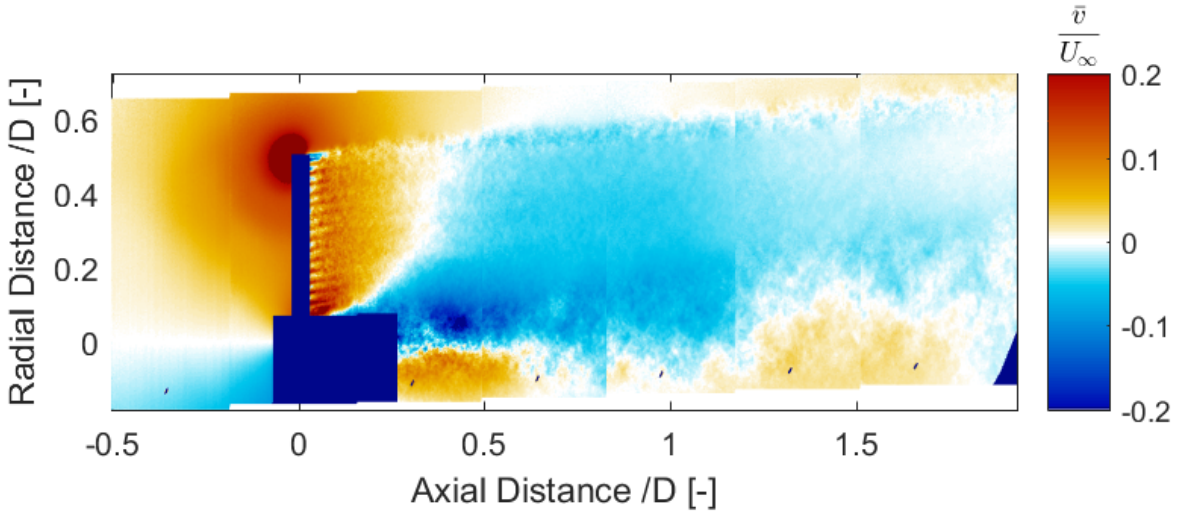

(b) Porosity = 47% (increasing porosity) and C_T = 0.616

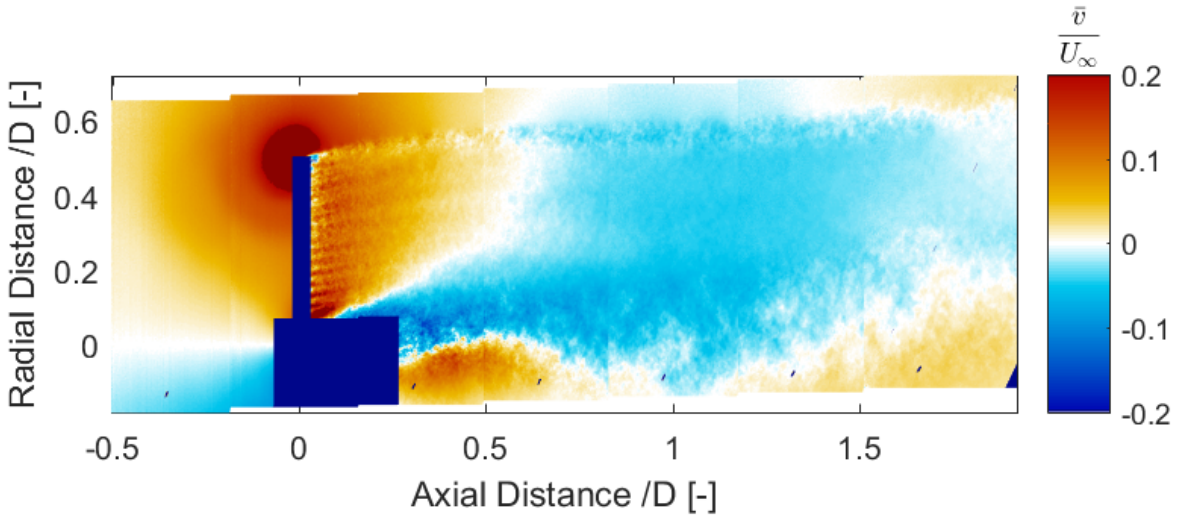

(c) Porosity = 59% (increasing porosity) and C_T = 0.575

Figure 7.37: Normalized Radial Velocity Field for porosity changing with frequency = 1.5Hz and reduced frequency = 0.47 (Experiment)

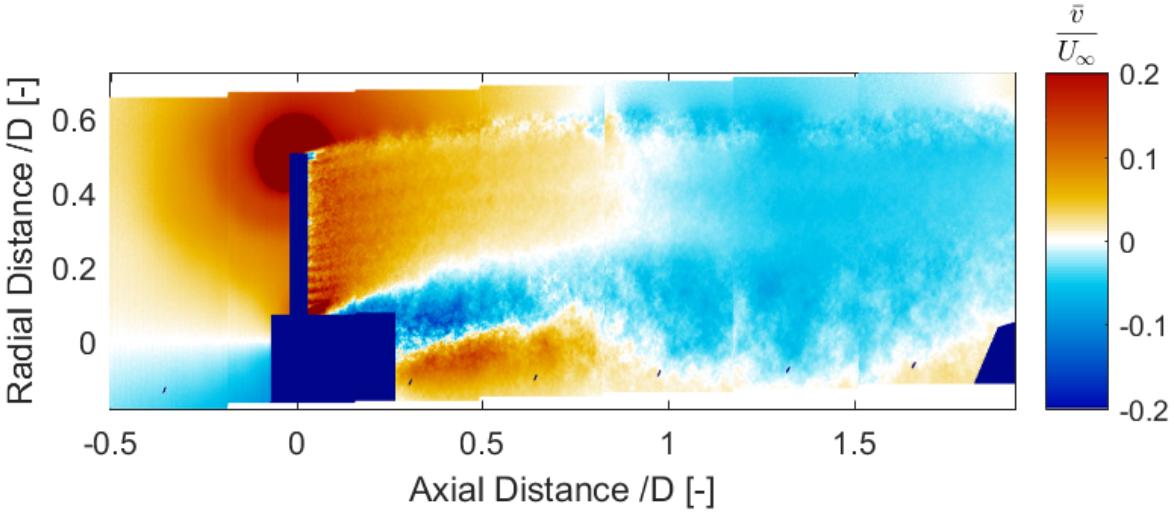

(a) Porosity = 64% (maximum porosity) and C_T = 0.555

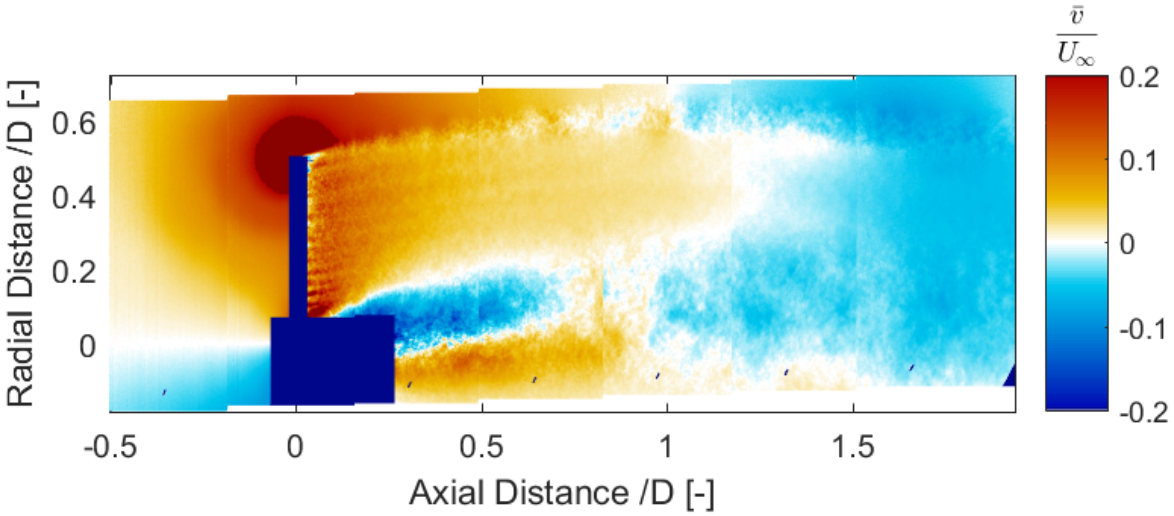

(b) Porosity = 59% (decreasing porosity) and C_T = 0.565

Figure 7.38: Normalized Radial Velocity Field for porosity changing with frequency = 1.5Hz and reduced frequency = 0.47 (Experiment)

VORTICITY

Figure 7.39 - Figure 7.42 show the normalized vorticity fields for changing porosity with frequency of 1.5Hz and k = 0.47. Like the other load cases (both steady and unsteady), the vorticity is strongest near the wake edge and behind the disc. However, for this case, the vorticity does not roll up till x/D = 2 like the other two unsteady load cases. The vorticity fields for this load case are more like the steady load cases.

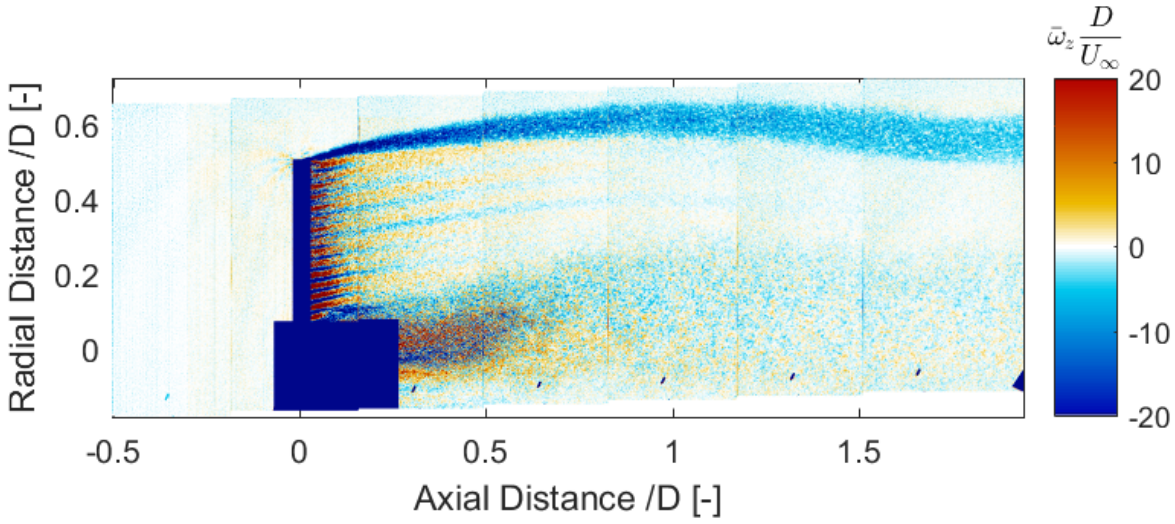

(a) Porosity = 59% (decreasing porosity) and C_T = 0.565

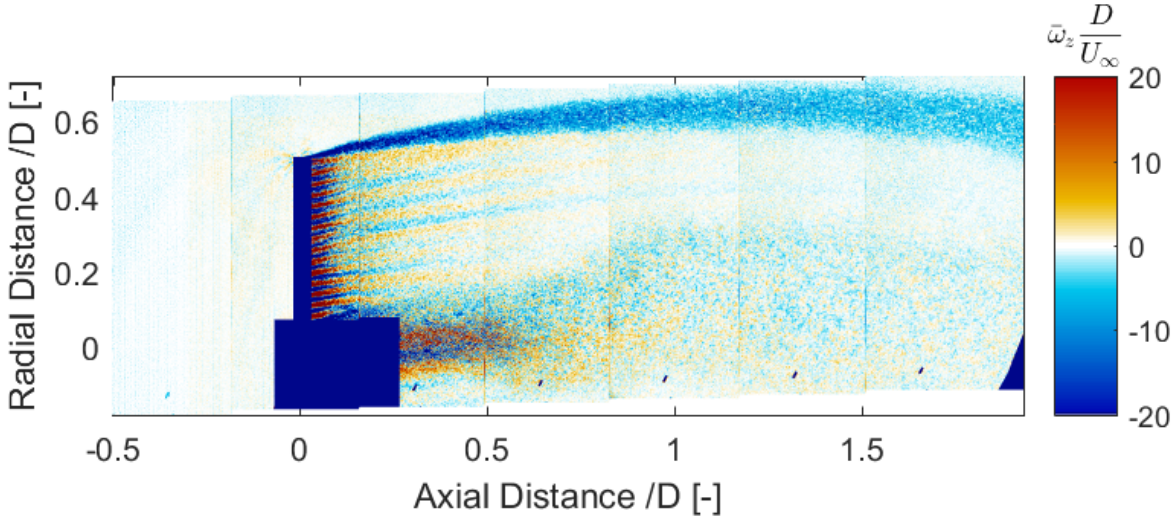

(b) Porosity = 47% (decreasing porosity) and C_T = 0.605

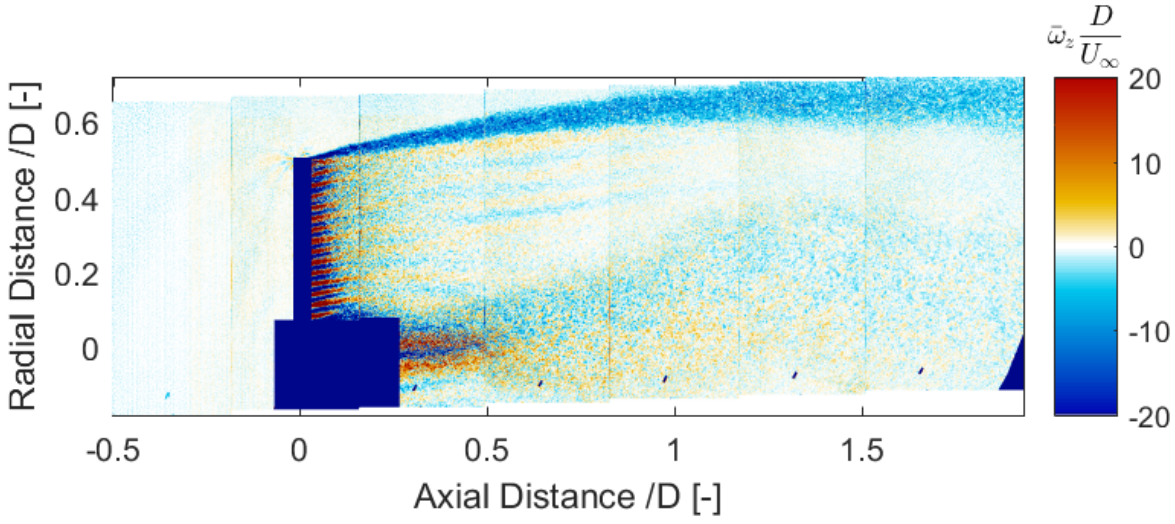

(c) Porosity = 31% (decreasing porosity) and C_T = 0.639

Figure 7.39: Normalized Vorticity Field for porosity changing with frequency = 1.5Hz and reduced frequency = 0.47 (Experiment)

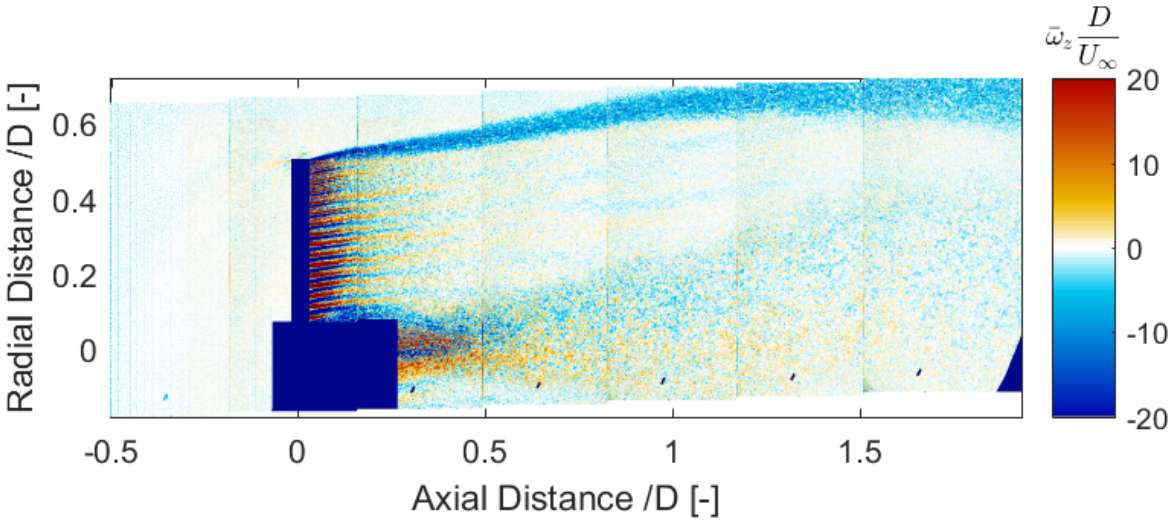

(a) Porosity = 19% (decreasing porosity) and C_T = 0.666

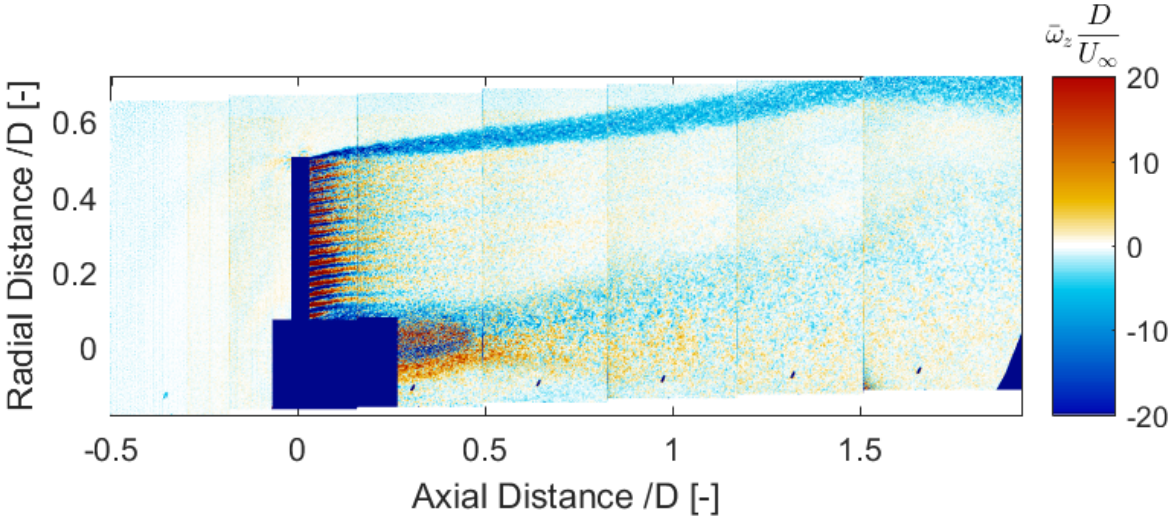

(b) Porosity = 14% (minimum porosity) and C_T = 0.692

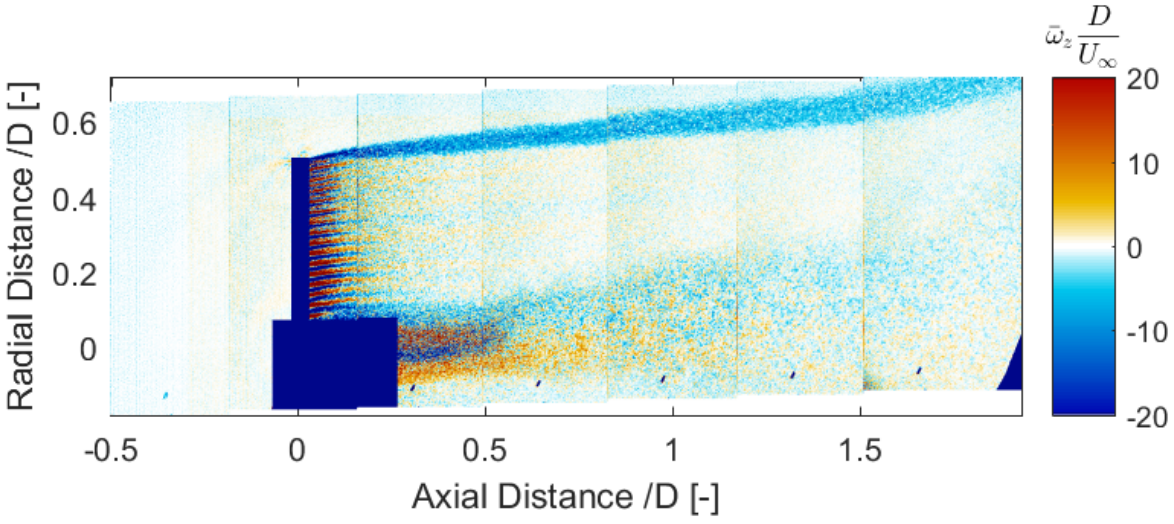

(c) Porosity = 19% (increasing porosity) and C_T = 0.675

Figure 7.40: Normalized Vorticity Field for porosity changing with frequency = 1.5Hz and reduced frequency = 0.47 (Experiment)

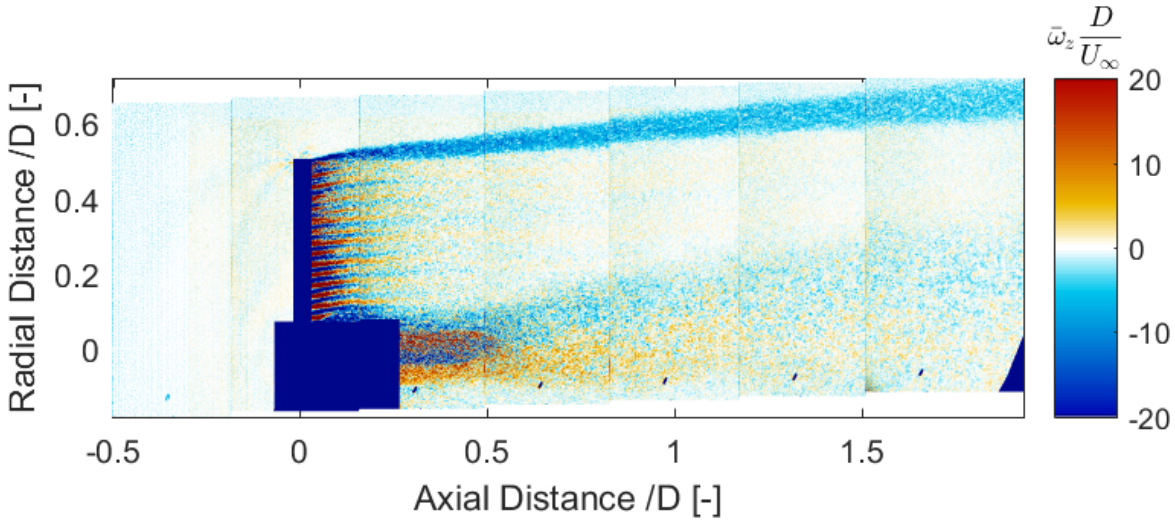

(a) Porosity = 31% (increasing porosity) and C_T = 0.651

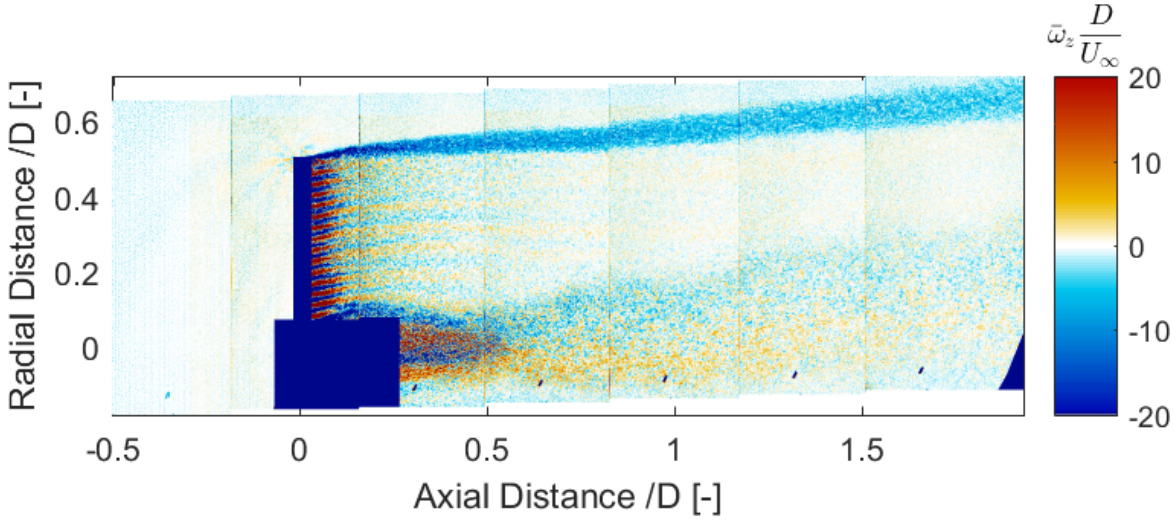

(b) Porosity = 47% (increasing porosity) and C_T = 0.616

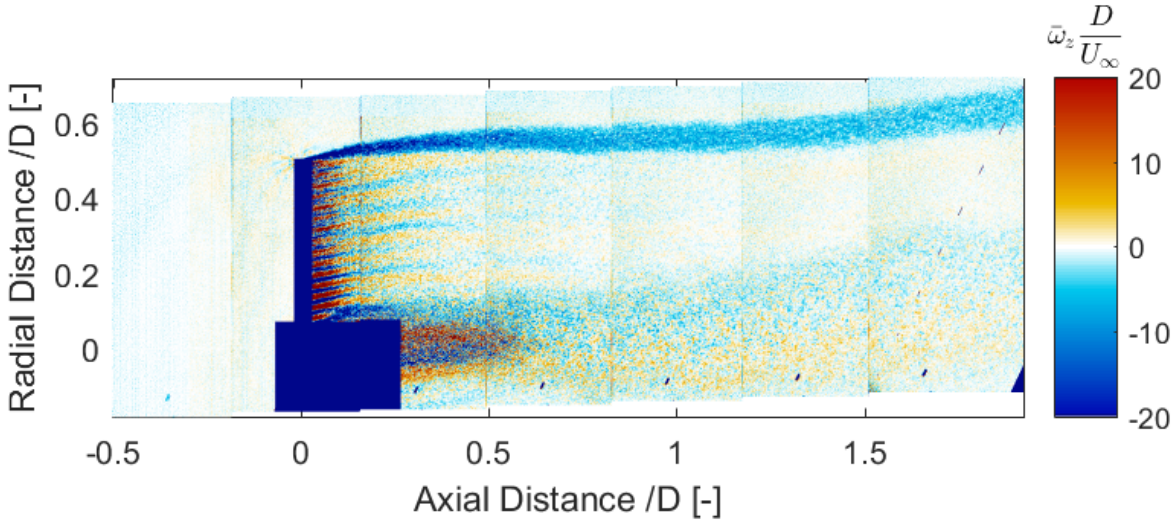

(c) Porosity = 59% (increasing porosity) and C_T = 0.575

Figure 7.41: Normalized Vorticity Field for porosity changing with frequency = 1.5Hz and reduced frequency = 0.47 (Experiment)

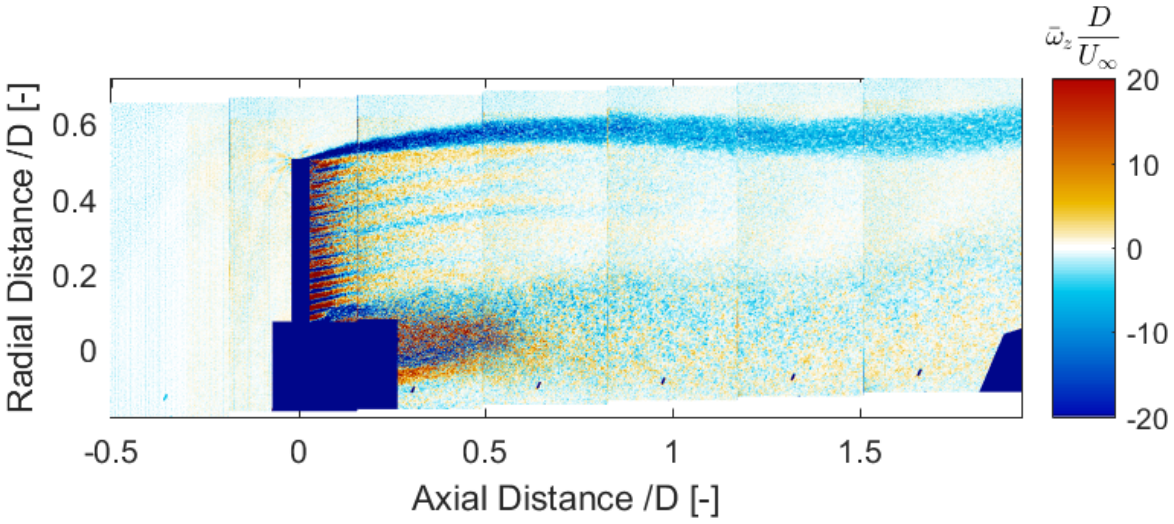

(a) Porosity = 64% (maximum porosity) and C_T = 0.555

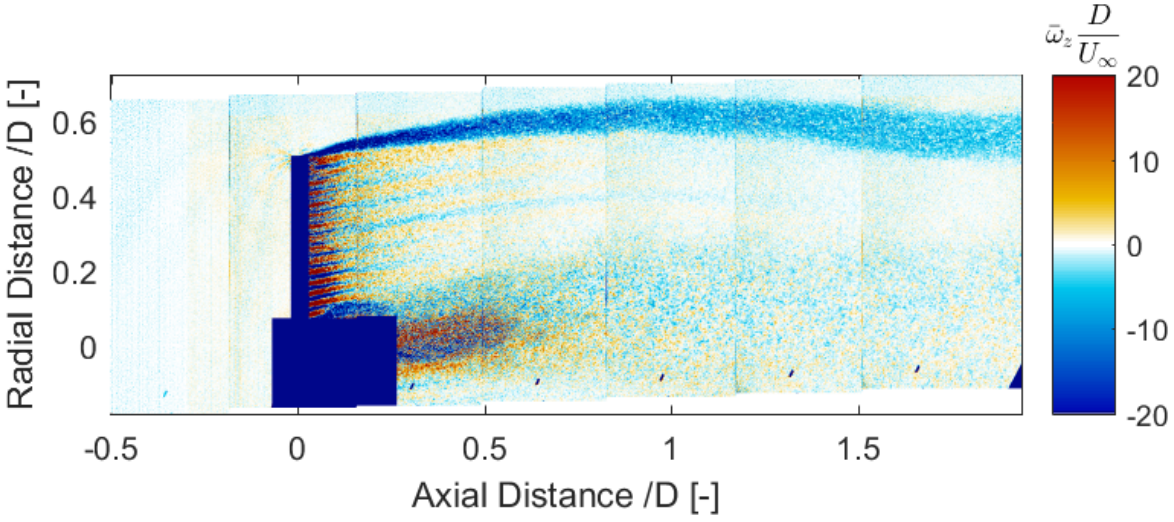

(b) Porosity = 59% (decreasing porosity) and C_T = 0.565

Figure 7.42: Normalized Vorticity Field for porosity changing with frequency = 1.5Hz and reduced frequency = 0.47 (Experiment)

7.2.4. ANALYSIS OF UNSTEADY LOADING ON THE FLOW FIELD

COMPARISON OF AXIAL VELOCITY

The main effect of the sinusoidal change in porosity is seen to be expanding and contracting wake (where velocity field is equal to the free-stream velocity). The reasons for this have already been explained. However, it can also be noticed that with increasing frequency, the phenomenon is more evident. The expansion and contraction of the wake are more frequent within the same distance for the cases with frequency of 5Hz than that for the other two unsteady load cases.

From the axial velocity fields, it could not be seen how the velocity field varies at a point with change in porosity. For that velocity data at a few points in the wake are plotted to see the trend. These locations on the flow field are shown in Figure 7.43. These points are selected such that they are not in the region heavily influenced by shear layer, disc mesh and nacelle. Figure 7.44-Figure 7.46 and Figure E.6-Figure E.8 show axial velocity for different axial locations and same radial location in the

field. As shown in the figure, for the same porosity value, but as loading is different, the value of the velocity also changes. Hence, due to the sinusoidal change in porosity, there is different loading on the disc which causes a different velocity induction. It should also be noted that in order to analyse the velocity trend, more data points per load cycle are needed. At the regions where overlap of FOV takes place uncertainty is higher. Although for the first and the last time-node, porosity and phase are same, loadings are not same. Hence, due to this there is a difference in the velocity induction. This is as explained before, is most likely caused by uncertainty in disc alignment and uncertainties in PIV measurements. Unlike porosity and load cycle, axial velocity does not follow a clear trend.

The figures also show the normalized axial velocity for the same locations for steady loading. As the steady load cases have different range in thrust coefficient, the velocity induction range is different. The figures also show that for the second steady load case (C_T = 0.61), velocity is higher behind the disk than that for the first steady load case (C_T = 0.56). But it should be noted that velocity jump across the disc is higher for the higher load. It might be caused by the discontinuity in vorticity due to mesh of the disk.

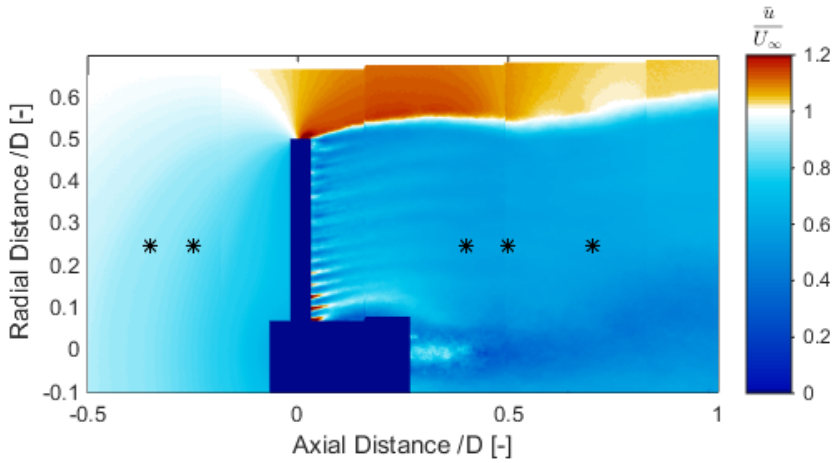

Figure 7.43: Flow field with selected points for which velocity magnitude are compared.

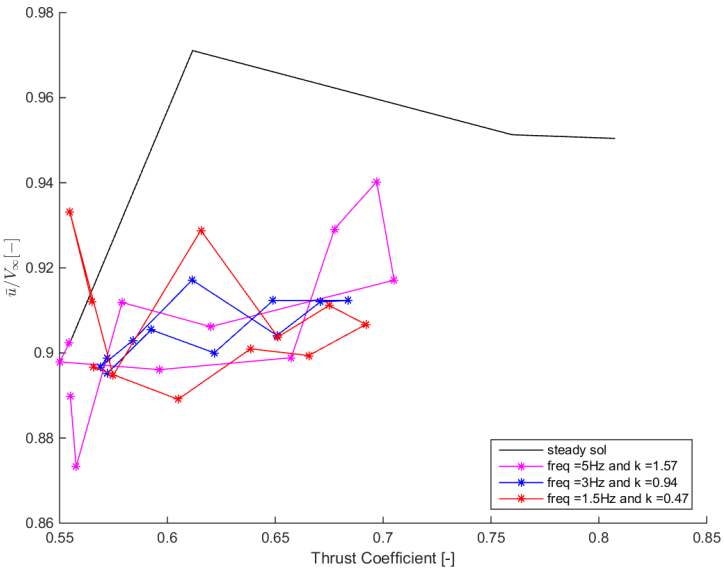

(a) x/D = -0.35, r/D = 0.25

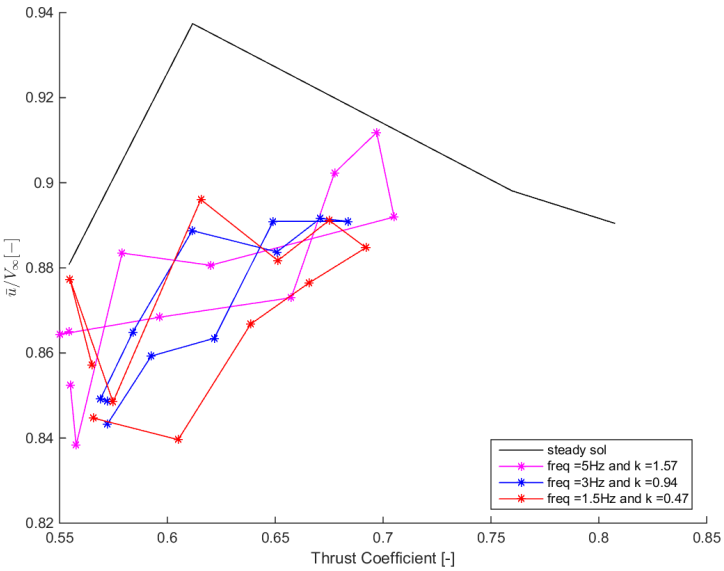

(b) x/D = -0.25, r/D = 0.25

Figure 7.44: Normalized axial velocity vs. C_T at a point in wake for different unsteady load cases

Figure 7.45a shows the normalized axial velocity at x/D = 0.4 and r/D = 0.25. Contrary to the steady load cases, where with increase in load on the disc, velocity induction is higher, the trend for unsteady load cases is different. This is likely due to the effect of previous loading. The axial velocity also does not form a smooth cycle, apart from the first and the last load cases not coinciding.

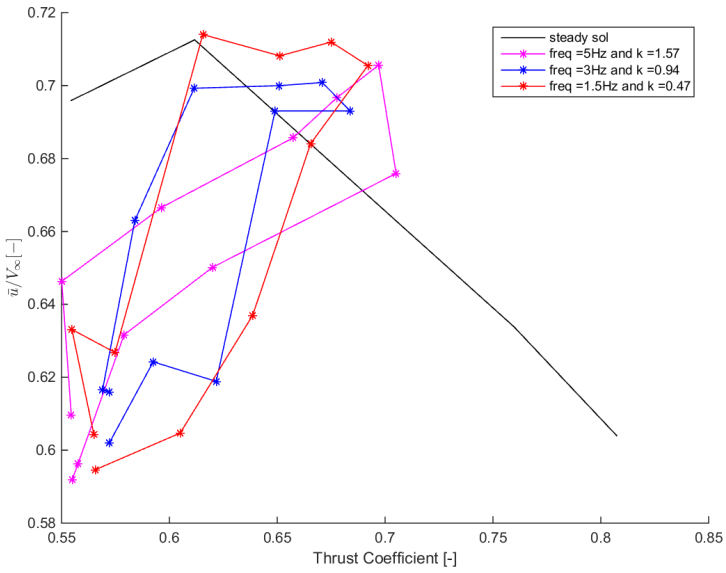

(a) x/D = 0.4, r/D = 0.25

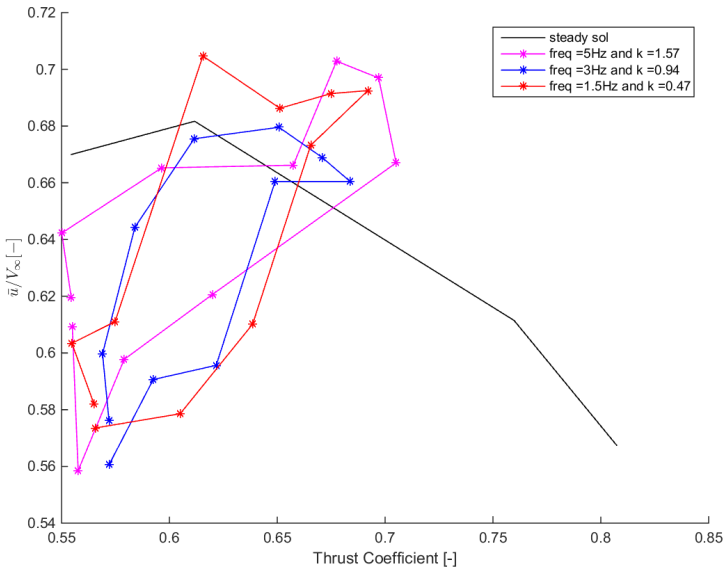

(b) x/D = 0.5, r/D = 0.25

Figure 7.45: Normalized axial velocity vs. C_T at a point in wake for different unsteady load cases

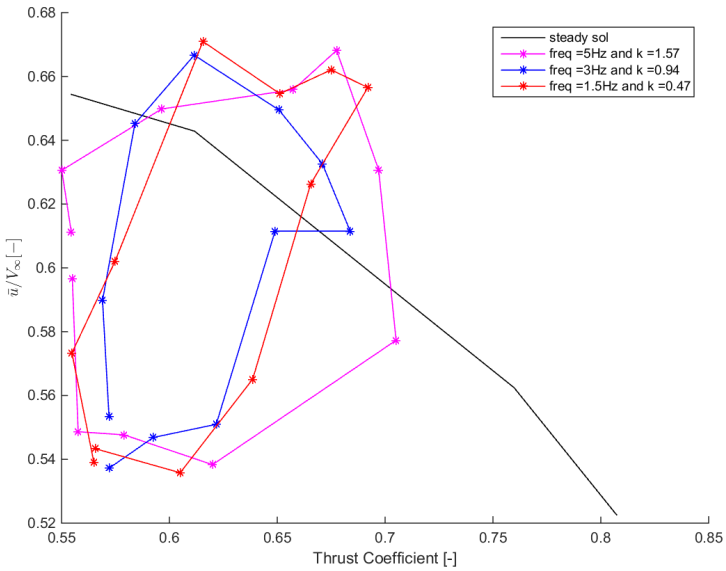

(a) x/D = 0.7, r/D = 0.25

Figure 7.46: Normalized axial velocity vs. C_T at a point in wake for different unsteady load cases

COMPARISON OF RADIAL VELOCITY

In order to see trend in radial velocity at one point, five different locations with different axial positions but same radial position are chosen. The radial velocities for these locations are plotted against the disc loading and porosity. Figure 7.47-Figure 7.49 and Figure E.9-Figure E.11 show the normalized radial velocity for different points in wake for different unsteady load cases. Contrary to the steady load cases, radial velocity decreases with increasing load. The figures also show that the radial velocity also does not form a complete cycle similar to the axial velocities. This is possibly because of difference in the disc loading and the uncertainties in the experiment.

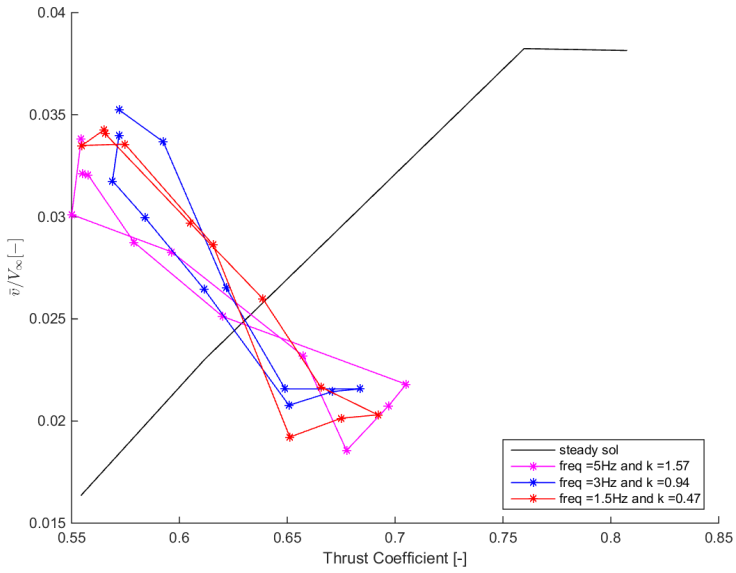

(a) x/D = -0.35, r/D = 0.25D

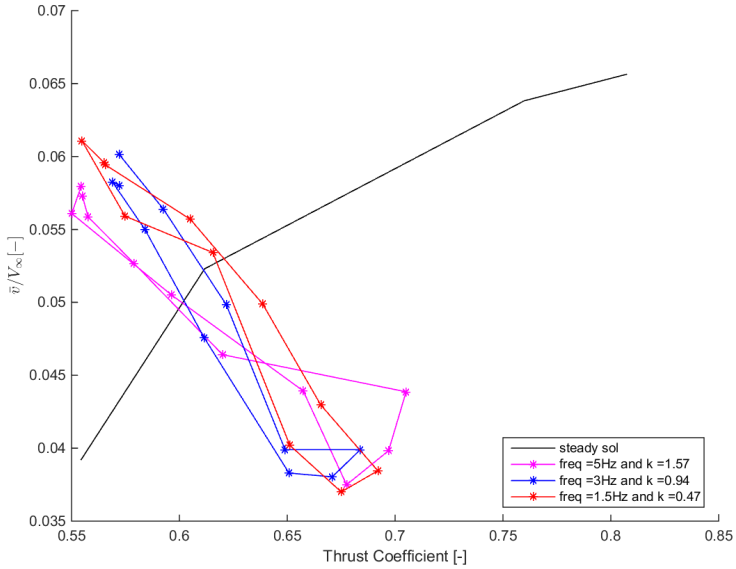

(b) x/D = -0.25, r/D = 0.25D

Figure 7.47: Normalized radial velocity vs. C_T at a point in wake for different unsteady load cases

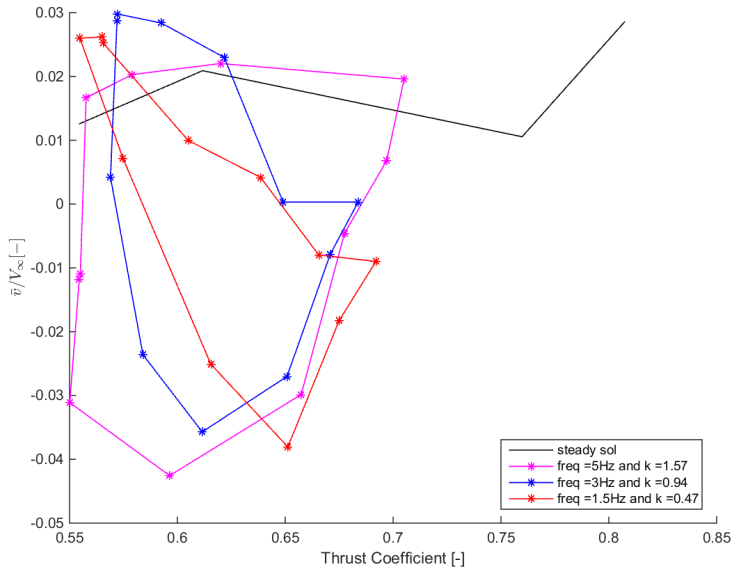

(a) x/D = 0.4, r/D = 0.25D

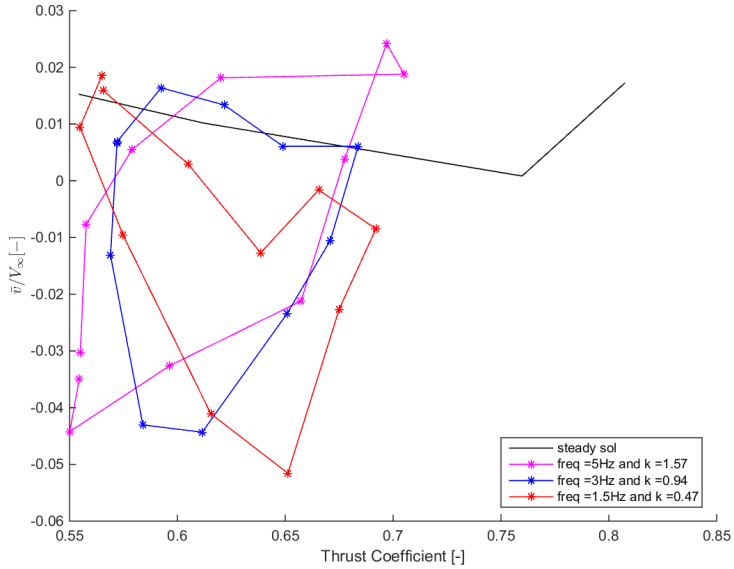

(b) x/D = 0.5, r/D = 0.25D

Figure 7.48: Normalized radial velocity vs. C_T at a point in wake for different unsteady load cases

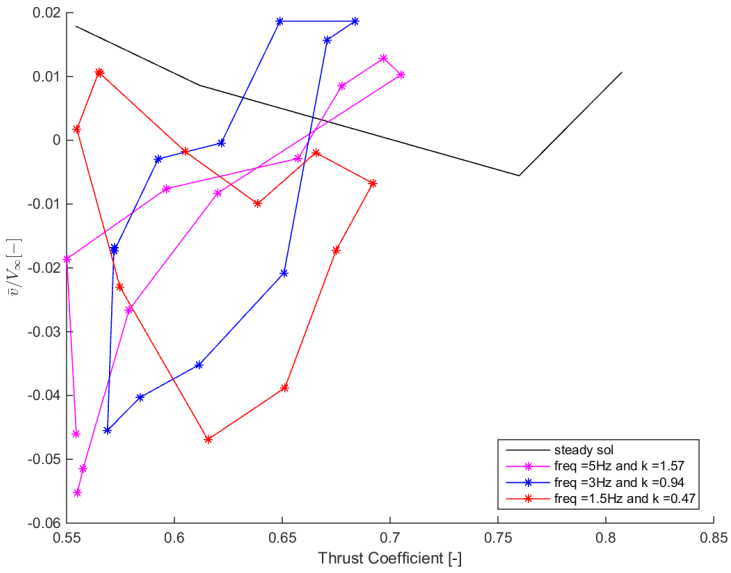

(a) x/D = 0.7, r/D = 0.25D

Figure 7.49: Normalized radial velocity vs. C_T at a point in wake for different unsteady load cases

COMPARISON OF VORTICITY

From the vorticity fields presented in the previous sections, it is seen that for the unsteady load cases, vortices roll up except for the minimum frequency case. It is found that with increasing porosity, this phenomena is more frequent over the same distance. This is due to the fact that with changing porosity, the velocity and magnitude of shed vortices change. Due to this, the 'new' and the 'old' vortices have different velocity from each other and they eventually interact with each other. However, with decrease in load cycle frequency, change in vorticity is less frequent.

7.3. VORTEX RING SOLUTION OF THE FLOW FIELD USING EXPERIMENTAL DATA

In this section, axial and radial velocity fields estimated using the VR model for cyclic load cases are analysed. Strength of the wake is estimated from the experimental data as described in section 6.3.

7.3.1. FREQUENCY = 5HZ AND REDUCED FREQUENCY = 1.57

In this section, axial and radial velocity fields calculated using the VR model disc load cycle with a frequency of 5Hz and k = 1.57 are discussed.

Axial Velocity: Figure 7.50-Figure 7.53 displays axial velocity field calculated using Vortex Ring models for unsteady load case of 5Hz frequency. Following can be seen in the figures:

1. Wake for all cases is expanding and contracting due to cyclic change in loading on the disc, similar to the experimental data.

2. Across the disk, there is a velocity jump. Figure E.12a show that axial velocity also forms a cycle.

3. The axial velocity field is not axisymmetric around the R = 0. This is because the VR model assumes axisymmetric flow so velocity estimations below r/D = 0 are irrelevant.

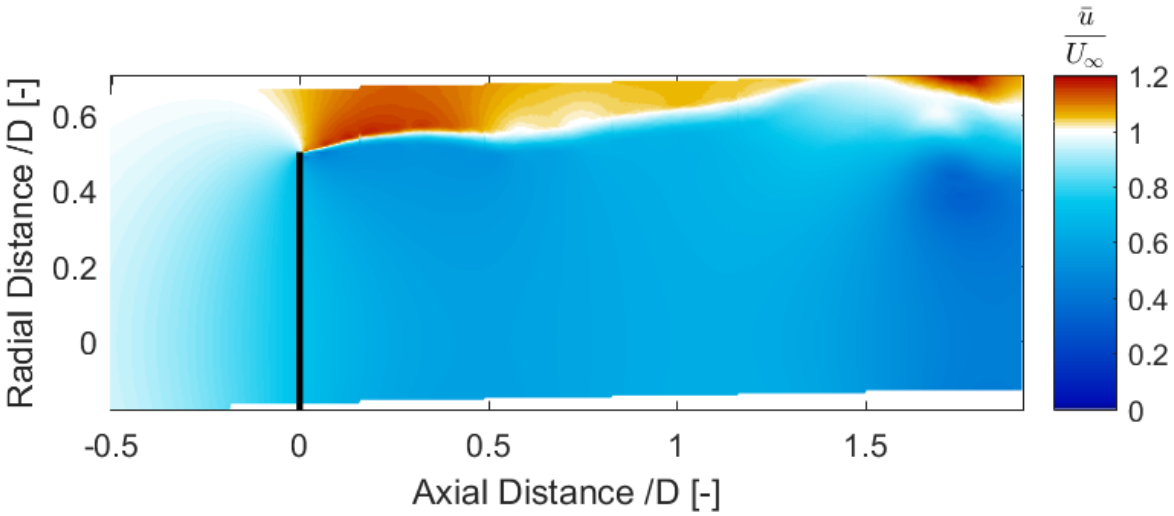

(a) Porosity = 59% (decreasing porosity) and C_T = 0.555

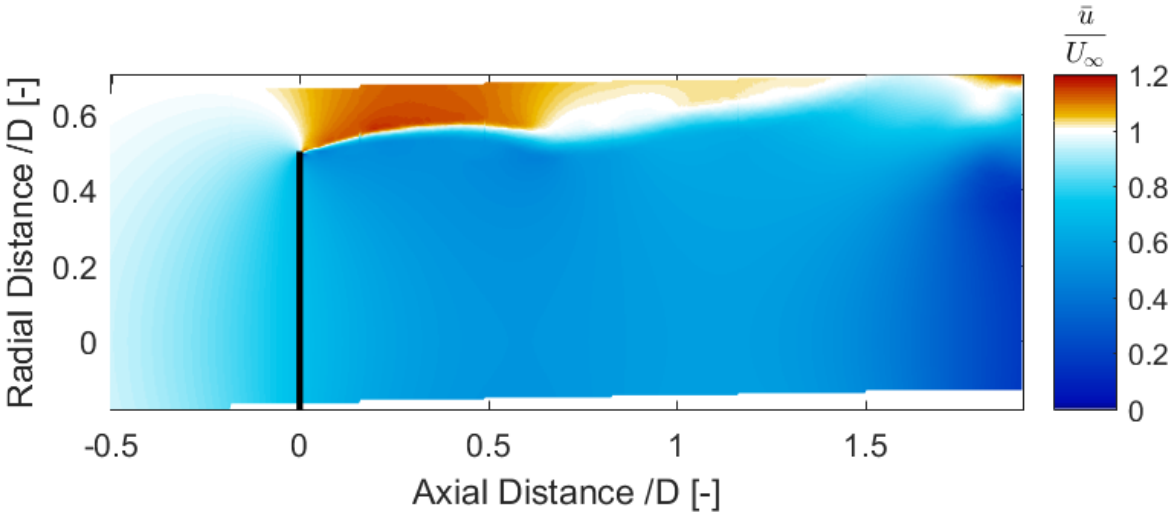

(b) Porosity = 47% (decreasing porosity) and C_T = 0.557

Figure 7.50: Normalized Axial Velocity Field for porosity changing with frequency = 5Hz and reduced frequency = 1.57 (Vortex Ring model)

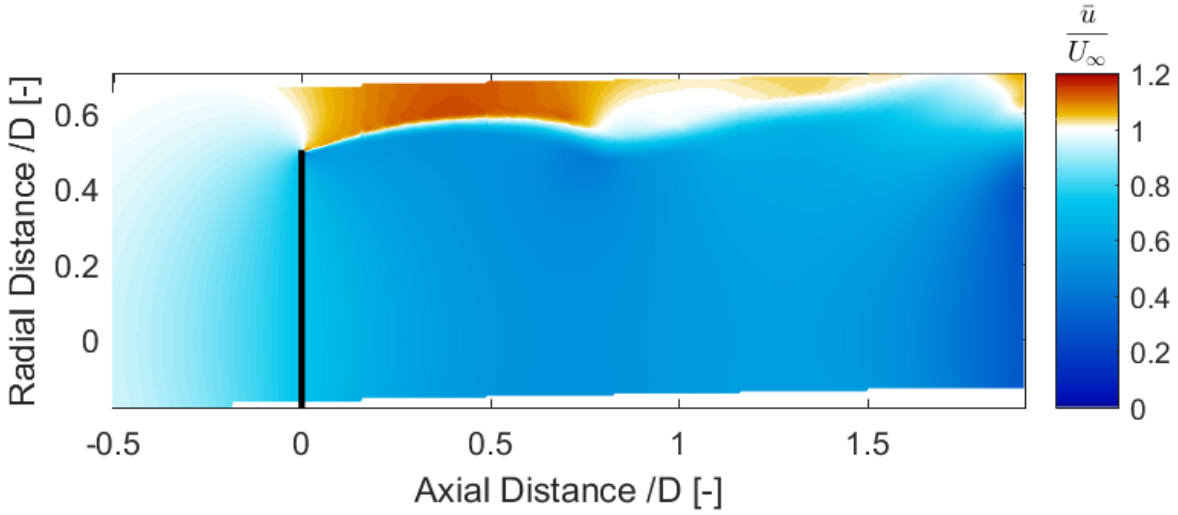

(a) Porosity = 31% (decreasing porosity) and C_T = 0.579

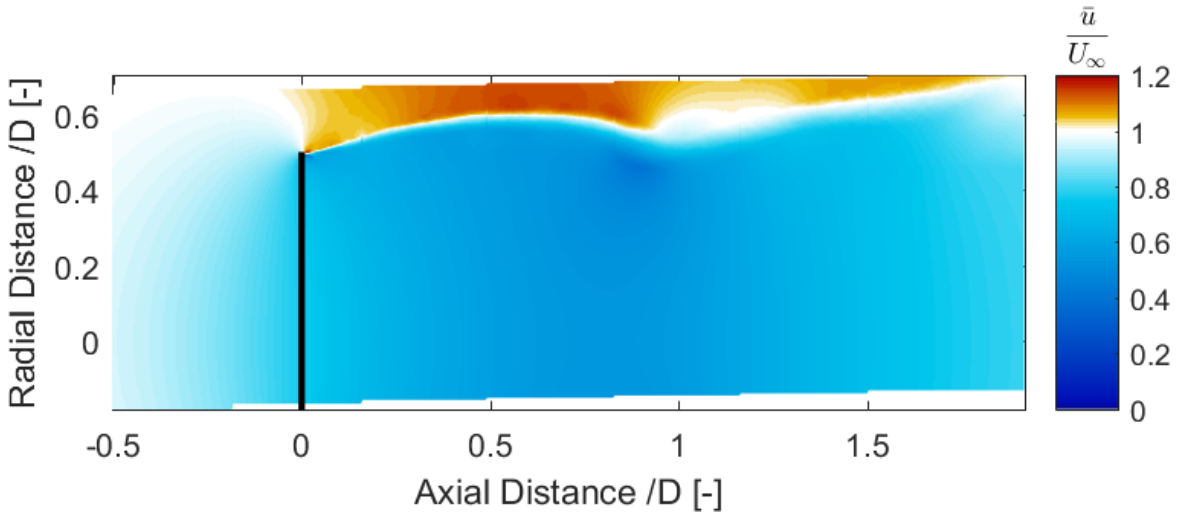

(b) Porosity = 19% (decreasing porosity) and C_T = 0.620

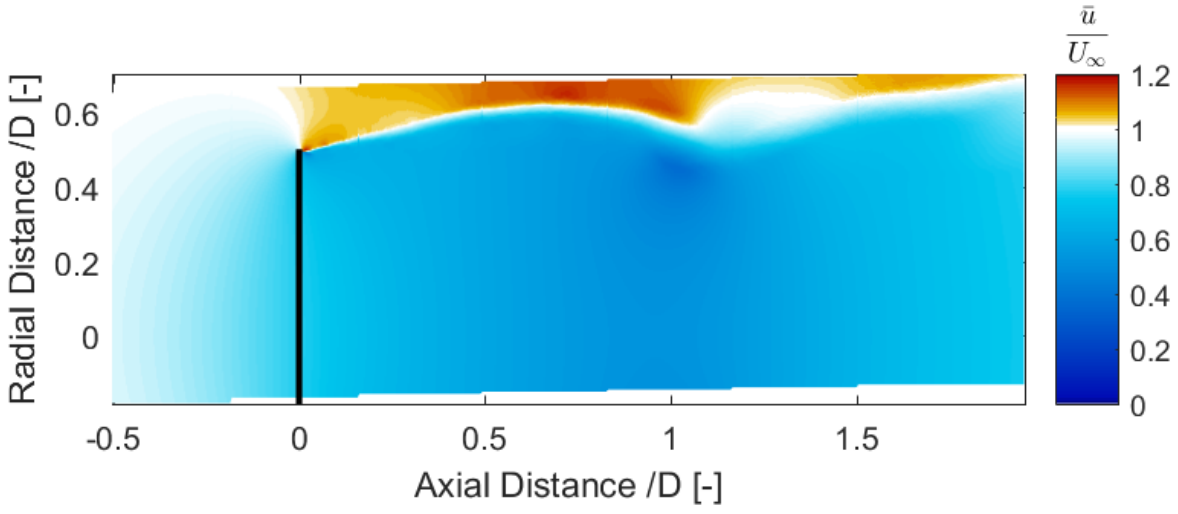

(c) Porosity = 14% (minimum porosity) and C_T = 0.705

Figure 7.51: Normalized Axial Velocity Field for porosity changing with frequency = 5Hz and reduced frequency = 1.57 (Vortex Ring model)

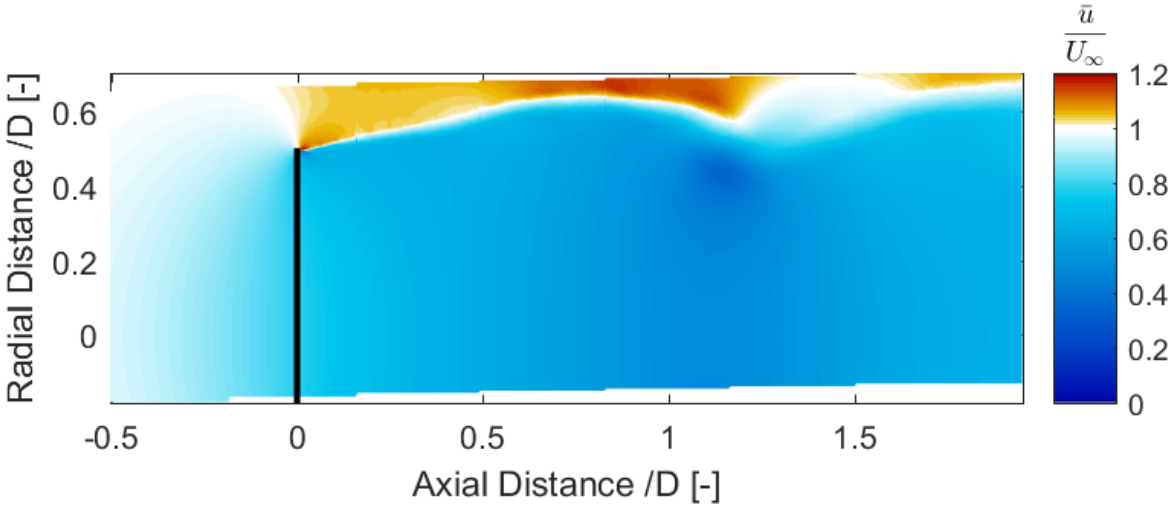

(a) Porosity = 19% (increasing porosity) and C_T = 0.697

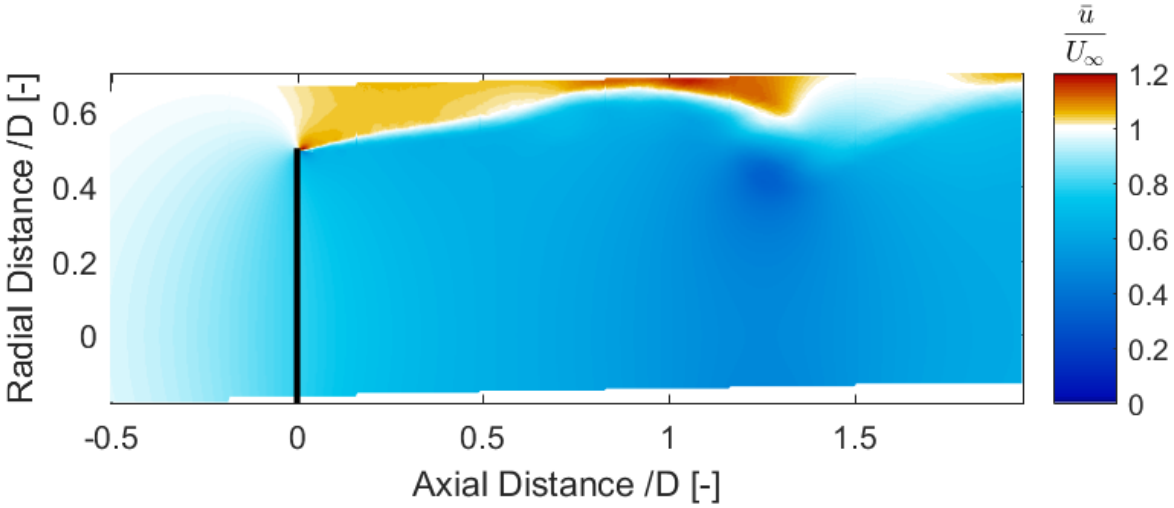

(b) Porosity = 31% (increasing porosity) C_T = 0.678

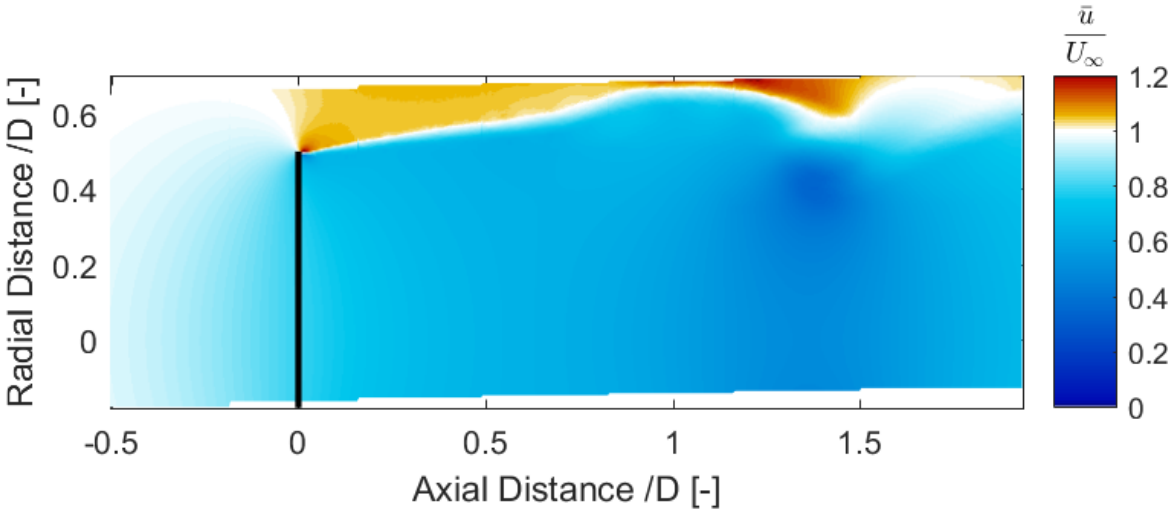

(c) Porosity = 47% (increasing porosity) and C_T = 0.657

Figure 7.52: Normalized Axial Velocity Field for porosity changing with frequency = 5Hz and reduced frequency = 1.57 (Vortex Ring model)

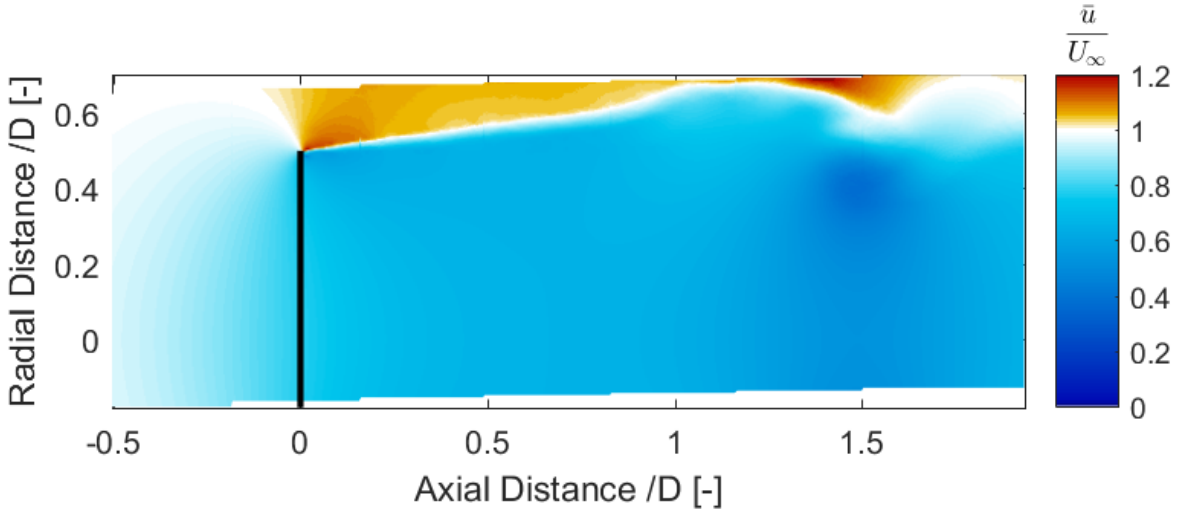

(a) Porosity = 59% (increasing porosity) and C_T = 0.596

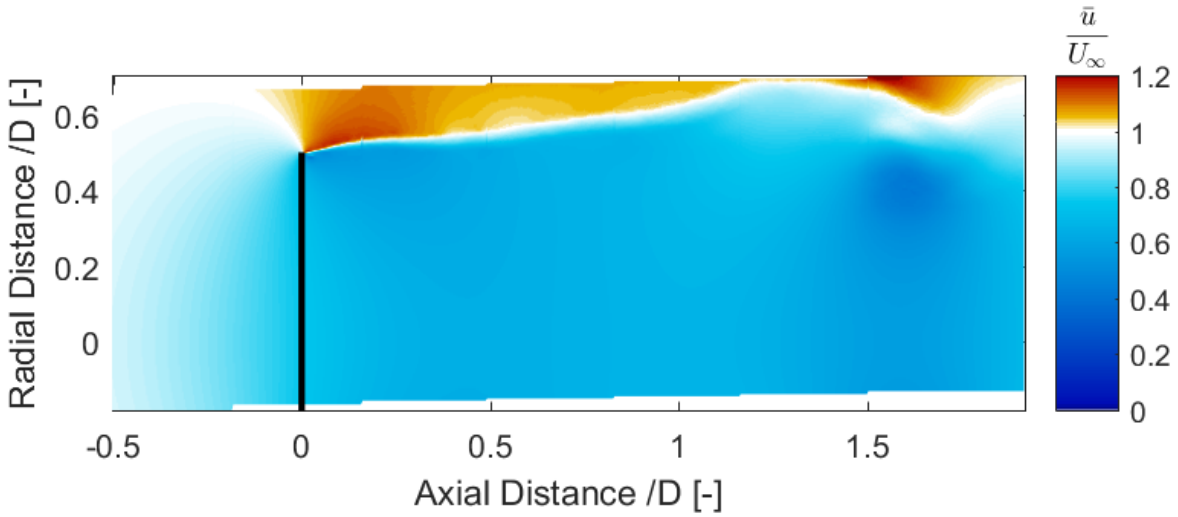

(b) Porosity = 64% (maximum porosity) and C_T = 0.550

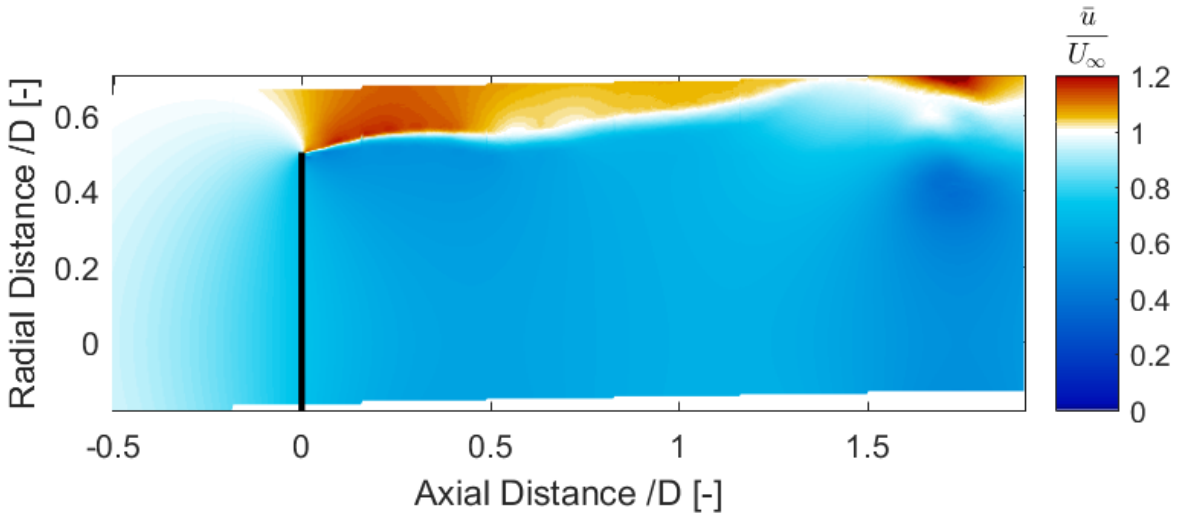

(c) Porosity = 59% (decreasing porosity) and C_T = 0.554

Figure 7.53: Normalized Axial Velocity Field for porosity changing with frequency = 5Hz and reduced frequency = 1.57 (Vortex Ring model)

Radial Velocity: Figure 7.54-Figure 7.58 show the average normalized radial velocity fields for changing porosity with frequency of 5Hz. Following points can be noticed from these figures:

1. Compared to the axial velocity fields, radial velocity is small. This is similar to the experimental data.

2. Figure E.12b show that radial velocity is periodic.

3. For first half of the load cycle, there is a region between x/D = 0.5 and x/D = 1.25 (different for different loads), where the radial velocity field is negative. For the second half, this region moves downstream. However, for the second half of the load cycle, region with radial velocity less than or equal to 0 starts appearing between x/D = 0.4 and x/D = 1. This is same as the experimental results.

4. The flow is not axisymmetric as the VR model assumes axisymmetric velocity and takes square of radial positions, thereby, estimating the same velocity for both negative and positive radial positions.

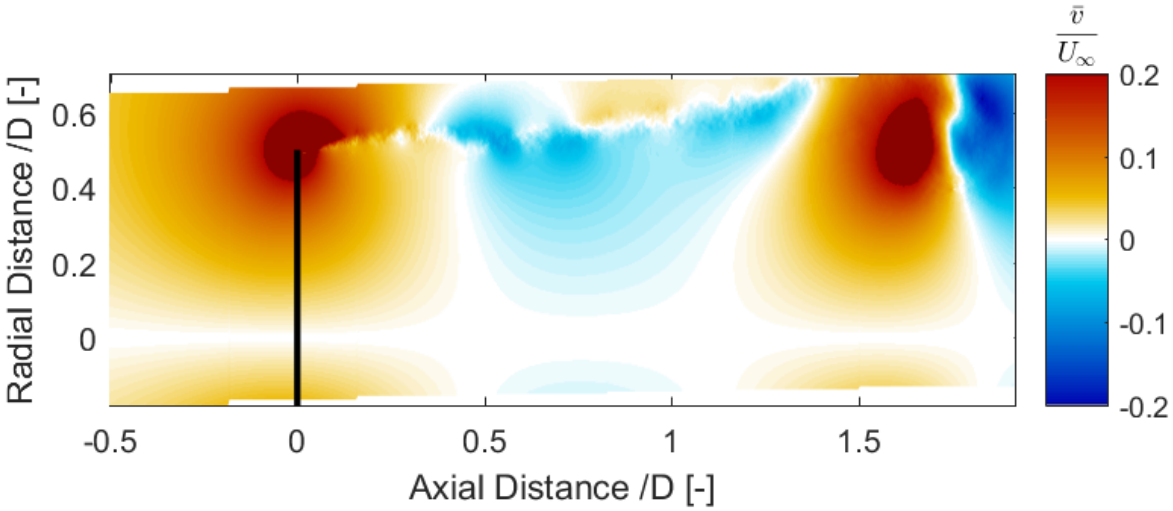

(a) Porosity = 59% (decreasing porosity) and C_T = 0.555

Figure 7.54: Normalized Radial Velocity Field for porosity changing with frequency = 5Hz and reduced frequency = 1.57 (Vortex Ring model)

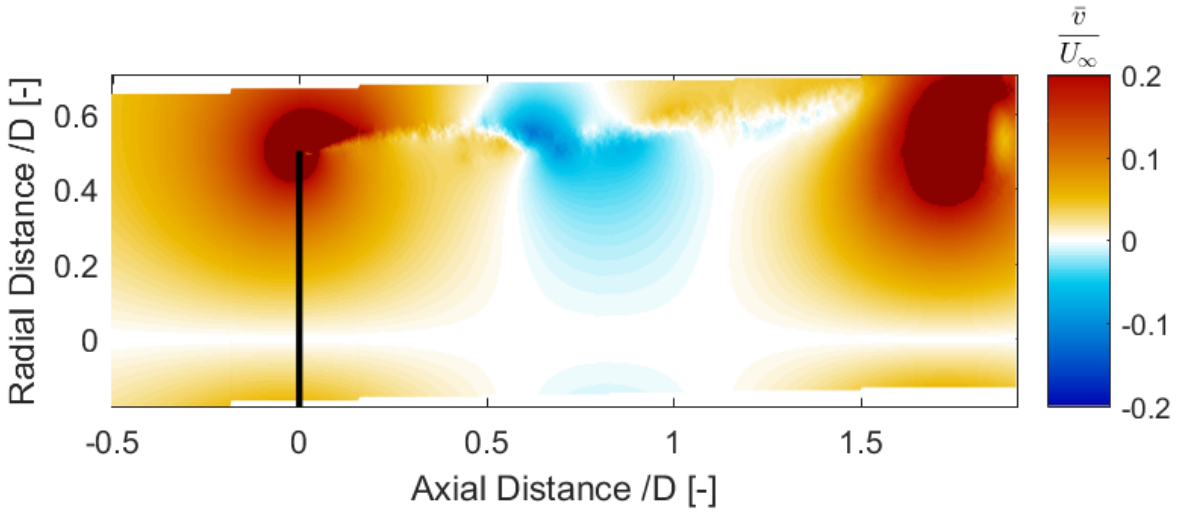

(a) Porosity = 47% (decreasing porosity) and C_T = 0.557

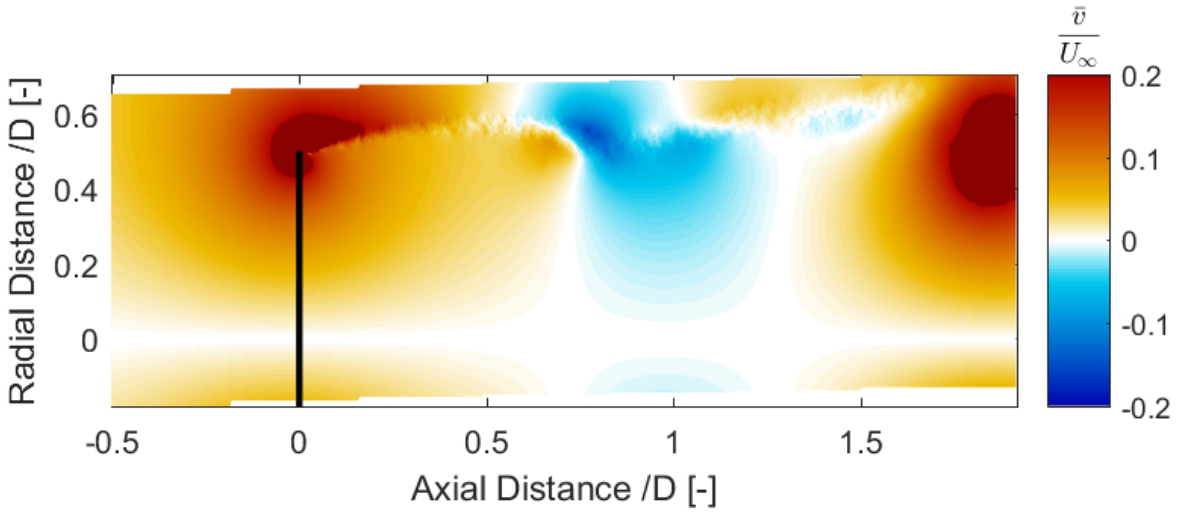

(b) Porosity = 31% (decreasing porosity) and C_T = 0.579

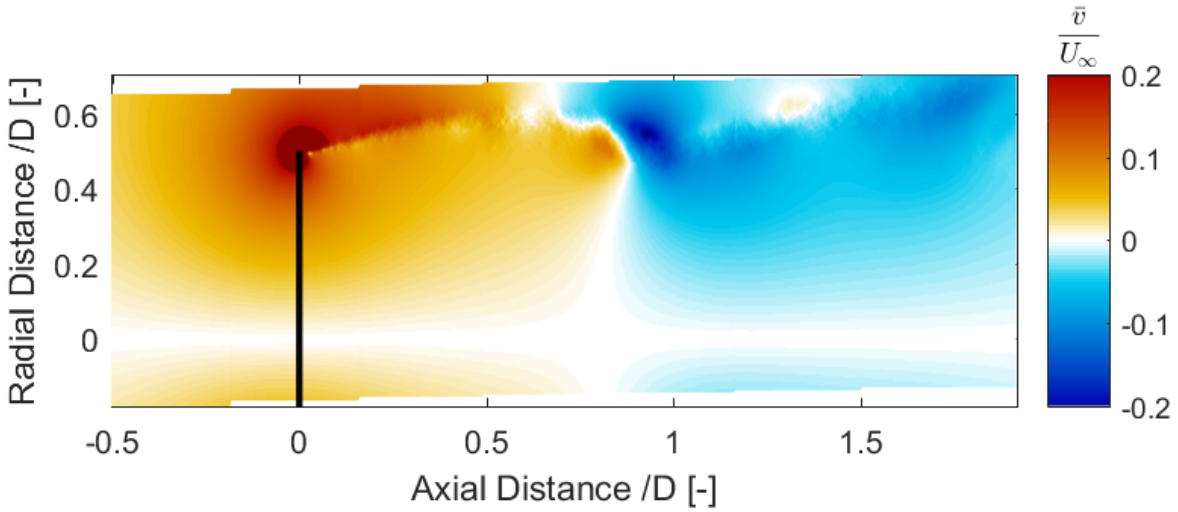

(c) Porosity = 19% (decreasing porosity) and C_T = 0.620

Figure 7.55: Normalized Radial Velocity Field for porosity changing with frequency = 5Hz and reduced frequency = 1.57 (Vortex Ring model)

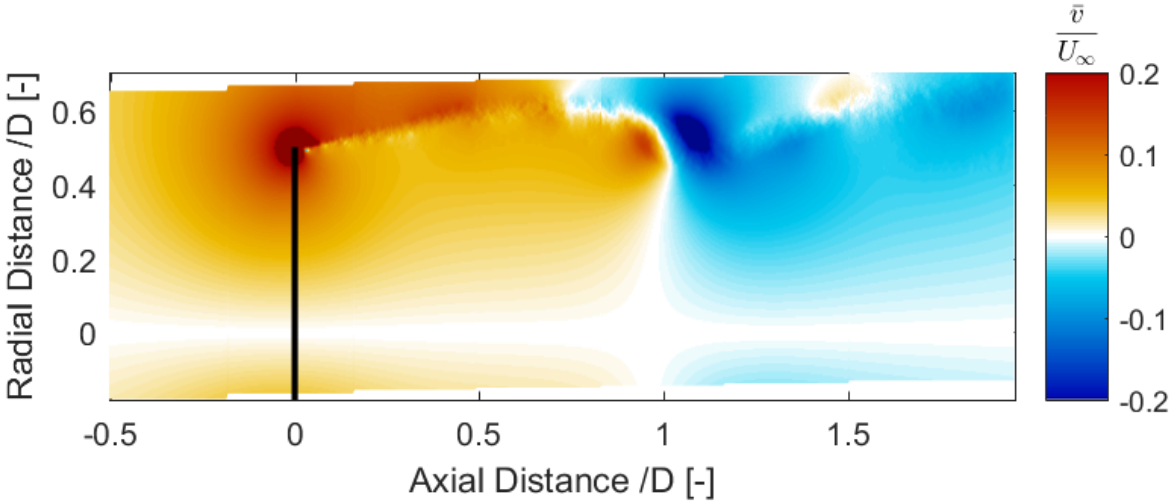

(a) Porosity = 14% (minimum porosity) and C_T = 0.705

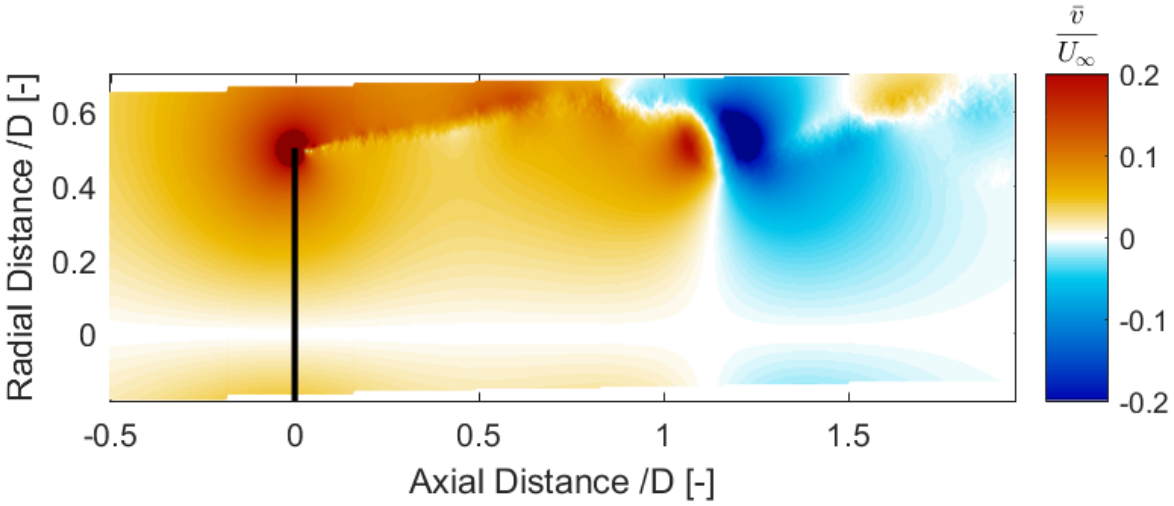

(b) Porosity = 19% (increasing porosity) and C_T = 0.697

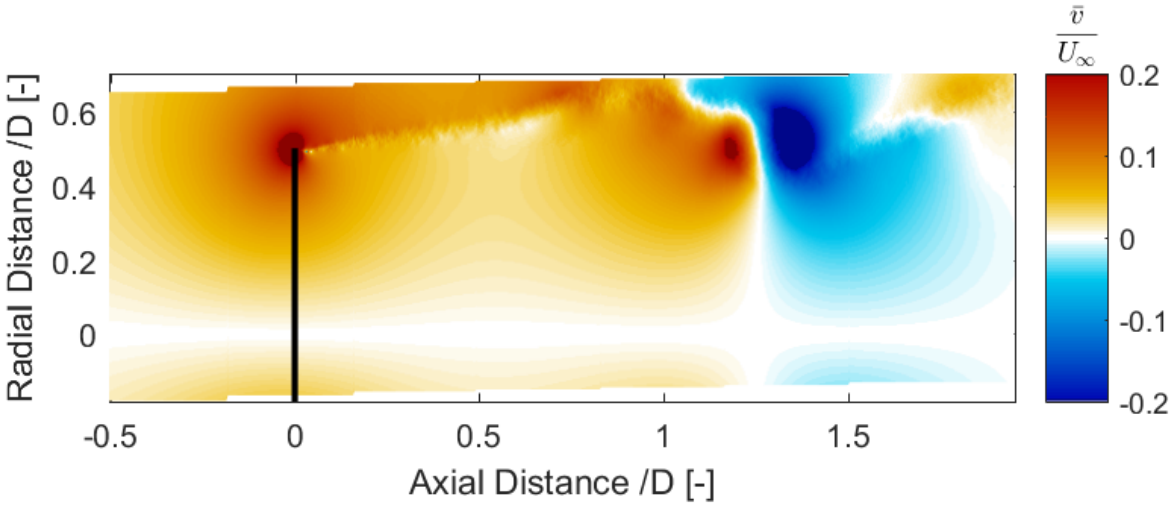

(c) Porosity = 31% (increasing porosity) C_T = 0.678

Figure 7.56: Normalized Radial Velocity Field for porosity changing with frequency = 5Hz and reduced frequency = 1.57 (Vortex Ring model)

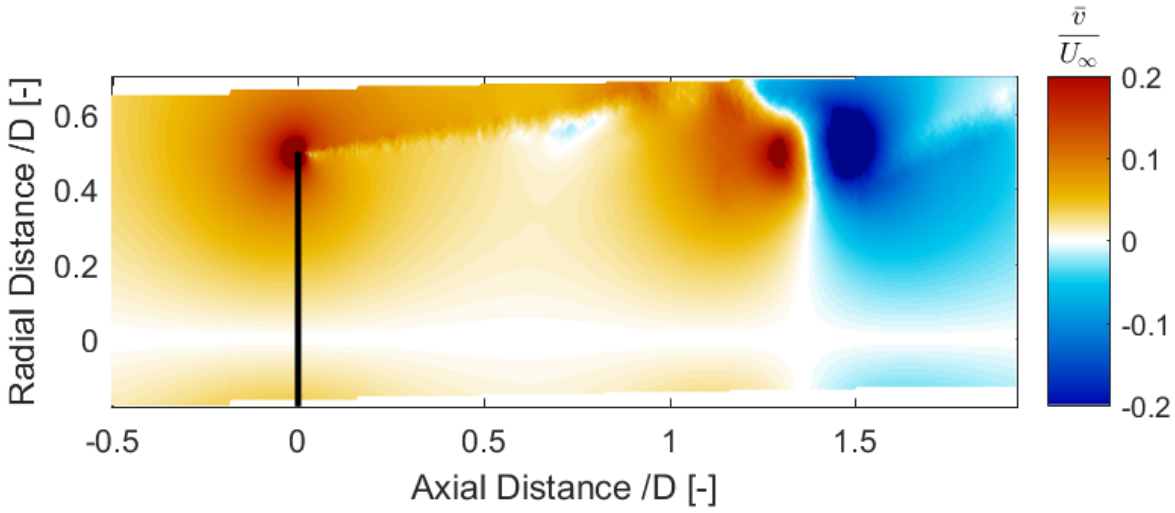

(a) Porosity = 47% (increasing porosity) and C_T = 0.657

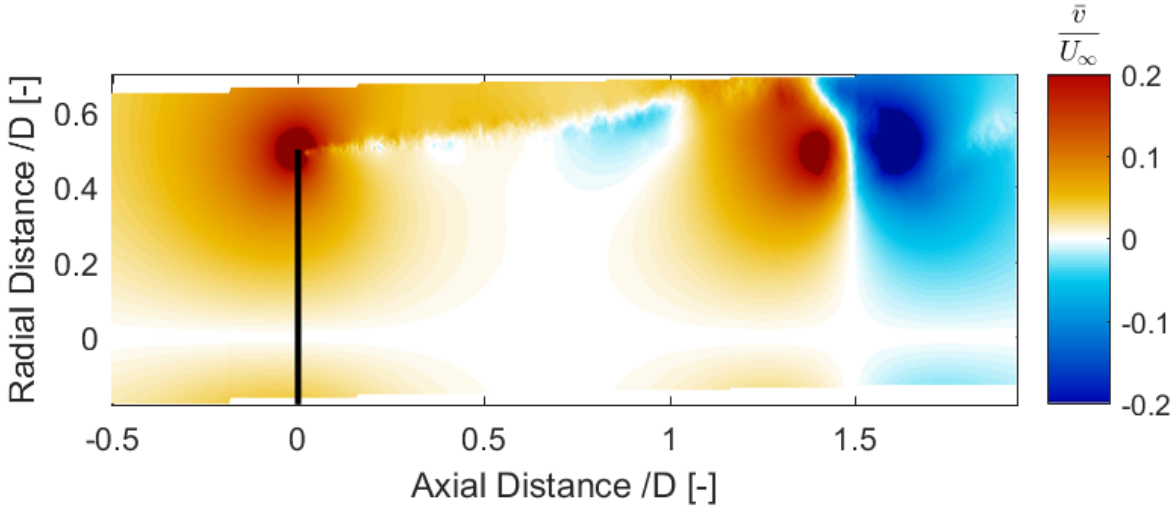

(b) Porosity = 59% (increasing porosity) and C_T = 0.596

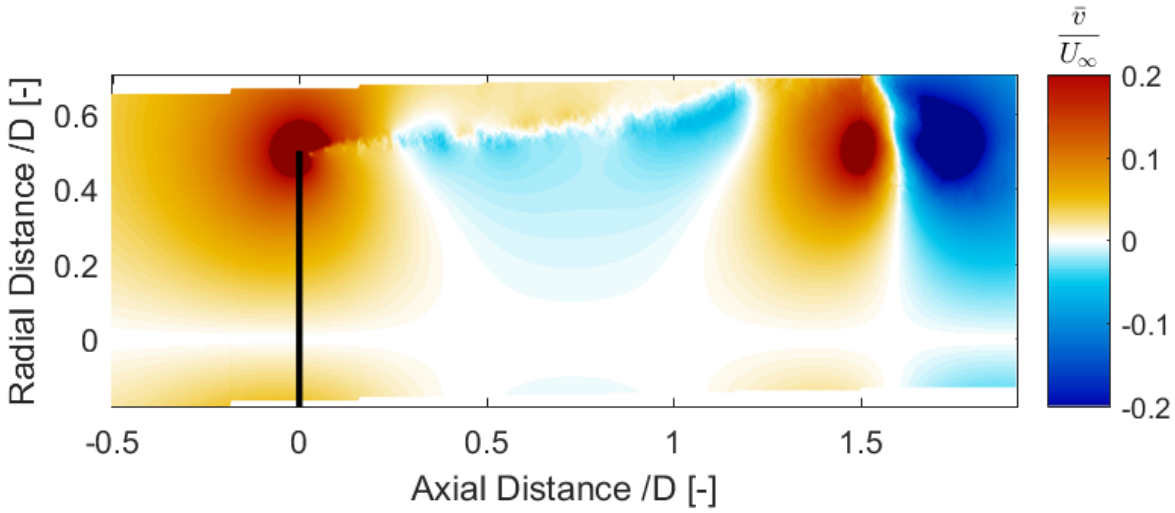

(c) Porosity = 64% (maximum porosity) and C_T = 0.550

Figure 7.57: Normalized Radial Velocity Field for porosity changing with frequency = 5Hz and reduced frequency = 1.57 (Vortex Ring model)

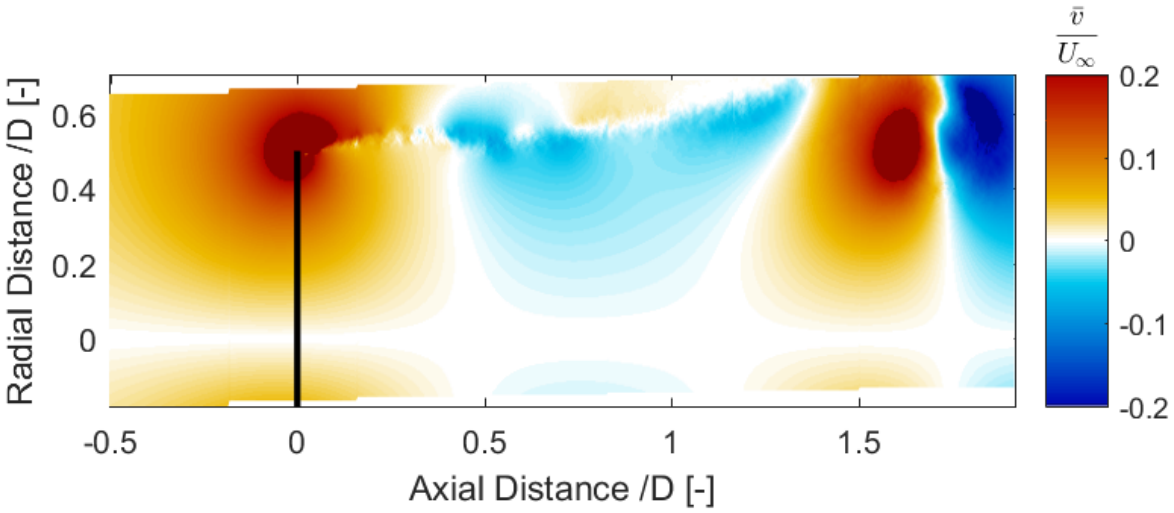

(a) Porosity = 59% (decreasing porosity) and C_T = 0.554

Figure 7.58: Normalized Radial Velocity Field for porosity changing with frequency = 5Hz and reduced frequency = 1.57 (Vortex Ring model)

7.3.2. FREQUENCY = 3HZ AND REDUCED FREQUENCY = 0.94

In this section, axial and radial velocity fields for unsteady load case in which the disc load cycle has a frequency of 3Hz and k = 0.47 are analysed.

Axial Velocity: Figure 7.59-Figure 7.62 show the normalized axial velocity field for the second unsteady load case. Following trends can be observed in the figures:

1. Wake is expanding and contracting owing to the cyclic change in loading, similar to the previous case. Figure E.12a shows that axial velocity estimated using the VR model for this case is also periodic.

2. For all cases, there is a region downstream the disk (near the wake edge) where axial velocity is really small. After which velocity field increases. At first, for the first five cases from 53.2% till 14%, this region increases in size and moves downstream.

3. For the second half of the load cycle, this region of low axial velocity is not seen till x/D = 2. This is because for this half, the rolling up of the vorticity has moved further downstream (as seen in the previous section).

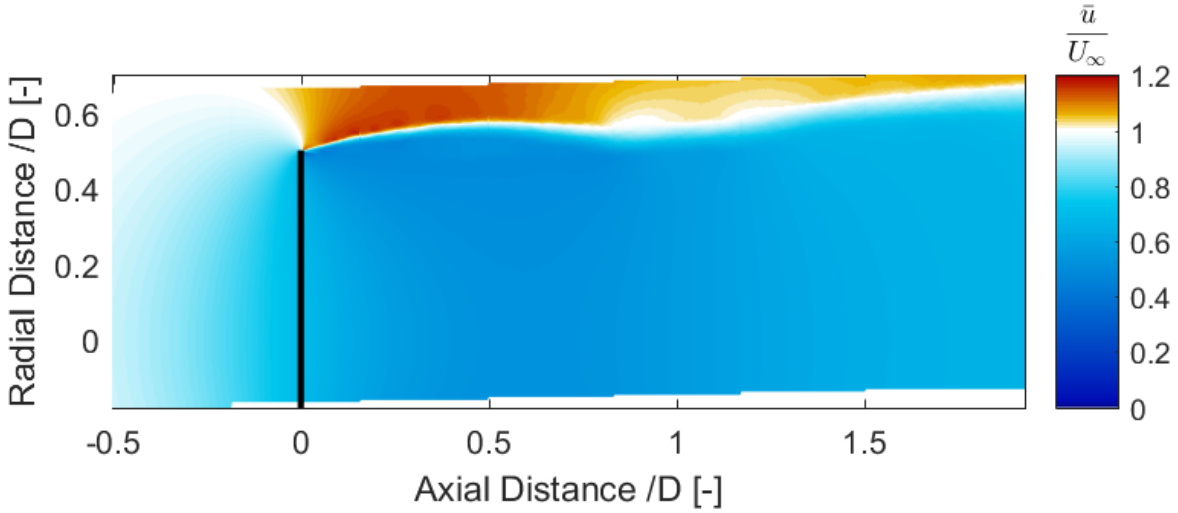

(a) Porosity = 59% (decreasing porosity) and C_T = 0.572

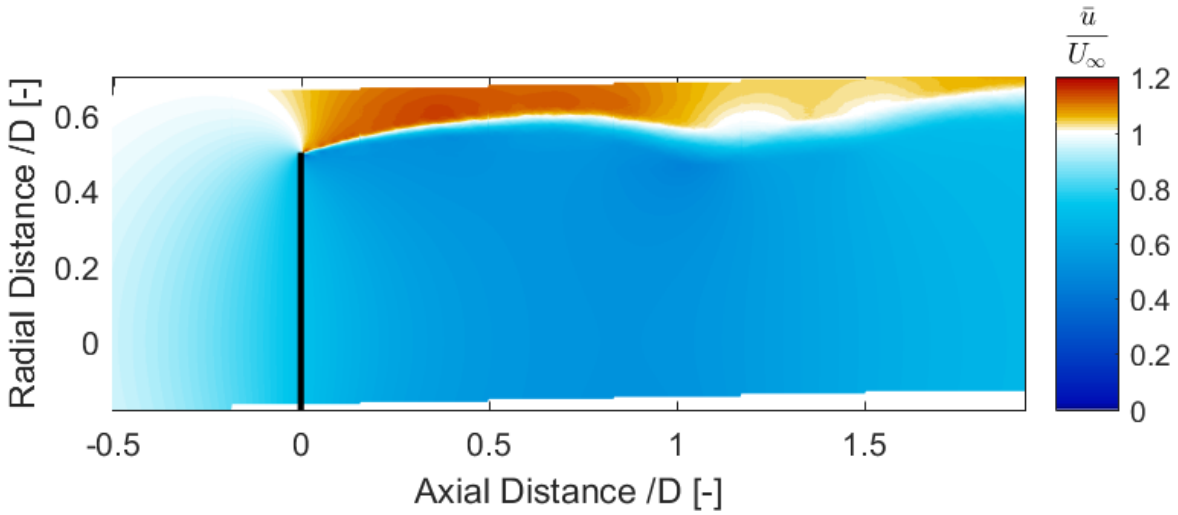

(b) Porosity = 47% (decreasing porosity) and C_T = 0.593

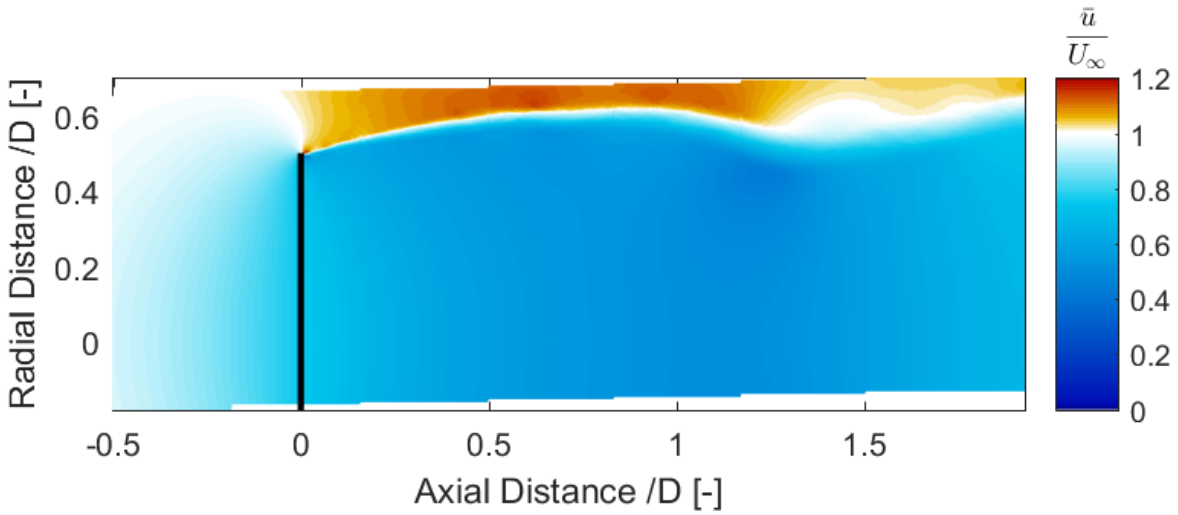

(c) Porosity = 31% (decreasing porosity) and C_T = 0.622

Figure 7.59: Normalized Axial Velocity Field for porosity changing with frequency = 3Hz and reduced frequency = 0.94 (Vortex Ring model)

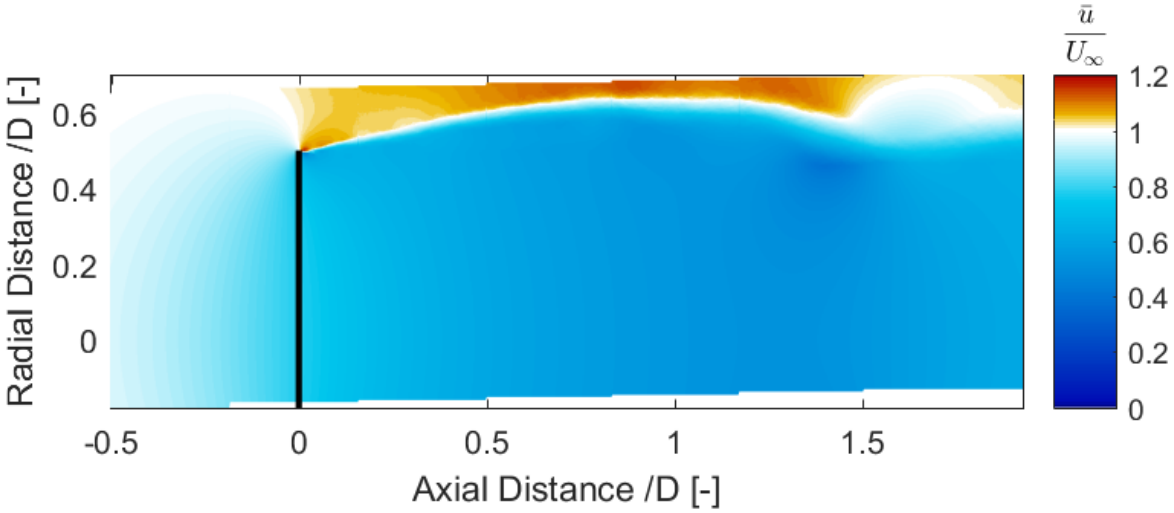

(a) Porosity = 19% (decreasing porosity) and C_T = 0.649

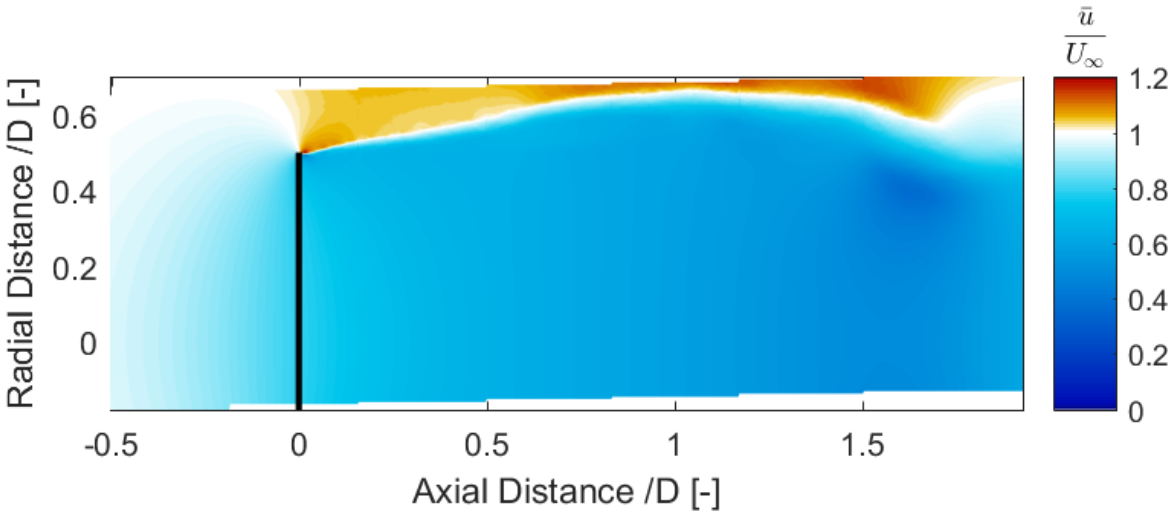

(b) Porosity = 14% (minimum porosity) and C_T = 0.684

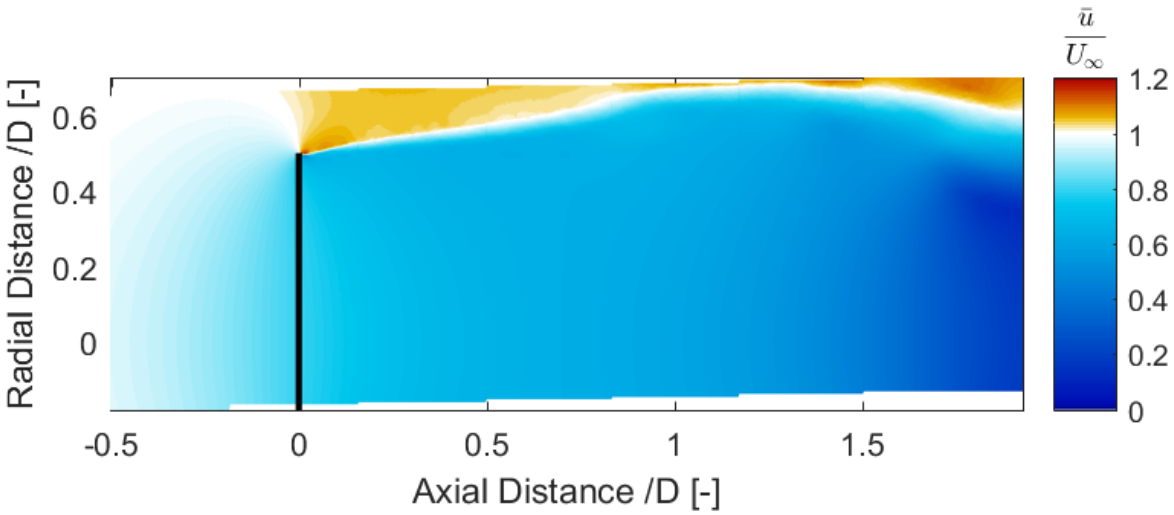

(c) Porosity = 19% (increasing porosity) and C_T = 0.671

Figure 7.60: Normalized Axial Velocity Field for porosity changing with frequency = 3Hz and reduced frequency = 0.94 (Vortex Ring model)

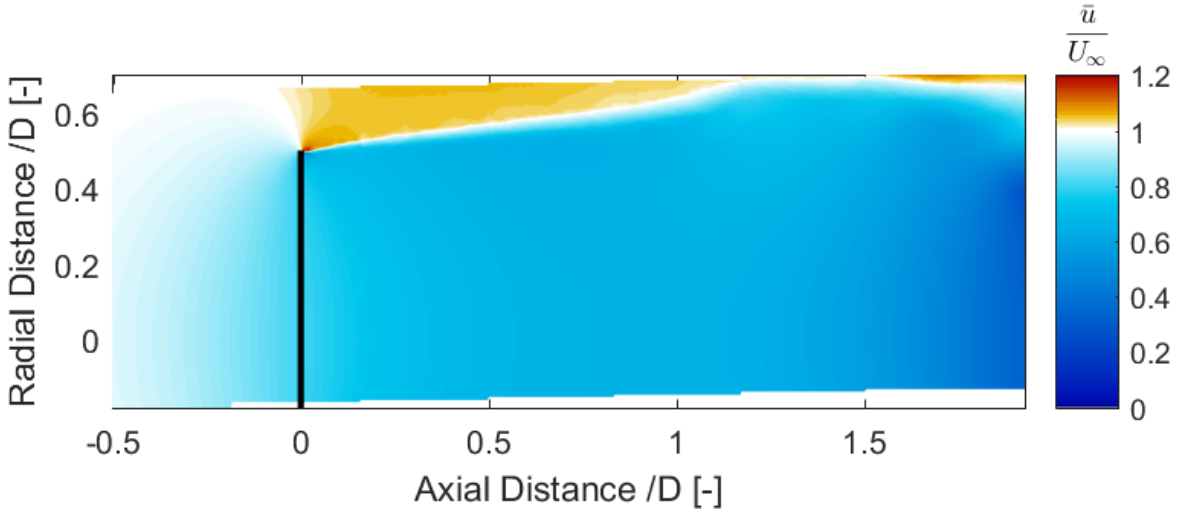

(a) Porosity = 31% (increasing porosity) and C_T = 0.651

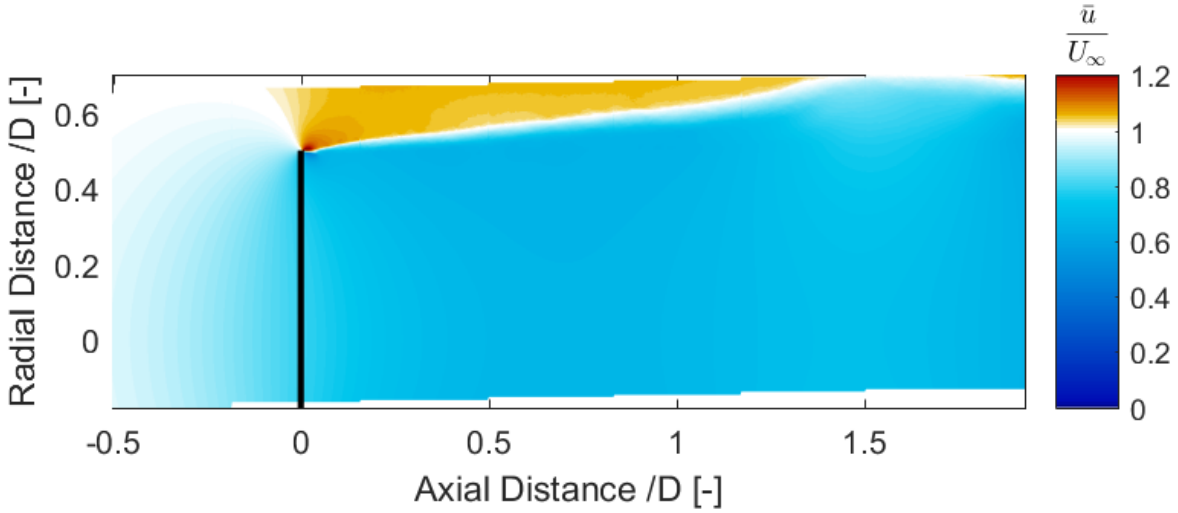

(b) Porosity = 47% (increasing porosity) and C_T = 0.612

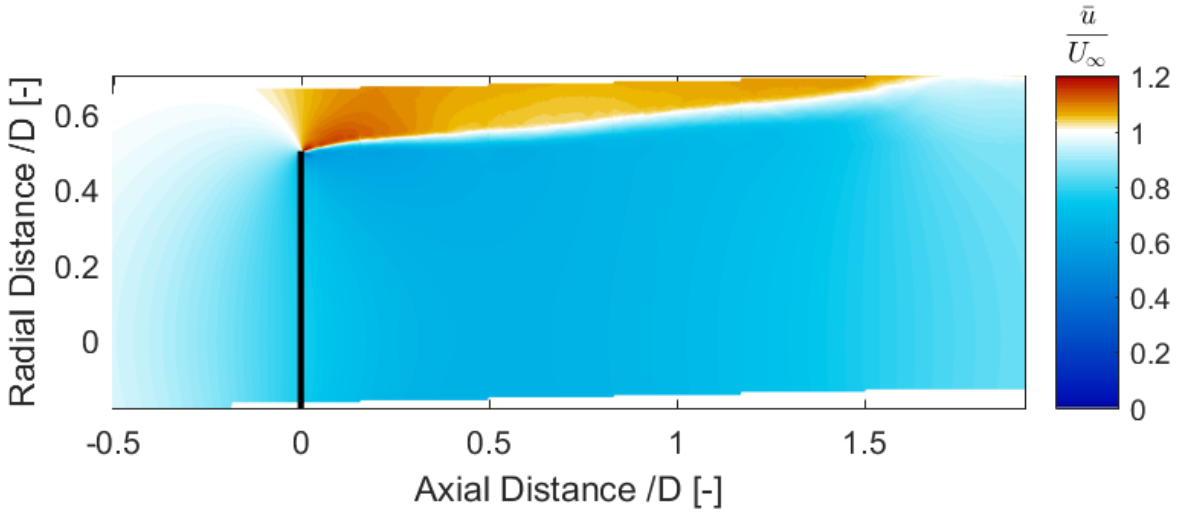

(c) Porosity = 59% (increasing porosity) and C_T = 0.584

Figure 7.61: Normalized Axial Velocity Field for porosity changing with frequency = 3Hz and reduced frequency = 0.94 (Vortex Ring model)

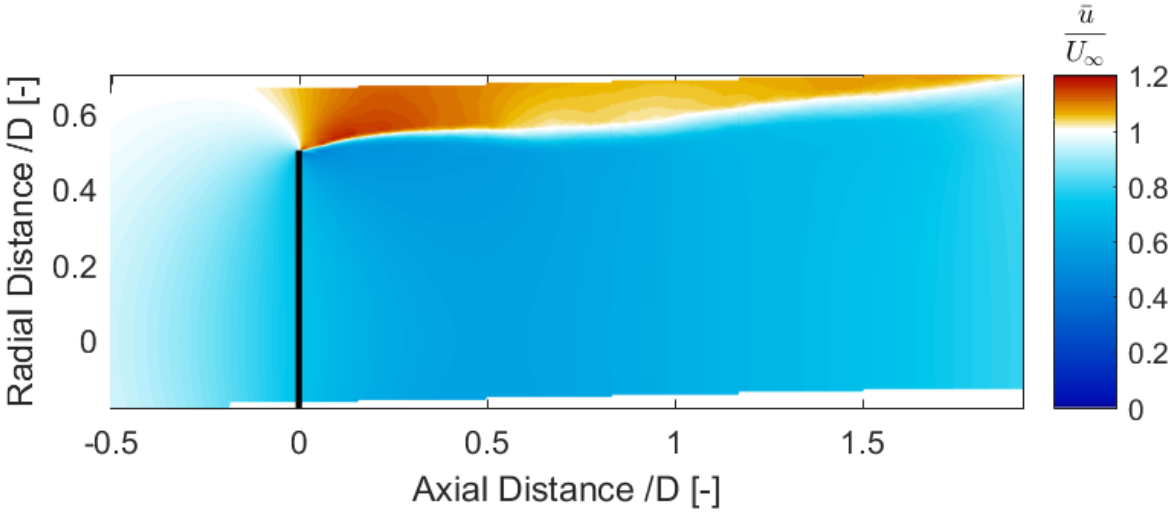

(a) Porosity = 64% (maximum porosity) and C_T = 0.569

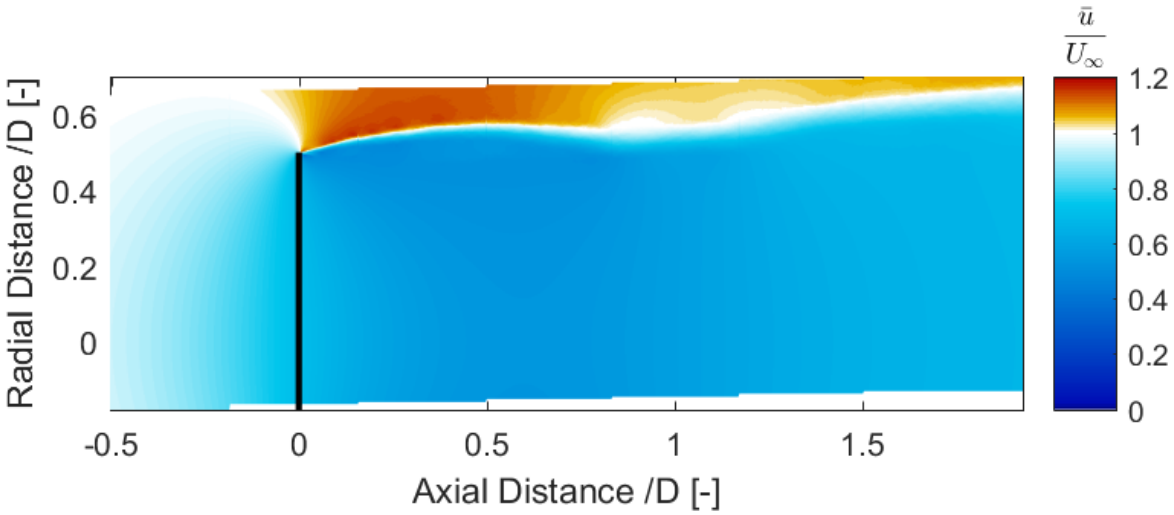

(b) Porosity = 59% (decreasing porosity) and C_T = 0.572

Figure 7.62: Normalized Axial Velocity Field for porosity changing with frequency = 3Hz and reduced frequency = 0.94 (Vortex Ring model)

Radial Velocity: Figure 7.63-Figure 7.67 show the average radial velocity fields for changing porosity with frequency of 3Hz and k = 0.94. Following analysis can be made from the figures:

1. The flow is not axisymmetric as the VR model assumes axisymmetric velocity and takes square of radial position, thereby estimating the same velocity for both negative and positive radial positions.

2. The maximum radial velocity is around the disc edge.

3. The radial velocity fields are both negative and positive for all cases.

4. For first 5 cases (59%-14%), the flow is positive just behind the disc and then negative. With increase in load, positive radial velocity region increases in size.

5. The case with thrust coefficient of 0.671 (after maximum loading) has mainly positive radial velocity till x/D = 2.

6. Then for the second half of the cycle, the radial velocity begins to become negative again around x/D = 0.75. This region increases with decrease in loading on the disk. By 59% porosity case, the field starts to reach the initial case of the cycle.

7. From these fields, it can be noticed that the radial velocity fields of the first and last time-node resemble each other. The positive and negative radial velocity is seen in the wake. This means flow is moving outboards in some regions in the field and in-boards towards the centre line in others. This is the effect of changing porosity in a sinusoidal way.

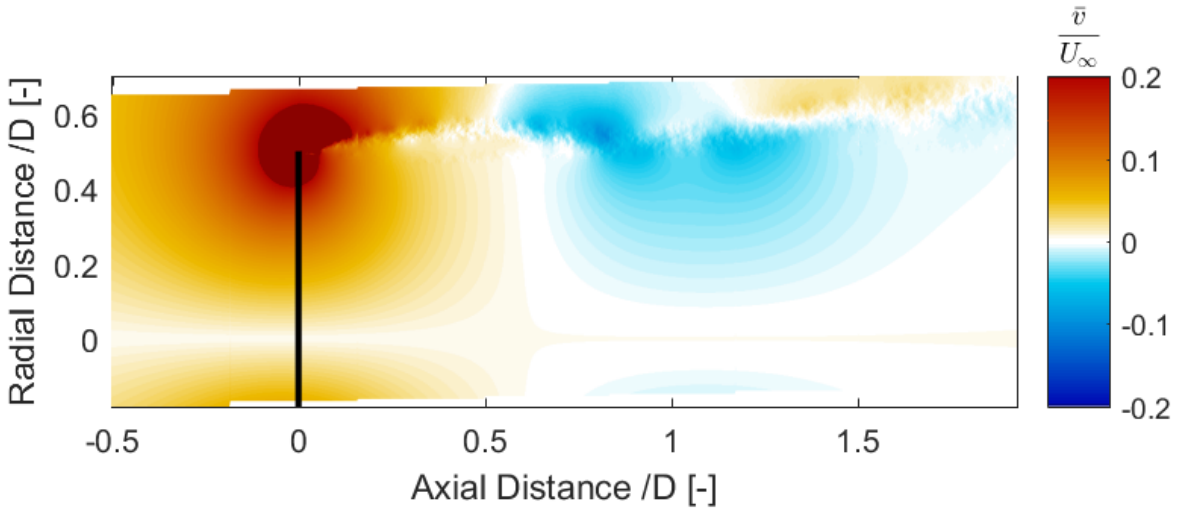

(a) Porosity = 59% (decreasing porosity) and C_T = 0.572

Figure 7.63: Normalized Radial Velocity Field for porosity changing with frequency = 3Hz and reduced frequency = 0.94 (Vortex Ring model)

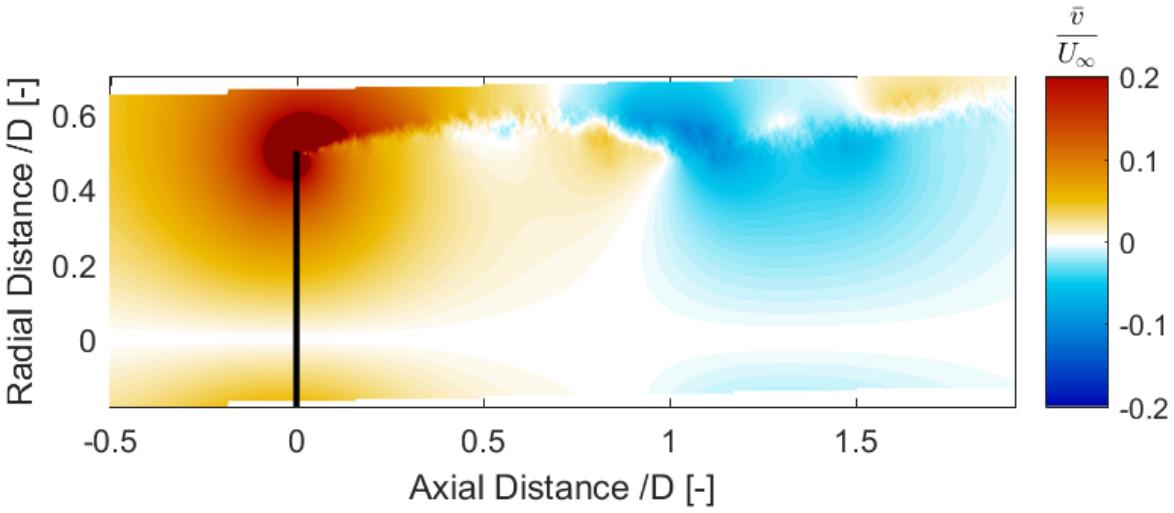

(a) Porosity = 47% (decreasing porosity) and C_T = 0.593

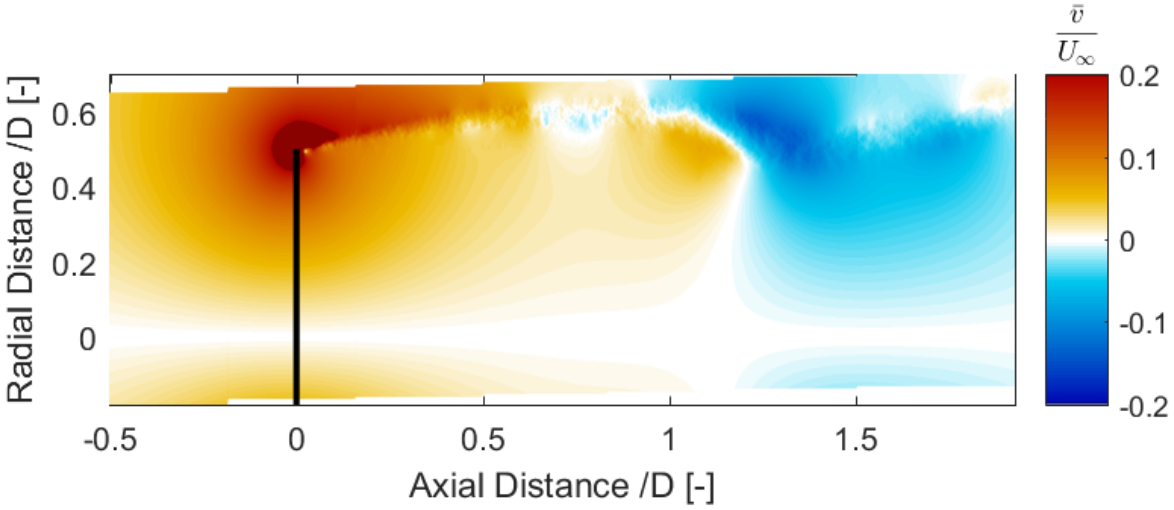

(b) Porosity = 31% (decreasing porosity) and C_T = 0.622

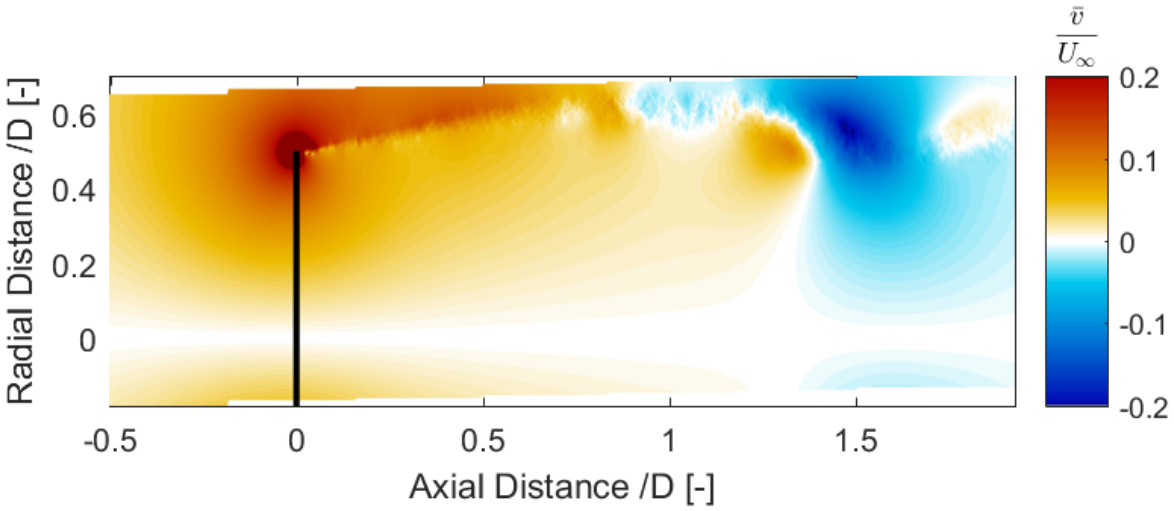

(c) Porosity = 19% (decreasing porosity) and C_T = 0.649

Figure 7.64: Normalized Radial Velocity Field for porosity changing with frequency = 3Hz and reduced frequency = 0.94 (Vortex Ring model)

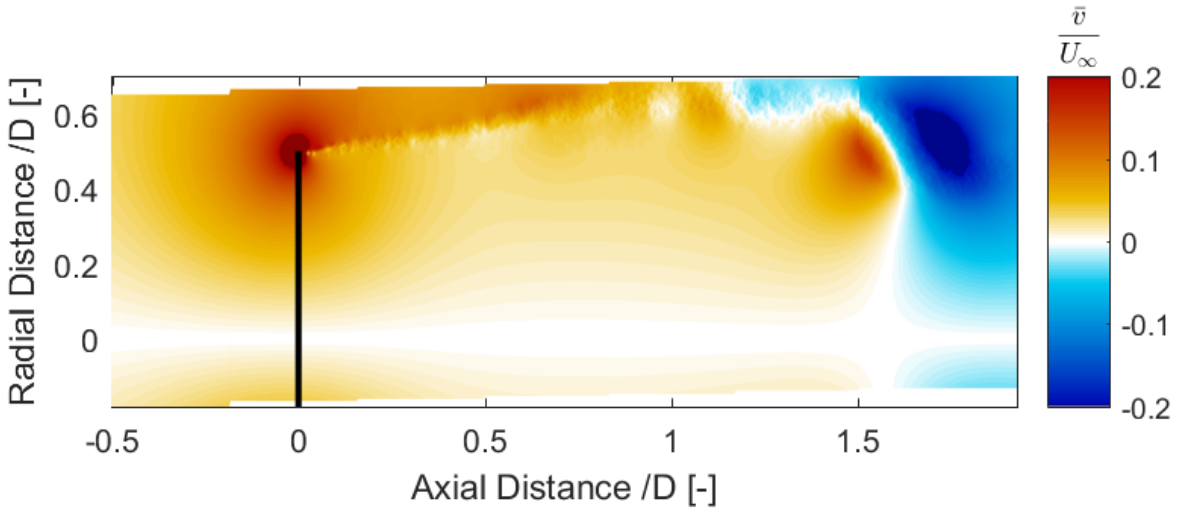

(a) Porosity = 14% (minimum porosity) and C_T = 0.684

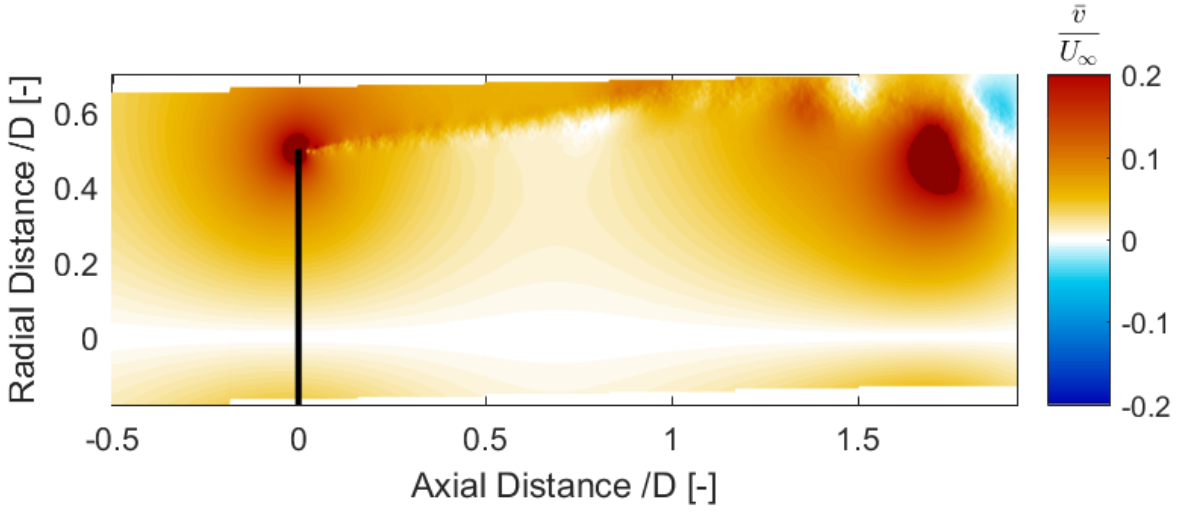

(b) Porosity = 19% (increasing porosity) and C_T = 0.671

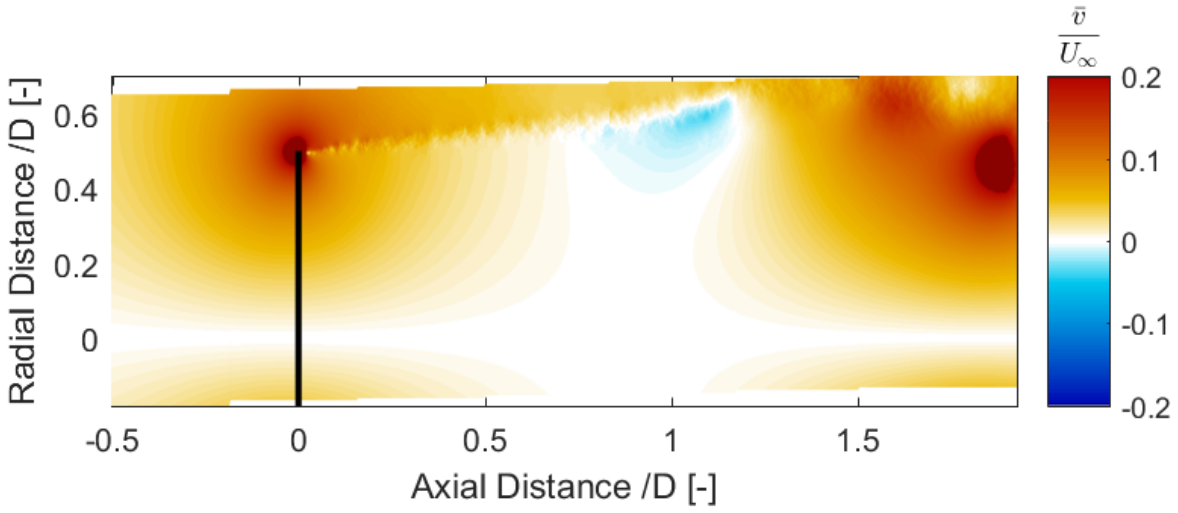

(c) Porosity = 31% (increasing porosity) and C_T = 0.651

Figure 7.65: Normalized Radial Velocity Field for porosity changing with frequency = 3Hz and reduced frequency = 0.94 (Vortex Ring model)

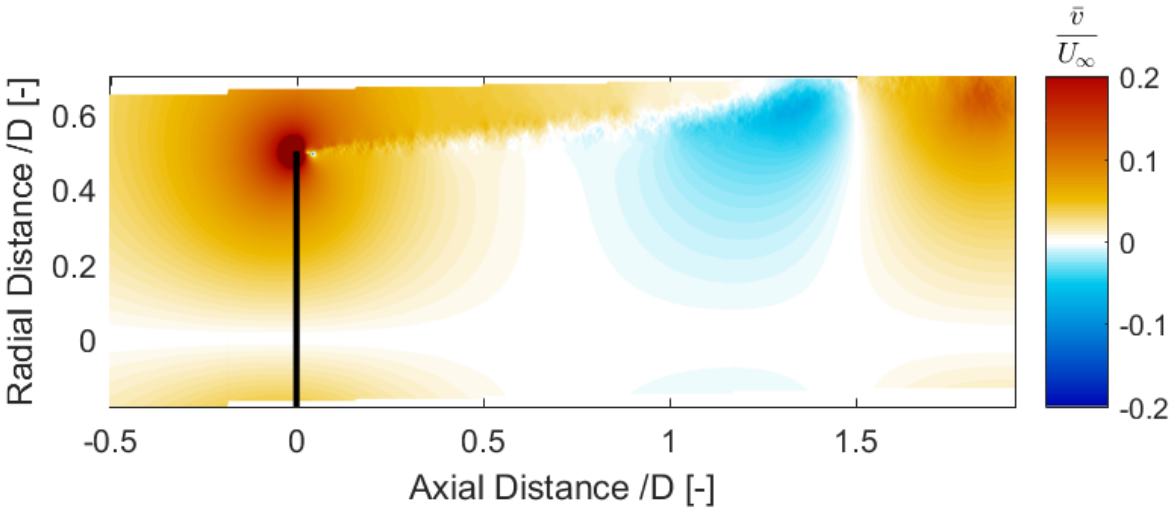

(a) Porosity = 47% (increasing porosity) and C_T = 0.612

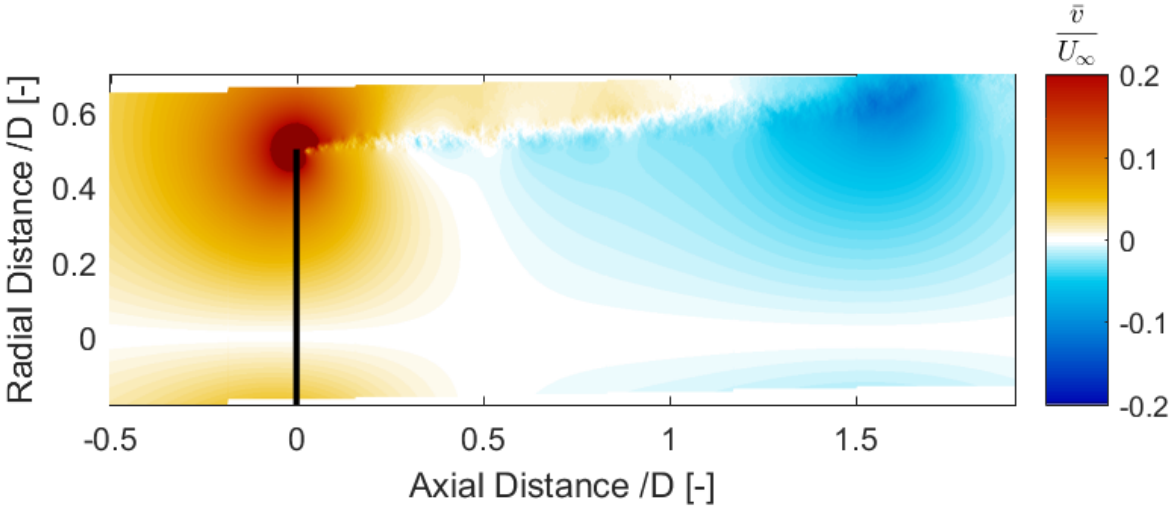

(b) Porosity = 59% (increasing porosity) and C_T = 0.584

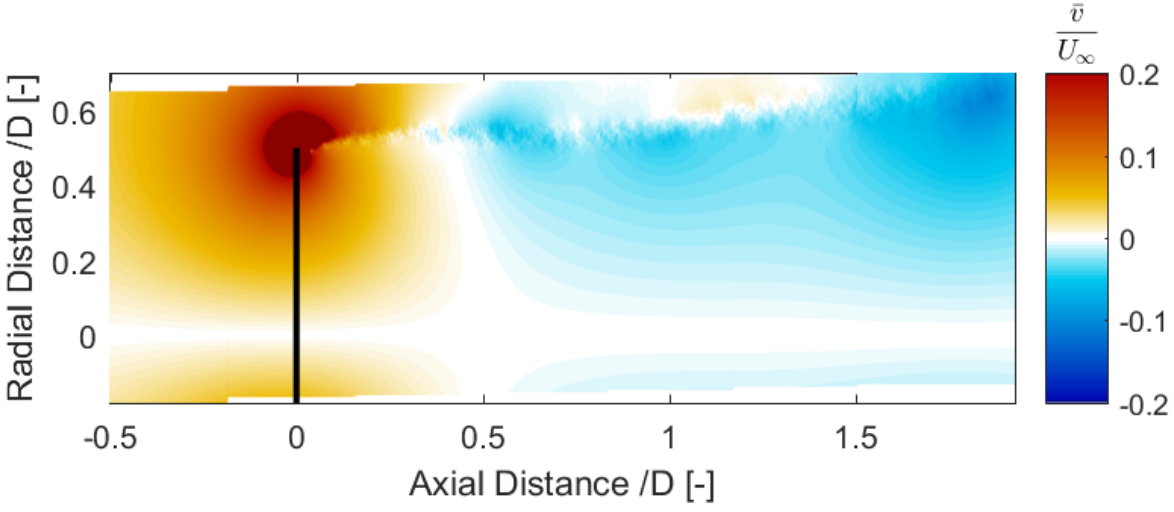

(c) Porosity = 64% (maximum porosity) and C_T = 0.569

Figure 7.66: Normalized Radial Velocity Field for porosity changing with frequency = 3Hz and reduced frequency = 0.94 (Vortex Ring model)

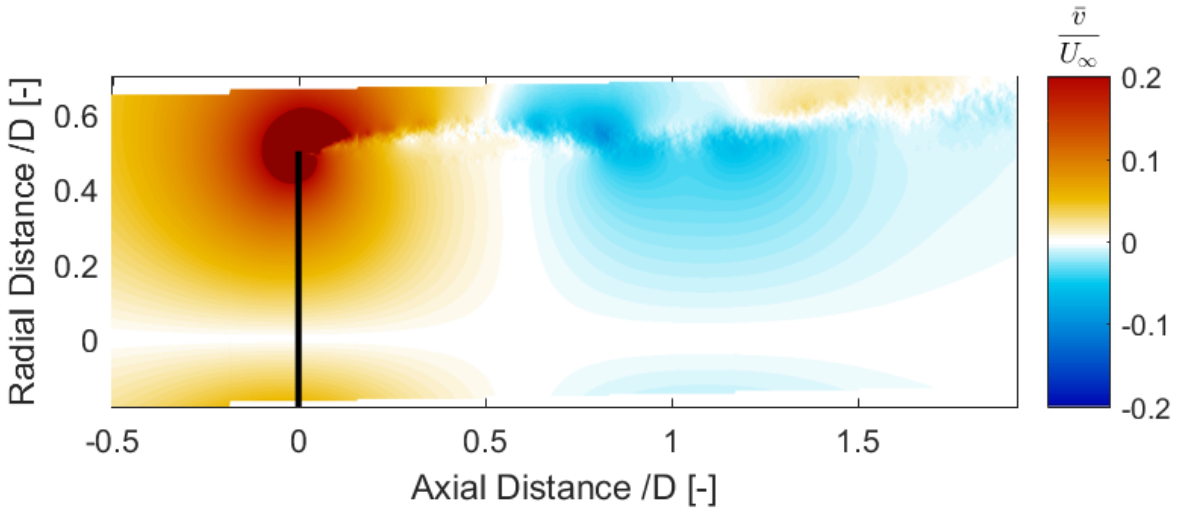

(a) Porosity = 59% (decreasing porosity) and C_T = 0.572

Figure 7.67: Normalized Radial Velocity Field for porosity changing with frequency = 3Hz and reduced frequency = 0.94 (Vortex Ring model)

7.3.3. FREQUENCY = 1.5HZ AND REDUCED FREQUENCY = 0.47

In this section, axial and radial velocity fields for unsteady load case in which the disc load cycle has a frequency of 3Hz and k = 0.47 are discussed.

Axial Velocity: Figure 7.68 -Figure 7.71 show the axial velocity field estimated by the Vortex Ring model for the unsteady load case of frequency = 1.5Hz and k = 0.47. It can be observed that with each change in the disc loading, the wake expansion behaviour (expanding and contracting wake) does not change as much as the previous cases. With increase in loading, wake expands more as seen in figures 7.68a,7.68b,7.68c,7.69a and 7.69b. When loading starts decreasing, figures 7.69c, 7.70a, 7.70b, 7.70c and 7.71a show that the wake expansion decreases.

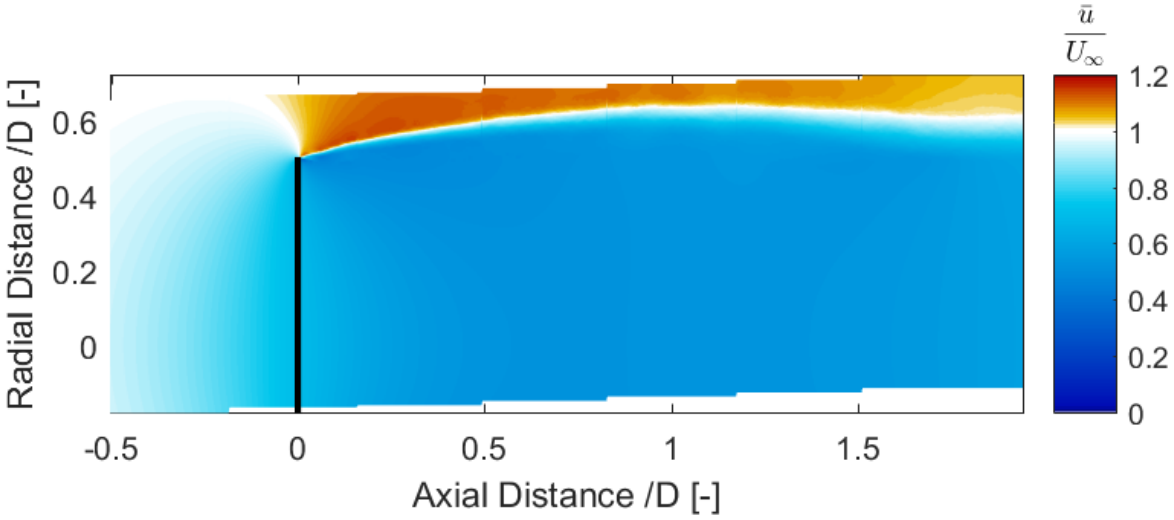

(a) Porosity = 59% (decreasing porosity) and C_T = 0.566

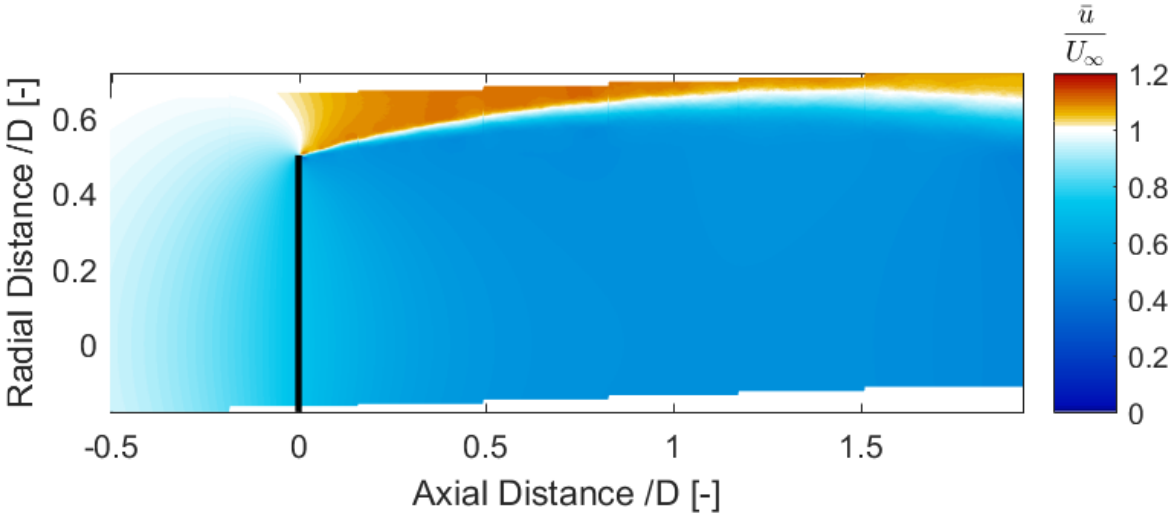

(b) Porosity = 47% (decreasing porosity) and C_T = 0.605

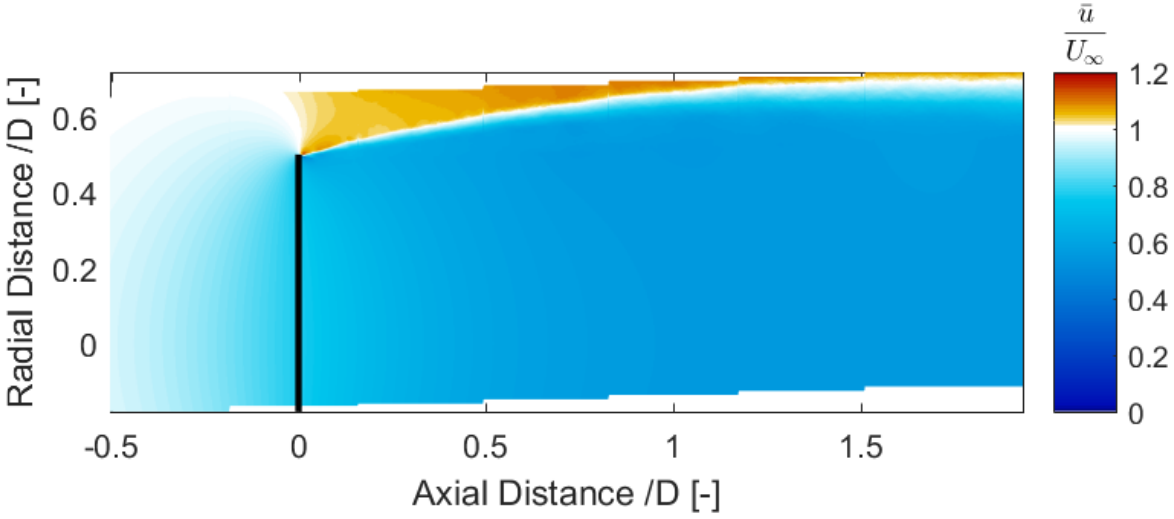

(c) Porosity = 31% (decreasing porosity) and C_T = 0.639

Figure 7.68: Normalized Axial Velocity Field for porosity changing with frequency = 1.5Hz and reduced frequency = 0.47 (Vortex Ring model)

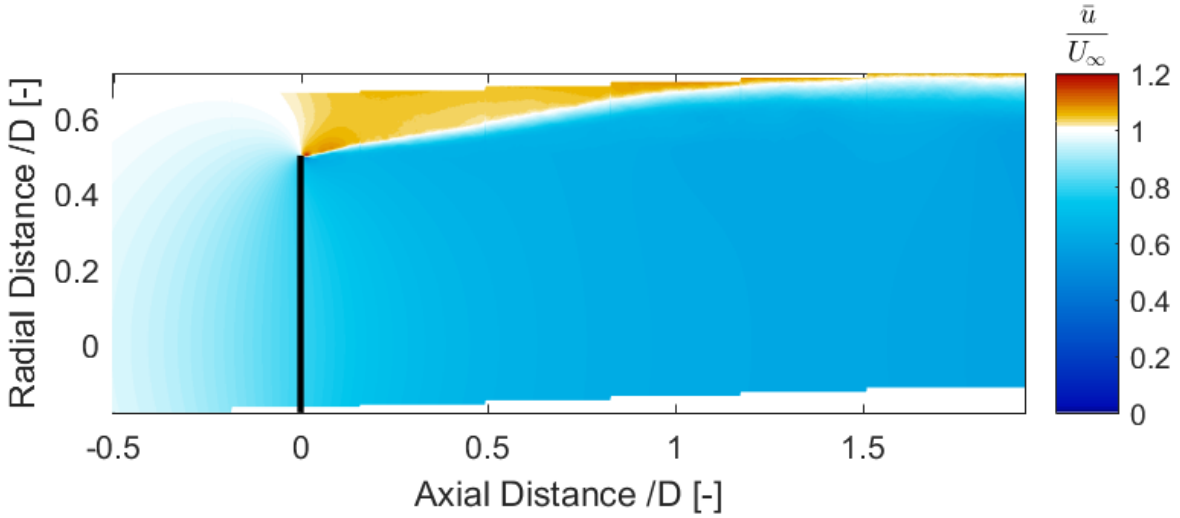

(a) Porosity = 19% (decreasing porosity) and C_T = 0.666

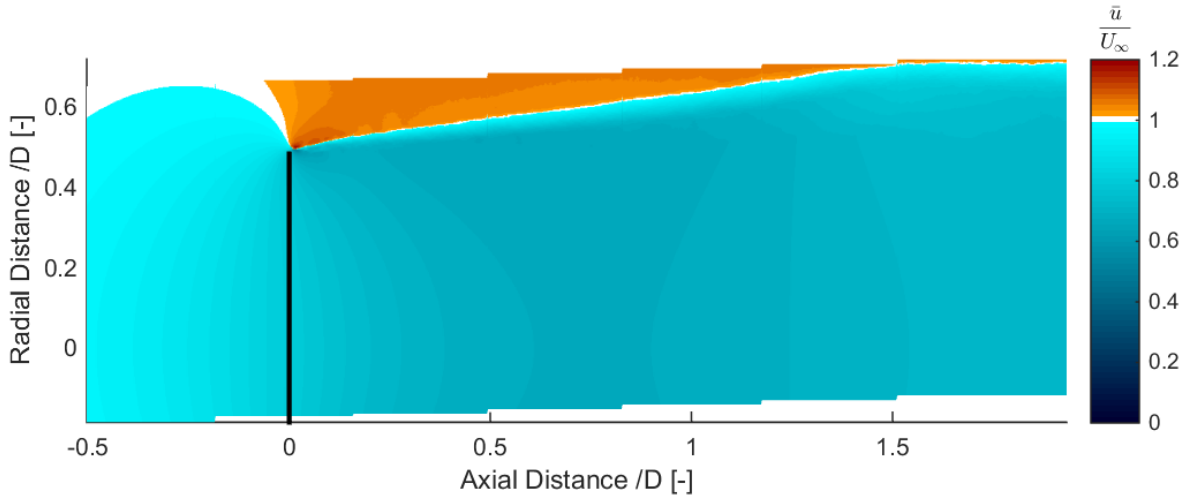

(b) Porosity = 14% (minimum porosity) and C_T = 0.692

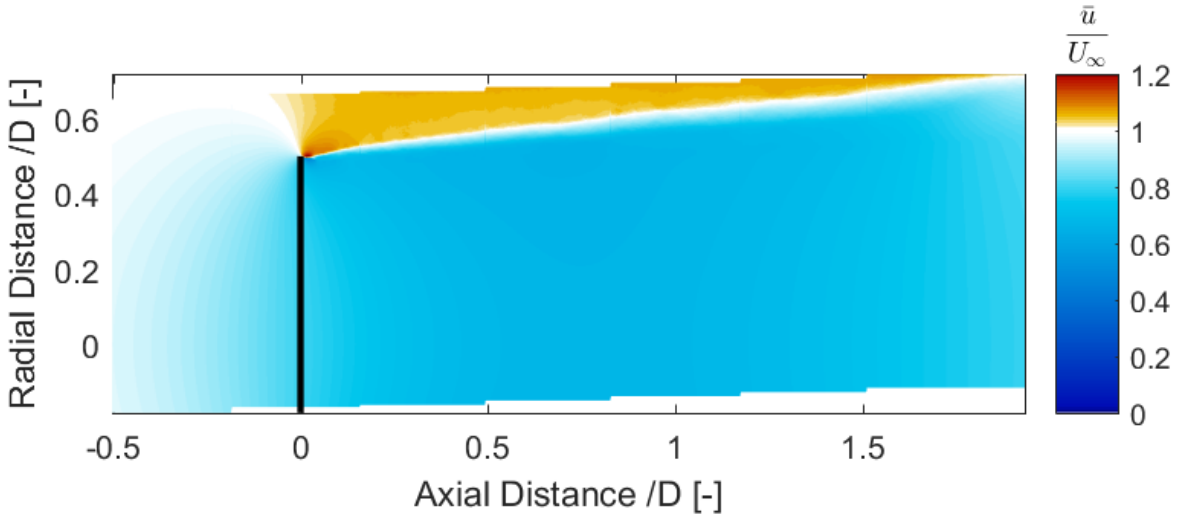

(c) Porosity = 19% (increasing porosity) and C_T = 0.675

Figure 7.69: Normalized Axial Velocity Field for porosity changing with frequency = 1.5Hz and reduced frequency = 0.47 (Vortex Ring model)

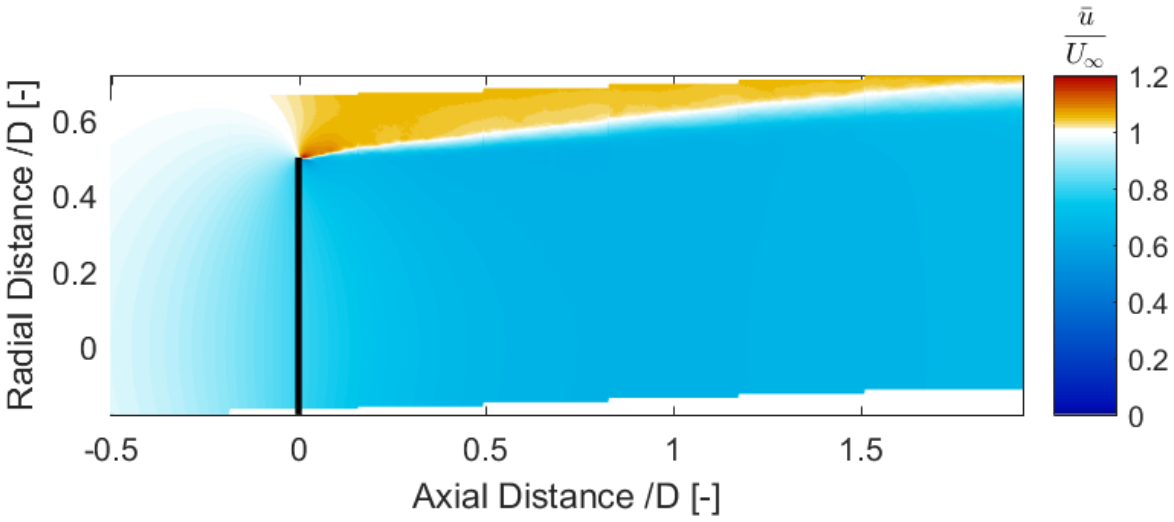

(a) Porosity = 31% (increasing porosity) and C_T = 0.651

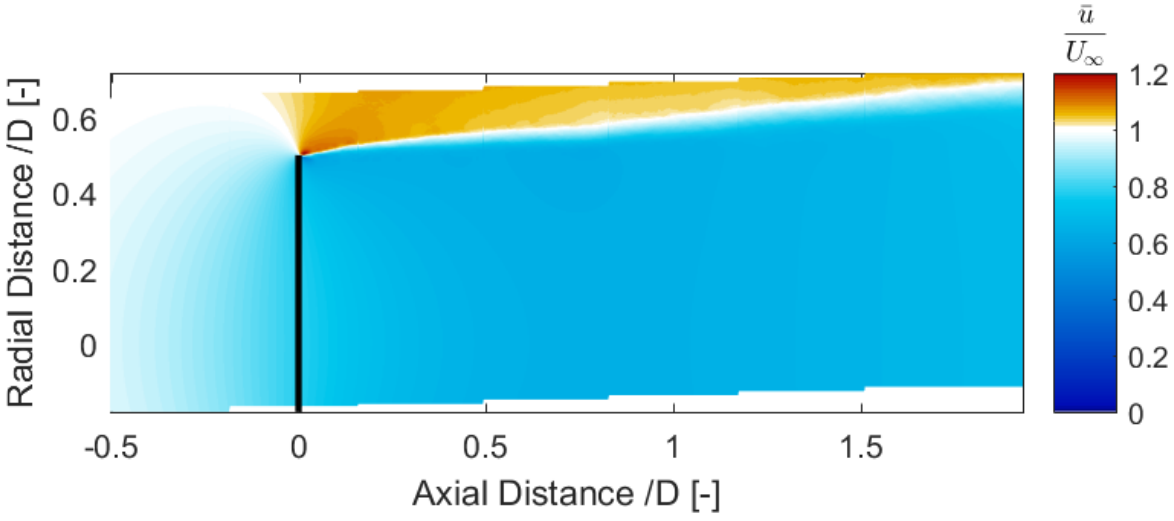

(b) Porosity = 47% (increasing porosity) and C_T = 0.616

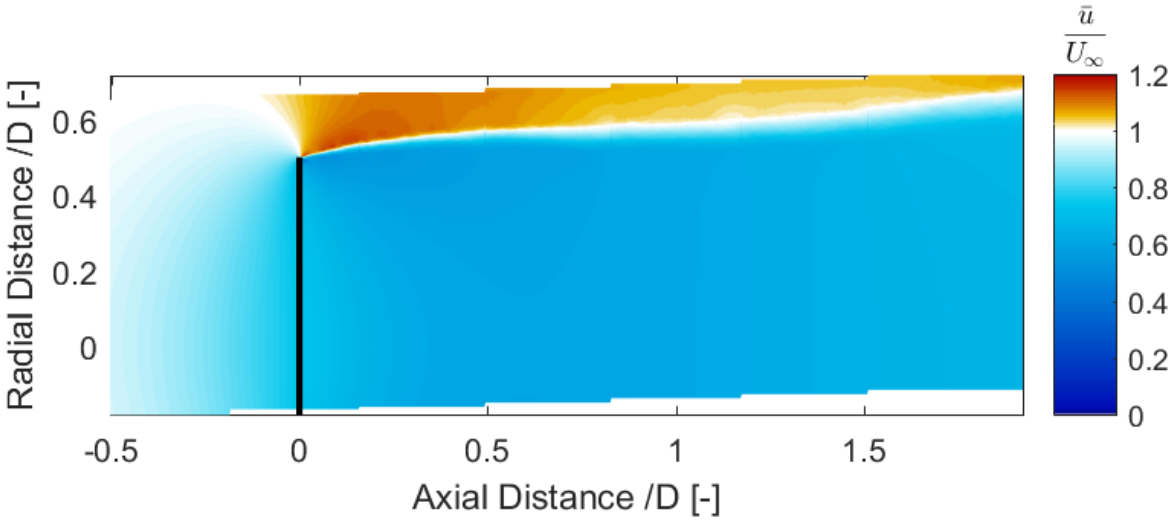

(c) Porosity = 59% (increasing porosity) and C_T = 0.575

Figure 7.70: Normalized Axial Velocity Field for porosity changing with frequency = 1.5Hz and reduced frequency = 0.47 (Vortex Ring model)

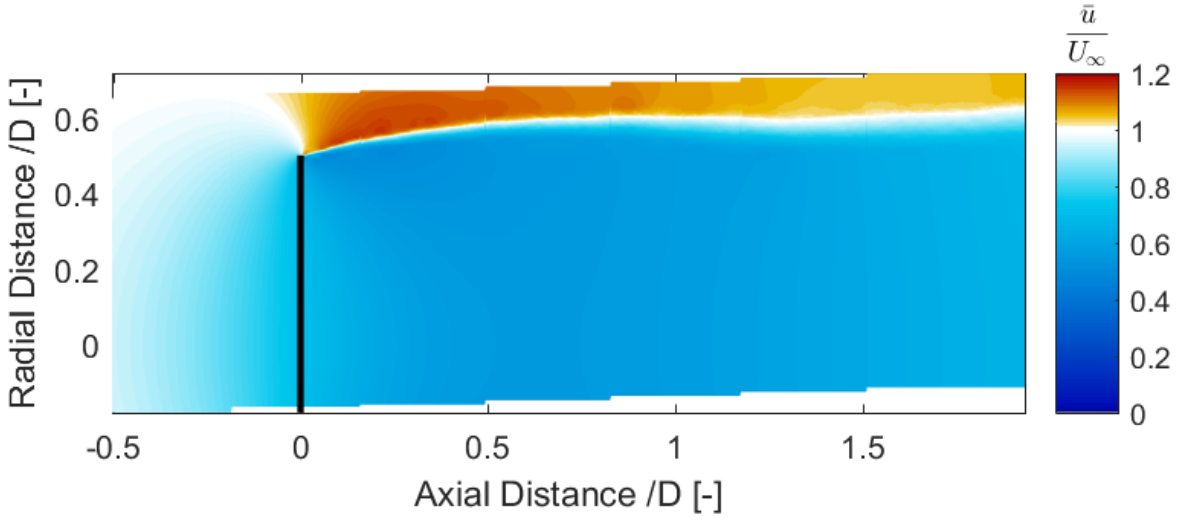

(a) Porosity = 64% (maximum porosity) and C_T = 0.555

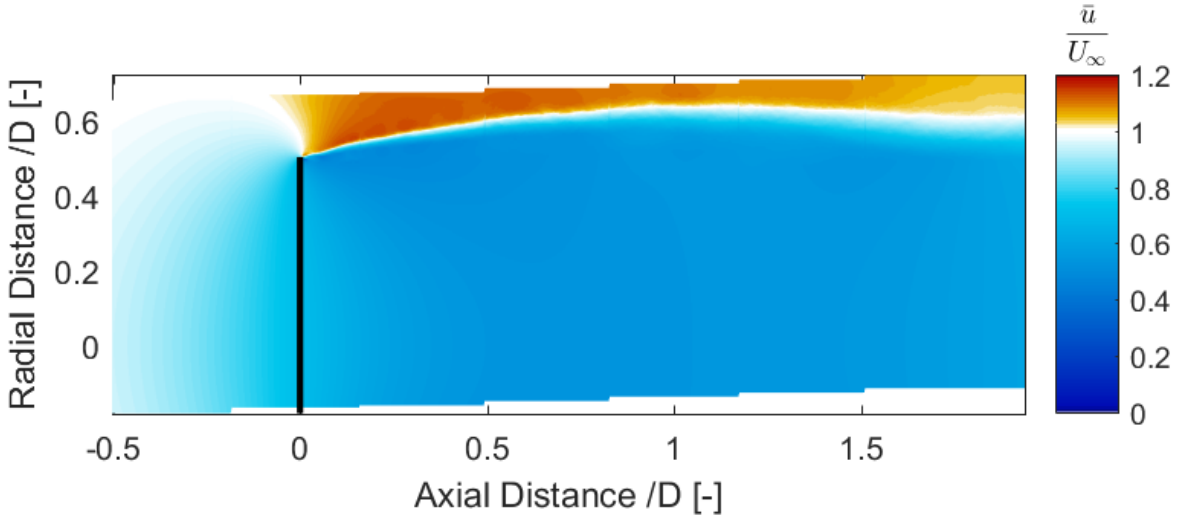

(b) Porosity = 59% (decreasing porosity) and C_T = 0.565

Figure 7.71: Normalized Axial Velocity Field for porosity changing with frequency = 1.5Hz and reduced frequency = 0.47 (Vortex Ring model)

Radial Velocity: Figure 7.72-Figure 7.75 show the average radial velocity fields for changing porosity with frequency of 1.5Hz. Following observations can be made:

1. Like the previous unsteady load cases, the VR model predicts radial velocity to be maximum near the tip. Compared to the axial velocity, it is small.

2. Again the fields are constituted of both negative and positive radial velocity field. For 59% till 14%, positive radial velocity region increase. Then, for increasing porosity cases, it gets smaller. This is caused by changes in the wake expansion.

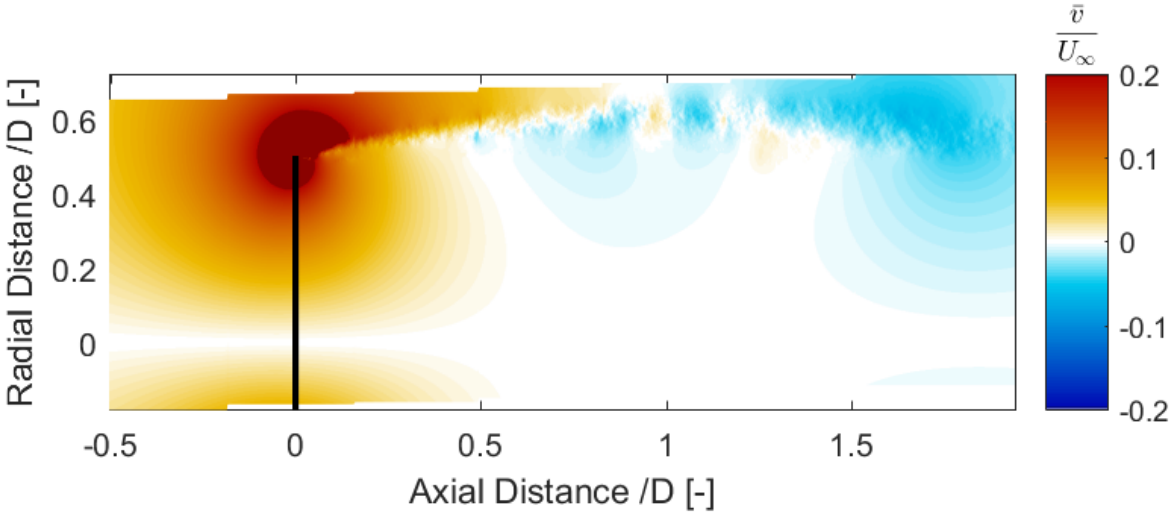

(a) Porosity = 59% (decreasing porosity) and C_T = 0.566

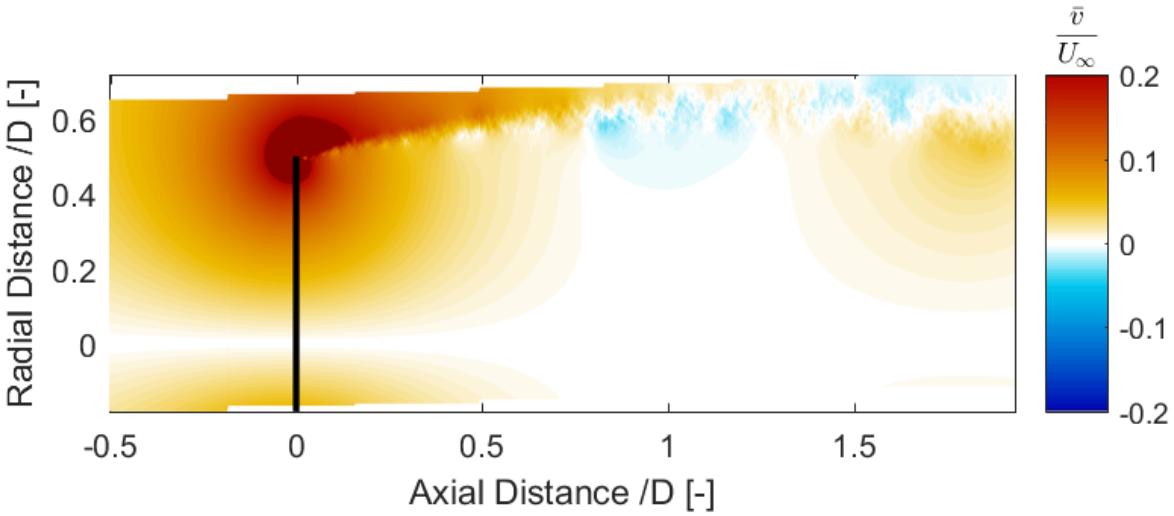

(b) Porosity = 47% (decreasing porosity) and C_T = 0.605

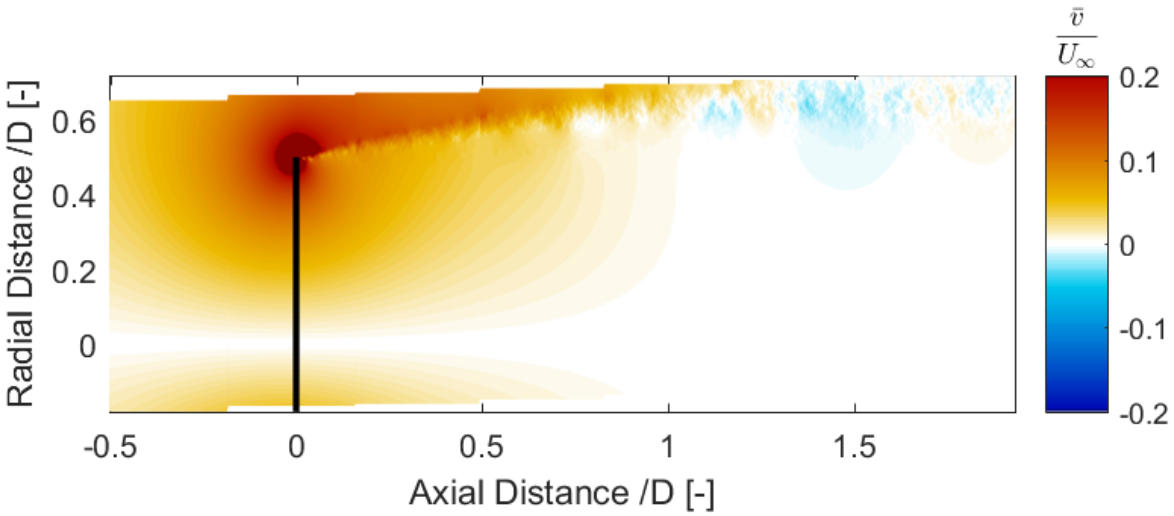

(c) Porosity = 31% (decreasing porosity) and C_T = 0.639

Figure 7.72: Normalized Radial Velocity Field for porosity changing with frequency = 1.5Hz and reduced frequency = 0.47 (Vortex Ring model)

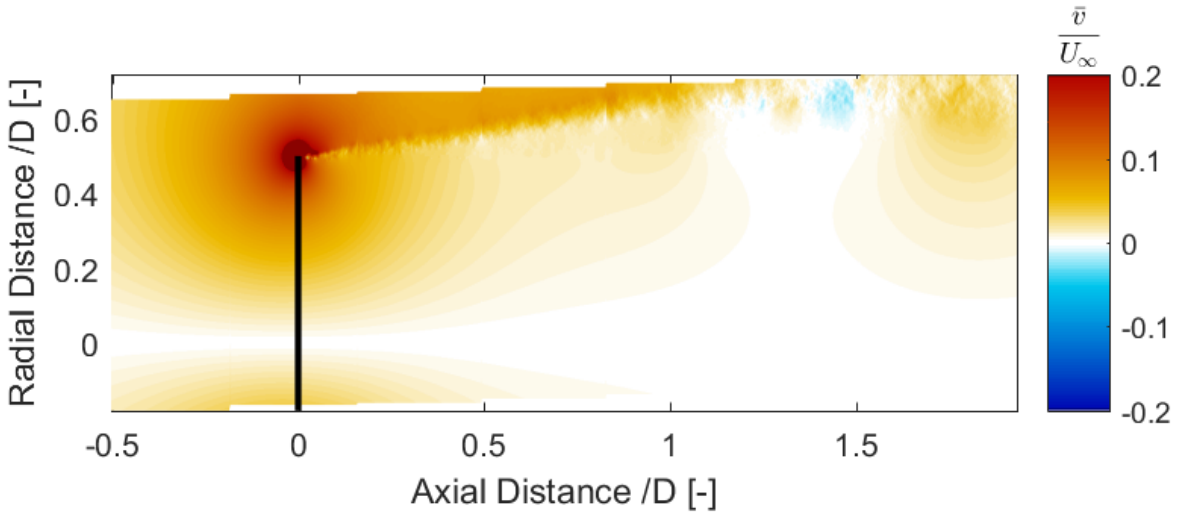

(a) Porosity = 19% (decreasing porosity) and C_T = 0.666

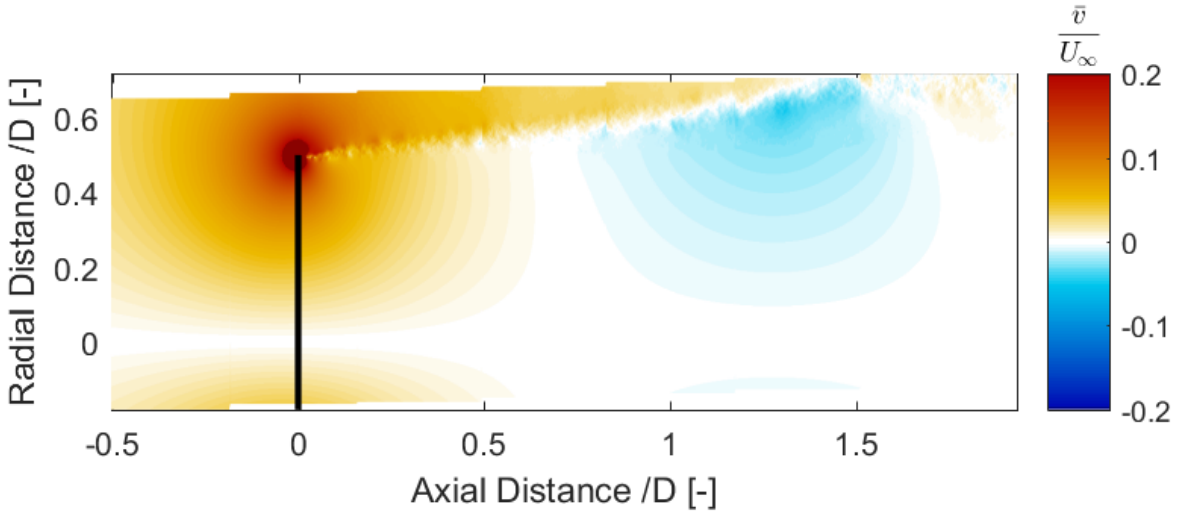

(b) Porosity = 14% (minimum porosity) and C_T = 0.692

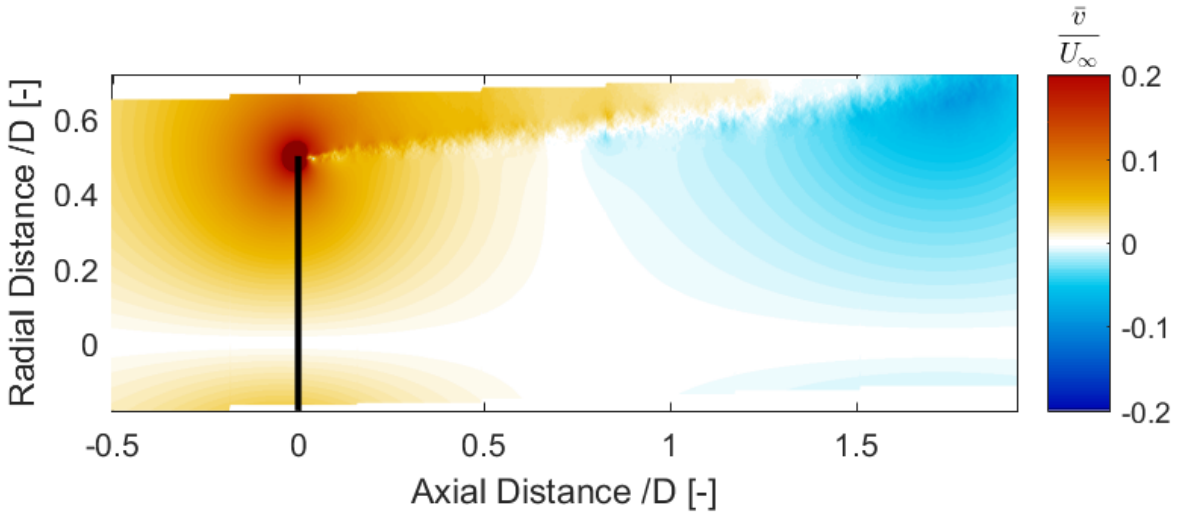

(c) Porosity = 19% (increasing porosity) and C_T = 0.675

Figure 7.73: Normalized Radial Velocity Field for porosity changing with frequency = 1.5Hz and reduced frequency = 0.47 (Vortex Ring model)

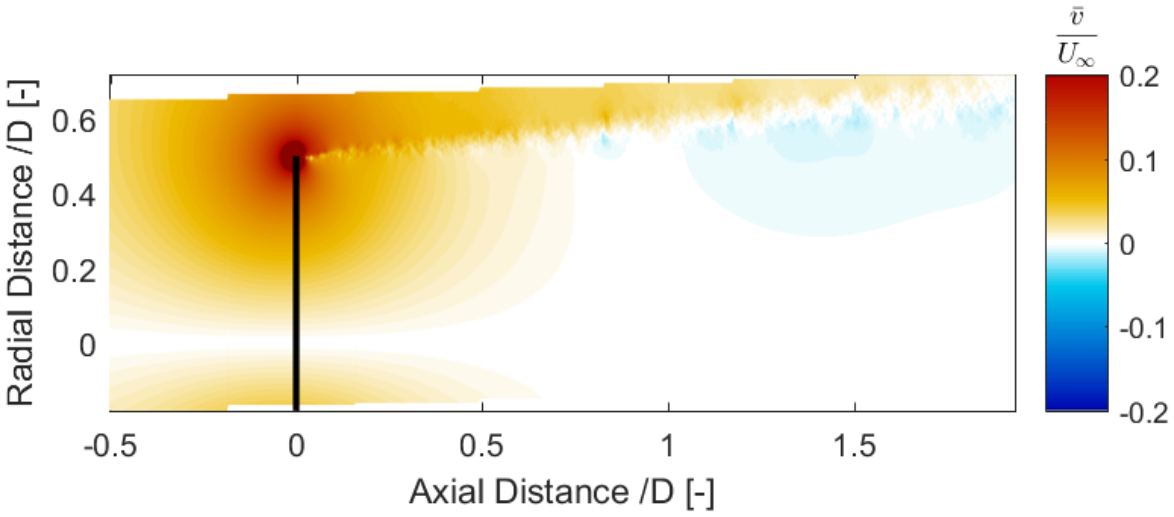

(a) Porosity = 31% (increasing porosity) and C_T = 0.651

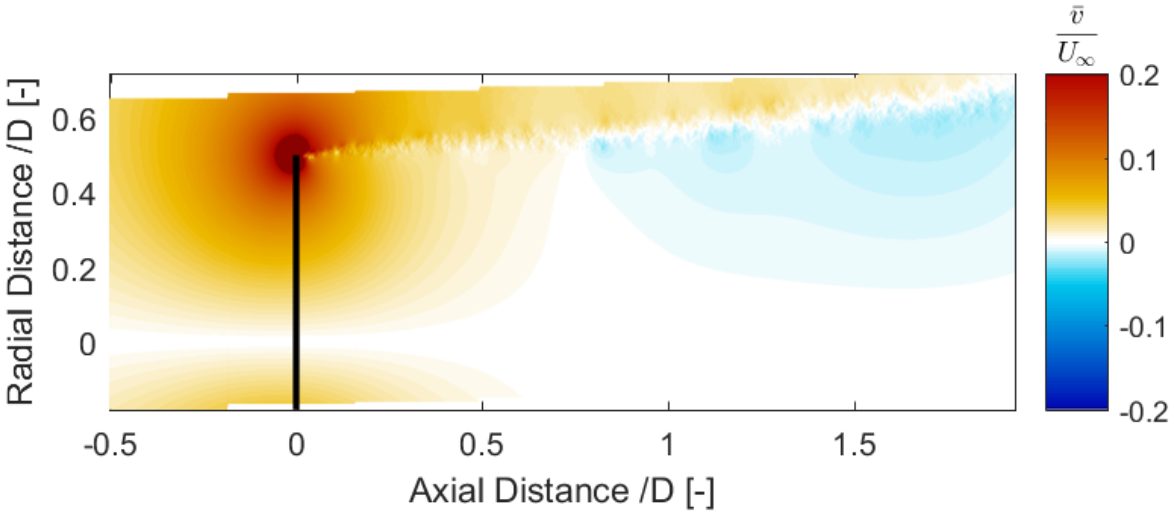

(b) Porosity = 47% (increasing porosity) and C_T = 0.616

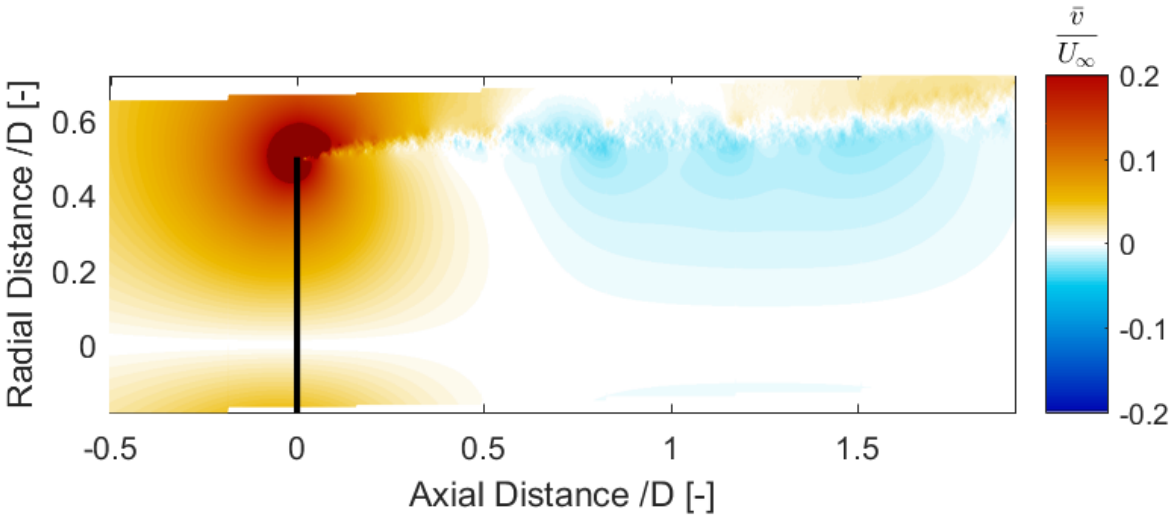

(c) Porosity = 59% (increasing porosity) and C_T = 0.575

Figure 7.74: Normalized Radial Velocity Field for porosity changing with frequency = 1.5Hz and reduced frequency = 0.47 (Vortex Ring model)

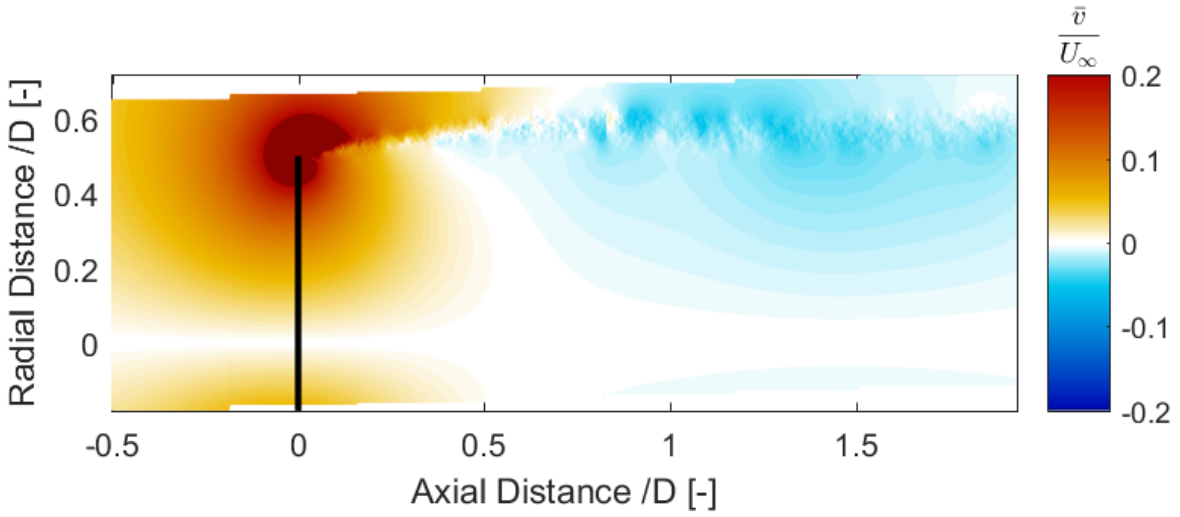

(a) Porosity = 64% (maximum porosity) and C_T = 0.555

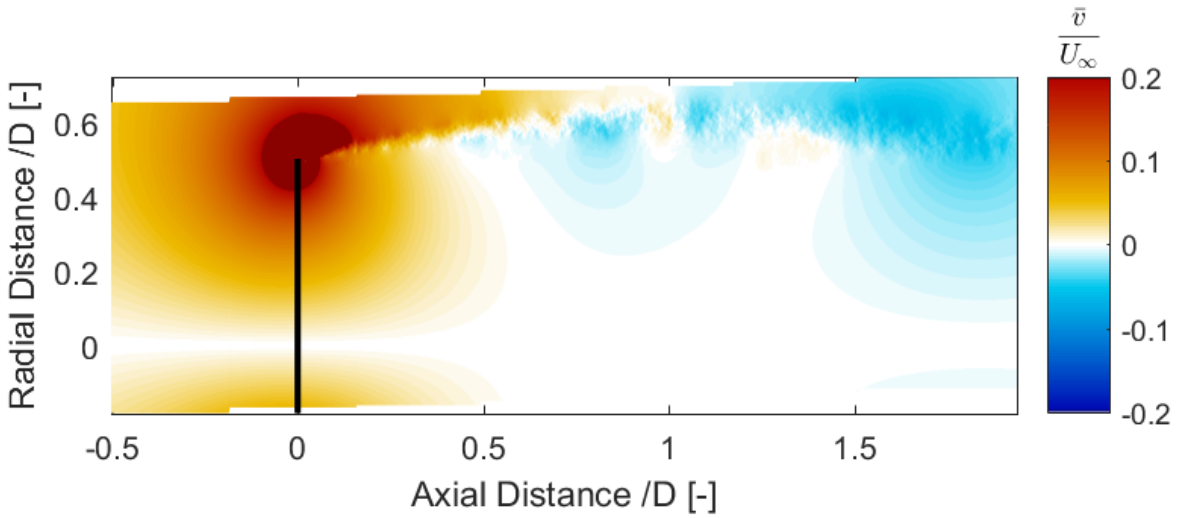

(b) Porosity = 59% (decreasing porosity) and C_T = 0.565

Figure 7.75: Normalized Radial Velocity Field for porosity changing with frequency = 1.5Hz and reduced frequency = 0.47 (Vortex Ring model)

7.3.4. ANALYSIS OF UNSTEADY LOADING ON THE FLOW FIELD

1. **Comparison of Axial Velocity:** By comparing all the unsteady load cases, it is found that as the frequency and reduced frequency of the load cycle decreases, the unsteady effects also decrease. The effect of frequency on the wake expansion is also noticeable for all the cases. As mentioned before, the wake is expanding and contracting. This is because of porosity changing fast in sinusoidal way. However, for the case of 1.5Hz frequency case, this effect decreases. Figure E.12a shows that velocity induction for load cycle with different frequencies is different. The frequency of 5Hz and k = 1.57 has the maximum difference between two velocity induction for same loading but opposite phases of the cycle.

2. **Comparison of Radial Velocity:** For all unsteady cases, main difference is seen in the directions of the flow field. Due to the cyclic loading on the disc, it is seen that the flow moves outwards and inwards with expanding and contracting wake owing to the cyclic loading on

the disc. However, as the wake expansion and contraction is less frequent for the load cycle with lower reduced frequency, regions of positive and negative radial velocity are larger in size for that case.

7.3.5. VALIDATION OF THE MODEL

In this section, the results from the VR model are validated using the experimental results.

FREQUENCY = 5HZ AND REDUCED FREQUENCY = 1.57

Figure 7.76-Figure 7.79 show the difference between results from the experiment and the VR model for the normalized axial velocity. Figure 7.80-Figure 7.83 show the difference between the two method for the normalized radial velocity. For the velocity fields, following remarks can be made:

1. **Tower-shadow effect:** This is one of the main differences between the two methods. In the VR model, it is assumed that the wake strength can be solely determined by vorticity near the wake edge, ignoring any other vorticity. However, as seen in the experimental results, flow field behind the hub of the disc has a major effect till a certain distance behind the disc. Due to this reason, the error is high behind the disc.
   It can also be seen from the normalized radial velocity fields from the experiment and the VR model that there is difference in the radial velocity behind the hub. In VR model, this region has mainly Vr = 0. However, in the experimental results, region of negative radial velocity due to the nacelle is seen around the disc centre line.

2. **Disc mesh effect:** Other region where error is high is just behind the disc. It was noticed earlier that due to porosity of the disc, the wake just behind the disc is characterized by discontinuity in vorticity. Similar to the tower-shadow effect, this effect was also ignored in the VR model. Hence, there is a high error just behind the disc both for the axial and the radial velocity fields.

3. **Other Regions:** In the other regions where vorticity is not strong, the error for the axial velocity field is less that 10% of the free-stream value. For the radial velocity, it is less than 2% of the free-stream velocity.

Axial Velocity Fields

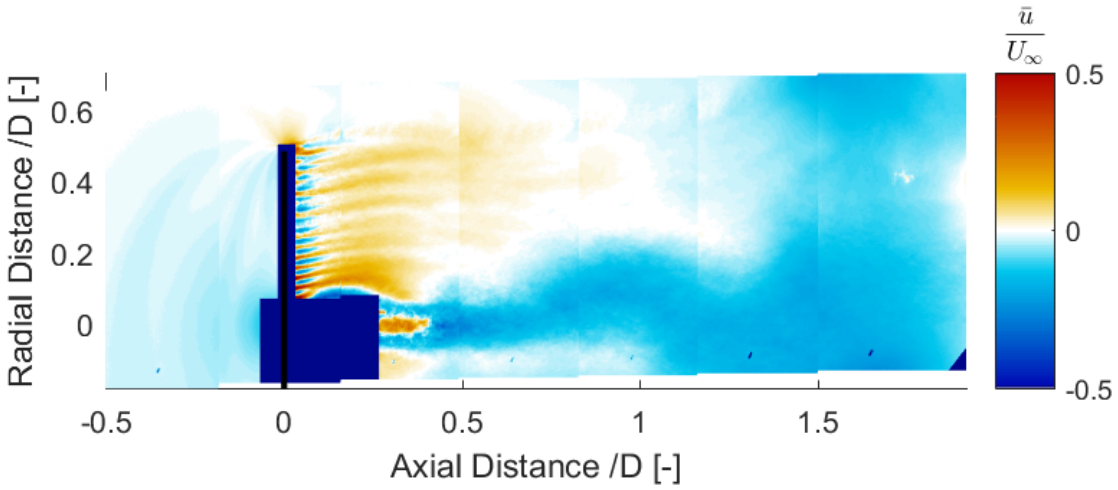

(a) Porosity = 59% (decreasing porosity) and C_T = 0.555

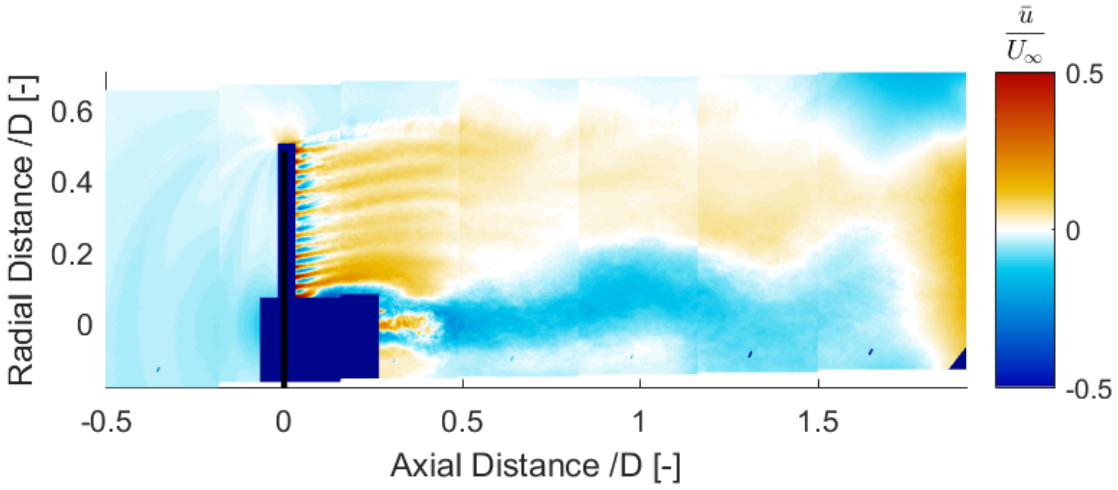

(b) Porosity = 47% (decreasing porosity) and C_T = 0.557

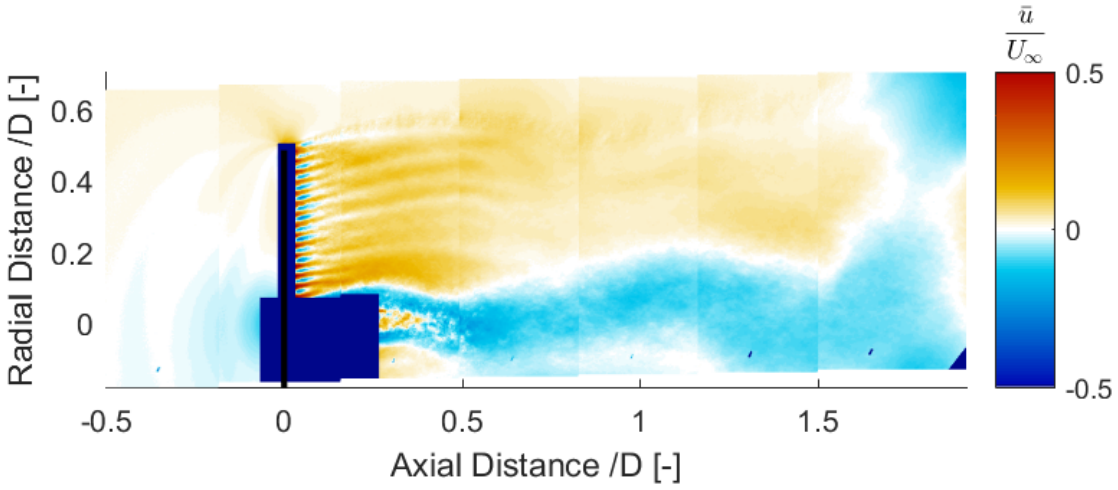

(c) Porosity = 31% (decreasing porosity) and C_T = 0.579

Figure 7.76: Error in axial velocity field for porosity changing with Frequency = 5Hz and reduced frequency = 1.57

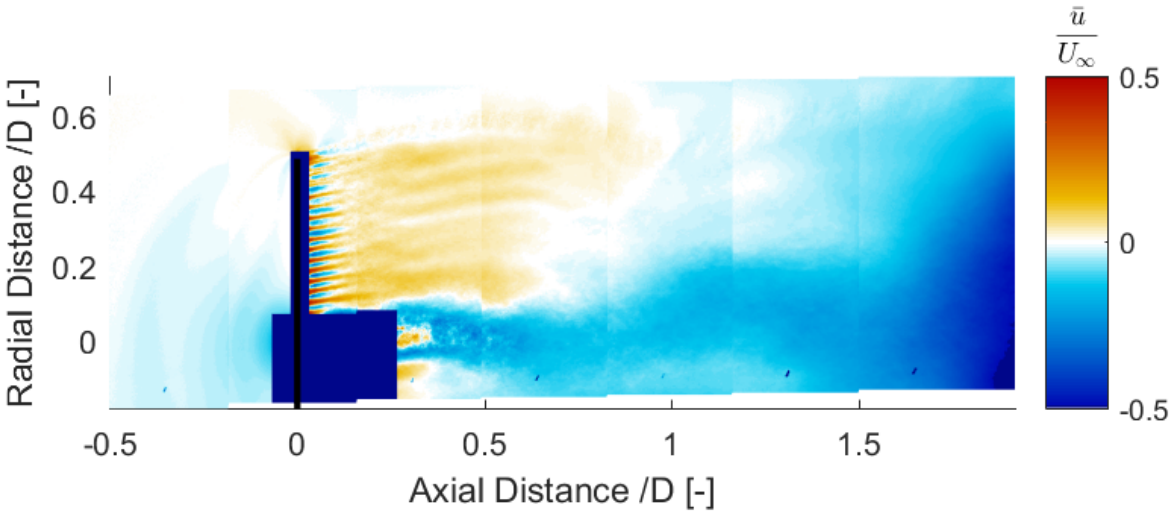

(a) Porosity = 19% (decreasing porosity) and C_T = 0.620

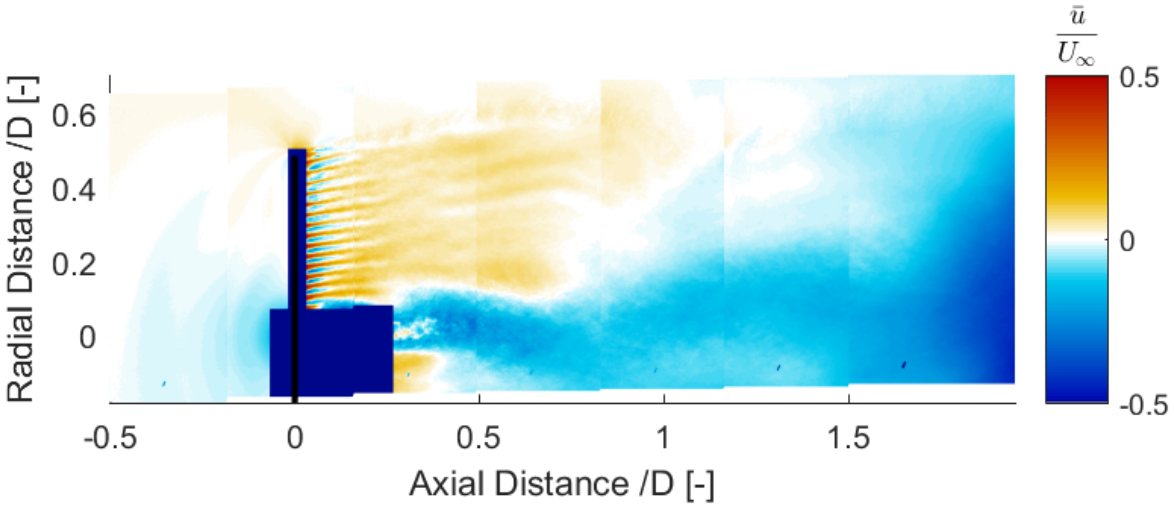

(b) Porosity = 14% (minimum porosity) and C_T = 0.705

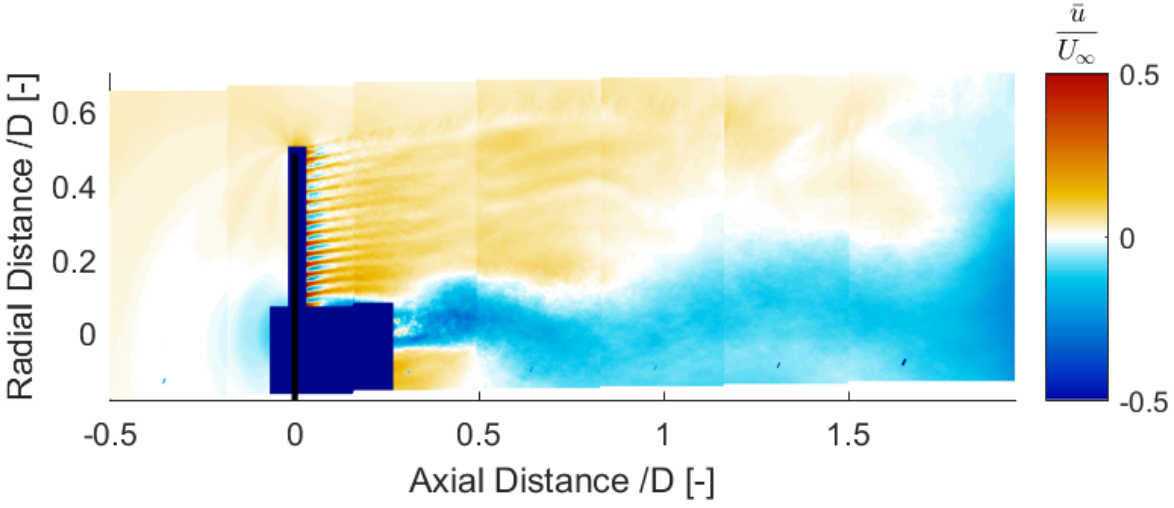

(c) Porosity = 19% (increasing porosity) and C_T = 0.697

Figure 7.77: Error in axial velocity field for porosity changing with Frequency = 5Hz and reduced frequency = 1.57

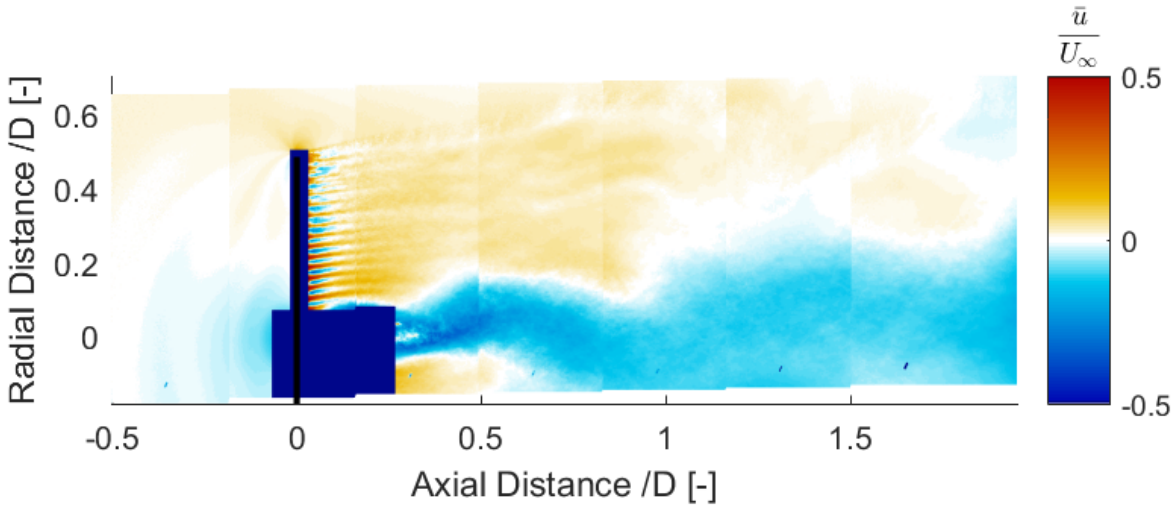

(a) Porosity = 31% (increasing porosity) C_T = 0.678

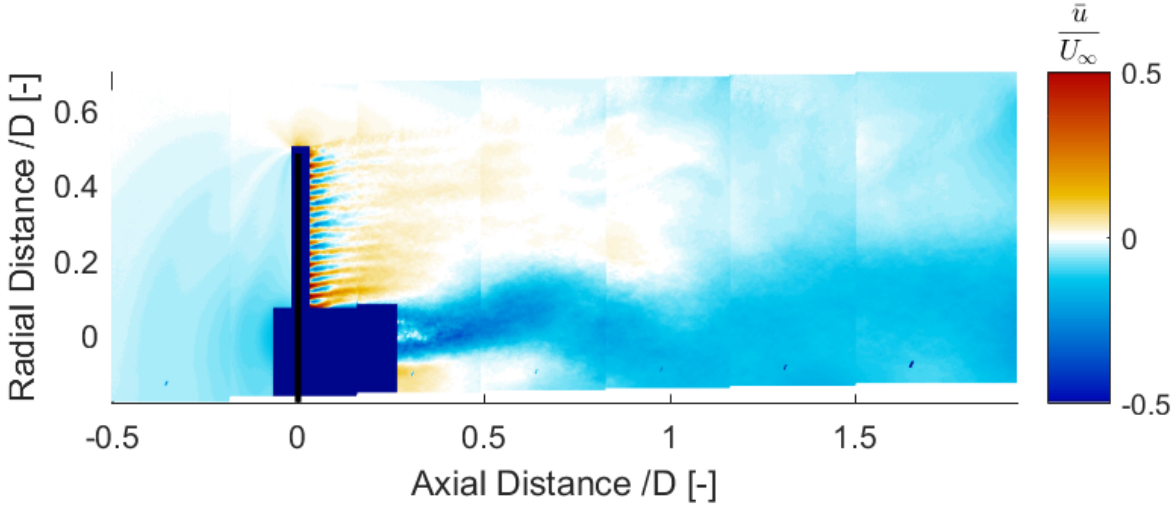

(b) Porosity = 47% (increasing porosity) and C_T = 0.657

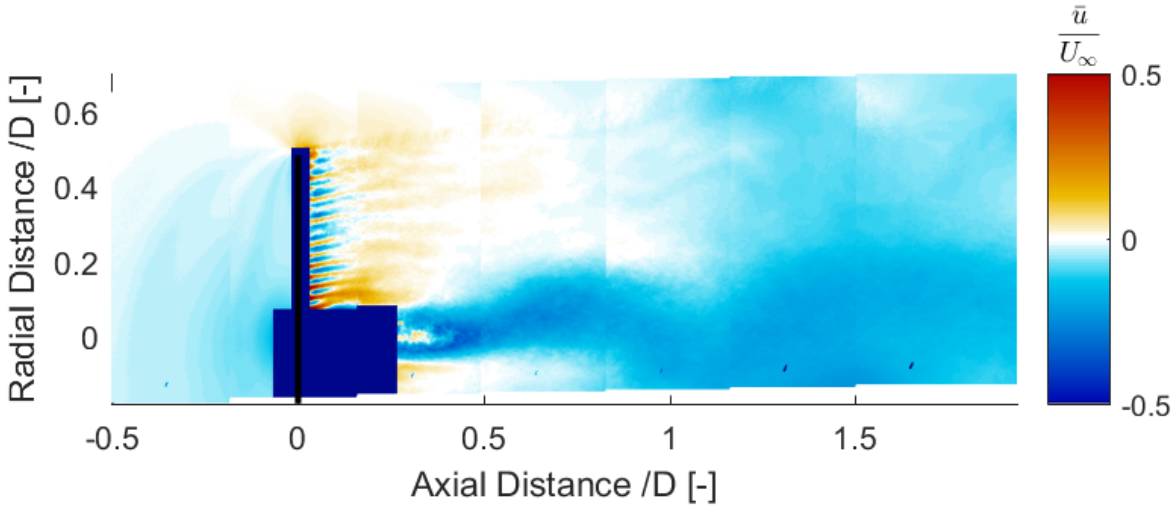

(c) Porosity = 59% (increasing porosity) and C_T = 0.596

Figure 7.78: Error in axial velocity field for porosity changing with Frequency = 5Hz and reduced frequency = 1.57

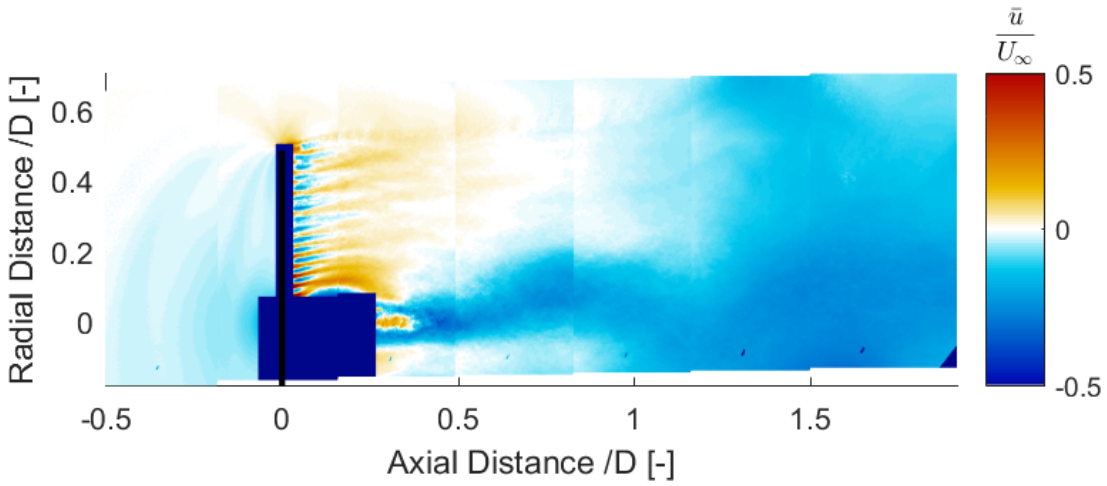

(a) Porosity = 64% (maximum porosity) and C_T = 0.550

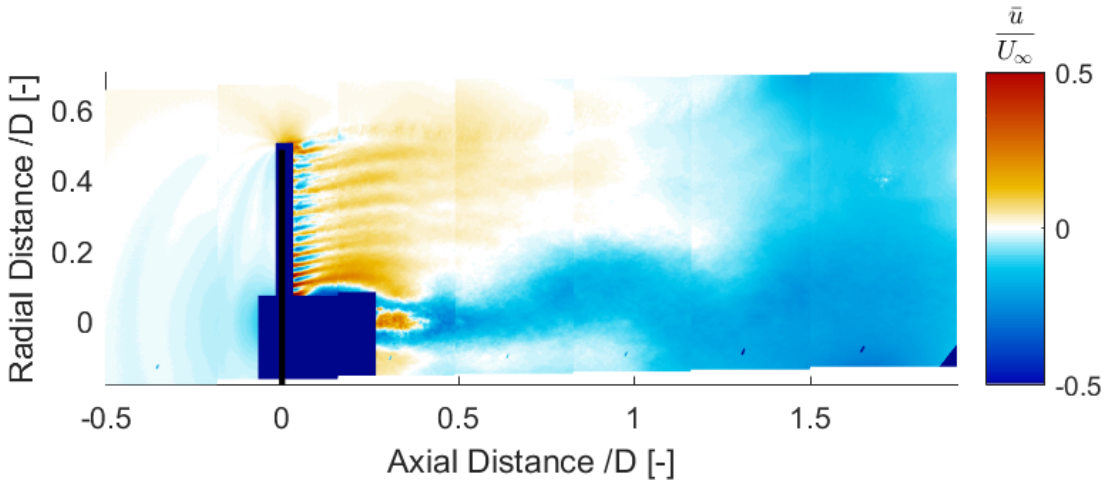

(b) Porosity = 59% (decreasing porosity) and C_T = 0.554

Figure 7.79: Error in axial velocity field for porosity changing with Frequency = 5Hz and reduced frequency = 1.57

Radial Velocity Fields

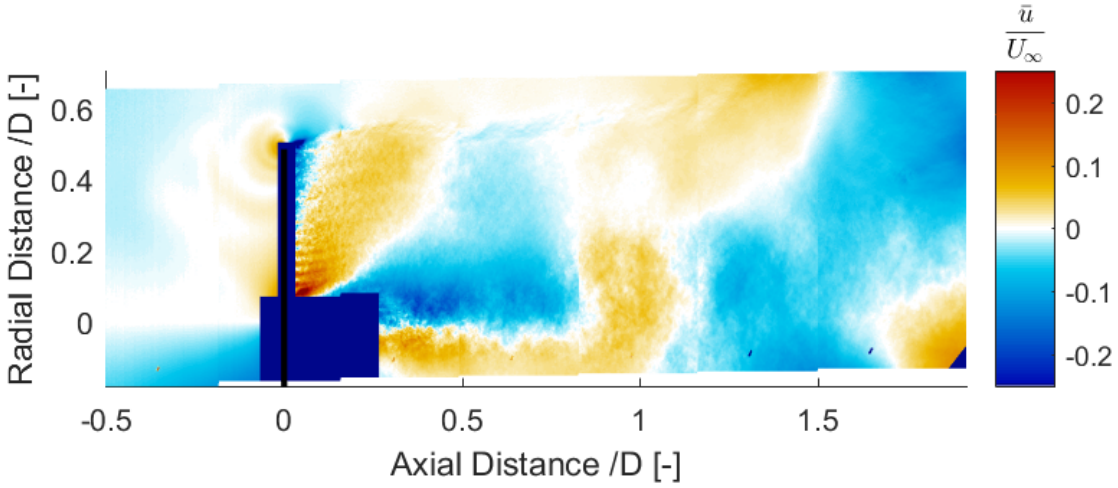

(a) Porosity = 59% (decreasing porosity) and C_T = 0.555

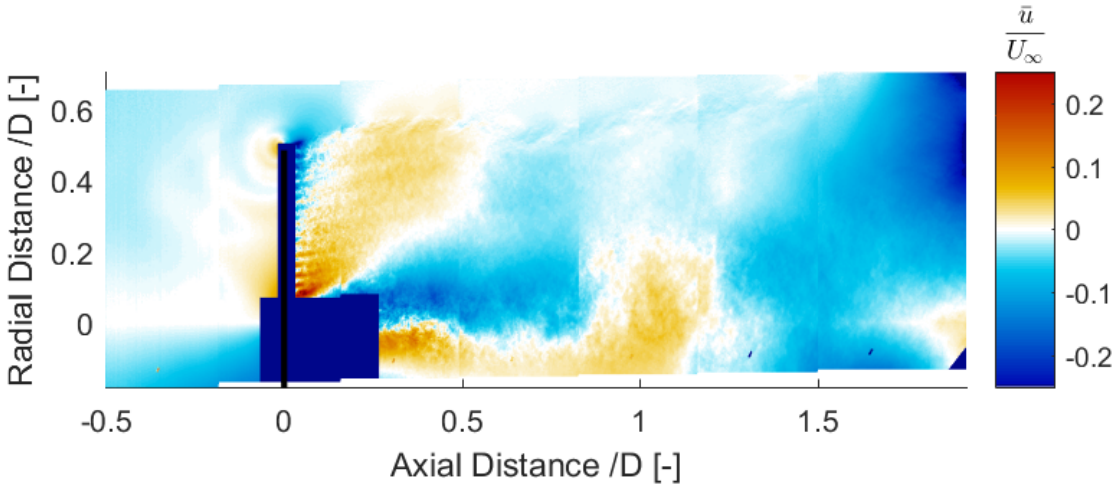

(b) Porosity = 47% (decreasing porosity) and C_T = 0.557

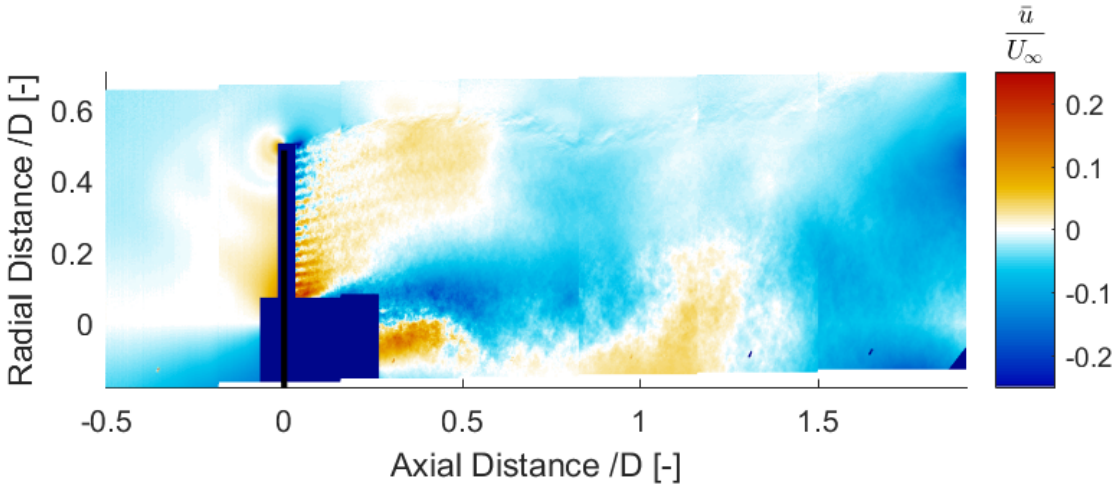

(c) Porosity = 31% (decreasing porosity) and C_T = 0.579

Figure 7.80: Error in radial velocity field for porosity changing with Frequency = 5Hz and reduced frequency = 1.57

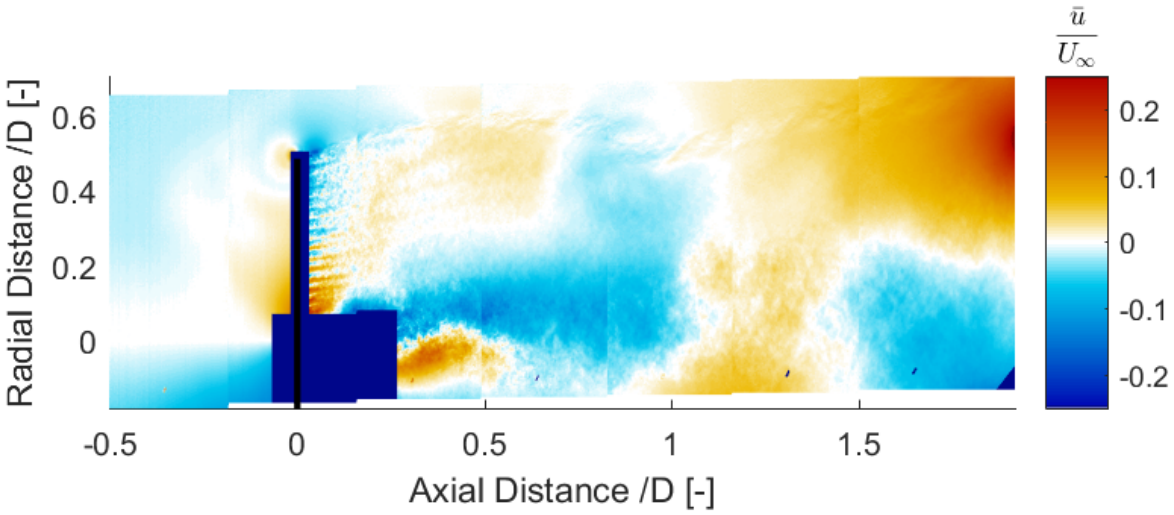

(a) Porosity = 19% (decreasing porosity) and C_T = 0.620

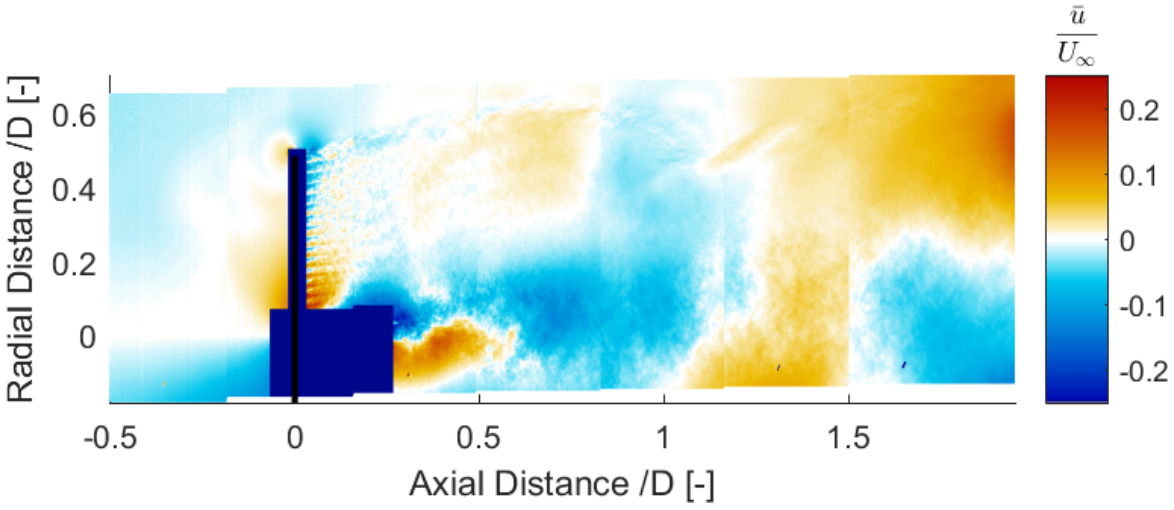

(b) Porosity = 14% (minimum porosity) and C_T = 0.705

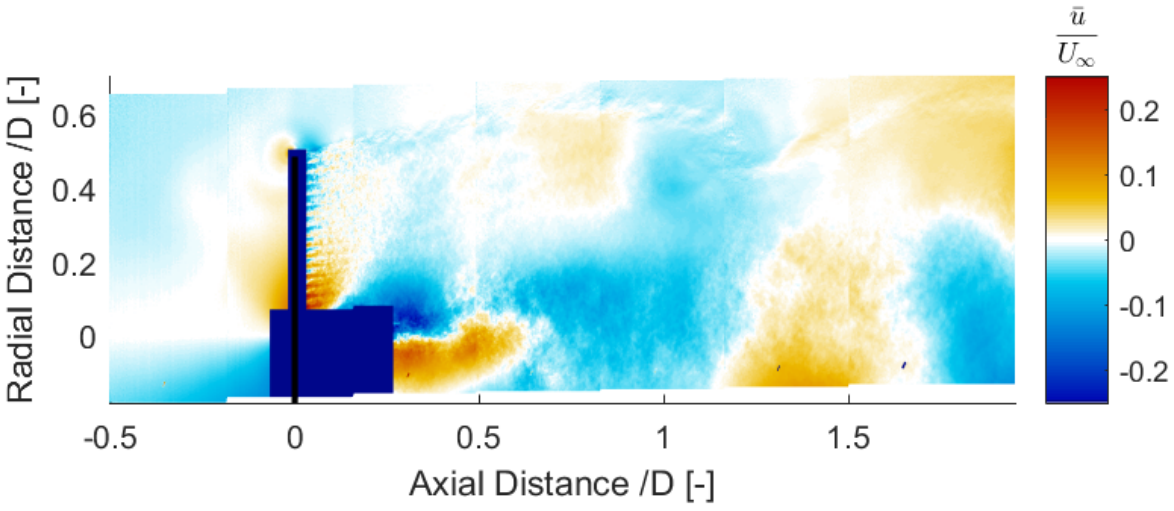

(c) Porosity = 19% (increasing porosity) and C_T = 0.697

Figure 7.81: Error in radial velocity field for porosity changing with Frequency = 5Hz and reduced frequency = 1.57

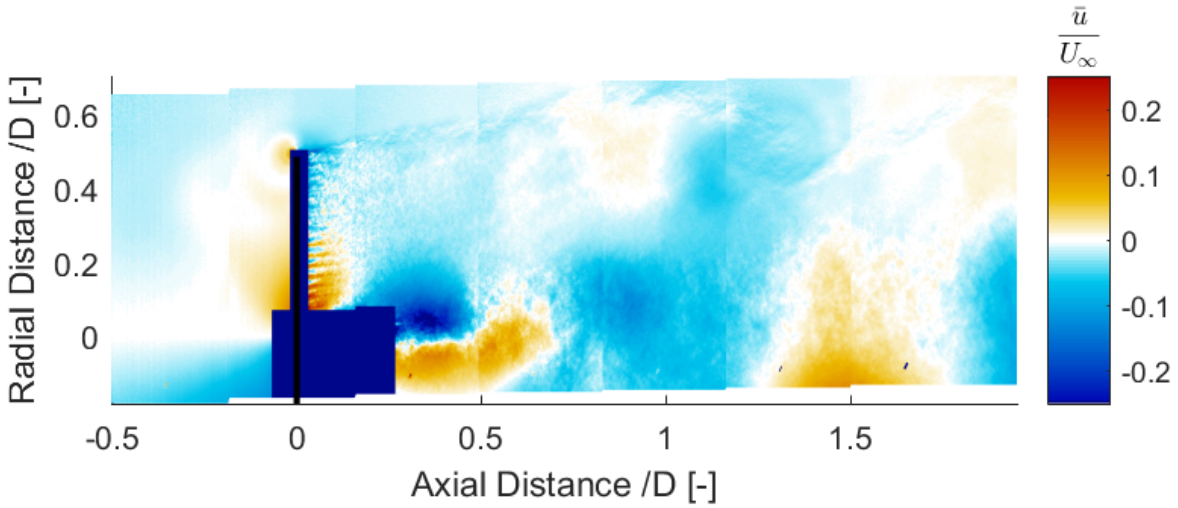

(a) Porosity = 31% (increasing porosity) C_T = 0.678

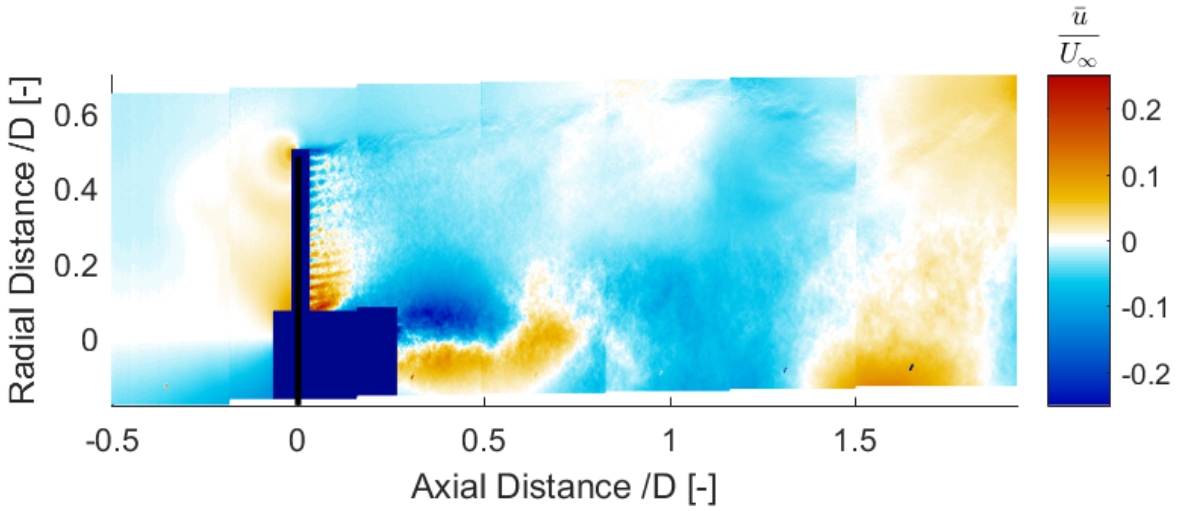

(b) Porosity = 47% (increasing porosity) and C_T = 0.657

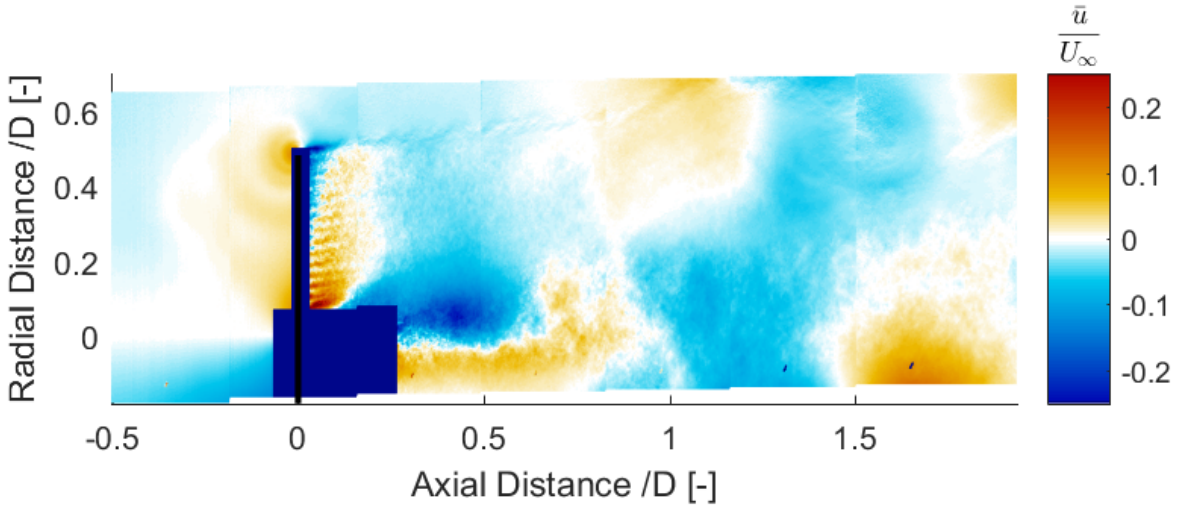

(c) Porosity = 59% (increasing porosity) and C_T = 0.596

Figure 7.82: Error in radial velocity field for porosity changing with Frequency = 5Hz and reduced frequency = 1.57

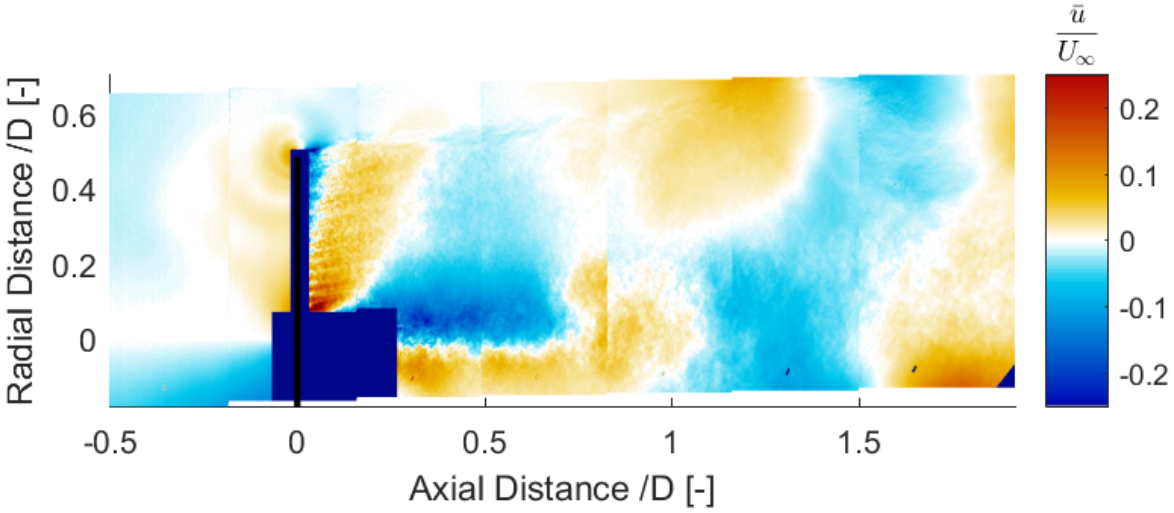

(a) Porosity = 64% (maximum porosity) and C_T = 0.550

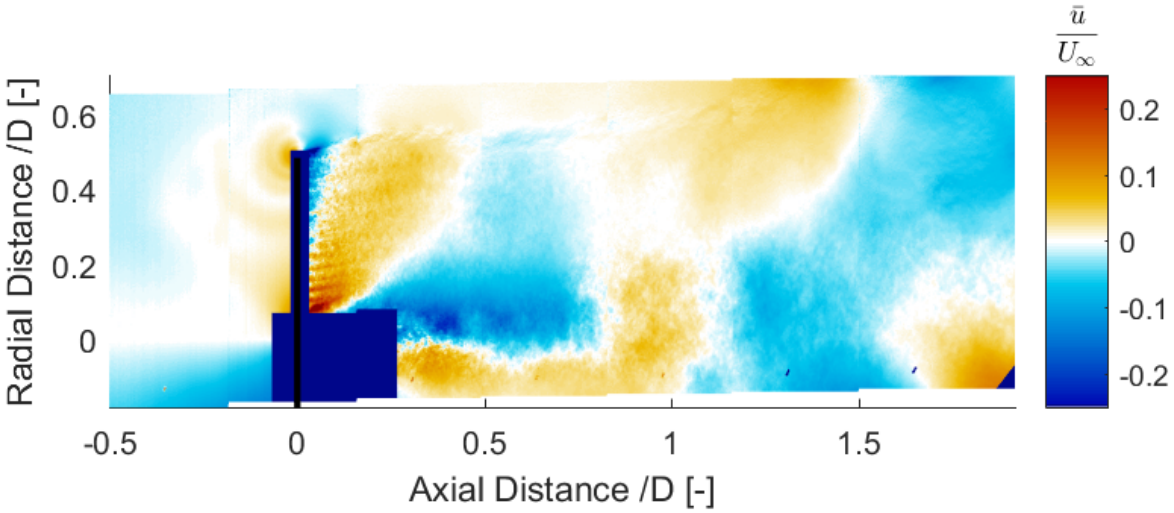

(b) Porosity = 59% (decreasing porosity) and C_T = 0.554

Figure 7.83: Error in radial velocity field for porosity changing with Frequency = 5Hz and reduced frequency = 1.57

FREQUENCY = 3HZ AND REDUCED FREQUENCY = 0.94

Figure 7.84-Figure 7.88 show error in the axial velocity for the unsteady load case of 3Hz frequency. Figure 7.89-Figure 7.93 show error in the radial velocity for the unsteady load case of 3Hz frequency. Following analysis can be made from the figures:

1. **Axial Velocity**

   (a) Similar to the steady load cases, the VR model does not take vorticity due to the mesh of the disc and tower-shadow effect into account. Due to this, the negative axial velocity behind the disc is not observed in velocity fields generated by VR model.

   (b) For all cases, the error (ε_x) is less than 10% of U_∞ in other regions. Near the wake boundary, it is smallest, as the wake strength used for VR model is estimated from vorticity in

that region only.

2. **Radial Velocity**

   (a) Compared to the axial velocity, error in the radial velocity is smaller for all unsteady load cases. ($-0.2 \leq \varepsilon_r \leq 0.2$)

   (b) Similar to the axial velocity fields, error (ε_r) is maximum behind the disc and the hub.

Axial Velocity fields

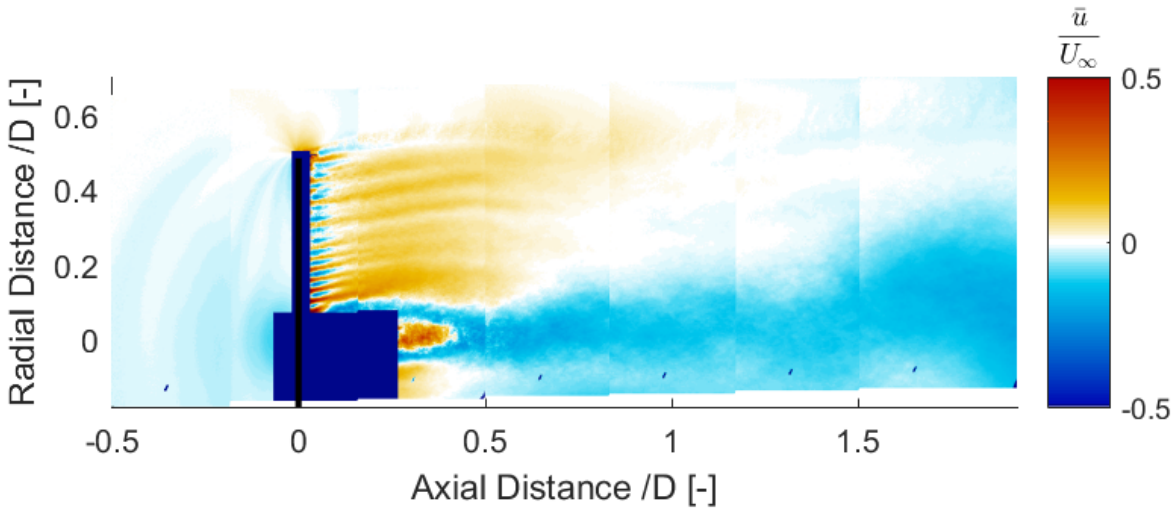

(a) Porosity = 59% (decreasing porosity) and C_T = 0.572

Figure 7.84: Error in axial velocity field for porosity changing with frequency = 3Hz and reduced frequency = 0.94

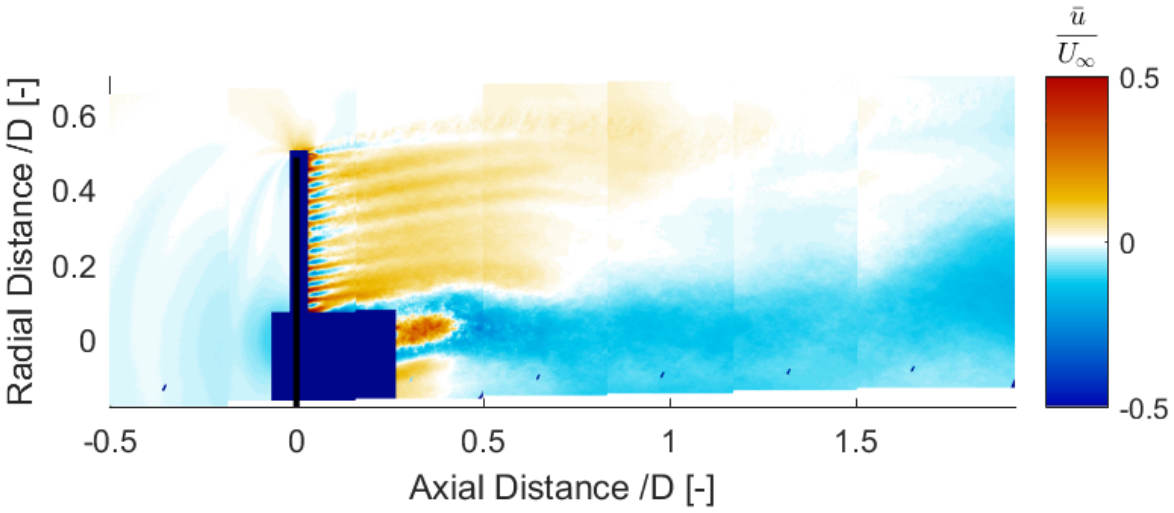

(a) Porosity = 47% (decreasing porosity) and C_T = 0.593

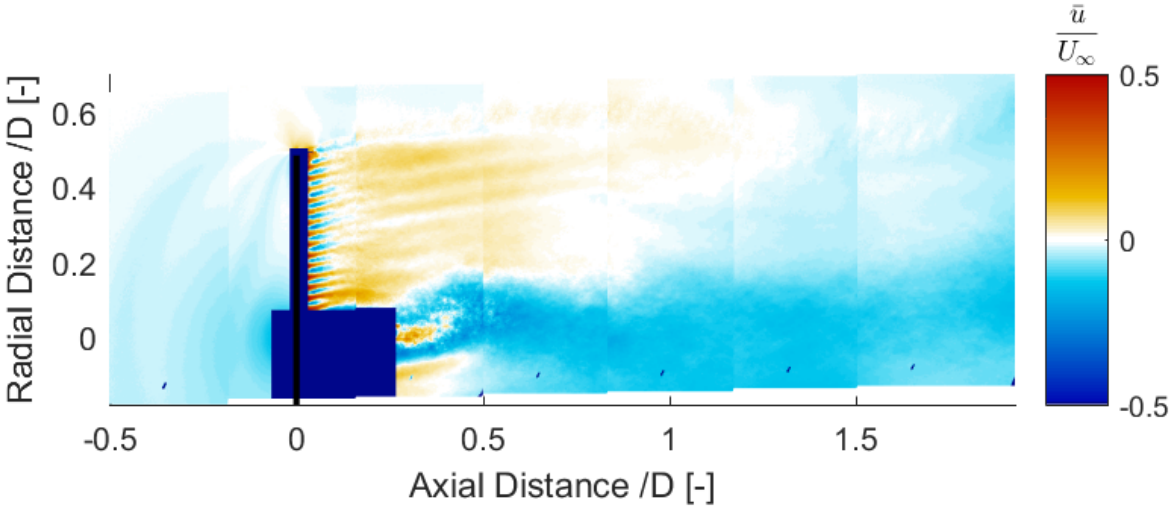

(b) Porosity = 31% (decreasing porosity) and C_T = 0.622

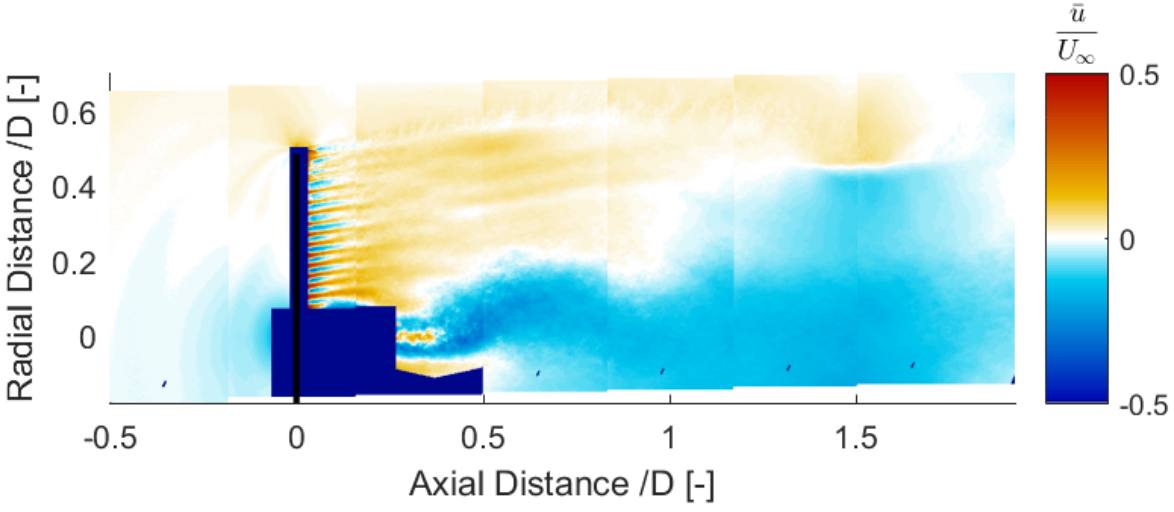

(c) Porosity = 19% (decreasing porosity) and C_T = 0.649

Figure 7.85: Error in axial velocity field for porosity changing with frequency = 3Hz and reduced frequency = 0.94

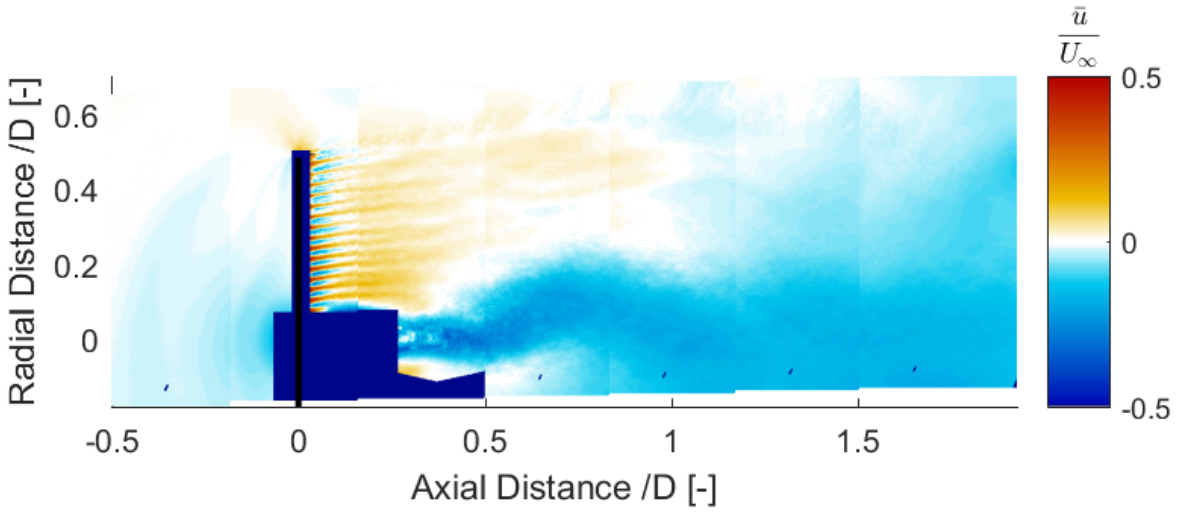

(a) Wake strength in the shear layer for porosity 43.4%

(b) Porosity = 14% (minimum porosity) and C_T = 0.684

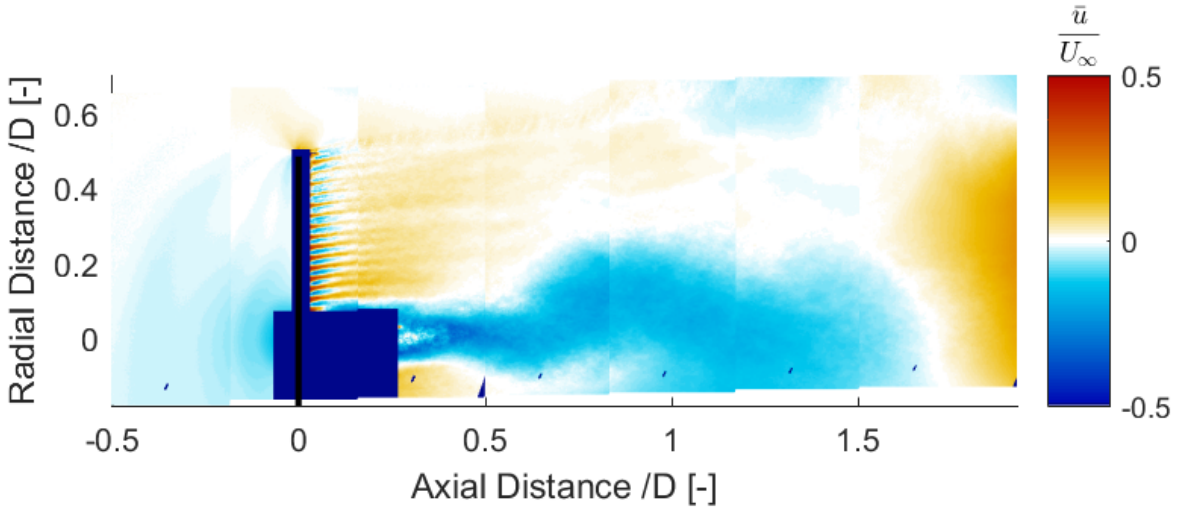

(c) Porosity = 19% (increasing porosity) and C_T = 0.671

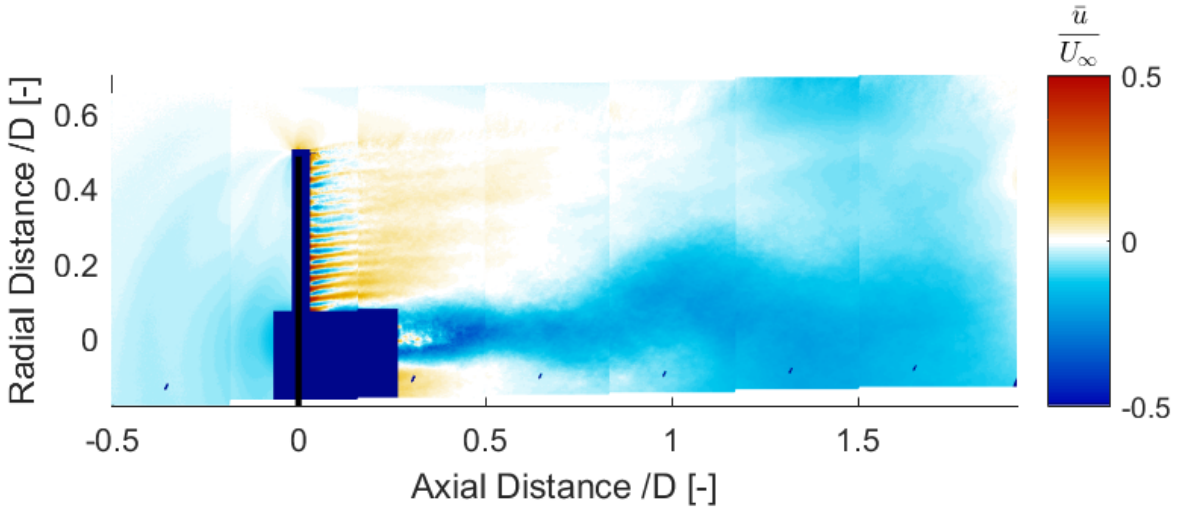

(d) Porosity = 31% (increasing porosity) and C_T = 0.651

Figure 7.86: Error in axial velocity field for porosity changing with frequency = 3Hz and reduced frequency = 0.94

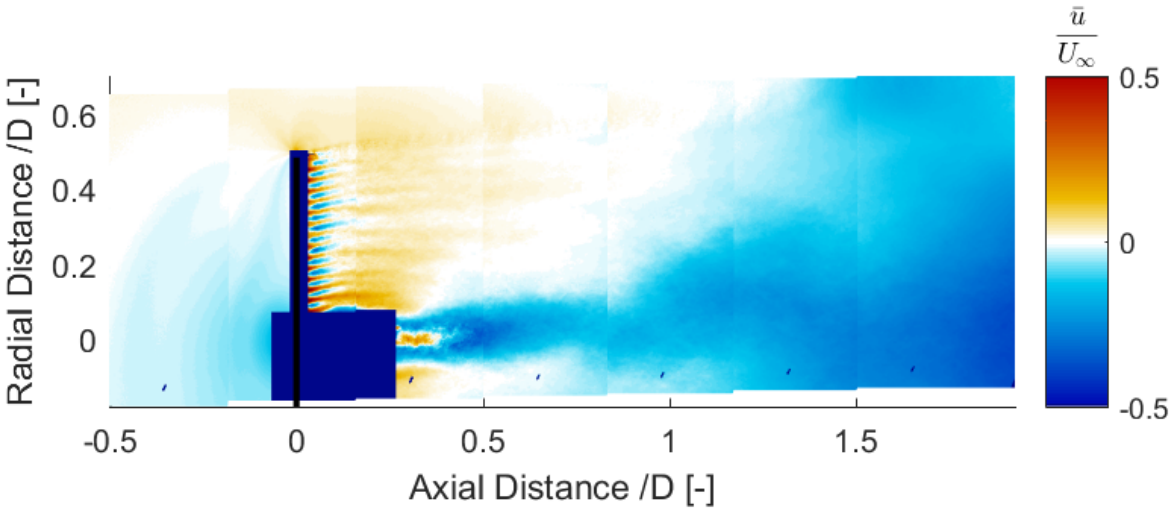

(a) Porosity = 47% (increasing porosity) and C_T = 0.612

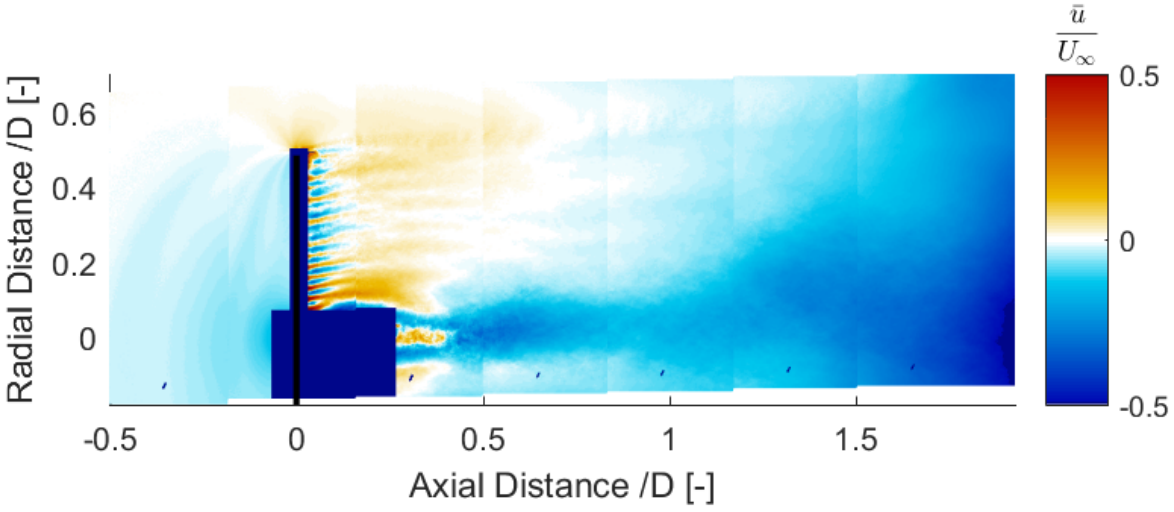

(b) Porosity = 59% (increasing porosity) and C_T = 0.584

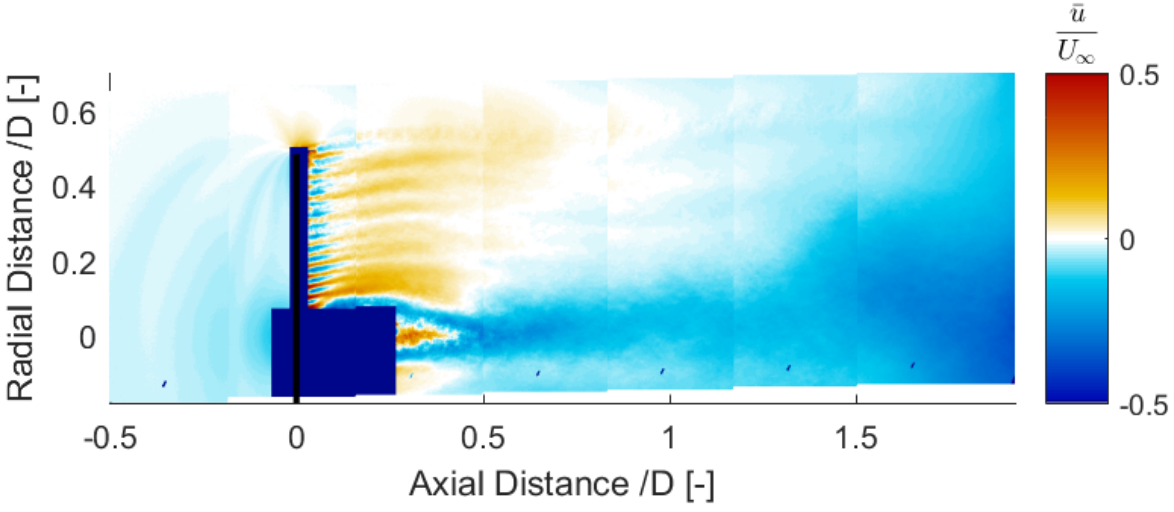

(c) Porosity = 64% (maximum porosity) and C_T = 0.569

Figure 7.87: Error in axial velocity field for porosity changing with frequency = 3Hz and reduced frequency = 0.94

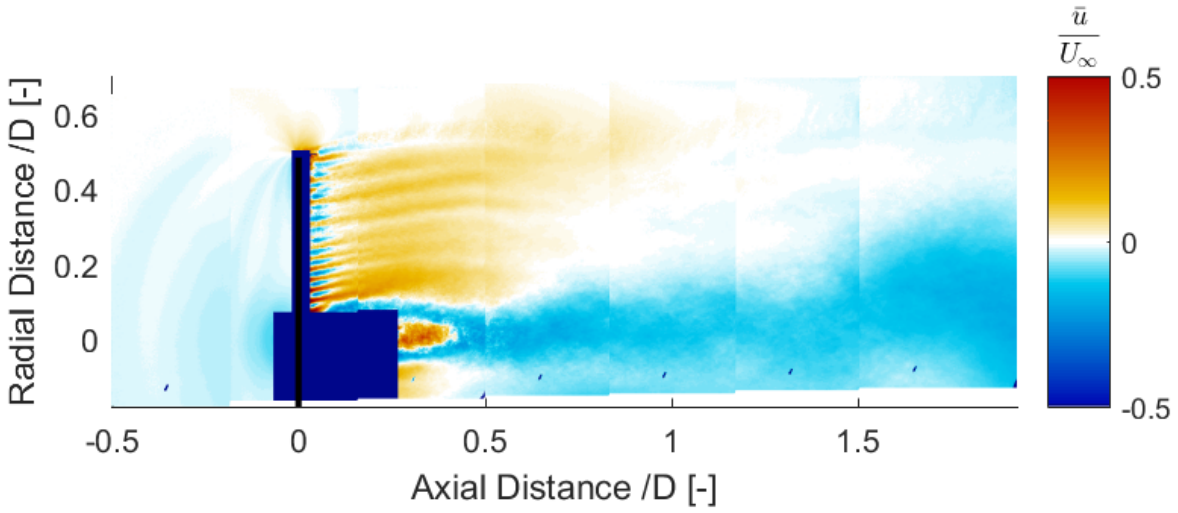

(a) Porosity = 59% (decreasing porosity) and C_T = 0.572

Figure 7.88: Error in axial velocity field for porosity changing with frequency = 3Hz and reduced frequency = 0.94

Radial Velocity fields

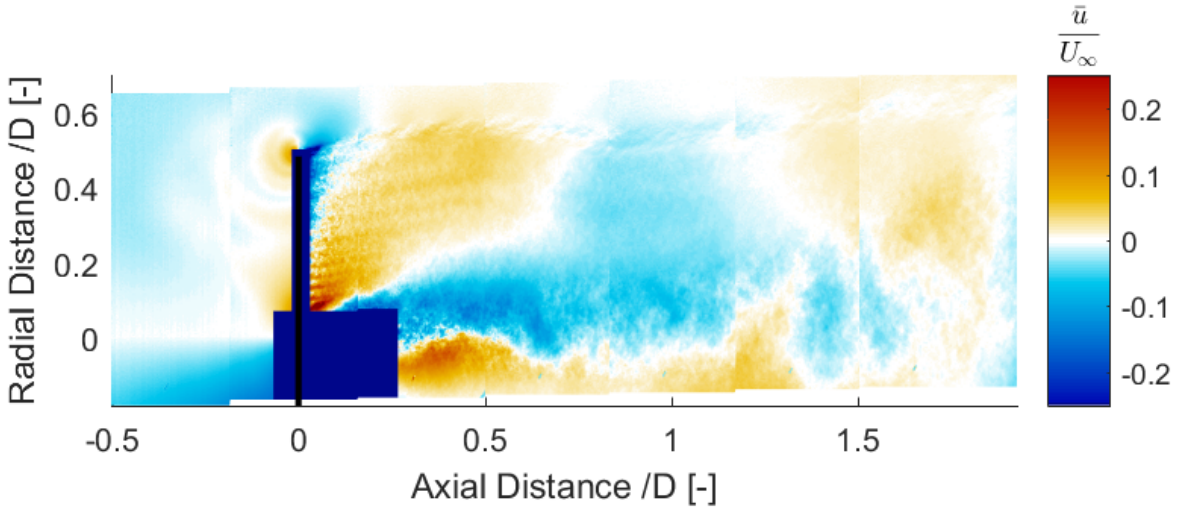

(a) Porosity = 59% (decreasing porosity) and C_T = 0.572

Figure 7.89: Error in radial velocity field for porosity changing with frequency = 3Hz and reduced frequency = 0.94

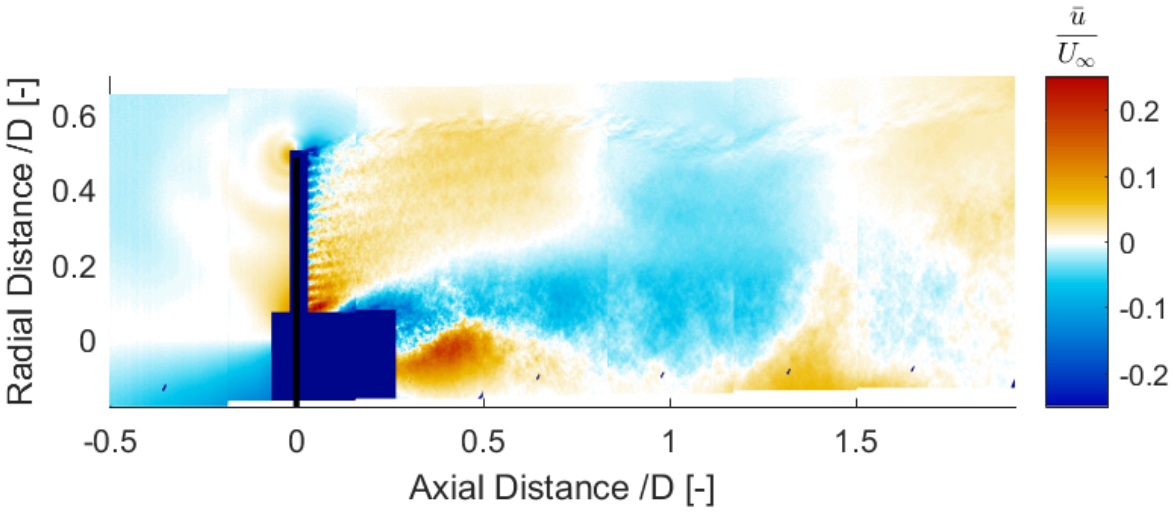

(a) Porosity = 47% (decreasing porosity) and C_T = 0.593

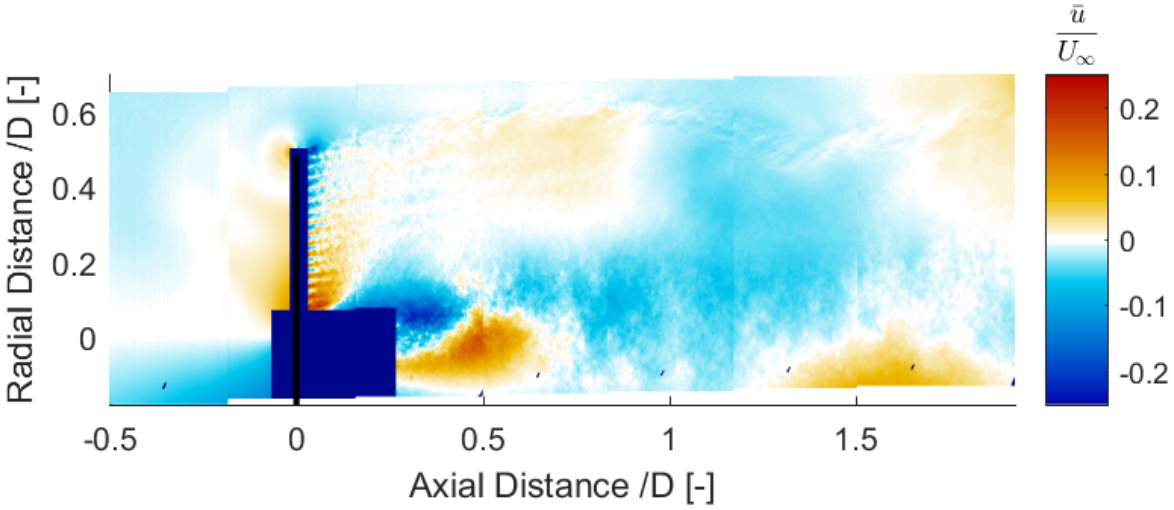

(b) Porosity = 31% (decreasing porosity) and C_T = 0.622

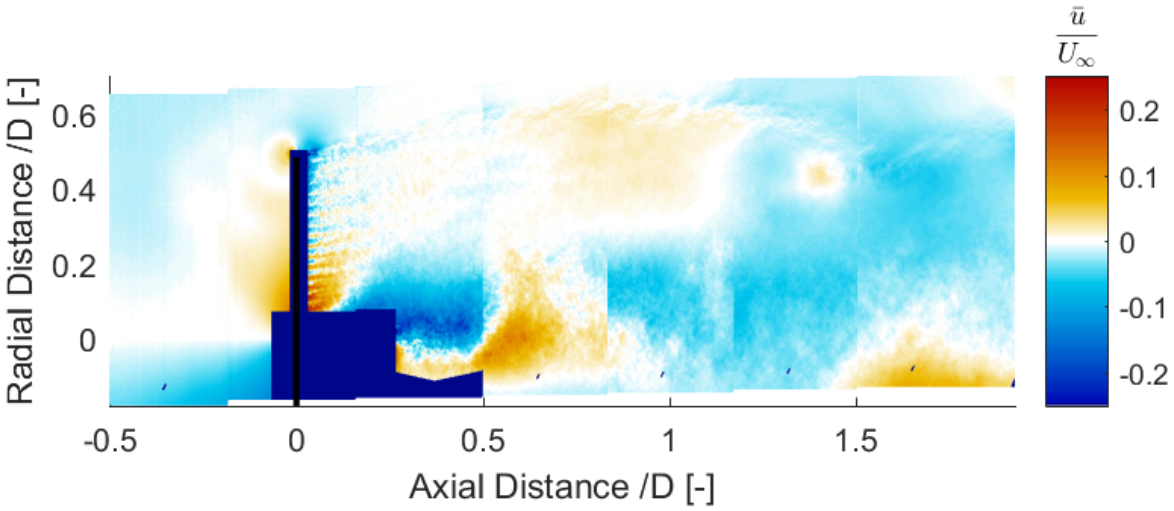

(c) Porosity = 19% (decreasing porosity) and C_T = 0.649

Figure 7.90: Error in radial velocity field for porosity changing with frequency = 3Hz and reduced frequency = 0.94

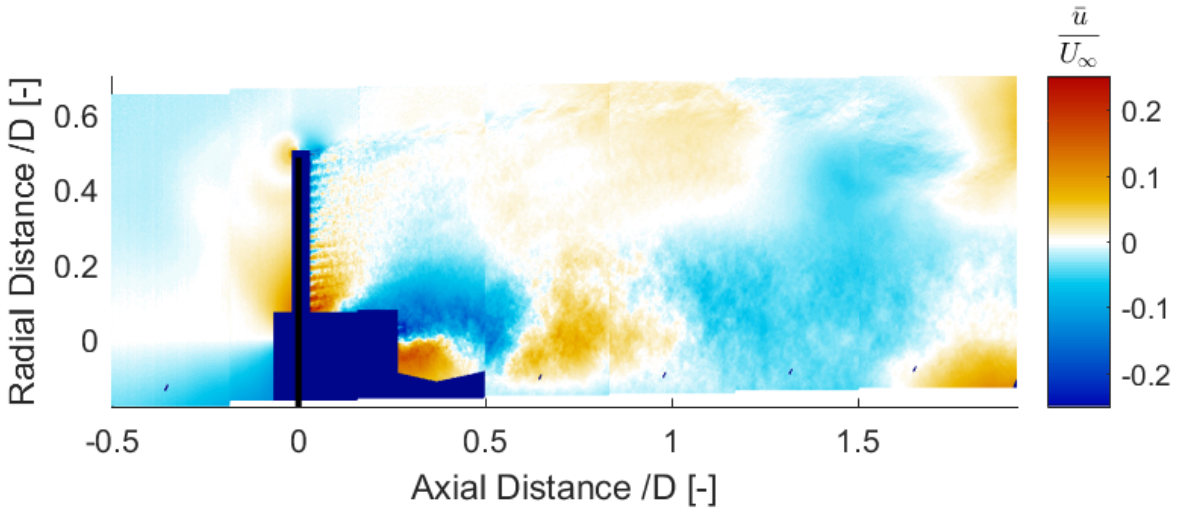

(a) Porosity = 14% (minimum porosity) and C_T = 0.684

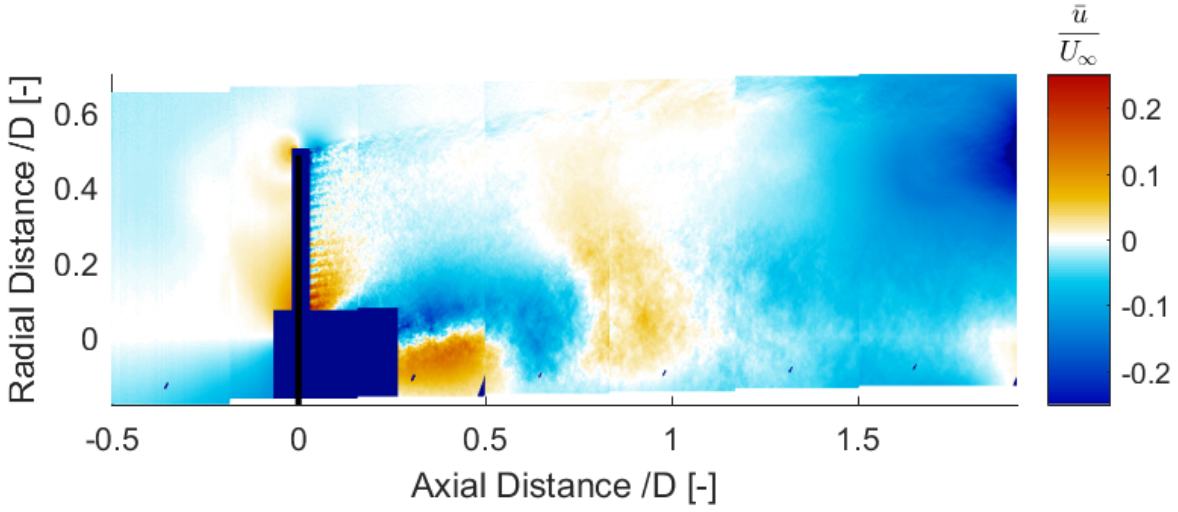

(b) Porosity = 19% (increasing porosity) and C_T = 0.671

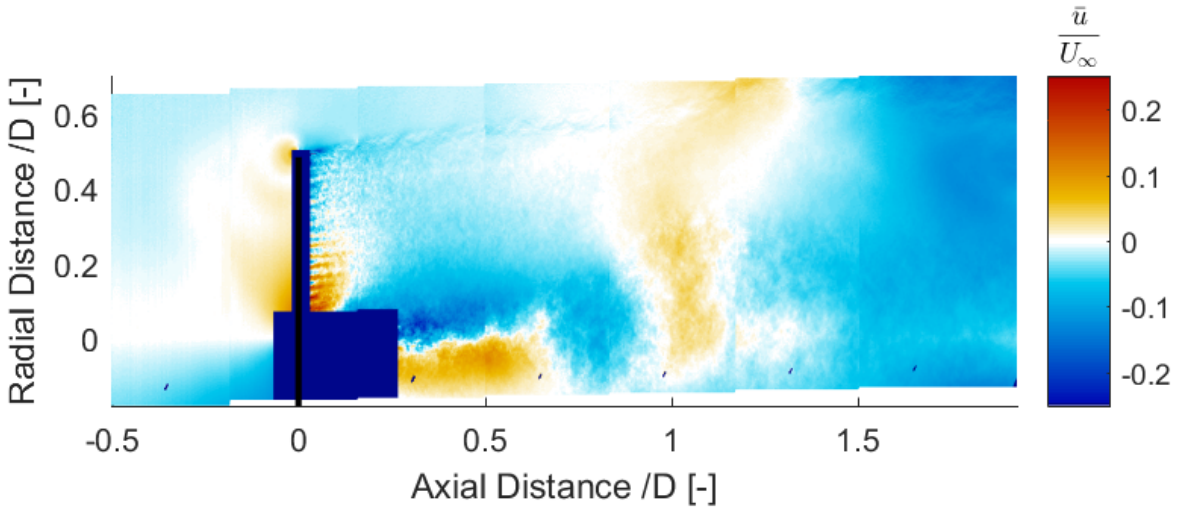

(c) Porosity = 31% (increasing porosity) and C_T = 0.651

Figure 7.91: Error in radial velocity field for porosity changing with frequency = 3Hz and reduced frequency = 0.94

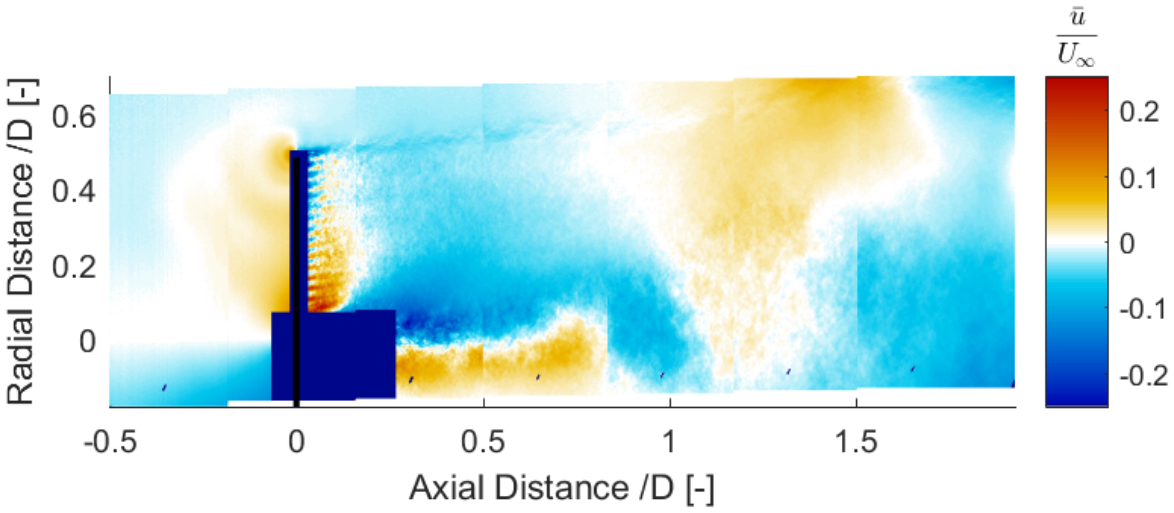

(a) Porosity = 47% (increasing porosity) and C_T = 0.612

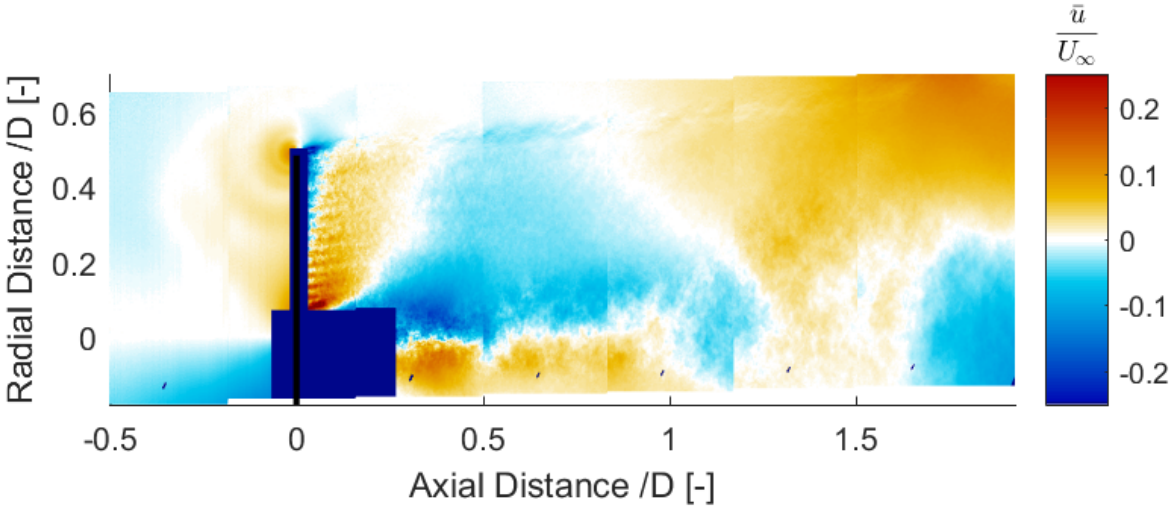

(b) Porosity = 59% (increasing porosity) and C_T = 0.584

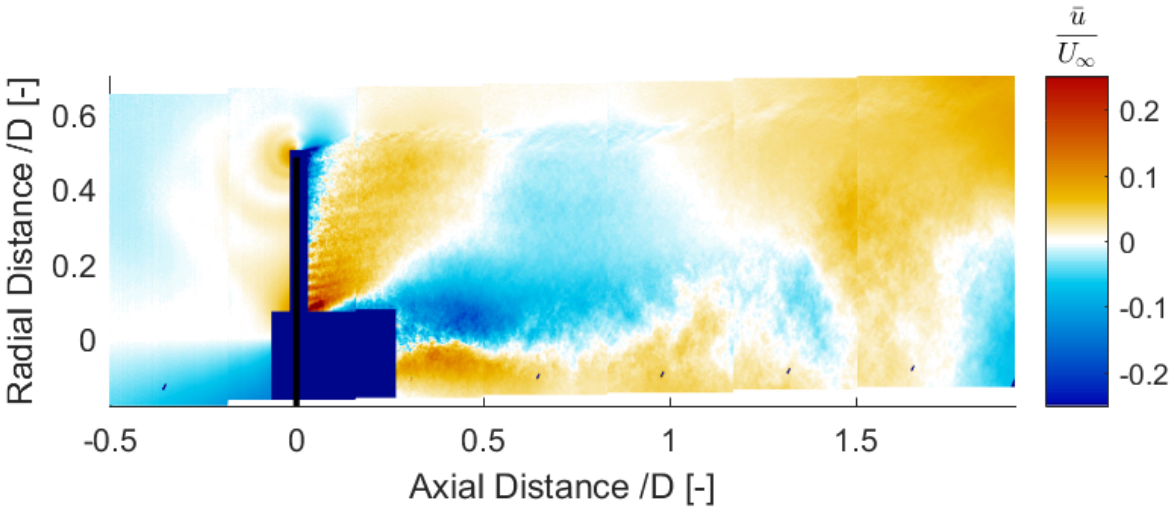

(c) Porosity = 64% (maximum porosity) and C_T = 0.569

Figure 7.92: Error in radial velocity field for porosity changing with frequency = 3Hz and reduced frequency = 0.94

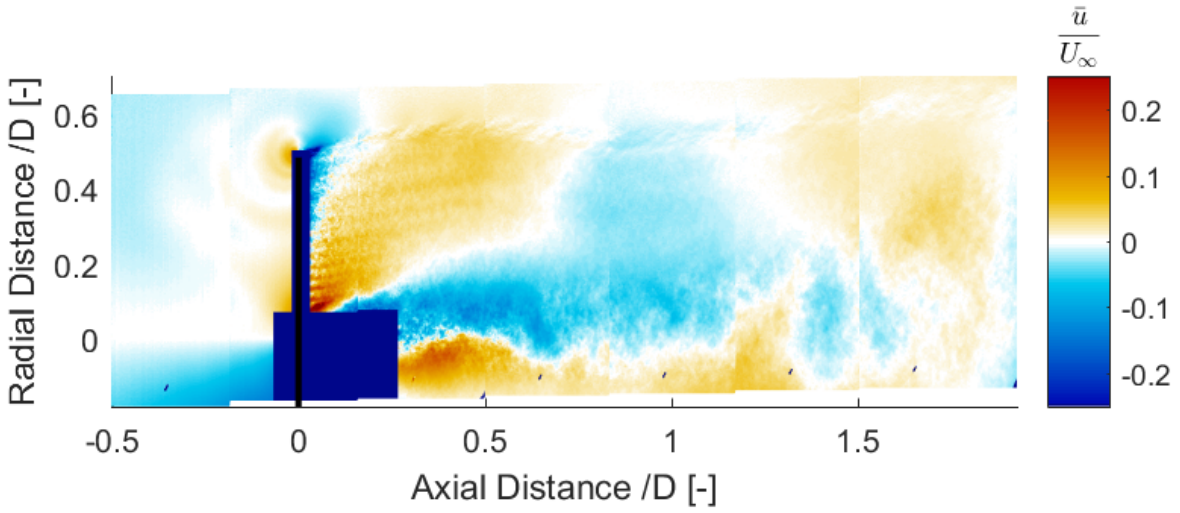

(a) Porosity = 59% (decreasing porosity) and C_T = 0.572

Figure 7.93: Error in radial velocity field for porosity changing with frequency = 3Hz and reduced frequency = 0.94

FREQUENCY = 1.5HZ AND REDUCED FREQUENCY = 0.47

Figure 7.94-Figure 7.98 show the difference in average axial velocity fields for changing load with frequency of 1.5Hz. Figure 7.99-Figure 7.103 show the difference in average radial velocity fields for changing load with frequency of 1.5Hz. Similar to the previous cases, error is maximum behind the disc, hub and in the region below r/D = 0. For axial velocity, difference in most regions is less than 10% of the free-stream velocity. For radial velocity, difference in other regions is less than 2% of the free-stream velocity.

Axial Velocity Fields

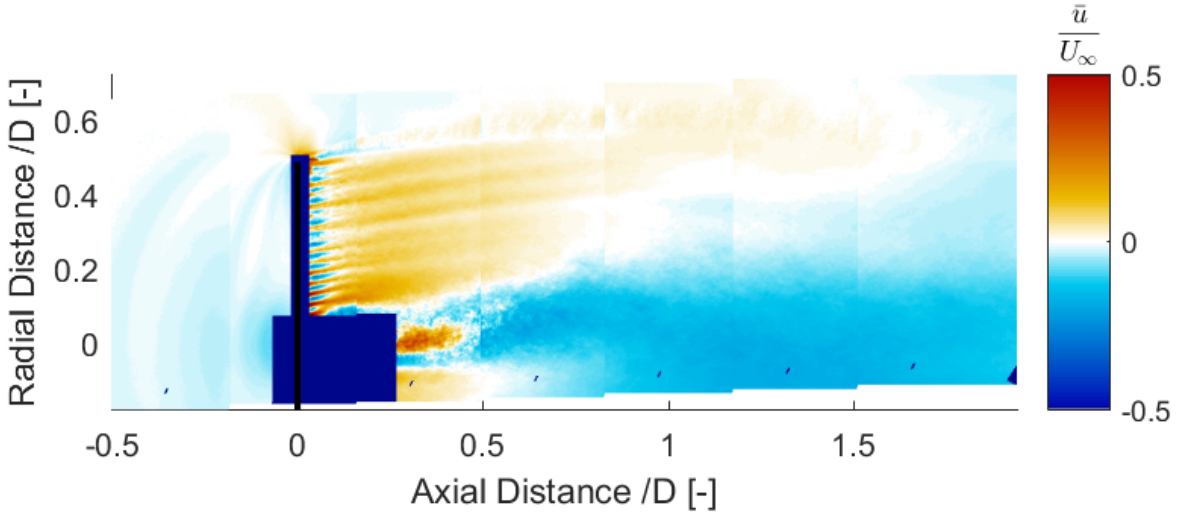

(a) Porosity = 59% (decreasing porosity) and C_T = 0.566

Figure 7.94: Error in axial velocity field for porosity changing with frequency = 1.5Hz and reduced frequency. = 0.47

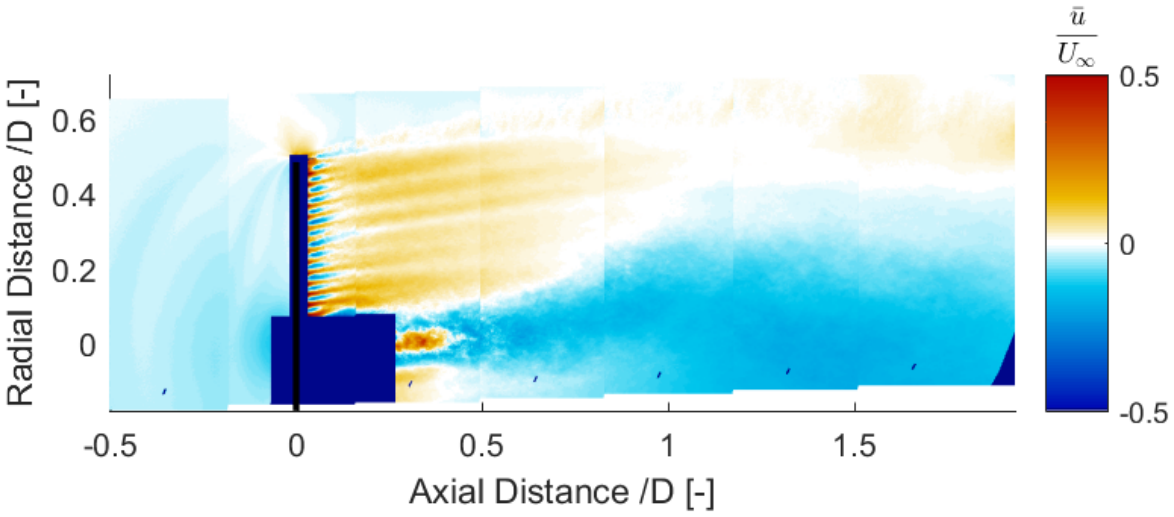

(a) Porosity = 47% (decreasing porosity) and C_T = 0.605

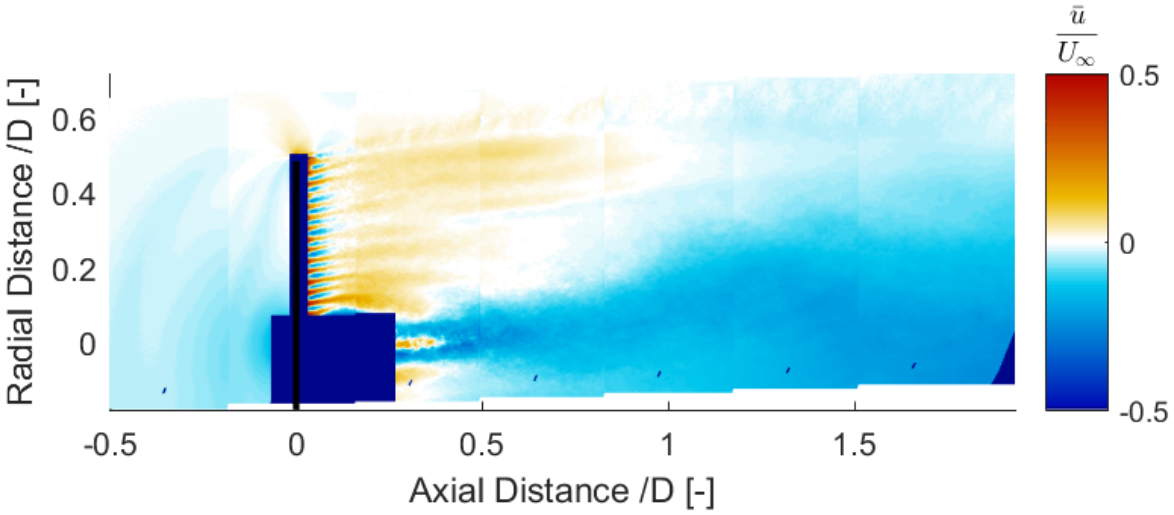

(b) Porosity = 31% (decreasing porosity) and C_T = 0.639

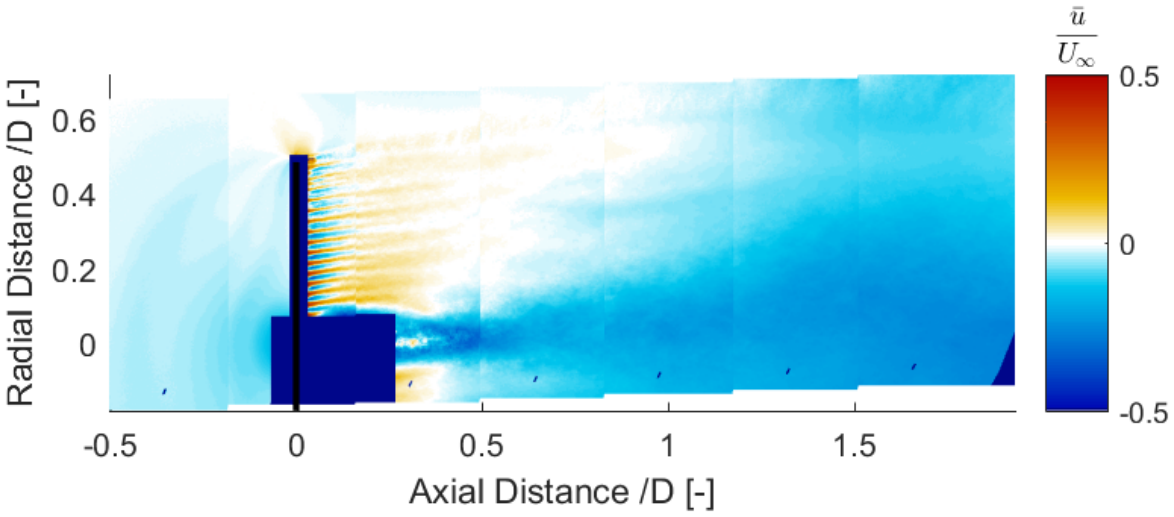

(c) Porosity = 19% (decreasing porosity) and C_T = 0.666

Figure 7.95: Error in axial velocity field for porosity changing with frequency = 1.5Hz and reduced frequency. = 0.47

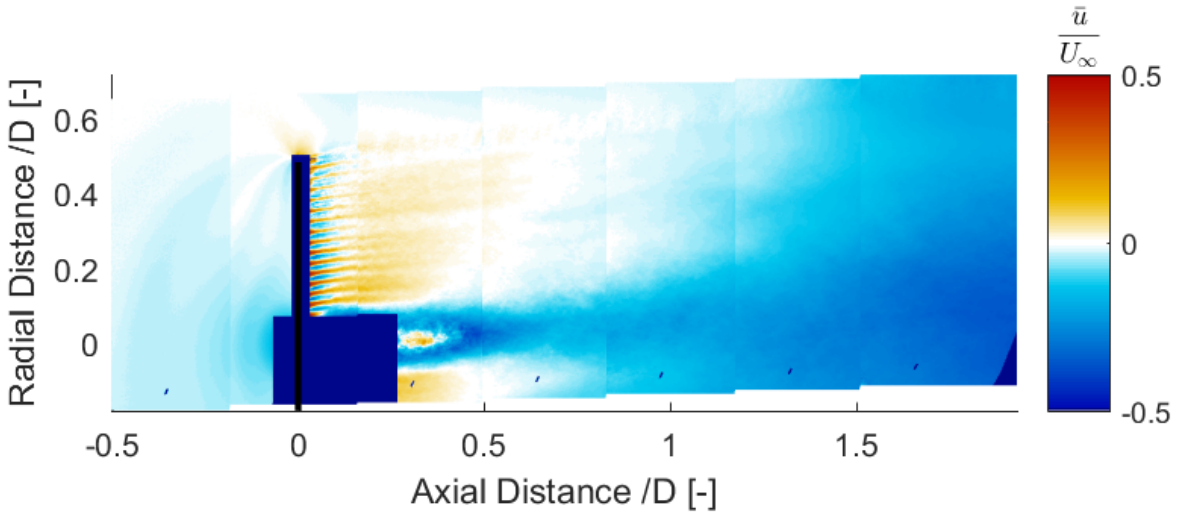

(a) Wake strength in the shear layer for porosity 43.4%

(b) Porosity = 14% (minimum porosity) and C_T = 0.692

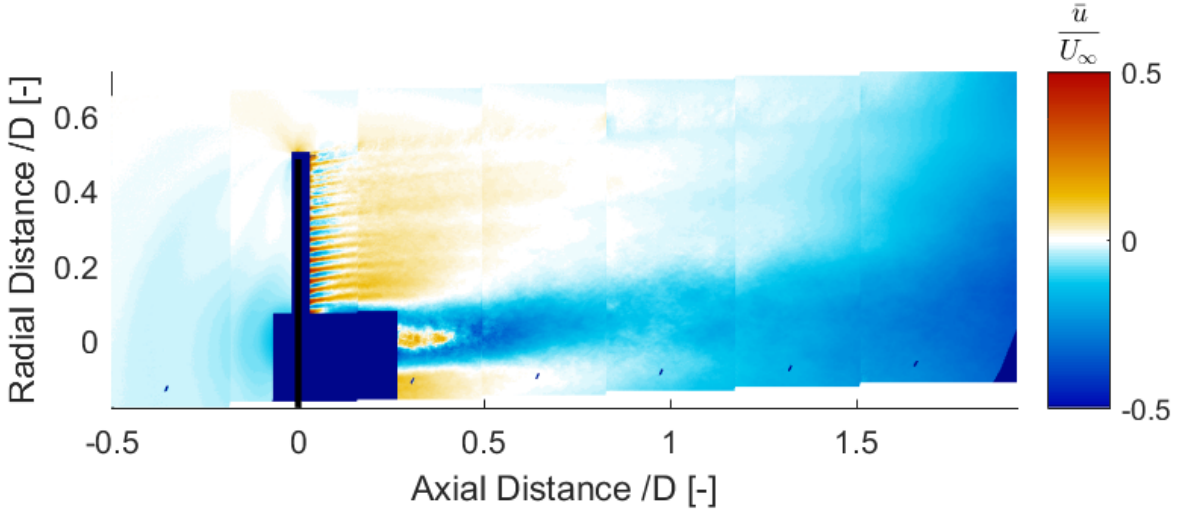

(c) Porosity = 19% (increasing porosity) and C_T = 0.675

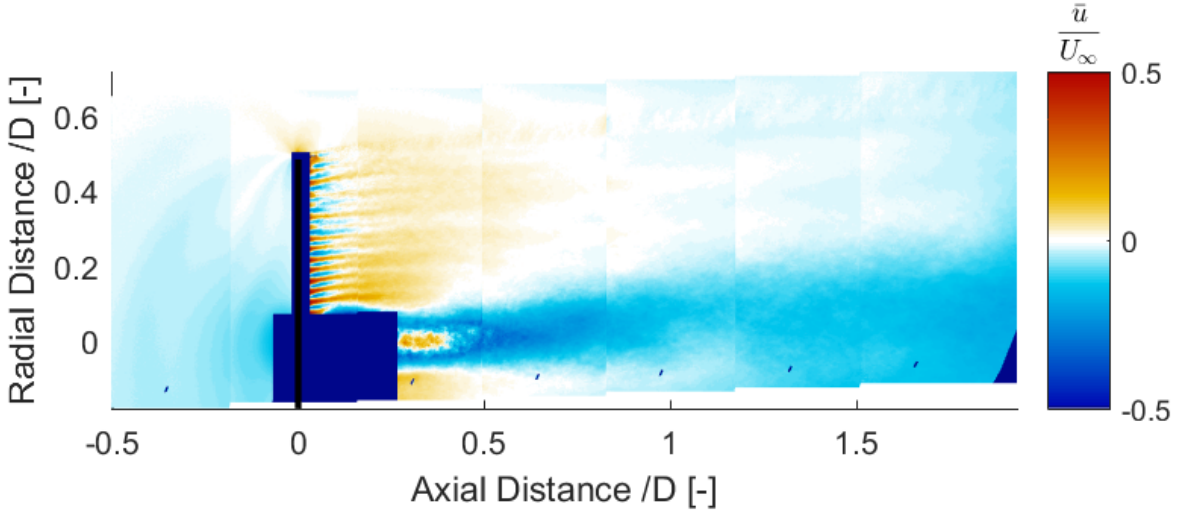

(d) Porosity = 31% (increasing porosity) and C_T = 0.651

Figure 7.96: Error in axial velocity field for porosity changing with frequency = 1.5Hz and reduced frequency. = 0.47

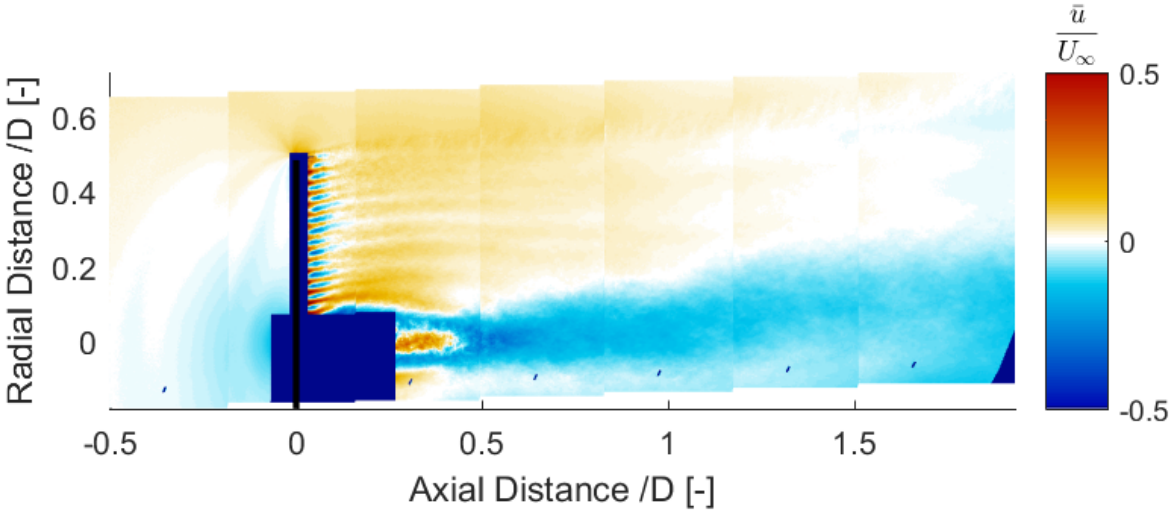

(a) Porosity = 47% (increasing porosity) and C_T = 0.616

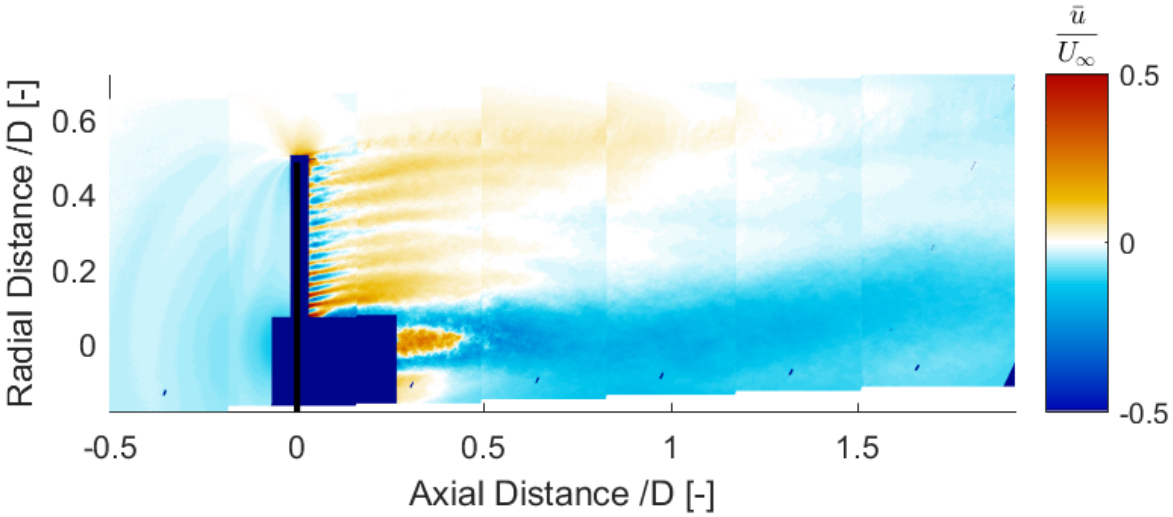

(b) Porosity = 59% (increasing porosity) and C_T = 0.575

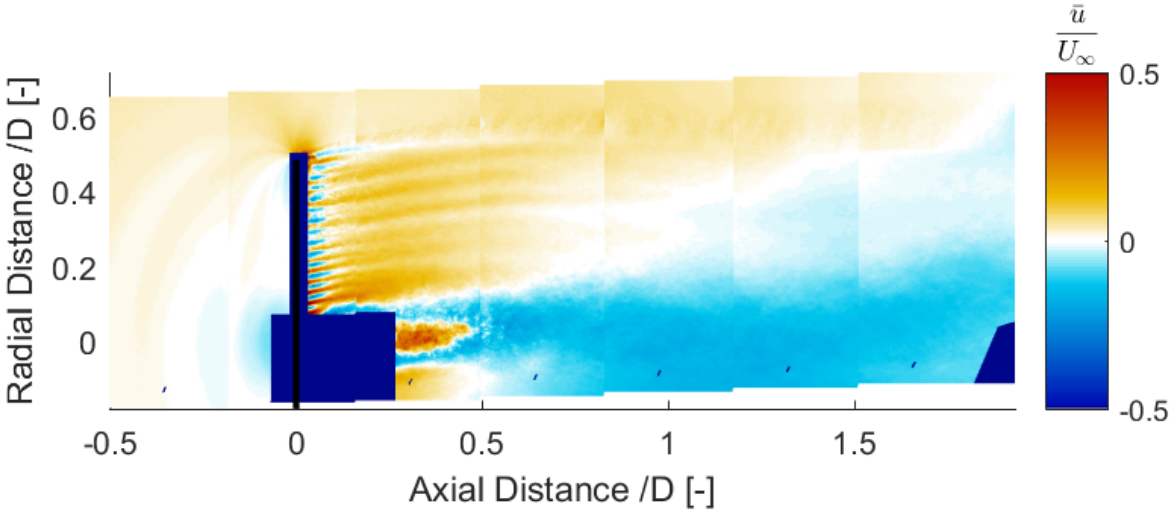

(c) Porosity = 64% (maximum porosity) and C_T = 0.555

Figure 7.97: Error in axial velocity field for porosity changing with frequency = 1.5Hz and reduced frequency. = 0.47

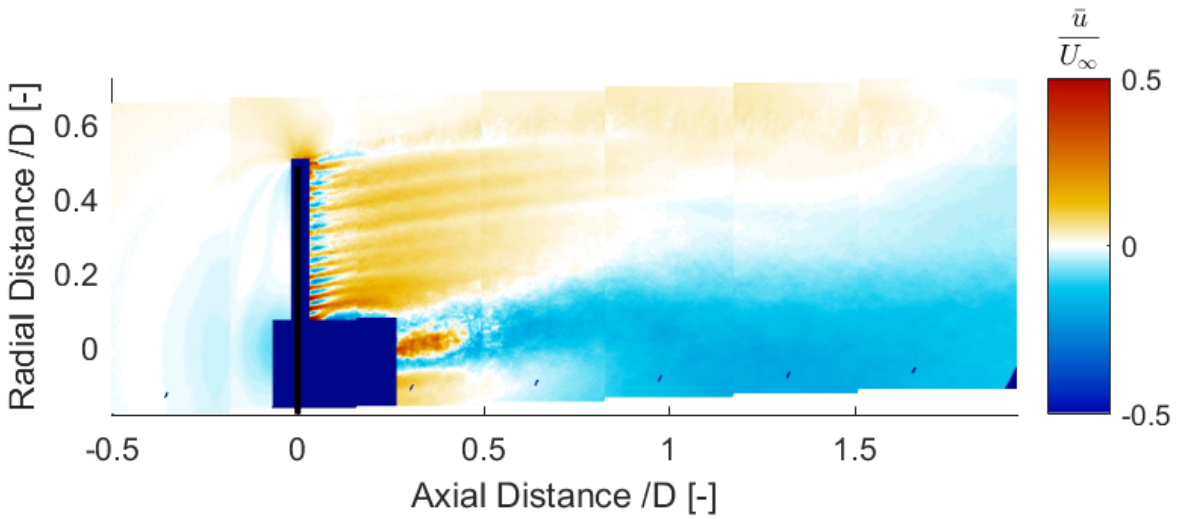

(a) Porosity = 59% (decreasing porosity) and C_T = 0.565

Figure 7.98: Error in axial velocity field for porosity changing with frequency = 1.5Hz and reduced frequency. = 0.47

Radial Velocity fields

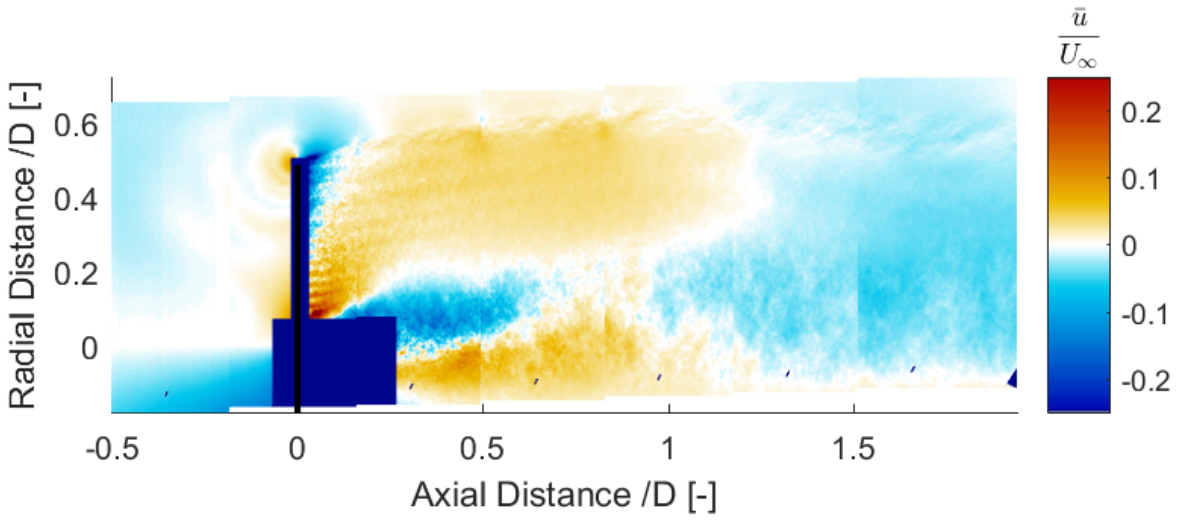

(a) Porosity = 59% (decreasing porosity) and C_T = 0.565

Figure 7.99: Error in radial velocity field for porosity changing with frequency = 1.5Hz and reduced frequency. = 0.47

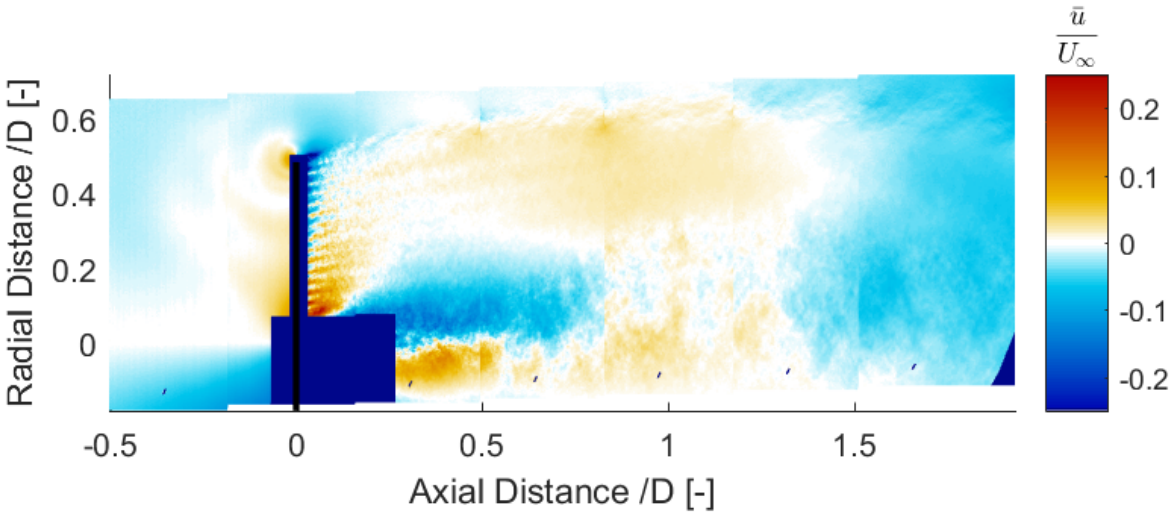

(a) Porosity = 47% (decreasing porosity) and C_T = 0.605

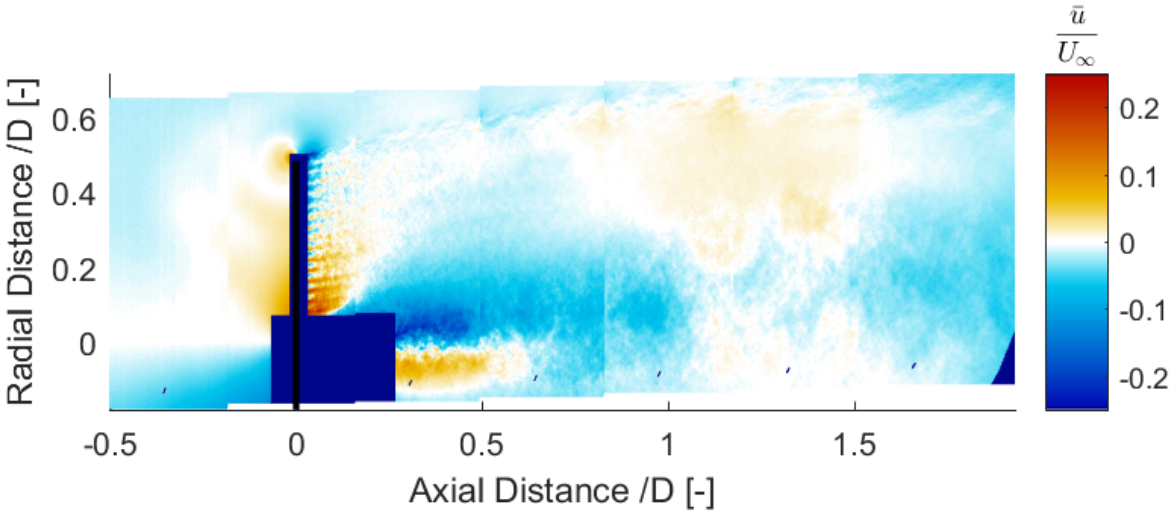

(b) Porosity = 31% (decreasing porosity) and C_T = 0.639

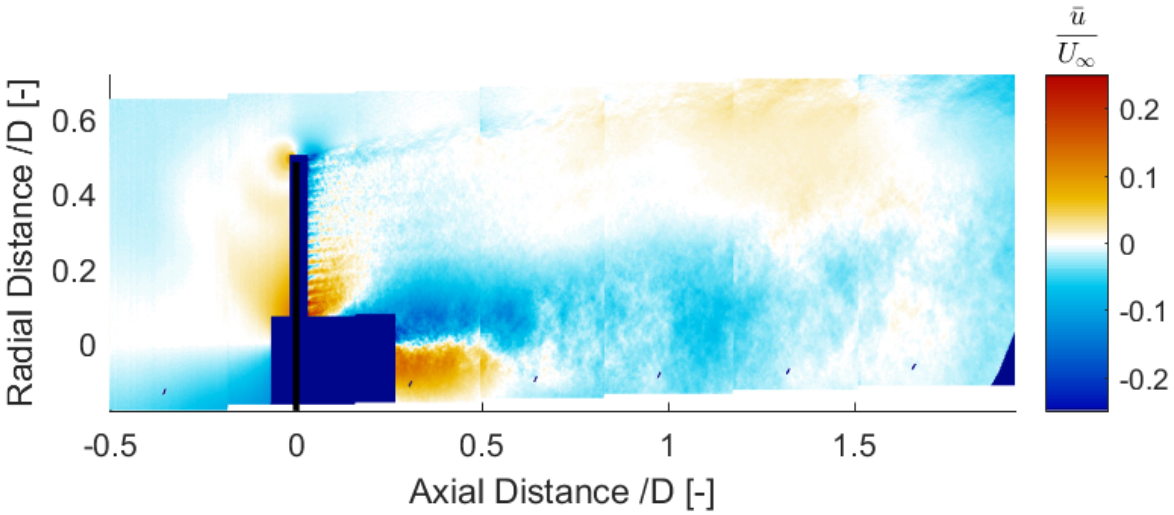

(c) Porosity = 19% (decreasing porosity) and C_T = 0.666

Figure 7.100: Error in radial velocity field for porosity changing with frequency = 1.5Hz and reduced frequency. = 0.47

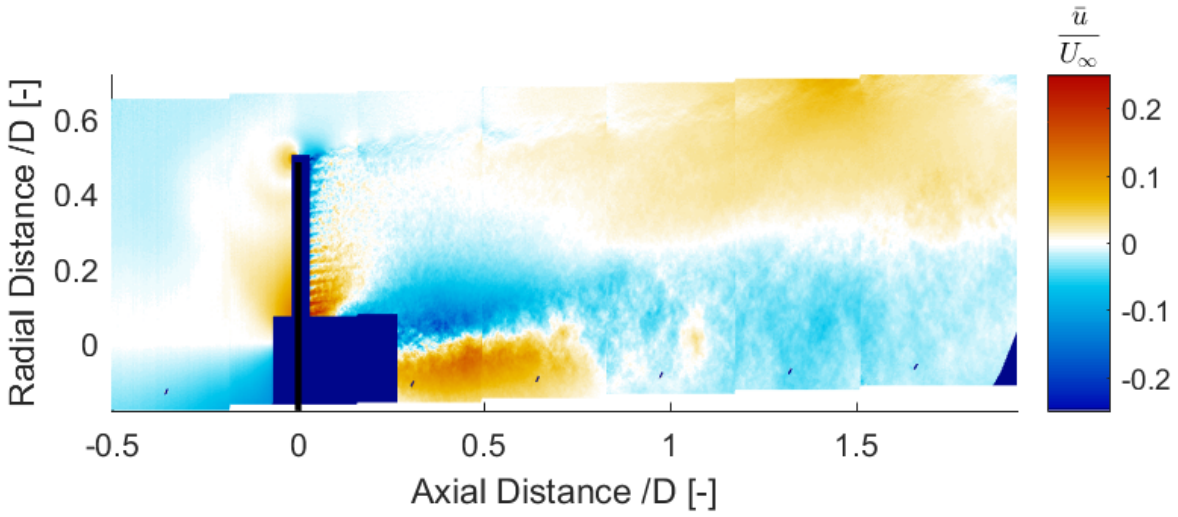

(a) Porosity = 14% (minimum porosity) and C_T = 0.692

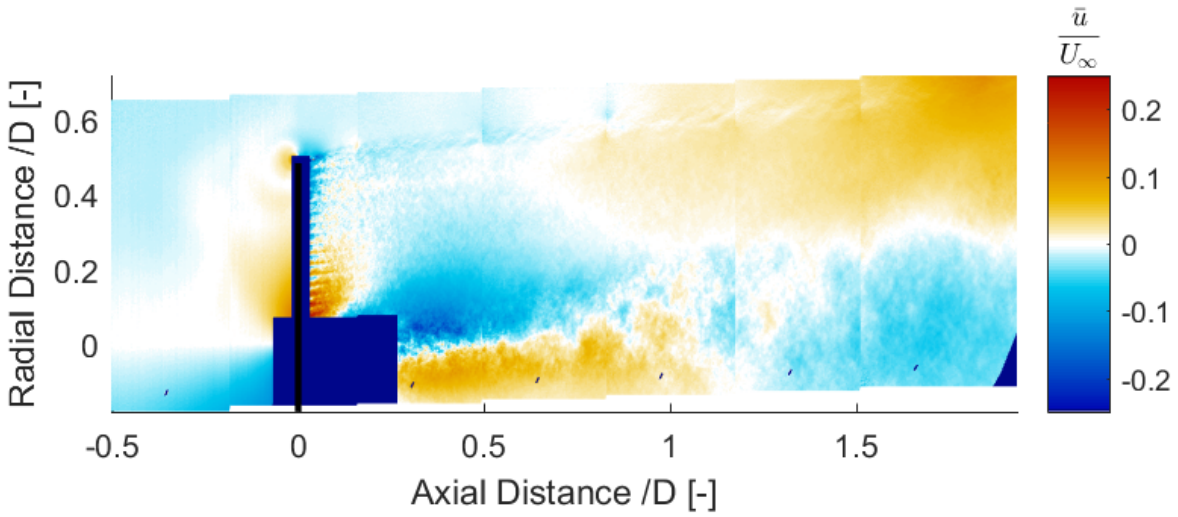

(b) Porosity = 19% (increasing porosity) and C_T = 0.675

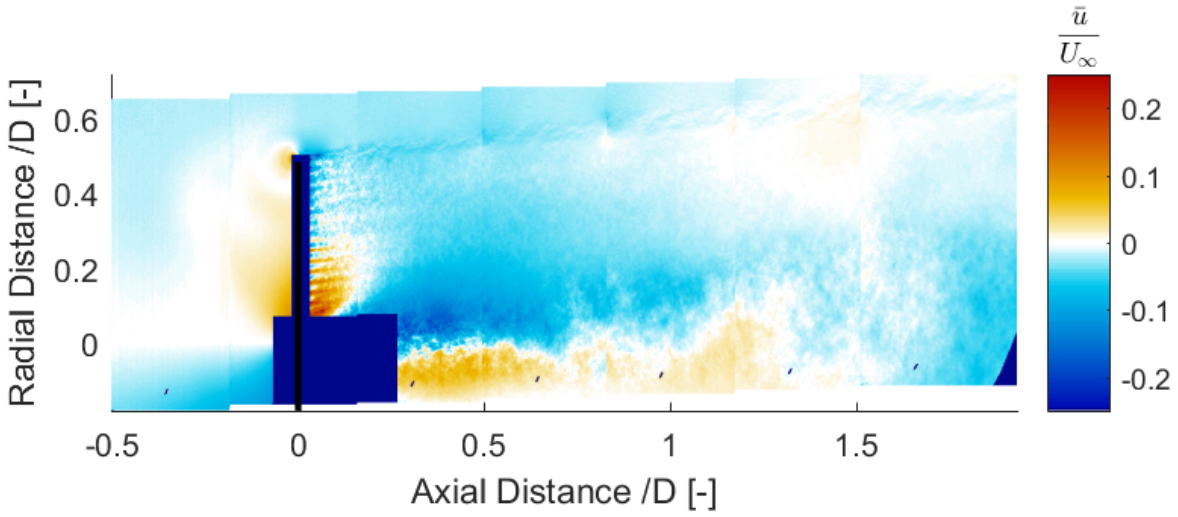

(c) Porosity = 31% (increasing porosity) and C_T = 0.651

Figure 7.101: Error in radial velocity field for porosity changing with frequency = 1.5Hz and reduced frequency. = 0.47

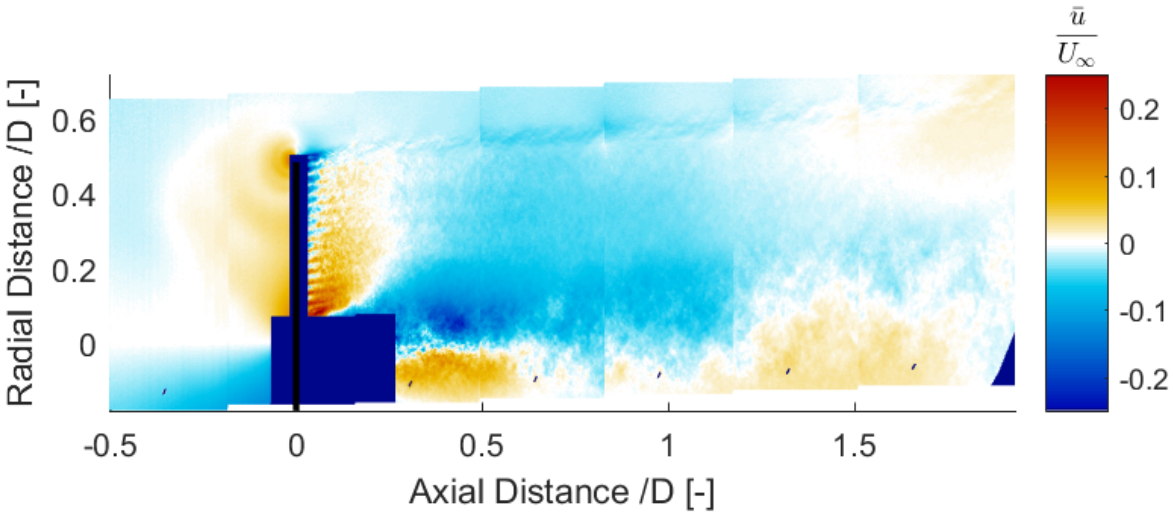

(a) Porosity = 47% (increasing porosity) and C_T = 0.616

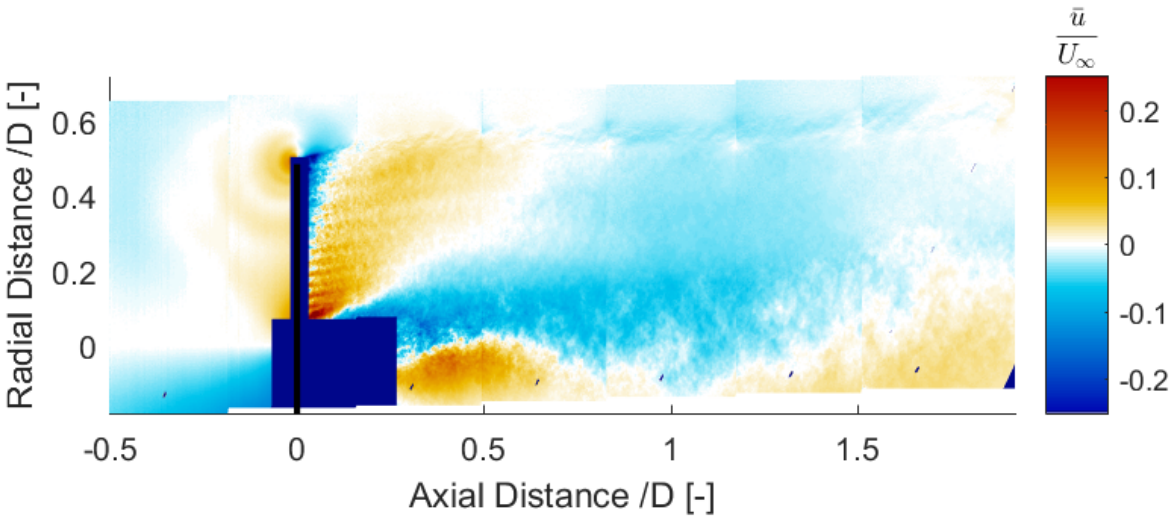

(b) Porosity = 59% (increasing porosity) and C_T = 0.575

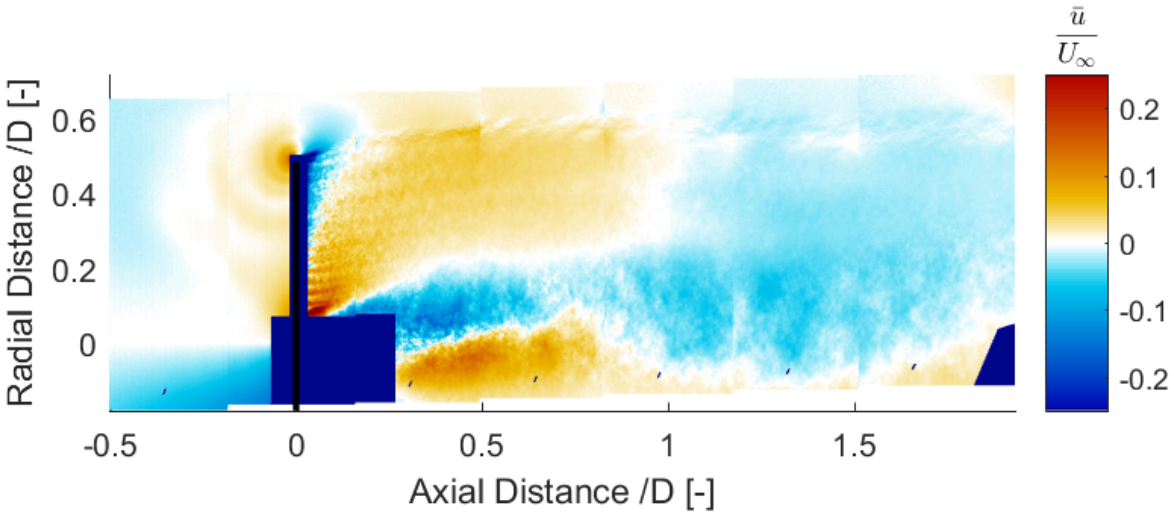

(c) Porosity = 64% (maximum porosity) and C_T = 0.555

Figure 7.102: Error in radial velocity field for porosity changing with frequency = 1.5Hz and reduced frequency. = 0.47

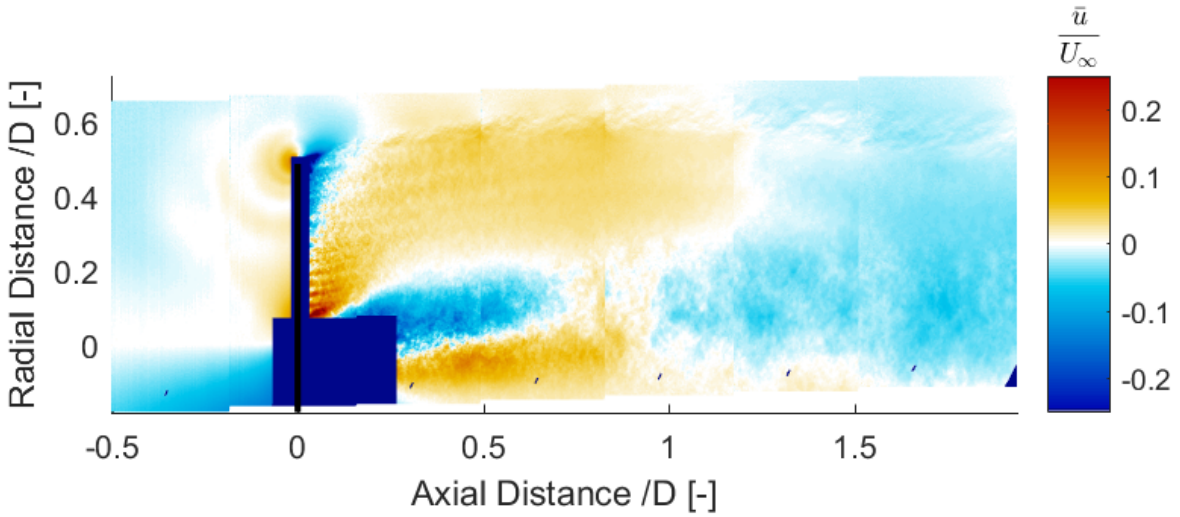

(a) Porosity = 59% (decreasing porosity) and C_T = 0.565

Figure 7.103: Error in radial velocity field for porosity changing with frequency = 1.5Hz and reduced frequency. = 0.47

COMPARISON WITH HOT-WIRE DATA

Figure 7.104, Figure 7.105 and Figure 7.106 present the normalized axial velocity results for HWA and VR model at the hot-wire location for 5Hz, 3Hz and 1.5Hz. For most cases, hot-wire results are lower than those of the VR model. As stated before, this can be due to several reasons. The position of the hot-wire was measured manually with a ruler of uncertainty $\pm 0.5mm$. As the hot-wire was not coordinated with the trigger system of the PIV, in order to find porosity, time of the first trigger is used. Whenever a initial trigger was given to PIV at the maximum porosity, it was saved in the system. Other causes for the difference can be the calibration of HWA, over-heating of the probe, wake-strength estimation for the VR model, etc.

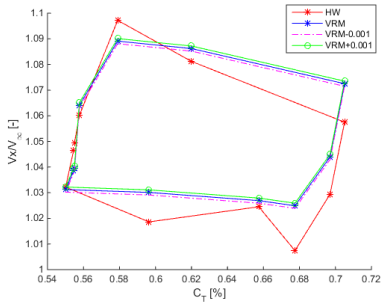

(a) Normalized Axial velocity vs. C_T

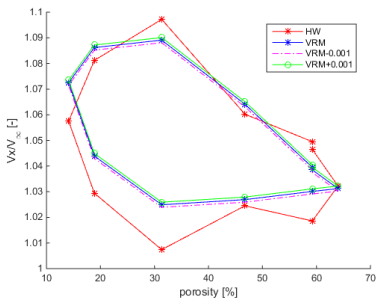

(b) Normalized Axial velocity vs. Porosity

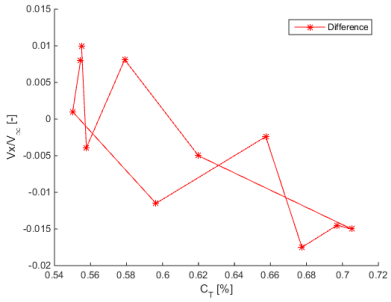

(c) Error in normalized Axial velocity

Figure 7.104: Normalized axial Velocity comparison between hot-wire results and VR model for unsteady load cases for frequency of 5Hz and k = 1.57

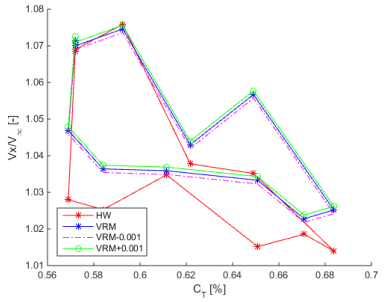

(a) Normalized Axial velocity vs. C_T

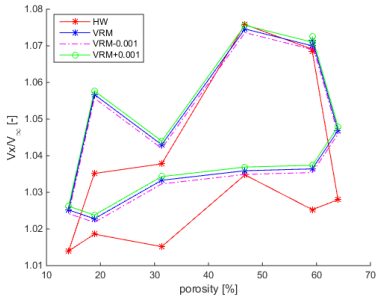

(b) Normalized Axial velocity vs. Porosity

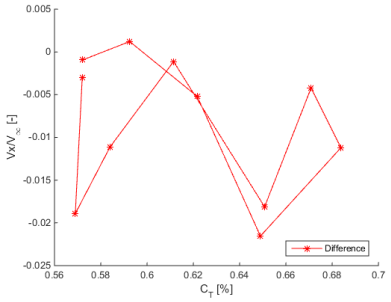

(c) Error in normalized Axial velocity

Figure 7.105: Normalized axial Velocity comparison between hot-wire results and VR model for unsteady load cases for frequency of 3Hz and k = 0.94

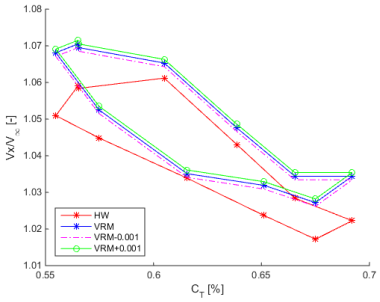

(a) Normalized Axial velocity vs. C_T

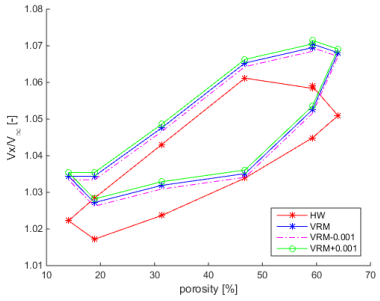

(b) Normalized Axial velocity vs. Porosity

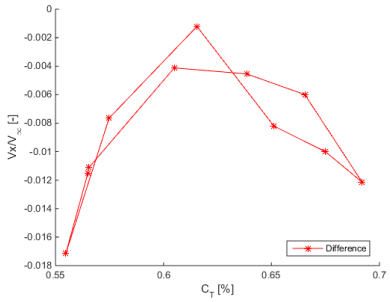

(c) Error in normalized Axial velocity

Figure 7.106: Normalized axial Velocity comparison between hot-wire results and VR model for unsteady load cases for frequency of 1.5Hz and k = 0.47

As discussed in this chapter, load and velocity for first and the last time-node does not coincide. This is expected to be due to uncertainty in experiment and post-processing. These uncertainties are discussed in the next chapter.

8

UNCERTAINTY ESTIMATION

The results analysed in the previous chapters are influenced by experimental errors. The experimental errors are both systematic and random. Although it is difficult to quantify these errors, a rough estimation of uncertainties are made in this chapter based on possible sources of errors.

8.1. UNCERTAINTY IN THE FREE-STREAM

As stated in section 5.2, OJF wind tunnel uses radiators to minimize temperature variation, but temperature variations were still observed. In order to quantify the error due to temperature variation, air is assumed to be an ideal fluid. Hence, ideal gas law (Equation 8.1) can be applied to estimate the effect of temperature variation.[10]

$$P_\infty = \rho RT \tag{8.1}$$

Minimum temperature was recorded to be 18.6°C and maximum temperature was recorded as 20.1°C. The average temperature was recorded to be 19.52°C. Hence, density variations were found to be: $\rho_{min} = 1.204 kg/m^3$,$\rho_{max} = 1.21 kg/m^3$ and $\rho_{avg} = 1.2065 kg/m^3$.

Using conservation of mass, variation in the free-stream velocity can be estimated: $\rho u = constant$. The average free-stream velocity was recorded to be $5.89 m/s$. Hence, the free-stream velocity variation can be estimated to be 5.868-5.898m/s. Therefore, uncertainty due to temperature variations is found to be less than 0.4% of the mean free-stream velocity value used.

Other sources of errors are model blockage, wind tunnel shear and turbulence. The data was acquired till an axial distance of 180cm from the wind tunnel opening and till the radial distance of 70cm from the wind tunnel centre. With every 1m downstream distance from the wind tunnel, the jet decreases by 16.7cm. At a distance of 2m, the jet has decreased by almost 35cm. Therefore, the measurement field is still in the region where shear layer and flow oscillations are negligible. At this distance, turbulence level is less than 0.5%. The flow inhomogeneity is found to be less that 1% at this distance. [10] Due to the wake of the model, the fluid next to the wake will be compressed and blocked, which induces model blockage uncertainty. But as the model area is less than 3% of the wind tunnel jet area, the error due to model blockage can also be estimated to be negligible

8.2. UNCERTAINTY IN PIV

Pressure and load uncertainty are related to uncertainty in the velocity field as these quantities are inferred from the velocity field. The errors in velocity field are both random and bias errors. [22] The random errors are mainly caused due to cross correlation and flow fluctuations.

Table 8.1: Uncertainty estimation due to random errors in PIV measurement [22]

	Error Type	Estimator	Typical mean value	Mean velocity uncertainty $[m/s]$	Mean velocity uncertainty % of V_∞
Random	cross-correlation	$\left[\frac{\varepsilon_u}{\sqrt{N}}\right]$	$\varepsilon_u = 0.1px$	0.03(steady)	0.05(steady)
				0.0025(unsteady)	0.04(unsteady)
	Velocity fluctuations	$\left[\frac{\sigma_u}{\sqrt{N}}\right]$	$\sigma_u = 0.5\%$	0.035(steady)	0.06(steady)
				0.0029(unsteady)	0.05(unsteady)

Table 8.1 summarizes the uncertainty estimation due to random errors. As the table shows, the random errors decreases by square root of number of samples. The number of samples for steady load cases were 70 and for unsteady load cases 100. Uncertainty due to cross-correlation is assumed typically to be 0.1px. Dividing this value by square root of N gives uncertainty of 0.05% of the free-stream value in steady loading and 0.04% of the free-stream value for unsteady loading. Random velocity fluctuations are taken to be 0.5% as the turbulence of OJF is very low. Uncertainty due to this is found to be 0.06% of the free-stream value in steady loading and 0.05% of the free-stream value in unsteady loading. Therefore, in total uncertainty due to random errors is 0.1% of the free-stream velocity. Uncertainty due to random errors carried forward in other calculations is following:

1. **Pressure from Bernoulli equation**: As $P_{BERN} \sim V^2$, uncertainty in pressure estimation from Bernoulli equation is $\frac{\Delta P_{Bern}}{P_{Bern}} = \sqrt{2\left(\frac{\Delta \vec{V}}{\vec{V}}\right)^2}$. Therefore, uncertainty in pressure calculated from Bernoulli equation is 0.15% of the free-stream value.

2. **Static pressure field**: It is difficult to quantify error in the pressure field, as it is not known how uncertainties are affected during Poisson integration. But by adding/subtracting the total uncertainty from the velocity fields, it is found that uncertainty due to random errors is really small.

3. **Load**: The uncertainty in the load calculated with both the methods ranges between 0.1% and 0.2% of original value.

Other sources of uncertainty in PIV measurements are:

- Peak locking: When particle image is bigger than pixel size, displacement is rounded to the nearest integer value. Due to this, error in velocity measurement occurs. If one particle image diameter is bigger than 2 pixel unit, than this uncertainty is of acceptable value. Typically it ranges between 0.05-0.1pixels.[67] Therefore, this will result in uncertainty of 0.02-0.04% of the free-stream velocity.

- Spatial resolution: Uncertainty due to spatial resolution is defined as the ration of window size to spatial wavelength.[68] As the value of spatial wavelength is not known, it cannot be estimated.

- Image matching: This is typically of 0.1px value, which gives 0.04% of the free-stream velocity.
- Uncertainty due to error in traversing: As seen in the flow fields, the regions where adjacent FOV are stitched together, there is a discontinuity. This discontinuity arises from small changes in the flow field but mainly due to error in traversing the camera setup. From the correlation analysis of the fields, this error was estimated to be 0-8mm in the radial direction. Therefore in these regions, the error in the velocity is higher than in the other locations in the field.

- Other sources of error are due to non-uniform seeding, particle slip, friction between the disc, misalignment of the disc, distortion of the acquired images, etc.

LOAD CHANGE DUE TO CONTOUR BOUNDARY VARIATIONS

Table 8.2 shows variation in load as boundary for momentum integration is changed. This table is for first time node for unsteady load case with frequency = 5Hz and k =1.57. This was repeated for all load cases, and similar results were found. As the table shows that for most variations, the change is less than 2% of the value used. This value increases to 5-15% when axial boundaries moved to less than 0.2m near the disc. This is because near the disc effect of porosity of the disc and the hub is maximum as seen in the previous chapters. Near the disc viscous affects are not negligible which was the assumption used for estimating load. It is also seen that when radial positions are also near the tip, the change in C_T is maximum. The reason being same that viscous affects cannot be ignored.

Table 8.2: Uncertainty Estimation in load due to contour variation

x/D upstream boundary [-]	**x/D downstream boundary** [-]	**r/D top boundary** [-]	**r/D bottom boundary** [-]	C_T [-]	**% change in** C_T [%]
-0.5030	0.9270	0.6530	0.0647	0.5586	-0.649
-0.5030	0.9270	0.3168	0.0653	0.2926	47.279
-0.1665	0.9270	0.6680	0.0647	0.4781	13.856
-0.4010	0.9265	0.6530	0.0647	0.5395	2.793
-0.4525	0.9267	0.6530	0.0647	0.5494	1.009
-0.2968	0.9313	0.6530	0.0647	0.5182	6.631
-0.4833	0.9267	0.6530	0.0647	0.5560	-0.180
-0.4783	0.9267	0.6530	0.0647	0.5553	-0.054
-0.4732	0.9267	0.6530	0.0647	0.5542	0.144
-0.4732	0.8960	0.6530	0.0647	0.5506	0.793
-0.5030	0.8962	0.6530	0.0647	0.5550	0.000
-0.5030	0.8753	0.6530	0.0647	0.5520	0.541
-0.5030	0.4170	0.6530	0.0588	0.5263	5.171
-0.5030	0.8752	0.5200	0.0650	0.4973	10.396
-0.5030	0.8752	0.6025	0.0650	0.5629	-1.423
-0.5030	0.8752	0.6283	0.0650	0.5574	-0.432
-0.5030	0.9270	0.6283	0.0650	0.5643	-1.676

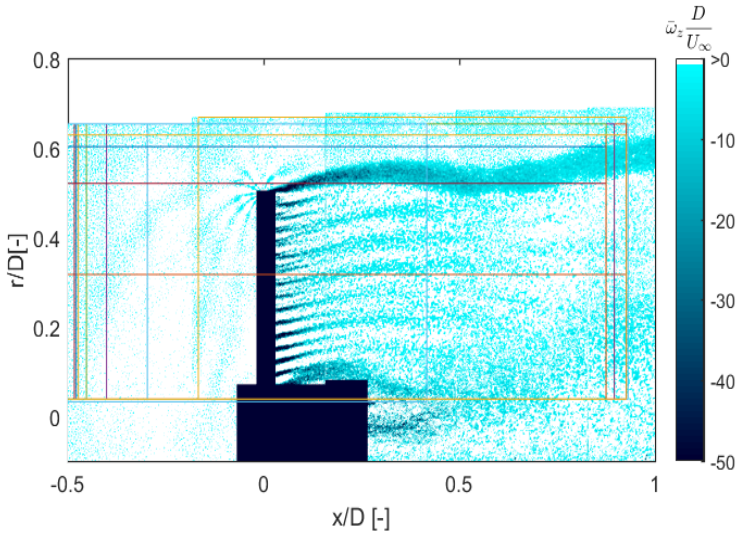

Figure 8.1: Different boundaries considered for momentum integration of the flow field

9

CONCLUSION AND RECOMMENDATIONS

The wake of a porous disc is captured using Particle Image Velocimetry till x/d = 1 for steady load cases and till x/D = 2 for unsteady load cases. In this chapter, main results are summarized along with recommendations for further research projects:

9.1. STEADY LOAD CASES

The following major conclusions are made for the actuator disc under steady loading:

1. **Effect of porosity on pressure distribution and disc loading**: Pressure fields estimated using Poisson integration show that pressure increases as the flow approaches the disc, and decreases after it. Pressure also decreases towards the disc centre line. This is the result of wake expansion. From the radial distribution of pressure field, it can be shown that load on the disc non-uniform. This is contrary to the AD model assumption that the disc is uniformly loaded.

   Load on the disc decreases as porosity is varied from 14% to 64%. This is because as disc porosity decreases, a more strong boundary is created against the flow and pressure difference across the disc increases. The disc load does not vary linearly with porosity, likely due to the uncertainty stated in the previous chapter also has an effect of the estimation of load.

2. **Effect of loading on axial velocity**: The axial velocity induction increases with the disc load. The velocity induction is higher behind the disc hub resulting from the tower shadow effect. The wake directly behind the disc constitutes of discontinuity of vorticity resulting from the mesh of the disc. Due to this, axial velocity field just behind the disc is also discontinuous.

3. **Effect of loading on radial velocity**: Compared to the axial velocity, radial velocity is very small. It is the highest around the disc edge. This region around the disc edge with high radial velocity increases in size with loading. As the wake is expanding, the radial velocity field is mainly positive (except in the region behind the hub), indicating outward movement towards the free-stream

4. **Effect of loading on vorticity distribution**: Vorticity is the strongest near the wake edge and just behind the disc. These are regions of strong velocity gradient. The tip vorticity is more persistent for higher loading.

5. **Effect of loading on wake expansion and recovery**: Wake expands more with increase in load on the disc. Recovery for higher load cases takes a longer downstream distance to recover. The gradient of decrease in velocity with downstream distance is higher for those cases. For none of the load cases, the flow has fully recovered till x/D = 1. However, gradient of velocity change is increasing with distance, which indicates velocity reaching a minimum.

6. **Vortex Ring Method**: Solutions from Vortex Ring method is in good agreement with the experimental data. The regions with maximum difference between the two methods are regions behind nacelle and just behind the disc. The wake expansion (region where $u/U_\infty = 1$) is estimated to be similar to the experimental data, with less than 0.5% error in the location. As experimental data was only collected till x/D = 1, the model assumes that for steady load cases, wake has stopped expanding after this point, resulting in negative radial velocity near x/D = 1. This further introduces an error in the model.

9.2. UNSTEADY LOAD CASES

1. **Effect of sinusoidal change in porosity on the pressure and loading**: Pressure increases with wake expansion and decreases with wake contraction. This is caused due to cyclic loading on the disk. As there is a small gradient in the pressure coefficient for all axial locations, the assumption of uniform loading is not completely true. This is due to the non-uniform velocity field.

   The loading calculated using both MT and momentum integration is cyclic, which was the intention of changing porosity harmonically. For higher frequency load case, the difference between the loads is higher for the same porosity with different phase.

   Difference between step-change in porosity and sinusoidal change in porosity can be seen in the load calculations. As seen in [1, 27], when there is a step decrease in porosity, there is an overshoot in loading and velocity, before a subsequent decay to a steady-state. This is because of difference in dynamic inflow for two types of unsteady loading.

2. **Effect of sinusoidal change in the porosity and cyclic loading on the axial velocity field**: The axial velocity forms a loop for cyclic loading. For same loading, different induction is seen when phase of the load cycle is different. A small difference exits between the first and the last velocity fields (the first and the eleventh disc alignments) of the same unsteady load case. This is likely because of the possible disc alignment errors and other uncertainties resulting in variations on the disc loading.

   With changing load in a cyclic manner, the wake expands and contracts which is contrary to the steady loading during which wake only expands (within the region of x/D = 1). For the higher frequencies, this effect is higher. During the first half of the load cycle in which load is increasing, the wake near the disc expands more. During the next half of the cycle, in which porosity increases and the loading decreases, wake expansion near the disc decreases. The

lowest frequency load case show the least effect, but still the wake expansion is not similar to the steady cases. Velocity induction for this case is also different for same loading with different phase. Downstream the disc, wake is expanding and contracting for all the unsteady load cases, however when compared to the other two cases, the last case with minimum frequency the effect is very small.

3. **Effect of sinusoidal change in porosity and cyclic loading on the radial velocity**: Similar to the steady cases, radial velocity is small in comparison to the axial velocity fields. The radial velocity fields show the rotation of vortices. The regions with high radial velocity indicates strong vortex. However as the frequency decreases, the size of these regions decrease.

   However, contrary to the steady load cases, radial velocity fields for unsteady load cases have regions with both positive and negative value. This indicates flow is going outward and inwards. This is due to the wake expanding and contracting with increase and decrease in loading respectively. For the first half of the load cycle, where loading on the disc increases, radial velocity is positive next to the disc. However, for the second half, region of negative radial velocity starts to appear as the wake expansion is decreasing.

4. **Effect of sinusoidal change in porosity on the vorticity**: Two regions of vorticity roll up were seen within the region up to x/D =2 during the first half of the load cycle for the highest frequency load case. For the second half, the first roll-up position moves downstream and no second roll-up is seen within that distance. This is likely because of higher velocity induction for the first half of the load cycle. Hence, flow velocity is lower than the second half of the load cycle.

   For the load case with 3Hz frequency, the vorticity roll-up position moves downstream with increasing load. However, vorticity only rolls up for two maximum loadings. For all other cases of 3Hz frequency. For the load case with 1.5Hz frequency, vorticity rolling up phenomena is not seen, but wake expansion process as observed in axial velocity fields is noticeable.

5. **Vortex Ring Method**: Results from the VR method are in good agreement with the experimental results other than the tower shadow effect and porous disc effect.

   (a) **Axial Velocity**: The results estimated using the VR method are in good agreement regarding axial velocity with results from the experiment. Other than the regions just behind the disc and the hub, the difference between the two results is less than 10% of the free-stream value.

   (b) **Radial Velocity**: The radial velocity fields estimated using VR method also show positive and negative region denoting the effect of cyclic loading on the wake. For radial velocity, the difference is less than 2% of the free-stream in most regions.

9.3. LIMITATIONS AND FURTHER WORK RECOMMENDATIONS

1. **Improvements in the Experiment**:

   (a) During the experiment, towers of the disc and hot-wire had oscillations. This can be reduced by mechanically clamping the tower to increase its stability.

   (b) Random error can be further decreased by increasing the number of samples.

   (c) One of the uncertainties that could not be quantified was friction of the two discs. As two discs were used to vary the porosity, while keeping them as close as possible, uncertainty was introduced.

   (d) Error in traversing the PIV set-up can easily be reduced as the traversing system in OJF has less than 0.4mm of uncertainty.

   (e) The load cell used in this experiment had a small Signal-to-Noise ratio, this affected the results.

   (f) As seen in chapter 8, uncertainty estimation is only made for random errors and peak locking, while there are other sources of errors too, which need to be quantified as well.

   (g) In order to analyse trends in detail, more data points per load cycle should be measured.

2. **Further recommendations**

   (a) Increasing the sampling size of image per PIV measurement.

   (b) Interpolating pressure distribution at the disc from both upstream and downstream regions. Then load can be estimated from the pressure jump across the disc.

   (c) Validating velocity fields estimated using Free Wake Vortex Ring method for cyclic loading.

   (d) Validating dynamic inflow engineering models.

   (e) Validating CFD (RANS) model for cyclic change in the load.

   (f) Collecting experimental data using PIV for a step change in the loading. In [1], hot-wire was used to collect data, but hot-wire does not provide whole flow field.

A

PARTICLE IMAGE VELOCIMETRY

In this chapter, working principles of Particle Image Velocimetry are discussed. Unlike the hot-wire anemometry , PIV is a non-intrusive method to measure velocity field (see Appendix B for working principles of HWA).

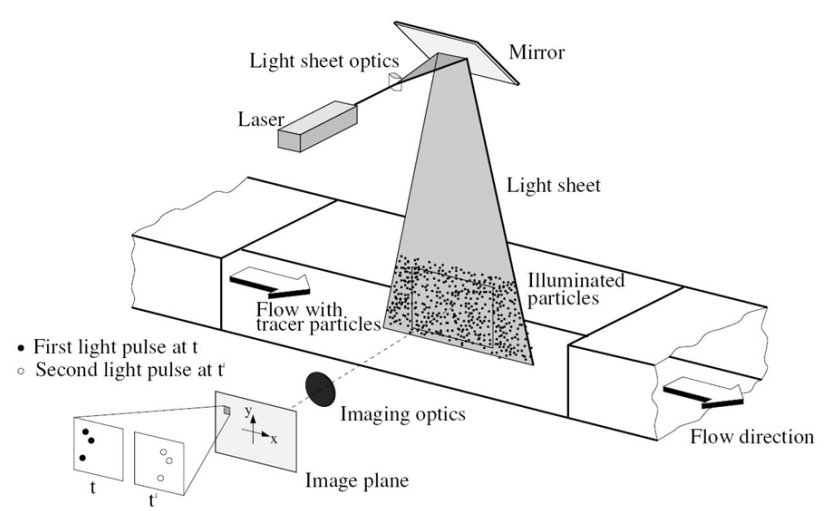

Figure A.1: Experimental arrangement of PIV in a wind tunnel [18]

It is one of the most successful flow measurements techniques. It has many advantages:

- It is a non-intrusive method, so the instruments do not need to immersed in the flow. Hence there is no much disturbance to the flow.
- It is possible to capture the whole field both for quantitative and visualization purposes. [19]
- It can be used to measure vorticity.[19]
- Unlike HWA, it does not require daily calibration as it does not dependent on ambient temperature or pressure changes.[19]

However along with these advantages, PIV has some disadvantages too. PIV has a complex set-up and needs more optical access. It has low temporal resolution and post processing is time consuming. [19]

A.1. WORKING PRINCIPLE

Figure A.1 shows a schematic of planar PIV set-up. PIV allows to measure instantaneous velocity field, by using displacement of tracer particles which are carried by the fluid over short time interval. These tracer particles should be small enough to not alter the fluid properties and should be able to scatter light. This light scattered is captured by a digital imaging device, which is placed perpendicular to the measurement plane. [19],[18]

A.2. FLOW SEEDING

Tracer particles used are usually microscopic particles which should not affect the flow properties. The concentration of these particles is generally between $10^9 - 10^{12} particles/m^3$. Beyond this limit, the particles start affecting the flow properties. The main parameter that is used to check this property of tracer particles is mass ratio. Mass ratio is defined as ratio of fluid mass to the mass of particle. This ratio should be less than 10^{-3}, in order for particles to follow the flow without altering its properties. [19],[18]

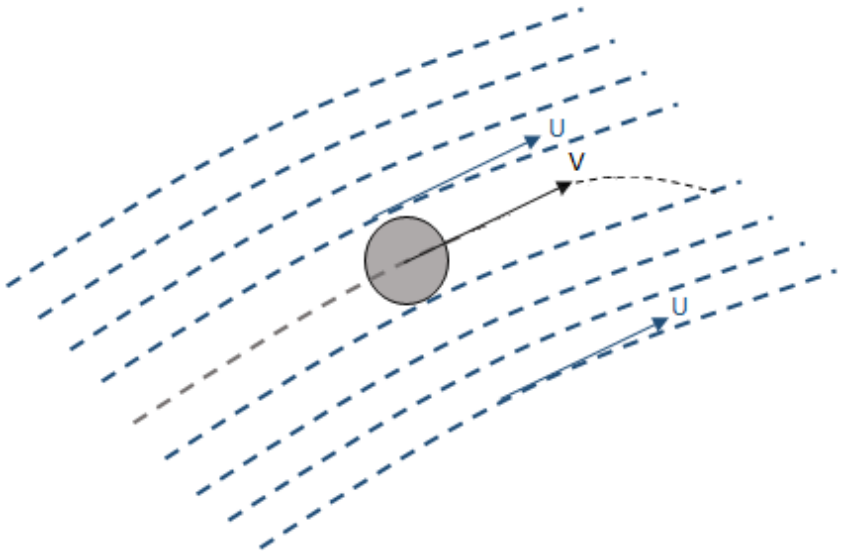

Figure A.2: Discrepancy between the particle and the flow [19]

Along with the size of these particles, material of these is also really crucial to meet these properties. The choice of material depends on the mechanical properties of the particle. Imaging device should be able to clearly capture the light scattered by these particles. Therefore important parameters to consider here are: size of these particles and refractive index. [19],[18]

The requirement of not altering the flow properties and being able to scatter light properly demands opposite parameters. For the former, it should be as small as possible but in order to scatter light properly, particles should be large enough. [19],[18]

In order for particles to accurately follow the flow, buoyancy neutral particles are used. These are particles such that $\frac{(\rho_p - \rho_f)}{\rho_f} \ll 1$. This is easy to get for liquid flows, but as gas has very low density, it gets difficult to get such particles. For gaseous flows, therefore very small particles are required. [19],[18]

Another property that can be taken into account is particle response time, τ_p. It is the time after which particle changes its velocity to 63% of ΔU_{1-2}. This property is very crucial for turbulent flows as it should be less than the small time scale of the flow. Figure A.3 shows that increasing the particle diameter increases its response time. Therefore, smaller particle is preferred as it adapts to flow changes more quickly. For turbulent flows, selection of particle can be done using Stokes number, SK=$\frac{\tau_p}{\tau_f}$ and τ_f can be found using dimensional analysis [19],[18]

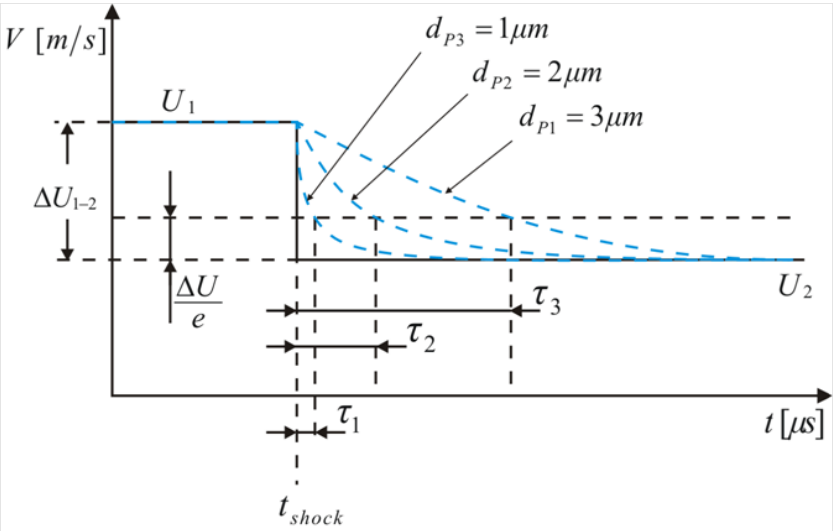

Figure A.3: Particle Response time with respect to its size [19]

Apart from the particles being able to scatter light properly and not affecting the fluid properties, there are other requirements for particles. Particles should not be hazardous to health and should be non-corrosive and non reactive as otherwise they will affect the flow facility. Particle should also leave minimum residue after use, therefore, they should be self evaporating.[19],[18]

Scattering Properties of Tracer Particles: As mentioned before, particles should be able to scatter light properly. This depends on the diameter of the particles, refractive index and wavelength of the light.[18]

According to Mie's theory, if $d_p > \gamma$, then normalized diameter, q, can be used to determine this property of particles.[18]

$$q = \frac{\pi d_p}{\gamma}$$

As q increases, ratio of forward to backward increases, as also shown in Figure A.4. Therefore, it is better to place imaging device at forward position, i.e., 0 degrees or 180 degrees. However due to

limited optical access, it is generally placed at 90 degrees, where scattering is least.[19],[18]

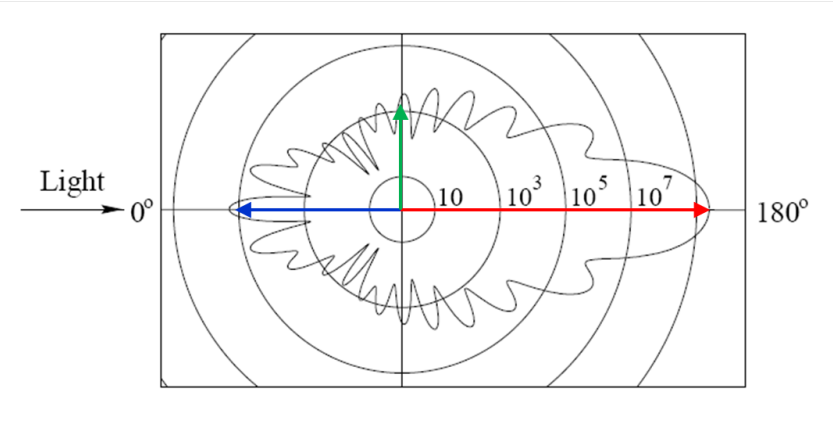

Figure A.4: Particle Illumination in PIV [19]

Seeding Technique: In order to meet the above mentioned requirements, it is important to seed these particles properly, but optimum seeding is very difficult. For liquid flows, particles are simply dispersed in the liquid, while for gaseous flows, they are first entrained in the fluid and then injected before measuring instruments. [19],[18]

A.3. ILLUMINATION

For illumination of these particles, a light source is needed. Lasers are most commonly used devices for the particle illumination as they are able to omit high intensity monochromatic light. The laser sheet needs to be very thin so that only the particles in the field of measurement are captured in the image. This thickness is obtained using optics.

The pulse time, i.e., the duration of illumination should be such that the particle should not appear like a line but rather dots. Therefore, pulse time needs to be short enough to avoid blurring of the images and out of plane movement of the particles. However it should also be long enough to be able to measure the displacement of particles between two images with sufficient resolution. The light source needs to illuminate the measurement plane twice by separation of short time, known as separation time. [19],[18]

A.4. IMAGING EVALUATION

This section will discuss the post processing process. In order to acquire velocity field from images, two factors are very important: image window size and cross correlation. The parameters that are needed for it are magnification factor, pixel size, window size, separation time and overlap ratio.

Calculate the magnification factor M.

$$M = \frac{\text{sensor size}}{\text{imaged object size}} = \frac{\text{pixel size} \times \text{number of pixels in the sensor}}{FOV} \tag{A.1}$$

$$M = \frac{d_i}{d_o} \tag{A.2}$$

(A.3)

together with

$$\frac{1}{f} = \frac{1}{d_i} + \frac{1}{d_o} \tag{A.4}$$

Image Window size :As shown in Figure A.5, image is divided into small areas known as "interrogation windows". Approximately each window should have about 10 particles. Size of the window should be small enough to be able to capture flow details properly, but too small window means a lot of redundant and false vectors.[10] The displacement of these particles is found using correlation methods. An assumption of homogeneous movement of particles between two images is made for this. [18]

Cross-Correlation :Cross Correlation is basically similarities between two separate measurements. For each window, cross-correlation value is found and place where maximum of this function takes place indicates the average displacement of the particles in that window. This is repeated for all windows and velocity field is found using dividing this displacement by separation time and scaling factor (M/number of pixels) (see Figure A.5). [19] This is done for each interrogation window. Ideally adjacent interrogation areas should have some overlap as the particles on the edge which might have moved out of the window in two different frames.

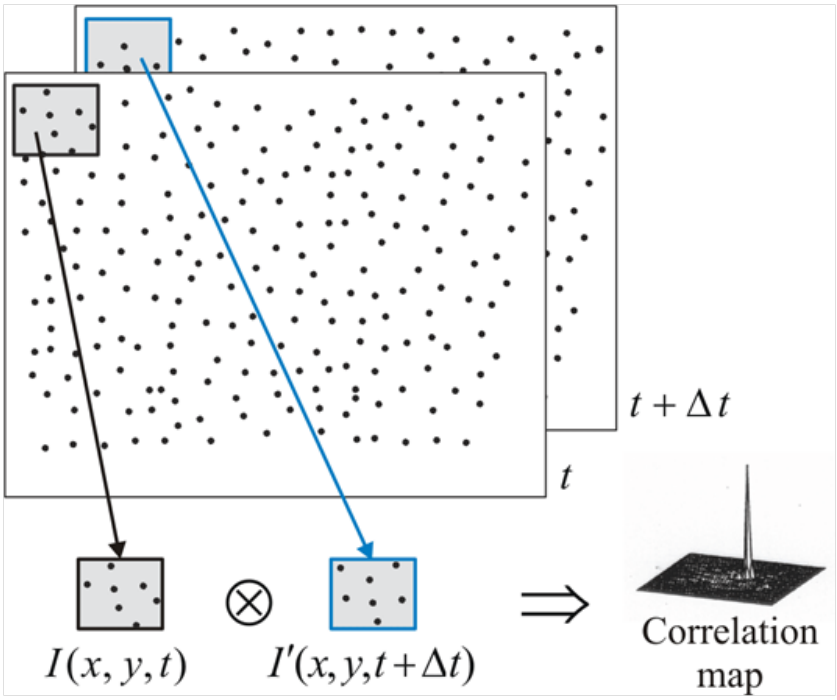

Figure A.5: Cross Correlation Process for PIV [19]

Uncertainty Calculation: As stated in the earlier section, that velocity is derived using mean displacement of particles, so velocity found is mean velocity. Uncertainty in velocity can be found from uncertainty in displacement and separation time using error propagation. [19]

$$\varepsilon_u = \sqrt{\left(\frac{\partial U}{\partial t}\varepsilon_{\Delta t}\right)^2 + \left(\frac{\partial U}{\partial x}\varepsilon_{\Delta x}\right)^2} \tag{A.5}$$

$$\varepsilon_u = \sqrt{\left(-\frac{\Delta x}{\Delta t^2}\varepsilon_{\Delta t}\right)^2 + \left(\frac{1}{\Delta t}\varepsilon_{\Delta x}\right)^2} \tag{A.6}$$

$$\varepsilon_u = \frac{1}{\Delta t}\sqrt{(-U\varepsilon_{\Delta t})^2 + (\varepsilon_{\Delta x})^2} \tag{A.7}$$

B

HOT-WIRE ANEMOMETRY

Hot-wire anemometry is based on the velocity measurement by measuring changes in heat by placing a heat sensor in the fluid flow. This heat sensor is usually a thin cylindrical wire which is electrically conductive.[19]

B.1. WORKING PRINCIPLE

HWA uses a electricity conducting wire. When current, I, passes through it, electricity is dissipated into thermal energy by Joule's effect. [19] This power generation due to Joule's effect is given by Equation B.1 and Figure B.1:

$$P_{input} = I^2 R_{wire} \tag{B.1}$$

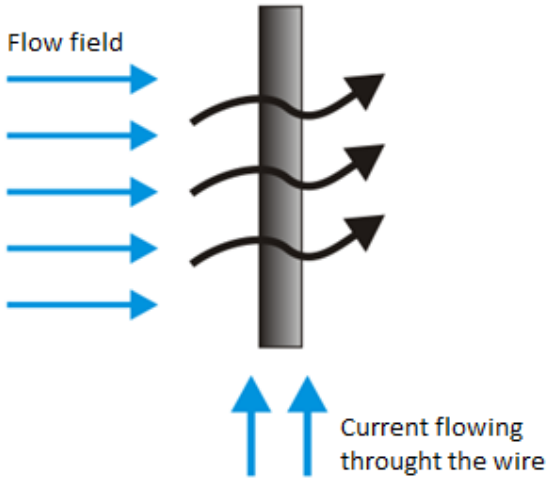

Figure B.1: Heat transfer through a wire [19]

As the wire is in an equilibrium state, the power generated by Joule's effect is equal to the heat loss to the fluid. As the velocity changes, the heat transfer changes, and the wire temperature changes to acquire a new equilibrium. Therefore, rate of heat exchange between the wire and the fluid depends on the temperature difference between them. [19]

Most commonly used operating principle for HWA is Constant Temperature Anemometry (CTA). There are others such as constant Current Anemometry, but they are less commonly used. In the CTA operating hot-wire anemometry, current through the wire changes to keep the temperature of the wire, T_w, constant. When the flow passes over the probe, there is a heat loss from the wire and in order to maintain a constant temperature, voltage across the wire changes. Therefore, the heat loss is equal to the power generation by Joule's effect. [19]

Heat loss is given by Equation B.2:

$$P_{lost} = Q_{conv} + Q_{cond} + Q_{rad} \tag{B.2}$$

Heat loss due to conduction and radiation are considered negligible as:

- The flow velocity is normal the axis of wire, and uniform over its length. [19]
- Temperature and density of the fluid are constant. [19]
- Temperature of the wire is uniform over its length. [19]
- Area of the wire is very small. [19]

Therefore, the power loss can be estimated by Equation B.3:

$$P_{lost} = h \cdot A_{wire} \left(T_{wire} - T_{fluid}\right) \tag{B.3a}$$
$$P_{input} = P_{lost} \tag{B.3b}$$
$$\tag{B.3c}$$

where P_{input} is the electrical power input to keep the temperature of the wire constant, I is the current needed, R_{wire} is the resistance of the wire, P_{lost} is the loss of power due to convection, h is the forced convection coefficient, A_{wire} is the area of the wire, T_{wire} is the temperature of the wire and T_{fluid} is the temperature of the air. [19]

For a forced convection case, the h is given by the Equation B.4. [19].

$$h = \frac{Nu \cdot k_f}{d} \tag{B.4a}$$
$$Nu = \left(a + b \cdot U_{fluid}^{n}\right) \tag{B.4b}$$

where Nu is the Nusselt number, k_f is the heat conductivity of the air, d is the diameter of the wire, a and b are constant and U_{fluid} is the fluid velocity.[19]

Therefore:

$$I^2 R_{wire} = h \cdot A_{wire} \left(T_{wire} - T_{fluid}\right) \tag{B.5}$$

Using Equation B.4, equation for power loss in terms of Nusselt's number, area of wire and temperature difference can be found:

$$I^2 R_{wire} = \frac{Nu \cdot k_f}{d} \cdot A_{wire}\left(T_{wire} - T_{fluid}\right) \tag{B.6}$$

B.2. VELOCITY CALIBRATION

Before starting an experiment with HWA, velocity calibration needs to be done, i.e. velocity is found in terms of voltage gradient across the wire in order to maintain constant temperature.

At the first, the flow conditions are set, and velocity of the flow is measured using some other equipment such as a pitot tube. Then the hot-wire probe is immersed in the flow and voltage is measured using a voltmeter. These steps are repeated for several velocities and data for velocity and related voltage is collected. As $Nu = a_1 + b_1 Re^n$, therefore $Nu = a_2 + b_2 Re^n$ Along with this, using Equation B.3 and Equation B.4, it can be found that $E^2 \propto U^n_{fluid}$. (seeEquation B.7) [19]

$$E^2 = I^2 R^2_{wire} \tag{B.7a}$$

$$\therefore E^2 = \left(T_{wire} - T_{fluid}\right)\left(a_3 + b_3 \cdot U^n_{fluid}\right) \tag{B.7b}$$

$$\therefore E^2 \propto U^n_{fluid} \;\; within \approx 0.5 \tag{B.7c}$$

Temperature and Pressure Correction: During the measurements, temperature and pressure might vary from the calibration conditions. This will have an effect on the relationship between voltage difference across the hot-wire and the measured velocity. To take the temperature variation into account, Equation B.8 is used, where E_{corr} is the corrected voltage difference, E_{un} is the measured voltage difference, $T_{opr,HWA}$ is the operating temperature of hot-wire, T_{calib} is the temperature during calibration and T_{amb} is the temperature during actual measurements.

$$E_{corr} = E_{un}\sqrt{\frac{T_{opr,HWA} - T_{calib}}{T_{opr,HWA} - T_{amb}}} \tag{B.8}$$

Using E_{corr} from Equation B.8 in Equation B.7, V_{un} is found and then corrected using Equation B.9. This equation is for correction in velocity for the pressure variation. In this equation, V_{corr} represents the corrected velocity, P_{calib} and P_{meas} are the pressure during calibration and measurement campaigns respectively.

$$V_{corr} = V_{un}\frac{P_{calib}}{P_{meas}} \tag{B.9}$$

B.3. HOT-WIRE ANEMOMETRY MEASUREMENTS IN 2D AND 3D

Generally the hot-wire anemometry is used for one dimensional flows, but it is also possible to do 2-dimensional and 3-dimensional measurements with it. There are many types of probes available: Miniature probe, Gold-plated probe, Film Probe, Fibre Film probe, X-probe, Split fibre probe and tri-axial probe. X-probe and Split fibre probe can be used for 2D measurements and tri-axial probe

is used for 3D measurements. [19]

Figure B.2 shows a X-probe. In this 2D velocity component can be found using Equation B.10 and Equation B.11. [19]

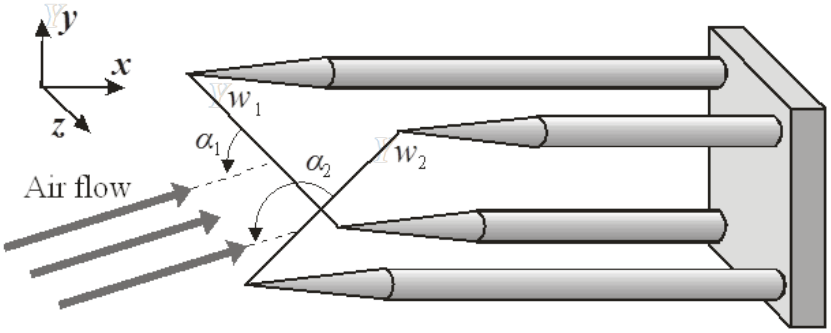

Figure B.2: X-probe for HWA [19]

$$U = U_1 cos\alpha_1 + U_2 sin\alpha_2 \tag{B.10}$$

$$V = U_1 sin\alpha_1 - U_2 cos\alpha_2 \tag{B.11}$$

where U_1 and U_2 can be found from directional calibrations and yaw coefficients. [19]

Using an tri- axial probe, velocity measurements in 70 degrees around the probe axis can be made.

C

Load Determination from Velocity Field

In this section, principles of load distribution from velocity field is discussed. There have been many methods purposed for load determination: Imaichi and Ohmi (1983) for 2D incompressible flows, NOCA *et al.* [69], Noca *et al.* [70] and van Oudheusden *et al.* [66]. In this section, method described uses momentum equation to acquire forces acting on the body from velocity field and its derivative.

C.1. Steady, In-compressible Flows

At first, method for steady incompressible flows is discussed. Figure C.1 shows and airfoil immersed in a steady, incompressible flow. Using integral form of momentum equation for the complete control volume, i.e., S = a-b-c-d-e-f-g-h-i-a, gives Equation C.1 in case there is no body in the volume: [20]

$$-\oiint_S (\rho \vec{V} \cdot dS)\, u - \oiint_S (p dS) + \oiint_S \tau dS = 0 \tag{C.1}$$

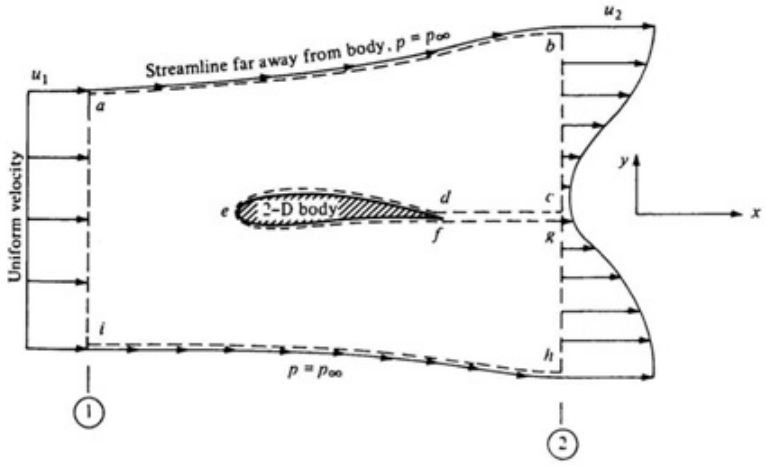

Figure C.1: Control Volume around the body [20]

where first term represent momentum flux through the control surface, second term represents forces due to pressure and last term is for viscous shear stresses. Contribution from c-d and f-g is not taken into account as flux, pressure forces and viscous forces cancel each other out here. [20]

As stated by Newton's third law, for every action there is equal and opposite reaction. When a body is immersed in the flow, the body exerts equal and opposite force back on the flow, hence, this force is given by Equation C.3

$$-\oiint_S (\rho \vec{V} \cdot dS)\, u - \oiint_S (p dS) + \oiint_S \tau dS = \vec{F} \tag{C.2}$$

When control volume is taken far from the body, it can be assumed that viscous forces are negligible. The velocity data is provided from PIV. Hence the only unknown is pressure.[20]

Pressure can be found using differential form of momentum equation:

$$\begin{aligned} \frac{D\vec{V}}{Dt} &= -\frac{\nabla p}{\rho} + \vec{F} + \vec{F}_{visc} \\ \frac{\partial \vec{V}}{dt} + \vec{V} \cdot \nabla \vec{V} &= -\frac{\nabla p}{\rho} + \vec{F} + \vec{F}_{visc} \end{aligned} \tag{C.3}$$

As the flow is steady and viscous forces are negligible, the equation becomes: [20]

$$\vec{V} \cdot \nabla \vec{V} = -\frac{\nabla p}{\rho} + \vec{F} \tag{C.4}$$

$$\nabla p = -\rho \left(\vec{V} \cdot \nabla \vec{V}\right) + \mu \nabla^2 \vec{V} \tag{C.5}$$

Right hand side of the equation can be computed from velocity data from PIV. Then pressure can be found by integrating the pressure gradient, assuming pressure, p_0 near the wall of control volume is known. Now that pressure is known, Equation C.2 can be solved to get force distribution. [20]

C.2. UNSTEADY FLOWS

Method for unsteady flows is very similar, where pressure gradient is computed using Equation C.6, which is then integrated for pressure

$$\nabla p = -\rho \left(\frac{\partial \vec{V}}{dt} + \vec{V} \cdot \nabla \vec{V} \right) + \mu \nabla^2 \vec{V} \tag{C.6}$$

As Equation C.3 is valid for both steady and unsteady, force distribution can then be found from that equation. In integral form, this equation becomes:

$$\vec{F} = -\rho \int\int\int \frac{\partial \left(\rho \vec{V}\right)}{\partial t} dV(t) - \oiint_S \rho \left(\vec{V}.\vec{n}\right) \cdot \vec{V} dS - \oiint_S p \vec{n} dS + \oiint_S \tau \vec{n} dS \tag{C.7}$$

Therefore, for stationary frame of reference, force in axial and radial direction is given by Equation C.8: [71]

$$\begin{aligned}\begin{bmatrix} F_x \\ F_y \end{bmatrix} &= \int \mu \begin{bmatrix} 2\frac{du}{dx} & \left(\frac{du}{dy}+\frac{dv}{dx}\right) \\ \left(\frac{du}{dy}+\frac{dv}{dx}\right) & 2\frac{dv}{dy} \end{bmatrix} \cdot \vec{n} ds \\ &- \int \rho \begin{bmatrix} uu & uv \\ uv & vv \end{bmatrix} \cdot \vec{n} ds - \frac{d}{dt} \int \rho \begin{bmatrix} u \\ v \end{bmatrix} dxdy \\ &- \int \rho \begin{bmatrix} \overline{u'u'} & \overline{u'v'} \\ \overline{u'v'} & \overline{v'v'} \end{bmatrix} \cdot \vec{n} ds - \int \begin{bmatrix} p & 0 \\ 0 & p \end{bmatrix} \cdot \vec{n} ds \end{aligned} \tag{C.8}$$

$$C_t = \frac{\vec{F}_x}{0.5\rho V_\infty^2} \tag{C.9}$$

where $\vec{n}ds = \begin{bmatrix} -dy \\ dx \end{bmatrix}$

Equation C.10 and Equation C.11 show expressions to calculate pressure gradient: [71]

$$\nabla p = -\rho \left(\frac{\partial \vec{V}}{dt} + \vec{V} \cdot \nabla \vec{V} \right) + \mu \nabla^2 \vec{V} \tag{C.10}$$

$$\begin{aligned}\begin{bmatrix} \frac{dp}{dx} \\ \frac{dp}{dy} \end{bmatrix} &= -\rho \begin{bmatrix} \frac{du}{dt} \\ \frac{dv}{dt} \end{bmatrix} - \rho \begin{bmatrix} u\frac{du}{dx} + v\frac{du}{dv} \\ u\frac{dv}{dx} + v\frac{dv}{dy} \end{bmatrix} \\ &- \rho \begin{bmatrix} \frac{d\overline{u'u'}}{dx} + \frac{d\overline{u'v'}}{dv} \\ \frac{du'v'}{dx} + \frac{dv'v'}{dy} \end{bmatrix} \\ &+ \mu \begin{bmatrix} \frac{d^2u}{dx^2} + \frac{d^2u}{dy^2} \\ \frac{d^2v}{dx^2} + \frac{d^2v}{dy^2} \end{bmatrix} \end{aligned} \tag{C.11}$$

C.2.1. PRESSURE CALCULATION USING POISSON INTEGRATION

As seen in the equations for load calculation, pressure needs to be calculated first. Pressure can be calculated using Poisson integration as shown by Equation C.12:

$$\nabla^2 p = -\rho \nabla (u \cdot \nabla u) \tag{C.12}$$

In order to calculate pressure, at first pressure gradient is found using Equation C.11. After that pressure is found by solving Poisson pressure equation, given by Equation C.13. [71]

$$\nabla^2 p \approx Dp = g(u,v) \Rightarrow p = D^{-1} p \tag{C.13}$$

where matrix D is found by discretization of Laplace operator using second order finite difference method (as shown in Equation C.14) and $g(u,v)$ is a forcing function found from momentum equation using central finite difference method, given by Equation C.15. [71]

$$Dp = \frac{p_{i+1,j} - 2p_{i,j} + p_{i-1,j}}{\Delta x^2} + \frac{p_{i,j+1} - 2p_{i,j} + p_{i,j-1}}{\Delta y^2} \tag{C.14}$$

$$g(u,v)_{i,j} = \frac{\left(\frac{dp}{dx}\right)_{i+1,j} - \left(\frac{dp}{dx}\right)_{i-1,j}}{2\Delta x} + \frac{\left(\frac{dp}{dy}\right)_{i,j+1} - \left(\frac{dp}{dy}\right)_{i,j-1}}{2\Delta y} \tag{C.15}$$

for $i = 1...n$ and $j = 1...m$

To solve this equation, Neumann condition and Dirchlet boundary conditions on the wake boundaries can be used by calculating pressure with Bernoulli theorem. [71]

C.3. NOCA'S METHOD FOR LOAD DETERMINATION

There is another method of force determination from velocity field presented by NOCA *et al.* [69] (1999). It gives closed form force distribution and is based on momentum distribution. Figure C.2 gives control volume of a body with contour S_b and volume boundary, S.

As represented in NOCA (1999), fluid dynamics force per unit density is represented by *Flux Equation*, given by Equation C.16

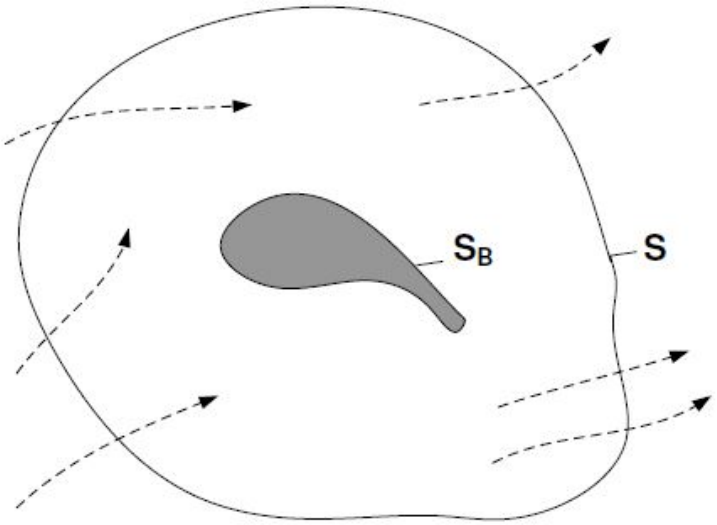

Figure C.2: Control Volume around the body for momentum integration of the flow field [21]

$$\frac{F}{\rho} = -\frac{d}{dt}\oint_{S_b(t)} (\hat{n}\cdot(ux))\,dS + \oint_{S(t)} (\hat{n}\cdot\gamma_{flux})\,dS - \oint_{S_b(t)} (\hat{n}\cdot(u-u_s)\,u)\,dS \tag{C.16}$$

where $\hat{n}$ is normal vector to the body. T is the stress tensor give by $T = \mu\left(\nabla u + \nabla u^T\right)$ and γ_{flux} is given by Equation C.17

$$\begin{aligned}\gamma_{flux} = {} & \frac{1}{2}u^2 I - uu - \frac{1}{N-1}u(x\times\omega) + \frac{1}{N-1}\omega(x\times u) \\ & -\frac{1}{N-1}\left[\left(x\cdot\frac{du}{dt}\right)I - x\frac{du}{dt} + (N-1)\frac{du}{dt}x\right] \\ & +\frac{1}{N-1}\left[x\cdot(\nabla\cdot T)\,I - x(\nabla\cdot T)\right] + T\end{aligned} \tag{C.17}$$

However as shown in the Equation C.17, this method requires determination vorticity, which can lead to source of error for thin boundary layer bodies. Due to this γ_{flux} is represented is terms of pressure:

$$\gamma_{flux} = \frac{p}{\rho} I - uu - \frac{du}{dt} x + T \tag{C.18}$$

However this method also requires determination of pressure. This can be done in the same way as in the previous method using Equation C.19:

$$\nabla p = -\rho \left(\frac{\partial \vec{V}}{dt} + \vec{V} \cdot \nabla \vec{V} \right) + \mu \nabla^2 \vec{V} \tag{C.19}$$

D

ACTUATOR DISC UNDER UNSTEADY LOADING : PRESSURE DISTRIBUTION

D.1. FREQUENCY = 5HZ AND RED. FREQUENCY = 1.57

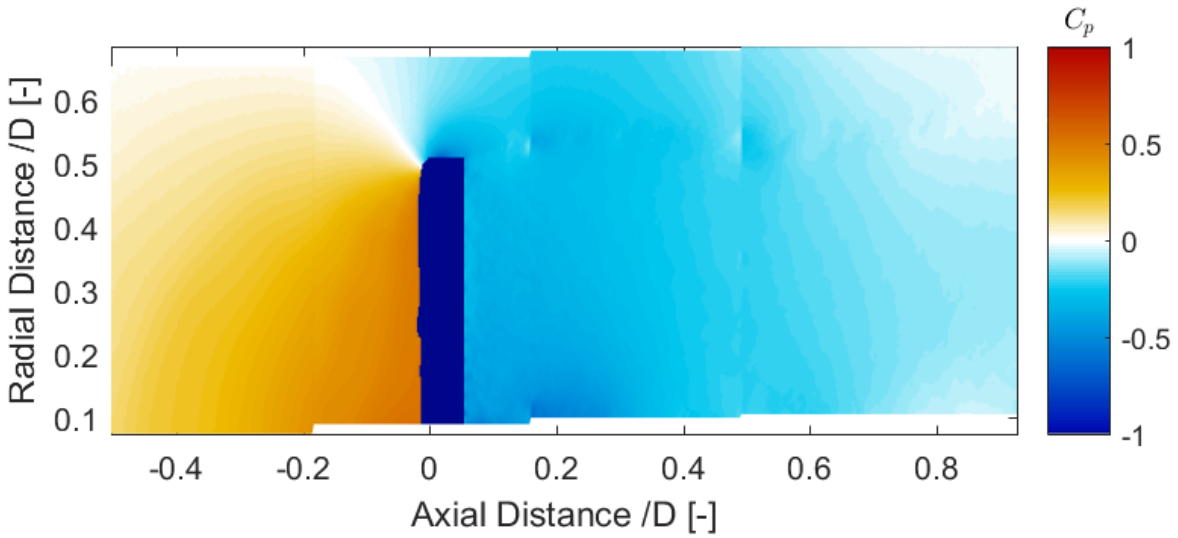

(a) Porosity = 59% (decreasing porosity) and C_T = 0.555

Figure D.1: Pressure Field for porosity change with frequency of 5Hz and Reduced Frequency = 1.57

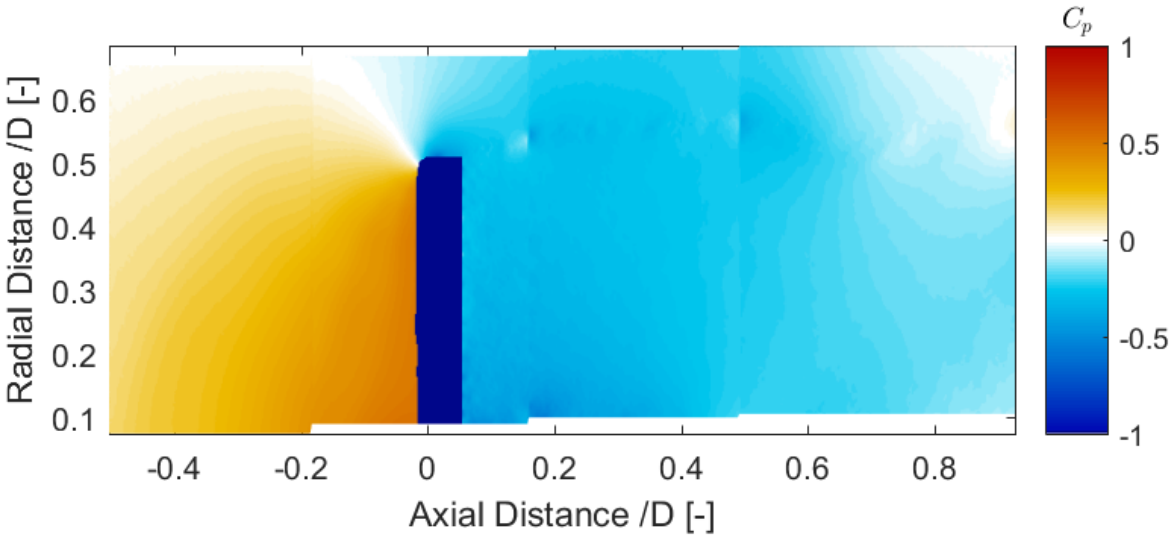

(a) Porosity = 47% (decreasing porosity) and C_T =0.558

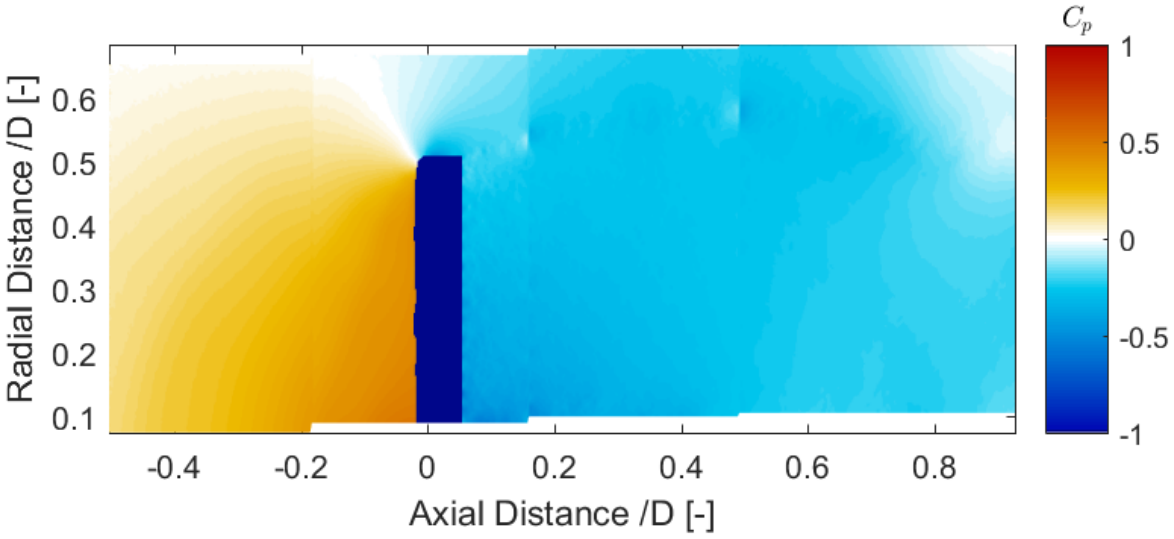

(b) Porosity = 31% (decreasing porosity) and C_T =0.579

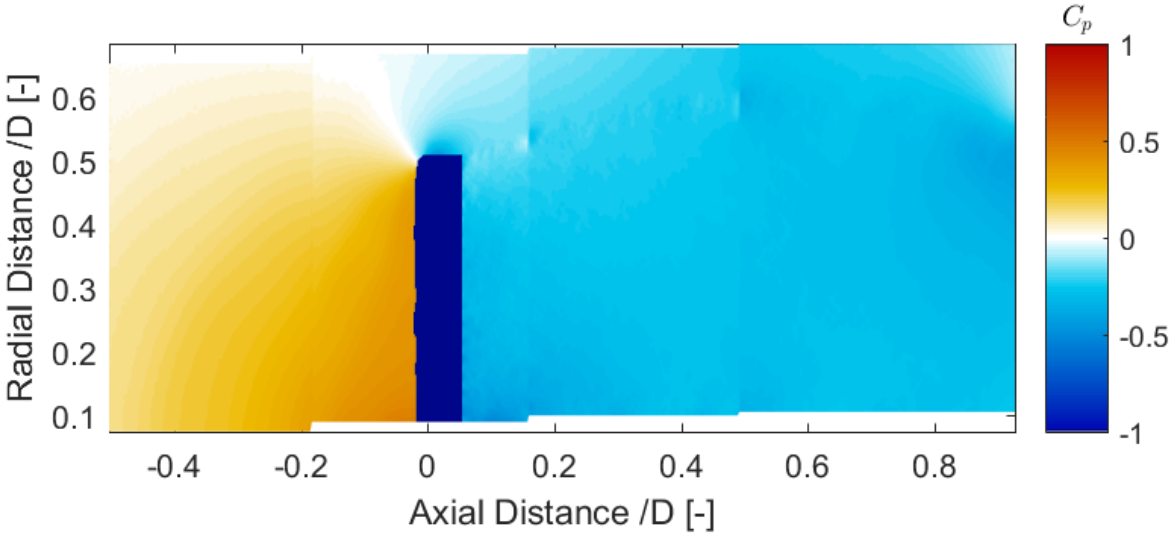

(c) Porosity = 19% (decreasing porosity) and C_T =0.620

Figure D.2: Pressure Field for porosity change with frequency of 5Hz and Reduced Frequency = 1.57

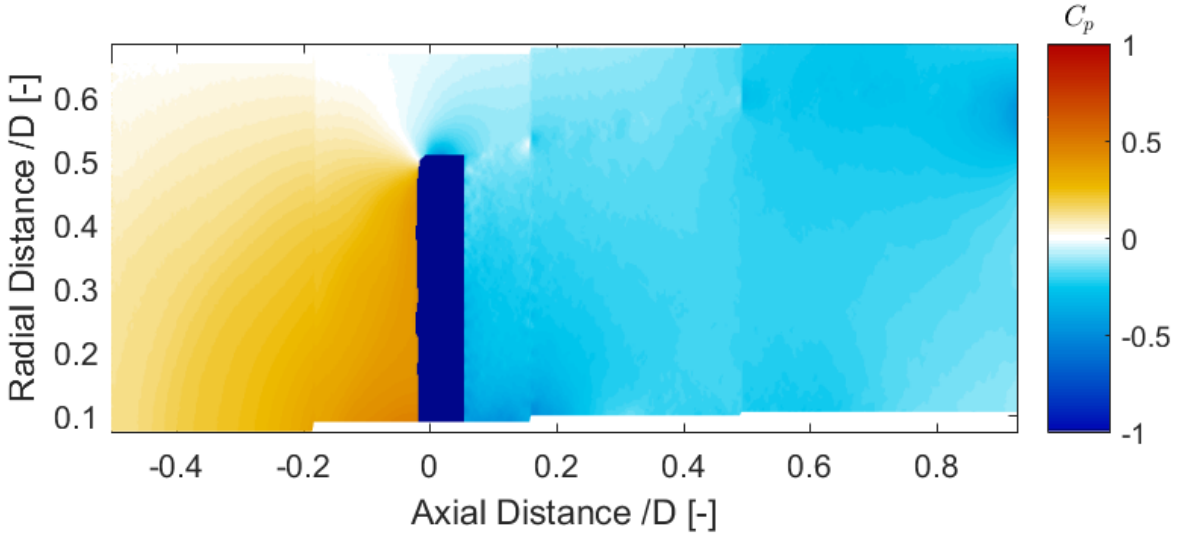

(a) Porosity = 14% (minimum porosity) and C_T = 0.705

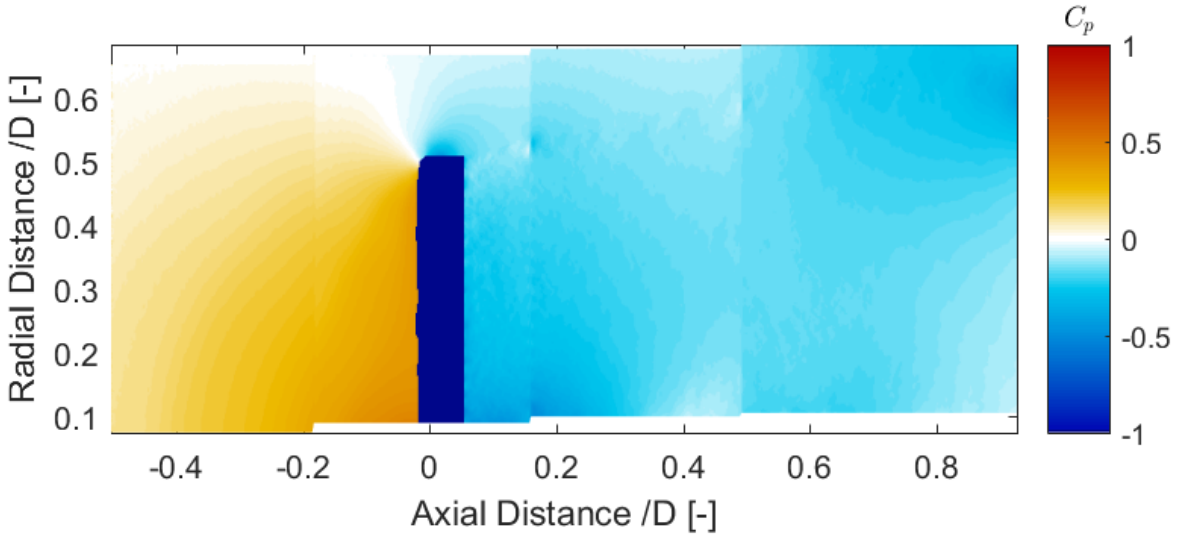

(b) Porosity 19% (increasing porosity) and C_T = 0.697

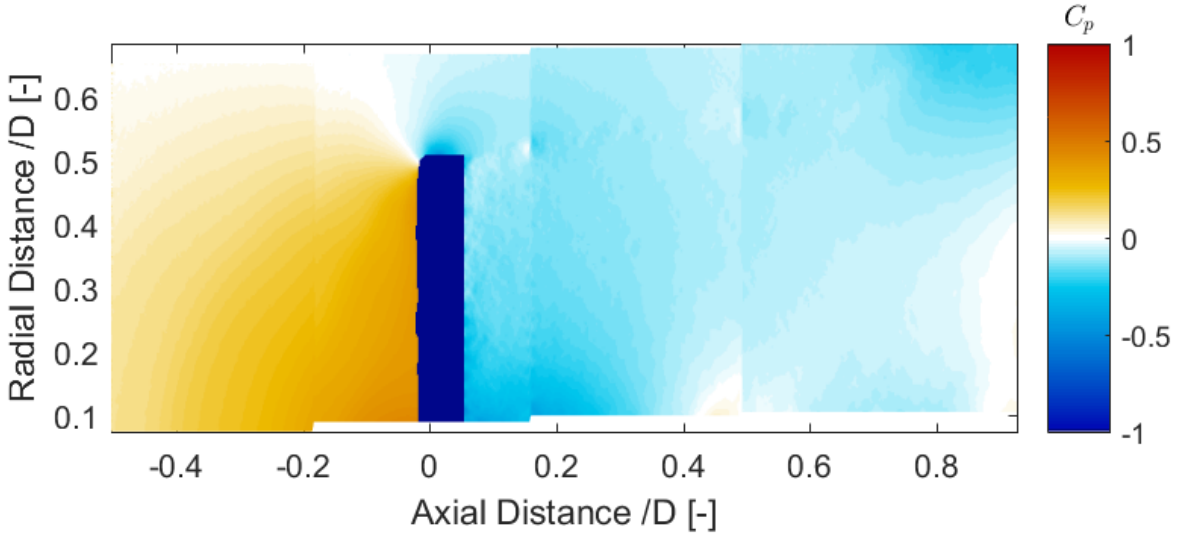

(c) Porosity = 31% (increasing porosity) and C_T = 0.678

Figure D.3: Pressure Field for porosity change with frequency of 5Hz and Reduced Frequency = 1.57

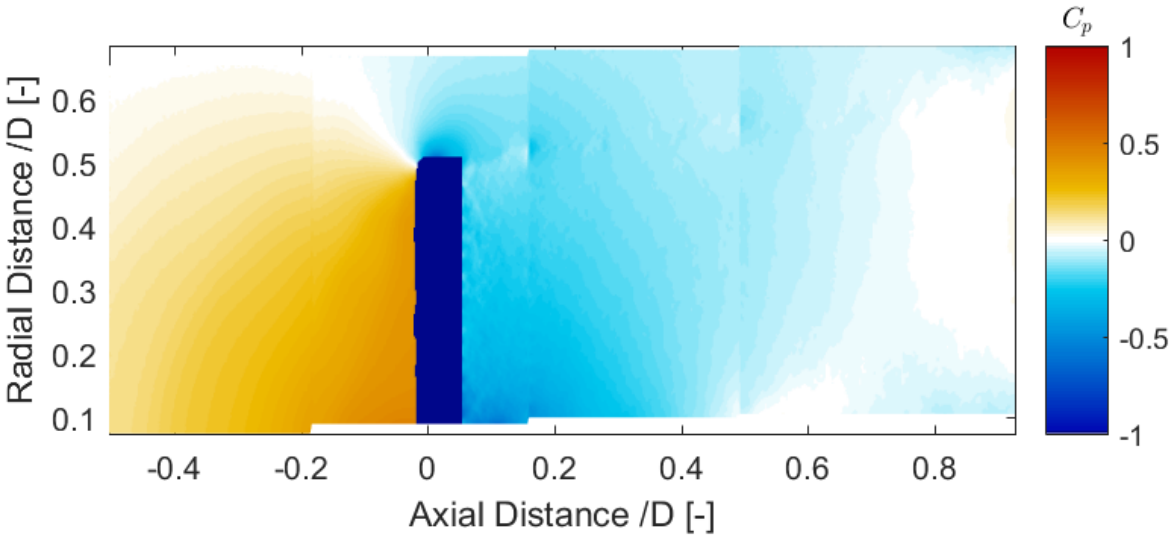

(a) Porosity = 47% (increasing porosity) and C_T = 0.657

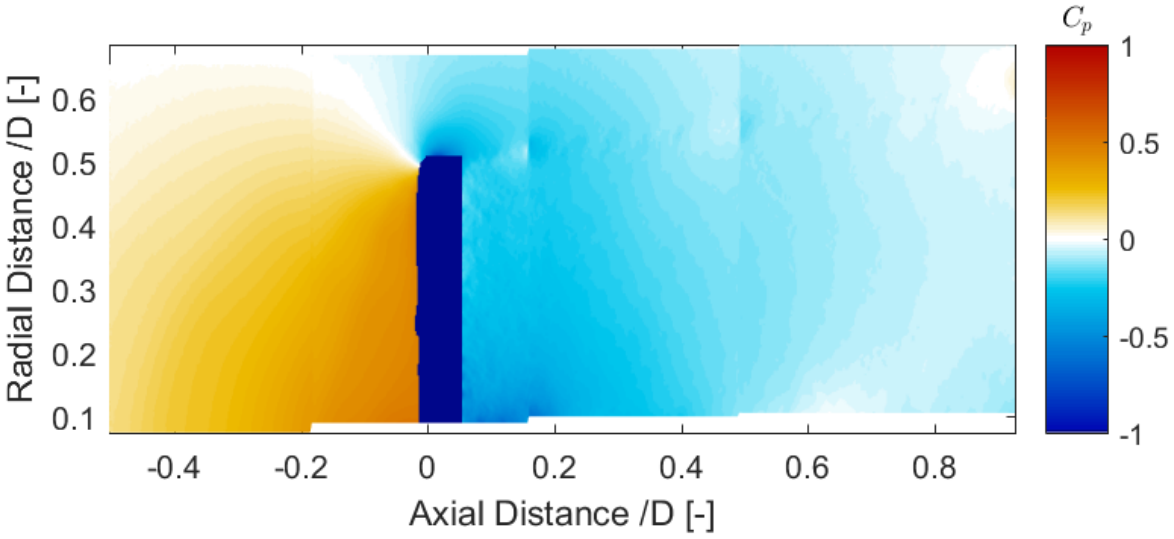

(b) Porosity = 59% (increasing porosity) and C_T = 0.596

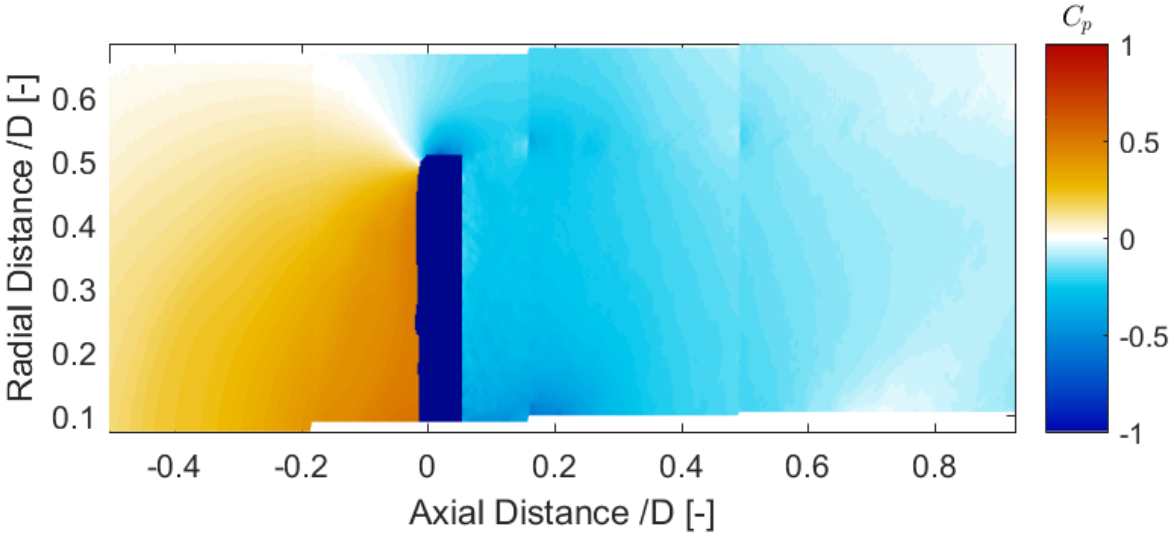

(c) Porosity = 64% (maximum porosity) and C_T = 0.550

Figure D.4: Pressure Field for porosity change with frequency of 5Hz and Reduced Frequency = 1.57

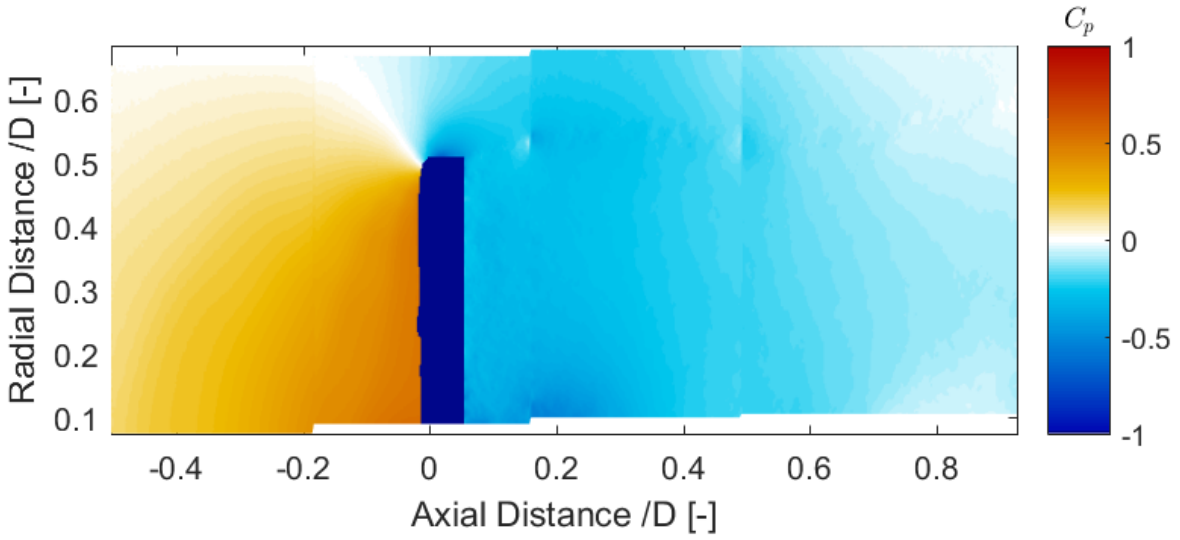

(a) Porosity = 59% (decreasing porosity) and C_T = 0.554

Figure D.5: Pressure Field for porosity change with frequency of 5Hz and Reduced Frequency = 1.57

D.2. FREQUENCY = 3HZ AND RED. FREQUENCY = 0.94

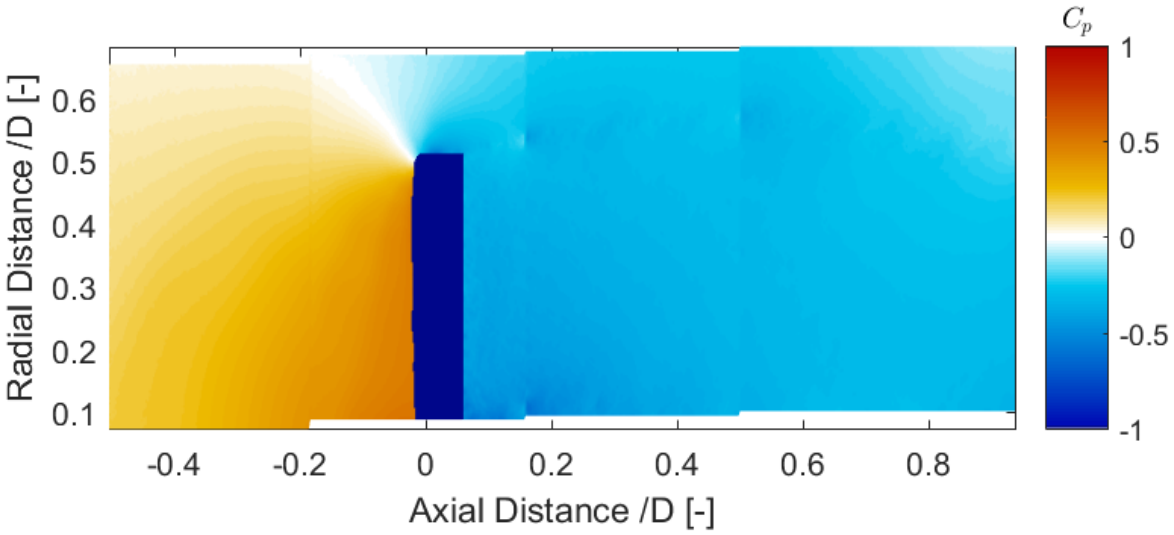

(a) Porosity = 59% (decreasing porosity) and C_T = 0.527

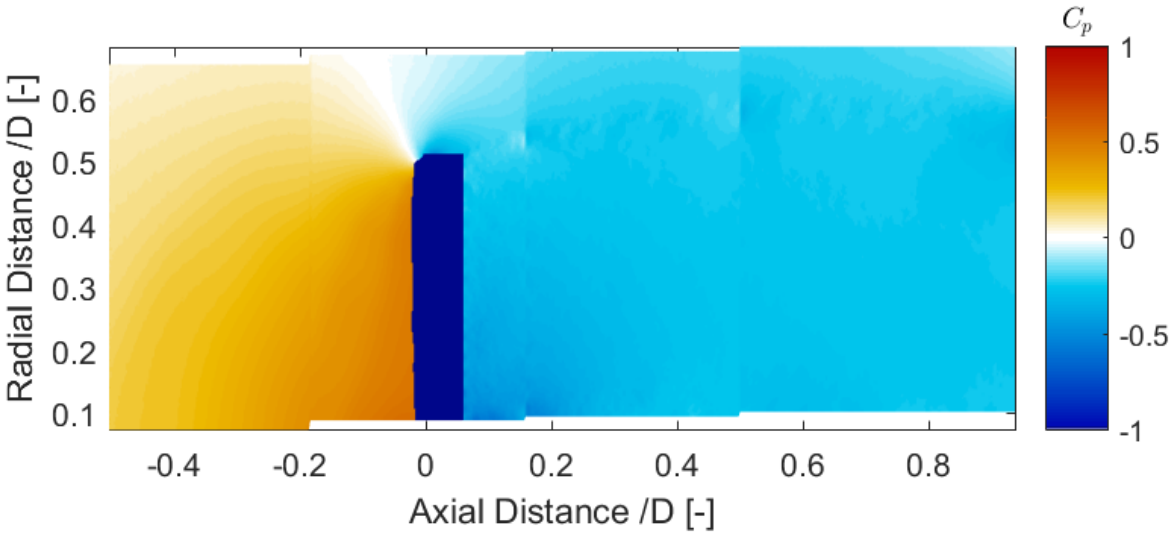

(b) Porosity = 47% (decreasing porosity) and C_T = 0.593

Figure D.6: Pressure Field for porosity change with frequency of 3Hz and Red. Freq = 0.94

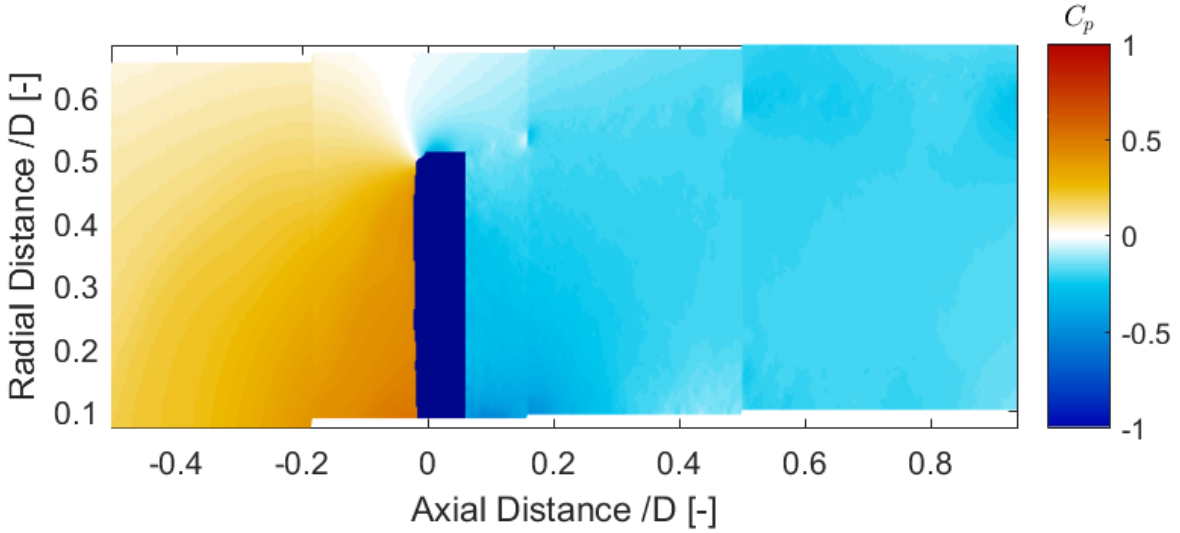

(a) Porosity = 31% (decreasing porosity) and C_T = 0.622

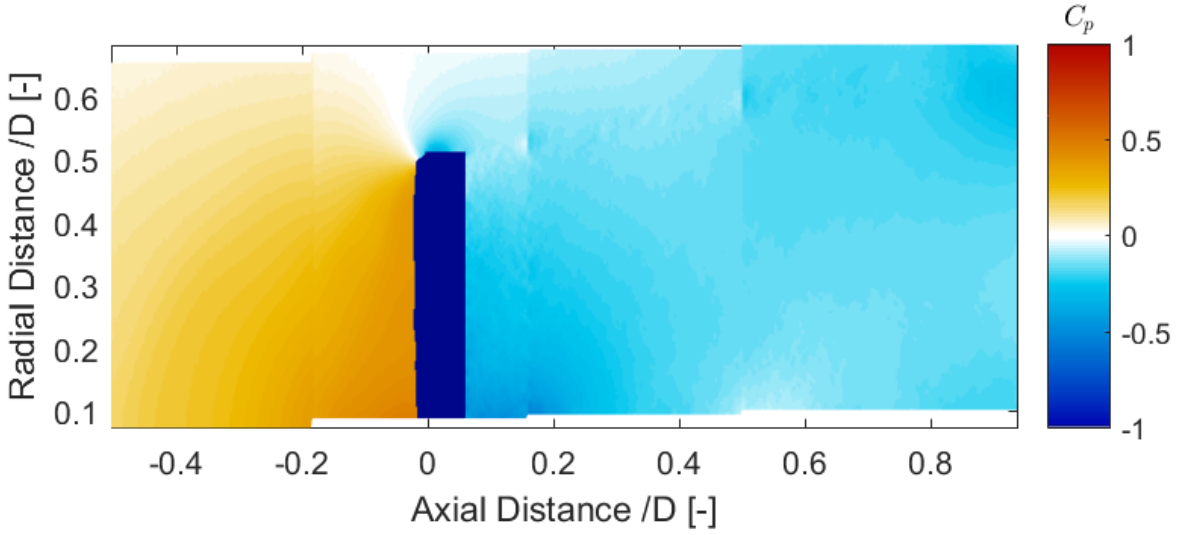

(b) Porosity = 19% (decreasing porosity) and C_T = 0.649

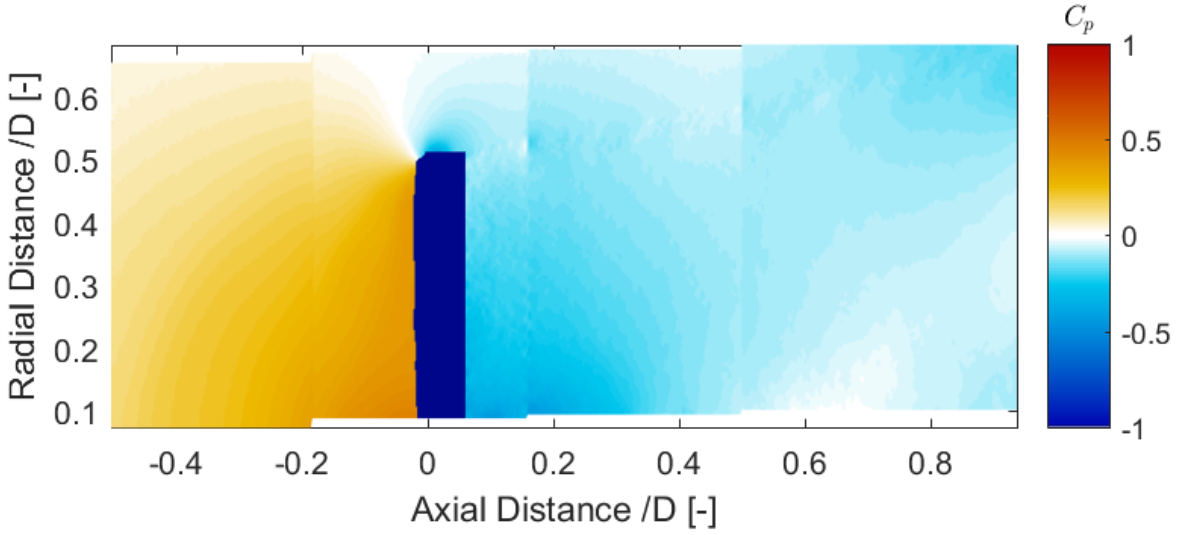

(c) Porosity = 14% (minimum porosity) and C_T = 0.684

Figure D.7: Pressure Field for porosity change with frequency of 3Hz and Red. Freq = 0.94

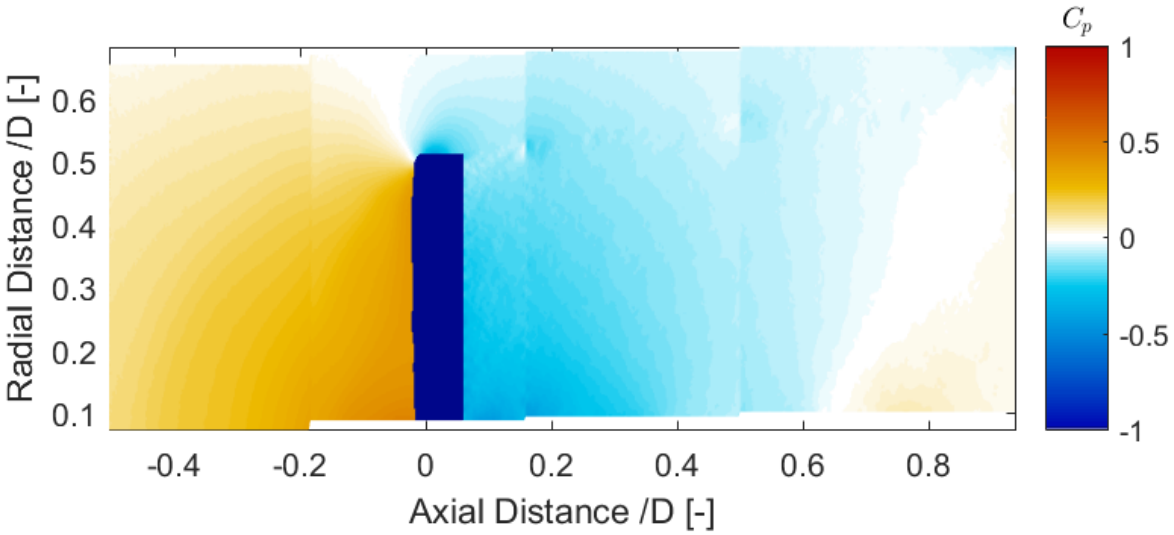

(a) Porosity = 19% (increasing porosity) and C_T = 0.671

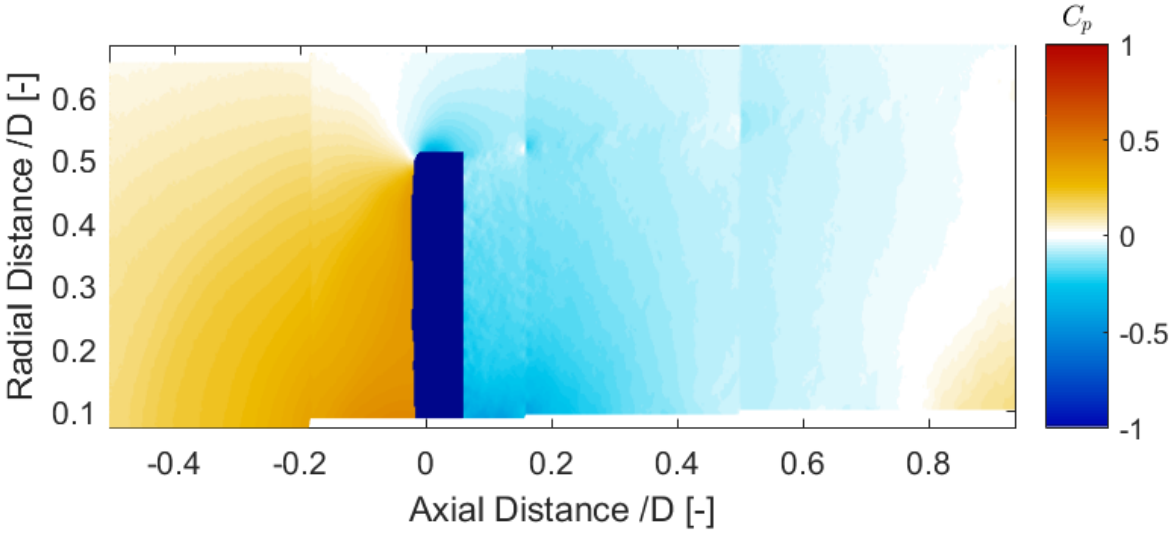

(b) Porosity = 31% (increasing porosity) and C_T = 0.651

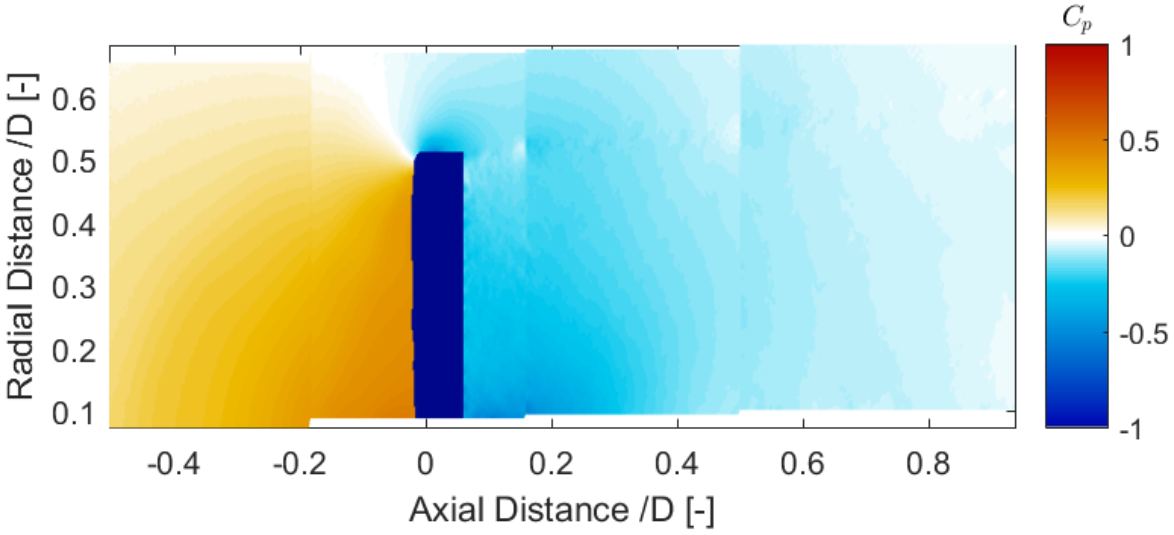

(c) Porosity = 47% (increasing porosity) and C_T = 0.612

Figure D.8: Pressure Field for porosity change with frequency of 3Hz and Red. Freq = 0.94

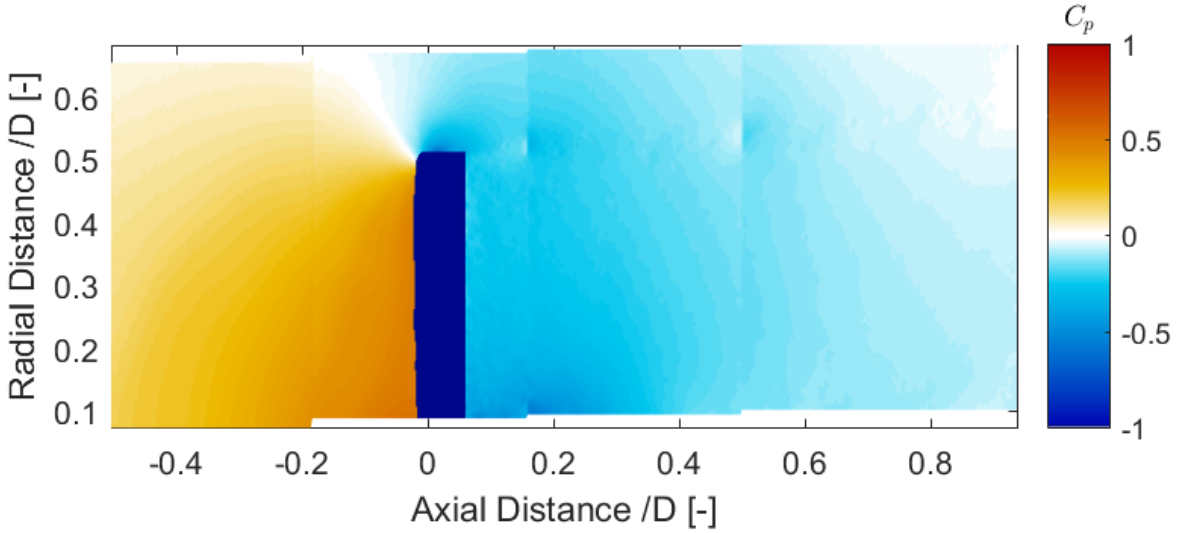

(a) Porosity = 59% (increasing porosity) and C_T = 0.584

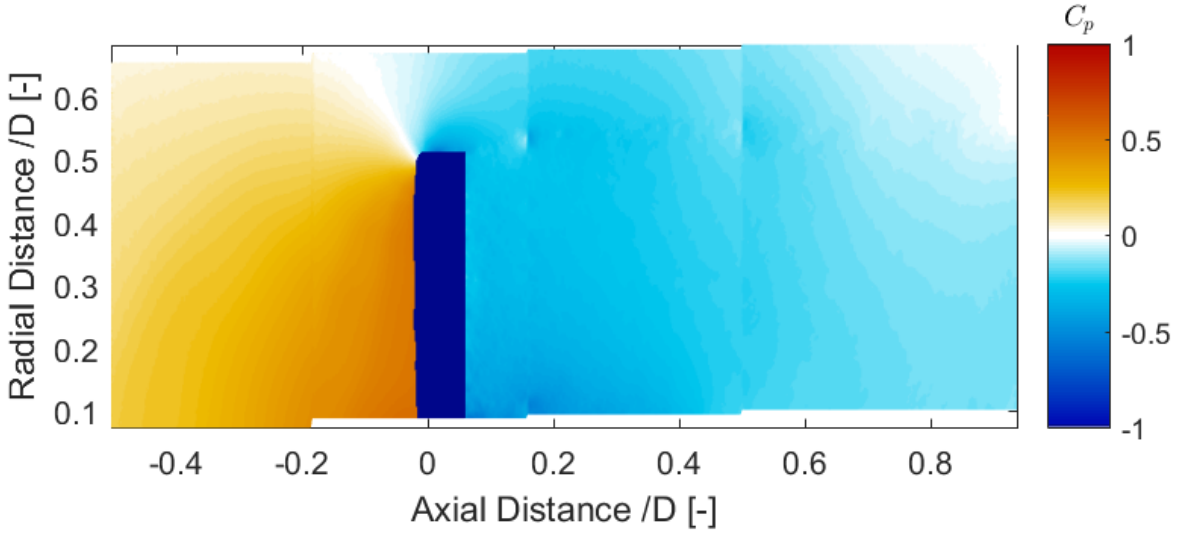

(b) Porosity = 64% (maximum porosity) and C_T = 0.569

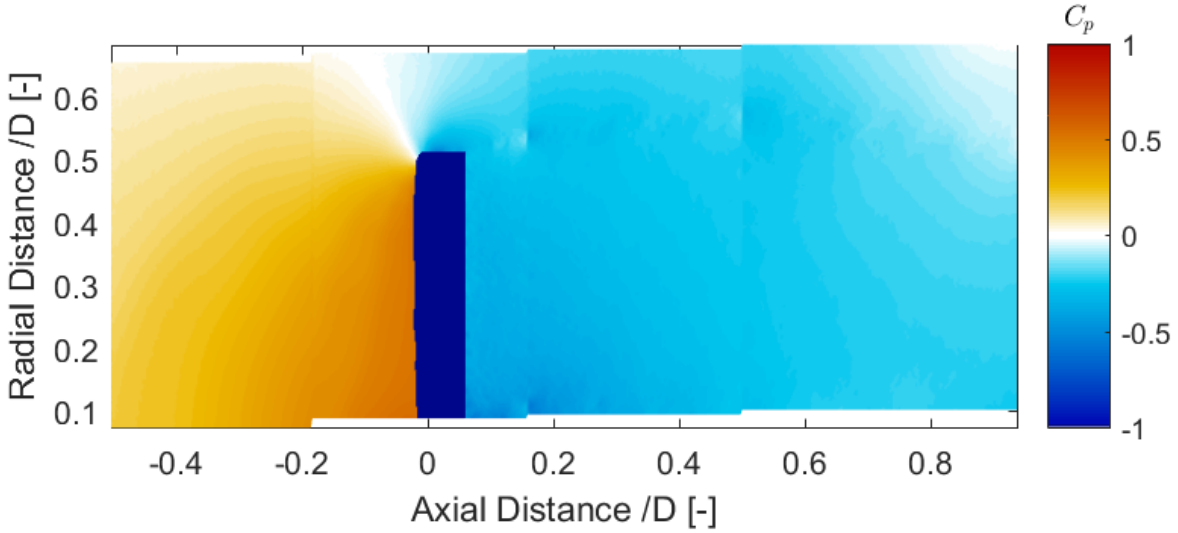

(c) Porosity = 59% (decreasing porosity) and C_T = 0.572

Figure D.9: Pressure Field for porosity change with frequency of 3Hz and Red. Freq = 0.94

D.3. FREQUENCY = 1.5HZ AND RED. FREQUENCY = 0.47

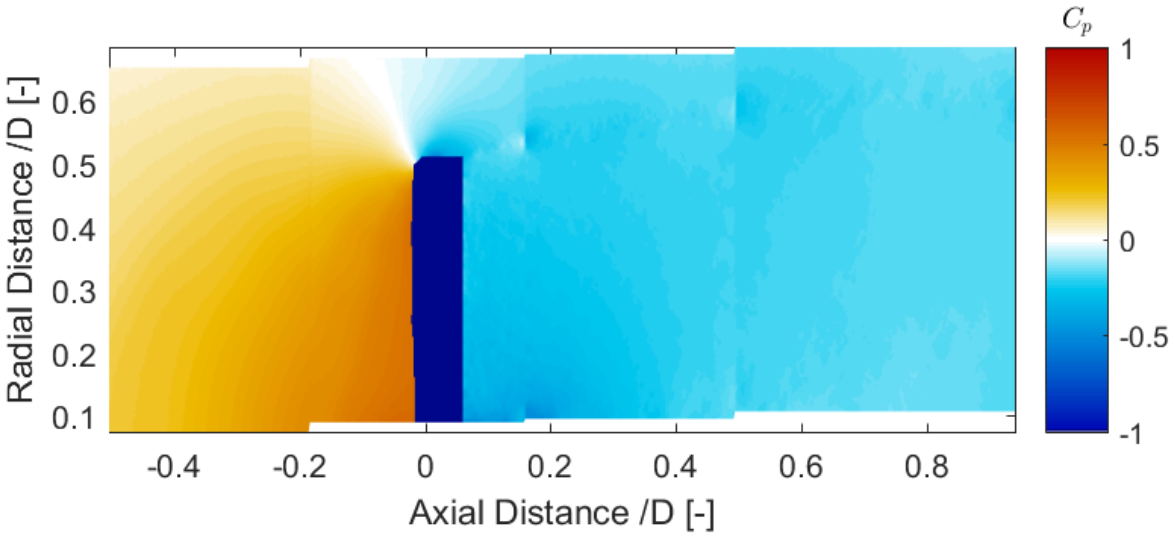

(a) Porosity = 59% (decreasing porosity) and C_T = 0.566

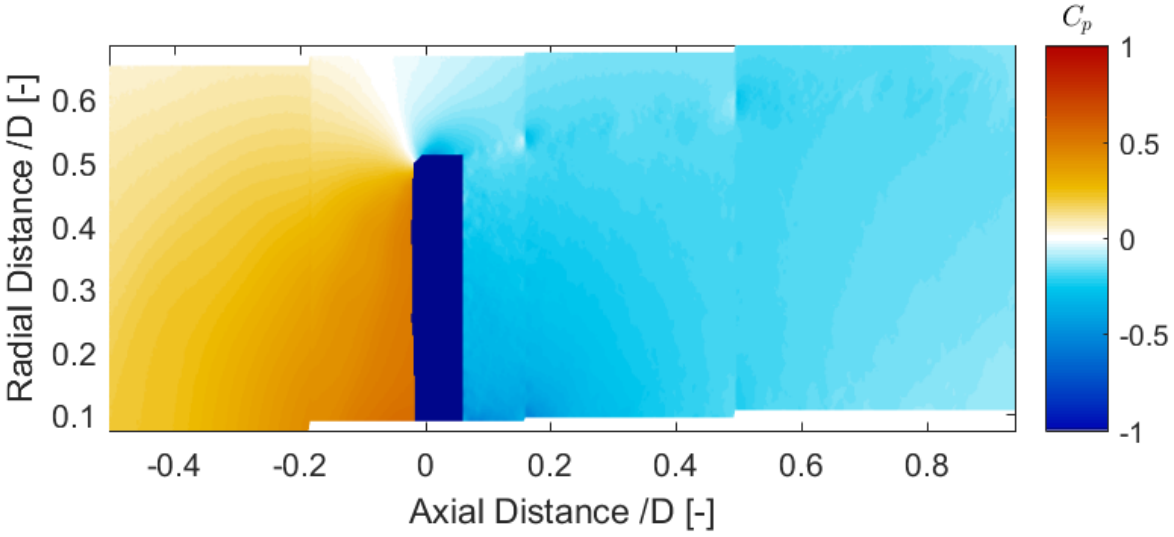

(b) Porosity = 47% (decreasing porosity) and C_T = 0.605

Figure D.10: Pressure Field for porosity change with frequency of 1.5Hz and Red. Frequency = 0.47

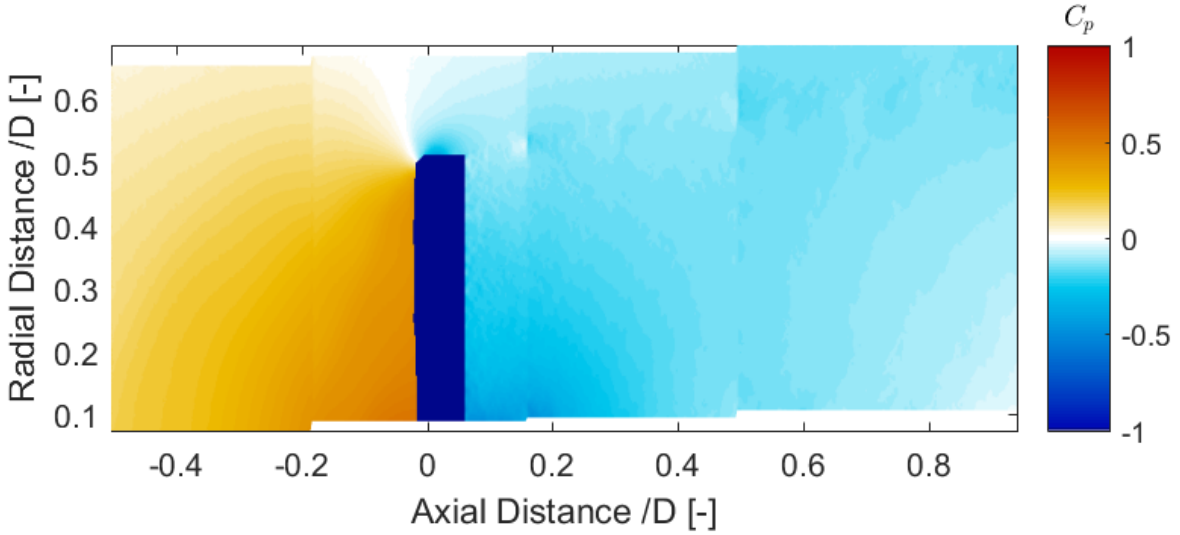

(a) Porosity = 31% (decreasing porosity) and C_T = 0.639

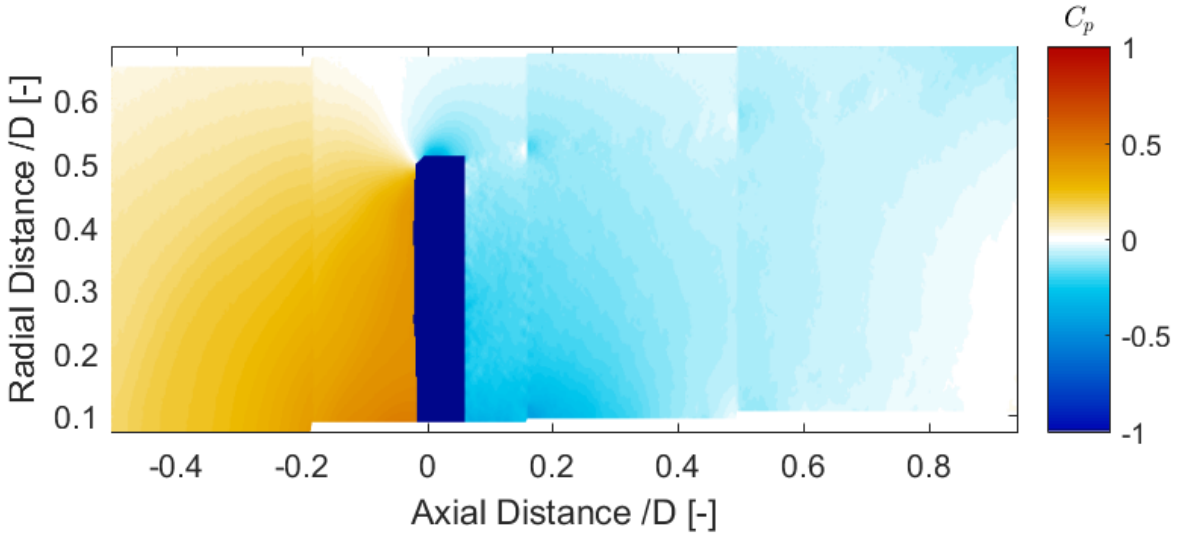

(b) Porosity = 19% (decreasing porosity) and C_T = 0.666

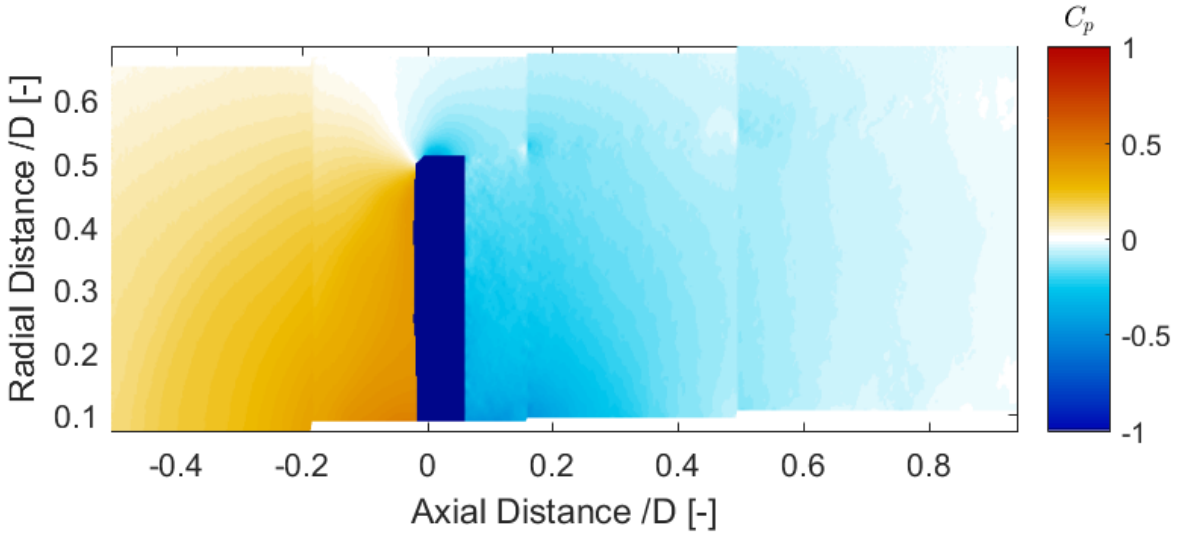

(c) Porosity = 14% (minimum porosity) and C_T = 0.692

Figure D.11: Pressure Field for porosity change with frequency of 1.5Hz and Red. Frequency = 0.47

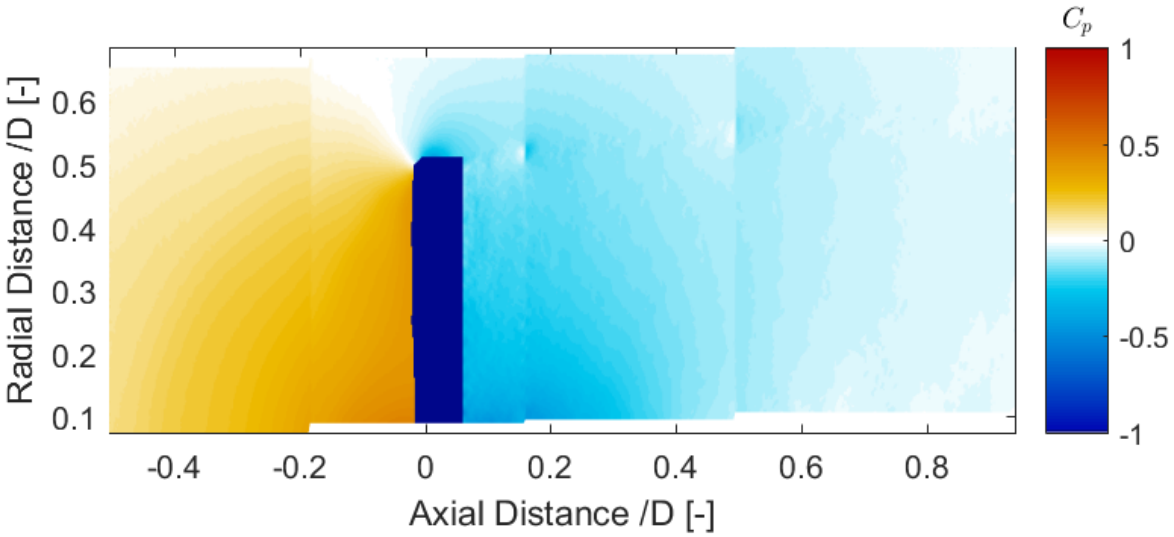

(a) Porosity = 19% (increasing porosity) and C_T = 0.675

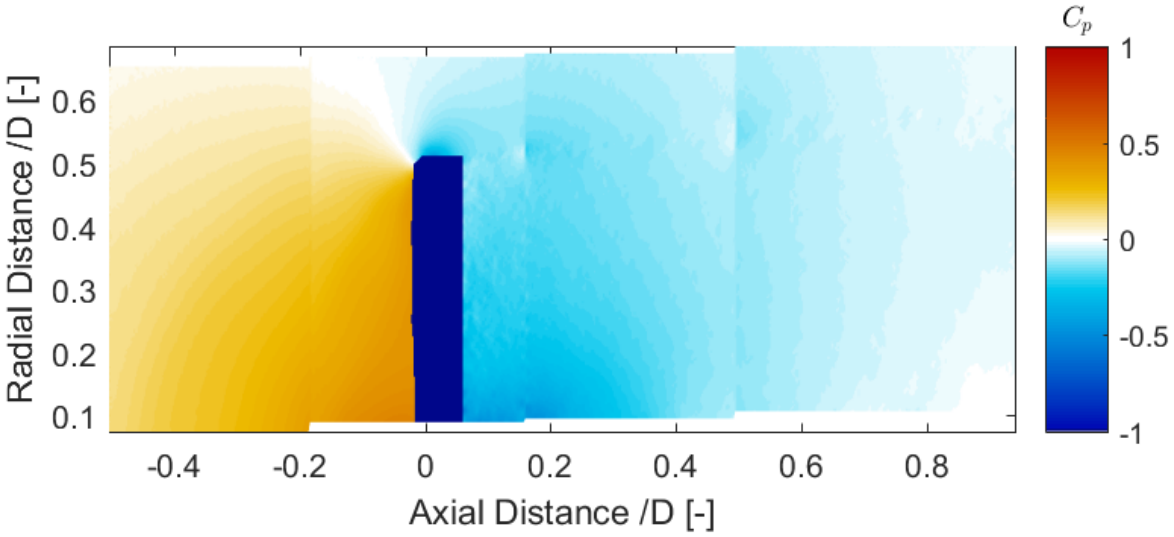

(b) Porosity = 31% (increasing porosity) and C_T = 0.651

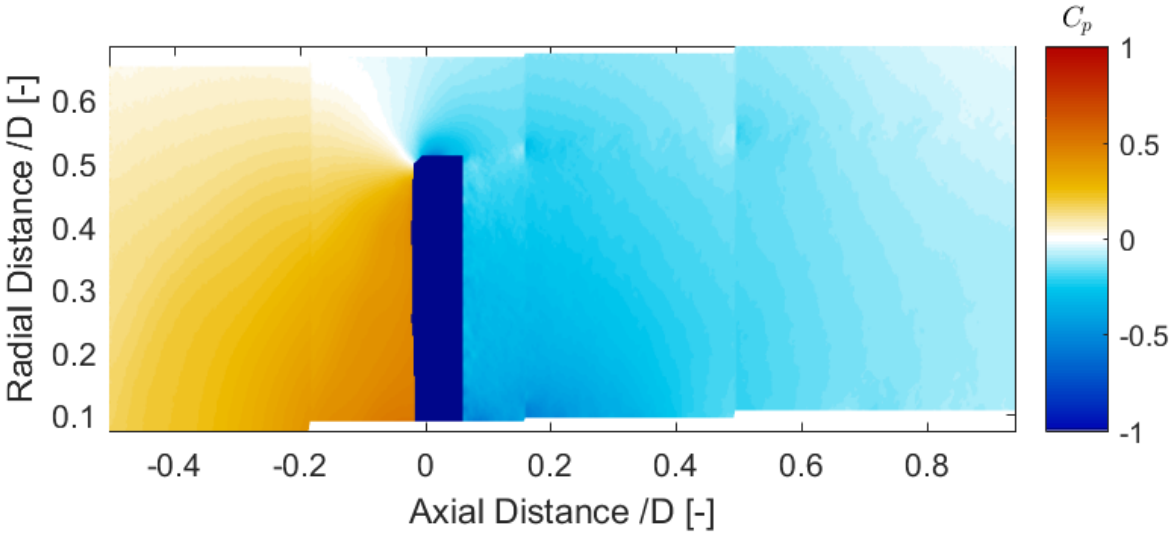

(c) Porosity = 47% (increasing porosity) and C_T = 0.616

Figure D.12: Pressure Field for porosity change with frequency of 1.5Hz and Red. Frequency = 0.47

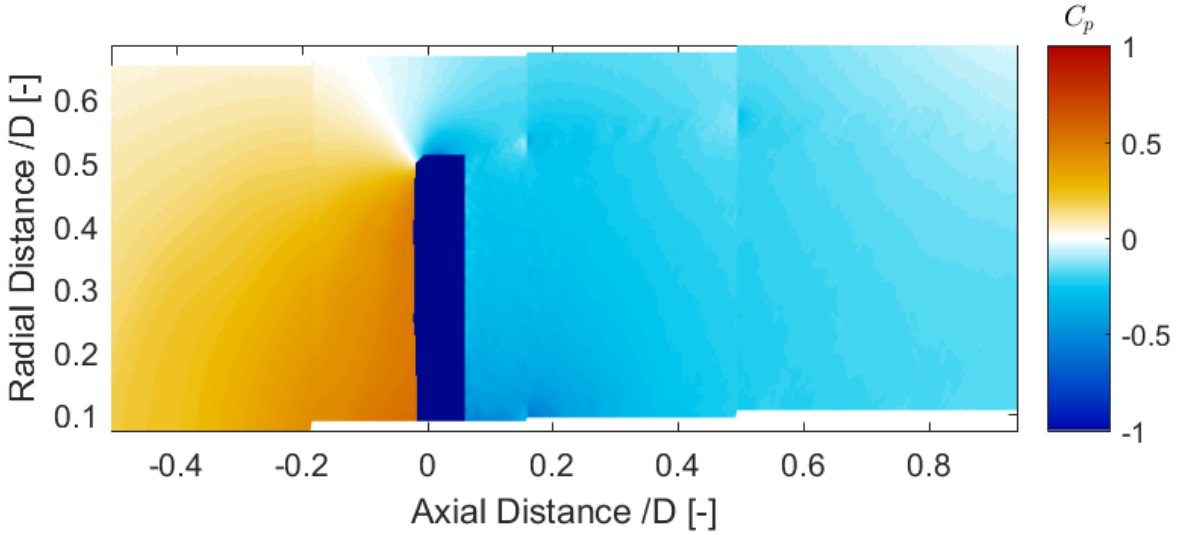

(a) Porosity = 59% (increasing porosity) and C_T = 0.575

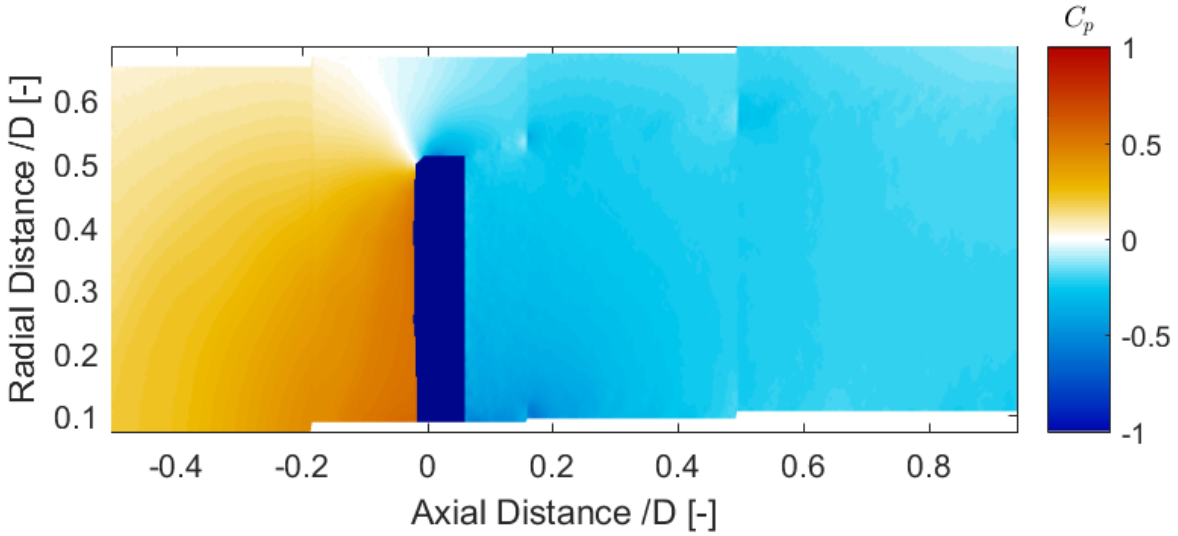

(b) Porosity = 64% (maximum porosity) and C_T = 0.555

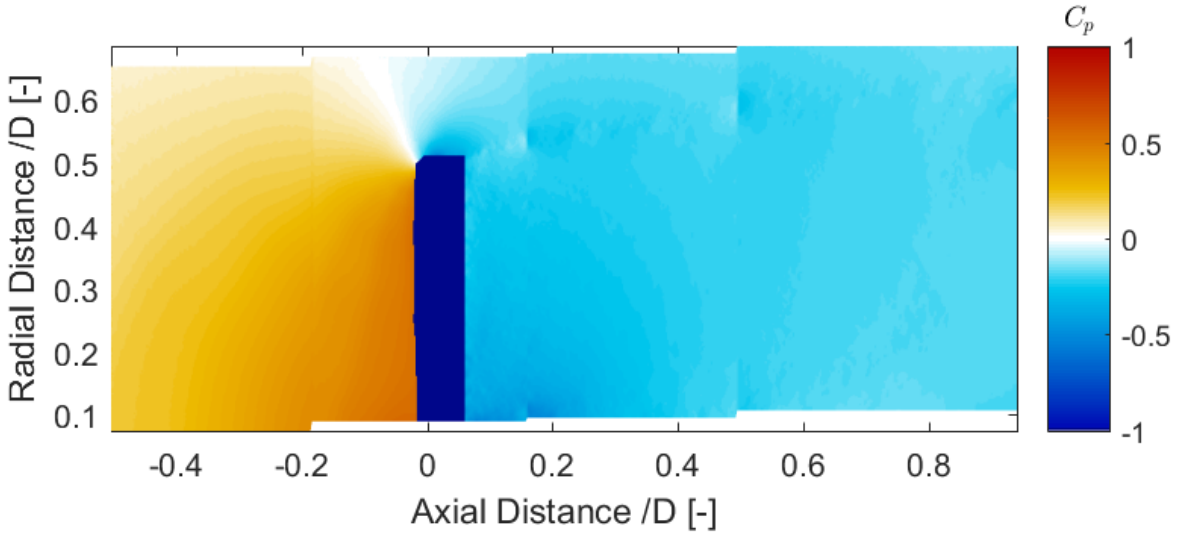

(c) Porosity = 59% (decreasing porosity) and C_T = 0.565

Figure D.13: Pressure Field for porosity change with frequency of 1.5Hz and Red. Frequency = 0.47

E

Extra plots for unsteady loading over Actuator Disc

E.1. Frequency = 5Hz and Reduced Frequency = 1.57

In this section, normalized axial velocity field from the experiment are presented for the 5Hz frequency load case. These fields are same as in subsection 7.2.1 with different colour scale.

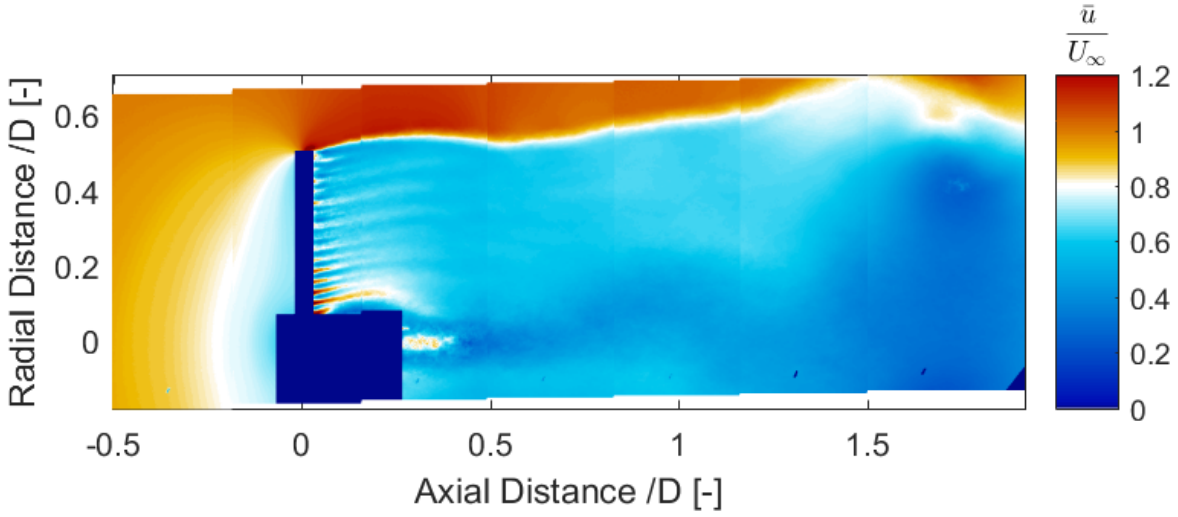

(a) Porosity = 59% (decreasing porosity) and C_T = 0.555

Figure E.1: Normalized Axial Velocity Field used for porosity changing with frequency = 5Hz and reduced frequency = 1.57 (Experiment)

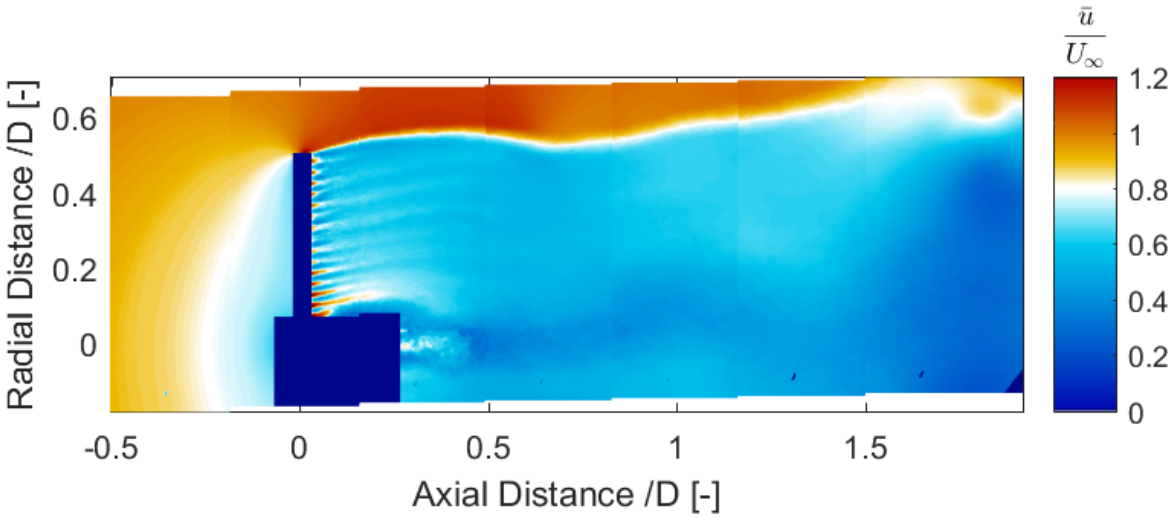

(a) Porosity = 47% (decreasing porosity) and C_T = 0.557

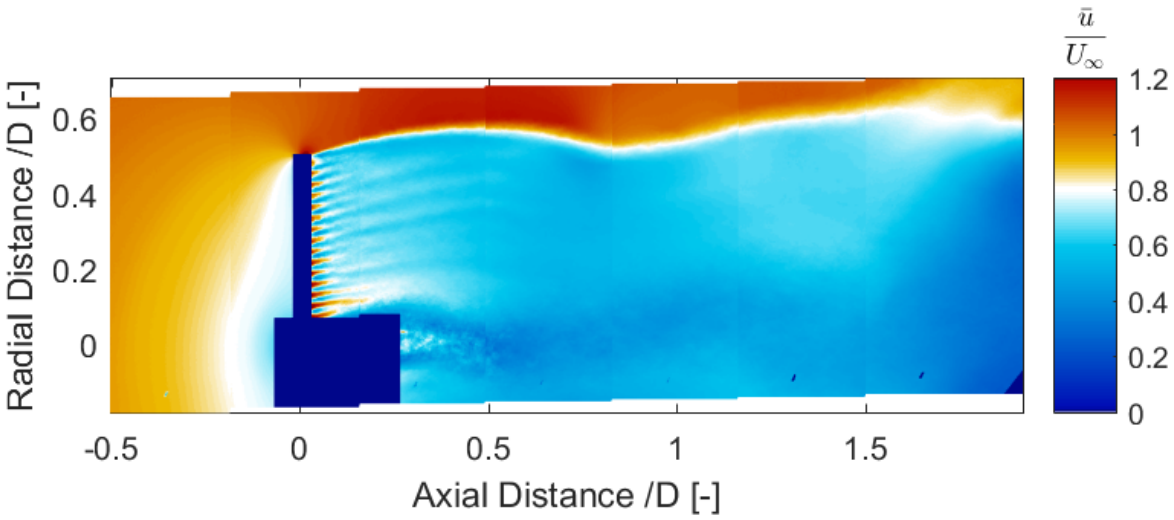

(b) Porosity = 31% (decreasing porosity) and C_T = 0.579

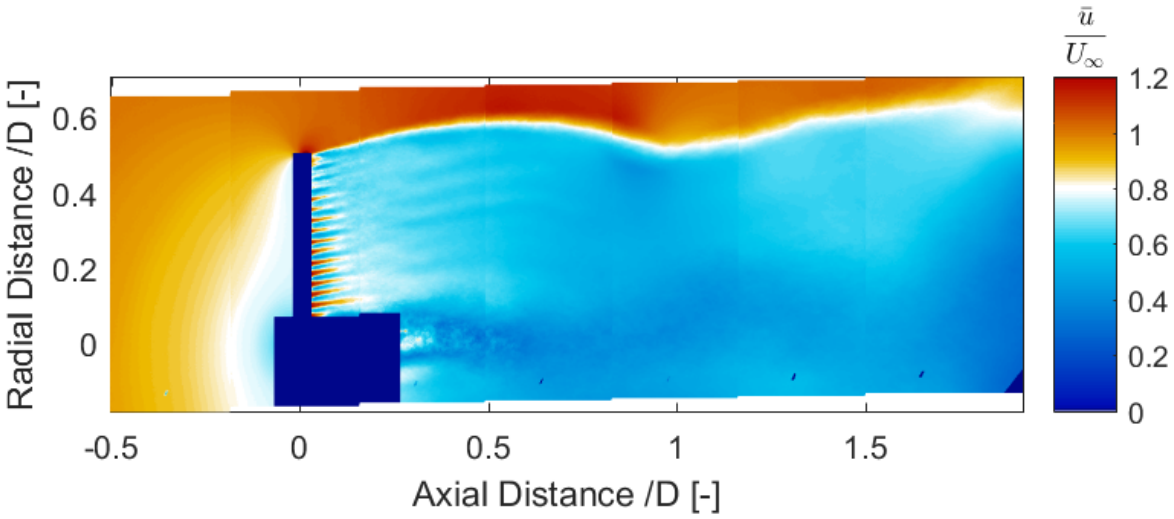

(c) Porosity = 19% (decreasing porosity) and C_T = 0.620

Figure E.2: Normalized Axial Velocity Field used for porosity changing with frequency = 5Hz and reduced frequency = 1.57 (Experiment)

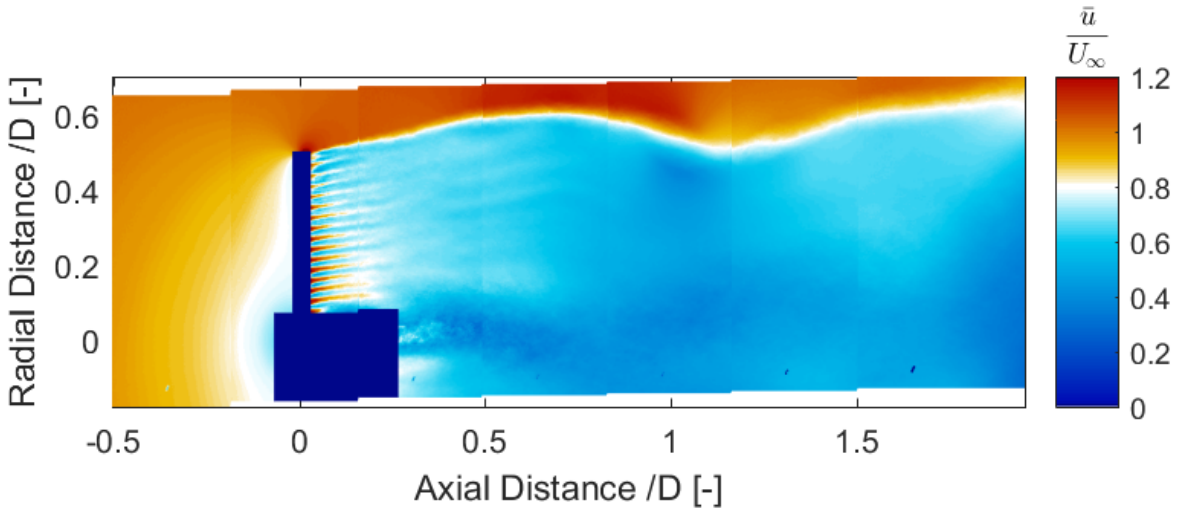

(a) Porosity = 14% (minimum porosity) and C_T = 0.705

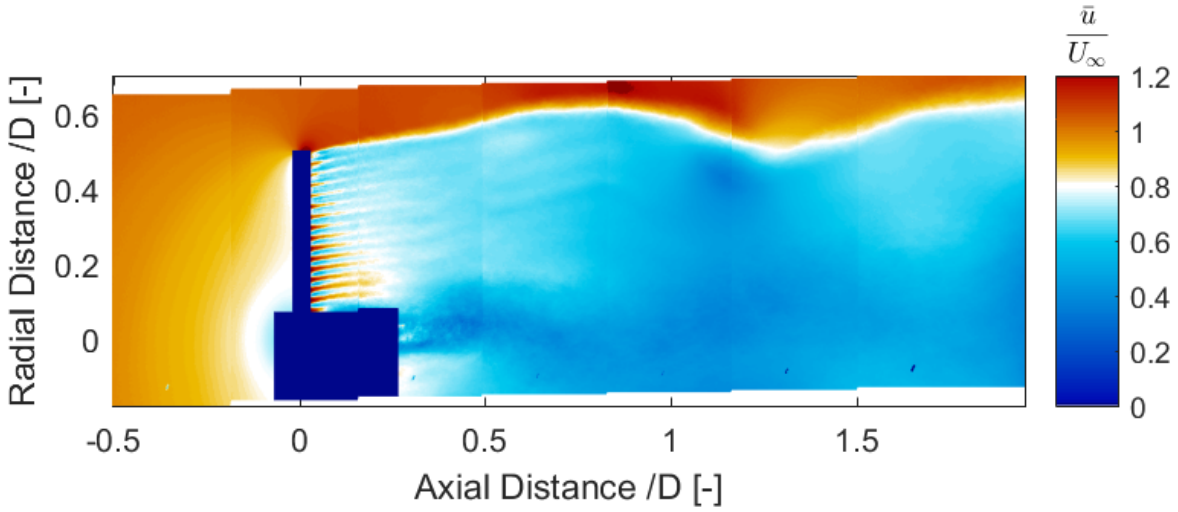

(b) Porosity = 19% (increasing porosity) and C_T = 0.697

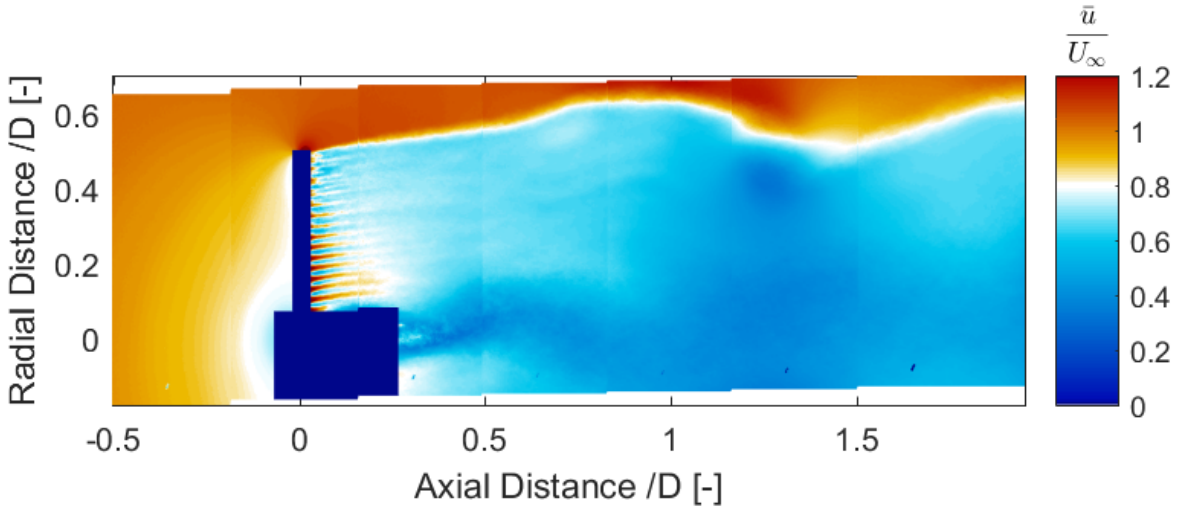

(c) Porosity = 31% (increasing porosity) C_T = 0.678

Figure E.3: Normalized Axial Velocity Field for porosity changing with frequency = 5Hz and reduced frequency = 1.57 (Experiment)

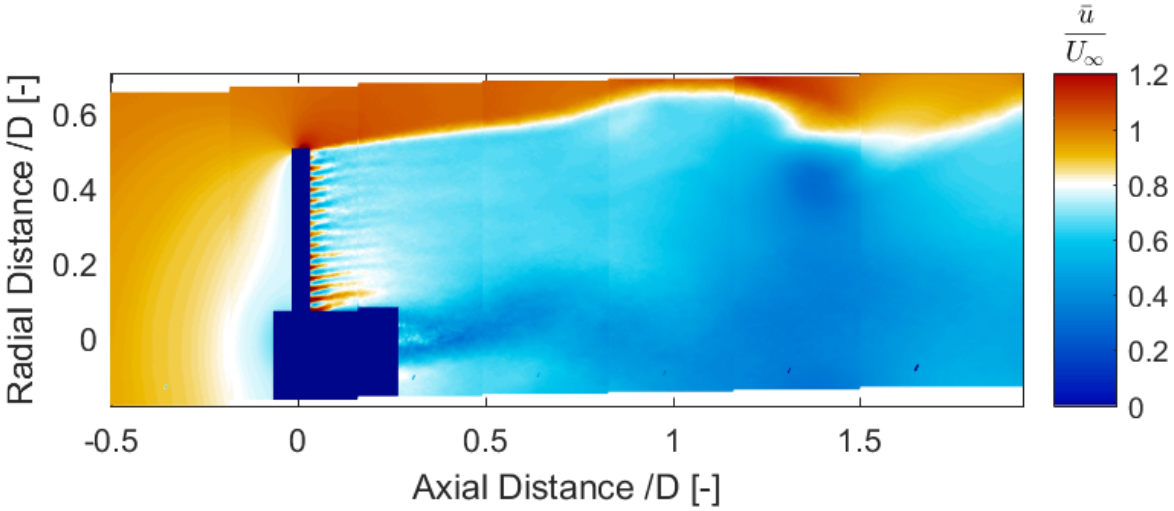

(a) Porosity = 47% (increasing porosity) and C_T = 0.657

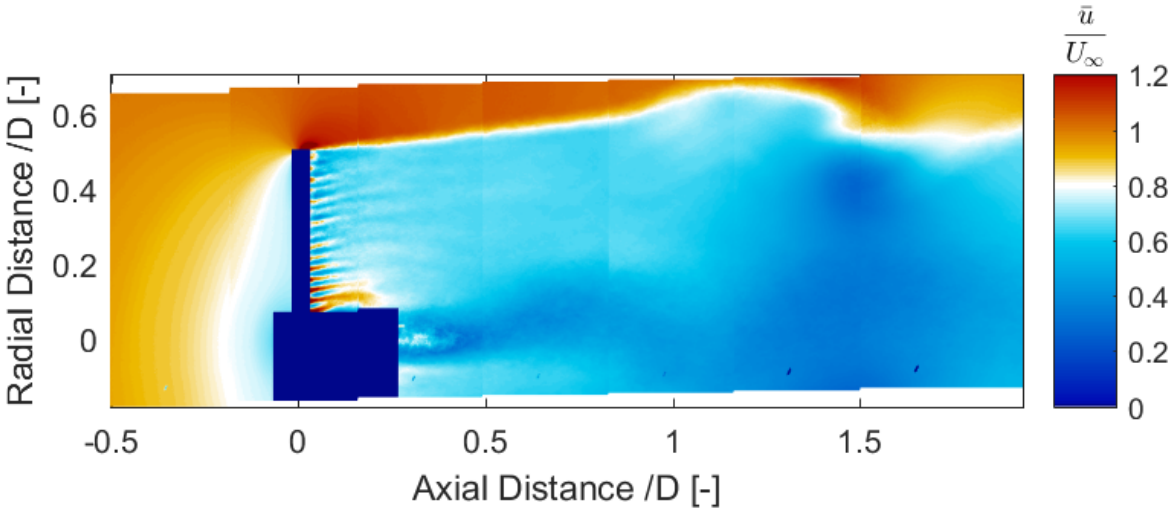

(b) Porosity = 59% (increasing porosity) and C_T = 0.596

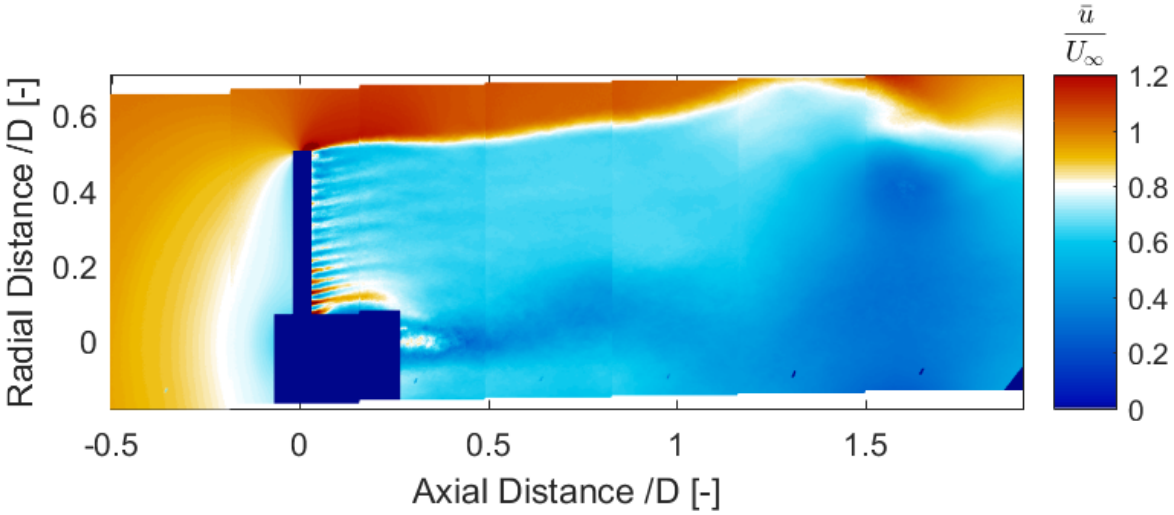

(c) Porosity = 64% (maximum porosity) and C_T = 0.550

Figure E.4: Normalized Axial Velocity Field for porosity changing with frequency = 5Hz and reduced frequency = 1.57 (Experiment)

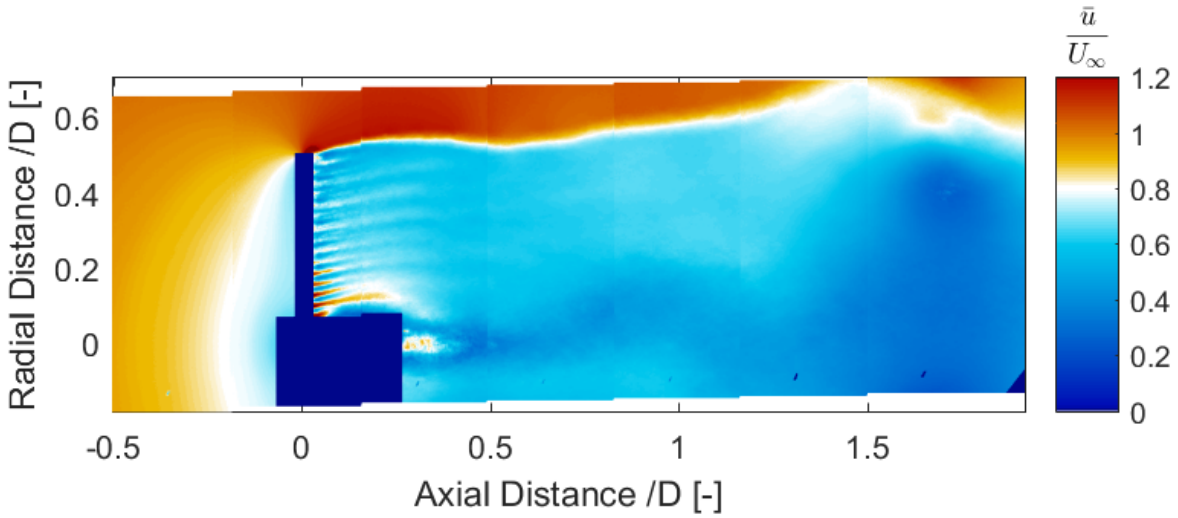

(a) Porosity = 59% (decreasing porosity) and C_T = 0.554

Figure E.5: Normalized Axial Velocity Field for porosity changing with frequency = 5Hz and reduced frequency = 1.57 (Experiment)

E.2. NORMALIZED AXIAL VELOCITY VS. POROSITY FOR SELECTED POINTS

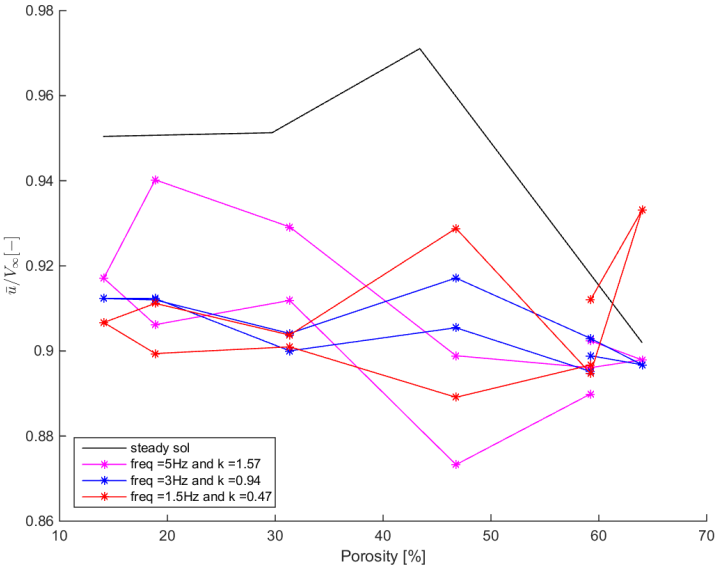

(a) x/D = -0.35, r/D = 0.25

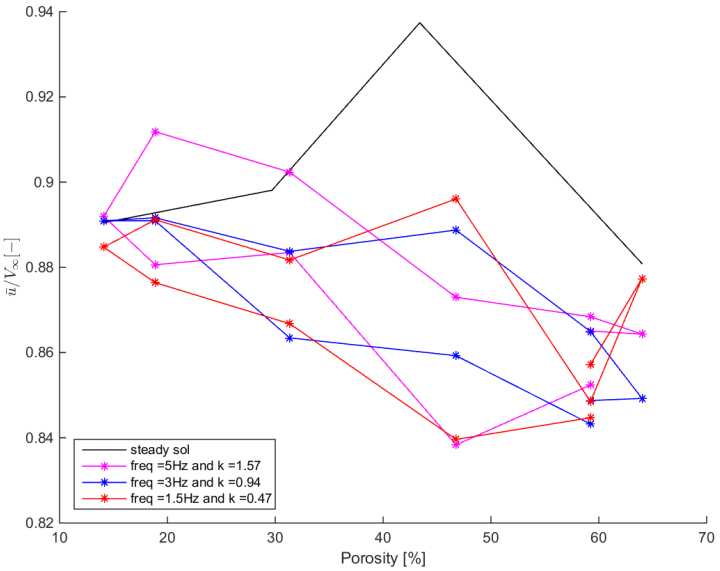

(b) x/D = -0.25, r/D = 0.25

Figure E.6: Normalized axial velocity Vs. C_T for two different points in wake for different unsteady load cases

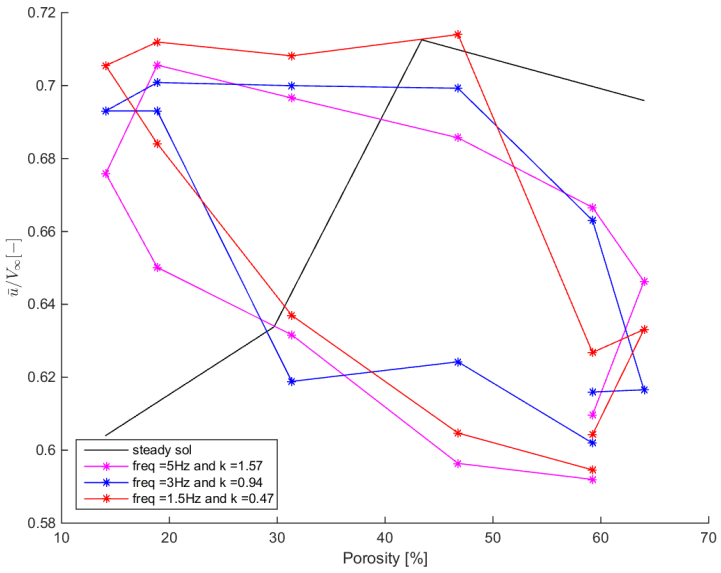

(a) x/D = 0.4, r/D = 0.25

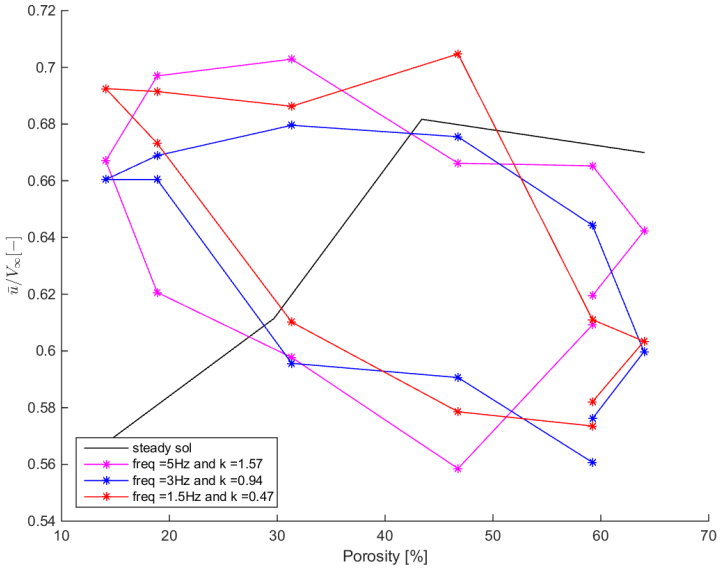

(b) x/D = 0.5, r/D = 0.25

Figure E.7: Normalized axial velocity Vs. C_T for two different points in wake for different unsteady load cases

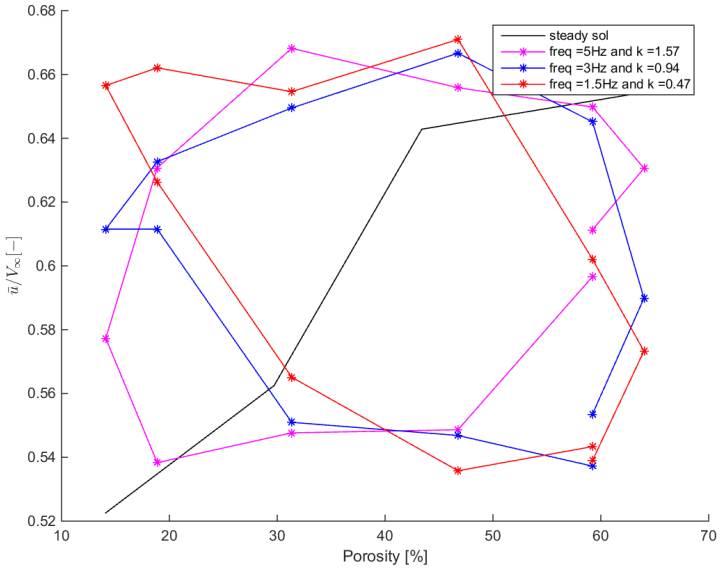

(a) x/D = 0.7, r/D = 0.25

Figure E.8: Normalized axial velocity Vs. porosity for different points in wake for different unsteady load cases

E.3. NORMALIZED RADIAL VELOCITY VS. POROSITY FOR SELECTED POINTS

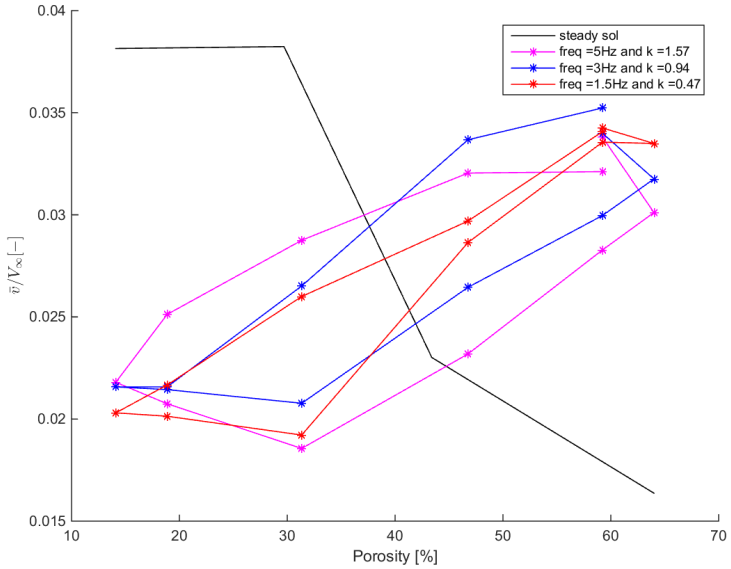

(a) x/D = -0.35, r/D = 0.25D

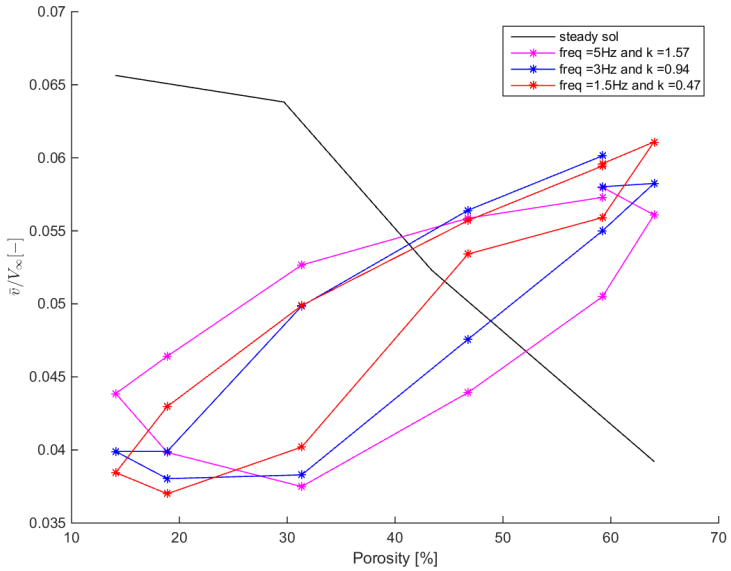

(b) x/D = -0.25, r/D = 0.25D

Figure E.9: Normalized radial velocity Vs. C_T for two different points in wake for different unsteady load cases

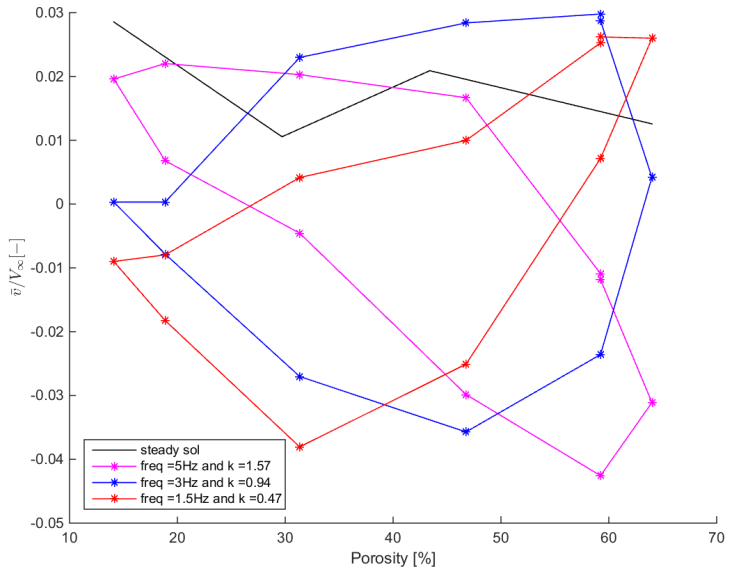

(a) x/D = 0.4, r/D = 0.25D

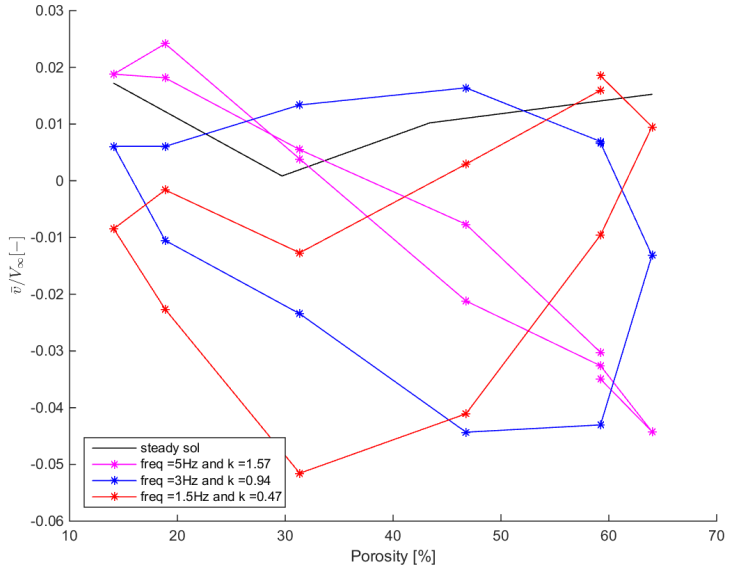

(b) x/D = 0.5, r/D = 0.25D

Figure E.10: Normalized radial velocity Vs. C_T for two different points in wake for different unsteady load cases

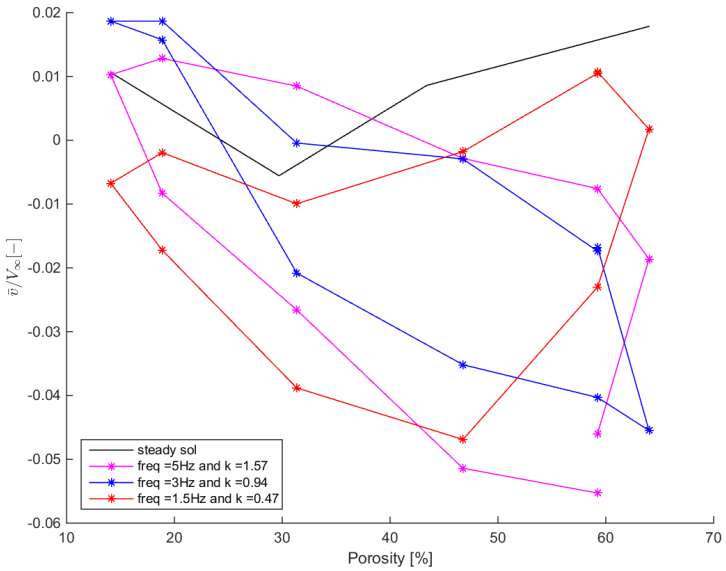

(a) x/D = 0.7, r/D = 0.25D

Figure E.11: Normalized radial velocity Vs. porosity for different points in wake for different unsteady load cases

E.4. VELOCITY AT ONE LOCATION IN THE FIELD USING VR METHOD

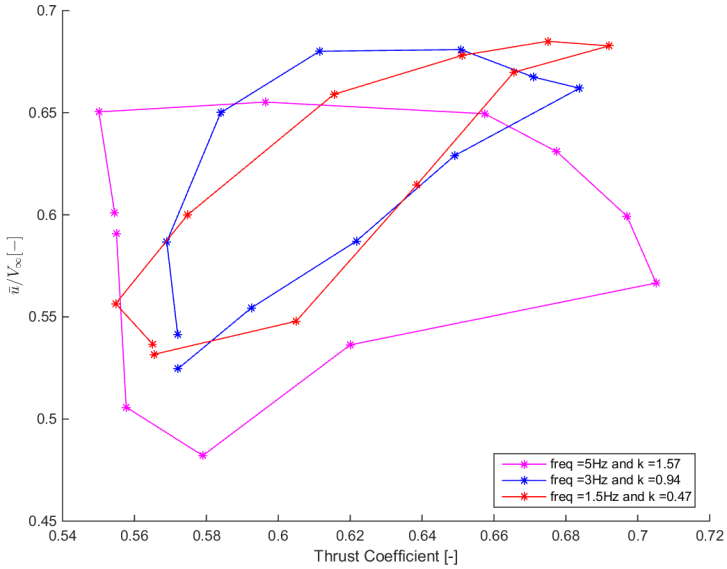

(a) Porosity = 59% (decreasing porosity) and C_T = 0.555

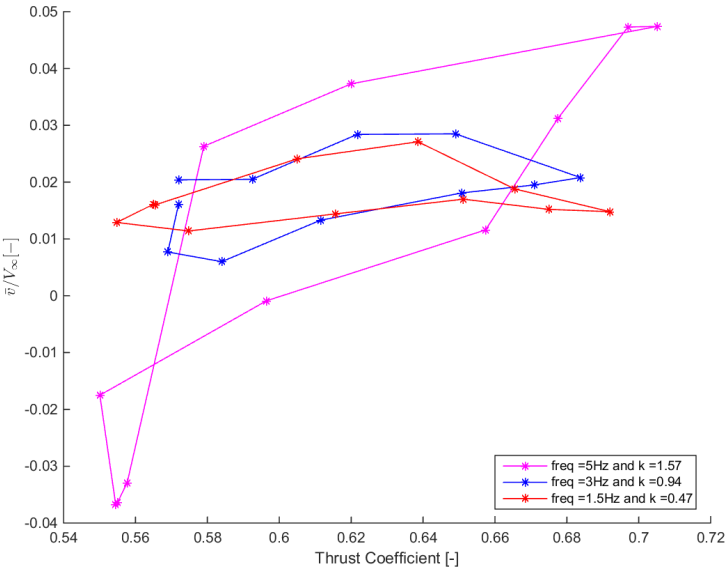

(b) Porosity = 47% (decreasing porosity) and C_T = 0.557

Figure E.12: Velocity calculations at x/D = 0.4 and r/D = 0.25 (Vortex Ring Method)

BIBLIOGRAPHY

[1] V. Hong, *Analysis of an actuator disc under unsteady loading,* M.Sc. Thesis report,TU Delft,The Netherlands (Sept 2015).

[2] D. Medici and P. H. Alfredsson, *Measurements on a wind turbine wake: 3d effects and bluff body vortex shedding,* Wind Energy **9**, 219 (2006).

[3] D. Medici and P. H. Alfredsson, *Wind turbine near wakes and comparisons to the wake behind a disc,* Proc. of the 43rd Aerospace Sciences Meeting and Exhibit, no. 595, pp. 1-12 (2005), 10.2514/6.2005-59.

[4] L. E. M. Lignarolo, D. Ragni, C. J. Ferreira, and G. J. W. van Bussel, *Experimental comparison of a wind-turbine and of an actuator-disc near wake,* Journal of renewable and sustainable energy **8** (2016).

[5] L. E. Lignarolo, D. Mehta, R. J. Stevens, A. E. Yilmaz, G. van Kuik, S. J. Andersen, C. Meneveau, C. J. Ferreira, D. Ragni, J. Meyers, G. J. van Bussel, and J. Holierhoek, *Validation of four {LES} and a vortex model against stereo-piv measurements in the near wake of an actuator disc and a wind turbine,* Renewable Energy **94**, 510 (2016).

[6] G. A. M. van Kuik and L. E. M. Lignarolo, *Potential flow solutions for energy extracting actuator disc flows,* Wind Energy **19**, 1391 (2016), we.1902.

[7] M. O. L. Hansen, *Aerodynamics of wind turbine,* (2008).

[8] M. Stock and A. Gharakhani, *Modeling rotor wakes with a hybrid overflow-vortex method on a gpu cluster,* `http://markjstock.org/research/AIAA_AA10_pres.pdf` (Aug 2016).

[9] B. Sanderse, *Aerodynamics of wind turbine wakes,* (January 2015).

[10] C. Krishnaswami, *Experimental analysis of near and transitional wind turbine wake using stereo particle image velocimetry,* M.Sc. Thesis, Technical University of Delft, The Netherlands (Sept 2013).

[11] M. Hand, D. Simms, L. Fingersh, D. Jager, J. Cotrell, S. Schreck, and S. Larwood, *Unsteady aerodynamics experiment phase vi: Wind tunnel test configurations and available data campaigns.* Technical report NREL/TP- 500-29955, NREL (2001).

[12] L. E. M. Lignarolo, D. Ragni, F. Scarano, C. J. Simão Ferreira, and G. J. W. van Bussel, *Tip-vortex instability and turbulent mixing in wind-turbine wakes,* Journal of Fluid Mechanics **781**, 467–493 (2015).

[13] R. Barthelmie, S. Frandsen, K. Hansen, J. Schepers, K. Rados, and SchlezW., *Modelling the impact of wakes on power output at nysted and horns rev,* European Wind Energy Conference (2009).

[14] J. Schepers (ECN), *Engineering models of wind energy aerodynamics,* P.hD thesis (Nov 2012).

[15] J. Schepers (ECN) and R. van Rooij (TU Delft), *Analysis of aerodynamic measurements on a model wind turbine placed in the nasa-ames tunnel,* ECN's and TUD's contribution to IEA Wind Task XX (June, 2015).

[16] H. Snel and J. Schepers, *Investigation and modelling of dynamic inflow effects,* https://www.ecn.nl/docs/library/report/1993/rx93029.pdf (March, 1993).

[17] J. W. van Heemst, *Improving the jensen and larsen wake deficit models,* M.Sc. thesis report, (June, 2015).

[18] M. Raffel, C. Willert, S. Wereley, and J. Kompenhans, *Particle image velocimetry, a practical guide,* 2nd Edition, Springer (2007).

[19] F. Scarano, *Ae4-180 flow measurement techniques lecture notes,* Available on Blacboard (2015-16).

[20] L. Souverein, *Piv based load determination in supersonic flows,* M.Sc. thesis, TU Delft, The Netherlands (Feb 2006).

[21] C. Ferreira, G. J. W. van Bussel, F. Scarano, and G. van Kuik, *Piv visualization of dynamic stall vawt and blade load determination,* 46th AIAA Aerospace Sciences Meeting and Exhibit (Jan 2008), 10.2514/6.2008-1317.

[22] D. Ragni, *Piv-based load determination in aircraft propellers.* PhD Thesis, Technical University of Delft, The Netherlands (Feb 2012).

[23] T. W. A. Council, *Wind energy: A vision for europe in 2030,* European Wind Energy Technology Platform (2015-16).

[24] J. D. Anderson, *Fundamentals of Aerodynamics*, 4th ed. (February 2006).

[25] R. Froude, *On the part played in propulsion by differences of fluid pressure,* Institute of Naval Architects , 390 (1989).

[26] H. Snel and J. Schepers, *Joint investigation of dynamic inflow effects and implementation of an engineering method,* Technical report,ECN (1995).

[27] W. Yu, C. Ferreira, G. van Kuik, and D. Baldacchino, *Vortex ring model analysis of an actuator disc with unsteady, non-uniform load,* Wind Energy (2014).

[28] D. M. Pitt and D. A. Peters, *Theoretical prediction of dynamic-in ow derivatives,* Vertica 5(1): 21–34. (Jan 1981).

[29] S. Øye, *Unsteady wake effects caused by pitch-angle changes,* Proceedings of the First IEA Symposium on the aerodynamic of wind turbines (London) pp 58-74 (1986).

[30] W. Yu, C. S. Ferreira, and G. van Kuik, *Analytical actuator disc solution for unsteady load,* 34th Wind Energy Symposium, AIAA SciTech Forum, (AIAA 2016-0751) http://dx.doi.org/10.2514/6.2016-0751.

[31] S. Andersen, L. Lignarolo, D. Ragni, C. Ferreira, J. Sørensen, R. Mikkelsen, and G. van Bussel, *Comparison between piv measurements and computations of the near-wake of an actuator disc,* Journal of Physics: Conference Series (Online) **524** (2014), 10.1088/1742-6596/524/1/012173.

[32] L. Lignarolo, D. Ragni, C. Ferreira, and G. van Bussel, *Kinetic energy entrainment in wind turbine and actuator disc wakes: an experimental analysis,* Journal of Physics: Conference Series **524**, 012163 (2014).

[33] N. Sørensen and H. Aagaard Madsen, *Modelling of transient wind turbine loads during pitch motion (paper and poster),* in *Proceedings (online)* (European Wind Energy Association (EWEA), 2006).

[34] P.-E. Réthoré, P. van der Laan, N. Troldborg, F. Zahle, and N. N. Sørensen, *Verification and validation of an actuator disc model,* Wind Energy **17**, 919 (2014).

[35] J. N. Sørensen and G. A. M. van Kuik, *General momentum theory for wind turbines at low tip speed ratios,* Wind Energy **14**, 821 (2011).

[36] G. van Kuik, *The edge singularity of an actuator disc with a constant normal load,* 22nd AIAA/ASME Wind Energy Symposium, Reno USA (2003), 10.1115/WIND2003-356.

[37] S. Aubrun, P. Devinant, G. Espana, L. Mécanique, and V. L.D, *Physical modelling of the far wake from wind turbines,* Application to wind turbine interactions. Ewec, 1-8. (2007).

[38] S. Aubrun, S. Loyer, P. Hancock, and P. Hayden, *Wind turbine wake properties: Comparison between a non-rotating simplified wind turbine model and a rotating model,* Journal of Wind Engineering and Industrial Aerodynamics 120 (2013).

[39] J. Ainslie, *Calculating the flowfield in the wake of wind turbines,* Journal of Wind Engineering and Industrial Aerodynamics **27**, 213 (1988).

[40] J. Schepers, *Endow: Validation and improvement of ecn's wake model,* Technical Report ECN-C-03-034, Energy research Centre of the Netherlands (2003).

[41] S. Lynum, *Wind turbine wake meandering,* M.Sc. thesis, Norwegian University of Science and Technology (June, 2013).

[42] L. Vermeer, *A review of wind turbine wake research at tu delft,* A Collection of the 2001 ASME Wind Energy Symposium Technical Papers. New York: ASME, pp 103–13. (2001).

[43] T. Lutz, K. Meister, and E. Krämer, *Near wake studies of the mexico rotor,* In In proceedings of the EWEC conference, pages 161-165 (March 2011).

[44] L. Vermeer, J. Briaire, and C. van Doorne, *How strong is a tip vortex?* British Wind Energy Association Annual Wind Energy Conference, Warwick, UK, page 5964 (1995).

[45] N. Vermeer, *How fast is a tip vortex?* Nineth IEA Symposium on the Aerodynamics of Wind Turbines,Stockholm, Sweden , 15 (1995).

[46] N. Vermeer, *How big is a tip vortex?* Tenth IEA Symposium on the Aerodynamics of Wind Turbines, Edinburgh, UK , 77 (1996).

[47] L. Vermeer and A. Sorensen, J.N.and Crespo, *Wind turbine wake aerodynamics,* Progress in Aerospace Sciences 39, pp 467–510 (2003).

[48] C. D. Winant and F. K. Browand, *Vortex pairing : the mechanism of turbulent mixing-layer growth at moderate reynolds number,* Journal of Fluid Mechanics **63**, 237–255 (1974).

[49] M.-K. Liu, M. Yocke, and T. Myers, *Mathematical model for the analysis of wind turbine wakes,* Journal of Energy **7**, 73 (1983).

[50] D. Medici, *Experimental studies of wind turbine wakes - power optimisation and meandering.* PhD thesis, KTH Mechanics, Royal Institute of Technology (2005).

[51] G. Larsen, H. Madsen, F. Bingöl, J. Mann, S. Ott, and et.al., *Dynamic wake meandering modeling,* Technical Report R-1607, Risø National Laboratory, Technical University of Denmark (2007).

[52] G. España, S. Aubrun, S. Loyer, and P. Devinant, *Wind tunnel study of the wake meandering downstream of a modelled wind turbine as an effect of large scale turbulent eddies,* Journal of Wind Engineering and Industrial Aerodynamics **101**, 24 (2012).

[53] M. Adaramola and P.-. Krogstad, *Experimental investigation of wake effects on wind turbine performance,* Renewable Energy **36**, 2078 (2011).

[54] P. B. S. Lissaman, ed., *AIAA, Aerospace Sciences Meeting* (1979).

[55] H. Aagaard Madsen, G. Larsen, and K. Thomsen, *Wake flow characteristics in low ambient turbulence conditions,* (2005).

[56] D. L. Elliott, *Status of wake and array loss research,* in *Presented at the 21st American Wind Energy Association Conference: Windpower 1991, Palm Springs, CA, 24-27 Sep. 1991* (1991).

[57] D. Milborrow and J. Ross, *The influence of turbulence and rotor thrust on wind turbine wake characteristics,* Memorandum TPRD/L/AP/0098/M83 (1983).

[58] S. McTavish, D. Feszty, and F. Nitzsche, *A study of the performance benefits of closely-spaced lateral wind farm configurations,* Renewable Energy **59**, 128 (2013).

[59] S. J.G. and S. H, *Joule2: Dynamic inflow: Yawed conditions and partial span pitch,* ECN-C-95-056, Energy Research Centre of the Netherlands, ECN (1995).

[60] M. Hansen, J. Sørensen, S. Voutsinas, N. Sørensen, and H. Madsen, *State of the art in wind turbine aerodynamics and aeroelasticity,* Progress in Aerospace Sciences **42**, 285 (2006).

[61] J. Chattot, *Actuator disk theory steady and unsteady models,* Journal of Solar Energy Engineering **136** (2014), 10.1115/1.4026947.

[62] S. Øye, *Simple vortex model for turbine,* TU Denmark (1990).

[63] M. Stock, *Summary of vortex methods literature,* (2007).

[64] S. S. Yoon and S. D. Heister, *Analytical formulas for the velocity field induced by an infinitely thin vortex ring,* International Journal for Numerical Methods in Fluids **44**, 665 (2004).

[65] S. S. Yoon and S. D. Heister, *Analytical formulas for the velocity field induced by an infinitely thin vortex ring,* International Journal for Numerical Methods in Fluids **44**, 665 (2004).

[66] B. van Oudheusden, F. Scarano, E. Roosenboom, E. W. Casimiri, and L. Souverein, *Evaluation of integral forces and pressure fields from planar velocimetry data for incompressible and compressible flows,* Experiments in Fluids,43(2-3):153–162 (2007), DOI: 10.1007/s00348-007-0261-y.

[67] E. Overmars, N. Warncke, C. Poelma, and J. Westerweel, *Bias errors in piv: the pixel locking effect revisited.* 15th Int Symp on Applications of Laser Techniques to Fluid Mechanics (2010).

[68] F. Schrijer, G. Mignoli, F. Scarano, and W. L.M.G.F.M., *Experimental capsule afterbody flow investigation,* G Saccoccia (Ed.), proceedings of the Sixth European Symposium on Aerothermodynamics for Space Vehicles (2008).

[69] F. NOCA, D. SHIELS, and D. JEON, *A comparison of methods for evaluating time-dependent fluid dynamic forces on bodies, using only velocity fields and their derivatives,* Journal of Fluids and Structures **13**, 551 (1999).

[70] F. Noca, D. Shiels, and D. Jeon, *Measuring instantaneous fluid dynamic forces on bodies, using only velocity fields and their derivatives,* Journal of Fluids and Structures **11**, 345 (1997).

[71] V. del Campo, D. Ragni, D. Micallef, B. Akay, F. J. Diez, and C. Simão Ferreira, *3d load estimation on a horizontal axis wind turbine using spiv,* Wind Energy **17**, 1645 (2014).